

Simulation and Optimisation of Hydraulic Fracturing and Flowback in Unconventional Reservoirs: A Case Study in the Cooper Basin, South Australia

Kunakorn Pokalai

The Australian School of Petroleum
The University of Adelaide

This thesis is submitted in fulfilment of the requirements for the degree of
Doctor of Philosophy in the Faculty of Engineering, Computer and
Mathematical Sciences, The University of Adelaide

June 2018



Table of Contents

Table of Contents	ii
List of Figures	iv
List of Tables	vi
Nomenclatures	vii
Abstract	x
Declaration.....	xii
Acknowledgement	xiii
List of Publications	xiv
Statement of Authorship	xv
Chapter 1 : Introduction	1
1.1 Background	1
1.2 Hydraulic Fracturing in Unconventional Reservoirs in Australia	3
1.3 Regional Geology	5
1.3.1 The Cowralli Field	10
1.4 Geomechanics	12
1.5 In-Situ Stress.....	14
1.6 Pressure Diagnostic Tests	18
1.6.1 Step Rate Tests.....	18
1.6.2 Diagnostic Fracture Injection Test (DFIT).....	18
1.6.2.1 Before Closure Analysis.....	19
1.6.2.2 After-Closure Analysis.....	25
1.6.3 Nolte-Smith Log-Log Plot.....	26
1.7 Flow Back Analysis	27
1.8 Research Objective	30
1.9 Methodology and Work Flow	31
1.10 Thesis Structure	33
Chapter 2 : Mathematical Modelling of Hydraulic Fracturing	35
2.1 Overview.....	35
2.2 History of Hydraulic Fracturing Models	35
2.3 Mathematical Formulation Based on Fracture Mechanic Concept	38
2.4 Mathematical for 3D Planar Fracture Propagation	42
2.4.1 Elasticity	42
2.4.2 Fluid Flow	47
2.4.3 Leak-Off.....	52
2.4.4 Coupling Schemes of Elasticity, Fluid Flow and Leak-Off.....	53

2.4.5	Comparison of Hydraulic Fracturing Models	54
2.5	Stress Shadowing and Fracture Interference	56
2.6	Non-Planar 3D Hydraulic Fracturing Model	56
2.7	Fracture Roughness.....	59
2.8	Summary.....	60
Chapter 3	: Data Review	62
3.1	Drilling and Completion History	62
3.2	Data Quality Control and Limitations	65
3.2.1.1	Sonic Log Data	65
3.2.1.2	Diagnostic Fracture Injection Test Data.....	68
Chapter 4	: Development of a New Approach for Hydraulic Fracturing in Tight Sand with Pre-Existing Natural Fractures.....	69
Chapter 5	: Investigation of the Effects of Near-Wellbore Pressure Loss and Pressure Dependent Leak-off on Flowback during Hydraulic Fracturing with Pre-Existing Natural Fractures	84
Chapter 6	: Integrated 3D Modelling of Hydraulic Fracturing in Tight Reservoirs with Pre- Existing Natural Fractures and Complex Stress Conditions: A Case Study from the Cooper Basin, Australia.....	107
Chapter 7	: Design and Optimization of Multi-Stage Hydraulic Fracturing in A Horizontal Well in A Shale Gas Reservoir in Cooper Basin, South Australia	135
Chapter 8	: Conclusions	150
References	152
Appendix A	: Petrophysics Properties	159
Appendix B	: Geomechanics Properties	167
Appendix C	: Diagnostics Fracture Injection Test Plots.....	171
Appendix D	: Step Down Test Plots.....	177
Appendix E	: Pre-Closure Analysis Plots	188
Appendix F	: After Closure Analysis Plots	199
Appendix G	: 3-D Hydraulic Fracturing Models.....	209
Appendix H	: A Comprehensive Review of the Intracratonic Cooper and Eromanga Basins, Australia	219
Appendix I	: Cooper Basin Simulation Study of Flow-back after Hydraulic Fracturing in Tight Gas Wells	292
Appendix J	: Alternative Fracturing Fluid Systems.....	317
J1	: Simulation of Hydraulic Fracturing with Propane-Based Fluid using a Fracture Propagation Model Coupled with Multiphase Flow Simulation in the Cooper Basin, South Australia	317

J2: 3D Simulation of Hydraulic Fracturing by Foam Based Fluids Using a Fracture Propagation Model Coupled with Geomechanics in an Unconventional Reservoir the Cooper Basin, South Australia.....	330
J3: Experimental and Simulation Study of Foam Stability and the Effects on Hydraulic Fracture Proppant Placement.....	341
J4: Experimental and Numerical Investigation into Nano-Stabilized Foams in Low Permeability Reservoir Hydraulic Fracturing Applications	353

List of Figures

Figure 1-1 : Fracture fluid and proppant stages in hydraulic fracturing (Bellarby, 2009)....	2
Figure 1-2 : Unconventional play in the Cooper Basin (Greenstreet, 2015)	4
Figure 1-3 : Map of the Cooper (blue) and Eromanga (green) basins (McGowen et al., 2007).	6
Figure 1-4 : Map of major structural highs and troughs in the Cooper Basin (Alexander et al., 1998).	8
Figure 1-5 : Stratigraphy of the Cooper Basin (Alexander et al., 1998).....	9
Figure 1-6 : Structural map and seismic cross-section in the Cowralli Field.	12
Figure 1-7 : The relationship of tectonic regimes (Zoback, 2007)	15
Figure 1-8 : Fracture propagation in a normal faulting stress regime.....	15
Figure 1-10 : Typical Diagnostic Fracture Injection Test (DFIT) pressure profile.	19
Figure 1-11 : Leak-off behaviour in G-function plots.	24
Figure 1-9 : Nolte-Smith net pressure log-log plot (Smith and Montgomery, 2015).....	26
Figure 1-12 : Workflow diagram for the integrated simulation study.	32
Figure 2-1 : The history of hydraulic fracturing models.....	38
Figure 2-2 : Strain energy from stress-strain plot	39
Figure 2-3 : The line crack of a pressurized plane (Sneddon, 1973).	41
Figure 2-4 : Force on boundary of a semi-infinite body (Timoshenko and Goodie, 1951).	42
Figure 2-5 : Load distribution over the semi-infinite body (Timoshenko and Goodie, 1951).	46
Figure 2-6 : Analytical fracture model solution for: (a) PKN; and (b) KGD models.....	46
Figure 2-7 : Poiseuille flow between parallel plates.....	48
Figure 2-8 : Mass Conservation in 1D of hydraulic fracturing.....	49
Figure 2-9 : Laminar fluid flow (Poiseuille) in the fracture.	50
Figure 2-10 : Non-Newtonian fracturing fluid rheology.	51
Figure 2-11 : Workflow diagram for coupling of elasticity, fluid flow and leak-off for 3D hydraulic fracturing model.....	54
Figure 2-12 : Hydraulic fracturing models.	55
Figure 2-13 : Hydraulic fracture propagation interaction with pre-existing natural fracture (Weng, 2015).	58
Figure 2-14 : Fluid injection pressure profile in the fracture distance between 10, 20 and 40 m respectively (Kresse et al., 2013).....	59
Figure 3-1 : Construction of conventional and unconventional wells in the Cooper Basin (Santos, 2015).	65

Figure 3-2 : Geomechanical properties derived based on compressional travel time (DTC).
 (a) Poisson’s Ratio estimation vs DTC; and (b) Young’s Modulus/Density ratio estimation
 vs DTC..... 67

Figure A- 1 : Petrophysics Summary of Cowralli 6 Stage1..... 159
Figure A- 2 : Petrophysics Summary of Cowralli 6 Stage2..... 160
Figure A- 3 : Petrophysics Summary of Cowralli 7 Stage1..... 161
Figure A- 4 : Petrophysics Summary of Cowralli 7 Stage2..... 162
Figure A- 5 : Petrophysics Summary of Cowralli 8 Stage1..... 163
Figure A- 6 : Petrophysics Summary of Cowralli 8 Stage 2..... 164
Figure A- 7 : Petrophysics Summary of Cowralli 8 Stage 3 and Stage 4..... 165
Figure A- 8 : Petrophysics Summary of Cowralli 8 Stage 5, 6 and Stage 7 166

Figure B- 1 : Geomechanics Properties of Cowralli 6 Stage 1 167
Figure B- 2 : Geomechanics Properties of Cowralli 6 Stage 2 167
Figure B- 3 : Geomechanics Properties of Cowralli 7 Stage 1 168
Figure B- 4 : Geomechanics Properties of Cowralli 7 Stage 2 168
Figure B- 5 : Geomechanics Properties of Cowralli 8 Stage 1 169
Figure B- 6 : Geomechanics Properties of Cowralli 8 Stage 2 169
Figure B- 7 : Geomechanics Properties of Cowralli 8 Stage 3 and Stage 4 170
Figure B- 8 : Geomechanics Properties of Cowralli 8 Stage 5 Stage 6 and Stage 7 170

Figure C- 1 : Diagnostic fracture injection test plots in well Cowralli 6 Stage 1 171
Figure C- 2 : Diagnostic fracture injection test plots in well Cowralli 6 Stage 2..... 171
Figure C- 3 : Diagnostic fracture injection test plots in well Cowralli 7 Stage 1 172
Figure C- 4 : Diagnostic fracture injection test plots in well Cowralli 7 Stage 2..... 172
Figure C- 5 : Diagnostic fracture injection test plots in well Cowralli 8 Stage 1 173
Figure C- 6 : Diagnostic fracture injection test plots in well Cowralli 8 Stage 2..... 173
Figure C- 7 : Diagnostic fracture injection test plots in well Cowralli 8 Stage 3..... 174
Figure C- 8 : Diagnostic fracture injection test plots in well Cowralli 8 Stage 4..... 174
Figure C- 9 : Diagnostic fracture injection test plots in well Cowralli 8 Stage 5..... 175
Figure C- 10 : Diagnostic fracture injection test plots in well Cowralli 8 Stage 6..... 175
Figure C- 11 : Diagnostic fracture injection test plots in well Cowralli 8 Stage 7..... 176

Figure D- 1 : Step Down Test Plot in well Cowralli 6 Stage 1..... 177
Figure D- 2: Step Down Test Plot in well Cowralli 6 Stage 2 178
Figure D- 3 : Step Down Test Plot in well Cowralli 7 Stage 1..... 179
Figure D- 4 : Step Down Test Plot in well Cowralli 7 Stage 2..... 180
Figure D- 5 : Step Down Test Plot in well Cowralli 8 Stage 1..... 181
Figure D- 6 : Step Down Test Plot in well Cowralli 8 Stage 2..... 182
Figure D- 7 : Step Down Test Plot in well Cowralli 8 Stage 3..... 183
Figure D- 8 : Step Down Test Plot in well Cowralli 8 Stage 4..... 184
Figure D- 9 : Step Down Test Plot in well Cowralli 8 Stage 5..... 185
Figure D- 10 : Step Down Test Plot in well Cowralli 8 Stage 6..... 186
Figure D- 11 : Step Down Test Plot in well Cowralli 8 Stage 7..... 187

Figure E- 1 : Pre-Closure analysis plots in Cowralli 6 Stage 1	188
Figure E- 2 : Pre-Closure analysis plots in Cowralli 6 Stage 2	189
Figure F- 3 : Pre-Closure analysis plots in Cowralli 7 Stage 1	190
Figure E- 4 : Pre-Closure analysis plots in Cowralli 7 Stage 2	191
Figure E- 5 : Pre-Closure analysis plots in Cowralli 8 Stage 1	192
Figure E- 6 : Pre-Closure analysis plots in Cowralli 8 Stage 2	193
Figure E- 7 : Pre-Closure analysis plots in Cowralli 8 Stage 3	194
Figure E- 8 : Pre-Closure analysis plots in Cowralli 8 Stage 4	195
Figure E- 9 : Pre-Closure analysis plots in Cowralli 8 Stage 5	196
Figure E- 10 : Pre-Closure analysis plots in Cowralli 8 Stage 6	197
Figure E- 11 : Pre-Closure analysis plots in Cowralli 8 Stage 7	198
Figure F - 1 : After-Closure analysis plots in Cowralli 6 Stage 1	199
Figure F - 2 : After-Closure analysis plots in Cowralli 6 Stage 2	200
Figure F - 3 : After-Closure analysis plots in Cowralli 7 Stage 1	201
Figure F - 4 : After-Closure analysis plots in Cowralli 7 Stage 2	202
Figure F - 5 : After-Closure analysis plots in Cowralli 8 Stage 1	203
Figure F - 6 : After-Closure analysis plots in Cowralli 8 Stage 2	204
Figure F - 7 : After-Closure analysis plots in Cowralli 8 Stage 3	205
Figure F - 8 : After-Closure analysis plots in Cowralli 8 Stage 5	206
Figure F - 9 : After-Closure analysis plots in Cowralli 8 Stage 6	207
Figure F - 10 : After-Closure analysis plots in Cowralli 8 Stage 7	208
Figure G- 1 : Hydraulic Fracturing Models in Cowralli 6 Stage 1	209
Figure G- 2 : Hydraulic Fracturing Models in Cowralli 6 Stage 2	210
Figure G- 3 : Hydraulic Fracturing Models in Cowralli 7 Stage 1	211
Figure G- 4 : Hydraulic Fracturing Models in Cowralli 7 Stage 2	212
Figure G- 5 : Hydraulic Fracturing Models in Cowralli 8 Stage 2	213
Figure G- 6 : Hydraulic Fracturing Models in Cowralli 8 Stage 3	214
Figure G- 7 : Hydraulic Fracturing Models in Cowralli 8 Stage 4	215
Figure G- 8 : Hydraulic Fracturing Models in Cowralli 8 Stage 5	216
Figure G- 9 : Hydraulic Fracturing Models in Cowralli 8 Stage 6	217
Figure G- 10 : Hydraulic Fracturing Models in Cowralli 8 Stage 7	218

List of Tables

Table 2-1 : Advantages and limitations of numerical models for hydraulic fracturing simulation (Mao, 2011).....	59
Table 3-1 : Data Set for Cowralli 6, Cowralli 7 and Cowralli 8.....	62

Nomenclatures

A_f = Fracture area

c = crack length, ft

C_L = Leak-off coefficient

D = Diameter of the proppant, m

E = Young's modulus, MMpsi

K_I = Stress intensity factor

K_{IC} = Critical fracture toughness

k' = Consistency index

n' = flow behaviour index

P_p = Initial pore pressure, psi

q_i = Injection rate

U_E = Potential energy

U_S = Surface energy

u_L = Leak-off velocity

W_L = external work

w = Fracture width, in

\bar{w} = Average fracture width, in

V_s = Settling velocity, m/s

ν = Poisson's ratio, dimensionless

σ_θ = Tangential stress, psi

σ_c = In-situ stress or Total horizontal stress, psi

σ_v = Vertical stress, psi

σ_{hmin} = Minimum horizontal stress, psi

σ_{Hmax} = Maximum horizontal stress, psi

α_h = Horizontal Poroelastic Constant, dimensionless

α_v = Vertical Poroelastic Constant, dimensionless

w_{bo} = Borehole breakout width, radians

P_0 = Far-field pore pressure, psi

P_{ob} = Overburden pressure, psi

P_w = Wellbore fluid pressure, psi

ΔP_{NWBPL} = Total pressure drop based on near-wellbore pressure loss, psi

k_{perf} = Perforation pressure loss coefficient, psi/(stb/d)²

k_{tort} = Tortuosity pressure loss coefficient, $\text{psi}/(\text{stb/d})^2$
 q_{in} = Fluid injection rate, bpm
 N = Number of perforation
 C_d = Coefficient of discharge
 $G(\Delta t_D)$ = G-function time
 $g(\Delta t_D)$ = Fluid loss at dimensionless time
 g_0 = Dimensionless loss-volume function at the shut-in
 Δt_D = Dimensionless pumping time
 k = Reservoir Permeability, md
 k_f = Fracture Permeability, md
 r = Distance from wellbore, in
 r_w = Wellbore radius, in
 σ_h = Minimum horizontal net stress, psi
 σ_H = Maximum horizontal net stress, psi
 σ_r = Radial net stress, psi
 σ_t = Tangential (Hoop) net stress, psi
 $\tau_{r\theta}$ = Shear stress in the plane of the borehole stress, psi
 θ = Angle from the direction of minimum horizontal stress, degrees
 α = Inclination from the vertical direction, degrees
 β = Azimuth relative to maximum horizontal stress, degrees
 ε_H = Tectonic strain in maximum horizontal direction, microstrains
 ε_h = Tectonic strain minimum horizontal direction, microstrains
 $[[u_l]]$ = Displacement discontinuity
 μ_{app} = Apparent viscosity, cp
 $\dot{\gamma}$ = shear rate, sec^{-1}
 ρ_p = Proppant Density, kg/m^3
 ρ_f = Fluid Density, kg/m^3
GR = Gamma Ray, API
RHOB = Bulk density, g/cc
CNC = Neutron Porosity, fraction
CCL = Casing Collar Locator
CBL = Cement Bond Log
DTC = Compressional Travel Time, microsec/ft
DTS = Shear Travel Time, microsec/ft

RD, RMILL, RS = Resistivity logs, ohm
CAL = Caliper, in
NWBPL = Near-wellbore pressure loss, psi
PDL= Pressure dependent leak-off
DFIT = Diagnostic fracture injection tests
SDT = Step down test
PCA = Pre-closure analysis
ACA = After-closure analysis
ISIP = Instantaneous shut-in pressure, psi

Abstract

This thesis presents and discusses the results of simulation and optimisation of hydraulic fracturing and flowback design in unconventional reservoirs using a case study from the Cooper Basin, South Australia. The Cooper Basin has a very large raw recoverable gas from unconventional gas resources estimated to be up to 187 trillion cubic feet. These resources are locked away in unconventional gas reservoirs such as tight sand, shale gas and deep coal seam gas. Hydraulic fracturing is a key technical approach to economical extraction of gas from these reservoirs.

Hydraulic Fracturing has been used throughout the Cooper Basin as a method of gas extraction for several decades. However, there are numerous problems which have not yet been fully addressed leading to a sub-optimal gas production and higher operational costs which, typically, represents nearly half of the total project cost. Also, the downturn in the pricing of oil and gas over the past few years requires production companies to optimise their production methods in order to increase the volume of production without significantly increasing costs so as to remain competitive in the market. Extraction of gas from the Cooper Basin therefore demands proper data analysis and selection of wells to be undertaken carefully to achieve the best results.

In this thesis, the following key issues are addressed for the optimization of hydraulic fracturing and flowback in the Cooper Basin:

1. The complexity of the stress regime is believed to be the main reason for the failure in some hydraulic fracturing operations in the Cooper Basin, as the stress can alternate between strike-slip, reverse and normal regimes along the wellbore. To better understand the complex stress, a validated Mechanical Earth Model (MEM) is developed using petrophysical log data. Then, the model was tuned by Diagnostic Fracturing Injection Test data to find a reliable in-situ stress and rock mechanical

validate the modelling of hydraulic fracturing and flowback using generalised reduced gradients or nonlinear solving method.

2. Using an integrated simulation method and using advances in data analysis, a 3D planar hydraulic fracturing model integrated with a reservoir flow simulation is constructed for a tight sands in the Cowralli Field in the Cooper Basin and flow-back was predicted.
3. Because of pre-existing natural fractures and the complex stress regime, there is usually high Near-Wellbore Pressure Loss (NWBPL) and pressure dependent leak-off during hydraulic fracturing. In this thesis, tortuosity around the wellbore was found as the main reason and linked to 3D hydraulic fracturing simulation.
4. Using Discrete Fracture Network (DFNs) model, the well trajectory was optimized such that the interaction with pre-existing natural fractures are maximized. This optimised well placement was found to generate up to six times greater stimulated reservoir volume compared to the base model (without considering pre-existing natural fractures)
5. Alternatives to water-based fracturing fluid, Liquefied Petroleum Gas (LPG) and foam have also been used in the fracture propagation model and coupled with multiphase flow simulation and the optimized scenario was investigated.

This thesis is presented in a “combination” form between conventional and publication formats. As such, it contains several peer reviewed publications, together with detailed chapters that describe the mathematical theory behind hydraulic fracturing and a comprehensive review of the Cooper Basin case study.

Declaration

I certify that this work contains no material which has been accepted for the award of any other degree or diploma in my name, in any university or other tertiary institution and, to the best of my knowledge and belief, contains no material previously published or written by another person, except where due reference has been made in the text. In addition, I certify that no part of this work will, in the future, be used in a submission in my name, for any other degree or diploma in any university or other tertiary institution without the prior approval of the University of Adelaide and where applicable, any partner institution responsible for the joint-award of this degree.

I give consent to this copy of my thesis when deposited in the University Library, being made available for loan and photocopying, subject to the provisions of the Copyright Act 1968. I acknowledge that copyright of published works contained within this thesis resides with the copyright holder(s) of those works.

I also give permission for the digital version of my thesis to be made available on the web, via the University's digital research repository, the Library Search and also through web search engines, unless permission has been granted by the University to restrict access for a period of time.

Kunakorn Pokalai

Acknowledgement

I would like to express my special thanks and gratitude to my principle supervisor, Manouchehr Haghghi, for his creative ideas, supervision, technical expertise and support during my PhD studies. Without his guidance and persistent help this thesis would not have been possible. I would like to thank my co-supervisor, Dennis Cooke, who initiated the flowback project and provided ongoing support with the principles of geomechanics. In Addition, a thank you to Ray Johnson, Jr. who improved my understanding of hydraulic fracturing and provided an overview of the key issues and methods relevant to the exploration, assessment and development of unconventional reservoirs.

I would also like to acknowledge the work of PhD students and my friends Yang Fei and David Kulikowski who I worked closely with while researching fracturing fluid, structural geology and pre-existing natural fractures in the Cooper Basin, Australia. My gratitude also extends to Santos for providing data, and all the staff at the Australian School of Petroleum for their kind help and co-operation. It is my privilege to thank you my mother Mrs. Threetip Wongsala, for her constant encouragement throughout my study period. Also, my friends Pavel Polach, Shane Clay and Stephanie Wikan Tyiasning for their support.

List of Publications

Paper 1: Pokalai, K., Kulikowski, D., Johnson, Jr., R.L., Haghghi, M., & Cooke, D. 2016. 'Development of a new approach for hydraulic fracturing in tight sand with pre-existing natural fractures', The APPEA Journal, 56, 225-238, doi:10.1071/AJ15017.

Paper 2: Pokalai, K., Fei, Y., Ahmad, M., Haghghi, M. & Gonzalez, M. 2015. 'Design and Optimisation of Multi-Stage Hydraulic Fracturing in a Horizontal Well in a Shale Gas Reservoir in the Cooper Basin, South Australia', The APPEA Journal, vol. 55.

Paper 3: Pokalai, K., Haghghi, M., Sarkar, S., Tyiasning, S. & Cooke, D. 2015. 'Investigation of the Effects of Near-Wellbore Pressure Loss and Pressure-Dependent Leak-off on Flowback during Hydraulic Fracturing With Pre-Existing Natural Fractures', paper presented at The SPE/IATMI Asia Pacific Oil & Gas Conference and Exhibition Nusa Dua, Bali, Indonesia, 20–22 October 2015, doi:10.2118/176440-MS.

Paper 4: Pokalai, K., Kulikowski, D., Amrouch, K., Haghghi, M., & Johnson, Jr., R.L. 2017. 'Integrated 3D modelling of hydraulic fracturing in tight reservoirs with pre-existing natural fractures and complex stress conditions: A case study from the Cooper Basin, Australia', Journal of Petroleum Science and Engineering, under review by Journal.

Paper 5: Sarkar, S, Haghghi, M, Sayyafzadeh, M, Cooke D, Pokalai, K. & Mohamed. F, 2016. 'A Cooper Basin Simulation Study of Flow-Back after Hydraulic Fracturing in Tight Gas Wells'.The APPEA Journal, vol. 56.

Paper 6: Kulikowski, D., Amrouch, K., Pokalai, K., & Gray, M.E. 2017. 'A Comprehensive Review of the Cooper and Eromanga Basins, Australia'. Earth-Science Reviews, Manuscript Submitted.

Paper 7: Fei, Y., Gonzalez, Nguyen, M, Lei, ZY, Pokalai, K., Sarkar, S & Haghghi, M. 2016. 'Simulation of Hydraulic Fracturing with Propane-Based Fluid using a Fracture Propagation Model Coupled with Multiphase Flow Simulation in the Cooper Basin, South Australia'. The APPEA Journal, vol. 56.

Paper 8: Fei, Y., Gonzalez, M., Pokalai, K., and Haghghi, M., 2016 'Simulation of Hydraulic Fracturing with CO2 Foam Using a Fracture Propagation Model Coupled with Geomechanics in a Shale Gas Reservoir from Cooper Basin, South Australia, paper presented at International Conference on Geo-mechanics, Geo-energy and Geo-resources, 28-29 September.

Paper 9: Fei, Y., Pokalai, K., Johnson, R., Gonzalez, M., & Haghghi, M. 2017. 'Experimental and simulation study of foam stability and the effects on hydraulic fracture proppant placement. Journal of Natural Gas Science and Engineering', Vol 46, Pages 544-554, doi:http://dx.doi.org/10.1016/j.jngse.2017.08.020

Paper 10: Fei, Y., Johnson, R., Gonzalez, M., Haghghi, M. & Pokalai, K. 2018. 'Experimental and numerical investigation into nano-stabilized foams in low permeability reservoir hydraulic fracturing applications', Fuel, 213. 123-140.

Statement of Authorship

Paper 1

Statement of Authorship

Title of Paper:	Development of a new approach for hydraulic fracturing in tight sand with pre-existing natural fractures
Publication Status:	Manuscript Published
Publication Details:	Pokalai, K., Kulikowski, D., Johnson, Jr., R.L., Haghghi, M., & Cooke, D. (2018). Development of a new approach for hydraulic fracturing in tight sand with pre-existing natural fractures. The APPEA Journal, 56, 225-238. doi:10.1071/AJ15017.

Principal Author

Principal Author (Candidate):	Kunakorn Pokalai		
Contribution to the Paper:	Data collection, interpretation, analysis, and writing.		
Overall percentage (%):	60%		
Certification:	This paper reports on original research I conducted during the period of my Higher Degree by Research candidature and is not subject to any obligations or contractual agreements with a third party that would constrain its inclusion in this thesis. I am the primary author of this paper.		
Signature:		Date:	08 March 2017

Co-Author Contribution

By signing the Statement of Authorship, each author certifies that:

- i. the candidate's stated contribution to the publication is accurate (as detailed above);
- ii. permission is granted for the candidate to include the publication in the thesis; and
- iii. the sum of all co-author contributions is equal to 100% less the candidate's stated contribution.

Name of Co-Author:	David Kulikowski (10%)		
Contribution to the Paper:	Interpreted the image log, wrote geology section, and review of paper.		
Signature:		Date:	08 March 2017

Name of Co-Author:	Raymond (Ray) L. Johnson, Jr		
Contribution to the Paper:	Interpreted D MEM and review the paper (10%)		
Signature:		Date:	4/6/2017

Name of Co-Author:	Manouchehr Haghghi (10%)		
Contribution to the Paper:	Supported with the structure, writing and review of paper.		
Signature:		Date:	09 March 2017

Name of Co-Author:	Dennis Cooke (10%)		
Contribution to the Paper:	Initiated the research and review of paper.		
Signature:		Date:	28 March 2017

Paper 2

Statement of Authorship

Title of Paper	Design and Optimisation of Multi-Stage Hydraulic Fracturing in a Horizontal Well in a Shale Gas Reservoir in the Cooper Basin
Publication Status	<input checked="" type="radio"/> Published <input type="radio"/> Accepted for publication <input type="radio"/> Submitted for publication <input type="radio"/> Unsubmitted but in manuscript form
Publication Details	Pokalai, K, Fei, Y, Ahmad, M, Haghghi, M & Gonzalez, M 2015, 'Design and Optimisation of Multi-Stage Hydraulic Fracturing in a Horizontal Well in a Shale Gas Reservoir in the Cooper Basin, South Australia', The APPEA Journal, vol. 55.

Principal Author

Name of Principal Author (Candidate)	Kunakorn Pokalai		
Contribution to the Paper	Data collection, interpretation, analysis, and writing.		
Overall percentage (%)	60%		
Certification:	This paper reports on original research I conducted during the period of my Higher Degree by Research candidature and is not subject to any obligations or contractual agreements with a third party that would constrain its inclusion in this thesis. I am the primary author of this paper.		
Signature		Date	08/03/17

Co-Author Contribution

By signing the Statement of Authorship, each author certifies that:

- i. the candidate's stated contribution to the publication is accurate (as detailed above);
- ii. permission is granted for the candidate to include the publication in the thesis; and
- iii. the sum of all co-author contributions is equal to 100% less the candidate's stated contribution.

Name of Co-Author	Yang Fei		
Contribution to the Paper	Production data analysis and review the paper (10 %)		
Signature		Date	8/3/17

Name of Co-Author	Maqsood Ahmad		
Contribution to the Paper	Interpreted 1 D MEM and review the paper (10 %)		
Signature		Date	8/3/17

Name of Co-Author	Manouchehr (Manny) Haghghi		
Contribution to the Paper	Supported with the structure, writing and review of paper. (10 %)		
Signature		Date	9-3-17

Name of Co-Author	Mary Gonzalez		
Contribution to the Paper	Review of paper. (10%)		
Signature		Date	01/08/2017

Statement of Authorship

Title of Paper	Investigation of the Effects of Near-Wellbore Pressure Loss and Pressure-Dependent Leakoff on Flowback during Hydraulic Fracturing With Pre-Existing Natural Fractures
Publication Status	<input checked="" type="radio"/> Published <input type="radio"/> Accepted for publication <input type="radio"/> Submitted for publication <input type="radio"/> Unsubmitted but in manuscript form
Publication Details	Pokalai, K, Haghghi, M, Sarkar, S, Tyiasning, S & Cooke, D 2015. 'Investigation of the Effects of Near-Wellbore Pressure Loss and Pressure-Dependent Leakoff on Flowback during Hydraulic Fracturing With Pre-Existing Natural Fractures', paper presented at The SPE/IATMI Asia Pacific Oil & Gas Conference and Exhibition Nusa Dua, Bali, Indonesia, 20-22 October 2015, SPE-176440-MS

Principal Author

Name of Principal Author (Candidate)	Kunakorn Pokalai		
Contribution to the Paper	Data collection, interpretation, analysis, and writing.		
Overall percentage (%)	60%		
Certification:	This paper reports on original research I conducted during the period of my Higher Degree by Research candidature and is not subject to any obligations or contractual agreements with a third party that would constrain its inclusion in this thesis. I am the primary author of this paper.		
Signature		Date	08/03/17

Co-Author Contribution

By signing the Statement of Authorship, each author certifies that:

- i. the candidate's stated contribution to the publication is accurate (as detailed above);
- ii. permission is granted for the candidate to include the publication in the thesis; and
- iii. the sum of all co-author contributions is equal to 100% less the candidate's stated contribution.

Name of Co-Author	Manouchehr (Manny) Haghghi		
Contribution to the Paper	Supported with the structure, writing and review of paper. (10 %)		
Signature		Date	9-7-2017

Name of Co-Author	Sume Sarkar		
Contribution to the Paper	Performed reservoir simulation (10 %)		
Signature		Date	08/03/07

Name of Co-Author	Stephanie Tyiasning		
Contribution to the Paper	Interpreted image log and fracture (10 %)		
Signature		Date	28/03/07

Name of Co-Author	Dennis Cooke		
Contribution to the Paper	Review of paper. (10%)		
Signature		Date	28 Mar 2017

Statement of Authorship

Title of Paper:	Integrated 3D modelling of hydraulic fracturing in tight reservoirs with pre-existing natural fractures and complex stress conditions: A case study from the Cooper Basin, Australia
Publication Status:	Manuscript Submitted
Publication Details:	Pokalai, K., Kulikowski, D., Amrouch, K., Haghghi, M., & Johnson, Jr., R.L. (2017). Integrated 3D modelling of hydraulic fracturing in tight reservoirs with pre-existing natural fractures and complex stress conditions: A case study from the Cooper Basin, Australia. <i>Journal of Petroleum Science and Engineering</i> , under review.

Principal Author

Principal Author (Candidate):	Kunakorn Pokalai
Contribution to the Paper:	Data collection, model building, interpretation, analysis, writing, and review of paper.
Overall percentage (%):	40%
Certification:	This paper reports on original research I conducted during the period of my Higher Degree by Research candidature and is not subject to any obligations or contractual agreements with a third party that would constrain its inclusion in this thesis. I am the primary author of this paper.
Signature:	<div style="border-bottom: 1px solid black; width: 100%;"></div>
Date:	11 July 2017

Co-Author Contribution

By signing the Statement of Authorship, each author certifies that:

- i. the candidate's stated contribution to the publication is accurate (as detailed above);
- ii. permission is granted for the candidate to include the publication in the thesis; and
- iii. the sum of all co-author contributions is equal to 100% less the candidate's stated contribution.

Name of Co-Author:	David Kulikowski (40%)
Contribution to the Paper:	Data collection, model building, interpretation, analysis, writing, and review of paper.
Signature:	<div style="border-bottom: 1px solid black; width: 100%;"></div>
Date:	11 July 2017

Name of Co-Author:	Khalid Amrouch (10%)
Contribution to the Paper:	Supported with the structure, writing and review of paper.
Signature:	<div style="border-bottom: 1px solid black; width: 100%;"></div>
Date:	11 July 2017

Name of Co-Author:	Manouchehr Haghghi (5%)
Contribution to the Paper:	Supported with the structure, writing and review of paper.
Signature:	<div style="border-bottom: 1px solid black; width: 100%;"></div>
Date:	21 September 2017

Name of Co-Author:	Raymond Johnson (5%)
Contribution to the Paper:	Supported with the structure, writing and review of paper.
Signature:	<div style="border-bottom: 1px solid black; width: 100%;"></div>
Date:	21 September 2017

Statement of Authorship

Title of Paper	A Cooper Basin Simulation Study of Flow-Back after Hydraulic Fracturing in Tight Gas Wells
Publication Status	<input checked="" type="radio"/> Published <input type="radio"/> Accepted for publication <input type="radio"/> Submitted for publication <input type="radio"/> Unsubmitted but in manuscript form
Publication Details	Sarkar, S, Haghghi, M, Sayyafzadeh, M, Cooke D, Pokalai, K & Mohamed. F, 2016 'A Cooper Basin Simulation Study of Flow-Back after Hydraulic Fracturing in Tight Gas Wells'. The APPEA Journal, vol. 56.

Principal Author

Name of Principal Author (Candidate)	Sume Sarkar		
Contribution to the Paper	Data collection & analysis, 3D Multiphase Flow Model Development, History Matching, Sensitivity analysis, Optimization and writing.		
Overall percentage (%)	65 %		
Certification:	This paper reports on original research I conducted during the period of my Higher Degree by Research candidature and is not subject to any obligations or contractual agreements with a third party that would constrain its inclusion in this thesis. I am the primary author of this paper.		
Signature		Date	14/03/17

Co-Author Contribution

- By signing the Statement of Authorship, each author certifies that:
- i. the candidate's stated contribution to the publication is accurate (as detailed above);
 - ii. permission is granted for the candidate to include the publication in the thesis; and
 - iii. the sum of all co-author contributions is equal to 100% less the candidate's stated contribution.

Name of Co-Author	Manouchehr Haghghi		
Contribution to the Paper	Supported with the structure, writing and review of paper. (10 %)		
Signature		Date	29-3-2017

Name of Co-Author	Mohammad Sayyafzadeh		
Contribution to the Paper	Supported with the structure, writing and review of paper. (5 %)		
Signature		Date	28/03/2017

Name of Co-Author	Dennis Cooke		
Contribution to the Paper	Supported with the structure, writing and review of paper. (5 %)		
Signature		Date	28 March 2017

Name of Co-Author	Kunakorn Pokalai		
Contribution to the Paper	Collected data, performed 3D planar hydraulic fracturing model, history matched of surface treating pressure and gas production (10 %)		
Signature		Date	28/03/17

Name of Co-Author	Fathima Mohamed		
Contribution to the Paper	Supported with the structure, writing and review of paper. (5 %)		
Signature		Date	28/03/17

Statement of Authorship

Title of Paper:	A Comprehensive Review of the Intracratonic Cooper and Eromanga Basins, Australia
Publication Status:	Manuscript Submitted
Publication Details:	Kulkowski, D., Amrouch, K., Pokalal, K., & Gray, M.E. (2017). A Comprehensive Review of the Intracratonic Cooper and Eromanga Basins, Australia. Earth-Science Reviews. Submitted.

Principal Author

Principal Author (Candidate):	David Kulkowski		
Contribution to the Paper:	Data collection, interpretation, analysis, and writing.		
Overall percentage (%):	75%		
Certification:	This paper reports on original research I conducted during the period of my Higher Degree by Research candidature and is not subject to any obligations or contractual agreements with a third party that would constrain its inclusion in this thesis. I am the primary author of this paper.		
Signature:		Date:	29 March 2017

Co-Author Contribution

By signing the Statement of Authorship, each author certifies that:

- i. the candidate's stated contribution to the publication is accurate (as detailed above);
- ii. permission is granted for the candidate to include the publication in the thesis; and
- iii. the sum of all co-author contributions is equal to 100% less the candidate's stated contribution.

Name of Co-Author:	Khalid Amrouch (10%)		
Contribution to the Paper:	Supported with the structure, writing and review of paper.		
Signature:		Date:	29 March 2017

Name of Co-Author:	Kunakorn Pokalal (10%)		
Contribution to the Paper:	Writing hydraulic fracture stimulation chapter and support with the writing and review of paper.		
Signature:		Date:	28 March 2017

Name of Co-Author:	Michael E. Gray (5%)		
Contribution to the Paper:	Supported with the structure, writing and review of paper.		
Signature:		Date:	29 March 2017

Statement of Authorship

Title of Paper	Simulation of Hydraulic Fracturing with Propane-Based Fluid using a Fracture Propagation Model Coupled with Multiphase Flow Simulation in the Cooper Basin, South Australia.
Publication Status	<input checked="" type="radio"/> Published <input type="radio"/> Accepted for publication <input type="radio"/> Submitted for publication <input type="radio"/> Unsubmitted but in manuscript form
Publication Details	Fel, Y., Gonzalez, Nguyen, V, Lei, ZY, Pokalai, K., Sarkar, S & Haghghi, M 2016 Simulation of Hydraulic Fracturing with Propane-Based Fluid using a Fracture Propagation Model Coupled with Multiphase Flow Simulation in the Cooper Basin, South Australia. The APPEA Journal, vol. 56.

Principal Author

Name of Principal Author (Candidate)	Yang Fei		
Contribution to the Paper	Data collection, interpretation, analysis, and writing.		
Overall percentage (%)	60%		
Certification:	This paper reports on original research I conducted during the period of my Higher Degree by Research candidature and is not subject to any obligations or contractual agreements with a third party that would constrain its inclusion in this thesis. I am the primary author of this paper.		
Signature		Date	28/03/17

Co-Author Contribution

By signing the Statement of Authorship, each author certifies that:

- i. the candidate's stated contribution to the publication is accurate (as detailed above);
- ii. permission is granted for the candidate to include the publication in the thesis; and
- iii. the sum of all co-author contributions is equal to 100% less the candidate's stated contribution.

Name of Co-Author	Mary Gonzalez Perdomo		
Contribution to the Paper	Supported with the structure, writing and review of paper. (10 %)		
Signature		Date	01/08/2017

Name of Co-Author	Viet Quoc Nguyen		
Contribution to the Paper	Supported with the structure, writing and review (5 %)		
Signature		Date	14/08/2017

Name of Co-Author	Zhongyu Lei		
Contribution to the Paper	Interpreted Image log and fracture (5 %)		
Signature		Date	16/08/2017

Name of Co-Author	Kunakorn Pokalai		
Contribution to the Paper	Supported with the structure and review of paper (5 %)		
Signature		Date	29/03/17

Name of Co-Author	Sume Sarkar		
Contribution to the Paper	Review of paper. (5 %)		
Signature		Date	07/08/2017

Name of Co-Author	Manouchehr (Manny) Haghghi		
Contribution to the Paper	Review of paper. (10 %)		
Signature		Date	27/3/2017

Statement of Authorship

Title of Paper	Simulation of Hydraulic Fracturing with CO ₂ Foam Using a Fracture Propagation Model Coupled with Geomechanics in a Shale Gas Reservoir from Cooper Basin, South Australia
Publication Status	<input checked="" type="radio"/> Published <input type="radio"/> Accepted for publication <input type="radio"/> Submitted for publication <input type="radio"/> Unsubmitted but in manuscript form
Publication Details	Fei, Y., Gonzalez, M., Pokalaf, K., and Haghghi, M., 2016 'Simulation of Hydraulic Fracturing with CO ₂ Foam Using a Fracture Propagation Model Coupled with Geomechanics in a Shale Gas Reservoir from Cooper Basin, South Australia, paper presented at International Conference on Geo-mechanics, Geo-energy and Geo-resources, 28-29 September.

Principal Author

Name of Principal Author (Candidate)	Yang Fei		
Contribution to the Paper	Data collection, interpretation, analysis, and writing.		
Overall percentage (%)	60 %		
Certification:	This paper reports on original research I conducted during the period of my Higher Degree by Research candidature and is not subject to any obligations or contractual agreements with a third party that would constrain its inclusion in this thesis. I am the primary author of this paper.		
Signature		Date	28/03/17

Co-Author Contribution

By signing the Statement of Authorship, each author certifies that:

- i. the candidate's stated contribution to the publication is accurate (as detailed above);
- ii. permission is granted for the candidate to include the publication in the thesis; and
- iii. the sum of all co-author contributions is equal to 100% less the candidate's stated contribution.

Name of Co-Author	Mary Gonzalez Perdomo		
Contribution to the Paper	Supported with the structure, writing and review of paper. (10 %)		
Signature		Date	01/08/2017

Name of Co-Author	Kunakorn Pokalaf		
Contribution to the Paper	Supported with the structure and review of paper (20 %)		
Signature		Date	29/03/17

Name of Co-Author	Manouchehr Haghghi		
Contribution to the Paper	Supported with the structure, writing and review of paper. (10 %)		
Signature		Date	29/3/2017

Statement of Authorship

Title of Paper	Experimental and simulation study of foam stability and the effects on hydraulic fracture proppant placement
Publication Status	<input checked="" type="radio"/> Published <input type="radio"/> Accepted for publication <input type="radio"/> Submitted for publication <input type="radio"/> Unsubmitted but in manuscript form
Publication Details	Fei, Y., Pokalai, K., Johnson, R., Gonzalez, M., & Haghghi, M. 2017. 'Experimental and simulation study of foam stability and the effects on hydraulic fracture proppant placement. <i>Journal of Natural Gas Science and Engineering</i> , Vol 46, Pages 544-554, doi:http://dx.doi.org/10.1016/j.jngse.2017.05.020

Principal Author

Name of Principal Author (Candidate)	Yang Fei		
Contribution to the Paper	Data collection, interpretation, analysis, and writing.		
Overall percentage (%)	60%		
Certification:	This paper reports on original research I conducted during the period of my Higher Degree by Research candidature and is not subject to any obligations or contractual agreements with a third party that would constrain its inclusion in this thesis. I am the primary author of this paper.		
Signature		Date	1/8/2017

Co-Author Contribution

- By signing the Statement of Authorship, each author certifies that:
- i. the candidate's stated contribution to the publication is accurate (as detailed above);
 - ii. permission is granted for the candidate to include the publication in the thesis; and
 - iii. the sum of all co-author contributions is equal to 100% less the candidate's stated contribution.

Name of Co-Author	Kunakorn Pokalai		
Contribution to the Paper	Supported with the structure and review of paper (10 %)		
Signature		Date	16/08/17

Name of Co-Author	Raymond (Ray) L. Johnson, Jr		
Contribution to the Paper	Supported with the structure, writing and review of paper. (10 %)		
Signature		Date	16/8/2017

Name of Co-Author	Mary Gonzalez Perdomo		
Contribution to the Paper	Supported with the structure, writing and review of paper. (10 %)		
Signature		Date	01/08/2017

Name of Co-Author	Manouchehr Haghghi		
Contribution to the Paper	Supported with the structure, writing and review of paper. (10 %)		
Signature		Date	4-8-2017

Statement of Authorship

Title of Paper	Experimental and Numerical Investigation into Nano-Stabilized Foams in Low Permeability Reservoir Hydraulic Fracturing Applications
Publication Status	<input checked="" type="checkbox"/> Published <input type="checkbox"/> Accepted for publication <input type="checkbox"/> Submitted for publication <input type="checkbox"/> Unsubmitted but in manuscript form
Publication Details	Fei, Y., Johnson, R., Gonzalez, M., Haghghi, M., & Pokalai, K. (2017). Experimental and Numerical Investigation into Nano-Stabilized Foams in Low Permeability Reservoir Hydraulic Fracturing Applications, Fuel, 213, 123-140.

Principal Author

Name of Principal Author (Candidate)	Yang Fei		
Contribution to the Paper	Data collection, interpretation, analysis, and writing.		
Overall percentage (%)	65%		
Certification:	This paper reports on original research I conducted during the period of my Higher Degree by Research candidature and is not subject to any obligations or contractual agreements with a third party that would constrain its inclusion in this thesis. I am the primary author of this paper.		
Signature		Date	1/8/2017

Co-Author Contribution

By signing the Statement of Authorship, each author certifies that:

- i. the candidate's stated contribution to the publication is accurate (as detailed above);
- ii. permission is granted for the candidate to include the publication in the thesis; and
- iii. the sum of all co-author contributions is equal to 100% less the candidate's stated contribution.

Name of Co-Author	Raymond (Ray) L. Johnson, Jr		
Contribution to the Paper	Supported with the structure, writing and review of paper. (20%)		
Signature		Date	1/4/8/2017
Name of Co-Author	Mary Gonzalez Perdomo		
Contribution to the Paper	Supported with the review of paper. (5%)		
Signature		Date	01/08/2017
Name of Co-Author	Manouchehr Haghghi		
Contribution to the Paper	Supported with the review of paper. (5%)		
Signature		Date	4-8-2017
Name of Co-Author	Kunakorn Pokalai		
Contribution to the Paper	Supported with the mathematical formulas (5%)		
Signature		Date	16/08/2017

Chapter 1 : Introduction

1.1 Background

Hydraulic fracturing is a common method for producing gas from unconventional reservoirs which provides highly conductive channel flow in low-permeability rocks. Hydraulic fracturing was first introduced in the Hugoton gas field in Western Kansas in 1947 with low gas well deliverability because of low fracture conductivity (Clark, 1949). In the 1960s, the propped fluid (slurry of fracturing fluid with sand) was used in the same field. This improved the gas productivity; however, with a large amount of fluid usage, the cost of running such stimulation process was still too high (Economides and Martin, 2007). To lower the cost, different materials and energy consumption have been used and developed.

Different steps in hydraulic fracturing procedure can be seen in Figure 1-1. The first step is pumping a fracturing fluid (pad) at high rates to reach the breakdown pressure and initiate the fracture in the formation. Then, different stages of proppant slurry will be injected to displace the pad. In the first stage, the slurry concentration is increased and the pad is nearly consumed by the fracturing fluid leak-off to the surrounding formations. In the final stage, the leak-off decreases and the slurry concentration will be close to the original concentration. Once the propagating process stops, the proppant remains in the fracture against the fracture closure to create the flow path for hydrocarbon production. Hydraulic fracturing models can predict the fracture geometry and design the operation requirements.

For modelling, reliable in-situ stresses, mechanical and petrophysical rock properties near the wellbore must be determined to predict how the fracture propagates, activates the pre-existing natural fractures, and how the fracturing fluid flows back from

the subsurface.(Nelson et al., 2007). Obviously, any uncertainty in input data results in uncertainty in the hydraulic fracturing models. This problem can be addressed by data calibration using pressure diagnostics tests and using petrophysical log data to estimate the in-situ stress and the mechanical rock properties.

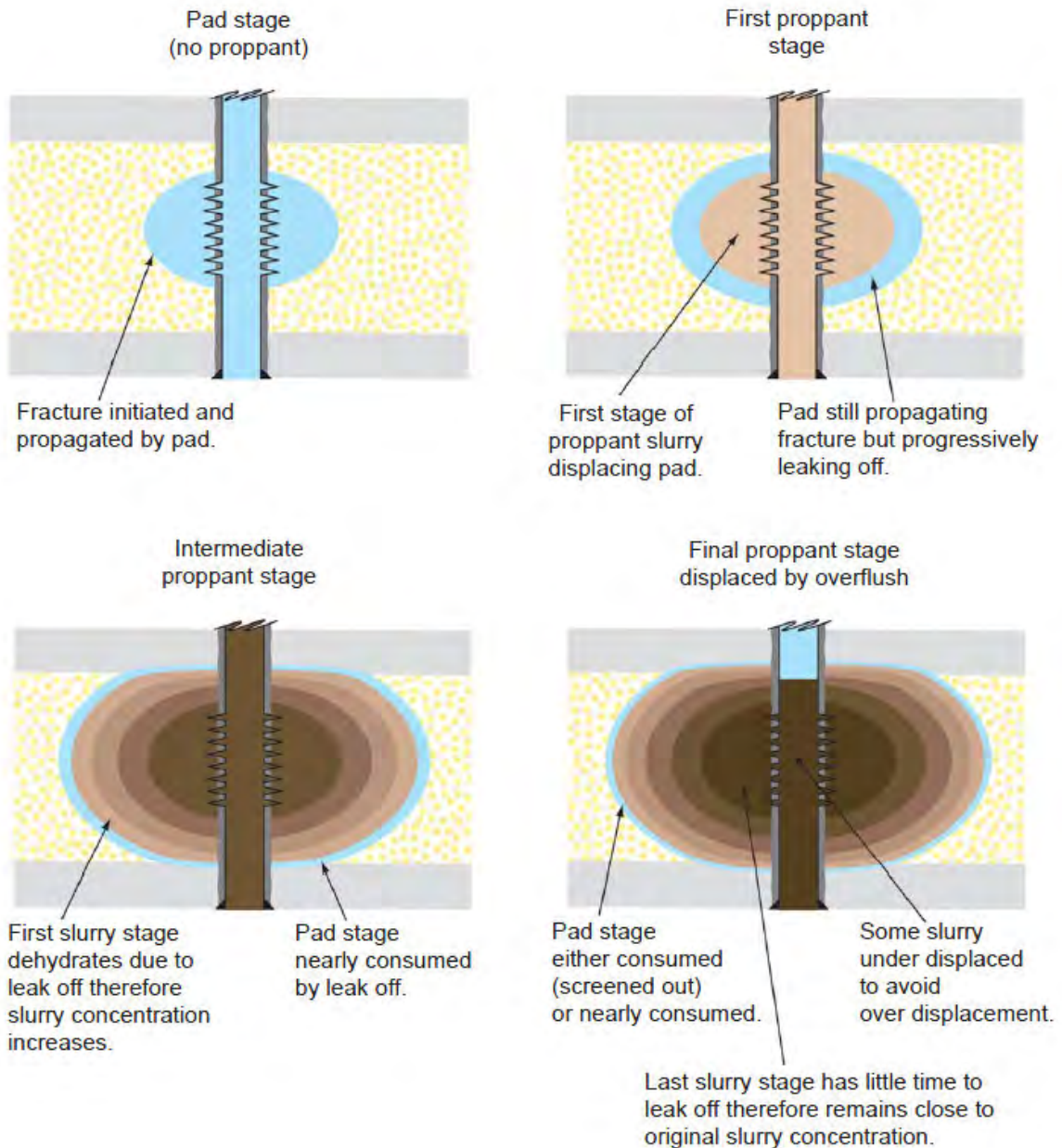


Figure 1-1 : Fracture fluid and proppant stages in hydraulic fracturing (Bellarby, 2009).

After hydraulic fracturing, the hydrocarbon production will not commence immediately due to production constraints. Thus, the fracturing fluid will remain in the reservoir for some time (soaking time). During hydrocarbon production, the remaining

fracturing fluid needs to be brought to the surface (flowback). The incomplete return of fracturing fluids from induced fracture to the surface can be a reason for the failure of hydraulic fracturing, as it can decrease the relative permeability to hydrocarbons. There has been a significant amount of research conducted in the past aimed at studying fluid entrapment in the fracture. Sharma (2005) simulated hydraulic fracturing design in the laboratory and led to more realistic design models and production strategies from tight gas reservoirs. Further research by Gdanski et al. (2005) attempted to understand the flowback behaviour. Wang et al. (2009) conducted parametric studies to better understand the proppant embedment, reservoir pressure, gel residue, and flowback on the performance of fracture treatment.

1.2 Hydraulic Fracturing in Unconventional Reservoirs in Australia

Hydraulic fracturing in Australia was firstly conducted in the Cooper Basin in 1968 (McGowen et al., 2007). Most hydraulic fracturing treatments in Australia are focused on the predominately Permian sandstone reservoirs, especially in the tight sand Patchawarra Formation. There is a significant gas potential to explore and develop in this area; however, the stress complexity and high pressure and temperature conditions are challenging to effectively execute hydraulic fracturing. The Cooper Basin has a very large raw recoverable gas for unconventional gas resources estimated to be up to 187 trillion cubic feet. (Menpes et al., 2013).

Hillis et al. (2001) described the gas accumulation as abasin-centred gas (BCG) in the Nappamerri Trough. Based on that study and making comparisons between the Cooper Basin and the North American deep basin, a new play for developing future unconventional gas reservoirs was indicated. Unconventional reservoir exploration have increased since 2009, with most plays being discovered in the tight BCG, deep dry coal seam gas in Patchawarra and Toolachee formations, and shale plays in the Roseneath,

Epsilon and Murteree (REM) sections (Hall et al., 2016). Greenstreet (2015) also classified the unconventional resources based on the lithotypes in Permian age (Figure 1-2).

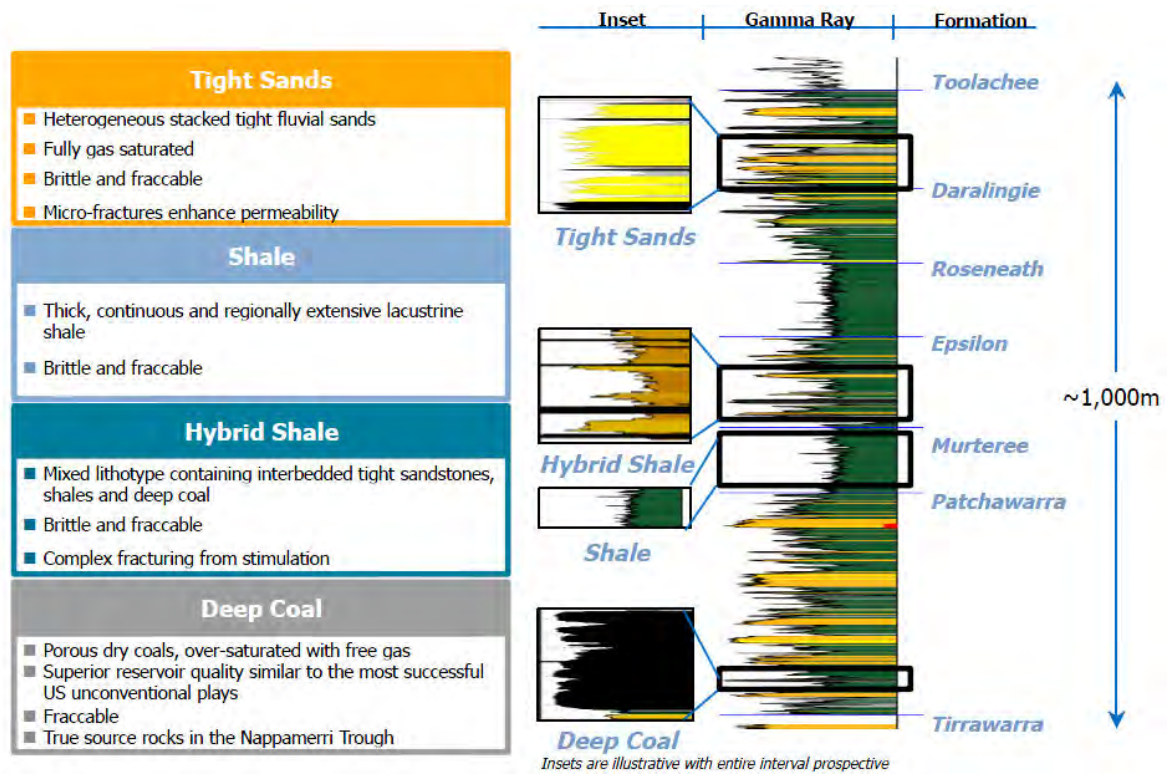


Figure 1-2 : Unconventional play in the Cooper Basin (Greenstreet, 2015)

BCG plays have been explored since 1971, mainly focused on the significantly low permeability and overpressured Patchawarra Formation. Shale gas pilot wells have been drilled by Beach Energy in 2011 (Pitkin et al., 2012). Holdfast-1 and Encounter-1 have provided gas production of more than 2 MMscf/D in the REM. The discovery and potential of unconventional reservoirs has given rise to a need to understand the drilling technologies available, infrastructure required and the market (Goldstein et al., 2012).

During hydraulic fracturing in some cases, a considerable pressure loss is observed near the wellbore. NWBPL was first discussed by Chipperfield et al. (2000) and Roberts et al. (2000). They stated that the causes of NWBPL are pressure loss within the perforations, and tortuosity within the induced fracture path near the wellbore. Johnson et al. (2002) and Johnson and Greenstreet (2003) discussed pressure dependent leak-off (PDL) and NWBPL

in the Cooper Basin and showed their significant impacts on production performance. High NWBPL can result in a lower percentage of proppant placed within the target reservoir. Four different types of fracture propagation can result from high tortuosity including fracture turning, fracture twisting, multiple fractures and fracture growth. When pre-existing natural fractures are present within a reservoir, NWBPL analysis will be even more complicated (Pokalai et al., 2015).

Furthermore, the Patchawarra Formation consists of thick sand intervals that cycle between coal measures and shale and is currently exposed to high pressure, high stress, and high temperature conditions. Therefore, the fracturing fluid and proppant need to be selected to suit to these conditions. Fracturing fluid is commonly a water based fluid system comprising of either a Linear Gel or a Borate Crosslink Gel that is injected during the pad, slurry stage and the flushing. Proppant is typically 100 mesh sand which is pumped into the target zone to reduce NWBPL and to bridge-off the PDL. This is followed by the injection of ceramic proppant to provide high fracture conductivity. The perforations that the target formation is initiated into are typically made by lowering expendable hollow carrier (EHC) or link guns down the wellbore to perforate the casing completion at the target location. The style of perforating guns is primarily dependant on well completion with EHC guns commonly used in monoboires to mitigate rat-hole loss, and link guns are used in conventional completion designs with high density shot strategy of 5 shot/ft and 60 degree phasing (Johnson et al., 2002).

1.3 Regional Geology

Our case study focuses on the Patchawarra Formation in the Cowralli Field, Cooper Basin. The Cooper Basin is located on-shore in Eastern Central Australia (Figure 1-4) covering an area of ~130,000 km² across north-east South Australia and south-west Queensland (Cotton et al., 2007) and is Australia's largest onshore hydrocarbon province. The Jurassic-

Cretaceous Eromanga Basin overlies the Permian-Triassic Cooper Basin.



Figure 1-3 : Map of the Cooper (blue) and Eromanga (green) basins (McGowen et al., 2007).

The Cooper Basin is a Permian-Carboniferous to Late Triassic intra-cratonic basin with an unconformity separating it from the underlying early Palaeozoic sediments of the Warburton Basin that were deposited in a non-marine environment (Hall et al., 2016). The Gidgealpa-Merrimelia-Innaminka (GMI) and Murteree-Nappacoongee (MN) ridges form two major intra-basin structural highs that separate the northeast-southwest elongated Patchawarra, Nappamerri and Tennapera troughs (Figure 1-4).

According to the stratigraphy presented by Alexander et al. (1998), the major target intervals have been found in the Permian sandstones that compose the Early Permian Tirrawarra and Patchawarra formations, and the Late Permian Toolachee Formation. The gross sand thickness in the Patchawarra Formation varies between 500 and 2,500 ft at

depths of between 7,000 and 10,500 ft (Figure 1-5) in the study area. A thorough review of the geology and geophysics in the Cooper Basin was reviewed in section 1.7 (Paper 6).

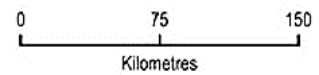
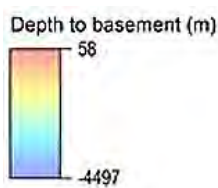
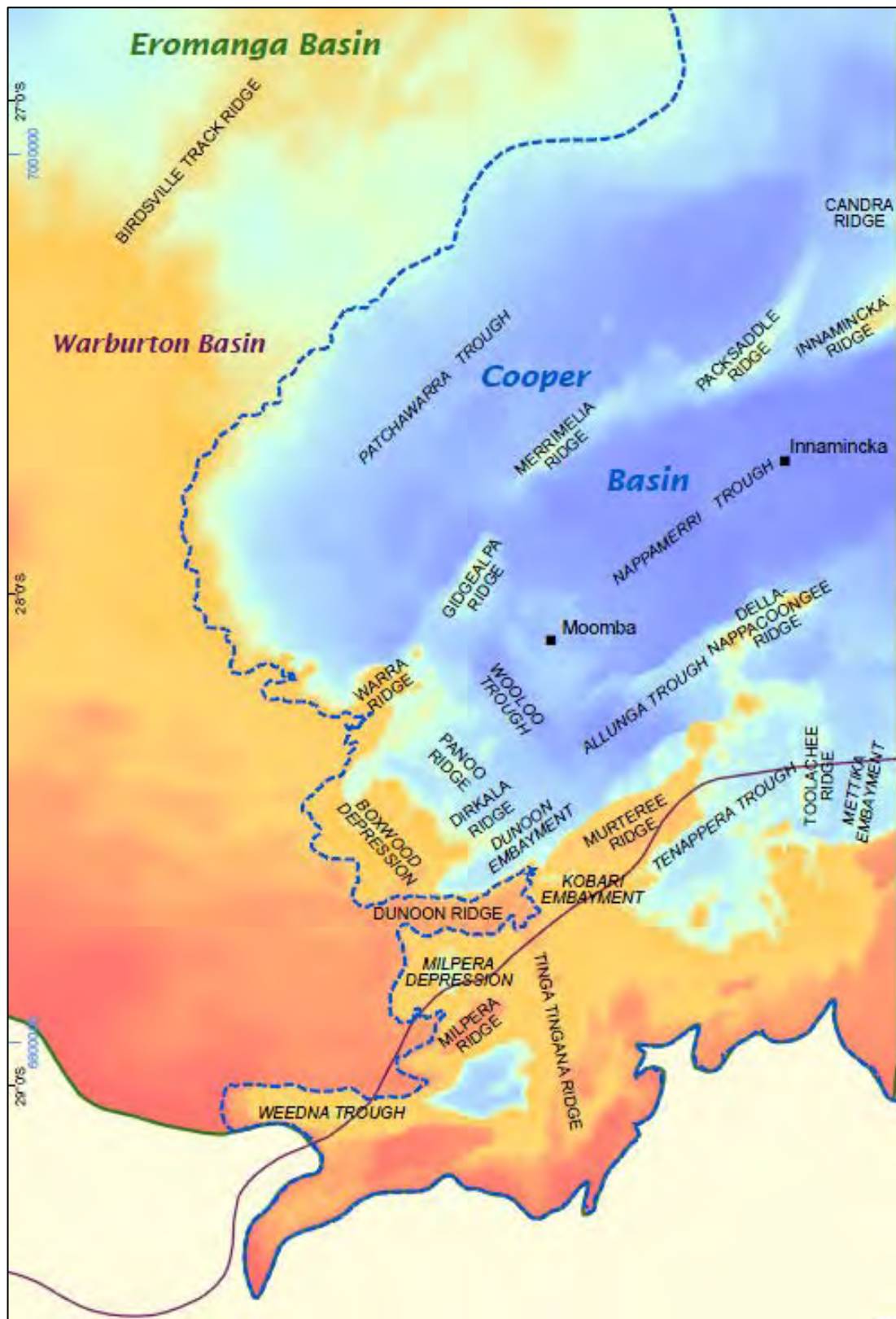


Figure 1-4 : Map of major structural highs and troughs in the Cooper Basin (Alexander et al., 1998).

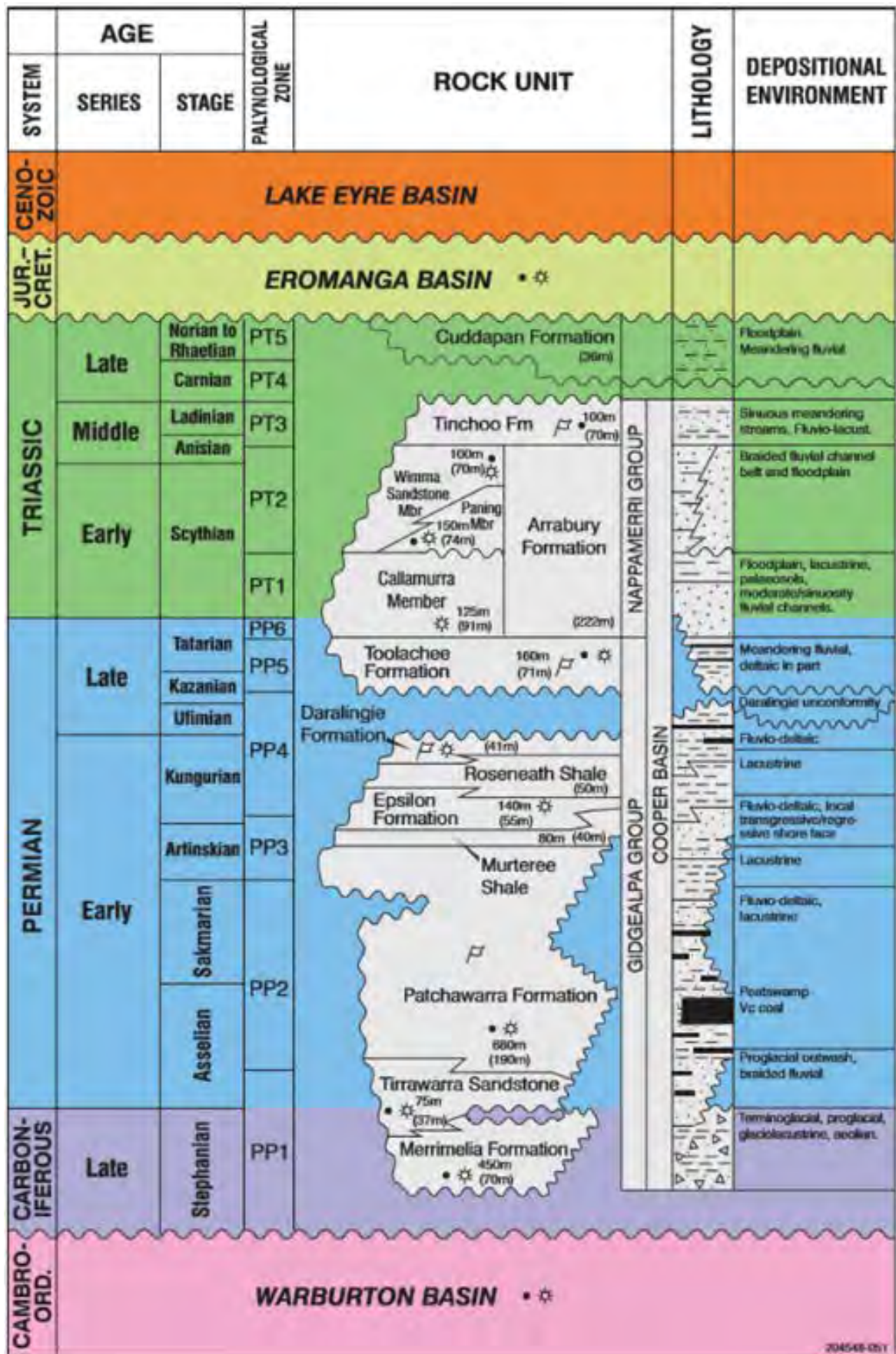


Figure 1-5 : Stratigraphy of the Cooper Basin (Alexander et al., 1998).

The Patchawarra Formation shows interbedded sandstone, siltstone, shale and coal as a result of lithology deposited in a high sinuosity fluvial system over a floodplain with peat swamp, lakes and gentle uplands (Kapel, 1972). The gas reservoir thickness varies between 300 ft and 1,500 ft with Carbon Dioxide Gas (CO₂) concentrations of 8 – 40 %. The permeability ranges between 0.01 and 10 mD, which is considered low permeability, therefore requires hydraulic fracturing to achieve economical gas production.

Kulikowski and Amrouch (2017) presented the timing of natural fracture development and the geometry of regional pre-existing natural fractures by using borehole image logs and core from 27 wells across the basin. They found 5 different natural fracture sets within the Patchawarra Formation in the Cooper Basin that include two high (60°) dip angle conjugate sets striking NE-SW and SE-NW, as well as three low (30°) dip angle conjugate sets striking NE-SW, N-S, and E-W.

Furthermore, there are two mechanisms in order to reactivate or open the pre-existing natural fractures, namely shear reactivation and tensile reactivation. Based on Zhang and Li (2016), the shearing of natural fractures is the most important process to enhance gas recovery and create larger and complex fracture networks.. In the Patchawarra Formation, the orientation of the shear reactivation is $\pm 30^\circ$ from the maximum horizontal stress direction. The plane of tensile reactivation is parallel to the planes of maximum horizontal and vertical stress, and perpendicular to the minimum principal stress direction. The hydraulic fracturing interactions with pre-existing natural fractures is described in more detail in Chapter 2.

1.3.1 The Cwralli Field

The Cwralli Field is located in the Patchawarra Trough and contains an approximate gas column of 1,640 ft within the cyclically deposited very fine grained sandstone, siltstone, shales and coals that form the Patchawarra Formation. The field contains a low to

moderate relief structure elongate in a northeast-southwest direction. The structure aligns with the northeast-southwest trending GMI Ridge and is located 35 km west of the Moomba Gas Plant (Figure 1-6). The first well, Cowralli 1, was drilled in 1986 targeting the Patchawarra interval, which is found to be high in gas saturated sands and was extremely successful (Leonov, 2009). The total of 29 wells were spudded by 2014 along the low relief structure, which is shown in Figure 1-6 and includes the location of 4 wells used in our case study.

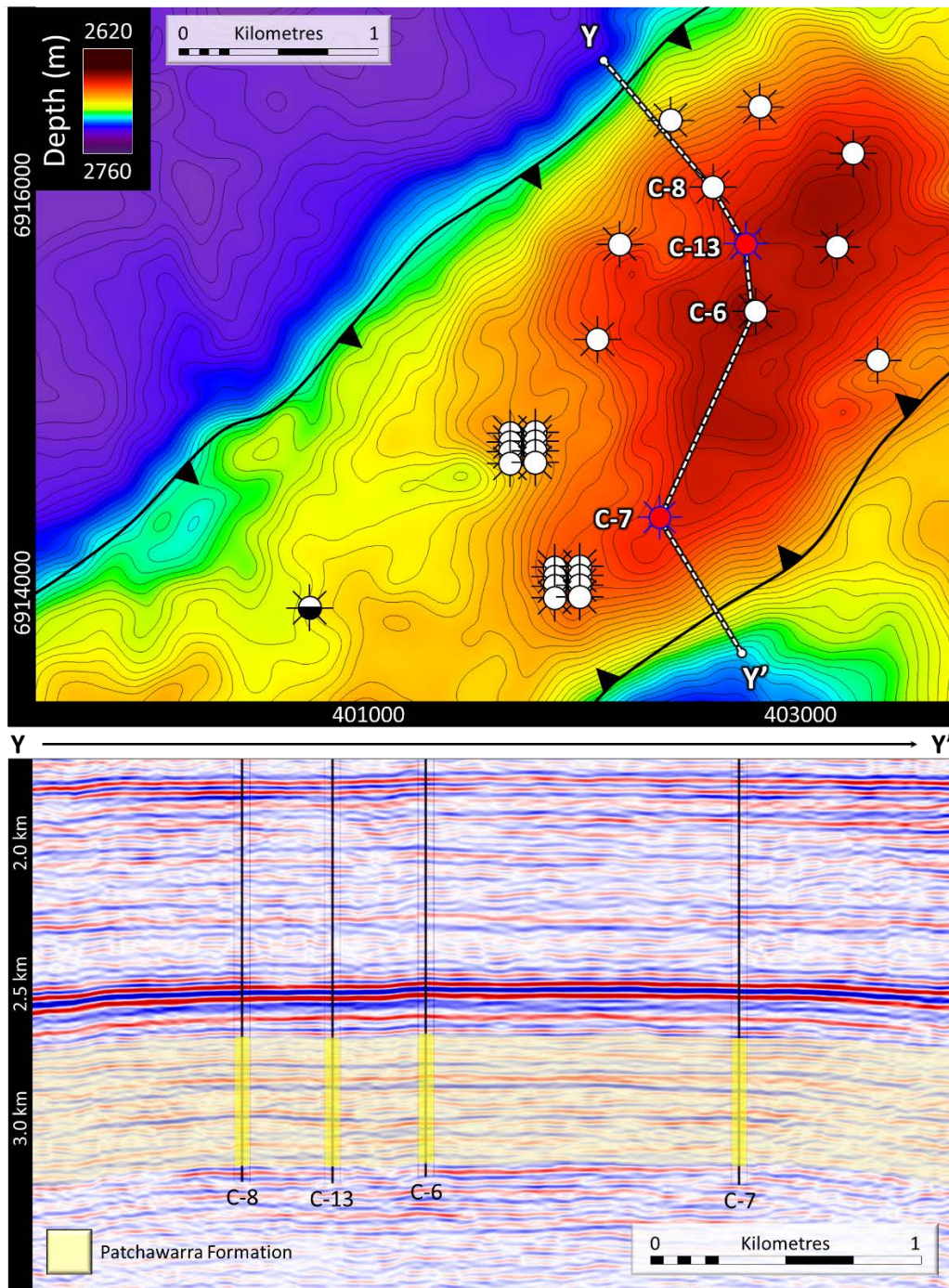


Figure 1-6 : Structural map and seismic cross-section in the Cowralli Field.

1.4 Geomechanics

Rock mechanics are the rocks physical behaviour as it responds to the forces in the environment. Warpinski and Smith (1989) stated that in order to determine the in-situ stress, the mechanical rock properties need to be measured. The hydraulic fracture geometry and treatment design relates to the analysis of the important rock properties such as stress and strain, the Poisson's Ratio and Young's Modulus. Another critical parameter

is the in-situ stresses profile (Nelson et al., 2007). The study area contains complex and high in-situ stress gradient (>0.95 psi/ft), high rock strength and the hydraulic fracture complexity increases due largely to the weakness of geological fabrics (i.e. bedding, fractures, faults, etc.).

Tiab and Donaldson (2011) described rock deformation based on the linear elasticity theory. Hooke's law can be used to describe the deformation of rock properties into four stages: (1) elastic; (2) elastic-viscous; (3) plastic; and (4) rupture. The linear function of stress (σ) behaviour in purely elastic material is associated with Young's Modulus (E) and strain (ε) as shown in Equation 1-1.

$$\sigma = E\varepsilon \quad \text{Equation 1-1}$$

Young's Modulus is a measure of the resistance against the axial load, that can be expressed as the ratio between load per unit area (F/A) and the deformation, or strain, where ΔL is the change in length and L_o is the original length.

$$E = \frac{\sigma}{\varepsilon} = \frac{F/A}{\Delta L/L_o} \quad \text{Equation 1-2}$$

Poisson's ratio (ν) measures the ability of a material stretch and is the ratio between the lateral expansion ($\varepsilon_{lateral}$) and axial strain (ε_{axial}) as shown in Equation 1-3.

$$\nu = \frac{\varepsilon_{lateral}}{\varepsilon_{axial}} \quad \text{Equation 1-3}$$

The dynamic moduli of rock can be calculated from the elastic wave velocity or the sonic and density from logging measurements (Barree et al., 2009b), which depend on the rock types. The full-wave log from shear (DTS) and compressional wave travel (DTC) are used to generate the elastic properties, the sonic and bulk density (ρ_b) log used to estimate Young's Modulus (E) and Poisson's ratio (ν), such that the value can be defined as;

$$E = 13447\rho_b \frac{(3R - 4)}{(DTC^2 R(R - 1))} \quad \text{Equation 1-4}$$

$$\nu = \frac{(R - 2)}{(2R - 2)} \quad \text{Equation 1-5}$$

Where R is the square of the sonic log travel time between shear (DTS) and compressional wave travel (DTC) as shown below.

$$R = \frac{DTS^2}{DTC^2} \quad \text{Equation 1-6}$$

1.5 In-Situ Stress

Considering that the intra-formational lithology can change in the Patchawarra Formation between sands, shales, and coals, the in-situ stress can vary locally as a result of the changing rock properties with depth. The three principle stresses are the main factors in controlling the hydraulic fracture azimuth and orientation, fracture growth, fluid and proppant treatment. Where σ_v is the vertical stress, σ_{Hmax} is the maximum horizontal stress and σ_{Hmin} is the minimum horizontal stress. The fracture propagation depends on the magnitude and direction of the three principle stresses. The fracturing fluid being pumped into the wellbore initiates the fracture in the formation. The fracture will then propagate perpendicular to the lowest stress or parallel to the maximum principle stress.

Based on the Anderson faulting theory (Anderson, 1905) in Figure 1-7, if the vertical stress is the maximum stress, the state of earth stresses is in a normal faulting stress regime. This will provide the vertical fracture growth that is perpendicular to the minimum horizontal stress direction when drilling a vertical well, as shown Figure 1-8. If the vertical stress is the intermediate stress, the stress is in a strike-slip faulting stress regime and finally, if the vertical stress is the minimum stress, then the stress is in a reverse faulting stress regime (Figure 1-7).

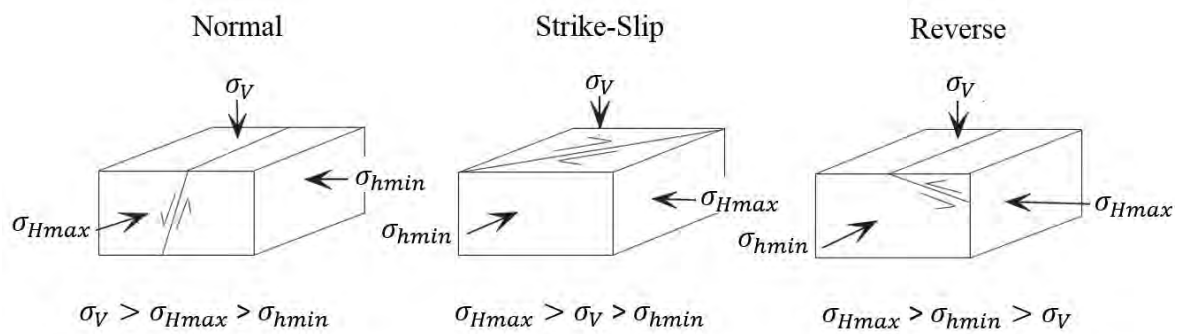


Figure 1-7 : The relationship of tectonic regimes (Zoback, 2007)

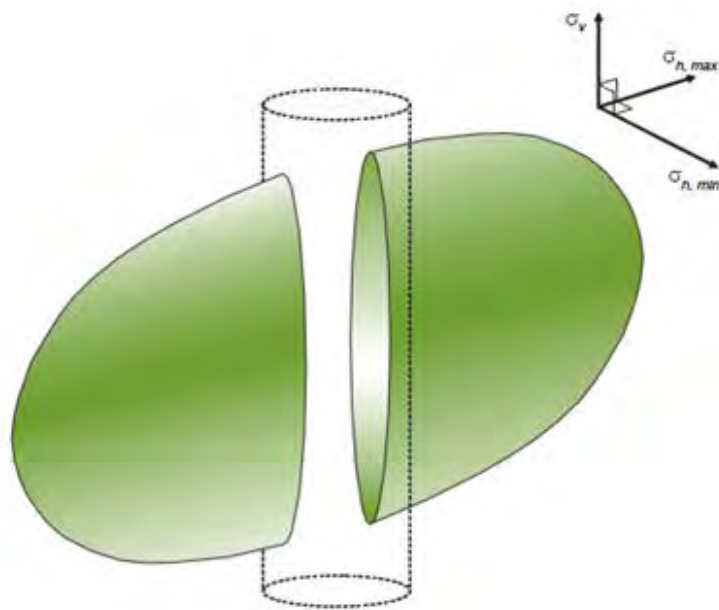


Figure 1-8 : Fracture propagation in a normal faulting stress regime

To quantify the magnitude of in-situ stresses in the Cooper Basin, leak-off test analysis was conducted on 24 wells by Reynolds et al. (2006) by pumped fluid into the wellbore. The result showed that the gradient of minimum horizontal stress was 15.5 MPa/km and the drilling-induced tensile fractures provided the maximum horizontal stress orientation and magnitude. A strike-slip fault stress regime has been found at the depths between 1 to 3 km, and in some areas showed that the stress regime changes with depth to reverse fault stress regime. Therefore, for a reverse fault regime the maximum stress will be in a horizontal direction and the minimum stress will be in a vertical direction. This

would affect the fracture propagation, which would be parallel to the horizontal stress directions in the Cooper Basin. This has led to fracture propagation complexity in this area.

Based on the hydraulic fracture treatment design, the in-situ stresses need to be determined in a multi-layer reservoir, especially, considering that the Cooper Basin stratigraphy varies between sandstone, siltstone, shale and coal. As in-situ stresses are associated with the rock properties, the stresses can change between adjacent rock types.

The weight of rock, increasing with depth, causes the vertical stress. This can be found by using the integration of density logs (Jaeger et al., 2007), where $\rho(z)$ is the density at any z depth from the surface, and g is the acceleration from gravity as shown in Equation 1-7.

$$\sigma_v = \int_0^z \rho(z)gdz \quad \text{Equation 1-7}$$

The classical approach of minimum stress calculations (Equation 1-8) is based on the behaviour of rock elastically (Whitehead et al., 1987).

$$\sigma_c = \frac{\nu}{1 - \nu} (\sigma_v - P_p) + P_p \quad \text{Equation 1-8}$$

The effective stress is the difference between the total stress and the pore pressure. Equation 1-8 shows the total horizontal stress (σ_c), with the first term considering the linear elasticity in the vertical stress direction by including Poisson's Ratio (ν). This is an important consideration because the vertical forced applied to the rock is transposed to the effective horizontal stress while including the effect of pore fluid pressure (P_p) to achieve a stabilised stress system. The second term includes the stress that is created from the pore pressure.

Despite considering the elastic part of vertical stress (σ_v) and pore pressure (P_p), the minimum horizontal stress (σ_{hmin}) needs to account for the regional stress field, or tectonic force. The majority of the maximum horizontal stress is in the east to west direction in Cooper Basin, which corresponds to far-field tectonics stresses along eastern Australia (Reynolds et al., 2006). Therefore, the tectonic part, or the stress from the external force (σ_{ext}), needs to be taken into account when calculating the closure pressure below.

$$\sigma_{hmin} = \frac{\nu}{1-\nu} (\sigma_v - P_p) + P_p + \sigma_{ext} \quad \text{Equation 1-9}$$

Prats (1981) considered the minimum horizontal strain (ϵ_h) and maximum horizontal strain (ϵ_H) in the stress model, which shows the amount of lateral tectonic movement based on the regional geological structures. Furthermore, the most important parameters in the stress model are the minimum (σ_{hmin}) and maximum (σ_{Hmax}) horizontal stress magnitudes. An extensive explanation of these parameters is given in Chapter 4. The four equations below are solved based on the observed by Diagnostic Fracture Injection Test (DFIT) data and well logs.

$$\sigma_{hmin} = \frac{\nu}{1-\nu} (\sigma_v - \alpha_v p_p) + \frac{E}{1-\nu^2} \epsilon_h + \frac{E\nu}{1-\nu^2} \epsilon_H + \alpha_h p_p \quad \text{Equation 1-10}$$

$$\sigma_{Hmax} = \frac{\nu}{1-\nu} (\sigma_v - \alpha_v p_p) + \frac{E}{1-\nu^2} \epsilon_H + \frac{E\nu}{1-\nu^2} \epsilon_h + \alpha_h p_p \quad \text{Equation 1-11}$$

$$P_{Breakdown} \text{ or } P_{wb} = 3\sigma_{hmin} - \sigma_{Hmax} - P_{Pore} + T_0 \quad \text{Equation 1-12}$$

$$P_{FissureOpening} \text{ or } P_{fo} = \frac{1}{2}(\sigma_{Hmax} + \sigma_{hmin}) + \frac{1}{2}(\sigma_{Hmax} - \sigma_{hmin}) \cos 2\theta \quad \text{Equation 1-13}$$

Typically, all the formation layers will be impacted by the stress created from tectonic movement. Tectonic strains are one of the unknown parameters that need to be solved and constrained in 2D: (1) minimum horizontal tectonic strain (ϵ_h); and (2) maximum horizontal tectonic strain (ϵ_H). The error function is used to minimise the stress tolerance by using the Generalized Reduced Gradient (GRG) nonlinear solving method

(Lasdon et al., 1978) shown in Equation 1-14, where x represents the observed values and \hat{x} is the log derived value.

$$\text{Error function (ErrFn)} = \sum (x - \hat{x})^2 \quad \text{Equation 1-14}$$

1.6 Pressure Diagnostic Tests

Pre-fracturing tests are usually conducted to obtain the estimation of the minimum horizontal stress, or closure pressure, which is the minimum stress that is required to keep the fracture open. This method is performed by injecting the fluid without the proppant and observing the pressure response. There are important parameters such as leak-off characteristic, closure pressure, reservoir pressure, and fluid transmissibility (Barree et al., 2009a), which can be determined by the diagnostic fracture injection tests (DFIT), also known as mini-frac testing and injection/falloff tests. This information helps to design hydraulic fracturing treatment.

1.6.1 Step Rate Tests

The step rate tests are conducted to determine the fracture pressure, or the maximum safe injection pressure without fracturing, for hydraulic fracture design, casing design, and preparation of adequate surface pumps. Also, the tests can provide idealized values for wellbore skin and the presence of pre-existing natural fractures, which provide characteristic pressure responses that are recorded when the pumping rate is increase at low rates (Step Up Test) or when the pumping rate is decreases (Step Down Test) step by step. More detail on step rate tests is included in Chapter 5.

1.6.2 Diagnostic Fracture Injection Test (DFIT)

Diagnostic Fracture Injection Test (DFIT) is the injection/falloff process by pumping small amounts of fluid at a low pumping rate in order to create a small fracture to establish the pressure communication between the fracture dominated area, reservoir dominated area

and the wellbore as shown in **Figure 1-10** (Craig and Brown, 1999). The DFIT test can be classified into two parts, the fracture dominated before closure analysis (BCA) and the reservoir dominated after-closure analysis (ACA) shown in **Figure 1-10**.

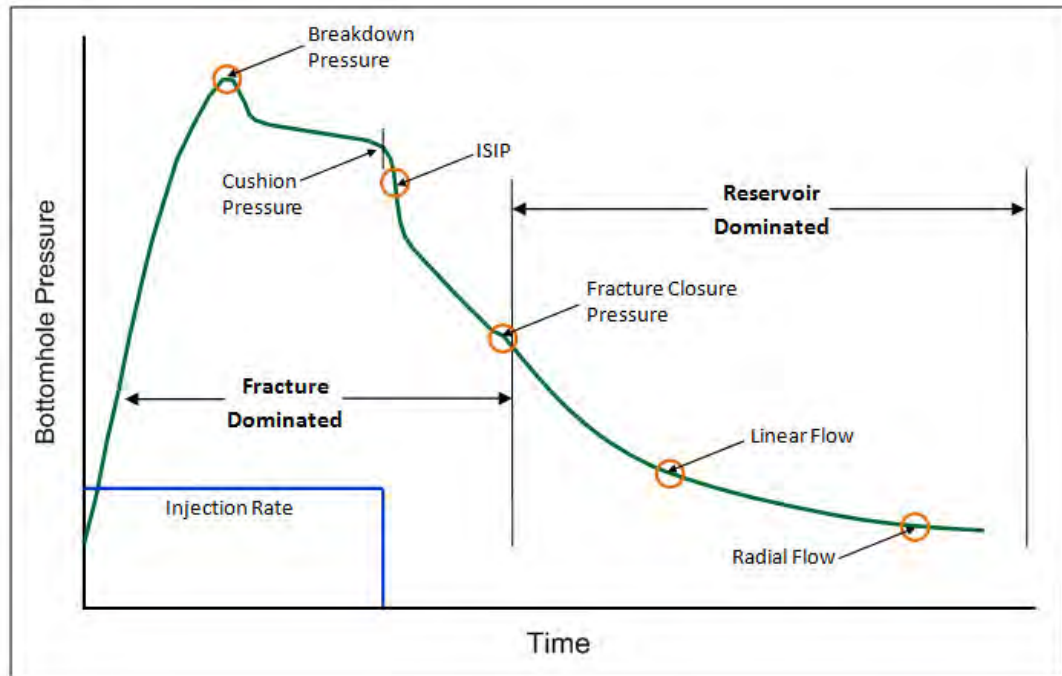


Figure 1-9 : Typical Diagnostic Fracture Injection Test (DFIT) pressure profile.

1.6.2.1 Before Closure Analysis

The before closure analysis (BCA) is used to determine the closure pressure (P_c), instantaneous shut-in pressure (ISIP) and fluid leak-off type. Barree et al. (2007) presented three methods in order to identify these parameters: (1) G-function analysis; (2) square-root time analysis; and (3) log-log plot analysis. These require consistent interpretation as it can impact on the flow regimes identified during after-closure analysis and also the input data for calibrating the fracture model. In this thesis, a more detailed review and how to use DFIT interpretations are presented in Paper 1 and Paper 3.

G-Function Analysis

The G-function is dimensionless leak-off with elapsed time, beginning at the fracture initiation until shut-in time and uses the normalised fracture extension time (Castillo, 1987;

Nolte, 1986). Carter (1957) discussed the linear fluid leak-off in a reservoir, which is classified into three regions: (1) invasion filtrate zone; (2) fracture zone; and (3) reservoir zone. The model uses Equation 1-15, where C_L is the leak-off coefficient (length/time^{0.5}), t is the time elapsed since the start of the leak-off process, and v_L is the leak-off velocity.

$$v_L = \frac{C_L}{\sqrt{t}} \quad \text{Equation 1-15}$$

Considering the area of fluid leak-off (A_L) by multiplying and integrating from 0 to t , results in Equation 1-16 and Equation 1-17.

$$\int_0^t v_L A_L dt = \int_0^t \frac{C_L A_L}{\sqrt{t}} dt \quad \text{Equation 1-16}$$

$$v_L A_L t = C_L A_L 2\sqrt{t} + S_p \quad \text{Equation 1-17}$$

Spurt loss coefficient (S_p) is the instantaneous volume of fracturing fluid that pass through the formation, which are controlled by filter cake. Then rearranging Equation 1-17 on the right hand side into leak-off volume (V_L) gives the following equation.

$$V_L = C_L A_L 2\sqrt{t} + S_p \quad \text{Equation 1-18}$$

Considering the changing of any differential surface element (dA) during the leak of any time (τ_N) gives;

$$\partial V_L = \partial A \frac{C_L}{\sqrt{t - \tau_N}} \partial t \quad \text{Equation 1-19}$$

Based on the leak-off volume, fracturing fluid is pumped through two fracture faces of one fracture wing. The integration is applied into the leak-off rate from the beginning of pumping (0) to any specific time (t_e) and through any fracture face area (A_e) over each element as shown in Equation 1-20.

$$V_{Le} = 2 \int_0^{A_e} \int_{\tau_N}^{t_e} \frac{C_L}{\sqrt{t - \tau_N}} \partial A \partial t \quad \text{Equation 1-20}$$

Adjusting the Nolte pressure decline analysis assumes fracture growth during an injection is modelled by a power law relationship and is dimensionless in area (A_D) and time (τ_{ND}) where α_N is equal to the fracture growth exponent (0.5 – 1).

$$A_D = t^{\alpha_N}_{DN} = \frac{A(t)}{A_e} \quad \text{Equation 1-21}$$

$$\tau_{ND} = \frac{\tau_N}{t} = A^{\frac{1}{\alpha_N}}_D \quad \text{Equation 1-22}$$

The leak-off volume in the dimensionless area and time at the end of pumping can be expressed in Equation 1-23.

$$V_{Le} = 2C_L A_e \sqrt{t_e} \int_0^1 \int_{A^{\frac{1}{\alpha_N}}_D}^1 \frac{1}{\sqrt{t_{DN} - A^{\frac{1}{\alpha_N}}_D}} dt_D dA_D \quad \text{Equation 1-23}$$

The next important function is the dimensionless loss-volume function at the end of the injection, or at shut-in (g_0), based on the double integration of the dimensionless area and the fracture growth exponent, which can define the volume as follows.

$$g_0(\alpha_N) = \int_0^1 \int_{A^{\frac{1}{\alpha_N}}_D}^1 \frac{1}{\sqrt{t_{DN} - A^{\frac{1}{\alpha_N}}_D}} dt_D dA_D = \frac{V_{Le}}{2C_L A_e \sqrt{t_e}} \quad \text{Equation 1-24}$$

Nolte assumed a constant fracture area during the shut-in period prior to fracture closure, which allows the dimensionless loss-volume function (g_0) to be defined beyond the end of an injection. We can then define the Nolte dimensionless shut-in time, where t_p is the pumping time as shown in Equation 1-25.

$$\Delta t_D \text{ or } t_{DN} = \frac{(t - t_p)}{t_p} \quad \text{Equation 1-25}$$

Substituting Equation 1-25 into Equation 1-20 gives;

$$V_{L(t_p+\Delta t)} = 2 \int_0^{A_e} \int_{\tau_N}^{t_p+\Delta t} \frac{C_L}{\sqrt{t - \tau_N}} \partial A \partial t \quad \text{Equation 1-26}$$

Similar to Equation 1-23, the leak-off-volume integral can then be written as;

$$V_{L(t_p+\Delta t)} = 2C_L A_e \sqrt{t_e} \int_0^1 \int_{\tau_N}^{t_p+\Delta t N} \frac{1}{\sqrt{t_{DN} - A^{\frac{1}{\alpha_N}}}} dt_D dA_D \quad \text{Equation 1-27}$$

The dimensionless loss-volume function at any post shut-in time after the injection $g(\Delta t, \alpha_N)$ is defined as;

$$g(\Delta t, \alpha_N) = \frac{V_{L(t_p+\Delta t)}}{2C_L A_e \sqrt{t_e}} \int_0^1 \int_{\tau_N}^{t_p+\Delta t N} \frac{1}{\sqrt{t_{DN} - A^{\frac{1}{\alpha_N}}}} dt_D dA_D \quad \text{Equation 1-28}$$

The hypergeometric function is applied to give the closed-form solution below;

$$g(\Delta t, \alpha_N) = \frac{4\alpha_N \sqrt{\Delta t_{DN}} + [2\sqrt{1 + \Delta t_{DN}}] F\left[\frac{1}{2}, \alpha_N; 1 + \alpha_N; (1 + \Delta t_{DN})^{-1}\right]}{1 + 2\alpha_N} \quad \text{Equation 1-29}$$

The fracture growth exponent can be expressed into three typical solutions (4/5, 2/3 and 8/9) depending on the leak-off rate in the formation. The approximation of the G-function for various exponents is defined below.

$$g\left(\Delta t, \frac{4}{5}\right) = \frac{1.41495 + 79.4125\Delta t + 632.457\Delta t^2 + 1293.07\Delta t^3 + 763.19\Delta t^4 + 94.0367\Delta t^5}{1 + 54.853\Delta t + 383.11\Delta t^2 + 540.342\Delta t^3 + 167.741\Delta t^5 + 6.49129\Delta t^6} \quad \text{Equation 1-30}$$

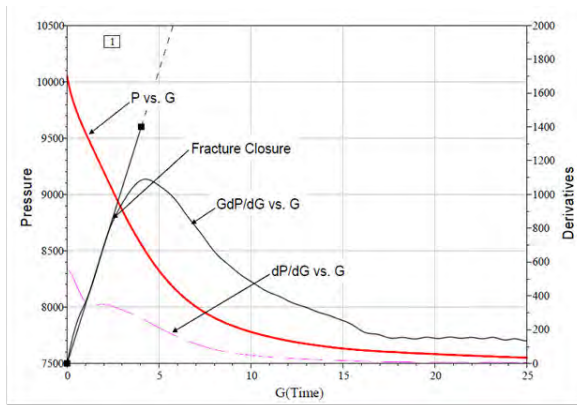
$$g\left(\Delta t, \frac{2}{3}\right) = \frac{1.47835 + 81.9445\Delta t + 635.354\Delta t^2 + 1251.53\Delta t^3 + 717.7\Delta t^4 + 86.843\Delta t^5}{1 + 54.2865\Delta t + 372.4\Delta t^2 + 512.374\Delta t^3 + 156.031\Delta t^4 + 5.95955\Delta t^5 - 0.0696905\Delta t^6} \quad \text{Equation 1-31}$$

$$g\left(\Delta t, \frac{8}{9}\right) = \frac{1.37689 + 77.8604\Delta t + 630.24\Delta t^2 + 1317.36\Delta t^3 + 790.7\Delta t^4 + 98.4497\Delta t^5}{1 + 55.1925\Delta t + 389.537\Delta t^2 + 557.22\Delta t^3 + 174.89\Delta t^4 + 6.8188\Delta t^5 - 0.0808317\Delta t^6} \quad \text{Equation 1-32}$$

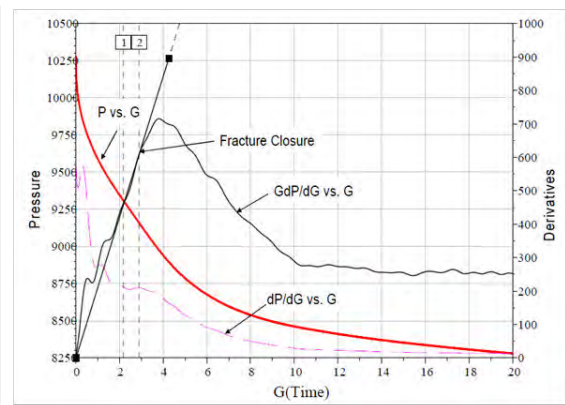
Based on Barree et al. (2007), the G-function, $G(\Delta t_D)$ is simplified by deriving from the intermediate function, where $g(\Delta t_D)$ is fluid loss at a dimensionless time, g_0 is the dimensionless loss-volume function at shut-in, and Δt_D is dimensionless pumping time.

$$G(\Delta t_D) = \frac{4}{\pi} [g(\Delta t_D) - g_0] \quad \text{Equation 1-33}$$

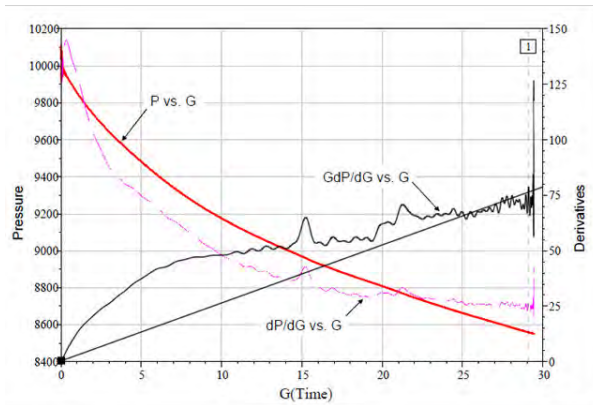
The plot of G-function time (G) and the G-function semilog derivatives, or superposition derivative (GdP/dG), is used to identify the fracture closure by using the straight line passing through the origin. The first derivative (dP/dG) is used to identify closure pressure when the flat peak of the curve or slope corresponds to the semilog derivatives. The square-root method identifies the closure pressure in a similar way to the G-function analysis. There are four leak-off characteristics that can be observed in G-function plots; (1) normal leak-off; (2) pressure dependent leak-off (PDL); (3) tip extension; and (4) height recession, or transverse storage (Figure 1-11).



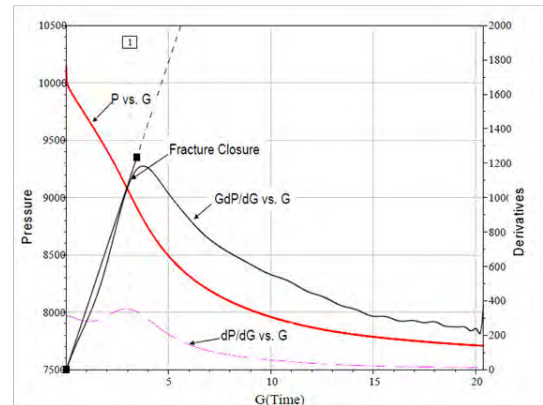
a) Normal Leakoff



b) Pressure Dependent Leakoff (PDL)



c) Tip Extension



d) Height Recession or Transverse Storage

Figure 1-10 : Leak-off behaviour in G-function plots.

The normal leak-off shows the fracturing fluid leak-off into the reservoir at a constant rate. Pressure dependent leak-off shows a characteristic large “hump” in the G-Function semilog derivative where the existence of secondary fractures intersecting the main fracture has been found. Tip extension initially exhibits a large positive slope that continues to decrease after shut-in, yielding a concave down curvature, which is a phenomenon in very low permeability reservoirs when a fracture continues to grow even after injection is stopped and the well is shut-in. Finally, height recession shows the G-Function derivative (GdP/dG) lying below a straight line extrapolated through the normal leak-off data when the fracture propagates through adjoining impermeable layers during injection. During early shut-in, the pressure declines at a relatively low constant rate since only the permeable zone allows fluid leak-off to occur.

1.6.2.2 After-Closure Analysis

After-closure analysis (ACA) provides estimates of reservoir pressure and reservoir transmissibility. However, the flow regime identification needs to be defined after the transition from linear flow in the fracture into the pseudo-linear flow and pseudo-radial flow in the formation (Nolte et al., 1997). Nolte's techniques use injected volume as the impulse volume and consider the closure point as the beginning of the falloff where the impulse linear and radial flow have slopes of -1/2 and -1, respectively.

Once the pseudo-linear flow is detected, Nolte Linear Time functions (F_L) can be used to define the leak-off coefficient and pore pressure estimates that are shown in Equation 1-34 to Equation 1-36.

$$F_L(t, t_c) = \frac{2}{\pi} \sin^{-1} \left(\sqrt{\frac{t_c}{t}} \right), t > t_c \quad \text{Equation 1-34}$$

$$p(t) - p_i = m_L F_L(t, t_c) \quad \text{Equation 1-35}$$

$$m_L = C_L \sqrt{\frac{\pi \mu}{k \phi c}} \quad \text{Equation 1-36}$$

If the imposed pseudo-radial flow is identified, slope (m_R) is extrapolated from the log-log plot of square linear flow and pressure derivative. Reservoir pressure and transmissibility are estimated, and the by-product of transmissibility can also be used to defined reservoir permeability (k).

$$F_R(t, t_c) = \frac{1}{4} \ln \left(1 + \frac{\chi t_c}{t - t_c} \right), t > t_c \quad \text{Equation 1-37}$$

$$p(t) - p_i = m_R F_R(t, t_c) \quad \text{Equation 1-38}$$

$$\frac{kh}{\mu} = 251,000 \left(\frac{V_i}{m_R t_c} \right) \quad \text{Equation 1-39}$$

1.6.3 Nolte-Smith Log-Log Plot

Nolte and Smith (1981) demonstrated the Log-Log plot of net pressure and elapse time during the injection until fracture shut-in time throughout the fracture closure time. This analysis indicates the fracture growth in each mode as shown in Figure 1-9. Mode I presents the confined-height fracture growth with unrestricted fracture growth in the lateral direction. The flat slope in Model II indicates the fracture height growth when the fracture starts to penetrate the high stress contrast. Mode II may be followed by either Mode III or Mode IV. Mode II being followed by Mode III suggests restricted fracture growth due to the proppant bridge-off, or block, at the wellbore. If the operator continues to pump proppant, the pressure will increase and the fracture will completely bridge-off, causing loss of proppant containment, or “screen-out”. Finally, Mode IV indicates the fracture height growth has broken through a formation barrier causing pressure to decrease.

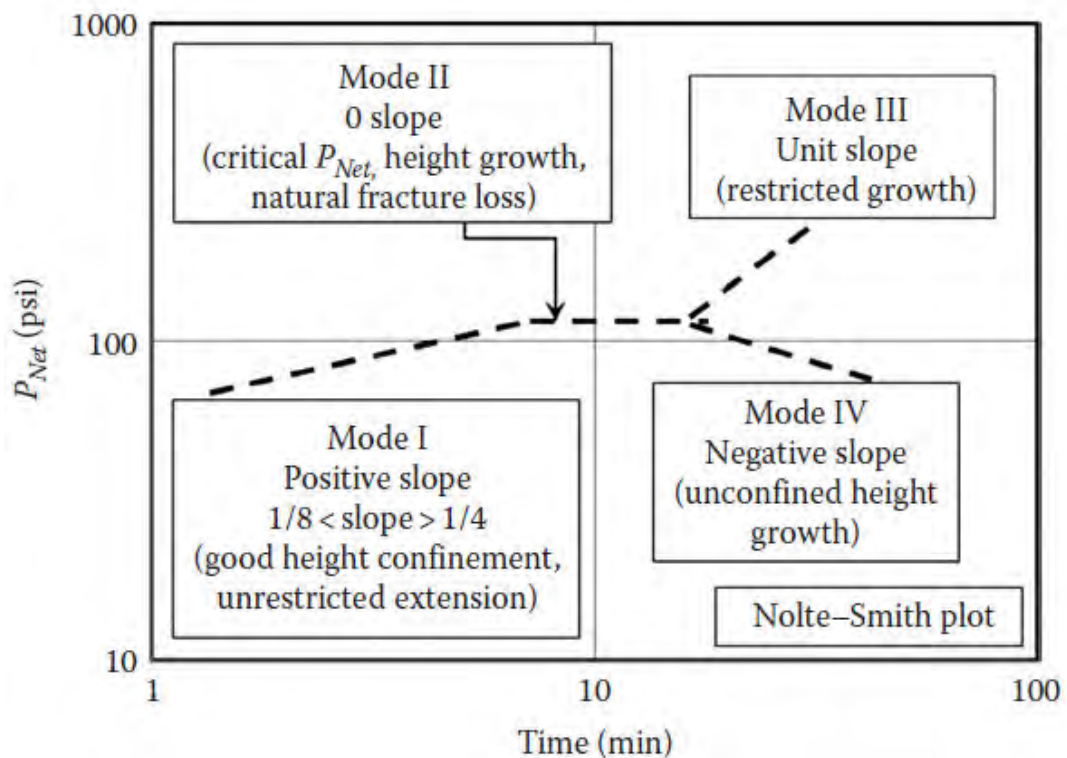


Figure 1-11 : Nolte-Smith net pressure log-log plot (Smith and Montgomery, 2015).

In the Cooper Basin, high stress magnitude in the horizontal direction and similar minimum and vertical stress magnitudes are indicated by a complex stress regime that can alternate between a strike-slip and reverse regime. This could create more complexity in the fracture, meaning that Mode I may last longer than expected before being followed by Mode II, or alternate between the two models.

1.7 Flow Back Analysis

Tannich (1975) described the fluid flowback mechanism in three steps. The first step is saturating the fracture with fracturing fluid. Once the production begins, the fluid flow near the wellbore will be moved first. This is followed by the flow along the fracture. This behaviour is controlled by fracturing fluid viscosity. Finally, the gas saturation will increase when the gas breaks through and the fracturing fluid is removed. Based on the simulation by Tannich (1975), the model areas are separated into different zones, such as the undamaged zone, invaded zone, fracture itself and the tubing zone. He used the concept of superposition to estimate the pressure distribution in the reservoir model. The result is that with shorter conductive fracture length, the fluid removal will be faster. However, the effect of capillary pressure and closure pressure is not considered in the model and this leads to unrealistic results when compared with the actual data.

The effects of water blockage in low permeability gas wells is introduced by Holditch (1979). His numerical simulation considered a J-function that relates to capillary pressure, which reduces the permeability in the invaded zone. The fluid cleanup improves when the pressure drawdown is in excess of the capillary pressure in the damaged zone. Based on this result, we should consider the importance of how to define an accurate J-function, which could impact the water mobility in the low permeability gas reservoir. Even though Holditch (1979) emphasis was on the low productivity based on the effect of drawdown pressure, there are other factors that should be considered. For example, gel

residue that can cause fracture face plugging, proppant crushing based on closure stress, and proppant flowback. This should be investigated as part of sensitivity analysis in fracturing models. Also, the relative permeability hysteresis should be taken into account when the mathematical model of the cleanup and well productivity performance is considered.

Robinson et al. (1988) indicated that the estimation of closure pressure is very important for flowback and cleanup. This is important for selecting the appropriate proppant to reduce the effect of proppant crushing. According to the authors, recorded data from the low gas reservoir in Indonesia relates to the opening of the wellhead choke to maintain the higher bottom-hole flowing pressure that helps to maximise the flowrate and minimises the fracture face damage that could reduce the flowback efficiency.

Another research group that was led by Sharma (2005), targeted the tight gas formation in the Bossier play in East Texas. This work focuses on laboratory and modelling studies to design the optimum hydraulic fracturing strategy. One of the problems mentioned in the study was the large fluid injected that was not recovered due to the water being trapped in the tight gas matrix. Mahadevan and Sharma (2003) conducted the experiment study to provide the basic principles on how cleanup water block occurs. The first mechanism is the displacement of water during which the drawdown pressure is greater than the capillary pressure and then followed by vaporization of flowing gas which impacts the long term result of water cleanup. Better results are further achieved by adding methanol that improves the volatility of the fluid, which increases water retention. Increasing the reservoir temperature changes the limestone from water-wet to oil-wet, which affects the displacement mechanism.

Parekh and Sharma (2004) proposed a parametric study in depleted low permeability reservoirs by using reservoir simulation and gridding separation. The

simulation assumes the use of the Brooks-Corey function that helps to define the capillary pressure and relative permeability. The research also recommended that the drawdown pressure should be at least three times higher than the capillary pressure to ensure appropriate fluid cleanup. In addition, leak-off behaviour must be considered in order to indicate the fluid invaded zone and productivity recovery. Mahadevan et al. (2005) provided modelling for evaporation of fluids that affected the gas well deliverability. The papers also proposed the mass conservation comparison between the evaporation effect and non-evaporation effect. This helps to set up the initial condition, pressure and saturation distribution based on the dimensionless capillary pressure.

Gdanski et al. (2005) discussed the decreasing fluid recovery and gas production due to the effect of fracture face damage. The transmissibility and the simultaneous solution methods take into account the two-phase model. The authors of Gdanski et al. (2005) looked at the research by Holditch (1979), and concluded that fracture face damage (e.g. gelation, proppant embedment, or fracturing fluid invasion) of 90% or more increases the capillary pressure and this causes the decrease in gas production. As a result of their research, Gdanski and Funkhouser (2011) introduced the alternative method of fracture cleanup and chemistry simulator (FCCS), which enhances the fracture cleanup by modelling the changing wettability with adsorption to constrain the contact angle between 0 to 89 degrees.

According to the study, surfactant helps to reduce the capillary pressure to improve the load recovery. The surfactant is most effective when the reservoir has indicated good quality relative permeability, moderate dimensionless fracture conductivity and low reservoir pressure. A similar concept was also developed by modelling and observing the impacts of filter cake on water cleanup (Gdanski and Bryant, 2012a; Gdanski and Bryant, 2012b). The first mechanism is the FCCS with dilution, which requires two phase relative

permeability. The second mechanism requires three phase relative permeability between water, gel filter cake and gas phase in the proppant pack. It is thus important to consider how filter cake forms and the dissolution of gel filter cake recovery during the cleanup process.

Wills et al. (2009) developed a 3D numerical model during fracture cleanup with varying shut-in periods and drawdown pressures. The fluid viscosity between slickwater and gelled fluid must also be considered. This can be concluded that the higher differential pressure and shorter shut-in time improves the fracturing fluid retention. The injection fluid viscosity can cause fracture face damage even with low viscosity values.

Wang et al. (2009) have done extensive modelling of fracture fluid cleanup in tight gas reservoirs. The single phase flow begins with simulation and is then followed by two-phase flow simulation with the effect of proppant crushing, polymer filter cake and gel residue considered. The takeaway from the research is how to configure the input parameters for reservoir models in order to improve the water cleanup process. It is very important to identify the effective fracture length of the model because the realistic value is still uncertain when comparing the hydraulic fracture model with microseismic monitoring. To conclude, a dimensionless fracture conductivity of 10 or more is good for faster fluid load recovery.

1.8 Research Objective

The first objective of this research is to better understand and quantify the localised subsurface stress near the wellbore and the rock mechanical properties in each target zone. For this purpose, a one-dimensional (1D) mechanical earth model is developed with petrophysical log data. Then, in-situ stress and mechanical rock properties are calibrated with well pressure test data. We consider the tectonic stress and strain due to the stress from the Earth's crust and/or the stress from the dynamics of continental boundaries.

Mechanical earth modelling can help to interpret the closure pressure (minimum horizontal stress), the net pressure, pressure dependent leak-off (PDL) and NWBPL. Specifically, 1D mechanical earth modelling can help to predict hydraulic fracturing geometry when pre-existing natural fractures are available.

The second objective is to determine the leak-off mechanism, especially PDL, that is associated with NWBPL in the Cooper Basin. The leak-off mechanism for each well varies significantly between areas, formations and wellbore depths. The correlation between PDL and NWBPL can reveal the impact of the interaction between hydraulic fracturing and the pre-existing natural fractures. This interaction also impacts upon the well productivity.

The third objective is building a 3D planar hydraulic fracturing model that is integrated with a reservoir simulation to optimize the operating parameters, well placement, and the fracturing fluid flowback on gas production. The case study area (Cowralli Field) is a unique field in comparison to tight gas fields found in other parts of the world.

The fourth objective is to investigate the effect that pre-existing natural fractures can have on effective hydraulic fracturing in the complex stress environment. This is done by integrating a 1D mechanical earth model with borehole image log interpretation and a discrete fracture network model to estimate the stimulated rock volume under multiple scenarios that considers the complex stress conditions and trajectory of wells. The final objective is to model the effectiveness of different fracturing fluids to increasing the flow back volume and improve hydrocarbon productivity.

1.9 Methodology and Work Flow

The workflow diagram in Figure 1-12 shows the fully integrated methodology that was

used to achieve the research objectives in this dissertation. The workflow starts with petrophysical log data review and processing to calculate the petrophysical properties and evaluate the potential of the target zone, such as lithology, water saturation, porosity and net pay sand. Another important parameter is permeability, which can be obtained by after-closure well test analysis that will be discussed in the next section. Then, well logs are used to derive rock mechanical properties in each formation.

A 1D Mechanical Earth Model (1D MEM) is then built and validated by pressure test data (DFIT). This process is discussed in more detail in Chapter 4 and Paper 1. The 1D MEM results can be used as input data to determine the stress profile for the 3D planar hydraulic fracturing models and gives the fracture orientation. That orientation can help us to predict the optimum well placement. For this purpose, we incorporate the fundamentals of the Kirsch equations and pre-existing natural fractures.

The workflow for the study of near wellbore pressure loss starts with the interpretation of the diagnostic fracture injection tests (DFIT). The rigorous process of DFIT involves step-down test, pre-closure analysis and after-closure analysis which are discussed in Chapter 5. The outcome of these studies is the closure pressure and breakdown pressure for validating of 1D MEM. The effect of pre-existing natural fractures on DFIT also provide information about the leak-off characteristic. The workflow for the third objective is the integration of a 3D planar hydraulic fracturing model with reservoir simulation. For running the 3D planar hydraulic fracturing simulation, the input data includes the volume of fracturing fluid, proppant, pumping rate and time while the output is fracture properties and fracture geometries in three-dimensions. All models are validated by matching the surface treating pressure data. We used GOHFER from Barree & Associates for modelling of hydraulic fracturing and Eclipse from Schlumberger for

reservoir simulation. The Cartesian grids with two-phase flow reservoir simulator are used to predict the fluid flowback.

The workflow for the fourth objective begins with natural fracture interpretation from a borehole image log. The fracture intensity and distribution is analysed and used to develop a representative discrete fracture network (DFN) model of the Patchawarra Formation. The in-situ stresses and rock properties calculated from the 1D MEM in the first objective are used as input data for the DFN model. The hydraulic fracturing parameters from the third objective are used to estimate the stimulated rock volume in three scenarios. One scenario is the optimised well trajectory that was proposed in objective three. The workflow for the final objective continues on from objective three and involves the simulation of different hydraulic fracturing fluids (LPG and nano-stabilized foams) to maximise fluid flow back.

Optimisation of Hydraulic Fracturing and Flowback in Unconventional Reservoirs in the Cooper Basin

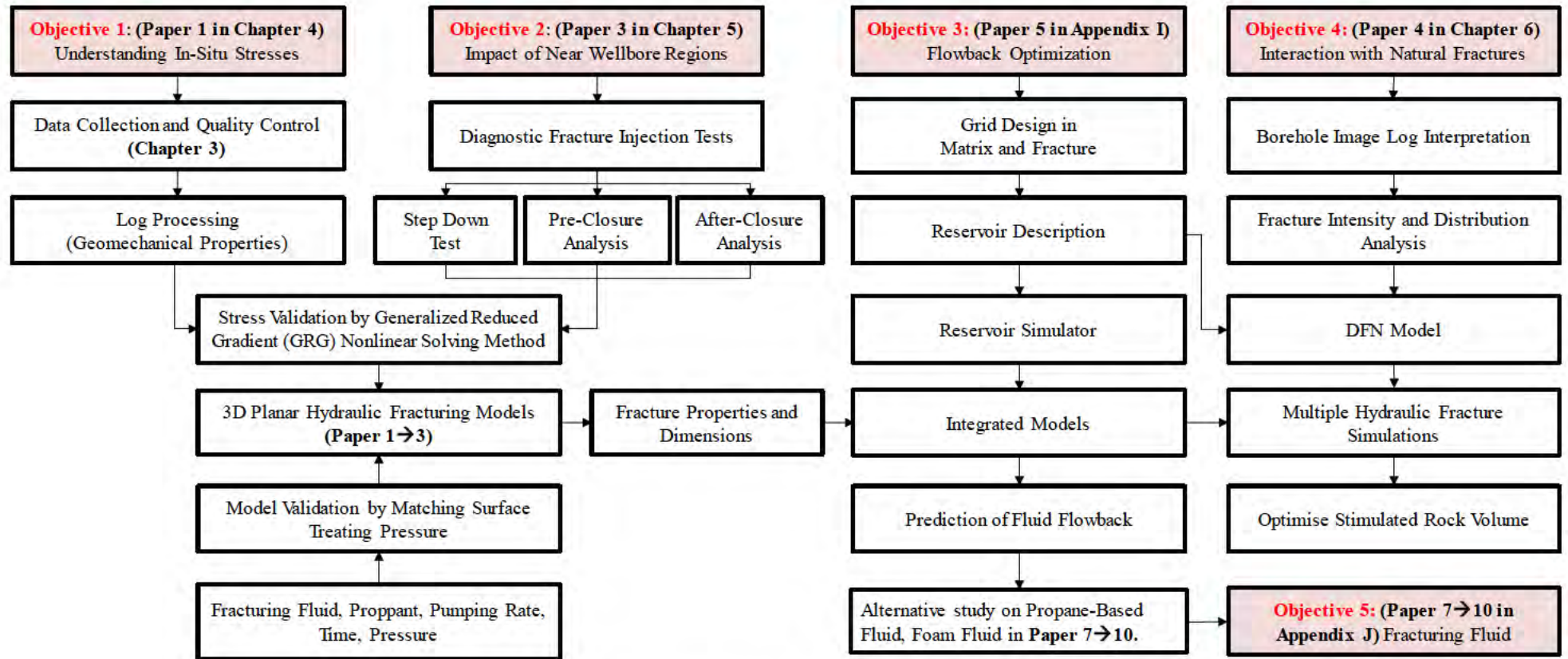


Figure 1-12 : Workflow diagram for the integrated simulation study.

1.10 Thesis Structure

The following is a brief summary of the thesis chapters.

Chapter 2 explores the overview of mathematical modelling of hydraulic fracturing starting with the history of modelling. The required equations of elasticity, fluid flow and material balance are derived for 3D modelling. The comparison between 2D, 3D planar and non-planar 3D hydraulic fracturing models is also discussed.

Chapter 3 reviews the input data which are required in this research and provides an overview of the quality and limitations of the dataset from the Cowralli Field, Cooper Basin.

Chapter 4 provides insight into the mechanical earth model and its application to generate reliable stress data. The highlight of this chapter is the simultaneous methods which are used to solve the minimum horizontal stress, maximum horizontal stress and tectonic strains to build the 1D MEM. This chapter uses the Cowralli Field as a case study to provide the optimum well trajectory to intersect the maximum number of pre-existing natural fractures that would likely improve the stimulated rock volume and result in more efficient hydrocarbon production.

Chapter 5 presents the results from pressure diagnostic tests data analysis. The step down test indicates friction loss in the near wellbore regions while pre-closure analysis provides the leak-off characteristic that can be used to detect pre-existing natural fracture. The resulting closure pressure can be used for in-situ stress validation. Finally, after closure analysis gives the reservoir parameters such as reservoir pressure and transmissibility. The results show that the near wellbore pressure loss impacts the fracture length and fracture pressure distribution, which has a strong influence on the recovery of fracturing fluid.

Chapter 6 investigates the effectiveness of hydraulic fracture interactions with pre-existing natural fractures by integrating a calibrated mechanical earth model with a discrete fracture network model to simulate hydraulic fracture treatments under an alternating (compressional and strike-slip) stress regime in both a vertical and inclined well. The trajectory of the inclined well was optimised to intersect the largest number of pre-existing natural fractures. The chapter provides a methodology that can be implemented to improve the stimulated rock volume in tight reservoir with pre-existing natural fractures.

Chapter 7 shows the application of optimised 3D hydraulic fracturing design in a horizontal well with multiple stages. Several scenarios were simulated with changing well length, stage spacing, and the number of stages to compare the stimulated rock volume and hydrocarbon productivity.

Chapter 8 summarises the findings in this thesis with several conclusive remarks.

Chapter 2 : Mathematical Modelling of Hydraulic Fracturing

2.1 Overview

Hydraulic fracturing is a multi-physics problem that involves the following mechanisms:

1. Fluid flow from wellhead through wellbore, perforations, and the formation.
2. Failure (Fracture initiation) of a saturated pore-elastic material (formation) which is under different principal stress regimes.
3. Fracture propagation in a pore-elastic material by the net pressure resulting from the fracturing fluid flow and in-situ stress.
4. Filtration of fracturing fluid from the induced fracture into the surrounding heterogamous formations.

Therefore, the mathematical modelling of hydraulic fracturing is developed by the coupling of following four equations:

1. Flow equation for power-law non-Newtonian fluid.
2. Failure criterion of pore-elastic material in a cylindrical geometry under in-situ far field stresses (Kirsch's equation ,1898).
3. The crack propagation equation developed for a semi-infinite pore-elastic material by combining of energy balance (Griffith ,1920) and fracture stress intensity (Irwin ,1957 and Sneddon,1973).
4. The equation for deep filtration of fracturing fluid through a fracture surface into the formation developed by Carter (1957).

2.2 History of Hydraulic Fracturing Models

The history of mathematical modelling of hydraulic fracturing started by Sack (1946) who derived a mathematical formulation for the centre of a crack in an infinite elastic medium and developed a model for opening a penny-shaped crack. The model does not take into account the volume of the crack or its geomechanical properties. Then, Sneddon (1946) introduced the net pressure and crack volume to the fracture propagation mathematics. Sneddon and Elliott (1946) further derived an equation to determine the fracture width by

using the solid mechanics. The fracture width was predicted based on the net pressure and fixed height with no leak-off.

Later, Khristianovic and Zheltov (1955) developed a two-dimensional (2D) model by analytical solution of vertical fracture propagation under the assumption of horizontal plane strain conditions. Later, Perkins and Kern (1961) developed a 2D model (PK model) using the Griffith-Sneddon approach in which two phenomena were involved: (1) the rupture of brittle and elastic material that related to a surface energy (Griffith, 1920); and (2) the solution of plane strain in elasticity equation (Sneddon, 1946). In the PK model, the width of the fracture does not vary in the vertical direction. Geertsma and De Klerk (1969) further developed the so-called 'KGD' model by considering the effect of fracture tip. The KGD model is also in two dimensions with fixed fracture height and constant flow rate in the fracture. Later, Nordgren (1972) developed the PKN model by considering fluid leak-off using mass balance that related the changing of flow rate in the fracture along the length.

To consider the fracture propagation in the vertical direction (fracture height), different models were developed based on elliptical shape along the fracture length. These models are called pseudo 3D models (P3D). These models can be classified into two categories: (1) cell-based models; and (2) lumped models.

Cell-based models are developed in a grid network of connected cells around the fracture. In this approach, Simonson et al. (1978) assumed symmetric layers while Fung et al. (1987) described asymmetric multilayers in the vertical direction. In the lumped models, Cleary (1980) developed the approach where the fracture growth was described by three points in three directions. Mack and Warpinski (2000) discussed P3D models in more detail for any arbitrary shape. They also discussed that fully coupling of elasticity with

fluid flow cannot be considered in P3D because of the lack of fluid flow in the vertical direction and 3D elasticity in the formation (Mendelsohn, 1984).

Barree (1983) described fluid pressure and flow velocity within a fracture in the 2D finite difference scheme that was associated with the viscous flow of parallel plates defined by the Navier-Stokes equations. Understanding the fluid viscosity, which creates the pressure distribution in the fracture, can help estimate the fracture width. In 1990, a true 3D model was developed based on planar fracture, which is known as PL3D. The governing equations of PL3D will be discussed in detail in the next section. The limitation of PL3D has been described by Li et al. (2015). They mentioned that PL3D cannot simulate out of plane regions, and does not consider: (1) the complexity of stress; (2) anisotropy of rocks in the fracture propagation; (3) fracture reorientation in any direction of the rock fabric; and (4) presence of pre-existing natural fractures. This problem can be addressed by using non-planar 3D models which also includes the interaction of pre-existing natural fracture with hydraulic fracture propagation and the resulting equations are generally solved by finite element method (FEM). Yamamoto et al. (1999) developed a non-planar 3D model based on the concept of the Displacement Discontinuity Method to simulate the complex fractures. The overview of the history of hydraulic fracturing modelling is shown in Figure 2-1.

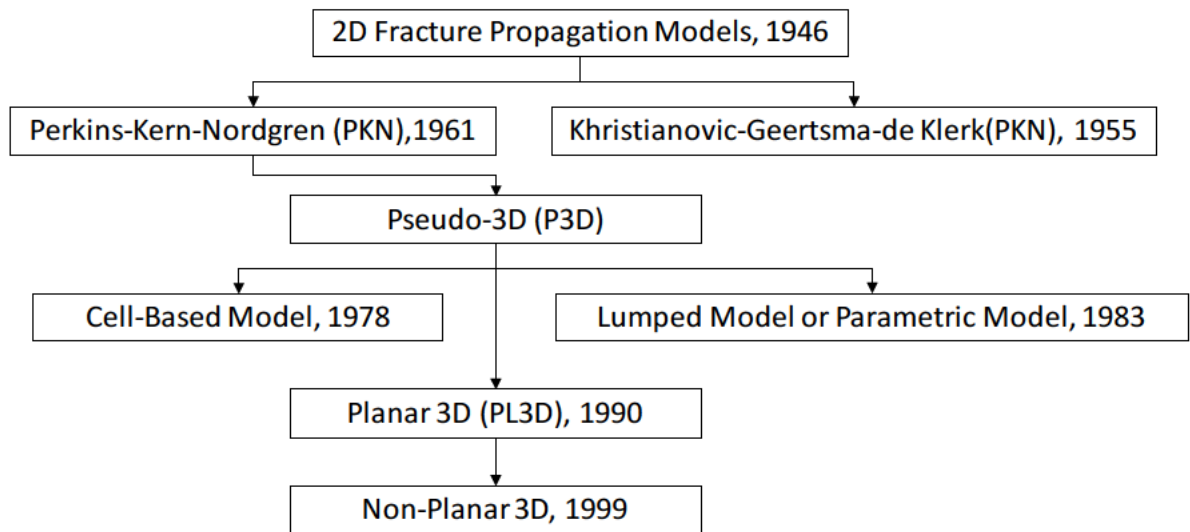


Figure 2-1 : The history of hydraulic fracturing models.

2.3 Mathematical Formulation Based on Fracture Mechanic Concept

The equation for fracture propagation started with two-dimensional crack problem developed by Griffith (1920). In that model, the fracture (crack) is assumed as a line in an infinite plane surface. He found that when load is applied constantly, the material fails and the crack will propagate as a line according to the energy balance equation in Equation 2-1, where U_E is potential energy, U_S is surface energy and W_L is external work.

$$U_E + U_S - W_L = 0 \quad \text{Equation 2-1}$$

The derivative of the above equation with respect to crack line (c) is in Equation 2-2.

$$\frac{\partial U_S}{\partial c} = \frac{\partial U_E}{\partial c} \quad \text{Equation 2-2}$$

Based on Equation 2-2, the rate of change of potential energy (strain energy release) is equal to the change of surface energy from the creation of two new incremental crack surfaces, which dissipate surface energy. The potential energy in an elastic material during deformation is the integration of the stress-strain function (Figure 2-2) and the relationship between stress and strain is shown in Equation 2-3.

$$\int \sigma d\varepsilon = \frac{1}{2} \sigma \varepsilon^2 \quad \text{Equation 2-3}$$

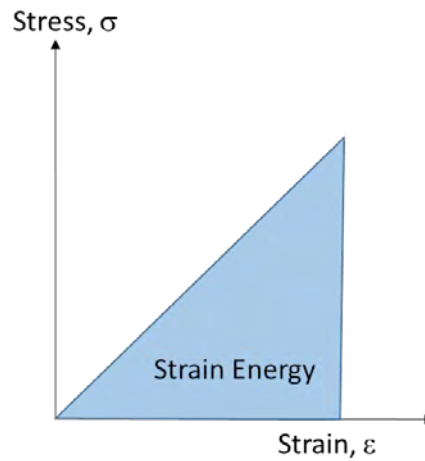


Figure 2-2 : Strain energy from stress-strain plot

Replacing ε with σ/E in Equation 2-3 results in Equation 2-4.

$$E = \frac{\sigma}{\varepsilon} \quad \text{Equation 2-4}$$

Therefore, the potential Energy per unit volume (u) defines in Equation 2-5

$$\int \sigma d\varepsilon = \frac{\sigma^2}{2E} \quad \text{Equation 2-5}$$

- As an example, the derivation of the required applied stress for fracture propagation in an elliptical surface is shown below.

$$u_E = \frac{\sigma^2}{2E} V - \frac{\sigma^2}{2E} B\pi c^2 \quad \text{Equation 2-6}$$

Where c is half of crack length and B is the fracture thickness. The surface energy for creation of two crack is shown in Equation 2-7, where γ_s is the surface energy per unit surface.

$$u_s = 2\gamma_s cB \quad \text{Equation 2-7}$$

Therefore, the total energy in the system will be the summation of Equation 2-6 and Equation 2-7 which is shown in Equation 2-8.

$$E_t = 2\gamma_s cB + \frac{\sigma^2}{2E}V - \frac{\sigma^2}{2E}B\pi c^2 \quad \text{Equation 2-8}$$

Based on Gibbs free energy concept, the change of energy in a system at equilibrium condition should be minimum, therefore the derivative of Equation 2-8 should be equal to zero (Equation 2-9).

$$\frac{dE_t}{dc} = 2\gamma_s B - \frac{\sigma^2}{E}B\pi c = 0 \quad \text{Equation 2-9}$$

From Equation 2-9, the required stress for the fracture propagation (σ_f) can be estimated and is shown in Equation 2-10.

$$\sigma_f = \sqrt{\frac{2\gamma_s E}{\pi a}} \quad \text{Equation 2-10}$$

Later, Erwin (1946) extended Griffith's concept for the plasticity at the tip of a fracture. The surface energy $2\gamma_s$ in brittle materials is replaced by G_c (Equation 2-11) and for ductile materials is replaced by $2(\gamma_s + \gamma_p)$, where γ_p is the plastic deformation energy or energy dissipation. Therefore, giving us:

$$G_c = 2(\gamma_s + \gamma_p) \quad \text{Equation 2-11}$$

$$\sigma_f = \sqrt{\frac{G_c E}{\pi a}} \quad \text{Equation 2-12}$$

Since the stress intensity factor for a penny shape crack is $K = \sigma\sqrt{\pi a}$ and the critical stress intensity factor for fracture propagation is K_c (fracture toughness), we have Equation 2-13.

$$K_c = \sigma_f \sqrt{\pi a} \quad \text{Equation 2-13}$$

Therefore, σ_f in Equation 2-12 is substituted into Equation 2-13, giving Equation 2-14 which will be derived for the fracture toughness in an elliptical fracture surface.

$$K_c = \sqrt{EG_c} \quad \text{Equation 2-14}$$

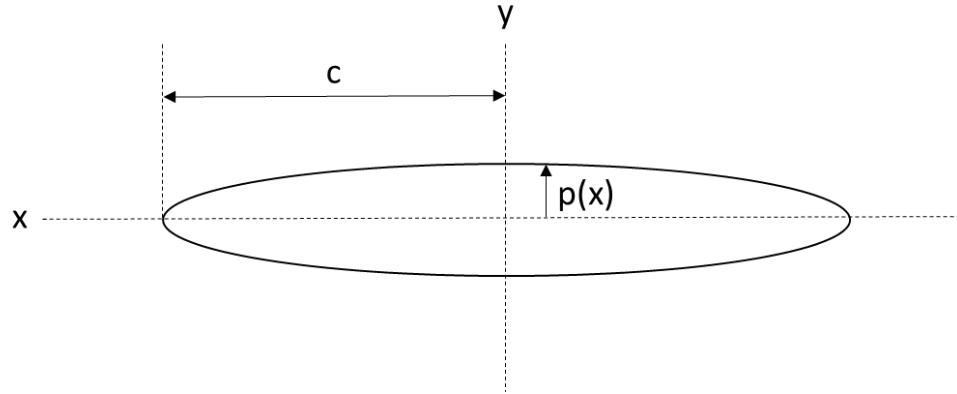


Figure 2-3 : The line crack of a pressurized plane (Sneddon, 1973).

For modelling of hydraulic fracturing, Sneddon (1973) used Griffith's concept and assumed symmetric pressure $p(x)$ in an x - y plane (Figure 2-3). This can be described in the half plane when the crack length c is related to $|x| \leq c, y = 0$, and the boundary conditions can be expressed when $y = 0$ (Equation 2-15 to Equation 2-17).

$$\sigma_{yy}(x, 0) = -p(x), \quad 0 \leq x \leq c, \quad \text{Equation 2-15}$$

$$u_y(x, 0) = 0, \quad x > c, \quad \text{Equation 2-16}$$

$$\sigma_{xy}(x, 0) = 0, \quad x \geq 0, \quad \text{Equation 2-17}$$

The fracture width as a function of fracture length is dependent on the constant pressure acting along the line crack (Equation 2-18).

$$w(x) = \frac{4p_0}{E'} \sqrt{c^2 - x^2} \quad \text{Equation 2-18}$$

The maximum width (w_0) in the middle of Figure 2-3 ($x=0$) is shown in Equation 2-19.

$$w_0 = \frac{4cp_0}{E'} \quad \text{Equation 2-19}$$

2.4 Mathematical for 3D Planar Fracture Propagation

The modelling of a 3D planar fracture relies on the coupling of linear elastic fracture mechanics (LEFM), fracturing fluid flow and the continuity equation. The model assumes that the fracture plane is oriented perpendicular to the far field minimum horizontal stress. The fracture is assumed to be grown in one direction only and is symmetrical. The fracture is defined by its width and shape at periphery which depend on the elapsed injection time.

2.4.1 Elasticity

For fracture propagation in 3D planar surface, the displacement of semi-infinite half space under the force (P) acting on the boundary plane ($z = 0$) was used (Boussinesq 1885).

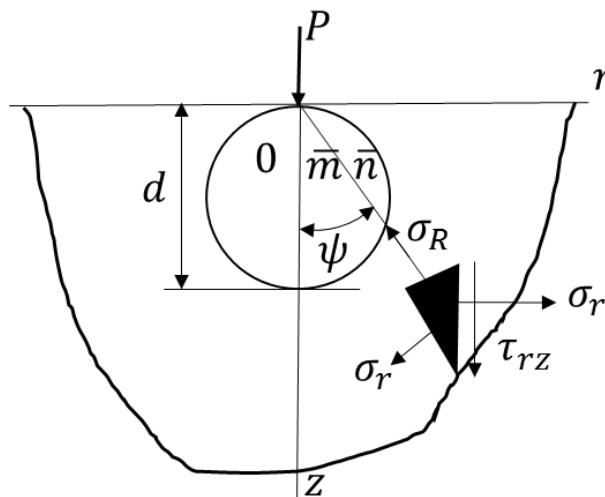


Figure 2-4 : Force on boundary of a semi-infinite body (Timoshenko and Goodie, 1951).

Figure 2-4 shows the stress distribution on a semi-infinite body on the polar coordinates.

Three stresses components in a cylindrical coordinate are radial stress (σ_r), tangential stress (σ_θ) and the z-axis stress (σ_z) (Equation 2-20 to Equation 2-22). The shearing stress (τ_{rz}) can be calculated at any location along the radial boundary (r) and in the vertical z-axis direction (z) (Equation 2-23) (Timoshenko and Goodie, 1951).

$$\sigma_r = \frac{P}{2\pi} \left\{ (1 - 2\nu) \left[\frac{1}{r^2} - \frac{z}{r^2} (r^2 + z^2)^{-\frac{1}{2}} \right] - 3r^2 z (r^2 + z^2)^{-\frac{5}{2}} \right\} \quad \text{Equation 2-20}$$

$$\sigma_\theta = \frac{P}{2\pi} (1 - 2\nu) \left\{ -\frac{1}{r^2} + \frac{z}{r^2} (r^2 + z^2)^{-\frac{1}{2}} - z (r^2 + z^2)^{-\frac{3}{2}} \right\} \quad \text{Equation 2-21}$$

$$\sigma_z = -\frac{3P}{2\pi} z^3 (r^2 + z^2)^{-\frac{5}{2}} \quad \text{Equation 2-22}$$

$$\tau_{rz} = -\frac{3P}{2\pi} r z^2 (r^2 + z^2)^{-\frac{5}{2}} \quad \text{Equation 2-23}$$

The ratio between the vertical z-axis and the shearing stress is shown in Equation 2-24.

$$\frac{\sigma_z}{\tau_{rz}} = \frac{z}{r} \quad \text{Equation 2-24}$$

The resultant stress (S) direction acted upon by the load through the origin, can be diminished with the inverse square of distance from the boundary z-plane (Equation 2-25).

$$S = \sqrt{\sigma_z^2 - \tau_{rz}^2} = \frac{3P}{2\pi} \frac{z^2}{(r^2 + z^2)^2} = \frac{3P}{2\pi} \frac{\cos^2 \psi}{(r^2 + z^2)} \quad \text{Equation 2-25}$$

In Figure 2-4, the sphere shows that the total stress on the horizontal plane can be expressed by Equation 2-26 and Equation 2-27 by substituting r and z in Equation 2-25 with the diameter (d) and tangent (ψ), respectively.

$$r^2 + z^2 = d^2 \cos^2 \psi \quad \text{Equation 2-26}$$

$$\sigma_{horizontal} = \frac{3P}{2\pi} \frac{\cos^2 \psi}{(d^2 \cos^2 \psi)} = \frac{3P}{2\pi d^2} \quad \text{Equation 2-27}$$

The lateral displacement (u) can be expressed in terms of the relationship between the

tangential elongation (ϵ_θ) and the semi-infinite radial boundary (r), which is related to all stresses and Poisson's ratio and Young's modulus, as shown in Equation 2-28.

$$u = \epsilon_\theta r = \frac{r}{E} [\sigma_\theta - \nu(\sigma_r - \sigma_z)] \quad \text{Equation 2-28}$$

Substituting Equation 2-20 through Equation 2-22 into Equation 2-28 allows us to determine the lateral displacement when considering the component of the z-direction force on the hemispherical surface (Equation 2-29 and Equation 2-30)

$$u = \frac{r}{E} \left[\frac{P}{2\pi} (1 - 2\nu) \left\{ -\frac{1}{r^2} + \frac{z}{r^2} (r^2 + z^2)^{-\frac{1}{2}} - z(r^2 + z^2)^{-\frac{3}{2}} \right\} \right. \\ \left. - \nu \left(\frac{P}{2\pi} \left\{ (1 - 2\nu) \left[\frac{1}{r^2} - \frac{z}{r^2} (r^2 + z^2)^{-\frac{1}{2}} \right] \right. \right. \right. \right. \\ \left. \left. \left. - 3r^2 z (r^2 + z^2)^{-\frac{5}{2}} \right\} + \frac{3P}{2\pi} z^3 (r^2 + z^2)^{-\frac{5}{2}} \right) \right] \quad \text{Equation 2-29}$$

$$u = \frac{(1 - 2\nu)(1 + \nu)P}{2\pi E r} \left[z(r^2 + z^2)^{-\frac{1}{2}} - 1 + \frac{1}{(1 - 2\nu)} z r^2 (r^2 + z^2)^{-\frac{3}{2}} \right] \quad \text{Equation 2-30}$$

The change in vertical displacement (w) respect to z-axis and r -axis can be derived from 3D Hook's law in Equation 2-31 and Equation 2-32

$$\frac{\partial w}{\partial z} = \epsilon_z = \frac{1}{E} [\sigma_z - \nu(\sigma_r - \sigma_\theta)] \quad \text{Equation 2-31}$$

$$\frac{\partial w}{\partial r} = \gamma_{rz} = \frac{\partial u}{\partial z} = \frac{2(1 + \nu)\tau_{rz}}{E} - \frac{\partial u}{\partial z} \quad \text{Equation 2-32}$$

Similar in Equation 2-29, we substitute Equation 2-20 through to Equation 2-22 into Equation 2-31 and Equation 2-32.

$$\begin{aligned} \frac{\partial w}{\partial z} = & \frac{1}{E} \left[\left(-\frac{3P}{2\pi} z^3 (r^2 + z^2)^{-\frac{5}{2}} \right) \right. \\ & - \nu \left(\left(\frac{P}{2\pi} \left\{ (1 - 2\nu) \left[\frac{1}{r^2} - \frac{z}{r^2} (r^2 + z^2)^{-\frac{1}{2}} \right] \right. \right. \right. \\ & \left. \left. \left. - 3r^2 z (r^2 + z^2)^{-\frac{5}{2}} \right\} \right) \right) \\ & \left. - \left(\frac{P}{2\pi} (1 - 2\nu) \left\{ -\frac{1}{r^2} + \frac{z}{r^2} (r^2 + z^2)^{-\frac{1}{2}} - z (r^2 + z^2)^{-\frac{3}{2}} \right\} \right) \right] \end{aligned} \quad \text{Equation 2-33}$$

$$\frac{\partial w}{\partial z} = \frac{P}{2\pi E} \left\{ 3(1 + \nu)r^2 z (r^2 + z^2)^{-\frac{5}{2}} - [3 + \nu(1 + 2\nu)]z (r^2 + z^2)^{-\frac{5}{2}} \right\} \quad \text{Equation 2-34}$$

$$\frac{\partial w}{\partial r} = -\frac{P(1 + \nu)}{2\pi E} \left[2(1 - \nu)r (r^2 + z^2)^{-\frac{3}{2}} + 3rz^2 (r^2 + z^2)^{-\frac{5}{2}} \right] \quad \text{Equation 2-35}$$

Integration of Equation 2-34 and Equation 2-35, with respect to the z-direction and radius, removes the constant of integration result in Equation 2-36

$$w = \frac{P}{2\pi E} \left[(1 + \nu)z^2 (r^2 + z^2)^{-\frac{3}{2}} + 2(1 - \nu^2)(r^2 + z^2)^{-\frac{1}{2}} \right] \quad \text{Equation 2-36}$$

Finally, we calculate the lateral displacement and vertical displacement at the boundary at $z = 0$ by using Equation 2-30 and Equation 2-36 respectively.

$$(u)_{z=0} = -\frac{(1 - 2\nu)(1 + \nu)P}{2\pi E r} \quad \text{Equation 2-37}$$

$$(w)_{z=0} = \frac{P(1 - \nu^2)}{\pi E r} \quad \text{Equation 2-38}$$

The next step, considering the load distribution over the semi-infinite body in Figure 2-5, the force, or pressure (P), on the point M with radius r , is represented by the changing angle $d\psi$ and radii (r) of the small element.

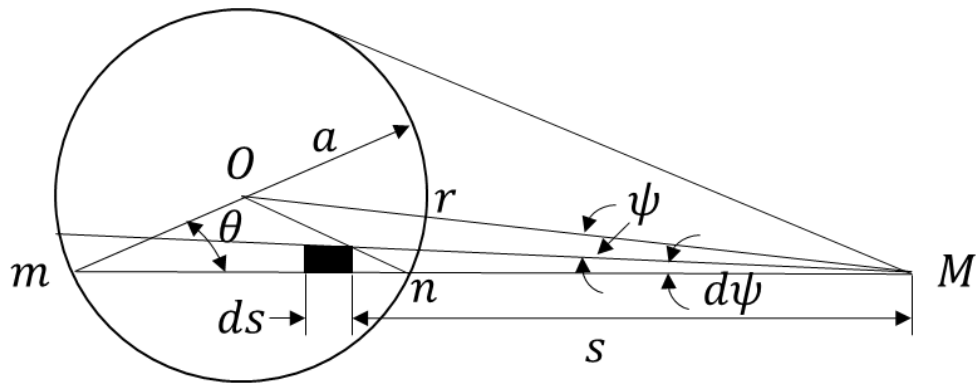


Figure 2-5 : Load distribution over the semi-infinite body (Timoshenko and Goodie, 1951).

Equation 2-39 defines the surface area of the total deflection by double integration with respect to the angle and radius as shown below.

$$w = \frac{(1 - \nu^2)P_{net}}{\pi E} \iint d\psi ds \quad \text{Equation 2-39}$$

$$w = \frac{(1 - \nu^2)P_{net}}{\pi E} \int_0^{2\pi} \int_0^r d\psi ds \quad \text{Equation 2-40}$$

$$w = \frac{2(1 - \nu^2)P_{net}r}{E} \quad \text{Equation 2-41}$$

Equation 2-41 is the edge of the loading area, and is comparable to Sneddon's equations and is used in Perkins-Kern-Nordgren (PKN) and Khristianovich-Geertsma-DeKlerk (KGD) models in the 2D geometry as shown in Figure 2-6.

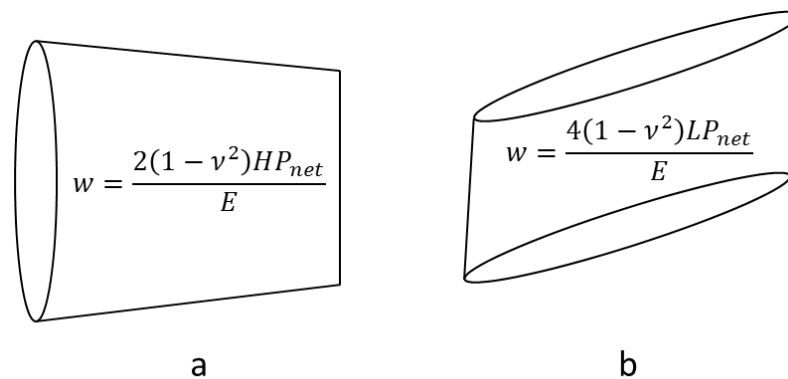


Figure 2-6 : Analytical fracture model solution for: (a) PKN; and (b) KGD models.

For the case with variable net pressure, based on Equation 2-39, the change of fracture width with respect to the accumulative net pressure can be derived (Equation 2-42)

$$\frac{\partial w}{\partial P} = \iint \frac{(1 - \nu^2)}{\pi E} d\psi ds \quad \text{Equation 2-42}$$

Where the change of pressure is the result of the pressure of fluid inside the fracture subtracted from the closure pressure or minimum horizontal stress magnitude.

2.4.2 Fluid Flow

The basic principle of fluid flow motion has been described by the Navier-Stokes equations. Navier-Stokes equation is basically a momentum balance equation derived from Newton's second law under the assumption of diffusing viscous fluid which is time dependent of the gradient of velocity proportional to the sum of the forces as shown in the equations below.

$$-\nabla p = \rho \frac{\partial u}{\partial t} + \rho u \cdot \nabla u \quad \text{Equation 2-43}$$

$$\mu \frac{\partial^2 u}{\partial x^2} + \mu \frac{\partial^2 u}{\partial y^2} + \mu \frac{\partial^2 u}{\partial z^2} - \nabla p = \rho \frac{du}{dt} + \rho u \cdot \nabla v \quad \text{Equation 2-44}$$

$$\mu(\nabla \cdot \nabla)u - \nabla p = \mu(\nabla^2)u - \nabla p = \rho \frac{du}{dt} + \rho u \cdot \nabla v \quad \text{Equation 2-45}$$

The summation of the total force is divided by density (ρ) as shown in Equation 2-46.

$$\frac{\partial u}{\partial t} + u \cdot \nabla u = \frac{\mu}{\rho} (\nabla^2)u - \frac{1}{\rho} \nabla p \quad \text{Equation 2-46}$$

The Navier-Stokes equation between two parallel plate (as a geometry for fracture) for steady state flow results in Equation 2-47.

$$0 = -\frac{1}{\rho} \frac{\partial p}{\partial x} + \frac{\mu}{\rho} \frac{\partial^2 u}{\partial y^2} \quad \text{Equation 2-47}$$

Assuming constant fluid density, the above equation gives Equation 2-48 and Equation 2-49.

$$0 = -\frac{\partial p}{\partial x} + \mu \frac{\partial^2 u}{\partial y^2} \quad \text{Equation 2-48}$$

$$\frac{\partial^2 u}{\partial y^2} = \frac{1}{\mu} \frac{\partial p}{\partial x} \quad \text{Equation 2-49}$$

The assumption has been set by using infinite plates between two boundaries and fluid flow symmetry around $y = 0$ as shown in Figure 2-7.

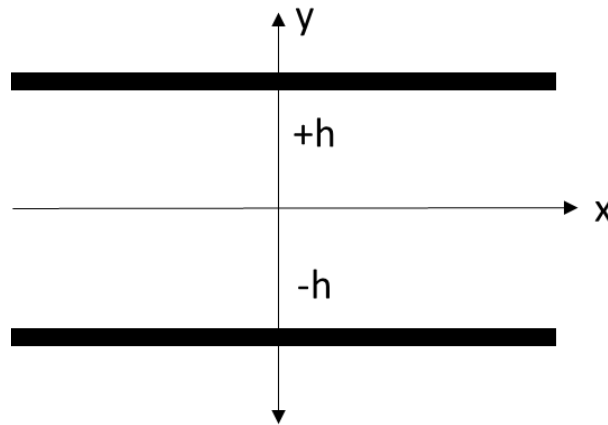


Figure 2-7 : Poiseuille flow between parallel plates.

In order to solve the flow velocity (u), double integration will be applied in Equation 2-49.

$$\frac{\partial u}{\partial y} = \frac{1}{\mu} \frac{\partial p}{\partial x} y + C_1 \quad \text{Equation 2-50}$$

$$u = \frac{1}{2\mu} \frac{\partial p}{\partial x} y^2 + C_1 y + C_2 \quad \text{Equation 2-51}$$

Two boundary conditions are set for no slip and no plate movement. This implies that the velocity at the boundary plate is 0 as shown below.

$$y = h, \quad u = 0 \quad \text{Equation 2-52}$$

$$y = -h, \quad u = 0 \quad \text{Equation 2-53}$$

Substituting Equation 2-52 and Equation 2-53 into Equation 2-51 gives the following.

$$0 = \frac{1}{2\mu} \frac{\partial p}{\partial x} h^2 + C_1 h + C_2 \quad \text{Equation 2-54}$$

$$0 = \frac{1}{2\mu} \frac{\partial p}{\partial x} h^2 - C_1 h + C_2 \quad \text{Equation 2-55}$$

Adding the two boundary conditions together allows us to solve the C_1 and C_2 parameters.

$$0 = \frac{1}{\mu} \frac{\partial p}{\partial x} h^2 + 2C_2 \quad \text{Equation 2-56}$$

$$C_2 = -\frac{1}{2\mu} \frac{\partial p}{\partial x} h^2 \quad \text{Equation 2-57}$$

$$0 = \frac{1}{2\mu} \frac{\partial p}{\partial x} h^2 - \frac{1}{2\mu} \frac{\partial p}{\partial x} h^2 - C_1 h \quad \text{Equation 2-58}$$

$$C_1 = 0, \quad u = \frac{1}{2\mu} \frac{\partial p}{\partial x} y^2 - \frac{1}{2\mu} \frac{\partial p}{\partial x} h^2 \quad \text{Equation 2-59}$$

The final form can be simplified to Equation 2-60.

$$u = \frac{1}{2\mu} \frac{\partial p}{\partial x} (y^2 - h^2) \quad \text{Equation 2-60}$$

The conservation of mass in 1D for an incompressible fluid is shown in Figure 2-8.

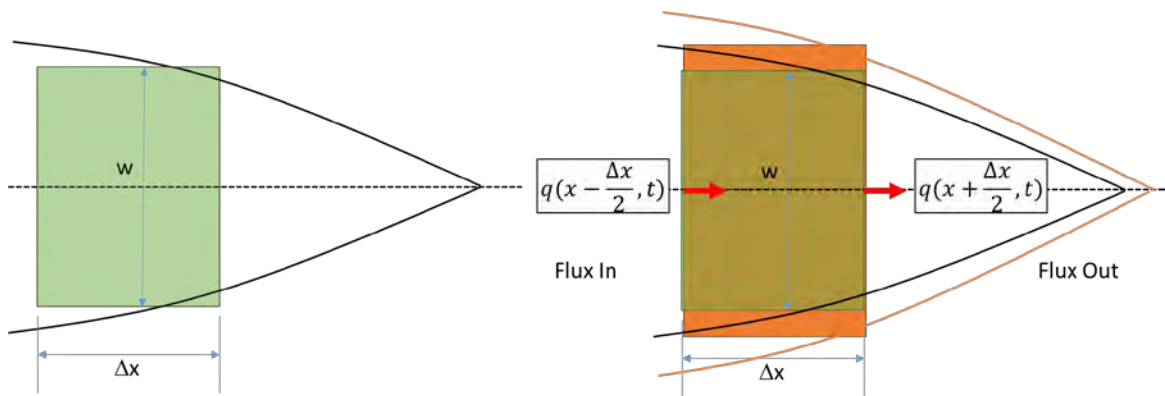


Figure 2-8 : Mass Conservation in 1D of hydraulic fracturing.

Total change in area per unit time is equal to the flux in minus flux out as it is shown in Figure 2-8 and in Equation 2-61 and Equation 2-62.

$$\frac{\Delta w \Delta x}{\Delta t} = q\left(x - \frac{\Delta x}{2}, t\right) - q\left(x + \frac{\Delta x}{2}, t\right) \quad \text{Equation 2-61}$$

$$\frac{\partial w(x, t)}{\partial t} = -\frac{\partial q(x, t)}{\partial x} \quad \text{Equation 2-62}$$

Based on the laminar fluid flow assumption in Equation 2-60, the flux has been integrated with respect to velocity in the y direction. Assuming that the velocity has become zero and the pressure gradient is infinite at the tip, velocity equation is derived called Poiseuille equation (Equation 2-63) as shown in Figure 2-9.

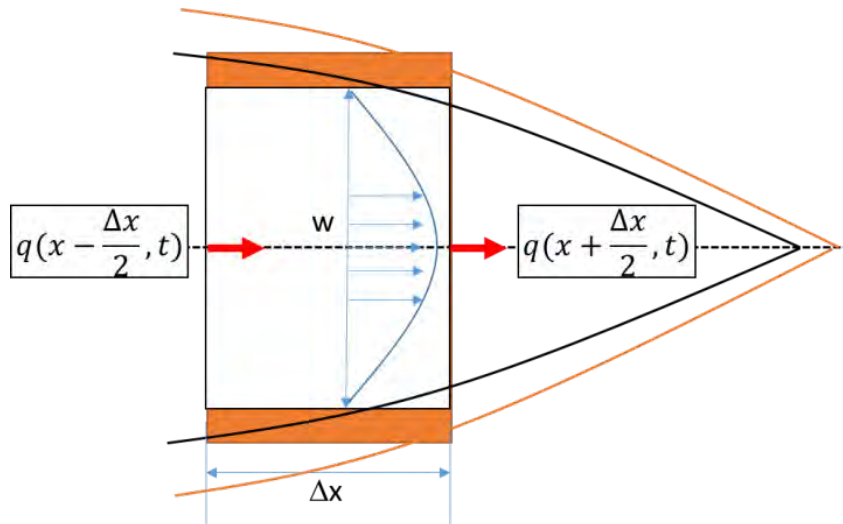


Figure 2-9 : Laminar fluid flow (Poiseuille) in the fracture.

$$v_x = -\frac{1}{2\mu} \frac{\partial p}{\partial x} \left(\frac{w^2}{4} - y^2 \right) \quad \text{Equation 2-63}$$

The total volumetric flux through the fracture can be determined by integrating the velocity across the fracture from $y = 0$ and $y = h$, shown in Equation 2-64. This equation is derived from Navier-Stokes equation and is for Newtonian fluid. In order to extend this equation

for non-Newtonian equation, the term viscosity (μ) is replaced by (μ'), which results in Equation 2-65 (Reynolds lubrication equation).

$$q(x, t) = -\frac{w^3}{12\mu} \frac{\partial p}{\partial x} \quad \text{Equation 2-64}$$

$$\frac{\partial w}{\partial t} = \frac{\partial}{\partial x} \left(\frac{w^3}{\mu'} \frac{\partial p}{\partial x} \right) \quad \text{Equation 2-65}$$

There are several types of fluid systems and the most conventional fracturing fluid is cross-linked gel with the rheology parameters obtained from a sample in the lab (Figure 2-10).

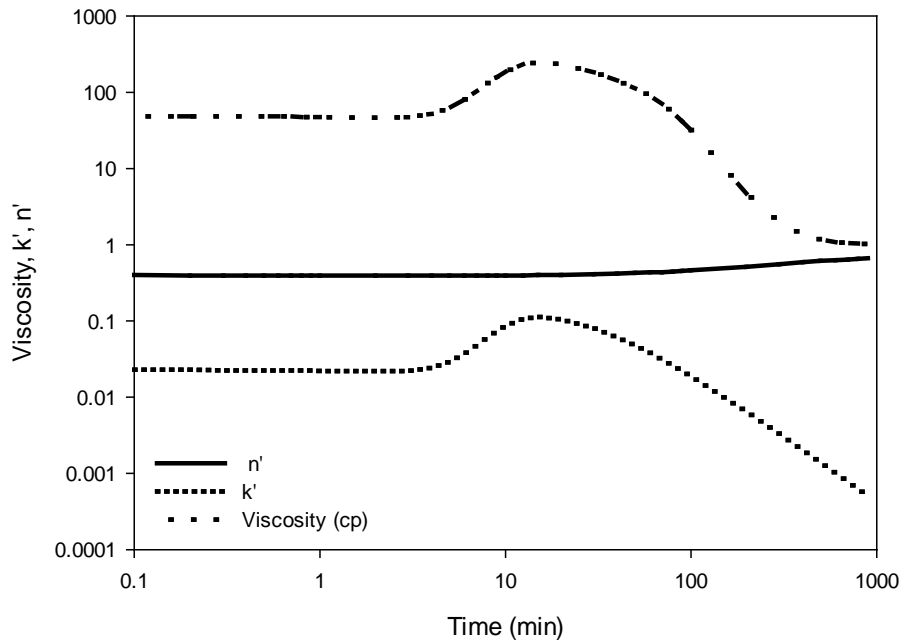


Figure 2-10 : Non-Newtonian fracturing fluid rheology.

The Non-Newtonian fluid contains a time dependent viscosity that is associated with shear rate. There are two primary parameters, flow behaviour index (n') and consistency index (k' , $\text{lbfsec}^{n'}/\text{ft}^2$), that relate to apparent viscosity (μ_{app} , cp) and shear rate ($\dot{\gamma}$, sec^{-1}). This can be expressed in the power law equation.

$$\mu_{app} = \frac{48000k'}{\dot{\gamma}^{1-n'}} \quad \text{Equation 2-66}$$

If n' is less than 1 then this fluid is a typical Non-Newtonian fracturing fluid and the apparent viscosity decreases with increasing shear rate. During fluid pumping through the target formation the fluid rheology must be determined and updated. The apparent viscosity will change in each time step. This updated viscosity data will be used in the workflow.

For slurry flow, the Stokes's equation has been used as a simple proppant transport models (Blyton et al., 2015).

$$V_s = \frac{2(\rho_p - \rho_f)}{36\mu} gD^2 \quad \text{Equation 2-67}$$

Where,

V_s = Settling velocity (m/s)

ρ_p = Proppant density (kg/m³)

ρ_f = Fluid density (kg/m³)

g = Gravitational acceleration (9.81 m/s²)

D = Diameter of the proppant (m)

2.4.3 Leak-Off

During injection of fracturing fluid, there is usually some fluid leak-off to the surrounding formations. The equation for deep filtration of fracturing fluid through formation developed by Carter (1957). He assumed the area of fracture surface is based on uniform fracture width where the fluid flow is perpendicular to the fracture face. He developed an analytical model for leak-off velocity (u_L) from the fracture which is related to the leak-off coefficient (C_L) and the leak-off time different between the current time (t) and the time

when the exposure occurs during the crack initiation (t_{exp}). (Equation 2-68).

$$u_L = \frac{C_L}{\sqrt{t - t_{exp}}} \quad \text{Equation 2-68}$$

The basic principle of the mass balance equation from the Carter equations is that the injection rate (q_i) is equal to the summation of the leak-off rate over the fracture propagation (q_L) and the volume rate (q_f).

$$q_i = q_L + q_f \quad \text{Equation 2-69}$$

In Carter's model, it is assumed that the leak-off from two fracture faces is the integration of leak-off velocity respect to fracture area (A_f) and the fracture rate is based on constant of fracture width (\bar{w}) and only the fracture area is changing overtime (Equation 2-70)

$$q_i = 2 \int_0^{A_f(t)} u_L dA_f + \bar{w} \frac{\partial A_f}{\partial t} \quad \text{Equation 2-70}$$

Since both fracture width and fracture height are assumed to be constant, the model is in one dimension and has a limited application for the fracture geometry when fluid leak-off occurs in two dimensional flow patterns.

2.4.4 Coupling Schemes of Elasticity, Fluid Flow and Leak-Off

For coupling of elasticity with fluid flow and leak off, there are 3 sets of unknowns of the fluid pressure, fracture width and fracture front location or displacement to be considered. Figure 2-11 shows the workflow for coupling of elasticity, fluid flow and leak off equations for finite difference numerical modelling. In the workflow, the fluid apparent viscosity is calculated based on the rheology of the fracturing fluid properties. Then, fracture width will be estimated from the elasticity equation. In the next step, the corresponding transmissibility of fluid for each grid will be calculated based on fluid flow

equation and flow rate for each grid will be estimated. Subsequently, fluid leakoff will be calculated and fluid flow and pressure for each node will be determined. In the next step, the stress at the boundary is updated and the new fracture width and fluid pressure will be calculated. The algorithm will be continued iteratively until the fracture width and pressure converge.

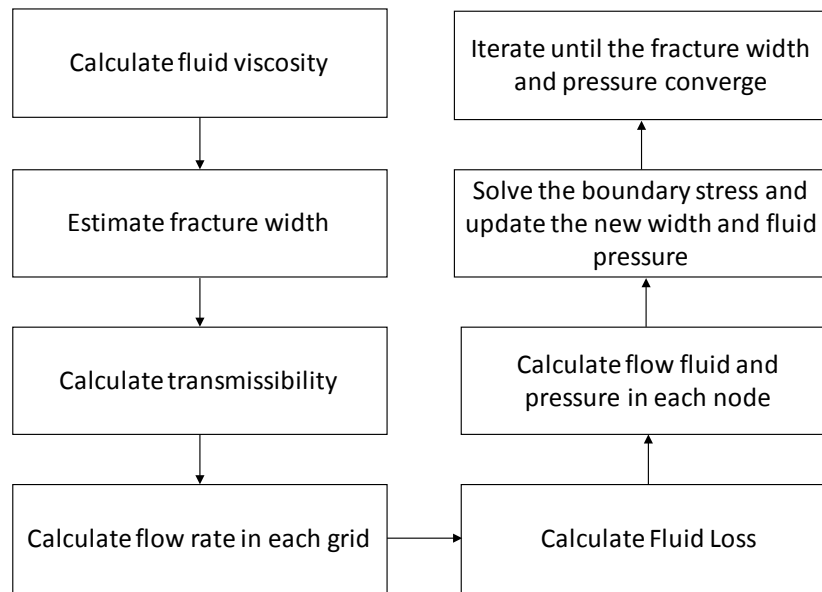


Figure 2-11 : Workflow diagram for coupling of elasticity, fluid flow and leak-off for 3D hydraulic fracturing model

2.4.5 Comparison of Hydraulic Fracturing Models

Figure 2-12 shows the results of various hydraulic fracturing models. Figure 2-12b shows the results of fracture height versus fracture length and fracture width distribution by colour scale for a fixed grid in planar 3D modelling. In this type of modelling, the fracture plane is discretised into a rectangular grid and the equations are solved by finite difference method to estimate by the iteration of the fracture width and fluid pressure in each node. Figure 2-12b also shows the fracture width profile which is determined by finite element method and the generation of triangular mesh in order to give a better resolution and more accurate results; however, the high amount of computation required for the 3D finite element method needs to be considered during the simulation. Figure 2-12c shows the

results of a Pseudo 3D model (P3D), that illustrates the simplified form of the model with non-linear partial differential equations and is solved by using integral methods. The simulated equations are similar to planar 3D hydraulic fracturing models that start with mass conservation during the injection of fracturing fluid, and use the continuity equation to balance the mass during the fluid injection and fluid leakoff area when the fracture width is changing. Disadvantages of P3D model are the inaccuracy of the equilibrium height growth and fracture length. (Dontsov and Peirce, 2015). The results of PKN and KGD models are shown in Figure 2-12d. The limitation requires fracture height to be fixed in order to calculate fracture width and pressure distribution along the fracture length. Planar 3D and P3D models can be used to calculate the fracture height as well.

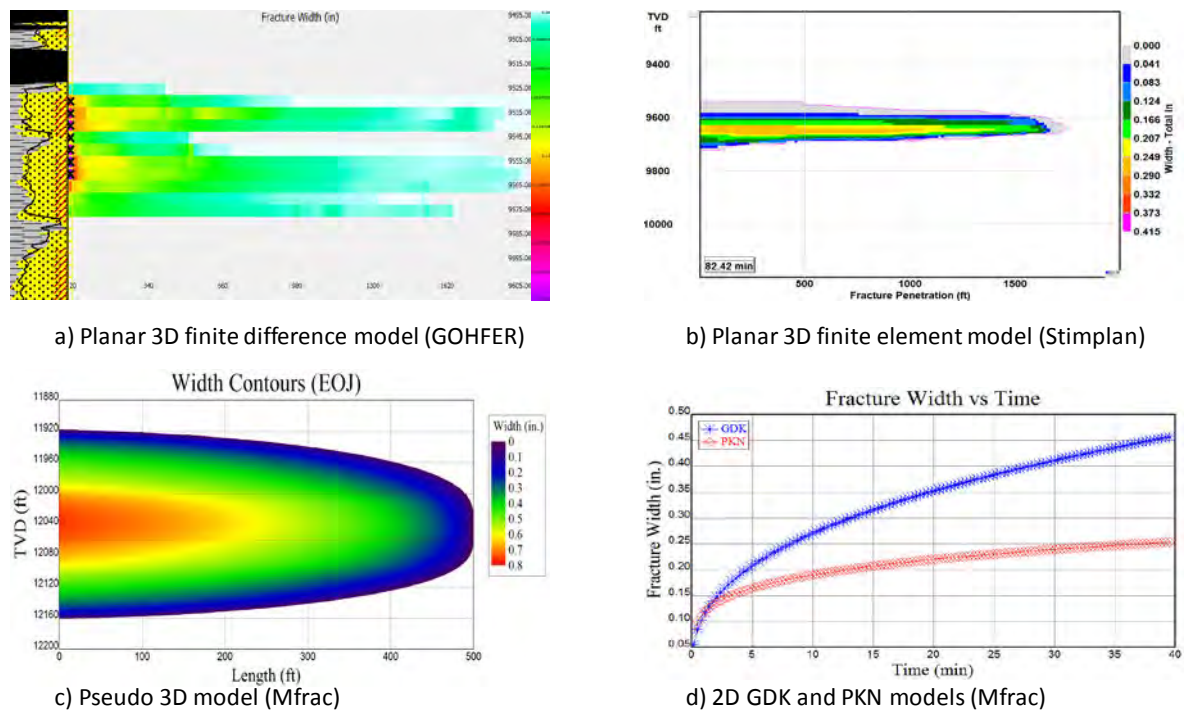


Figure 2-12 : Hydraulic fracturing models.

Warpinski et al. (1994) compared the model differences among PL3D commercial software such as FRACPRO, GOHFER, TRIFRAC, STIMPLAN, TERRAFRAC and MFRAC. The prediction results provided different fracture geometries according to stress and lithology. They concluded that it is not possible to determine which set of results

produced by these varying products has any advantages over each other. However, the models and predictions become more realistic and useful when the user better understands the rock physics, reservoir conditions and geological environment of the target zone.

2.5 Stress Shadowing and Fracture Interference

The concept of the stress shadowing in planar 3D hydraulic fracturing was defined by Barree (2015) as the force of stress that is transmitted to the surrounding rock due to stress and strain based on the linear elastic theory. Stress shadowing is important in spacing between different clusters of fractures in order to optimise the production of multi-stage hydraulic fracturing in horizontal wells in unconventional reservoirs. The high stress resulting from the stress shadowing creates interference between the two fractures. These can have an impact on the proppant transportation and how the fracture propagates, which can effect well productivity.

According to the undrained compaction in poroelastic materials which defined by Skempton's coefficient, the low permeability and overpressure in unconventional reservoirs can induce a stress field around the fracture. The stress interference relates to the distance from the fracture face (Z), net pressure (P), also the fracture width (w) and Young's Modulus (E). The characteristic of the fracture interference can be found during the injection and shut-in time until the closure pressure time. This is shown in Equation 2-71. Stress shadowing concepts is applied in some commercial software.

$$\sigma = \frac{3 \times 144 \times P}{2\pi Z^t} = \frac{wE}{12Z^t} \quad \text{Equation 2-71}$$

2.6 Non-Planar 3D Hydraulic Fracturing Model

Geological discontinuities, such as faults and bedding planes can significantly impact on fracture propagation. These discontinuities are not modelled in the 3D planar formulations. 2D non planar numerical models of HF and NF interaction have been simulated by Zhang

et al. (2009) based on the displacement discontinuity method (DDM). The infinite elastic medium has been used to determine the difference between normal stress and shear stress in each point of the fracture face, as shown in Equation 2-72 and Equation 2-73.

$$\sigma_n(x) - \sigma_n^\infty(x) = \int [G_{11}(x, s)w(s) + G_{12}(x, s)v(s)]ds \quad \text{Equation 2-72}$$

$$\tau(x) - \tau^\infty(x) = \int [G_{21}(x, s)w(s) + G_{22}(x, s)v(s)]ds \quad \text{Equation 2-73}$$

The recent model of Non-planar 3D hydraulic fracturing has been developed to include pre-existing natural fractures. By modifying the 2D displacement discontinuity method into 3D that computes the stress interference between the fractures when facing the pre-existing natural fracture (Kresse et al., 2013). According to Weng (2015), the hydraulic fracture (HF) propagation may interact with natural fractures (NF) in different scenarios such as: (1) HF directly crossing NF due to high stress; (2) HF arrested at NF due to interface failed in shear and slips; and (3) HF crossing with the an offset due to localized interface separation and shear slip at the point where the HF intersects the NF, which shifts the stress concentration away from the intersection (4) HF is branching at the intersection of NF because high fluid pressure exceeds closure pressure (5) HF is branching at the end of the NF or T-shape branch due to the fracture either turns itself to align with the preferred fracture direction (6) NF dilation due to shear slippage (Weng, 2015). These scenarios are shown in Figure 2-13.

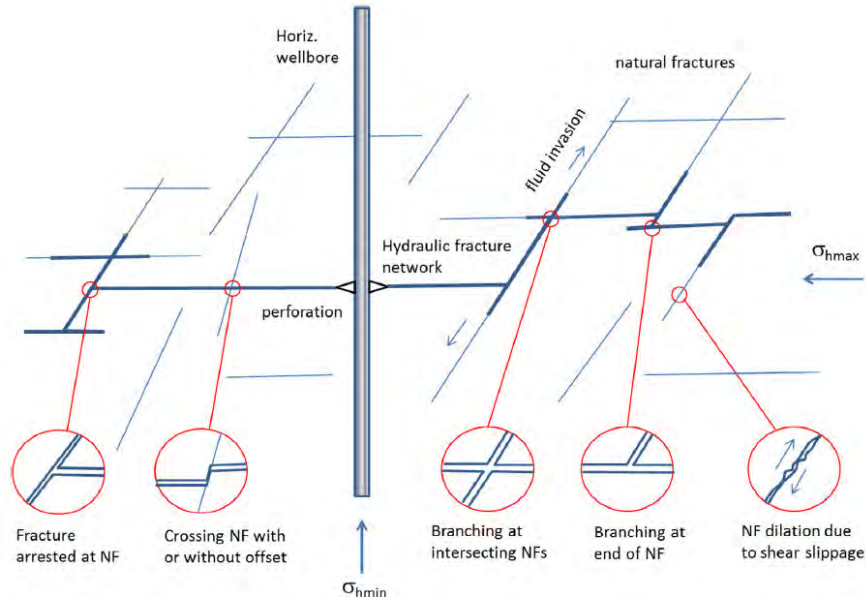


Figure 2-13 : Hydraulic fracture propagation interaction with pre-existing natural fracture (Weng, 2015).

The criteria for each above scenario are discussed by Gu et al. (2012). The shear dilation of a fracture can be modelled by the mass conservation which is shown in Equation 2-74, with the aperture of closed fractures (ω). The shear slip of the interface is dilated by fluid flow in the fracture as shown in Equation 2-75.

$$\frac{\partial q}{\partial s} + \frac{\partial(w + \omega)}{\partial t} + q_L = 0 \quad \text{Equation 2-74}$$

$$\frac{\partial p}{\partial s} = -2k \left(\frac{4n + 2}{n} \right)^n \frac{q^n}{(w + \omega)^{2n+1}} \quad \text{Equation 2-75}$$

As a result of numerical simulation, the HF and NF interaction can be simulated based on the dimensionless stress contrast and injection rate.

The result of a non-planar fracture numerical simulation is shown in Figure 2-14 presenting fluid injection pressure profile in the fracture distance between 10, 20 and 40 m respectively. The impact of distance between HF results in changes of the direction and conductivity of the fracture within the distance of 10 m.

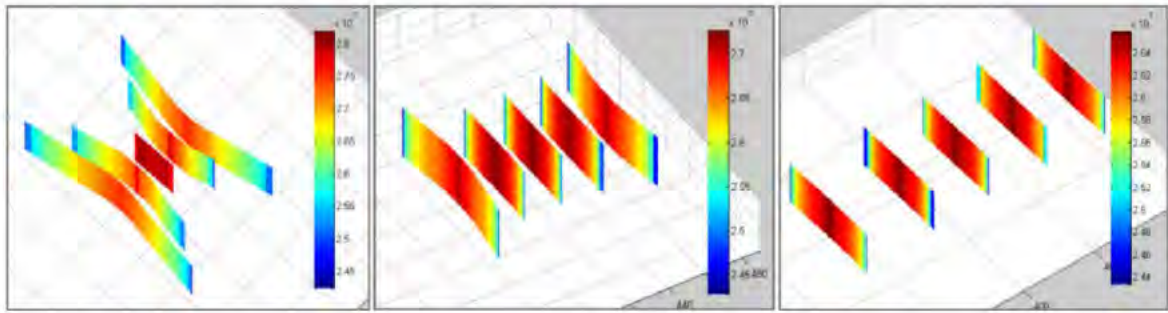


Figure 2-14 : Fluid injection pressure profile in the fracture distance between 10, 20 and 40 m respectively (Kresse et al., 2013).

Recently, the Boundary Element Method (BEM) and the Extended Finite Element Method (XFEM) have been developed in order to investigate the interaction of natural fractures and how they impact on the outcome of hydraulic fracturing (Areias and Belytschko, 2005). Mao (2011) has classified the advantages and limitations of four numerical methods (Table 2-1).

Table 2-1 : Advantages and limitations of numerical models for hydraulic fracturing simulation (Mao, 2011).

Model	Advantage	Limitation
Finite Difference Method	Simple because only mathematical equations are discretized.	Requires simple boundary conditions. May not accurately represent mechanical effects because the physical representation is not required at the element level.
Boundary Element Method	The solution beyond the fracture boundary is accurately represented.	Internal fracture shape is not evaluated and therefore the fracture development cannot be sensibly evaluated.
Finite Element Method	The solution inside the fracture boundary is accurately represented.	Solutions at the fracture boundary and beyond are approximately derived. The boundary conditions are difficult to determine.
Hybrid Boundary Element and Finite Element Methods	Solutions beyond the fracture boundary and at internal areas are accurately represented.	Requires more in-depth understanding of complex physical and mathematical processes.

2.7 Fracture Roughness

In hydraulic fracturing, fractures are created to provide a key pathway for fluid flow and mass transport. Although the experiments show that the induced fractures surfaces are not smooth, in hydraulic fracturing models, the effects of surface roughness are ignored. van

Dam and de Pater (2001) observed in field and lab tests that fracture surface roughness influences the mechanical and conductivity of fractures. A small displacement of opposing rough fracture surfaces relative to each other can cause imperfect closing, which leads to a residual width after closure. The root mean square (RMS) of fracture roughness has been used to measure the deviation of the roughness profile (A_{RMS}) from a centreline through a profile where the slope of the centreline is equal to the average slope of the roughness profile (\bar{m}) over a 1 cm interval. Equation 2-76 shows the equation of roughness profile.

$$\text{RMS Roughness} = \left[\frac{1}{n} \sum_{i=1}^n (y_{\text{profile},i} - y_{\text{centerline},i})^2 \right]^{\frac{1}{2}} \quad \text{Equation 2-76}$$

Where n indicates number of measured points and $y_{\text{profile},i}$ is the height of the measured profile at measuring point i. The average slope of the measured profile (\bar{m}) is defined as:

$$\bar{m} = \frac{1}{n-1} \sum_{i=2}^n \arctan \left[\left| \frac{y_{\text{profile},i} - y_{\text{profile},i-1}}{x_{\text{profile},i} - x_{\text{profile},i-1}} \right| \right] \quad \text{Equation 2-77}$$

Where $x_{\text{profile},i}$ indicates the position along the measuring interval at point i.

There are different ways for roughness characterization which are based on the experiment (van Dam and de Pater, 2001). In general, the roughness depends on rock properties, grain size and in-situ stresses. For different rock types, the increase of average surface roughness is associated with the decrease in critical normal stress required for fracture propagation across a layer interface. Therefore, fracturing and its propagation direction can be related to the anisotropy in fracture surface roughness. In summary, the roughness has an important role in fracture propagation and for better fracture dimension prediction and the current models need to include the roughness of their workflow.

2.8 Summary

In this chapter, the mathematical formulation for fracture propagation was derived based

on fracture mechanics and energy balance that was developed by Griffith. Then, Griffith's formulation was extended to include ductile materials and the formulae for fracture intensity factor and the fracture toughness are provided. The mathematical formulation for 3D planar fracture was derived based on three equations of elasticity, fluid flow and leak-off. The workflow for coupling the above three equations was presented and discussed for numerical modelling using the finite difference approach. The comparison of advantages and disadvantages of hydraulic models was discussed. The non-planar modelling was also discussed to include the interaction of hydraulic fractures with pre-existing natural fractures. The importance of the fracture roughness parameter was also discussed and should be included in the hydraulic fracture modelling.

Chapter 3 : Data Review

In this chapter, the data sets for three wells in the Cowralli Field (Cowralli 6, Cowralli 7, and Cowralli 8) are reviewed and summarised (Table 3-1). The data are collected from well completion reports, well log suits, DFIT, fracture treatments, and gas production.

Table 3-1 : Data Set for Cowralli 6, Cowralli 7 and Cowralli 8.

Wells Data	Cowralli 6 (2 Stages)	Cowralli 7 (2 Stages)	Cowralli 8 (7 Stages)
Well Completion Reports			
- Deviation Data			
- Log Interpretation (Petrophysics)	✓	✓	✓
- Lithological Descriptions			
- Well design and construction			
Well log suites			
- Gamma Ray (GR), API			
- Bulk density (RHOB), g/cc			
- Neutron Porosity (CNC), fraction			
- Compressional Travel Time (DTC), microsec/ft	✓	✓	✓
- Shear Travel Time (DTS), microsec/ft			
- Resistivity logs (RD, RMILL, RS), ohm			
- Caliper (CAL), in			
Hydraulic Fracturing Treatments			
- Formations summary			
- Frac Stages	✓	✓	✓
- Perforations			
- Pumping Schedule			
Diagnostic Fracture Injection Tests			
- Pressure, psi	✓	✓	✓
- Pumping Rate, bpm			
- Elapse Time, min			
Post-Hydraulic Fracturing Results			
- Gas Production, Mscf/d	✓	✓	✓
- Real time Pressure. Pumping Rate, Time			
- Production logging			

3.1 Drilling and Completion History

Cowralli 6 was drilled as a gas appraisal well in 2003. The production casing is 4½ inch 15.1 lb/ft P110 conventional completion. The well runs through the Patchawarra Formation at 10,314 ft. The well deviation survey shows the well to be vertical with a maximum

deviation of 3 degrees at 5,221 ft. The wireline logs were conducted and consist of GR, RHOB, CNC, DTC, DTS, RD, RMILL, RS and CAL (Table 3-1). These logs were evaluated to determine the lithology, volume of shale, water saturation, porosity, and net pay of intervals that are then used to identify the hydrocarbon potential (Appendix A). These well logs are also used for deriving the geomechanical properties (Appendix B). Based on the logging analysis, good gas columns were observed through the Patchawarra Formations with an average porosity of 9.9 %, a water saturation of 36.8 % and a net gas pay of 203 ft.

Cowralli 7 was drilled as a development well 22 days after Cowralli 6 was spudded and under similar drilling and completion conditions. The Patchawarra Formation was the primary target with the log analysis indicating a net gas pay of 267.5 ft with an average porosity of 9.9% and water saturation of 36.8%. Cowralli 8 was drilled in 2006 with multiple targets in the upper and lower Patchawarra Formation (convention completion). Net gas pay of 210.5 ft was found with an average porosity of 10.3% and water saturation of 26%.

Water based mud with Potassium Chloride (KCl) was used for drilling to control the clay swelling and improving the cement bonding. A production casing was inserted into the wellbore and cemented along the entire depth to protect the fresh water zone and prevent movement of hydrocarbons which may result in contamination. To assess the well and casing integrity, a circulating (pressure) test is performed and cased hole logging is performed (Gamma Ray (GR), Casing Collar Locator (CCL), Cement Bond Log (CBL)) (Santos, 2015). A conceptual overview of the well construction is shown in Figure 3-1.

Hydraulic fracturing in Cowralli 6 and Cowralli 7 was performed in two zones of the Patchawarra Formation, and seven stimulation stages were performed in Cowralli 8. Therefore, multi-stage hydraulic fracturing treatments needed to be performed and isolated

in each zone. Plug and Perforation (Plug-and-Perf) completion is used to operate perforations between stages. The perforation starts from the bottom zone then moves up to another zone by using a packer to isolate the above zone. The maximum surface treating pressure is 12,500 psi, which is the limit for surface pumping pressure. The calculation considers the burst pressure of P110 production casing and the annular pressure, including a 20% safety margin.

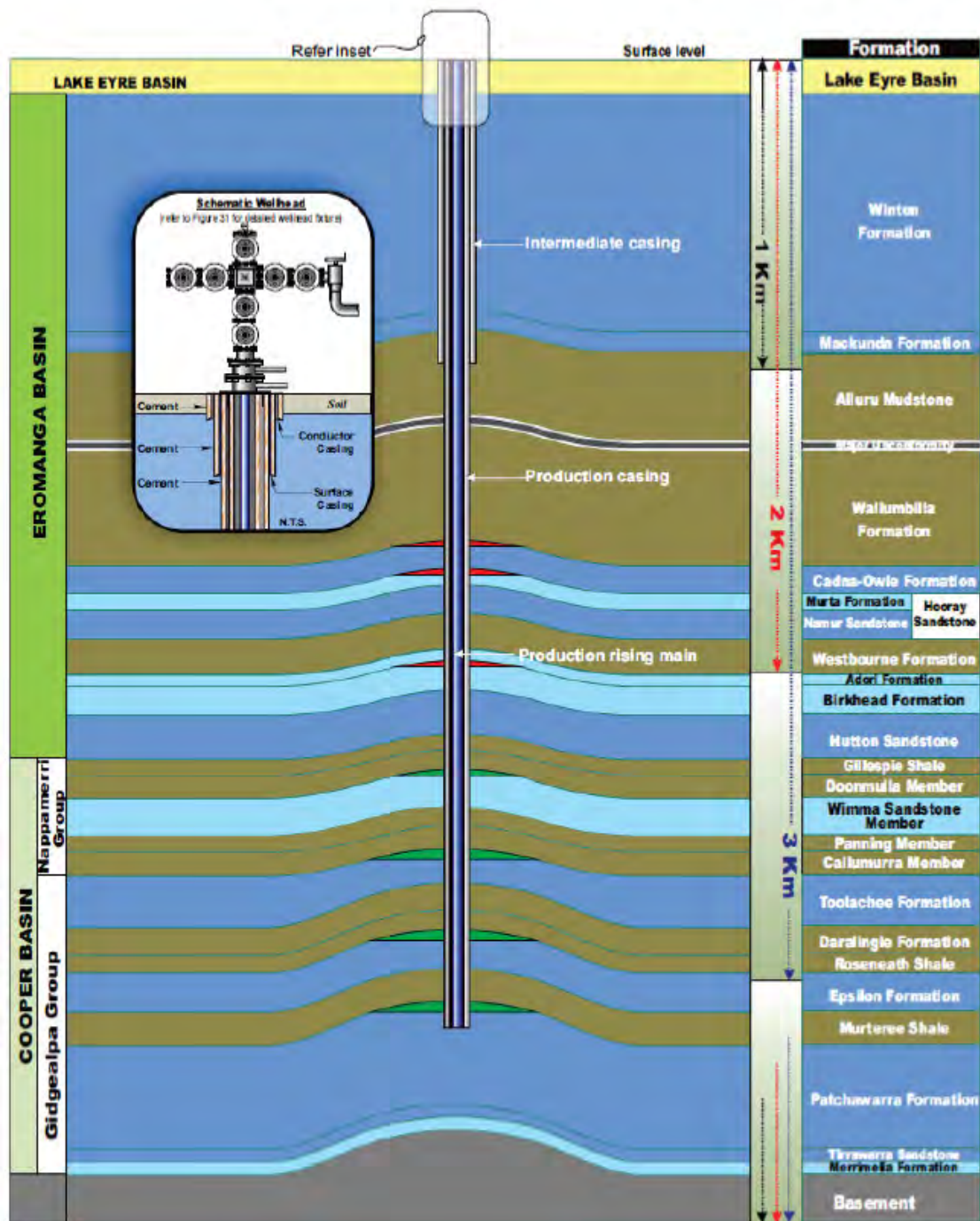


Figure 3-1 : Construction of conventional and unconventional wells in the Cooper Basin (Santos, 2015).

3.2 Data Quality Control and Limitations

3.2.1.1 Sonic Log Data

Sonic logs use a dynamic signal that is sent into the formation similar to sonar and radar. The signal reflection (response) is then used to determine properties such as porosity, lithology, and velocity that have been described in Paper 3 in Chapter 5. Petrophysical well logs can also be used to determine rock mechanical properties and geomechanical stress.

The sonic log and density log can be directly derived to determine overburden stress, Young's Modulus and Poisson's Ratio. These parameters will be used to calculate the minimum horizontal stress magnitude. Barree et al. (2009c) showed that derived rock properties using sonic log data can increase the error margin of the analysis by 28% between DTC and DTS which may be a result of gas saturation or total organic content (TOC). Synthetic sonic logs can be used to estimate the rock properties by using DTC only in order to estimate the Young's Modulus and Poisson's Ratio based on the lithology (Figure 3-2).

The generation of synthetic DTC curves is shown in Figure 3-2(a) and Figure 3-2(b), with the compressional velocity waves showing a difference response in the lithology types, such as quartz sands, limestones, dolomites, shales, and coals. Comparing the Poisson's Ratio at 80 microsec/ft of DTC, the Poisson's Ratio for quartz sands is 0.2 and 0.4 for coal. The Young's Modulus can also be estimated from Figure 3-2(b) by applying bulk density and compressional travel time.

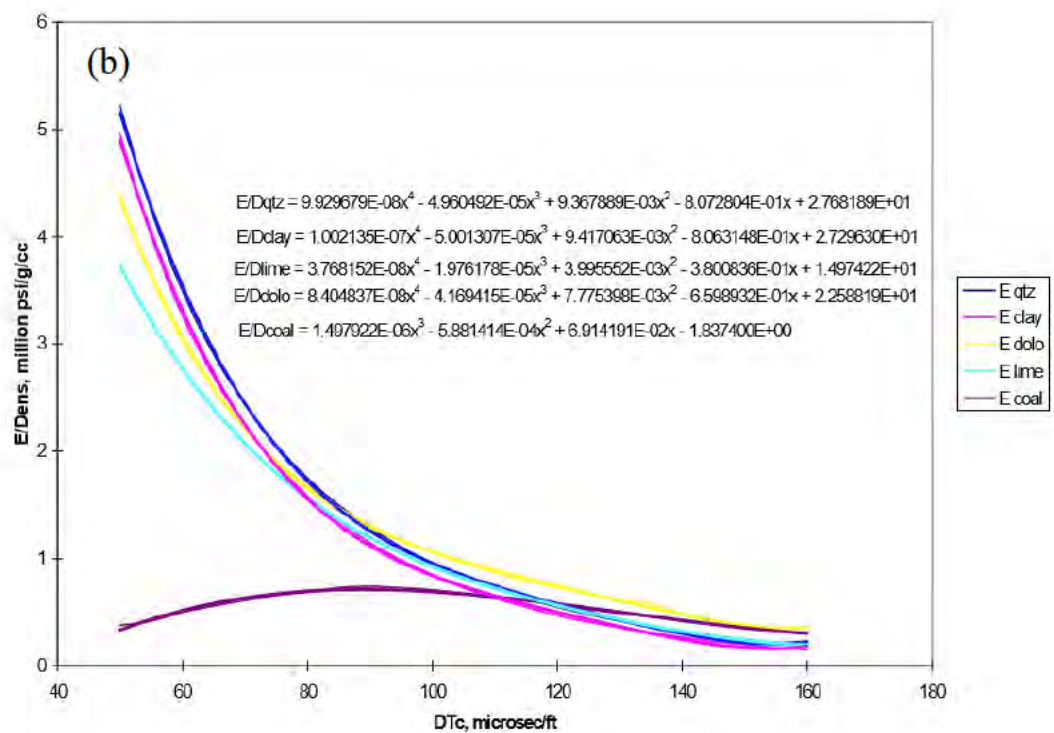
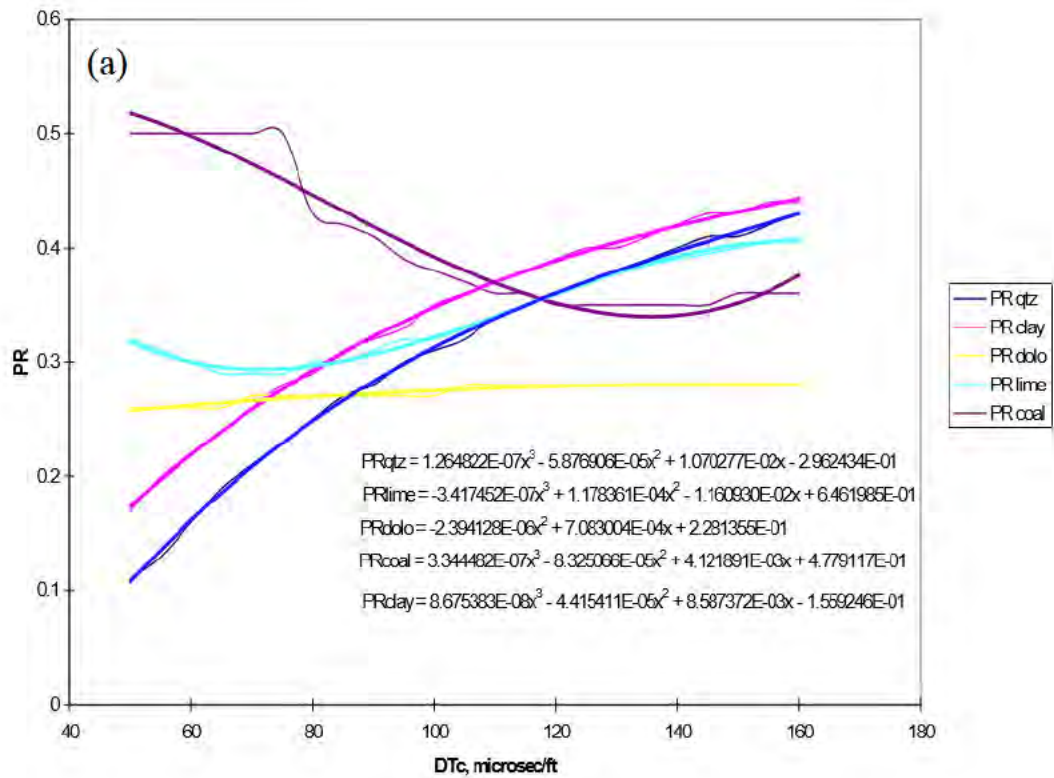


Figure 3-2 : Geomechanical properties derived based on compressional travel time (DTC). (a) Poisson's Ratio estimation vs DTC; and (b) Young's Modulus/Density ratio estimation vs DTC.

The Dipole sonic log (DTSD) can measure acoustic anisotropy along the wellbore based on shear wave splitting analysis (Mueller et al., 1994); however, the data from Cowralli 6, 7 and 8 only contains conventional DTS, therefore synthetic logging or using lithology derived from the geomechanical properties needs to be carried out before in-situ stress calculations.

3.2.1.2 Diagnostic Fracture Injection Test Data

DFIT is primarily used to obtain the minimum horizontal stress for validating and building the one-dimensional mechanical earth model. During this test, since the surface pressure is recorded, the tubing friction and fluid density are used in combination with the surface pressure data to calculate the bottom hole pressure. This calculation can introduce further uncertainty when trying to match the stress profile in comparison to using bottom-hole pressure recording devices.

In addition, the pressure data is used to determine the closure pressure. Any error in pressure measurement also has an impact on closure pressure estimation.

**Chapter 4 : Development of a New Approach for Hydraulic
Fracturing in Tight Sand with Pre-Existing Natural
Fractures**

Development of a new approach for hydraulic fracturing in tight sand with pre-existing natural fractures



Lead author
**Kunakorn
Pokalai**

K. Pokalai, D. Kulikowski, R.L. Johnson, Jr., M. Haghghi and D. Cooke

Australian School of Petroleum
University of Adelaide
Adelaide, SA 5005
kunakorn.pokalai@adelaide.edu.au

ABSTRACT

Hydraulic fracturing in tight gas reservoirs has been performed in the Cooper Basin for decades in reservoirs containing high stress and pre-existing natural fractures, especially near faults. The hydraulic fracture is affected by factors such as tortuosity, high entry pressures, and the rock fabric including natural fractures. These factors cause fracture plane rotation and complexities, leading to fracture disconnection or reduced proppant placement during the treatment.

In this paper, rock properties are estimated for a targeted formation using well logs to create a geomechanical model. Natural fracture and stress azimuths within the interval were interpreted from borehole image logs. The image log interpretations inferred that fissures are oriented 30–60° relative to the maximum horizontal stress. Next, diagnostic fracture injection test (DFIT) data was used with the poro-elastic stress equations to predict tectonic strains. Finally, the geomechanical model was history-matched with a planar 3D hydraulic fracturing simulator, and gave more insight into fracture propagation in an environment of pre-existing natural fractures.

The natural fracture azimuths and calibrated geomechanical model are input into a framework to evaluate varying scenarios that might result based on a vertical or inclined well design. A well design is proposed based on the natural fracture orientation relative to the hydraulic fracture that minimises complexity to optimise proppant placement. In addition, further models and diagnostics are proposed to aid predicting the hydraulically induced fracture geometry, its impact on gas production, and optimising wellbore trajectory to positively interact with pre-existing natural fractures.

KEYWORDS

Tight gas, Cooper Basin, hydraulic fracturing, pre-existing natural fractures, rock mechanical model.

INTRODUCTION

Hydraulic fracturing is a wellbore stimulation process using injected fluid and proppant to create a flow path in a low-permeability reservoir. Since most tight gas reservoirs often contain natural fractures, the interaction between natural fractures and hydraulically induced fractures is a complex process. Another issue is the existence of a complex stress regime (e.g., the Cooper Basin) where normal, strike-slip and reverse fault regimes exist (Reynolds et al, 2006). This can lead to complexity in fracture propagation, reducing effective proppant placement and leading to lower gas production.

In those areas like the Cooper Basin, highly complex stress regimes and pre-existing natural fractures can manifest near-wellbore pressure loss (NWBPL) and pressure dependent leak-off behavior during fluid injection (Johnson and Greenstreet, 2003). NWBPL is caused by fracture path tortuosity (Roberts et al, 2000) and can be predicted and estimated from the turning radius of the fracture (Johnson et al, 2015). To optimise the hydraulic fracturing treatment in such a complicated system, it was proposed that drilling an inclined well perpendicular to natural fracture orientation might maximise the intersection between open natural fracture networks and induced hydraulic fractures (Murphy and Fehler, 1986). Previous research by Zhou et al (1994) presented that inclined wellbores should consider the shear stress anisotropy that would impact wellbore stability, based on data from stress regimes in Australia. They recommended drilling in strike-slip stress regimes at 55–70° azimuth relative to the maximum horizontal stress. In a case with a similar strike-slip stress regime and anisotropy values similar to the Cooper Basin, Bentley et al (2013) used this drilling approach to reduce hydraulic fracture propagation complexity, based on surface deformation tiltmeter and microseismic monitoring results relative to vertical wells.

This paper attempts to use a multidisciplinary approach to study a tight gas reservoir in the Cooper Basin. First, borehole breakout geometries are interpreted from a wellbore image log and extrapolated to the remainder of the field. Then diagnostic fracture injection test (DFIT) data is used to calibrate a rock mechanical model constrained by the image log data for planar 3D hydraulic fracturing modelling of existing hydraulic fracturing data from the area. Finally, based on this modelling, an optimum well trajectory for drilling an inclined well is proposed.

THEORETICAL BACKGROUND

Deviated wellbore

For an inclined well, the stress distribution around the wellbore can be determined using analytical or numerical models. Kirsch equations (Kirsch, 1898) analytically describe the breakdown behavior around a vertical well (cylindrical geometry) under a linear elastic deformation assumption, where the effective radial stress (σ_r) and tangential stress (or hoop stress), shear stress ($\tau_{r\theta}$) and vertical stress (σ_v) are trigonometric functions of the horizontal stresses and reservoir pressure (Eqs 1–4).

$$\begin{aligned} \sigma_r = & \frac{\sigma_h + \sigma_H}{2} \left(1 - \frac{r_w^2}{r^2} \right) \\ & + \frac{\sigma_h - \sigma_H}{2} \left(1 - 4 \frac{r_w^2}{r^2} + 3 \frac{r_w^4}{r^4} \right) \cos 2\theta \\ & + \frac{r_w^2}{r^2} (P_w - \alpha P_0) \end{aligned} \quad (1)$$

$$\sigma_t = \frac{\sigma_h + \sigma_H}{2} \left(1 + \frac{r^2}{r^2} \right) - \frac{\sigma_h - \sigma_H}{2} \left(1 + 3 \frac{r_w^4}{r^4} \right) \cos 2\theta - \frac{r_w^2}{r^2} (P_w - \alpha P_0) \quad (2)$$

$$\tau_{r\theta} = -\frac{\sigma_h + \sigma_H}{2} \left(1 + 2 \frac{r_w^2}{r^2} - 3 \frac{r_w^4}{r^4} \right) \sin 2\theta - \frac{r_w^2}{r^2} (P_w - \alpha P_0) \quad (3)$$

$$\sigma_v = P_{ob} - \alpha P_0 \quad (4)$$

The Kirsch equations were modified by Barree and Misimins (2015) for a deviated wellbore with the principle stress tensor on the wellbore inclination, where azimuth (β) is defined relative to the maximum horizontal stress direction and the deviation angle (α) is defined relative to the vertical stress direction (Fig. 1). The transformed stresses can be described in three dimensions using Equations 5–10.

$$S_x = \sigma_H \sin(\beta)^2 + \sigma_h \cos(\beta)^2 \quad (5)$$

$$S_y = \cos(\alpha)^2 (\sigma_H \cos(\beta)^2 + \sigma_h \sin(\beta)^2) + \sigma_v \sin(\alpha)^2 \quad (6)$$

$$S_z = \sin(\alpha)^2 (\sigma_H \cos(\beta)^2 + \sigma_h \sin(\beta)^2) + \sigma_v \cos(\alpha)^2 \quad (7)$$

$$S_{xy} = \cos(\alpha) \sin(\beta) \cos(\beta) (\sigma_H - \sigma_h) \quad (8)$$

$$S_{yz} = \sin(\alpha) \cos(\alpha) (\sigma_v - \sigma_H \cos(\beta) - \sigma_h \sin(\beta)^2) \quad (9)$$

$$S_{zx} = \sin(\alpha) \sin(\beta) \cos(\beta) (\sigma_h - \sigma_H) \quad (10)$$

After transformation of the stress and shear stress along the wellbore axis, the resulting values can be substituted into Equations 1–4 to describe the radial (σ_r), tangential (σ_t) and axial (σ_z) well stress values. For the case of transverse fractures, if there are existing cracks, the internal pressure must exceed the axial stress and the tensile strength of any infill material. For breakdown criteria in a deviated or horizontal well, in the case of the longitudinal fracture, the internal pressure must exceed the minimum tangential stress plus the rock strength. Considering that the fractures are open, the breakdown pressure based on exceeding the axial stress is perpendicular to the fissure only, and can be estimated for a deviated or horizontal well using Equations 11–13.

$$\sigma_r = P_w - P_0 \quad (11)$$

$$\sigma_t = S_x + S_y - 2(S_x - S_y) \cos(2\lambda) - 4S_{xy} \sin(2\lambda) - \sigma_r \quad (12)$$

$$\sigma_z = S_z - 2v((S_x - S_y) \cos(2\lambda) + 2S_{xy} \sin(2\lambda)) \quad (13)$$

The angle for fracture propagation (λ) is given with respect to a vertical well; for example, in a vertical fracture $\lambda = 0$ and for a horizontal fracture $\lambda = 90$.

One-dimensional mechanical earth model

The construction and calibration of a one-dimensional (1D) rock mechanical model (1D MEM) is an important re-

quirement for hydraulic fracturing simulation and fracture containment assessment, and can be obtained using the following workflow. Firstly, the input data is obtained from well logging suites typical for hydraulic fracturing design; gamma ray, full-waveform sonic log and bulk density logs data are used to estimate elastic rock properties such as Poisson’s ratio (ν) and Young’s modulus (E). The DFIT provides observable values for breakdown pressure (P_{wb}) and closure pressure (P_c), a representative value for the minimum horizontal stress (σ_{hmin}) within an interval (Fig. 2). Formation pseudo radial flow behaviour may be observable in the shut-in data after the closure pressure has been observed using after-closure analysis (ACA) methods based on impulse test analytical solutions (Nolte et al, 1997). ACA can provide necessary data for the model such as pore pressure (p_p) and transmissibility. Then, estimates for the minimum horizontal (σ_{hmin}) and the maximum horizontal stress (σ_{Hmax}) can be derived by history matching the DFIT data using the isotropic form of the poro-elastic stress equations (Thiercelin and Plumb, 1994; Eqs 14 and 15) using the maximum (ϵ_H) and minimum horizontal (ϵ_h) strains to calibrate the model.

$$\sigma_{hmin} = \frac{\nu}{1-\nu} (\sigma_v - \alpha_v p_p) + \frac{E}{1-\nu^2} \epsilon_h + \frac{E\nu}{1-\nu^2} \epsilon_H + \alpha_h p_p \quad (14)$$

$$\sigma_{Hmax} = \frac{\nu}{1-\nu} (\sigma_v - \alpha_v p_p) + \frac{E}{1-\nu^2} \epsilon_H + \frac{E\nu}{1-\nu^2} \epsilon_h + \alpha_h p_p \quad (15)$$

The parameters of highest uncertainty in matching the observed values to the calculated values are the tectonic strains in the maximum (ϵ_H) and the minimum horizontal directions (ϵ_h). Previous research by Teufel (1983) described anelastic strain recovery measurements as a method to determine the strains

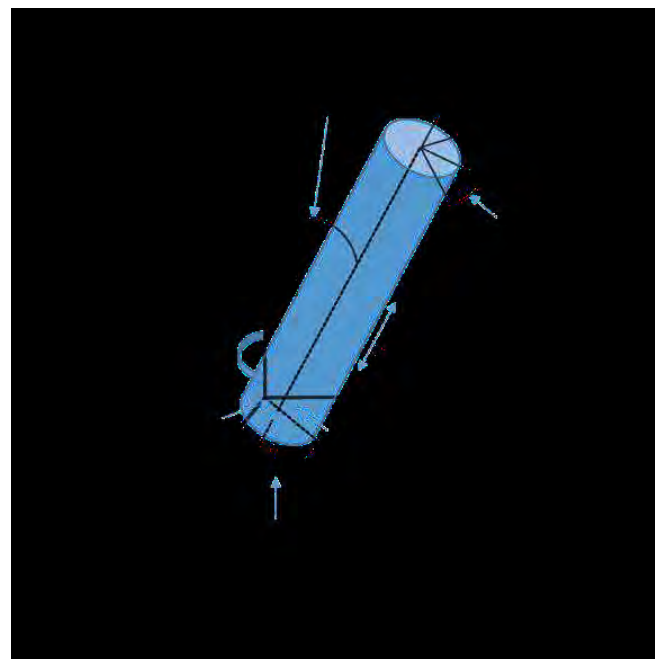


Figure 1. Borehole orientation in an inclined well.

based on the Blanton model (Blanton, 1983). This method, however, is based on core measurements that are obtained on a small scale and may not necessarily represent the reservoir scale.

To better constrain this process, the observed breakdown pressure and natural fissure opening pressures can also be used to constrain calculated values. The breakdown pressure during a DFIT is the pressure that acts on the rock and initiates the fracturing under an assumption that the rock is homogenous and elastic. It is the early and often maximum pressure, and pressure generally drops as more fluid is injected into the rock. The Kirsch equations can be resolved to describe the breakdown pressure for the horizontal stresses (Zoback, 2007) using Equation 16, based on the pore pressure and tensile rock strength (T_0).

$$P_{Breakdown} \text{ or } P_{wb} = 3\sigma_{hmin} - \sigma_{Hmax} - P_{Pore} + T_0 \quad (16)$$

T_0 can be estimated from core testing or observed values from past DFITs. The tensile strength can be neglected and the observed reopening fracture used when a second injection occurs for the same fracture after previous closure.

Another constraint for horizontal stresses can be derived from the fissure opening (closing) pressure (P_{fo}). The magnitude of pressure dependent leakoff (PDL) and P_{fo} can be determined from before-closure analysis (BCA) of a DFIT using the G-function time and semi G-function derivative (Barree et al, 2009) (Fig. 3). A characteristic hump in the semi G-function derivative is indicative of PDL behaviour in the early time shut-in pressure decline data of a DFIT. This effect is caused as fluid passes through pre-existing natural fractures, and can be described as an exponential fluid leak off rate relative to conventional leakoff. A Mohr circle failure criterion can be used to derive the fissure opening angle, or the angle at which a rock would preferentially break between the maximum and minimum horizontal stresses (Jaeger and Cook, 1979). Using this criterion, the angle (θ) of the natural fractures relative to the horizontal stress directions can be determined from P_{fo} using Equation 17 (Fig. 4), and further constraining the values of σ_{Hmax} and σ_{hmin} .

$$P_{FissureOpening} \text{ or } P_{fo} = \frac{1}{2}(\sigma_{Hmax} + \sigma_{hmin}) + \frac{1}{2}(\sigma_{Hmax} - \sigma_{hmin}) \cos 2\theta \quad (17)$$

In this paper, the tectonic strains and horizontal stress values have been determined by matching observed data to calculated data, solving Equations 14–17 simultaneously using a generalised reduced gradient (GRG) nonlinear solving method (Lasdon et al, 1978). This method, which is based on the genetic algorithm, helps to minimise the sum of the error function between the calculated and observed values derived from the logs to the values of closure pressure, breakdown pressure and fissure opening pressure observed from the DFIT data. For each value, Equation 18 describes the process where x represents the observed values and x is the value derived from logs for each parameter.

$$\text{Error function (ErrFn)} = \sum(x - x)^2 \quad (18)$$

Finally, the values of horizontal stress derived from this history matching process are compared with values predicted from image log analyses of borehole breakout and drilling induced tensile failure criteria (Zoback, 2007) to further constrain the resulting model.

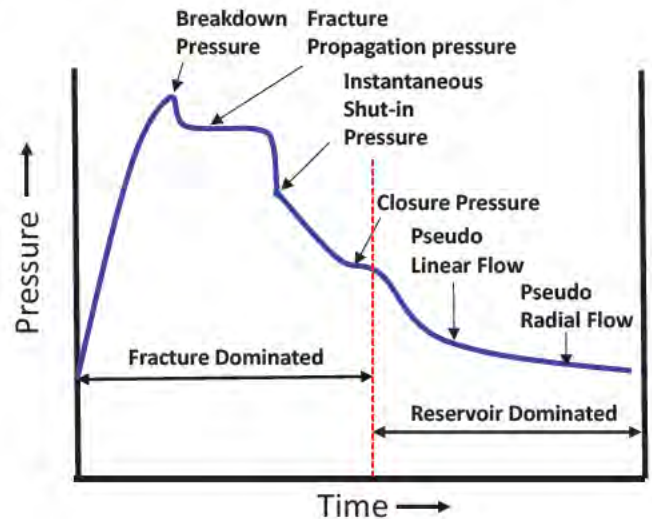


Figure 2. DFIT typical pressure profile.

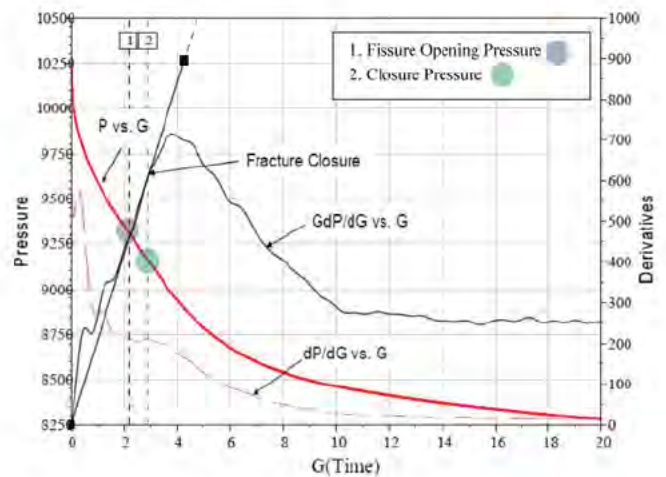


Figure 3. G-function analysis plot with PDL detected (Barree et al, 2009).



Figure 4. Hydraulic fracture interaction with a natural fracture.

CASE STUDY

The study area (C-Field) is located west of the Gidgealpa-Merrimelia-Innaminka (GMI) Ridge within the Greater Tindilpie (GT) region of the Permian to Triassic aged Cooper Basin (SA). The Cooper Basin is Australia's largest onshore hydrocarbon province, with tremendous unconventional hydrocarbon potential in low permeability fluvial to lacustrine reservoirs. The region contains northeast-southwest striking ridges (GMI and Murteree-Nappacoongee) that separate the northeast-southwest elongate Patchawarra, Nappamerri and Tenappera troughs. Initial accommodation space is believed to have generated through southeast-northwest oriented extension (650 Ma) developing northeast-southwest and southeast-northwest oriented structural lineaments (Kuang et al, 1985; Haines et al, 2001). Successive crustal shortening events during the Sakmarian, late Permian and Upper Triassic periods are believed to have reactivated pre-existing basement-involved faults and controlled the depositional patterns in the Cooper Basin and potentially influence hydrocarbon migration pathways (Apak et al, 1997; Kulikowski et al, 2015). These events likely controlled the development and possible reactivation of natural fractures within the Patchawarra Formation, which hosts the largest volume of known hydrocarbons within the basin.

Within the C-Field, the Early Permian aged Patchawarra Formation comprises of approximately 1,640 ft of gas charged and cyclically deposited very fine to coarse grained sandstone, siltstone, shales and coals under meandering fluvial to lacustrine conditions (Camac et al, 2012). The field is a low to moderate relief structure elongate in a northeast-southwest direction (Fig. 5) and bound from the east and west by northeast-southwest striking reverse faults. The wells used in this analysis (C-13 and C-7) are approximately 4,600 ft apart (Fig. 5). The maximum horizontal stress within the field is oriented approximately 116°N (Camac et al, 2012). Fracture stimulation treatments are becoming increasingly relied upon, with the majority of development wells requiring at least one fracture stimulation treatment, particularly within the relatively lower permeability C-Field (typically <1 mD). The influence of pre-existing natural fractures during fracture stimulation treatments within the Cooper Basin is not well understood in literature, albeit up to six regionally pervasive nat-

ural fracture sets may exist throughout the basin (Kulikowski et al, 2015; 2016). The authors' investigation into optimising well trajectory to positively interact with pre-existing natural fractures oriented parallel, 30°, 60° and perpendicular to the hydraulically induced fracture plane, while incorporating the local stress field, will provide a new approach for hydraulic fracturing in tight sand reservoirs to optimise hydrocarbon production.

Natural fracture planes typically exhibit a reduced strength and are favorably reactivated, rather than new fractures developing, and has been observed in prior studies in the Cooper Basin (Nelson et al, 2007). This fundamental rock failure principal is vital to better understanding the complex mechanics taking place during fracture stimulation treatments, and particularly in the stress and rock conditions of the Cooper Basin. The authors use wells C-7 and C-13, which contain an interpretable borehole image log, adequate well tests, and know effectiveness of fracture stimulation treatments, to showcase the effect that natural fractures play in tight sand hydrocarbon production. Natural fractures from the C-13 borehole image log were interpreted using Paradigm Geolog 7.2 software (Fig. 6). Natural fracture geometries ranged from horizontal to near vertical and with a large spread of strike orientations; however, up to three natural fracture sets can be realised. The dominant natural fracture set strikes north-northeast to south-southwest with a dip angle of 60° (Fig. 7). Fracture sets with dip angles of 30° are also present, dipping towards the east, south, west and northeast.

Together with natural fractures, the authors interpret borehole breakout occurrence to calculate the local maximum horizontal stress orientation and magnitude at the depth of interest (9,500 ft). The average strike of borehole breakouts is approximately 18.3°, inferring that the maximum horizontal stress orientation is approximately 108.3° (Fig. 7). The average borehole breakout width was approximately 74.1°, which was used for calculating the stress magnitude. The maximum horizontal stress magnitude—based on borehole breakout data, pore pressure, minimum horizontal stress magnitude (obtained from leak off tests), rock strength and the effect of temperature—was calculated within the C-13 well, and at 9,500 ft depth is approximately 9,900 psi, a value to constrain estimates from the DFIT data.

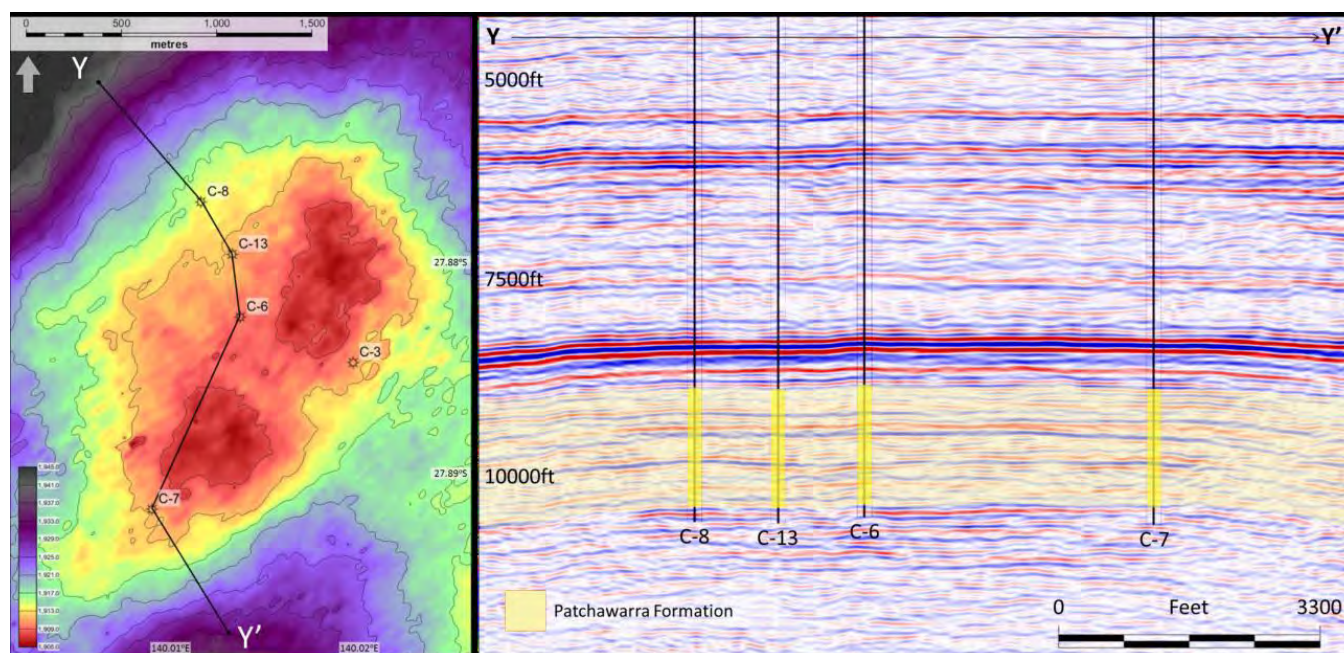


Figure 5. Structural map of the C-Field with a cross-section showing the Patchawarra Formation correlation across wells.

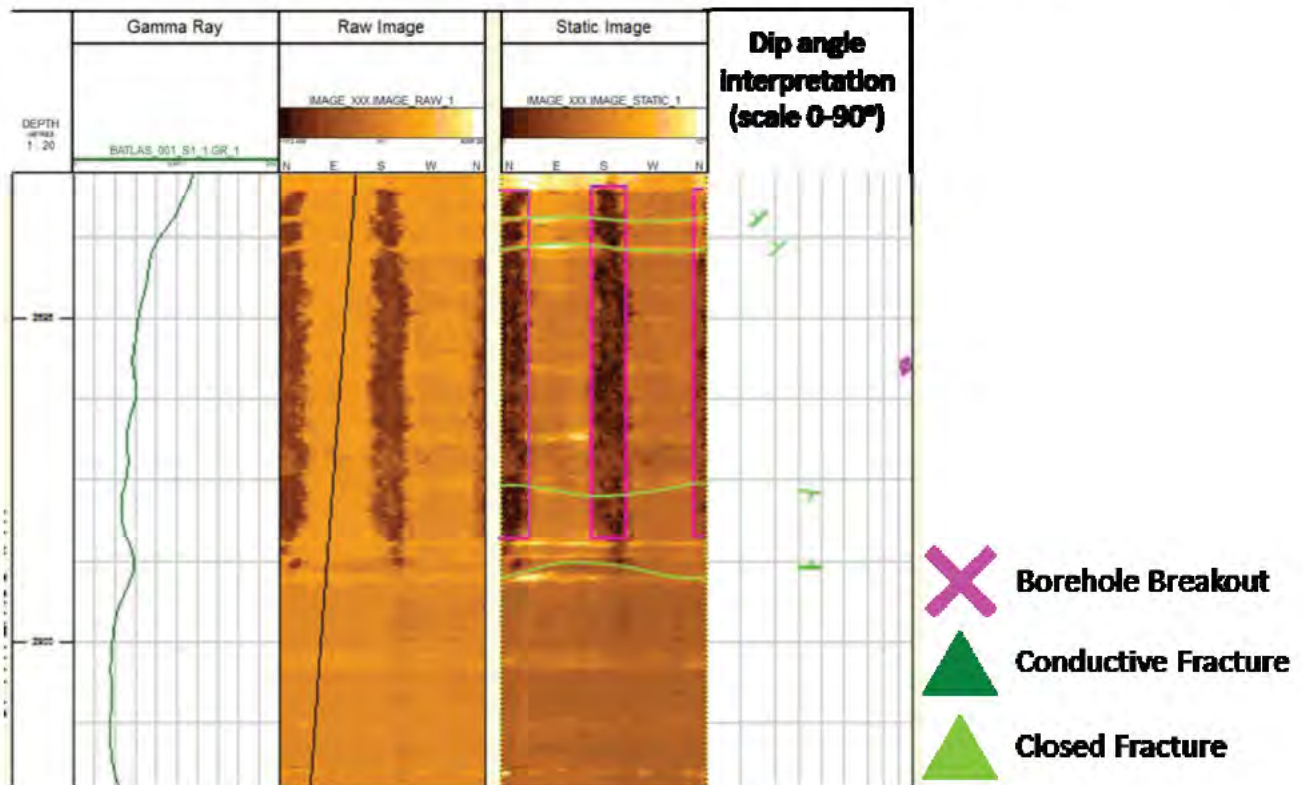


Figure 6. Acoustic image log interpretation.

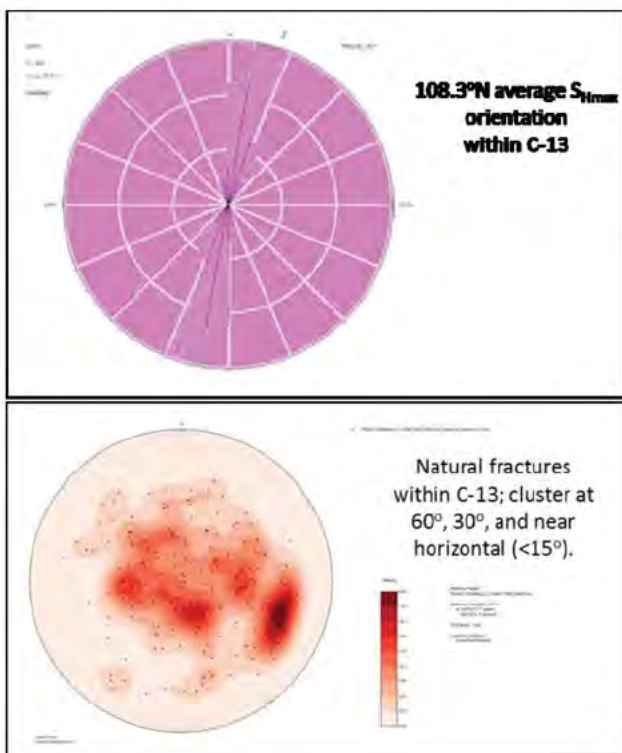


Figure 7. Borehole breakout and natural fracture analysis.

RESULTS AND DISCUSSION

There are two stages of fracture treatment that have been carried out in well C-7 to obtain commercial gas rates in the Patchawarra Formation (Fig. 8). Based on Pokalai et al (2015b), the tight gas target intervals have been analysed from depths between 9,000–10,000 ft with an average low permeability of 0.7 mD and temperatures up to 280°F, as shown in Table 1.

Interpretation of DFIT

STEP DOWN TEST

Well C-7 stage 1 and stage 2 were injected with the delayed borate crosslinked fluid for eight minutes with an average rate of 25 barrels per minute (bpm), with the total injected volume being 8,000 gallons (Fig. 9). The step down test was performed by reducing the injection rate by approximately 7.5 bpm in each step until pumping had been stopped. Stage 1 and stage 2 indicated average NWBPL of 522 psi (Table 2). This average indicates that the pressure's loss is dominated by tortuosity rather than pressure loss through perforations.

The delay borate crosslinked fluid was used for DFIT; the gel may damage the fracture and affect the fracture fluid cleanup during production. Also, because pumping time is held at eight minutes, it would impact the longer observe closure pressure and radial flow behavior.

BEFORE-CLOSURE ANALYSIS

During pumping, the breakdown pressure reached a value of 9,962 psi for stage 1 and 10,291 psi for stage 2. Once the pumping stopped, the stabilised pressure was observed within one hour. Based on the G-function analysis, both stages in well C-7's semi G-function (GdP/dG) versus G-function time (G) plot showed a hump, which means the leakoff type is pressure dependent leakoff (PDL) (Fig. 10). The fissure opening in stage 1 is shown at the G-function time of 1.28 with the fissure opening pressure (P_{fo}) of 7,822 psi. The closure pressure occurs at a G-function time of 1.58 at 7,596 psi, which is higher than stage 2 by 190 psi. In this case, the first derivative of the square root time plot confirmed the closure from the G-function analysis. Finally, the average fluid efficiency for the fracturing fluid injection was determined to be 56% from G-function analysis.

AFTER-CLOSURE ANALYSIS

As mentioned previously, ACA methods are used to identify different flow regimes in the post-closure fall-off data. In the data, a negative slope of 0.5 is observable in the plot of pressure difference and its derivative, an indication of a pseudo-linear formation flow regime, likely natural fracturing. Also, a negative slope of one in the late time data is observable, indicating a formation pseudo-radial flow regime. In Table 2, the pore pressure gradient reported from ACA is 0.443 psi/ft. Also, stage 1 provides the highest reservoir transmissibility of around 325 mD.ft/cP by using the net pay thickness of 36 ft, which gives a permeability of 0.116 mD.

Analysis of the mechanical earth model

A calibrated 1D MEM was developed based on the elastic rock properties from well log derived data (Fig. 11). The pore pressure and stress profiles have been generated for well C-7 encompassing the Patchawarra Formation stimulated for stages 1 and 2. Closure pressure, breakdown pressure and pore pressure have been determined from DFIT data for stages 1 and 2. For stages 1 and 2, the DFIT closure pressures are 7,596 psi and

7,406 psi, and breakdown pressures are 9,962 and 10,291 psi, respectively. These observed values were used to calibrate the log-derived values using the workflow described with Equations 14–16 and 18.

From this calibration process, the maximum horizontal tectonic strain is 504 microstrains and the minimum horizontal tectonic strain is 155 microstrains; this produces an effective tectonic strain of 338 microstrains in the minimum horizontal stress direction, based on the sum of the two tectonic strain components in Equation 14. As aforementioned, the borehole breakout data from the image log in the field was used to constrain the maximum horizontal stress magnitude to approximately 9,900 psi at 9,500 ft. The correlation between the observed closure pressure and calculation from log data generally show a good match. Some stress misalignment could, however, result from high near wellbore pressure losses observed in the breakdown pressures for both stages. In the coal, the stress values determined from full wave form sonic data appear to be unreliable and differ from values estimated from published compressional sonic travel time log models for a coal lithology. This is likely due to washouts affecting the shear wave data, giving inaccurate elastic rock properties and impacting the stress profile.

The stress regime in C-7 changes from the bottom of the Patchawarra Formation to the top of the well. As can be seen in Figure 11, the top part shows a strike-slip stress regime followed by a normal fault and reverse fault stress regime in other lithologies. A stress contrast of 1,200 psi is estimated between sand and coal at the level of the Patchawarra Formation; this stress contrast along with modulus changes could limit fracture initiation out of the sand section. There is, however, a high degree of uncertainty in the coal rock mechanical and stress values based on the sonic log data. Nevertheless, change in the stress regime can affect hydraulic fracturing propagation and potential cause orientation as it encounters strike slip, normal fault and thrust faulting conditions. In this case, hydraulic fracturing stage 1 and stage 2 indicate a normal fault condition, which is likely to propagate less complicated vertical fractures. At the boundaries of the Patchawarra, however, changes to reverse faulting may cause t-shaped fractures or blunting to occur at the boundaries, potentially limiting growth out of the intervals.

Hydraulic fracture simulation

3D hydraulic fracture models have been constructed for the C-7 well using a planar 3D hydraulic fracturing propagation simulator (GOHFER) (Barree, 1983) using the calibrated geomechanical model (1D MEM) as the initial input for the simulator to perform history-matching of observed pressures (Pokalai et al, 2015a). Figure 10a shows the plot of injection fluid rate and treating pressure in C-7 during stage 1. In this stage, 12,000 gal of delayed borate crosslinked fluid was injected as a pad stage, and calculated bottom hole treating pressures up to 9,000 psi were observed. In the next stage, 4,000 lbs of 100 mesh sand followed by slurry stages with increasing concentrations and mesh sizing of high-density ceramic proppant were used; both 20/40 then 16/30 proppant were used, pumped in concentrations from 0.5–8 lbm/gal. Finally, 5,500 gal of linear gel was pumped to displace the proppant stages and complete the job. A good match was obtained by history-matching observed and

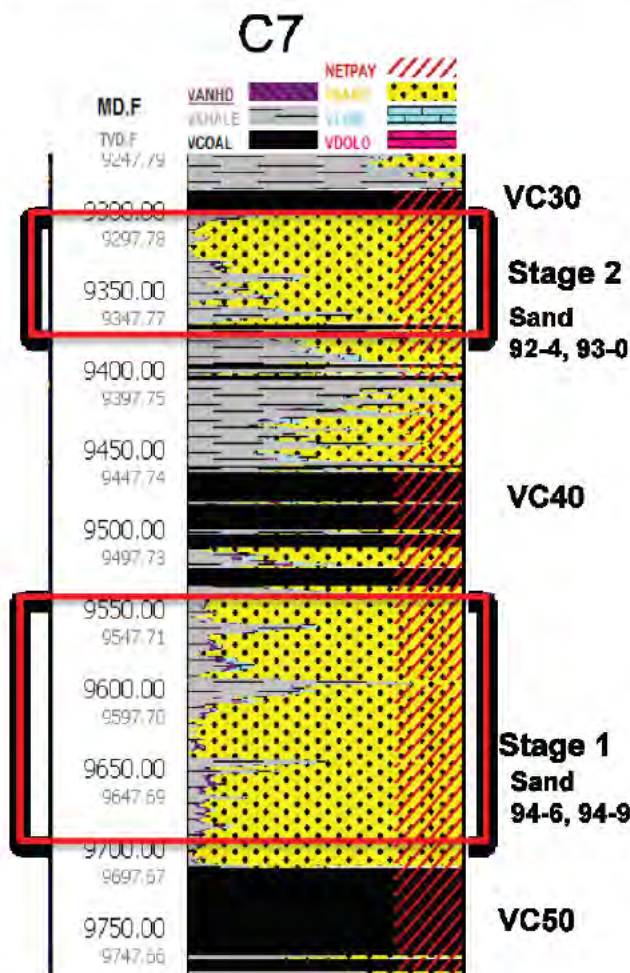


Figure 8. Different stages of hydraulic fracturing in well C-7.

Table 1. Petrophysical properties in well C-7.

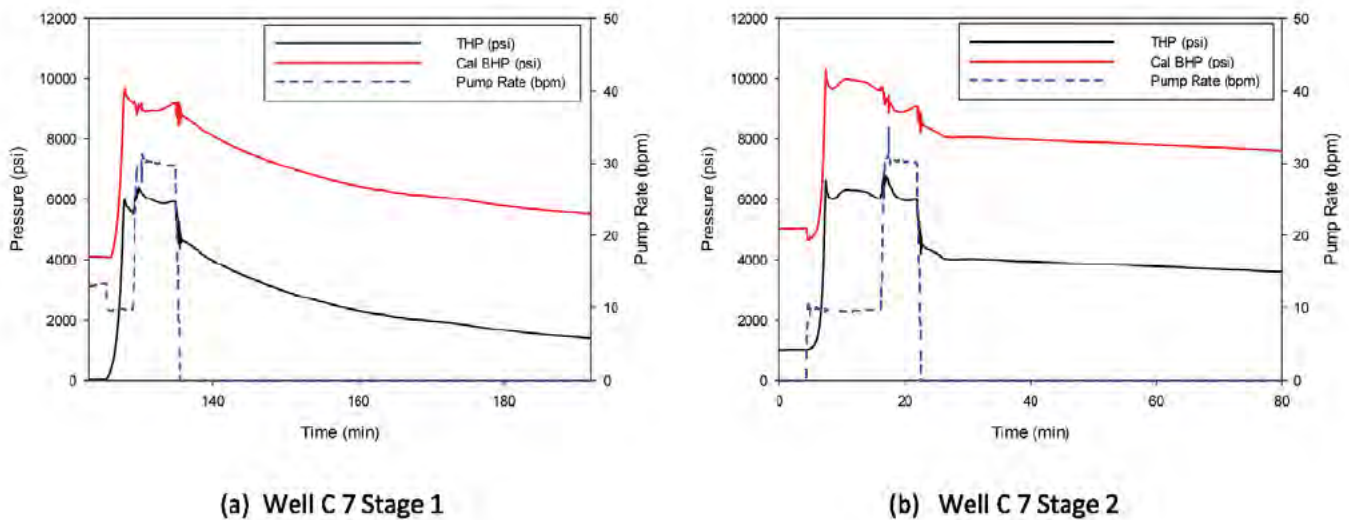
Well/stage	Depth	Net pay	Permeability	Porosity	Water saturation	Temperature
C-7, stage 1	9,533–9,634 ft	70 ft	0.12 mD	11.3%	34%	282 F
C-7, stage 2	9,294–9,351 ft	36 ft	0.06 mD	10.0%	31%	275 F

simulated surface results and calculated bottomhole pressures, and was used to further refine the geomechanical model. The purple dashed line in Figure 12a represents measured surface treating pressure (STP), and the solid purple line model predicted STP data. The pressure matching has been achieved by adjusting variables such as stress, fluid leak off (PDL) and excess pressure derived from the hydraulic fracture tortuosity.

Based on the fracture history matching (Fig. 12b), the fracture propagates with good height containment within the target formation and achieves an average baseline conductivity of 10 md.ft, with results shown in Table 3. This fracture geometry takes into account the geomechanical model and estimated fracturing fluid properties from the field reports, and models the proppant transport in the model based on extensive Stim-Lab modelling and conductivity studies. Furthermore, this modelling includes the impact of pressure independent leakoff and pressure drop from tortuosity. All these factors can impact the treating pressure resulting from the simulator and create a more realistic model; however, it cannot visually show the effects or fracture geometry induced from created versus natural fracture extension, being only a single planar model.

To complete the process of evaluation, the fracture propagation has also been interpreted using net pressure analysis (Nolte and Smith, 1981), which is derived using a log-log plot of net pressure versus time (Fig. 12c). Initially, Mode I behaviour was observed with a small positive slope, indicating the fracture was propagating in a confined height and length growing within the target zone. Next, a period of Mode II behaviour was observed (i.e., constant slope) inferring that a stable growth in fracture height or fissure opening was occurring. Then a period of Mode IV behaviour was observed (i.e., negative slope), which is generally associated with uncontrolled fracture growth. Finally, Mode II behavior was again observable until Mode III, or restricted fracture growth, was noted. Mode III often indicates a high positive slope and is associated with the beginning of proppant fill-up in the fracture, creating high treating pressures until a screen out or pressure out occurs.

Ultimately, the complex interaction between pre-existing natural fractures needs to be investigated more fully when performing hydraulic fracturing in high-stress unconventional reservoirs with natural fracturing. Areas for future investigations could include stochastic processing of multiple realisations



(a) Well C 7 Stage 1

(b) Well C 7 Stage 2

Figure 9. Diagnostic fracture injection test plots in well C-7.

Table 2. DFIT data observed in well C-7.

Rate-pressure step-down test analysis results						
Well/stage	ΔP tortuosity at 30 bpm	ΔP perforation at 30 bpm	Tortuosity pressure loss coefficient (K_{tort})	Perforation pressure loss coefficient (K_{perf})	NWBP	
C-7, stage 1	461 psi	67 psi	85 psi/(stb/d) ²	0.0076 psi/(stb/d) ²	528 psi	
C-7, stage 2	368 psi	148 psi	67 psi/(stb/d) ²	0.163 psi/(stb/d) ²	516 psi	
BCA results						
Well/stage	Breakdown pressure (P_{wb})	ISIP	Closure pressure (P_c)	Fissure opening pressure (P_{fo})	Leakoff type	Pressure dependent leakoff (PDL) coefficient
C-7, stage 1	9,962 psi	8,812 psi	7,596 psi	7,822 psi	PDL	0.005
C-7, stage 2	10,291 psi	8,528 psi	7,406 psi	8,064 psi	PDL and height recession	0.003
ACA results						
Well/stage	Reservoir pressure	Transmissibility (kH/ μ)	Flow capacity (kH)	Permeability (k)	Flow behaviours	
C-7, stage 1	4,520 psi	325 mD.ft/cp	8.12 mD.ft	0.116 mD	Pseudo linear and radial flow	
C-7, stage 2	4,262 psi	91 mD.ft/cp	2.27 mD.ft	0.063 mD	Pseudo linear and radial flow	

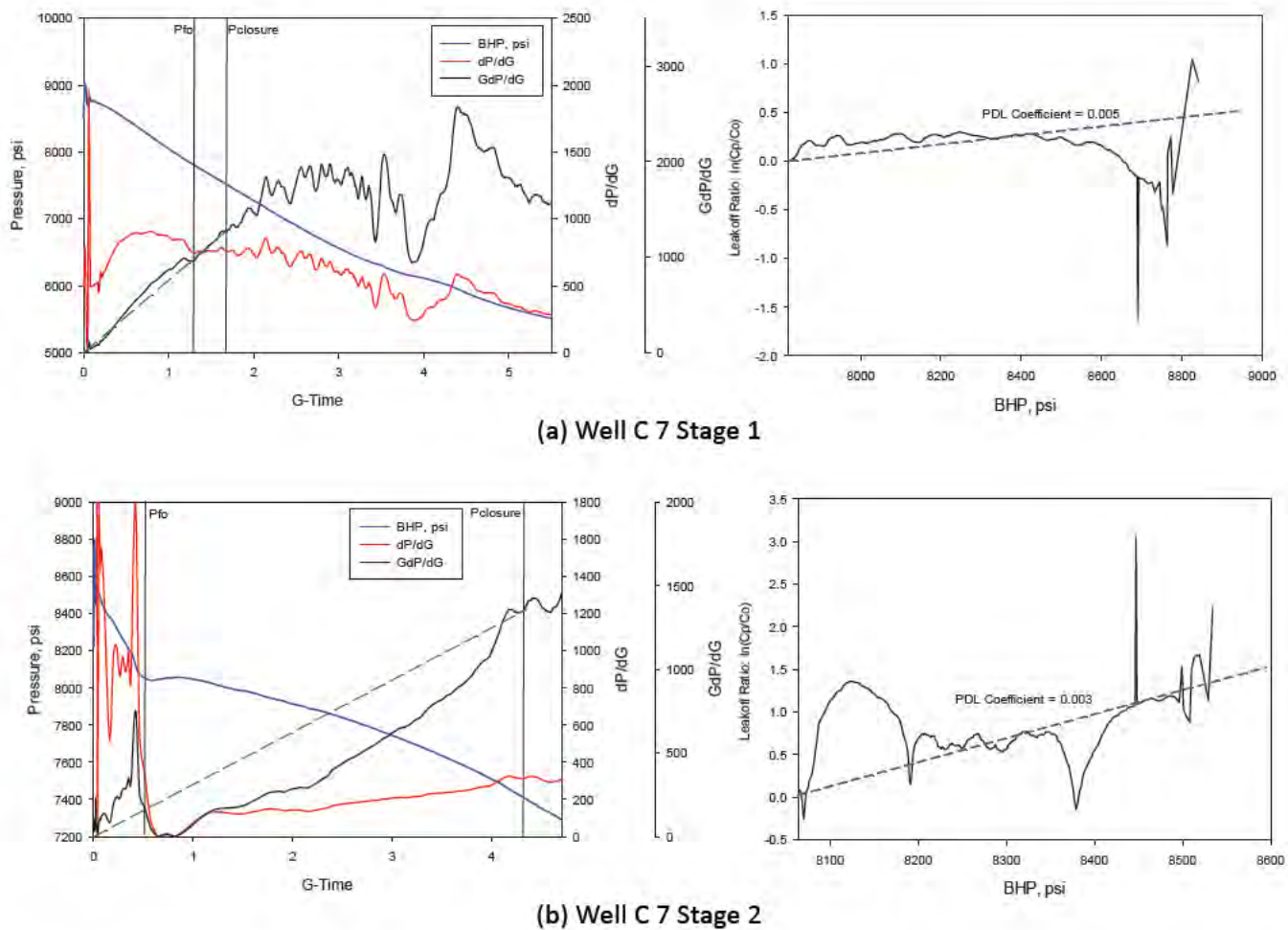


Figure 10. G-function and PDL plots in well C-7.

with discrete fracture networks and finite element methods to correctly account for the fluid flow in fractures. Although a simplistic planar model was used, predicted dimensions, production modelling and history-matching reasonably matched the observed average gas production rate of 300 Mscf/day across five years (Fig. 12d).

Fracture orientation and well design

Ultimately the greatest benefit of creating a calibrated geo-mechanical model and history matched hydraulic fracture model is to provide insight for future wells to better optimise stimulation treatments. To achieve this, the authors will show how the data can be used in a framework to provide insight on future wellbore deviation and inclination to optimise hydraulic fracture treatments for this environment. The authors will guide readers on their approach to achieve this optimisation.

Firstly, the existing data is summarised. Figure 13 shows the breakdown gradient and the breakdown angle in well C-7 at a depth of 9,500 ft. A Poisson's ratio value of 0.24, an overpressured reservoir gradient of 0.5 psi/ft, and an effective tectonic strain value of 338 microstrains in the σ_{hmin} direction creates a stress anisotropy or horizontal stress differential of 2,400 psi. Since this stress regime is considered to be in a strike-slip stress regime, the stress values are represented by a large ellipsoid shape and more anisotropic ratios in the figure.

The Kirsch modification equations (Eqs 5-13) have been applied for the breakdown pressure plot (Fig. 13a) and the breakdown angle (Fig. 13b.). The left-hand side of Figure 13a shows the azimuth starts from 0-360° north around the edge

of each circle. The vertical well falls in the centre of the plot, whereas the horizontal well falls on the outer plot. The light blue to grey colour shows the breakdown pressure, which ranges from 0.4-1.2 psi/ft; any pressure gradient greater than 1.2 psi/ft is shown as a grey color. The maximum stress direction shows 108° on the plot with an average breakdown gradient of 0.8 psi/ft. Figure 13b shows the fracture initiation angle from transverse fracture initiation (0° from vertical direction) to longitudinal fracture (90° from vertical direction). In this situation, the average fracture initiated with 20° from the vertical direction is shown in the inclined wellbore design.

Results from both the image log and the fissure opening equation can aid determination of an optimum drilling direction based on the fracture azimuth using Equation 19. In this case, using 60°—obtained from the DFIT data and Equation 17—results in the following natural fracture azimuth.

$$\begin{aligned} \text{Azimuth of fracture} &= \\ \text{Azimuth of maximum horizontal stress} &- 60^\circ \end{aligned} \tag{19}$$

The azimuth of drilling needs to be drilled perpendicular to the natural fracture system to enhance propagation in the pre-existing fractures, thereby maximising the number of fractures from an optimally inclined well placement. As shown in Equation 20, to perform an optimal hydraulic fracture stimulation within the well, the recommended drilling plan is to drill at an azimuth of 138° and with an inclination of 60° (Fig. 14).

$$\text{Azimuth of drilling} = \text{Azimuth of fracture} + 90^\circ \tag{20}$$

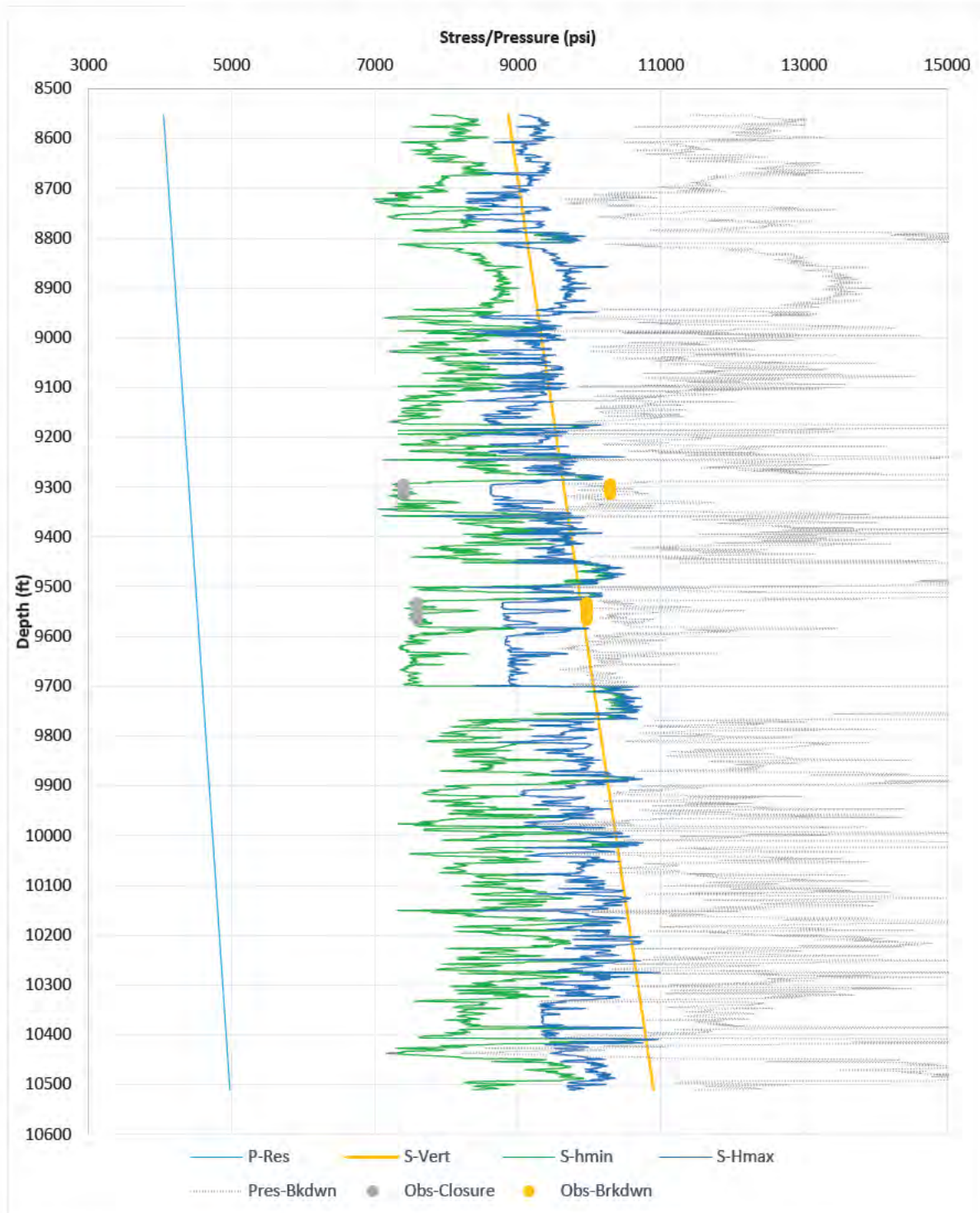


Figure 11. 1D MEM in well C-7.

In Figure 14, the blue color represents the fracture direction and the orange line represents the inclined well direction. In addition, the authors also make the assumption that the natural fractures interpreted from the C-13 image log are all present within well C-7. The distance between these wells is approximately 4,600 ft and covered the target formation. No image log was run within C-7, and an incomplete pressure data set was found in well C-13. As the distance between wells is quite large, the accuracy of the authors' natural fracture set geometries may be affected. This is often the case in fields where analog wells must be rationalised to provide the best go-forward plan.

Therefore, for new areas or areas where a number of wells are combined to generate the optimised plans, a pilot hole is

recommended to investigate the likely intersection between the hydraulic fracture and natural fractures. This pilot well can give more confidence in optimising fracture dilation and propagation using all the data from a single wellbore prior to sidetracking the deviated wellbore, reducing the costs relative to two wells. Finally, to fully close the optimisation loop, it is recommended to verify the results using microseismic monitoring and history-matching the geomechanical model using numerical methods. The results of this process can greatly enhance understanding of a complex fracture network and aid an optimal hydraulic fracture design for complex stress regimes as early as possible in the well development planning stage.

Continued from previous page.

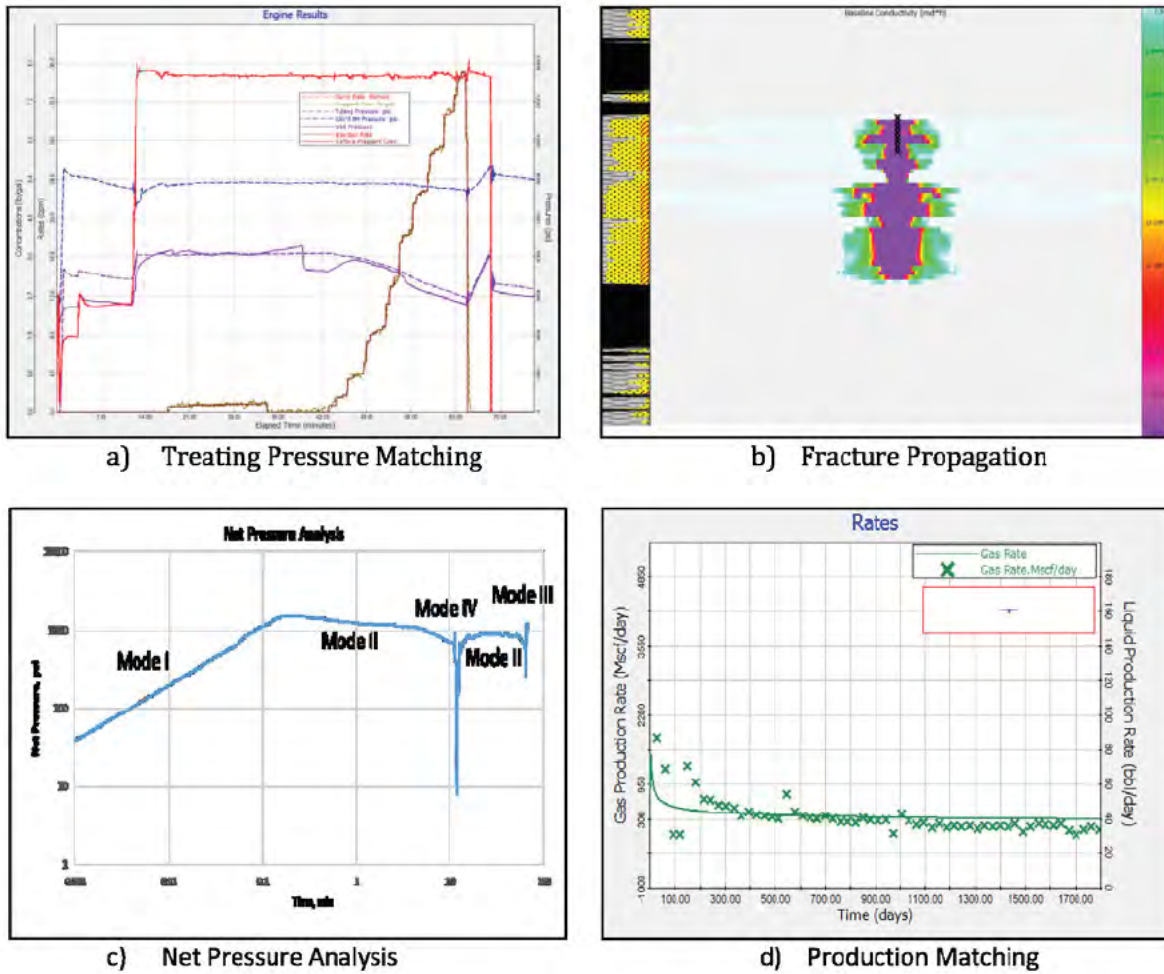


Figure 12. Results of 3D hydraulic fracturing simulation in well C-7, stage 1.

Table 3. Results of 3D hydraulic fracturing in well C-7.

Well/stage	Fracture half length	Fracture height	Fracture width	Fracture conductivity	Dimensionless fracture conductivity
C-7, stage 1	96 ft	175 ft	0.2 in	154 mD.ft	30
C-7, stage 2	176 ft	35 ft	0.2 in	315 mD.ft	30

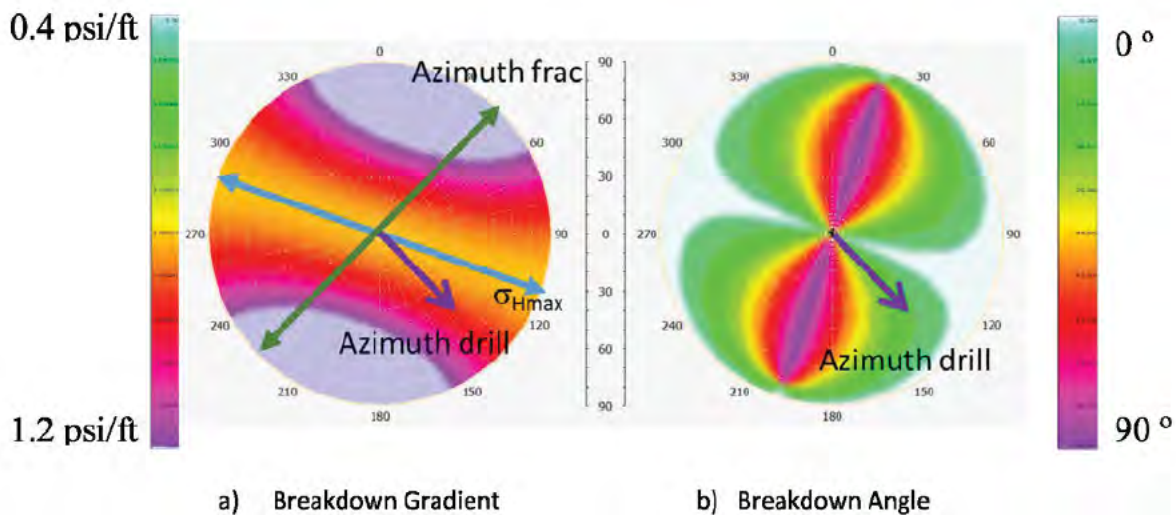


Figure 13. Fracture orientation.

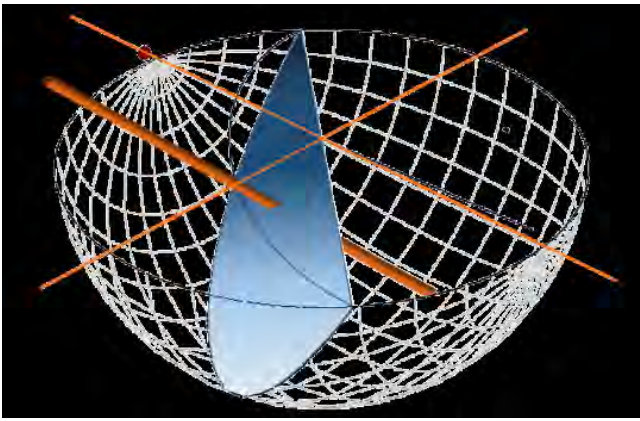


Figure 14. Well inclined drilling (azimuth 138° and inclination 60°).

CONCLUSIONS

New approaches and well-defined workflows for hydraulic fracturing planning have been proposed for tight sands in high stress environments with pre-existing natural fractures based on image log and DFIT data, and are refined using 3D planar hydraulic fracture history-matching. This multidisciplinary approach is extended to develop an optimised deviation/inclination for future well drilling to enhance hydraulic fracture stimulation of a natural fracture network. Key elements of this process are as follows.

- A rigorous process of DFIT interpretation has been proposed, incorporating step down, before closure and after closure analysis methods. In the example case, this process identified tortuosity in the fracture path as the dominant mechanism for near wellbore pressure loss. Furthermore, the data indicated a high-level pressure dependent leak off, supporting the theory that dominant fluid leakoff mechanism in this environment is leakoff occurring through natural fractures.
- The process of developing a 1D MEM has been presented for this case study in the Cooper Basin using the DFIT and image log data. The outcome confirms that strike-slip, normal and reverse stress regimes all exist within the wellbore. The minimum horizontal stress and the maximum horizontal stress values were estimated from well logs and calibrated by observed DFIT data using a non-linear, least-square based genetic algorithm. The key finding for this case is that the maximum horizontal tectonic strain is roughly three times higher than the minimum horizontal tectonic strain, creating a highly stressed and anisotropic stress environment.
- A calibrated hydraulic fracture model was developed and validated by pressure history matching. A good match was found between simulated and observed data, and indicated good fracture propagation and vertical coverage with good fracture height containment.
- From this data, a deviated well plan could be developed to maximise hydraulic fracture interaction by striking a well perpendicular to the natural fracture orientation and at an inclination favourable for fracture breakdown. In this case the plan was developed using a vertical wellbore fissure opening pressure and incorporating the natural fracture azimuth from image log data. For future wells in this case study area, the recommendation is for using a deviated and inclined wellbore with an azimuth of 138° and inclination of 60° to maximise natural fracture interaction. A similar process could be used for other wells in high-stress strike-slip stress regimes using offset or pilot hole image log and DFIT data.

ACKNOWLEDGEMENTS

The authors would like to acknowledge the financial contribution made by Santos. The authors would also like to thank GOHFER, Paradigm (Geolog 7.2), Down Under Geosolutions (DUG Insight 3.1), and Carlos H. Grohmann and Ginaldo A.C. Campanh (OpenStereo 0.1.2) for permissions to use their software.

NOMENCLATURE

α	Inclination from the vertical direction (°)
α_h	Horizontal poroelastic constant (dimensionless)
α_v	Vertical poroelastic constant (dimensionless)
β	Azimuth relative to maximum horizontal stress (°)
θ	Angle from the direction of minimum horizontal stress (°)
ν	Poisson's ratio (dimensionless)
σ	Vertical net stress (psi)
σ_h	Minimum horizontal net stress (psi)
σ_H	Maximum horizontal net stress (psi)
σ_{hmin}	Minimum horizontal stress (psi)
σ_{Hmax}	Maximum horizontal stress (psi)
σ_r	Radial net stress (psi)
σ_t	Tangential (hoop) net stress (psi)
σ_z	Axial well stress (psi)
$\tau_{\theta\theta}$	Shear stress in the plane of the borehole stress (psi)
P_0	Far-field pore pressure (psi)
P_{ob}	Overburden pressure (psi)
p_p	Pore pressure (psi)
P_w	Wellbore fluid pressure (psi)
r	Distance from wellbore (in)
r_w	Wellbore radius (in)
S_x	Transformed x-direction stress
S_y	Transformed y-direction stress
S_z	Transformed z-direction stress
S_{xy}	Shear stress in x-y plane
S_{yz}	Shear stress in y-z plane
S_{zx}	Shear stress in z-x plane

REFERENCES

- APAK, S.N., STUART, W.J., LEMON, N.M. AND WOOD, G., 1997—Structural evolution of the Permian Triassic Cooper Basin, Australia: relation to hydrocarbon trap styles. *AAPG Bulletin*, 81 (4), 533–55.
- BARREE, R.D., 1983—A Practical Numerical Simulator for Three-Dimensional Fracture Propagation in Heterogeneous Media. *SPE Reservoir Simulation Symposium*, San Francisco, California, 15–18 November, SPE-12273.
- BARREE, R.D., BARREE, V.L. AND CRAIG, D., 2009—Holistic fracture diagnostics: consistent interpretation of prefrac injection tests using multiple analysis methods. *SPE Production & Operations*, 24 (3), 396–406.
- BARREE, R.D. AND MISKIMINS, J.L., 2015—Calculation and Implications of Breakdown Pressures in Directional Wellbore Stimulation. *SPE Hydraulic Fracturing Technology Conference*, The Woodlands, Texas, 3–5 February, SPE-173356.
- BENTLEY, P.J.D., JIANG, H. AND MEGORDEN, M.P., 2013—Improving Hydraulic Fracture Geometry by Directional Drilling in Coal Seam Gas Formation. *SPE Unconventional Resources Conference and Exhibition-Asia Pacific*, Brisbane, Queensland, 11–13 November, SPE-167053.

- BLANTON, T.L., 1983—The Relation Between Recovery Deformation and In-Situ Stress Magnitudes. SPE/DOE Low Permeability Gas Reservoirs Symposium, Denver, Colorado, 14–16 March, SPE-11624.
- CAMAC, B.A., WALDRON, A.W., DONLEY, J.A. AND HUNT, S.P., 2012—Microseismic and 3D VSP for Infill Evaluation in Greater Tindilpie, Cooper Basin, Australia. 46th US Rock Mechanics/Geomechanics Symposium, Chicago, Illinois, 24–27 June, ARMA-2012-618.
- GROHMAN, C.H AND CAMPANHA G.A.C., 2010—OpenStereo: Open source, Cross-platform Software for Structural Geology Analysis. 2010 AGU Fall Meeting, San Francisco, California, 13–17 December, abstract #IN31C-06.
- HAINES, P.W., HAND, M. AND SANDIFORD, M., 2001—Palaeozoic synorogenic sedimentation in central and northern Australia: a review of distribution and timing with implications for the evolution of intracontinental orogens. *Australian Journal of Earth Sciences*, 48 (6), 911–28.
- JAEGER, J.C. AND COOK, N.G.W., 1979—Fundamentals of rock mechanics. London: Chapman and Hall.
- JOHNSON, R.L. JR., ABUL KHAIR, H.F., JEFFREY, R.G., MEYER, J.J., STARK, C. AND TAUCHINTZ, J., 2015—Improving fracture initiation and potential impact on fracture coverage by implementing optimal well planning and drilling methods for typical stress conditions in the Cooper Basin, Central Australia. *The APPEA Journal and Conference Proceedings*, 55, extended abstract.
- JOHNSON, R.L., JR. AND GREENSTREET, C.W., 2003—Managing Uncertainty Related to Hydraulic Fracturing Modeling in Complex Stress Environments with Pressure-Dependent Leakoff. *The SPE Annual Technical Conference and Exhibition*, Denver, Colorado, 5–8 October, SPE-84492.
- KIRSCH, E.G., 1898—Die Theorie der Elastizität und die Bedürfnisse der Festigkeitslehre. *Zeitschrift des Vereines Deutscher Ingenieure*, 42 (28), 797–807. Translation: The theory of elasticity and the requirements of the resistance of materials. *Journal of the Association of German Engineers*.
- KUANG, K.S., 1985—History and style of Cooper-Eromanga Basin structures. *Exploration Geophysics*, 16 (2/3), 245–8.
- KULIKOWSKI, D., AMROUCH, K., AL BARWANI, K.H.M., LIU, W. AND COOKE, D., 2015—Insights into the tectonic stress history and regional 4D natural fracture distribution in the Australian Cooper Basin using Etchecopar's calcite twin stress inversion technique, 2D/3D seismic interpretation and natural fracture data from image logs and core. *AAPG International Conference and Exhibition*, Melbourne, Victoria, 13–16 September, extended abstract #2224164.
- KULIKOWSKI, D., COOKE, D. AND AMROUCH, K., 2016—Constraining the distribution and relationship between overpressure, natural fracture density and temperature in the Cooper Basin. *The APPEA Journal*, this volume, in press.
- LASDON, L.S., WARREN, A.D., JAIN, A. AND RATNER, M., 1978—Design and testing of a generalized reduced gradient code for nonlinear. *ACM Transactions on Mathematical Software*, 4 (1), 34–50.
- MURPHY, H.D. AND FEHLER, M.C., 1986—Hydraulic Fracturing of Jointed Formations. *International Meeting on Petroleum Engineering*, Beijing, China, 17–20 March, SPE-14088.
- NELSON, E.J., CHIPPERFIELD, S.T., HILLIS, R.R., GILBERT, J., MCGOWEN, J. AND MILDREN, S.D., 2007—The relationship between closure pressures from fluid injection tests and the minimum principal stress in strong rocks. *International Journal of Rock Mechanics and Mining Sciences*, 44 (5), 787–801.
- NOLTE, K.G., MANIERE, J.L. AND OWENS, K.A., 1997—After-Closure Analysis of Fracture Calibration Tests. *SPE Annual Technical Conference and Exhibition*, San Antonio, Texas, 5–8 October, SPE-38676.
- NOLTE, K.G. AND SMITH, M.B., 1981—Interpretation of fracturing pressures. *Journal of Petroleum Technology*, 33 (9), 1,767–75.
- POKALAI, K., FEI, Y., AHMAD, M., HAGHIGHI, M. AND GONZALEZ, M., 2015—Design and optimisation of multi-stage hydraulic fracturing in a horizontal well in a shale gas reservoir in the Cooper Basin, South Australia. *The APPEA Journal*, 55, 1–14.
- POKALAI, K., HAGHIGHI, M., SARKAR, S., TYIASNING, S. AND COOKE, D., 2015—Investigation of the Effects of Near-Wellbore Pressure Loss and Pressure Dependent Leakoff on Flowback during Hydraulic Fracturing with Pre-Existing Natural Fractures. *SPE/IATMI Asia Pacific Oil and Gas Conference and Exhibition*, Nusa Dua, Bali, 20–22 October, SPE-176440.
- REYNOLDS, S.D., MILDREN, S.D., HILLIS, R.R. AND MEYER, J.J., 2006—Constraining stress magnitudes using petroleum exploration data in the Cooper-Eromanga Basins, Australia. *Tectonophysics*, 415 (1–4), 123–40.
- ROBERTS, G.A., CHIPPERFIELD, S.T. AND MILLER, W.K., II, 2000—The Evolution of a High Near-Wellbore Pressure Loss Treatment Strategy for the Australian Cooper Basin. *SPE Annual Technical Conference and Exhibition*, Dallas, Texas, 1–4 October, SPE-63029.
- TEUFEL, L.W., 1983—Determination of In-Situ Stress From Anelastic Strain Recovery Measurements of Oriented Core. *SPE/DOE Low Permeability Gas Reservoirs Symposium*, Denver, Colorado, 14–16 March, SPE-11649.
- THIERCELIN, M.J. AND PLUMB, R.A., 1994—A core-based prediction of lithologic stress contrasts in east Texas formations. *SPE Formation Evaluation*, 9 (4), 251–8.
- ZHOU, S., HILLIS, R. AND SANDIFORD, M., 1994—A study of the design of inclined wellbores with regard to both mechanical stability and fracture intersection, and its application to the Australian North West Shelf. *Journal of Applied Geophysics*, 32 (4), 293–304.
- ZOBACK, M.D., 2007—Reservoir geomechanics. Cambridge: Cambridge University Press.

Authors' biographies next page.

THE AUTHORS



Kunakorn Pokalai is presently a production engineering PhD candidate at the University of Adelaide. He has a BEng in petrochemical engineering from Silpakorn University (Thailand), and completed a Graduate Certificate in Management, and a master's in petroleum engineering from the University of Adelaide.

Kunakorn's research interests are in the simulation of unconventional reservoirs and hydraulic fracturing. He mainly focuses on the issue of fracturing fluid flowback in the Cooper Basin. He was the recipient of the prestigious AAPG Imperial Barrel Award in the Asia Pacific Region in 2014. Member: SPE and AAPG.

kunakorn.pokalai@adelaide.edu.au



David Kulikowski holds a BSc (Honours) in petroleum geoscience and geophysics, and is now completing a PhD by publication in structural geology at the Australian School of Petroleum, University of Adelaide. David's main research interests are in better understanding the structural and stress history of the Cooper Basin through the integration of micro- (calcite twinning), meso- (natural fractures) and macro-scale (faults) structural data.

David is a recipient of the 2015 American Association of Petroleum Geologists (AAPG) Grants-in-Aid Foundation Scholarship. He was also a team member in the first Australian team to win the prestigious Asia-Pacific Region AAPG Imperial Barrel Award (IBA) in 2014. During the early stages of his PhD, David was employed as a part-time technical assistant at Santos in the gas production and optimisation engineering team.

david.kulikowski@adelaide.edu.au



Raymond (Ray) L. Johnson, Jr. is presently Principal at Unconventional Reservoir Solutions, and serves as Adjunct Associate Professor at The University of Adelaide, and Senior Lecturer at The University of Queensland. He has a PhD in mining engineering, a MSc in petroleum engineering, a Graduate Diploma in information technology, and a BA in

chemistry. Ray has been active in the Society of Petroleum Engineers (SPE) as past Chair of the SPE Queensland Section, and served as 2013 and 2015 technical co-Chair of the SPE Unconventional Reservoir Conference and Exhibition Asia Pacific.

He has authored, co-authored and presented numerous papers on unconventional reservoir technologies at SPE and APPEA conferences, as well as published in peer-reviewed journals.

ray.johnson@adelaide.edu.au



Manouchehr (Manny) Haghighi is Associate Professor of Petroleum Engineering. His research and teaching focus is on unconventional reservoirs, reservoir simulation, well testing, and formation evaluation. He has supervised more than 40 MSc and 10 PhD students.

Before joining the University of Adelaide in 2009, Manouchehr was Associate Professor of Petroleum Engineering at the University of Tehran (Iran). From 2000–07 he was Head of the petroleum engineering program at the University of Tehran.

In 2000, Manouchehr established Simtech, a consulting company for the integrated reservoir simulation. He has been project director of several full field simulation projects for oil and gas reservoirs.

From 1995 to 2000, Manouchehr was working with the National Iranian Oil Company (NIOC) and was the director of a program for training NIOC staff at several universities in the US, UK, Canada, France, Australia and Norway. Manouchehr was a visiting professor at the University of Calgary from 2007–08.

Manouchehr has published more than 80 articles in peer review journals or presented in international conferences. He has served as a reviewer for different journals such as the Journal of Petroleum Science and Engineering. Member: SPE.

manouchehr.haghighi@adelaide.edu.au



Dennis Cooke has a PhD in geophysics from the Colorado School of Mines, and more than 25 years of experience in oil and gas exploration and development. He is a past-president of the Australian Society of Exploration Geophysicists (ASEG), and a former vice president of the Society of Exploration Geophysicists (SEG).

Dennis owns and operates ZDAC Geophysical Technology, which provides technology and services for seismic inversion and reservoir characterisation. He is an Adjunct Assistant Professor at the University of Adelaide's Australian School of Petroleum.

dennis.cooke@adelaide.edu.au

THIS PAGE LEFT BLANK INTENTIONALLY.

**Chapter 5 : Investigation of the Effects of Near-Wellbore
Pressure Loss and Pressure Dependent Leak-off on
Flowback during Hydraulic Fracturing with Pre-
Existing Natural Fractures**

SPE-176440-MS

Investigation of the Effects of Near-Wellbore Pressure Loss and Pressure Dependent Leakoff on Flowback during Hydraulic Fracturing with Pre-Existing Natural Fractures

K. Pokalai, M. Haghighi, S. Sarkar, S. Tyiasning, and D. Cooke, University of Adelaide

Copyright 2015, Society of Petroleum Engineers

This paper was prepared for presentation at the SPE/IATMI Asia Pacific Oil & Gas Conference and Exhibition held in Nusa Dua, Bali, Indonesia, 20–22 October 2015.

This paper was selected for presentation by an SPE program committee following review of information contained in an abstract submitted by the author(s). Contents of the paper have not been reviewed by the Society of Petroleum Engineers and are subject to correction by the author(s). The material does not necessarily reflect any position of the Society of Petroleum Engineers, its officers, or members. Electronic reproduction, distribution, or storage of any part of this paper without the written consent of the Society of Petroleum Engineers is prohibited. Permission to reproduce in print is restricted to an abstract of not more than 300 words; illustrations may not be copied. The abstract must contain conspicuous acknowledgment of SPE copyright.

Abstract

It is generally believed that the incomplete return of treating fluids (flowback) is a reason for the failure of hydraulic fracturing and it is associated with poor gas production. Capillary effects and fracture face skin are known to be the main parameters that limit flowback in tight gas sands. However, near-wellbore pressure loss during the main operation of hydraulic fracturing and its effects on flowback are not well understood.

In the case of pre-existing natural fractures in a reservoir, near-wellbore pressure loss is high mainly because multiple fractures with tortuous paths are often created. Also, it is believed that this tortuous path causes shear dilation in natural fractures and opens the closed fractures. As a result, there is a large amount of pressure dependent leakoff. Therefore, pressure dependent leakoff has both positive and negative impacts. It can increase rock permeability and at the same time it can cause a high near-wellbore pressure drop. Hence, near-wellbore pressure needs to be reduced in order to have better proppant placement and maximize the fracturing fluid flowback.

For this research, several hydraulic fracturing treatments in the Patchawarra formation in the Cooper Basin, South Australia have been studied. There are some pre-existing natural fractures in our case study. The bottom-hole treating pressure has been analysed with 600 psi of near-wellbore pressure loss causing a low percentage of proppant placement. We constructed a 3D hydraulic fracturing model coupled with multiphase flow simulation for the prediction of flowback of water and gas production.

Several injection fall-off tests were first interpreted and found that the leakoff is pressure dependent. Our simulation has shown that high near-wellbore pressure loss has an impact on the effectiveness of the fracture treatment. This results in a shorter fracture length and low pressure distribution inside the fracture that leads to a low recovery of fracturing fluid. As a result, we have successfully provided recommendations for best practice to reduce near-wellbore pressure loss.

Introduction

Hydraulic fracturing is a process that involves injecting of large volumes of fracturing fluid and proppant under high pressure in order to induce the fractures around the wellbore and to increase the flow path in

a low permeability reservoir. However, during injection and fracture propagation, in some situations, a considerable pressure loss is observed near wellbore. Near-wellbore pressure loss (NWBPL) was first discussed by [Chipperfield et al. \(2000\)](#) and [Roberts, Chipperfield, and Miller \(2000\)](#). They stated that the causes of NWBPL are pressure loss in perforation and tortuosity in induced fracture path near wellbore. [Johnson et al. \(2002\)](#) and [Johnson and Greenstreet \(2003\)](#) discussed pressure dependent leakoff (PDL) and NWBPL in the Cooper Basin and showed how these effects have an impact on the production performance by using 3D hydraulic fracturing simulation. [Lizak et al. \(2006\)](#) showed how different types of NWBPL can be detected by the step down test (SDT). Moreover, [Scott et al. \(2013\)](#) discussed the high NWBPL in tight gas and shale gas reservoirs and showed that NWBPL created high tortuosity in the Cooper Basin.

This research focuses on the study of diagnostic fracture injection tests by using both the step down test and the pre-closure analysis test to determine near-wellbore pressure loss and the leak off identification. These two tests help to better understand the physics of fracture propagation in the target stimulation. Then, the results of these tests were used in a 3D hydraulic fracturing modeling coupled with reservoir simulation in order to optimize the fracturing fluid flowback and gas production. Flowback which is the recovery of only a small portion of the amount of injected fluid may cause hydrocarbon entrapments in the low permeability reservoirs and lead to less expected gas production. The effect of fracturing fluid due to the capillary pressure and low relative permeability of gas has been described by [Holditch \(1979\)](#). There are many publications that describe how to prevent the fluid entrapment after stimulation by using chemicals or surfactants and explain the flow behavior by numerical simulation ([Agrawal and Sharma 2013](#)).

In this paper, first, the definition and the theoretical background of NWBPL and PDL are discussed. Then, the methodology is explained with a workflow diagram. After that, several test results and information about the case study are presented. Subsequently, the results of 3D hydraulic fracturing models and multiphase flow models are discussed. Finally some conclusive remarks are stated.

Theoretical Background

Near-Wellbore Pressure Loss (NWBPL)

Near-wellbore pressure loss is a combination of pressure drop near the wellbore based on perforation friction and tortuosity ([Chipperfield et al. 2000](#)). High NWBPL results in a lower percentage of proppant placement. NWBPL caused by tortuosity impacts fracture propagation. Four different types of fracture propagation due to tortuosity are reported including fracture turning, fracture twisting, multiple fracturing and fracture migration as shown in [Fig. 1](#). Fracture turning is caused by the change in lithology while fracture twisting is the result of complex stress regime in which the orientation of the minimum horizontal stress is changing. Multiple fracturing and fracturing migration are results of complex geometrical patterns caused by high tortuosity in the formation and the lower minimum horizontal stress in neighboring formation respectively.

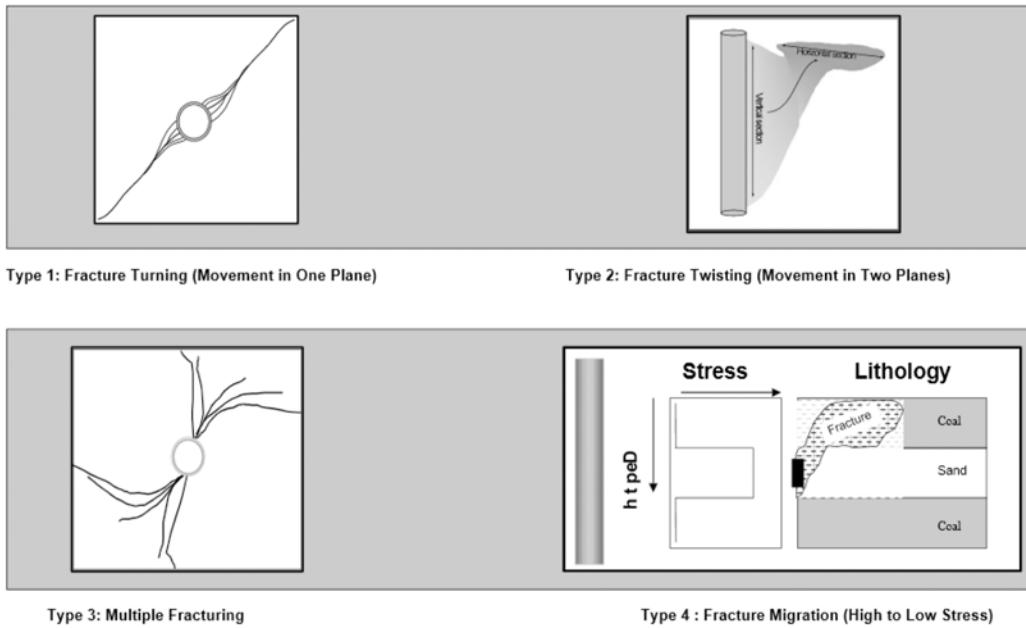


Figure 1—Four types of Near-Wellbore Pressure Loss cause by tortuosity (Roberts, Chipperfield, and Miller 2000)>

Near-wellbore pressure loss (NWBPL) can be identified by the step-down test in which the pressure is recorded while the injection rate is decreased step by step rather than by shutting in immediately. A plot of bottomhole treating pressure versus the slurry rate is shown in Fig. 2, if the plot exhibits a concave curve, tortuosity is dominated. In contrast, if the curve is convex, the perforation pressure drop is dominated. Equation 1 is an empirical model for the total NWBPL. The first term in the right hand side of the equation is related to perforation which is a function of high rate dependency (q^2) and the second term is related to tortuosity which is a function of low rate dependency ($q^{0.5}$). Equation 2 shows the perforation pressure loss coefficient (k_{perf}), which is a function of slurry density (ρ), perforation diameter (D_p), number of perforation (N) and coefficient of discharge (C_d). Tortuosity pressure loss coefficient (k_{tort}) is an empirical value which depends on the pressure-dependent opening and far-field stresses (Hildek and Weijers 2007).

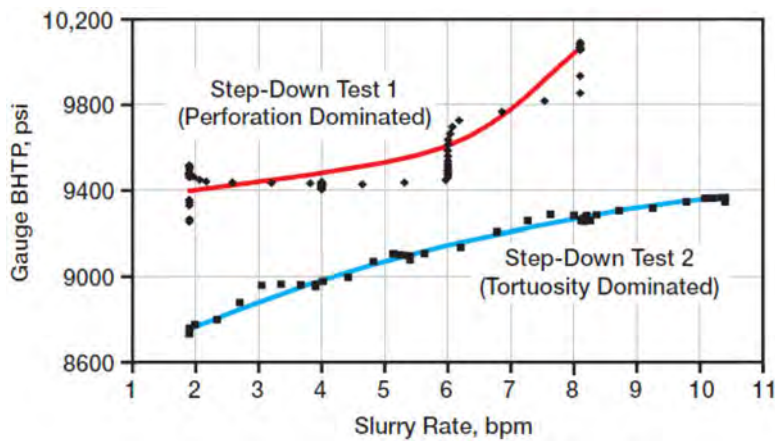


Figure 2—Step-Down Test (SDT) (Martin and Valko' 2007)

$$\Delta p_{NWBPL} = (k_{perf}q^2) + (k_{tort}q^{0.5}) \tag{1}$$

$$k_{perf} = 0.237 \frac{\rho}{N^2 D p^2 C_d^2} \quad (2)$$

Pressure Dependent Leakoff (PDL)

Pressure dependent leakoff is one type of leakoff which, fracturing fluid can be penetrated to the surrounding matrix, pre-existing natural fracture and fissures (Castillo 1987), (Barree and Mukherjee 1996). As it is shown in Fig. 3, the pre-existing natural fractures propagate perpendicular to the maximum horizontal stress. During the increase of the treating pressure along the main fracture, the dilation of natural fractures can be induced by resulting stress more than the maximum horizontal stress and keeps the natural fracture open (Chipperfield et al. 2007).

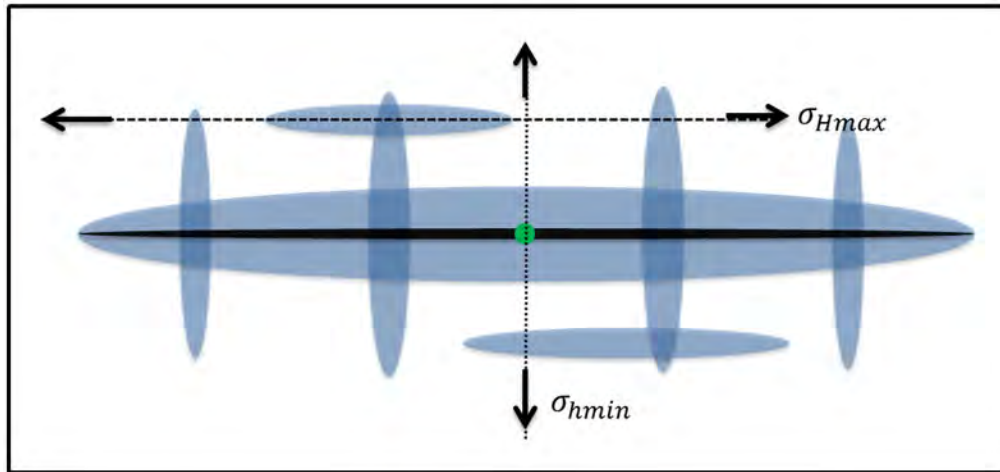


Figure 3—The conceptual model of Pressure Dependent Leakoff (PDL) (Baree & Associates Llc 2015)

By pre-closure analysis, the type of leakoff mechanism can be detected using G-function analysis (Barree et al. 2007). The G-function $G(\Delta t_D)$ is a dimensionless leakoff time function during fracture initiation and propagation. Equation 3 is a mathematical representation of G-function $G(\Delta t_D)$.

$$G(\Delta t_D) = \frac{4}{\pi} [g(\Delta t_D) - g_0] \quad (3)$$

High fluid leakoff is applied in this equation, where, $g(\Delta t_D)$ is fluid loss at dimensionless time, g_0 is dimensionless loss-volume function at the shut in time and Δt_D is dimensionless pumping time. Fig. 4 shows three different plots of pressure (p), pressure derivative (dP/dG) and semilog derivative of the pressure ($G[dP/dG]$) versus G-Function time respectively. The early increase in semilog pressure derivative can be observed as a hump. A straight line through the origin tangent to this plot gives the fracture closure pressure, however the first vertical dashed line indicates the fissure opening pressure and second dashed line indicates the closure pressure. To confirm the closure pressure, we should use the plot of first derivative of pressure ($dP/d\sqrt{t}$) versus \sqrt{t} where the optimum or peak of constant first derivative pressure indicates the closure pressure. Moreover, the PDL coefficient (C_{PDL}) can be determined as the difference between the overall PDL coefficient (C_P) and the original leakoff coefficient (C_O) as the pressure increases above the critical fissure opening pressure. This is described in Equation 4. The overall PDL coefficient increases based on the exponential function of the difference between fluid pressure and fissure opening (ΔP).

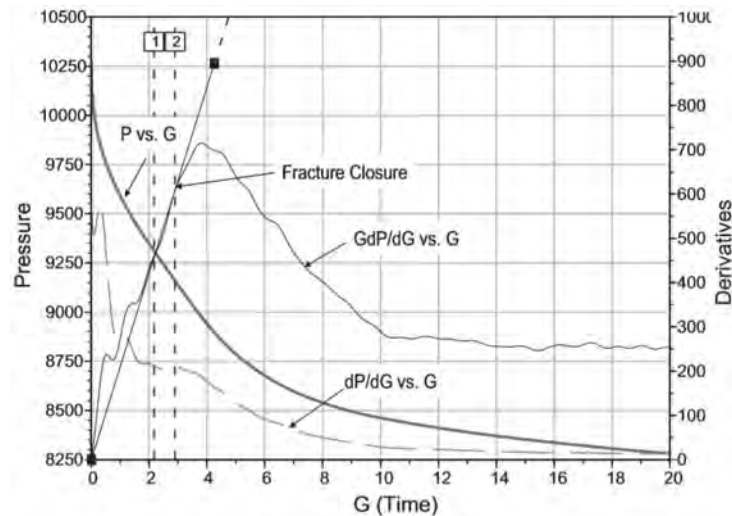


Figure 4—Pressure Dependent Leakoff (PDL) of G-function plot (Barree et al. 2009)

$$C_P = C_0 \exp[C_{PDL} \Delta P] \quad (4)$$

Ramurthy et al. (2013) showed that high pressure dependent leakoff leads to the screen-out effect. To prevent high PDL, the optimum injection rate and low mesh sand should be used in order to bridge-off the transverse fracture in the pre-existing natural fracture. Moreover, they found that high PDL could lead to good production. However, according to Johnson and Greenstreet (2003) and Johnson et al. (2002), high PDL and high NWBPL can lead to unsuccessful hydraulic fracture stimulation because of the high stress complexity in the Cooper Basin. This failure arises because the fracturing fluid could impair or damage the natural fractures in the formation.

Methodology

3D hydraulic fracturing model is first developed for multi-stage hydraulic fracturing in vertical wells using GOHFER (2015). Then, this model is coupled with reservoir simulation using Eclipse (2014). Coupling of hydraulic fracturing model with multi-phase flow simulation has been previously discussed for a multi-stage hydraulic fracturing in a horizontal well (Pokalai et al. 2015). Fig. 5 shows the workflow diagram starting with the well logging data which generates the geomechanical properties. The next step is to identify NWBPL from the step down test. The Pre-Closure Analysis is used to identify the leakoff mechanism, closure pressure and the pressure dependent leakoff coefficient. The models are validated by comparison with three different matching parameters which are the measured closure pressure, the treating pressure and the gas production rate.

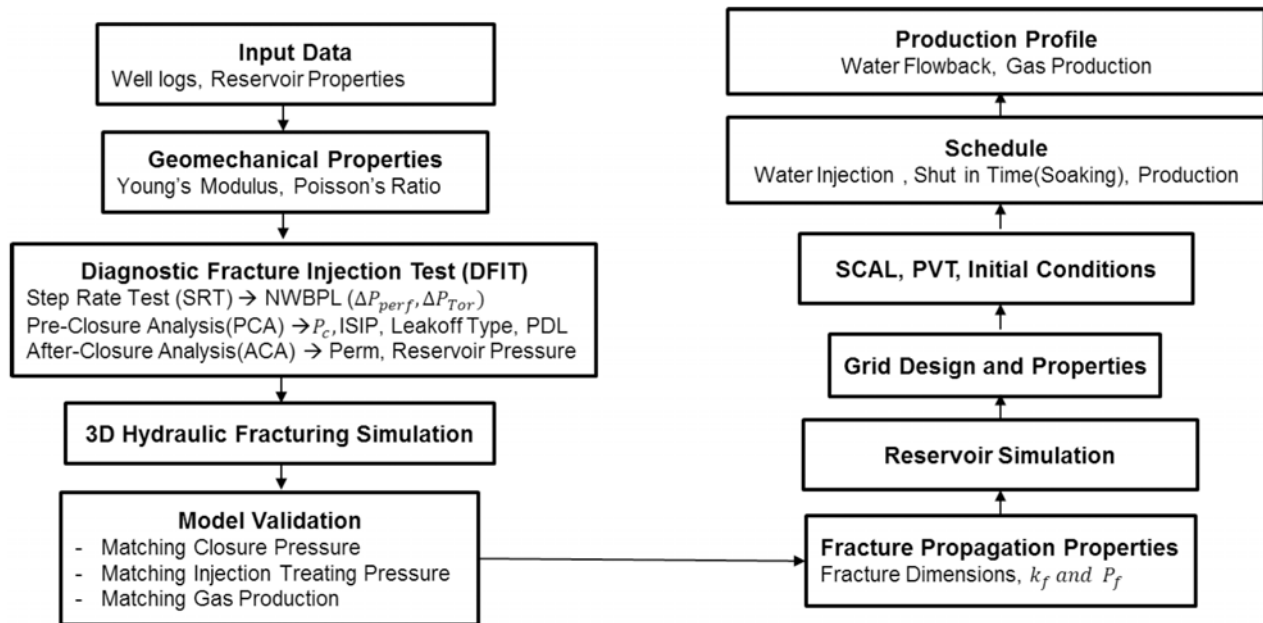


Figure 5— Workflow for coupling of 3D hydraulic fracturing model with reservoir simulations

The output of the 3D hydraulic fracturing model is fracture width, fracture height, propped fracture half-length and fracture conductivity. In order to couple hydraulic fracturing simulation with flow simulation. First the output of hydraulic fracturing model are imported for mesh generation in reservoir simulation. Later, all the required reservoir parameters for reservoir simulation are prepared are used in order to predict the gas and water production.

Case Study

Our case study is based on three vertical wells (C6, C7 and C8) in a tight sand gas field in the Cooper Basin, South Australia. The gas field is located in the Nappamerri trough with northeast and southwest alignment in Patchawarra formation in central South Australia. The location of the wells and stratigraphic map of the target wells are shown in Fig. 6. The target depths are approximately 9000 ft with net pay varying between 10 – 70 ft and an average permeability of 0.7 md and average porosity of 11 %. The petrophysical properties of each well are shown in Table 1.

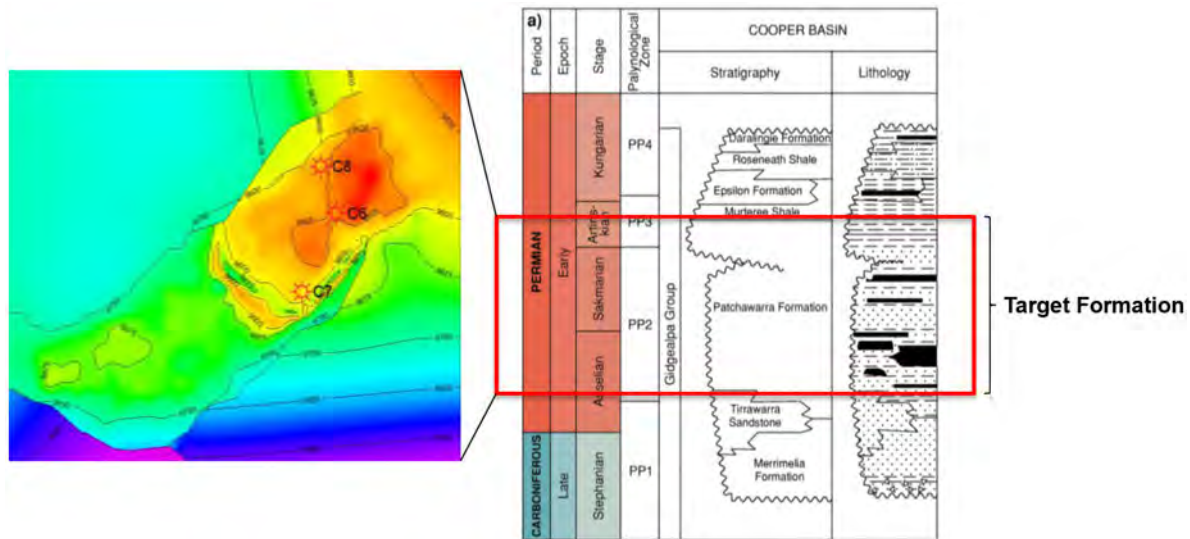


Figure 6— Location of the wells and stratigraphic map of target formation

Table 1—Petrophysical Properties of C6, C7 and C8

Well/Stage	Depth (ft)	Net Pay (ft)	Permeability (mD)	Porosity (%)	Water Saturation (%)	Temperature (°F)
C6						
Stage 1	9503–9581	43	0.65	10.4	36	278
Stage 2	9265–9306	27	1.62	10.5	27	272
C7						
Stage 1	9533–9634	70	0.12	11.3	34	282
Stage 2	9294–9351	36	0.06	10.0	31	275
C8						
Stage 1	10398–10410	27	0.03	8.8	19	282
Stage 2	9854–9879	24	0.30	10.6	40	274
Stage 3	9524–9610	34	0.60	7.8	34	272
Stage 4	9512–9524	11	0.30	9.0	27	260
Stage 5	9162–9186	20	2.40	9.0	32	249
Stage 6	9100–9120	18	0.70	10.5	31	246
Stage 7	9004–9016	10	1.00	10.0	21	246

Most of the Patchawarra formations consist of thick sand interval between coal and shale as shown in Fig. 7. Full set petrophysical logs were available including gamma ray, resistivity, sonic, density and neutron porosity. Well C6 and C7 were treated with two stages of hydraulic fracturing in Patchawarra formation. Well C8 was treated with 6 stages in Patchawarra and one stage in Tirrawarra, a total of 7 stages. The downhole was lined with a 4.5 inch production casing. Most of the perforation depths are between 9,000 and 10,000 ft.

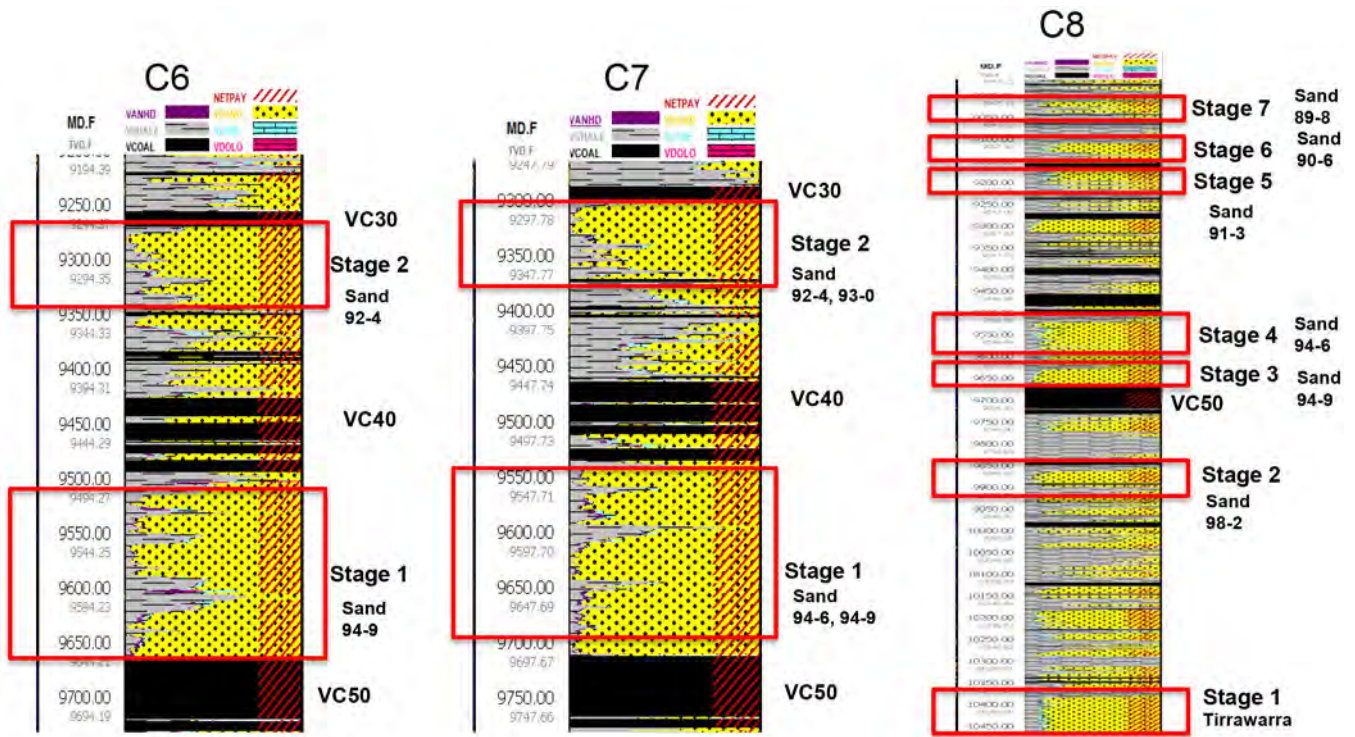


Figure 7—Different stages of hydraulic fracturing in C6, C7 and C8 wells

Hydraulic Fracturing Treatment

The fracturing fluid system and proppant which were used in well C6, C7 and C8 are shown in Table 2. The water based fluid system with Hydroxypropyl Guar (HPG) and Borate Crosslink gel were injected from the pad stage until the flushing stage. The average amount of fracturing fluid used per stage was 51,000 gallons. The 100 mesh sand was pumped into the target zone first in order to reduce NWBPL. Following that, the high density ceramic proppant was injected to provide high fracture conductivity around 3000 md-ft at the high closure stress, approximately 8000 psi in the Cooper Basin.

Table 2—Hydraulic fracturing treatment data

C 6	Fluid Type	Fluid Volume (gal)	Proppant type	Proppant Volume (lb)	Min/Max Proppant Conc (lbm/gal)	Slurry Rate (bpm)
Stage 1	40/HPG/Delay Br X-link	67000 (Pad 30000)	100 Mesh Sand 20/40 , 16/30 high- density ceramic	149000	0.5/8	35
Stage 2	40/HPG/Delay Br X-link	52000 (Pad 29000)	100 Mesh Sand 20/40 , 16/30 high- density ceramic	91000	0.5/8	35
C 7	Fluid Type	Fluid Volume (gal)	Proppant type	Proppant Volume (lb)	Min/Max Proppant Conc (lbm/gal)	Slurry Rate (bpm)
Stage 1	40/HPG/Delay Br X-link	67000 (Pad 30000)	100 Mesh Sand 20/40 , 16/30 high- density ceramic	149000	0.5/8	35
Stage 2	40/HPG/Delay Br X-link	52000 (Pad 29000)	100 Mesh Sand 20/40 , 16/30 high- density ceramic	91000	0.5/8	35
C8	Fluid Type	Fluid Volume (gal)	Proppant type	Proppant Volume (lb)	Min/Max Proppant Conc (lbm/gal)	Slurry Rate (bpm)
Stage 1	FR Water	115139	30/60 high-density ceramic	31500	0.2/1	35
Stage 2	40/HPG/Delay Br X-link	37695	100 Mesh Sand 20/40 , 16/30 intermediate- density ceramic	91000	0.5/6	20
Stage 3	40/HPG/Delay Br X-link	28434	100 Mesh Sand 20/40 , 16/30 intermediate- density ceramic	71255	1/6	20
Stage 4	40/HPG/Delay Br X-link	39386	100 Mesh Sand 20/40 , 16/30 intermediate- density ceramic	52293	0.5/6	20
Stage 5	40/HPG/Delay Br X-link	35684	100 Mesh Sand 20/40 , 16/30 intermediate- density ceramic	51043	1/6	20
Stage 6	40/HPG/Delay Br X-link	35667	100 Mesh Sand 20/40 , 16/30 intermediate- density ceramic	51043	0.5/6	20
Stage 7	40/HPG/Delay Br X-link	31341	100 Mesh Sand 20/40 , 16/30 intermediate- density ceramic	42658	0.5/6	20

Geomechanical Properties

The sonic logs (compressional travel time, DTC and shear travel time, DTS) and density logs were used to calculate the Poisson's ratio, Young's modulus and brittleness (Table 3). The range of Poisson's ratio in tight sand was varied between 0.20 – 0.23. The range of Young's modulus varied between 3.89 and 4.86 MMpsi.. The brittleness is moderate with an average of 0.5.

Table 3—Summary of geomechanical properties

Well/Stage	Poisson's ratio, Dimensionless	Young's Modulus, MMpsi	Brittleness, Fraction
C6			
Stage 1	0.22	4.21	0.49
Stage 2	0.20	4.53	0.53
C7			
Stage 1	0.21	4.33	0.50
Stage 2	0.21	4.43	0.51
C8			
Stage 1	0.20	4.86	0.55
Stage 2	0.21	4.67	0.53
Stage 3	0.21	4.56	0.52
Stage 4	0.22	4.35	0.50
Stage 5	0.23	4.20	0.48
Stage 6	0.22	4.48	0.51
Stage 7	0.23	3.89	0.45

Diagnostic Fracture Injection Test

Several diagnostic fracture injection tests were performed by using borate crosslink gel with an average injection of 20 bpm. The pretest injection starts with the fracture initiation, then decreasing the injection rate step by step and recording the pressure drop in each step (Step Down Test) in order to analyze NWBPL. After interpreting the test results, Pre-Closure Analysis and After-Closure Analysis have been carried out and the results are shown in [Table 4](#)

Table 4—Summary of Different Diagnostic Fracture Injection Tests

Step Rate Test			
<i>Well/Stage</i>	<i>NWBPL (psi)</i>	<i>ΔP Perforation (psi)</i>	<i>ΔP Tortuosity (psi)</i>
C6			
Stage 1	470	58	412
Stage 2	930	22	908
C7			
Stage 1	528	67	461
Stage 2	515	148	368
C8			
Stage 1	2737	2107	630
Stage 2	1710	342	1368
Stage 3	1093	91	1003
Stage 4	1427	1042	385
Stage 5	686	557	129
Stage 6	482	366	116
Stage 7	911	558	433

Pre-Closure Analysis

<i>Well/Stage</i>	<i>ISIP (psi)</i>	<i>Fracture Gradient (psi/ft)</i>	<i>Closure Pressure (psi)</i>	<i>Net Pressure (psi)</i>	<i>Leakoff Type</i>	<i>PDL (1/psi)</i>
C6						
Stage 1	8933	0.936	7426	1509	Height Recession	-
Stage 2	8577	0.925	8030	547	Height Recession	-
C7						
Stage 1	8816	0.923	7007	1809	PDL	0.008
Stage 2	8646	0.905	7509	1137	PDL and Tip Extension	0.003
C8						
Stage 1	11261	1.083	8953	2308	Tip Extension	-
Stage 2	9907	1.004	7257	2650	Height Recession and Tip Extension	-
Stage 3	9321	0.972	6265	3056	PDL	0.003
Stage 4	9178	0.957	6664	2514	Height Recession	-
Stage 5	8479	0.925	7133	1346	Height Recession	-
Stage 6	8391	0.919	6057	2323	PDL	0.002
Stage 7	8723	0.957	7897	826	PDL	0.002

After-Closure Analysis

<i>Well/Stage</i>	<i>Pressure (psi)</i>	<i>Permeability (mD)</i>	<i>Flow Capacity, kH (md-ft)</i>	<i>Flow Behaviors</i>
C6				
Stage 1	4562	0.214	9.2	Pseudo Radial Flow and Pseudo Linear Flow
Stage 2	2800	0.174	4.2	Pseudo Linear Flow
C7				
Stage 1	4572	0.115	8.0	Pseudo Radial Flow and Pseudo Linear Flow
Stage 2	4200	0.098	3.5	Pseudo Linear Flow
C8				
Stage 1	7765*	0.115	4.85	Pseudo Radial Flow
Stage 2	4318	0.098	1.78	Pseudo Radial Flow and Pseudo Linear Flow
Stage 3	4013	0.220	7.43	Pseudo Radial Flow and Pseudo Linear Flow
Stage 4	-	0.0128**	-	-
Stage 5	4274	0.126	2.52	Pseudo Radial Flow
Stage 6	2588	0.075	1.36	Pseudo Radial Flow
Stage 7	7101*	1.33	13.38	Pseudo Radial Flow

The average instantaneous shut-in pressure (ISIP) is estimated to be 9100 psi. From the results of the SDT, high NWBPL caused by mostly tortuosity which is 55 percent in all 11 stages. There are 7 stages where the NWBPL is higher than 600 psi. These high NWBPL are believed to cause lower proppant placement during the main hydraulic fracture stimulation. From the Pre-Closure Analysis, the type of leakoffs have been identified from the semilog derivative (Gdp/dG) of the G-Function. 42 percent of the leakoff behavior is height recession leakoff which indicates the fracture extended through the impermeable layer. Pressure Dependent Leakoff represents 41 % of the total target formation, which indicates the fluid loss rate is changed by the pre-existing natural fracture. The PDL coefficient indicates the leakoff range is between 0.002 and 0.008 1/psi. In addition, the image log interpretation in Fig. 8 from well C13 has been used to confirm the natural fracture in the Patchawarra formation. Most of the fractures are orientated at 120 degrees to North. The average closure pressure (P_c) or Minimum Horizontal Stress (σ_{hmin}) is 7300 psi. This value is used as matching parameter for the 3D hydraulic fracture simulation in the next step.

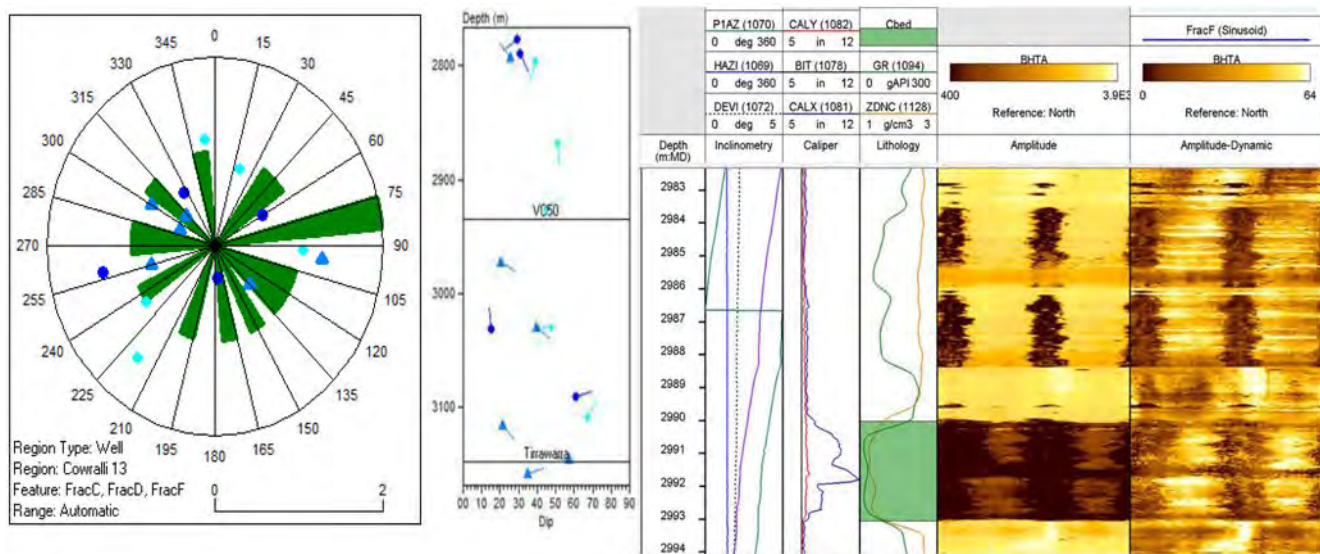


Figure 8—The result of image log interpretation in Well C13

Finally, the After-Closure Analysis has been done to obtain the reservoir properties. In this analysis, pseudo radial flow and pseudo linear flow have been detected, however, but not in all stages because the operator has not recorded the pressure for a sufficient amount of time. From ACA, the average reservoir permeability (k) is 0.2 md with 5.6 md-ft of flow capacity.

Simulation Results and Discussion

In order to investigate the effects of near-wellbore pressure loss and pressure dependent leakoff on flowback, a 3-D hydraulic fracturing model was coupled with multi-phase flow model. In the following subsections, the results of both hydraulic fracturing model and flow model are discussed.

3D Hydraulic Fracturing Model

The results of a 3D hydraulic fracturing model in each stage for three wells have been shown in Table 5. The resulting fracture dimensions are a function of the amount of fracturing fluid, proppant and the stress regime in each grid cell. The average fracture half-length is 200 ft with the fracture height up to 141 ft and an average fracture width of 0.3 in. The models have been validated by matching the surface treating pressure for well C6 stage 1 as shown in Fig 9. The purple dash line shows the actual data and the solid line shows the simulated data, which is in the range of 4000 to 7000 psi.

Table 5—Results of Hydraulic Fracturing Simulation

Well/Stage	Prop Fracture Half Length (ft)	Fracture Height (ft)	Average Fracture Width (in)	Fracture Conductivity (md.ft)	Dimensionless fracture conductivity (F_{CD})
C6					
Stage 1	246	69	0.2	239	4.24
Stage 2	198	45	0.4	479	30
C7					
Stage 1	78	57	0.1	136	4.40
Stage 2	114	51	0.4	189	2.17
C8					
Stage 1	20	65	0.1	67	2.74
Stage 2	272	27	0.3	178	9.72
Stage 3	270	21	0.5	190	1.23
Stage 4	120	141	0.1	153	4.35
Stage 5	468	24	0.3	135	0.49
Stage 6	330	24	0.4	427	2.04
Stage 7	120	45	0.2	55	0.47

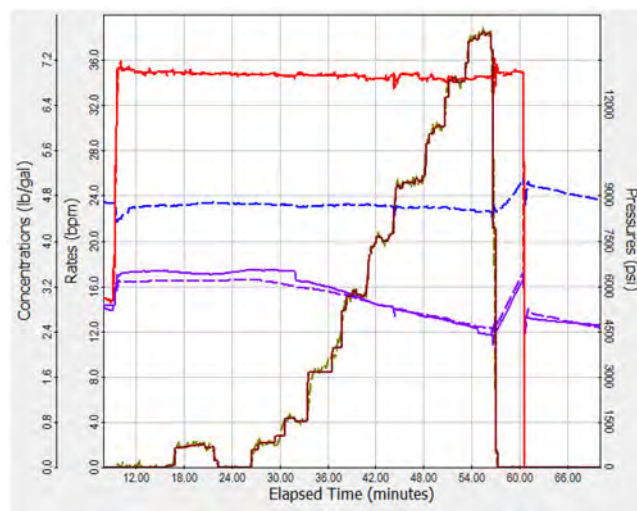


Figure 9—Surface Treating Pressure Matching in Stage 1 Well C6

After validating the model, the resulting proppant concentration is simulated and is shown in Fig 10. The impact of NWBPL and PDL (if detected) have been taken into account during the simulation of all three wells. It was observed that the increasing of the tortuosity leads to increasing treating pressure at the early stages of injection. Also, higher PDL can lead to a shorter fracture half-length when compared to no or lower PDL model.

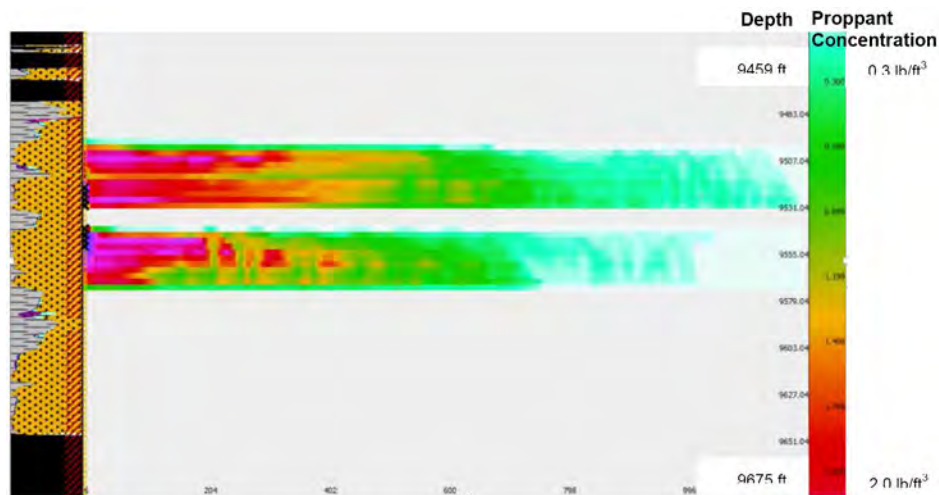


Figure 10—Proppant concentration (lb/ft³) of stage 1 of well C6

Production logging

The flow was measured with the memory production logging tool (MPLT) in each zone of the three wells. This tool provides the quantitative production data for the gas flow between bottomhole flow and shut-in pressure. As shown in the results of Table 6, we can identify the gas distribution across the entire well. The most productive sand is stage 1 in C6, followed by stage 2 in C7 and finally stage 2 in C8. In addition, the percentage of gas production in each stage is used for validating the modeling in each zone as shown in Fig 11. The points shows the actual data and the solid line shows the simulated data.

Table 6—Results of Production logging

Well/Stage	Gas Production Rate, Mscf/D	% Gas Production in Each Stage
C6		
Stage 1	2120	53
Stage 2	1400	35
C7		
Stage 1	395	23
Stage 2	912	53
C8		
Stage 1		
Stage 2	231	24
Stage 3	60	6
Stage 4	137	14
Stage 5	116	12
Stage 6	142	15
Stage 7	147	15

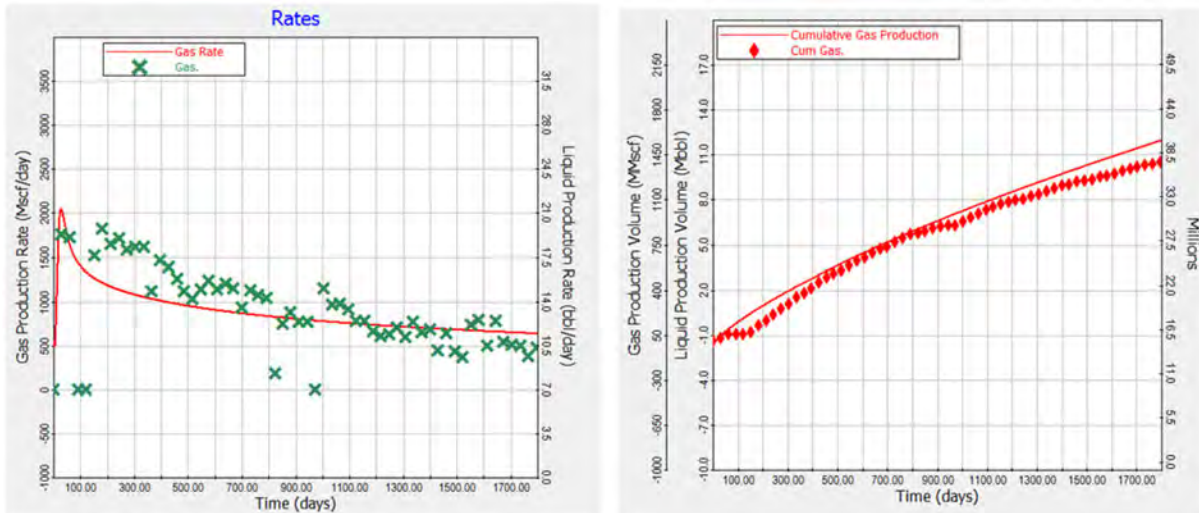


Figure 11—Gas production rate and cumulative gas production in stage 1 of well C6

Impact of Fracturing Fluid on PDL

In general, the larger amount of hydraulic fracturing fluid, the higher the gas production. However, not all the large amount of fluids can contribute to the high gas production rate. Fig 12 shows the relationship between gas production rate and fracturing fluid injection volume in Well C6, C7 and C8. For example, well C7 uses the highest amount of fluid (up to 85000 gal) during stage 1, however, it gives a lower gas production when compared with well C6 which has similar amount of fracturing fluid in stage 1. As a result, it is believe that a lower gas production caused by the PDL which was detected by G-function analysis with PDL coefficient of 0.008 1/psi.

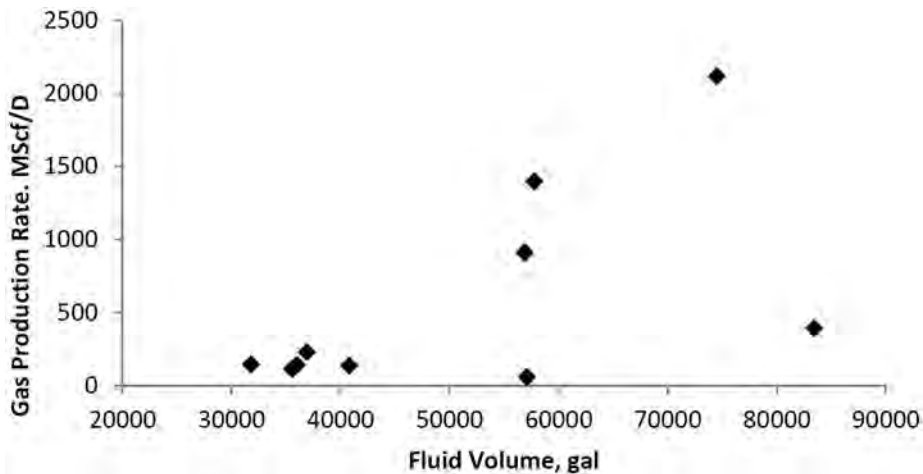


Figure 12—Gas production rate vs fracturing fluid volume

Impact of Gas Production Rate on NWBPL

Roberts, Chipperfield, and Miller (2000) indicated that a high NWBPL of more than 600 psi would lead to the reduction of hydraulic fracturing proppant placement. Results from the case study, which is depicted in Fig 13 shows similar results when the NWBPL is higher than 600 psi, the gas production rates are poor and they are generally smaller than 500 Mscf/d. However, the well C6 stage 2 with a high NWBPL around 900 psi provides a high gas production rate. This may be caused by the height recession leakoff behavior

that the fracture might have propagated to the impermeable layer. This might contribute to the overall gas production in that formation, particularly in the thick coal layers found in the Patchawarra formation.

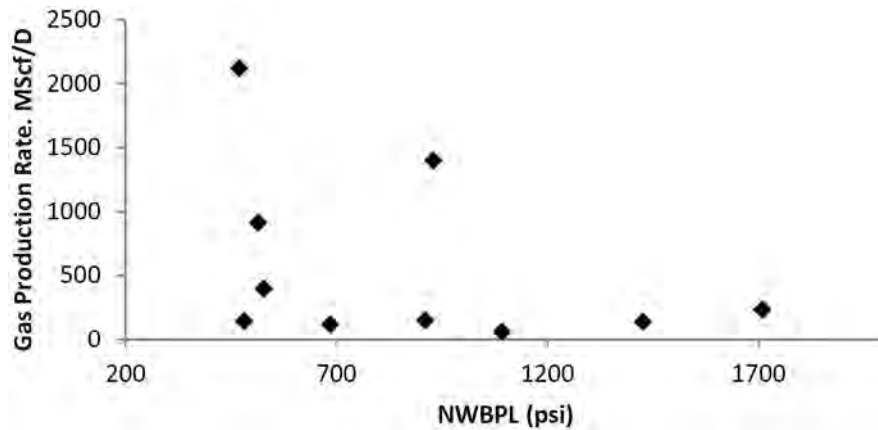


Figure 13—Gas production rate vs NWBPL

Impact of Fracture Pressure on Fracture Half-Length

During the fracture initiation period in hydraulic fracture stimulation, the treating bottomhole injection pressure to the target formation can be up to 10,000 psi. This pressure will be distributed and decrease based on the leakoff and the pressure drop near wellbore. Fig 14 shows the fracture pressure after stimulation and propped fracture half-length in wells C6 and C7. The fracture pressure varies between 7400 to 8500 psi whereas, the fracture half-length varies between 75 ft to 275 ft. It can be seen that the well C7 stage 1 has the lowest pressure distribution and fracture half-length. This effect might have been caused by high PDL and NWBPL with tortuosity dominated pressure loss. This pressure loss leads to losing driving force for fracture propagation which eventually leads to shorter fracture length.

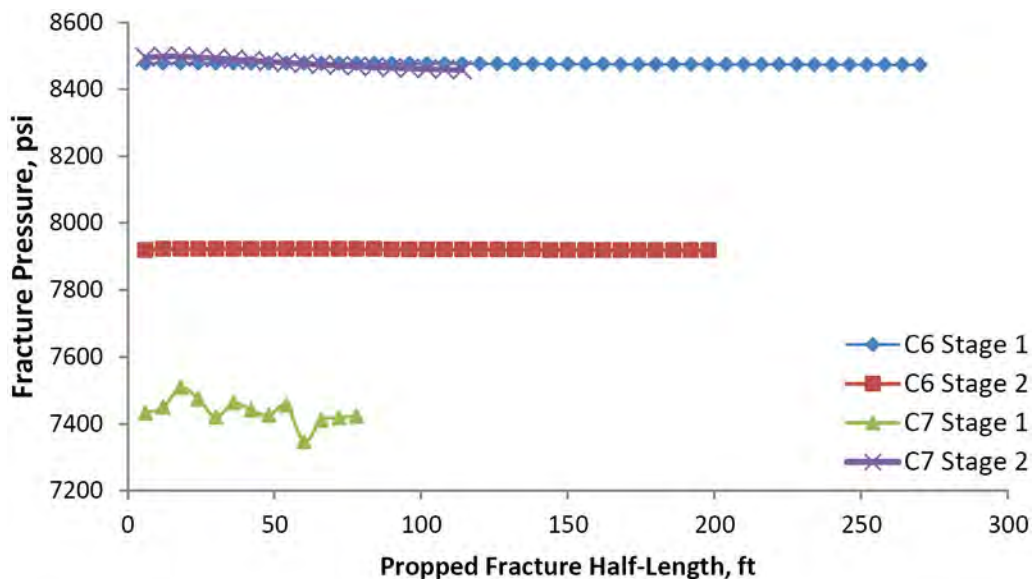


Figure 14—Fracture pressure distribution and propped fracture half-length in wells C6 and C7

Reservoir Simulation

A two-phase flow (gas and water) single porosity model is built by using Eclipse (2014). The reservoir properties from Table 1 are used. The Cartesian grid of 164500 cells have been created based on the fracture dimensions from the output of 3D hydraulic fracture stimulation. Fig. 15 shows the water saturation distribution after hydraulic fracture stimulation in C6 Stage 1. The model in the X direction is assigned to be the same as the fracture length of 246 ft, while in the Y direction with the fracture width of 0.2 in (0.017 ft). The grid spacing in the Y direction has been designed based on the exponential grid spacing, in which the grid spacing near the fracture face is concentrated and progressively widens out towards the boundary. The fracture height was found to be 69 ft based on the fracture height growth from 3D hydraulic fracturing model.

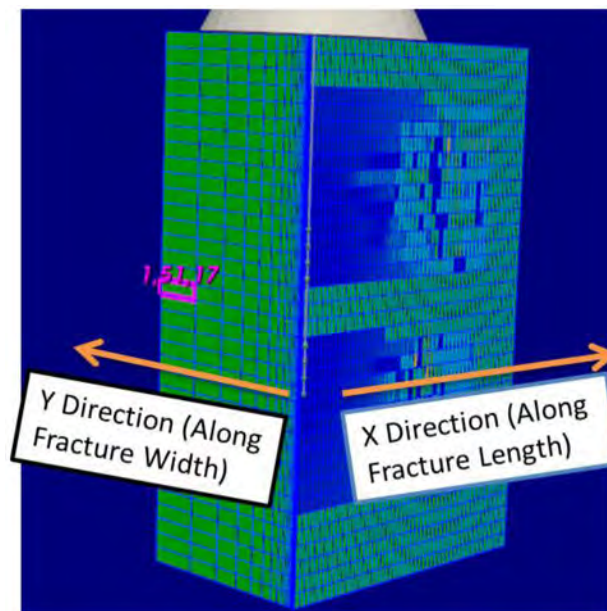


Figure 15—Water Saturation distribution after hydraulic fracture stimulation in well C6 stage 1 (Blue is high water saturation and Green is low water saturation)

Well C6 stage 1 has a fracture porosity of 0.4 and the fracture permeability ranges between 3,000 md and 50,000 md based on the fracture width and the fracture conductivity around 240 md-ft.

The initial condition of pressure distribution is also imported from 3D hydraulic fracturing model in each grid cell as shown in Fig. 14. The average pressure of 8500 psi has been applied in the fracture dimension in well C6 stage 1 while the reservoir pressure in the matrix is 4500 psi. There are three different regimes that affect the water saturation distribution as shown in Fig. 16. During injection, the water saturation within the fracture increases from 0.36 to 1 (blue indicates water saturation and the red color indicates gas saturation). However, at the fracture tips, there is less water saturation because of the small fracture conductivity in that area, Fig. 16a. After the injection, the well has been shut-in or kept soaking until the fracture closure and the proppant is settling and placed in the target zone. Also, during the soaking period, the effects of capillary pressure and gravity is observed as it can be seen in Fig. 16b, after 9 days of shut-in time, water accumulates at the bottom of the fracture due to gravity effects. When the production starts, the water near the wellbore is produce first. Then, gradually the water production continues through the entire fracture face. Finally, the gas breakthrough and single phase production starts. However, not all water can be removed from the matrix as shown in the Fig. 16c.

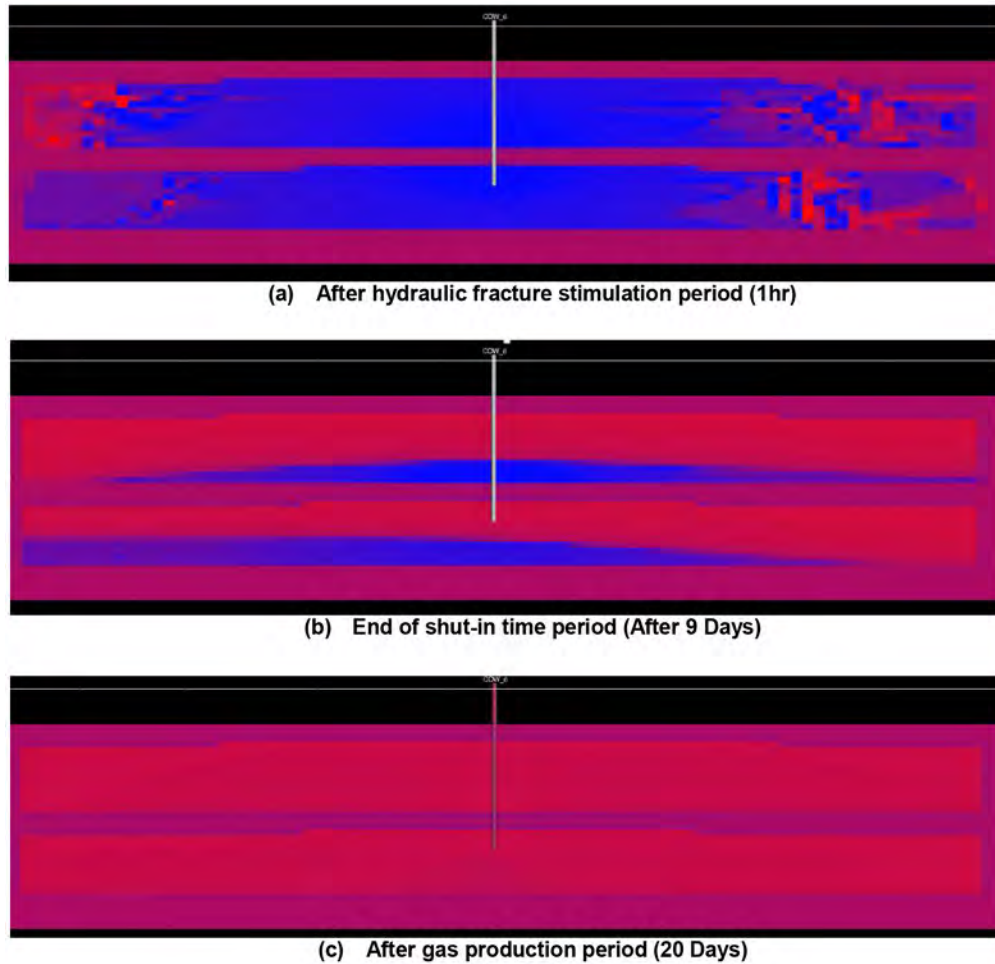


Figure 16—Water distribution during hydraulic fracture stimulation period (a), shut-in or soaking time (b) and gas production(c) (The blue is high water saturation and the red is low water saturation)

Fig 17 and Fig 18 show water saturation distribution in the X direction along the fracture length and Y direction along the fracture width respectively. We found that water is hardly removed from the fracture face along the width when compared with water distribution along the fracture length. The low permeability and high capillary in the Y direction could cause water entrapment inside the matrix. In the Y direction, it can be observed that the shut in period and the period after injection have the same water saturation profile. This means, It can be concluded that the water saturation in the Y direction does not change during the shut-in time and it can be attributed to the absence of gravity. After flowback period, the water surrounding the fracture is still higher than the water saturation inside fracture face near the boundary.

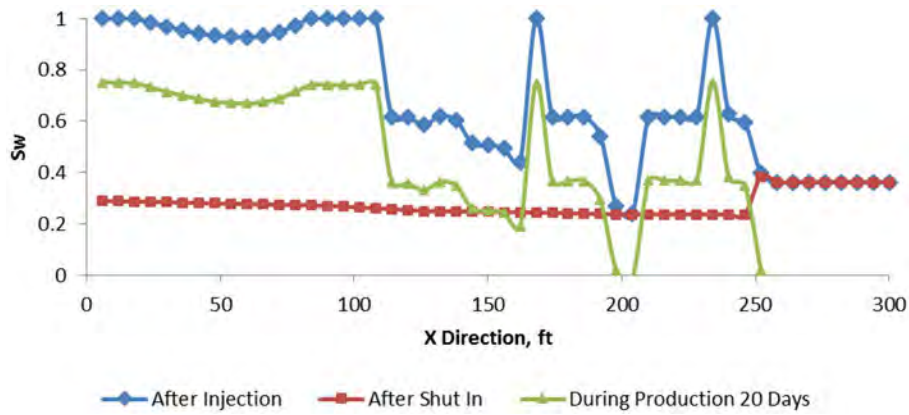


Figure 17—Water saturation in the X direction along the fracture length

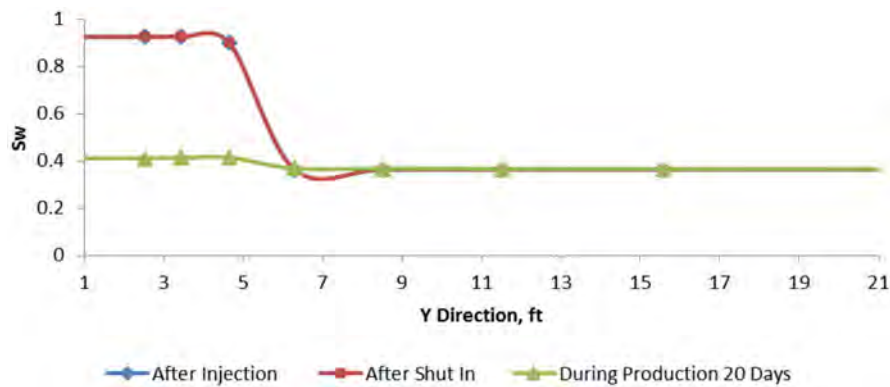


Figure 18—Water saturation in the Y direction along the fracture width

Fracturing Fluid Flowback Characterization

Fig. 19 shows an example of gas and water production from the reservoir simulation. The plot depicts three regions during the production. The first region has a high water production rate with relatively low gas production because the water dominates the bottom of the fracture. In the second region, the gas flow rate continuously increases and gas production gradually decreases. In the last region, the gas production dominates with relatively low water production.

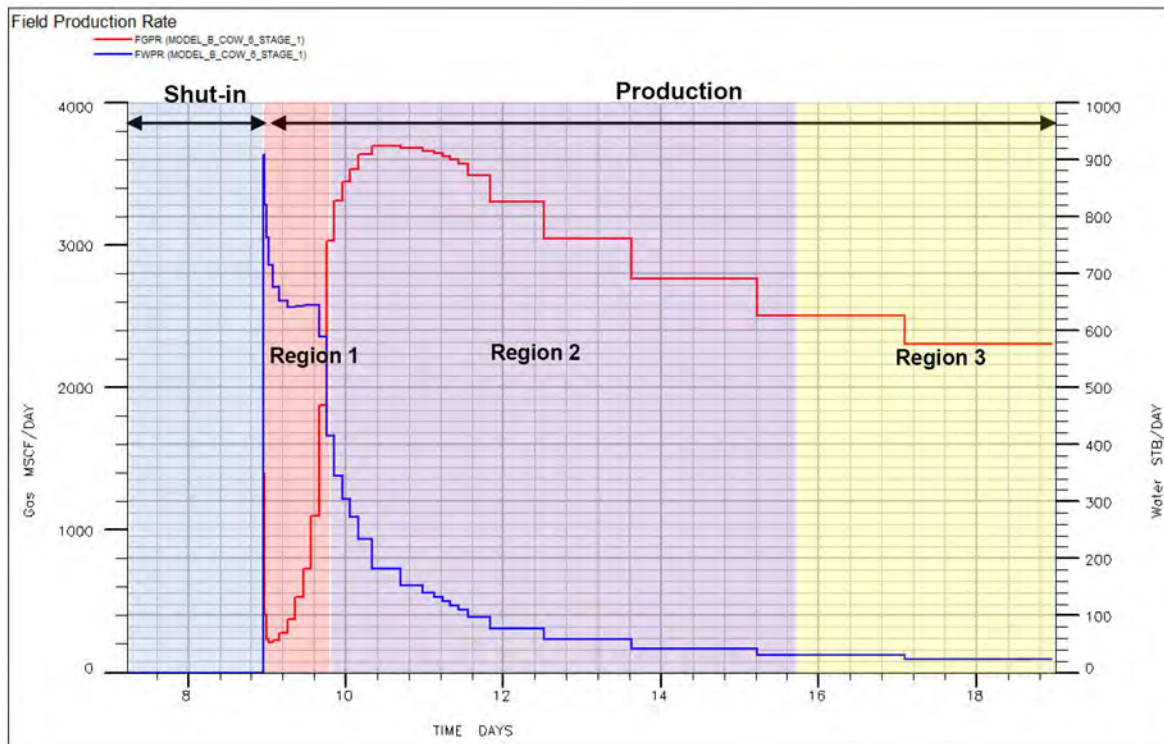


Figure 19—Gas and Water Production Rate of Well C6 in Stage 1

According to the results from the simulation, the water flowback is around 50% of the total fluid injection of 51,000 gal after 20 days. The percentage of flowback is higher than the expected, two reasons can be mentioned for this discrepancy. First, the simulation does not account for the impacts of different mechanism of formation damage in the fracture such as the gel effect in the fracture. Also, the permeability and porosity in the matrix were designed to be uniform which lead to an overestimation of the flowback.

Conclusion

- High NWBPL due to tortuosity is the predominant mechanism in the study area when compared to pressure drop due to perforation.
- NWBPL of more than 600 psi reduces the gas production rate. However the gas production does not decrease because of height recession, the other layers with good net pay might contribute to more gas production in the target formation.
- High PDL coefficient from 0.003 to 0.008 has a negative impact on the gas production because high amount of fluid will be injected into the formation and the fracturing fluid can impair the pre-existing fractures.
- The coupling between 3D hydraulic fracturing and reservoir simulation shows the relationship between hydraulic fracturing process cleanup and gas production. This allows for the optimization of fracturing fluid recovery to enhance gas flow.
- Based on the simulation results, the behavior of change in water saturation distribution due to the fracturing fluid loss was found.

Acknowledgments

The authors would like to thank Santos for providing data, Barree & Barree & Associates for GOHFER, Schlumberger for Eclipse, IHS for WellTest, Amarile for RE-Studio and Petrosys for mapping.

Nomenclature

$NWBPL$	= Near-wellbore pressure loss
PDL	= Pressure dependent leakoff
SDT	= Step down test
PCA	= Pre-closure analysis
ACA	= After-closure analysis
$ISIP$	= Instantaneous shut-in pressure, psi
P_C	= Closure Pressure, psi
ΔP_{NWBPL}	= Total pressure drop based on near-wellbore pressure loss, psi
k_{perf}	= Perforation pressure loss coefficient, psi/(stb/d) ²
k_{tort}	= Tortuosity pressure loss coefficient, psi/(stb/d) ²
q	= Fluid injection rate, bpm
N	= Number of perforation
C_d	= Coefficient of discharge
ρ	= Density of fluid, lb/gal
$G(\Delta t_D)$	= G-function time
$g(\Delta t_D)$	= Fluid loss at dimensionless time
g_0	= Dimensionless loss-volume function at the shut-in
Δt_D	= Dimensionless pumping time
k	= Reservoir Permeability, md
k_f	= Fracture Permeability, md

References

- Agrawal, S. and Sharma, M. M. 2013. Liquid Loading Within Hydraulic Fractures And Its Impact on Unconventional Reservoir Productivity. Presented at The Unconventional Resources Technology Conference Denver, Colorado, USA, 12–14 August. SPE-168781-MS. [10.1190/URTEC2013-115](https://doi.org/10.1190/URTEC2013-115).
- Baree & Associates Llc 2015, *GOHFER User Manual version 8.2.6*, viewed <http://www.gohfer.com/downloads.html>.
- Barree, D., Barree, L. and Craig, D. 2007. Holistic Fracture Diagnostics. Presented at SPE Rocky Mountain Oil & Gas Technology Symposium, Denver, Colorado, USA, 16–18 April 2007. SPE-107877-MS. [10.2118/107877-MS](https://doi.org/10.2118/107877-MS).
- Barree, R. D., Barree, V. L., and Craig, D. 2009. Holistic Fracture Diagnostics: Consistent Interpretation of Prefrac Injection Tests Using Multiple Analysis Methods. *SPE Prod & Oper* **24** (3): 396–406. SPE-107877-PA. [10.2118/107877-PA](https://doi.org/10.2118/107877-PA).
- Barree, R. D. and Mukherjee, H. 1996. Determination of Pressure Dependent Leakoff and Its Effect on Fracture Geometry', paper presented at The 71st Annual Technical Conference and Exhibition, Denver, CO, US., 6–9 October. SPE-36424-MS. [10.2118/36424-MS](https://doi.org/10.2118/36424-MS).
- Castillo, J. L. 1987. Modified Fracture Pressure Decline Analysis Including Pressure-Dependent Leakoff. Presented at SPE Low Permeability Reservoirs Symposium, Denver, Colorado, 18–19 May. SPE-16417-MS. [10.2118/16417-MS](https://doi.org/10.2118/16417-MS).
- Chipperfield, S. T., Roberts, G. A., Miller, W. K. and Vandersypen, R. S. 2000. Gel Slugs: A Near-Wellbore Pressure-Loss Remediation Technique for Propped Fracturing. Presented at the 2000 SPE/CERI Gas Technology Symposium Calgary, Alberta Canada, 3–5 April 2000. SPE-59777-MS. [10.2118/59777-MS](https://doi.org/10.2118/59777-MS).
- Chipperfield, S. T., Wong, J. R., Warner, D. S., Cipolla, C. L., Mayerhofer, M. J., Lolon, E. P. and

- Warpinski, N. R. 2007. Shear Dilation Diagnostics: A New Approach for Evaluating Tight Gas Stimulation Treatments. Presented at SPE Hydraulic Fracturing Technology Conference, College Station, Texas, U. S. A., 29–31 January. SPE-106289-MS. [10.2118/106289-MS](#).
- Hildek, B. and Weijers, L. 2007. Fracture -to-Well Conectivity. In *Modern Fracturing: Enhancing Natural Gas Production*, ed. Economides, M. J. and Martin T., *Chap. 6*, **216**, ET Publishing, Houston, TX.
- Holditch, S. A. 1979. Factors Affecting Water Blocking and Gas Flow From Hydraulically Fractured Gas Wells. *Journal of Petroleum Technology*, vol. **31**, no. 12, December, pp. 1515–1524. SPE-7561-PA. [10.2118/7561-PA](#).
- Johnson, R. L. Jr., Aw, K. P., Ball, D. and Willis, M. 2002. Completion, Perforating and Hydraulic Fracturing Design Changes Yield Success in an Area of Problematic Frac Placement - the Cooper Basin, Australia. Presented at the SPE Asia Pacific Oil & Gas Conference and Exhibition, Melbourne, Australia, 8–10 October. SPE-77906-MS. [10.2118/77906-MS](#).
- Johnson, R. L. Jr. and Greenstreet, C. W. 2003. Managing Uncertainty Related to Hydraulic Fracturing Modeling in Complex Stress Environments with Pressure-Dependent Leakoff. Presented at The SPE Annual Technical Conference and Exhibition, Denver, Colorado, US., 5 – 8 October. SPE-84492-MS [10.2118/84492-MS](#).
- Lizak, K. F., Bartko, K. M., Self, J. F., Izquierdo, G. A. and Al-Mumen, M. 2006. New Analysis of Step-Rate Injection Tests for Improved Fracture Stimulation Design. Presented at the 2006 SPE International Symposium and Exhibition on Formation Damage Control Lafayette, LA, 15–17 February. SPE-98098-MS. [10.2118/98098-MS](#).
- Martin, T. and Valko', P. 2007. Hydraulic Fracturing Design for Production Enhancement. In *Modern Fracturing: Enhancing Natural Gas Production*, ed. M. J. Economides and T. Martin(eds), *Chap. 4*, ET Publishing, Houston, TX.
- Pokalai, K., Fei, Y., Ahmad, M., Haghighi, M. and Gonzalez, M. 2015. Design and optimisation of multi-stage hydraulic fracturing in a horizontal well in a shale gas reservoir in the Cooper Basin, South Australia. *The APPEA Journal*, vol. **55**.
- Ramurthy, M., Towler, B. F., Harris, H. G. and Barree, R. D. 2013. Effects of High Pressure-Dependent Leakoff (PDL) and High Process-Zone Stress (PZS) on Stimulation Treatments and Production. Presented at The SPE Unconventional Resources Conference and Exhibition-Asia Pacific, Brisbane, Australia, 11 – 13 November. SPE-167038-MS. [10.2118/167038-MS](#).
- Roberts, G. A., Chipperfield, S. T. and Miller, W. K. 2000. The Evolution of a High Near-Wellbore Pressure Loss Treatment Strategy for the Australian Cooper Basin. Presented at The 2000 SPE Annual Technical Conference and Exhibition, Dallas, Texas, 1–4 October. SPE-63029-MS. [10.2118/63029-MS](#).
- Scott, M. P., Stephens, T., Durant, R., McGowen, J., Thom, W. and Woodroof, R. 2013. Investigating Hydraulic Fracturing in Tight Gas Sand and Shale Gas Reservoirs in the Cooper Basin. Presented at The SPE Unconventional Resources Conference and Exhibition-Asia Pacific, Brisbane, Australia, 11–13 November. SPE-167073-MS. [10.2118/167073-MS](#).

Chapter 6 : Integrated 3D Modelling of Hydraulic Fracturing in Tight Reservoirs with Pre-Existing Natural Fractures and Complex Stress Conditions: A Case Study from the Cooper Basin, Australia

*Kunakorn **Pokalai**^a (kunakorn.pokalai@adelaide.edu.au)

David **Kulikowski**^a (david.kulikowski@adelaide.edu.au)

Khalid **Amrouch**^a (khalid.amrouch@adelaide.edu.au)

Manouchehr **Haghighi**^a (manouchehr.haghighi@adelaide.edu.au)

Raymond L. **Johnson, Jr.**^a (ray.johnsonjr@adelaide.edu.au)

^aAustralian School of Petroleum, University of Adelaide, North Tce, 5005, South Australia, Australia

***Corresponding Author:** Kunakorn Pokalai (+61 449 044 385)

ABSTRACT

Hydraulic fracturing is an essential element of effective hydrocarbon production in low permeability reservoirs; however, subsurface geological features can be highly anisotropic and can lead to ineffective treatments. To provide a better understanding on the effectiveness of hydraulic fracture interactions with pre-existing natural fractures, we integrate a calibrated mechanical earth model with a discrete fracture network to simulate hydraulic fracture treatments under an alternating (compressional and strike-slip) stress regime in both a vertical and inclined well. The trajectory of the inclined well was optimised to intersect the largest number of pre-existing natural fractures and has been found to increase the stimulated reservoir volume (SRV) by five times compared to the base case (vertical well under a strike-slip stress regime and with no pre-existing natural fractures) and by three times in the vertical wells, irrespective of the stress regime. This presents valuable information on the effectiveness of hydraulic fracturing when the geometry of pre-existing natural fractures is established. A common phenomenon in the case study location (Cooper Basin, Australia) is the rotation of induced hydraulic fractures from a vertical position at the wellbore to horizontal with distance away from the well. This was discussed and found to be most likely related to the preferential migration of fluid through the path of least resistance, which will often be affected by high horizontal permeability intervals within tight sandstones, or alternatively through the reactivation of the interface plane between different lithologies or the reactivation of low dip angle natural fractures.

Key Words: Hydraulic Fracturing; Discrete Fracture Network; Stress; Fracture; Cooper Basin.

INTRODUCTION

The use of hydraulic fracturing to enhance the permeability of tight reservoirs can be a crucial aspect of effective hydrocarbon production as it can improve the economic feasibility. However, these treatments can become complicated in some provinces because of the: (1) complex stress conditions; (2) reactivation of pre-existing natural fractures and faults; and (3) intra-formational heterogeneities such as permeability anisotropy and changes in lithology (Hubbert and Willis, 1957; McGowen et al., 2007; Scott et al., 2013; Cooke et al., 2016). This study quantifies the effectiveness of hydraulic fracturing using a discrete fracture network (DFN) model and different scenarios that include: (1) altering the stress regime from strike-slip to compressional; and (2) simulating a hydraulic fracture program within a vertical and inclined well. A case study from the Cooper Basin, Australia, is chosen because of the abundance of publicly available data and extensive use of hydraulic fracturing within the low permeability gas reservoirs.

The Cooper-Eromanga Basin is Australia's largest onshore hydrocarbon province that has been producing hydrocarbons from low permeability reservoirs since the first natural gas discovery in 1963 (Radke, 2009; Mackie, 2015). Attempts have been made to better understand the growth of hydraulic fractures within the complex stress conditions of the Cooper Basin (e.g. Roberts et al., 2000; Johnson et al., 2002, 2015; McGowen et al., 2007; Camac et al., 2012; Cooke et al., 2016; Pokalai et al., 2016; Waldron and Camac, 2016). These studies found that the effect of near wellbore pressure loss (NWBPL) coupled with reactivation of pre-existing natural fractures, and a complex and alternating stress regime are the major contributors to ineffective hydraulic fracturing (Warpinski and Teufel, 1987; Reynolds et al., 2006; Nelson et al., 2007; Scott et al., 2013; Pokalai et al., 2015a, 2015b, 2016; Cooke et al., 2016). A significant concern within the basin is the unknown reason behind hydraulic fractures rotating from a vertical position at the wellbore to a horizontal position with increasing distance away from wellbore (Scott et al., 2013; Cooke et al., 2016).

The aim of this research is to: (1) better understand the complex interaction between hydraulic fracturing and pre-existing natural fractures; (2) quantify the effectiveness of hydraulic fracturing under strike-slip and compressional stress regime conditions in vertical and inclined wells; and (3) provide insights into why hydraulic fractures are rotating in the complex stress Cooper Basin. A DFN model is created for a tight sandstone interval within the prolific Patchawarra Formation using interpreted natural fractures from the C-13 borehole image log (Fig. 1). The DFN model was created by statistically populating these natural fractures within the interval using the Elliptical Fisher Distribution and using reservoir properties obtained from well logs and pressure diagnostic tests. Well logs are also used to develop a mechanical earth model (MEM) to constrain the tectonic stress and strain conditions, which is calibrated using well test data.

The DFN model is used to simulate a three-dimensional (3D) hydraulic fracture stimulation treatment in vertical and inclined wells and under compressional and strike-slip stress regimes to investigate the change in: (1) hydraulic fracture growth; (2) interaction with pre-existing natural fractures; and (3) stimulated reservoir volume (SRV). Rotation of the hydraulic fracture to the horizontal plane is also discussed. The results provide companies operating in the Cooper Basin with an improved understanding of hydraulic fracturing in the complex stress environment.

GEOLOGICAL SETTING

The Cooper Basin is an intracratonic Permian-Triassic aged hydrocarbon-rich province located within central Australia (Fig. 1a). Major hydrocarbon fields are commonly located along the NE-SW striking Gidgealpa-Merrimelia-Innaminka (GMI) and Murteree-Nappacoongee (MN) ridges, and within the NE-SW elongate Patchawarra, Nappamerri, and Tenappera troughs (Fig. 1a) (Apak et al., 1997; Kulikowski et al., 2017). Deposition of the oil and gas-rich Late Carboniferous to Early Permian aged Merrimelia and Tirrawarra formations under glacial and post-glacial outwash environments, respectively, marks the initial period of flexural relaxation that generated

accommodation space for Cooper Basin sediment deposition (Apak et al., 1997; Alexander et al., 1997).

Cyclic deposition of reservoir rocks (sands), seal rocks (shale and coal), and source rocks (coal and shale) during the Middle Permian formed the gas-rich Patchawarra Formation (Alexander et al., 1998). This thick, but low permeability, stratigraphic interval is the primary target for exploration companies in the basin; however, it requires hydraulic fracturing or the presence of pre-existing natural fractures to improve the economic significance (Kulikowski et al., 2016b; Pokalai et al., 2016). Within the study area (C-Field region), the top Patchawarra Formation is at a depth of approximately 2700m (Fig. 1b) and can reach a total thickness of 700 m (Fig. 1c). West of the GMI Ridge, significant accommodation space developed during the Middle Permian Event, where major NE-SW striking faults were reactivated and facilitated significant deposition of the middle Patchawarra Formation (VC30-VC50 coal) interval (Fig. 1c) (Kulikowski and Amrouch, 2017). Field scale NE-SW striking inverted normal faults are present throughout the basin and have a strong control on structural trap development, which includes the C-Field (Fig. 1d). This field was selected as a case study because it contains abundant well data and a thick Patchawarra Formation interval.

Insert Fig. 1

The depositional environment transitioned to fluvio-deltaic, shoreface, and lacustrine, which was coincident with an east to west transgression that deposited the Late Permian Murteree Shale, Epsilon Formation, Roseneath Shale, and Daralingie Formation (Alexander et al., 1998). The NE-SW oriented Daralingie Event regionally eroded much of the Daralingie Formation, upon which the fluvial to deltaic Toolachee Formation was deposited (Apak et al., 1997; Kulikowski and Amrouch, 2017). The Toolachee Formation contains cycles of sands, shales, and coals that are comparable to the Patchawarra Formation, but not nearly as thick (Alexander et al., 1998). The Triassic Nappamerri Group was deposited onto the Toolachee Formation under floodplain, lacustrine and fluvial environments, which continued until the Late Triassic E-W Hunter-Bowen

Event uplifted and peneplaned the Cooper Basin. This event created a regional unconformity that marks the top of the Cooper Basin (Apak et al., 1997; Alexander et al., 1998; Kulikowski and Amrouch, 2017).

The overlying Jurassic to Cretaceous Eromanga Basin was deposited under fluvial, lacustrine and shallow marine conditions during a prolonged period of tectonic quiescence (Apak et al., 1997; Kulikowski and Amrouch, 2017). The E-W Late Cretaceous Event created a regional unconformity that separates the Eromanga Basin from the overlying Paleogene to Quaternary Lake Eyre Basin (Apak et al., 1997; Alexander et al., 1998; Kulikowski and Amrouch, 2017). The subsequent N-S oriented Paleogene Event followed, and was succeeded by the in situ ESE-WNW oriented strike-slip to compressional stress regime (Müller et al., 2012; Pokalai et al., 2016; Kulikowski and Amrouch, 2017). The alternating stress regime (compressional to strike-slip) conditions present within the Cooper Basin may have a significant influence on the effectiveness of hydraulic fracturing treatments, as the induced fracture geometry, growth, and interaction with pre-existing natural fractures can change from highly effective to ineffective depending on the regime.

METHODOLOGY

Constructing a Mechanical Earth Model

Developing an accurate and calibrated mechanical earth model (MEM) is an important aspect for effective hydraulic fracturing, as it provides constraints on the elastic rock properties, pore pressure, transmissibility, and the in-situ stress and strain conditions present within a target interval (Nolte et al., 1997; Zoback, 2007; Johnson, 2016; Pokalai et al., 2016). The Poisson's ratio (ν), Young's modulus (E) and vertical (σ_v) stress magnitude are calculated from a series of wireline logs from the C-7 well (Fig. 1) that include the gamma ray log, full-waveform sonic logs, and bulk density log. The dynamic Young's Modulus obtained from the full-wave sonic log is converted to the static Young's Modulus following the Eissa-Kazi model (Barree et al., 2009a).

The values for E and ν are then used to constrain the minimum (σ_h) and maximum (σ_H) horizontal stress magnitudes that are calibrated to the diagnostic fracture injection test (DFIT) data using the isotropic form of the poro-elastic stress equations (Eq. 1 and Eq. 2; Thiercelin and Plumb, 1994). The DFIT data provides measured values for the breakdown (P_{wb}) and closure (P_c) pressures, and for the σ_h magnitude at two separate depths (2840m and 2920 m) within the formation, which are used to calibrate the MEM. The model is further calibrated to existing measurements (Nelson et al., 2007) by constraining the minimum (ε_h) and maximum (ε_H) horizontal tectonic strains (Eq. 1 and Eq. 2).

$$\sigma_h = \frac{\nu}{\nu-1} (\sigma_v - \alpha_v P_p) + \frac{E}{1-\nu^2} \varepsilon_h + \frac{E\nu}{1-\nu^2} \varepsilon_H + \alpha_h P_p \quad (\text{Eq. 1})$$

$$\sigma_H = \frac{\nu}{\nu-1} (\sigma_v - \alpha_v P_p) + \frac{E}{1-\nu^2} \varepsilon_H + \frac{E\nu}{1-\nu^2} \varepsilon_h + \alpha_h P_p \quad (\text{Eq. 2})$$

Where the Biot's poro-elastic constant (α) refers to transmissibility heterogeneities in the vertical (α_v) and horizontal (α_h) direction. The breakdown pressure (P_{wb}), pressure dependent leak-off (PDL) coefficient, and fissure opening pressures (P_{fo}), and closure pressure (P_c) or minimum horizontal stress (σ_h) magnitude, can be obtained directly or observed from the DFIT data during the before closure analysis (BCA) period using the G-function time and the semi derivative of the G-function (Barree et al., 2009b). These values are used to further calibrate the calculated σ_h and σ_H magnitudes by resolving the Kirsch's equations (Kirsch, 1898) to describe the P_{wb} in terms of the horizontal stresses, pore pressure, and tensile rock strength (T_o) (Eq. 3), and the P_{fo} in terms of the horizontal stress (σ_h and σ_H) magnitudes and the fissure opening angle (θ) (Eq. 4). The θ describes the angle at which fractures will preferentially develop with respect to the orientation of principal horizontal stresses and can also be obtained from Mohr's circle construction of in situ stresses (Jaeger et al., 2009).

$$P_{wb} = 3\sigma_h - \sigma_H - P_p + T_o \quad (\text{Eq. 3})$$

$$P_{fo} = \frac{1}{2}(\sigma_H + \sigma_h) + \frac{1}{2}(\sigma_H - \sigma_h)\cos 2\theta \quad (\text{Eq. 4})$$

The tectonic stress and strain magnitudes are determined by integrating several measured and theoretical methods to allow equations 1 to 4 to be solved simultaneously following the generalised reduced gradient (GRG) nonlinear solving method (Lasdon et al., 1978). An error function (ErrFn) is used to minimise the error between the observed (x) and calculated (\bar{x}) values (Eq. 5). Once the MEM is calibrated and representative of the interval, it provides valuable information on the Poisson's ratio, Young's modulus, the magnitude of principal stresses, and highlights differential stress contrasts between the target and surrounding rocks (Pokalai et al., 2016).

$$ErrFn = \sum(x - \bar{x})^2 \quad (\text{Eq. 5})$$

Interpretation of Pre-Existing Natural Fractures

Pre-existing natural fractures are interpreted from the C-13 wellbore image log, which covers the entire 434m Patchawarra Formation interval. As the South Australian portion of the Cooper Basin is entirely subsurface, geophysical data and core measurements are the only avenue for obtaining structural data (Kulikowski et al., 2016a; Kulikowski and Amrouch, 2017). Borehole image logs measure the electrical resistivity of the borehole at the centimetre scale by pressing six pads, containing a total of 150 microelectrodes, against the borehole wall. The digital data is converted into an oriented interpretable image of the borehole, highlighting changes in the micro-resistivity. Natural fractures will be imaged as sinuous features that are either resistive (open) or conductive (closed). Both resistive and conductive natural fractures were interpreted from the entire 434m image log interval. The data is used to populate the discrete Fracture Network (DFN) model and to analyse the natural fracture intensity for the entire Patchawarra Formation interval.

Discrete Fracture Network (DFN) Model

The subsurface distribution of pre-existing natural fractures can be modelled using a discrete fracture network (DFN), which incorporates natural fracture data measured from borehole image logs. Once the DFN model is populated with natural fractures, reservoir properties, stress conditions, and the hydraulic fracturing parameters, the simulation commences. The reactivation of pre-existing natural fractures during hydraulic fracturing is modelled as either tensile (dilation) or shear reactivation. These two interactions could be more stress economic than the development of new fractures (Hubbert and Willis, 1957; Jaeger et al., 2009).

The DFN model was created for the middle (VC30-VC50) Patchawarra Formation (2903-2955m) in the C-13 well using Golder Associates' FracMan 7 software. The C-13 well is vertical and contains 434m of Patchawarra Formation stratigraphy. The DFN model (grid size of 10m × 10m × 10m) represents a 52m sandstone reservoir interval with homogenous reservoir properties. In addition to this vertical well (which is simulated under a strike-slip and a compressional stress regime), a well with an inclination of 60° drilled towards the ESE is simulated within the DFN model using identical hydraulic fracturing properties and a strike-slip stress regime. The geometry of this additional well was suggested by previous works (Pokalai et al., 2016) to intersect the largest number of pre-existing natural fractures, and therefore would result in the largest stimulated reservoir volume (SRV). The effectiveness of this well geometry is compared to the results from the two vertical wells. Growth of the hydraulic fracture was simulated within a contained volume of $2.08 \times 10^8 m^3$ for each of the three scenarios. Importantly, this well trajectory is neither within the high-risk wellbore stability limits under the present-day stress conditions, nor within the best trajectory for maximum production, which was found using the modified Kirsch equations for breakdown pressure gradient and breakdown angle (Pokalai et al., 2016).

The Poisson's ratio, Young's modulus, and the magnitude of principal stresses for the target depth are obtained from the calibrated MEM. A reservoir porosity of 10%, permeability of 0.115mD, pressure of 27.6MPa, and temperature of 138°C were used. The maximum principal

stress direction was taken from previous works and assumed to be 101°N for the entire model (Pokalai et al., 2016). As the in situ stress can alternate between compressional and strike-slip stress regimes, two models were created to interchange the minimum and intermediate principal stress orientations. The distribution of pre-existing natural fractures within these two models remained constant and were controlled by the interpreted natural fractures from the C-13 borehole image log. The Elliptical Fisher Distribution was used to statistically populate the measured natural fractures within the model. This method was used because it captures the anisotropic variation of natural fracture geometries (strike and dip angles), whereas the Fisher Distribution requires a symmetrical variation around the mean pole, which is not observed in the dataset.

Three-Dimensional Hydraulic Fracture Simulation

Hydraulic fracturing is simulated within a sandstone reservoir at 2903-2955m depth, which belongs to the middle Patchawarra Formation (VC30-VC50) in the C-13 well. The growth of the hydraulic fracture and its interaction with the intersecting natural fractures is based on the orientation of principal stresses, such that opening (dilation) of the induced fracture will occur towards the minimum principal stress direction and its growth will be parallel to the maximum principal stress direction (mode 1 opening). Reactivation of pre-existing natural fractures followed the Mohr-Coulomb model using in situ stress conditions derived from the MEM and a standard friction angle of 30° (Kulikowski et al., 2016c). Natural fractures intersecting the hydraulic fracture (1^{st} order) must have an internal pore pressure greater than the normal stress magnitude to tensile reactivate. This continues for n^{th} order natural fracture intersections until the n^{th} fracture cannot accommodate the total volume of pumped material, at which point the hydraulic fracture is extended. To incorporate the pore pressure decrease in dilated natural fractures with increasing distance away from the wellbore (P_{pump}), a standard linear slope (s) (the standard value for s was used due to the lack of published information specific to the Cooper Basin) of 0.5

(Fig. 2a) was used to determine fracture pore pressure (P_{frac}) in Eq. (6) (Golder Associates Inc., 2015).

$$P_{frac} = (P_{pump} - \sigma_n) \left(1 - s \frac{d}{d_{max}}\right) + \sigma_n + \rho g(\Delta h) \quad (\text{Eq. 6})$$

Where P_{pump} is the pumping pressure, σ_n is the normal stress magnitude acting on the fracture end element, s is the slope representing fracture pore pressure (Fig. 2a), d is the flow distance from the well to the fracture element, d_{max} is the maximum hydraulic fracture distance, ρ is the slurry density, g is the gravitational acceleration, and Δh is the vertical elevation from the well intersection point to the fracture element (Golder Associates Inc., 2015). After the hydraulic fracture simulation is completed, the model comprises of the hydraulic fracture and the network of dilated natural fractures that act as fluid conduits. The next stage in the simulation is to calculate whether the pressure remaining at the tips of these fractures is sufficient enough to induce shear reactivation of uninflated natural fractures (Fig. 2c). Here the dissipating pressure (P_{dis}) at the fracture tip is calculated using Eq. (7) with a standard slope (s) (the standard value for s was used due to the lack of published information specific to the Cooper Basin) of 3 (Fig. 2b) (Golder Associates Inc., 2015).

$$P_{dis} = P_{tip} - (P_{tip} - P_R) \left(\frac{d - d_{tip}}{d_R - d_{tip}}\right)^s \quad (\text{Eq. 7})$$

Where P_{tip} is the pressure at the inflated fracture tip, P_R is the reservoir pressure at d_R , d_R is the path distance from the injection point to the point where the pore pressure is unperturbed by the hydraulic fracturing and equal to the P_R , d is the path distance from the injection point to the local point beyond the fracture tip, and d_{tip} is the path distance from the injection point to the fracture tip (Golder Associates Inc., 2015). Again, as the distance away from the fracture tip increases, the effect of pressure within dilate fractures is reduced (Fig. 2b). Reservoir pressure is 27.6MPa, and d_R is 1000m. A high-temperature, borate cross-linked, modified guar gelled fluid system consisting of $0.10m^3/s$ of clean water and $0.10m^3/s$ of slurry is used with 15 time steps

representing the viscosity profile over a period of 1.5 hours. Properties for a general ceramic (20/40) proppant type with a diameter of 0.854cm and a bulk density of $2099.55\text{kg}/\text{m}^3$ were used in the simulation. The fluid and proppants are consistent with current industry practice in the Cooper Basin. An initial shut-in pressure (ISIP) of 60.8MPa was observed from a DFIT data and matched to the fracture simulation model.

Insert Fig. 2

RESULTS

Calibrated Mechanical Earth Model

The mechanical earth model (MEM) was constructed across the entire Patchawarra Formation from well log derived data (Fig. 3a), and calibrated by DFIT data at two separate depths (Fig. 3b and 3d). Analysis of the DFIT data at 2920m and 2840m using the semi derivative (GdP/dG) of the G-function (dP/dG) found closure pressures (P_c) of approximately 52.4MPa and 51.0MPa, and breakdown pressures (P_{wb}) of approximately 68.6MPa and 71.0MPa, respectively (Fig. 3c and 3e). These values for P_c and P_{wb} were used to calibrate the log derived MEM using Eq. 1-3 and Eq. 5 and adjusting lateral tectonic strains as described in part 3.1. Further analysis of the GdP/dG shows a increase above ideal GdP/dG behaviour in the early G-Time (Fig. 3c), indicating fissure opening of natural fractures in this formation. In Figure 3e the GdP/dG behaviour in the early time illustrates height or transverse recession leak-off of the GdP/dG and suggests that the fracture stimulation has propagated vertically or laterally into less permeable regions. For these reasons, the bottom DFIT interval (2903-2955m) was selected for hydraulic fracture stimulation as it involves interaction with pre-existing natural fractures. The Poisson's ratio and Young's modulus were log derived with mean values of 0.245 and 31826.2MPa, over the target interval and were incorporated into MEM calibration and later DFN modelling.

This MEM calibration process produced tectonic strain values three times greater in the σ_H than in the σ_h directions, or approximately 600 and 200 microstrains, respectively. The resulting

magnitude of σ_h and σ_H were approximately 51.7MPa and 72.4MPa at the target depth (2910m), respectively (Fig. 3a). The σ_v magnitude within the Patchawarra Formation followed a gradient of approximately 0.0224MPa/m with a median magnitude of 65.5MPa at the target depth. The key observation from this MEM is that the σ_h and σ_v magnitudes can cross over and cause the MEM to alternate between a compressional ($\sigma_h > \sigma_v$) and strike-slip ($\sigma_h < \sigma_v$) stress regime based on moduli values (Barree et al., 2009a). The breakdown pressure, P_{wb} , rapidly decreases below the σ_H in regions of known coal presence, but is otherwise is greater than σ_H elsewhere in the MEM (Fig. 3a). The σ_h stress contrast between sandstones and coals (7MPa) is relatively low (Fig. 3a). Based on moduli value these low contrasts between σ_h in sandstones and coals would lead to containment issues when stimulating adjoining sandstone and coal sequences and as observed by prior researchers (Johnson and Greenstreet, 2003).

Insert Fig. 3

Analysis of Pre-Existing Natural Fractures

A total of 249 natural fractures were interpreted from the C-13 borehole image log covering the entire 434m Patchawarra Formation interval (Fig. 4a). The stereographic projection shows a significant cluster of natural fractures dipping towards the WNW at an angle of approximately 60° from horizontal. Low dipping (<40°) natural fractures are also common with no preference to dip direction. These form the main natural fracture clusters; however, a wide range of natural fracture geometries are present that vary from 70° dip angle to horizontal, and striking in all directions.

The cumulative fracture intensity with depth is presented for the upper (2727-2847m), middle (2847-2934m) and lower (2934-3161m) Patchawarra Formation (Fig. 4c). The P10 fracture intensity (fractures per meter) is much greater in the middle Patchawarra Formation (0.977012/m) than the upper (0.558333/m) and lower (0.405859/m) intervals. DFIT analysis within the target interval (2903-2955m) suggested interaction with natural fractures (Fig. 3c),

which is expected considering that this interval (middle Patchawarra Formation) contains the highest fracture intensity (Fig. 4c). The rock quality designation (RQD) is a statistic used to describe the expected core quality (number of separate pieces) and is defined as the total length of core pieces with lengths greater than 10cm divided by the total borehole length. High RQD values are found in the middle (RQD=33.6917) and upper (RQD=23.6923) intervals, with the lowest RQD value (RQD=8.51968) found in the lower Patchawarra Formation (Fig. 4c).

The three-dimensional distribution of natural fractures measured from the borehole image log is shown in Fig. 4b together with an example of an interpreted natural fracture. The distribution of natural fractures shows a dominant set dipping towards the WNW at a high dip angle, as well as a significant number of low angle fractures with no directional preference. To match this natural fracture distribution in the DFN model using the Elliptical Fisher Distribution, four natural fracture sets were statistically defined (pole plunge/pole trend): (1) 29/108°N; (2) 66/299°N; (3) 74/110°N; and (4) 32/111°N. The creation of these sets ensured that the software would distribute fractures within the DFN model (Fig. 4d) in a way that would ultimately represent the original interpreted borehole fracture data (Fig. 4a).

Insert Fig. 4

Three-Dimensional Hydraulic Fracture Simulation with Natural Fractures

VERTICAL WELL (C-13)

Strike-Slip Stress Regime

Under a strike-slip stress regime, the hydraulic fracture grew towards the maximum horizontal stress (σ_H) direction while opening towards the minimum horizontal stress (σ_h) direction (Fig. 5a) giving a total stimulated reservoir volume (SRV) of $116.4m^3$ (base case). The interaction between the hydraulically induced fracture and the pre-existing natural fractures displayed a consistent trend that preferentially reactivated high angled ($>50^\circ$) natural fractures striking ESE-WNW (Fig.

5b and 5c). A total of 9 pre-existing natural fractures were reactivated along the hydraulically induced fracture giving a total fracture area of $73516.4m^2$ and a SRV of $405.2m^3$.

Compressional Stress Regime

The hydraulic fracture growth under a compressional stress regime again grew towards the σ_H direction, but the opening was towards the σ_v direction (Fig. 5d) forming a pancake-like shape. This induced fracture geometry is sub-parallel to the stratigraphy and results in a fracture aspect ratio that is negligible (<1) and strongly dictated by the lack of vertical fracture growth. Inflation of near horizontal pre-existing natural fractures was strongly preferred under these stress conditions (Fig. 5e). The strike of these reactivated natural fractures was largely irrelevant and dominantly controlled by the dip angle; however, a slight preference for ESE-WNW striking fractures can be observed (Fig. 5f). A total of 11 pre-existing natural fractures were reactivated with significantly more second, and multiple, order interactions than under the strike-slip stress regime, with the reactivated natural fracture planes becoming increasingly more sub-horizontal with distance away from the wellbore (Fig. 5e). The hydraulic fracture covered an area of $64050.3m^2$ giving a SRV of $397.9m^3$.

Insert Fig. 5

INCLINED WELL

Strike-Slip Stress Regime

The inclined (30°) well scenario was modelled under a strike-slip stress regime and resulted in the hydraulic fracture growing parallel to the σ_H direction and opening towards σ_h (Fig. 5g). The induced hydraulic fracture reactivated seven pre-existing natural fractures (Fig. 5h). Again, this simulation contained multiple order interactions that covered an area of $60039.3m^2$, giving a SRV of $643.4m^3$. These reactivated pre-existing natural fractures were consistently high ($>50^\circ$) angled with a preferred ESE-WNW strike (Fig. 5i).

Discussion

The aims of this work were to quantify the effectiveness of hydraulic fracturing under different scenarios and attempt to better understand the complex interactions between the hydraulically induced fracture and pre-existing natural fractures. The calibrated mechanical earth model (MEM) shows high stress and strain conditions with a possible alternating stress regime between compressional and strike-slip (Fig. 3a). Such a complex stress environment can cause significant variations in hydraulic fracture growth and interaction with pre-existing natural fractures, which can ultimately compromise the effectiveness of hydrocarbon production.

Under both the vertical well (C-13) scenarios, the strike-slip stress regime conditions foster high (>50°) angled natural fractures to be preferentially reactivated (Fig. 5c), compared to the preferential reactivation of near horizontal natural fractures under a compressional stress regime (Fig. 5f). This contrast results in a slight increase in the stimulated reservoir volume (SRV) for the strike-slip stress regime scenario. Although this is only slight, a key difference comes from the difficulty of keeping near horizontal natural fractures dilated after reactivation due to the overlying weight of rock. Correct proppant placement is essential in this case and it may be beneficial to implement several stages of proppant, or coarse sand, placement to ensure that these natural fractures remain dilated. Horizontal hydraulic fractures may be preferred in some instances where vertical fracture growth would result in unwanted connection of previously isolated and vertically stacked reservoirs.

The work of Pokalai et al. (2016) suggested that an inclined (30°) well drilled towards the ESE-WNW would intersect a larger number of pre-existing natural fractures and result in a greater SRV. This well trajectory was modelled by Pokalai et al. (2016) without a DFN model, giving a SRV of $116.0m^3$ (base case), which was matched ($116.4m^3$) in our study. In addition to intersecting the largest number of pre-existing natural fractures using this well geometry, inclined wells have a larger wellbore contact in the reservoir compared to vertical wells, which in our case has a negligible effect on the SRV. The G-Function analysis shows a leak off behaviour consistent with

the interaction of pre-existing natural fractures during the shut-in time (Fig. 3c & 3e). This suggests that an understanding of natural fracture behaviour during hydraulic fracturing is essential.

To expand on previous work (Pokalai et al., 2016), hydraulic fracturing was simulated using this optimised well trajectory in the DFN model, finding that the SRV increased by five times compared to the vertical well scenario; albeit the total fracture area was larger in the vertical well. The reason behind this was the more complex multiple order interactions between natural fractures in the inclined well, which created a more intense fracture network compared to the vertical well. This infers that the effectiveness of hydraulic fracturing, and therefore hydrocarbon production, may be improved significantly by optimising the well trajectory to intersect the largest number of pre-existing natural fractures, which fostered greater multiple order natural fracture interactions. However, an inclined well can be subject to increased wellbore instability if the distribution of principal stress magnitudes and the stress regime are not carefully managed.

For each of the three modelled scenarios, the interaction between the hydraulic fracture and pre-existing natural fractures remains consistent within each case, and phenomenon such as hydraulic fracture plane rotation is not observed. Rotation of the hydraulic fracture from vertical at the wellbore to horizontal within the reservoir, as suggested by recent works (Scott et al., 2013; Cooke et al., 2016; Pokalai et al., 2016), would therefore require conditions that were not included in our model. For such a phenomenon to occur there can only be few reasons: (1) the stress regime transitions from strike-slip at the wellbore to compressional within the reservoir; (2) horizontal pre-existing natural fractures are preferentially reactivated; (3) the contact plane (bedding) between stacked lithologies is preferentially reactivated; (4) the hydraulic fracture initiates in the vertical position at the wellbore before the fracture fluid begins to preferentially flow through high permeability layers within the reservoir; or (5) a combination of the above.

It is unlikely that the stress regime consistently transitions from strike-slip at the wellbore to compressional within the reservoir for each of the many wells; however, it may be possible for the

hydraulic fracture to grow in height and interact with adjacent lithologies, which have contrasting mechanical properties that may foster a change in stress regime. This may be observed in the MEM where a change in lithology (and therefore a change in Poisson's ratio and Young's modulus) will influence the σ_h (and σ_H) magnitude (Fig. 3a). This is particularly the case between sandstones and coals where the difference in σ_h magnitude is approximately 7MPa and can contain the hydraulic fracture within the sandstone interval (Fig. 3a). Additionally, the significant decrease in the σ_h magnitude within coals can be sufficient enough to cause a transition from compressional to strike-slip stress regimes (Fig. 3a). Given that the σ_h and σ_v magnitudes are similar throughout the basin, the stress regime may alternate between strike-slip ($\sigma_h < \sigma_v$) and compressional ($\sigma_h > \sigma_v$) between adjacent lithologies (Fig. 3a). Vertical initiation of the hydraulic fracture at the wellbore (McGowen et al., 2007) implies a strike-slip stress regime (or extensional, but this is not the case here). To transition from a strike-slip stress regime at the wellbore to a compressional regime with increasing distance, the principal σ_v magnitude could be reduced, or the principal σ_h magnitude be increased.

As the stress regime must be strike-slip, preferential reactivation of horizontal natural fractures is geomechanically incorrect if high (>50°) angle ESE-WNW striking natural fractures are present (Anderson, 1905; Zoback, 2007). Based on these studies, historical evidences of high propagation pressures (i.e., ISIP gradients $> \sigma_v$) can be explained by a combination of tensile fracture and natural fracture reactivations in an environment of high σ_H magnitude. A more plausible explanation for observed horizontal fracture components from surface deformation tiltmeter experiments (Pitkin et al., 2012; Scott et al., 2013) is the potential for dip-slip or tensile fracture propagations along weak lithological boundaries. This occurs since the contact boundary between two lithologies forms a plane of weakness that may be preferentially reactivated if it is more stress economic than reactivating natural fractures, or initiating new fracture development (Warpinski and Teufel, 1987; Cooke et al., 2016). In this case, the cause of horizontal components would relate to the fracturing fluid seeking the path of least resistance, which is through high horizontal permeability sections in the tight sandstones that cycle to weaker boundaries with

shales and coals within the Patchawarra sequence. The fracturing fluid would traverse vertically through these high horizontal permeability sections within the tight sandstones then induce shear along the contact plane with adjacent shales and coals. Future work and additional diagnostics would be required to resolve this observation of horizontal fracture components from surface deformation tiltmeter experiments in the Cooper Basin.

Conclusions

Integrating a calibrated mechanical earth model, discrete fracture network model, and three-dimensional (3D) hydraulic fracture simulation has provided vital constraints on the effectiveness of hydraulic fracturing under different stress regimes and with different well trajectories. This 3D hydraulic fracture simulation study has also presented the unique interactions between hydraulic fractures and pre-existing natural fractures and quantified the in situ tectonic stress and strain conditions. Hydraulic fracturing within an optimised well trajectory under a strike-slip stress regime generated a stimulated reservoir volume (SRV) five times greater than the vertical well scenario (base case with no natural fracture interactions) under identical conditions. Compared to this base case the SRV under compressional and strike-slip stress regimes was three times greater if pre-existing natural fractures are present. High angled ($>50^\circ$) ESE-WNW striking natural fractures were found to exclusively reactivate under a strike-slip stress regime, and low angled ($<40^\circ$) to near horizontal natural fractures were found to reactivate under a compressional stress regime.

Although the simulations were not able to capture the hydraulic fracture plane rotation from vertical at the wellbore to horizontal within the reservoir, four likely reasons are presented, with the most likely reasons being a combination of two effects. The first is that fracturing fluid will preferentially seek the path of least resistance, which will typically be through high permeability fractures within the tight sandstones in either tensile or strike-slip mode generating higher than expected propagation pressures. The second plausible explanation for observed horizontal fracture components is that the contact plane between lithologies forms planes of weakness that

may be preferentially reactivated if it is more stress economic to do so than to reactivate the pre-existing natural fractures or induce rock failure. This paper provides the most plausible physical explanations for the complex hydraulic fracturing behaviour and high pressures observed in strike-slip stress regimes, and provides companies operating in the Cooper Basin with constraints on the in situ stress and strain conditions for future design considerations.

Acknowledgments

Thanks to DownUnder Geosolutions (DUG Insight 4.2), Paradigm (Geolog 7.2), Barree & Associates (GOHFER) and Golder Associates (FracMan 7) for academic licencing. We thank Carlos H. Grohmann and Ginaldo A.C. Campanha for the development of the 'OpenStereo 0.1.2' software.

References

- Alexander, E.M., Gravestock, D.I., Cubitt, C., Chaney, A., 1998. Lithostratigraphy and environments of deposition. In: Gravestock, D.I., Hibburt, J.E., Drexel, J.F., (Eds.), *The Petroleum Geology of South Australia*. Vol. 4: Cooper Basin, South Australia. Department of Primary Industries and Resources. Report Book, 98/9, 69-116.
- Anderson, E.M., 1905. The dynamics of faulting. *Transactions of the Edinburgh Geological Society*. 8(3), 387-402.
- Apak, S.N., Stuart, W.J., Lemon, N.M., Wood, G., 1997. Structural evolution of the Permian-Triassic Cooper Basin, Australia: Relation to hydrocarbon trap styles. *AAPG Bulletin*. 81, 533-555.
- Barree, R.D., Gilbert, J.V., Conway, M., 2009a. Stress and rock property profiling for unconventional reservoir stimulation. In: *SPE Hydraulic Fracturing Technology Conference*. 1-18, SPE 118703.
- Barree, R.D., Barree, V.L., Craig, D., 2009b. Holistic fracture diagnostics: consistent interpretation of prefrac injection tests using multiple analysis methods. *SPE Production & Operations*. 24(3), 396-406.
- Camac, B.A., Waldron, A.R., Donley, J.A., Hunt, S.P., 2012. Microseismic and 3D VSP for infill evaluation in Greater Tindilpie, Cooper Basin, Australia. In: *46th U. S. Rock Mechanics/Geomechanics Symposium*, American Rock Mechanics Association.

- Cooke, D., Tyiasning, S., Abul Khair, H., 2016. Unexpected behaviors of stimulated fractures in the high-stress Cooper Basin. *The Leading Edge*. 35(1), 78-84.
- Golder Associates Inc., 2015. *FracMan® Discrete Fracture Network Modelling Software*, FracMan 7.5 Workshop, Golder Associates Inc., Redmond.
- Grohmann, C.H., Campanha, G.A.C., 2010. OpenStereo: Open source, cross-platform software for structural geology analysis, paper presented at 2010 Fall Meeting, AGU, San Francisco, Calif.
- Hubbert, M.K., Willis, D.G., 1957. Mechanics of Hydraulic Fracturing. In: *Transactions of SPE of AIME*. 210, 153-168.
- Jaeger, J.C., Cook, N.G.W., Zimmerman, R., 2009. *Fundamentals of rock mechanics*, fourth edition. Blackwell Publishing Ltd., Oxford, UK.
- Johnson, Jr., R.L., Aw, K.P., Ball, D., Willis, M., 2002. Completion, Perforating and Hydraulic Fracturing Design Changes Yield Success in an Area of Problematic Frac Placement - the Cooper Basin, Australia. Presented at the SPE Asia Pacific Oil & Gas Conference and Exhibition, Melbourne, Australia, 8–10 October. SPE-77906-MS.
- Johnson, Jr., R.L., Greenstreet, C.W., 2003. Managing Uncertainty Related to Hydraulic Fracturing Modeling in Complex Stress Environments with Pressure-Dependent Leak-off. The SPE Annual Technical Conference and Exhibition, Denver, Colorado, 5–8 October, SPE-84492.
- Johnson, Jr., R.L., Abul Khair, H., Jeffrey, R., Meyer, J., Stark, C., Tauchnitz, J., 2015. Improving fracture initiation and potential impact on fracture coverage by implementing optimal well-planning and drilling methods for typical stress conditions in the Cooper Basin, central Australia. *The Australian Petroleum Production and Exploration Association Journal*. 55(2), 403-403.
- Johnson, Jr., R.L., 2016. Improving diagnostic fracture injection testing for in situ stress profiling, reservoir characterisation and well optimisation in unconventional gas reservoirs. International Conference on Geomechanics, Geo-Energy and Geo-resources (IC3G 2016), Melbourne, Australia, 28-29 September.
- Kirsch, E.G., 1898. Die Theorie der Elastizität und die Bedürfnisse der Festigkeitslehre. *Zeitschrift des Vereines Deutscher Ingenieure*. 42(28), 797-807.
- Kulikowski, D., Hochwald, C., Cooke, D., Amrouch, K., 2016a. A Statistical Approach to Assessing Depth Conversion Uncertainty on a Regional Dataset: Cooper-Eromanga Basin, Australia. ASEG-PESA-AIG 2016 Conference, Adelaide. Extended Abstract #200, 484-490.
- Kulikowski, D., Cooke, D., Amrouch, K., 2016b. Constraining the distribution and relationship between overpressure, natural fracture density and temperature in the Cooper Basin. *The Australian Petroleum Production and Exploration Association Journal*. 56, 11-28, doi:10.1071/AJ15002.
- Kulikowski, D., Amrouch, K., Cooke, D., 2016c. Geomechanical Modelling of Fault Reactivation in the Cooper Basin, Australia. *Australian Journal of Earth Sciences*. 63(3), 295-314, doi:10.1080/08120099.2016.1212925.
- Kulikowski, D., Amrouch, K., 2017. Combining Geophysical Data and Calcite Twin Stress Inversion Analysis to Refine the Structural and Stress History of Complex Provinces: A Case Study on the Cooper-Eromanga Basin, Australia. *Tectonics*. 36(3), 515-541, doi:10.1002/2016TC004366.
- Kulikowski, D., Amrouch, K., Cooke, D., Gray, M.E., 2017. Basement Structural Architecture and Hydrocarbon Conduit Potential of Polygonal Faults in the Cooper-Eromanga Basin, Australia. *Geophysical Prospecting*, in press, doi:10.1111/1365-2478.12531.

- Lasdon, L.S., Warren, A.D., Jain, A., Ratner, M., 1978. Design and testing of generalised reduced gradient code for nonlinear programming. *ACM Transactions on Mathematical Software*. 4(1), 34-50.
- Mackie, S., 2015. History of petroleum exploration and development in the Cooper and Eromanga basins. In: AAPG/SEG international conference and exhibition, 13-16 September, Melbourne, Australia. Search and Discovery Article #10814.
- McGowen, J.M., Gilbert, J.V., Samari, E., 2007. Hydraulic fracturing down under. SPE Hydraulic Fracturing Technology Conference, Texas, USA, 29-31 January.
- Müller, R.D., Dyksterhuis, S., Rey, P., 2012. Australian paleo-stress fields and tectonic reactivation over the past 100 Ma. *Australian Journal of Earth Sciences*. 59(1), 13-28.
- Nelson, E.J., Chipperfield, S.T., Hillis, R.R., Gilbert, J., McGowen, J., Mildren, S.D., 2007. The relationship between closure pressures from fluid injection tests and the minimum principal stress in strong rocks. *International Journal of Rock Mechanics and Mining Sciences*. 44(5), 787-801.
- Nolte, K.G., Smith, M.B., 1981. Interpretation of fracturing pressures. *Journal of Petroleum Technology*. 33(9), 1-767.
- Pitkin, M.C., Wadham, T.H., McGowen, J.M., Thom, W.W., 2012. Taking the First Steps: Stimulating the Nappamerri Trough Resource Play. SPE Asia Pacific Oil and Gas Conference and Exhibition, Perth, Australia, 22-24 October 2012.
- Pokalai, K., Fei, Y., Ahmad, M., Haghghi, M., Gonzalez, M., 2015a. Design and optimisation multi-stage hydraulic fracturing in a horizontal well in a shale gas reservoir in the Cooper Basin, South Australia. *The Australian Petroleum Production and Exploration Association Journal*. 55, 1-14.
- Pokalai, K., Haghghi, M., Sarkar, S., Tyiasning, S., Cooke, D., 2015b. Investigation of the Effects of Near Wellbore Pressure Loss and Pressure Dependent Leak-off on Flowback during Hydraulic Fracturing with pre-existing Natural Fractures. SPE/IATMI Asia Pacific Oil and Gas Conference and Exhibition, Nusa Dua, Bali. SPE-176440.
- Pokalai, K., Kulikowski, D., Johnson, Jr., R.L., Haghghi, M., Cooke, D., 2016. Development of a new approach for hydraulic fracturing in tight sand with pre-existing natural fractures. *The Australian Petroleum Production and Exploration Association Journal*. 56, 225-238.
- Radke, B., 2009. Hydrocarbon and Geothermal Prospectivity of Sedimentary Basins in Central Australia; Warburton, Cooper, Pedirka, Galilee, Simpson and Eromanga Basins. *Geoscience Australia Record* 2009/25.
- Reynolds, S.D., Mildren, S.D., Hillis, R.R., Meyer, J.J., 2006. Constraining stress magnitudes using petroleum exploration data in the Cooper–Eromanga Basins, Australia. *Tectonophysics*. 415(1), 123-140.
- Roberts, G.A., Chipperfield, S.T., Miller, W.K., 2000. The Evolution of a High Near-Wellbore Pressure Loss Treatment Strategy for the Australian Cooper Basin. Presented at the SPE Annual Technical Conference and Exhibition, Dallas, Texas, 1–4 October. SPE-63029-MS.
- Scott, M.P., Stephens, T., Durant, R., McGowen, J., Thom, W., Woodroof, R., 2013. Investigating Hydraulic Fracturing in Tight Gas Sand and Shale Gas Reservoirs in the Cooper Basin. Presented at The SPE Unconventional Resources Conference and Exhibition-Asia Pacific, Brisbane, Australia, 11–13 November. SPE-167073-MS.

- Thiercelin, M.J., Plumb, R.A., 1994. A core-based prediction of lithologic stress contrasts in east Texas formations. *SPE Formation Evaluation*. 9(4), 251-258.
- Waldron, A.R., Camac, B.A., 2016. Microseismic monitoring of hydraulic-fracturing programs in the Cooper Basin, Australia. *The Leading Edge*. 35(1), 72-76.
- Warpinski, N.R., Teufel, L.W., 1987. Influence of geologic discontinuities on hydraulic fracture propagation. *Journal of Petroleum Technology*. 39(2), 209-220.
- Zoback, M.D., 2007. *Reservoir geomechanics*. Cambridge University Press.

Figures

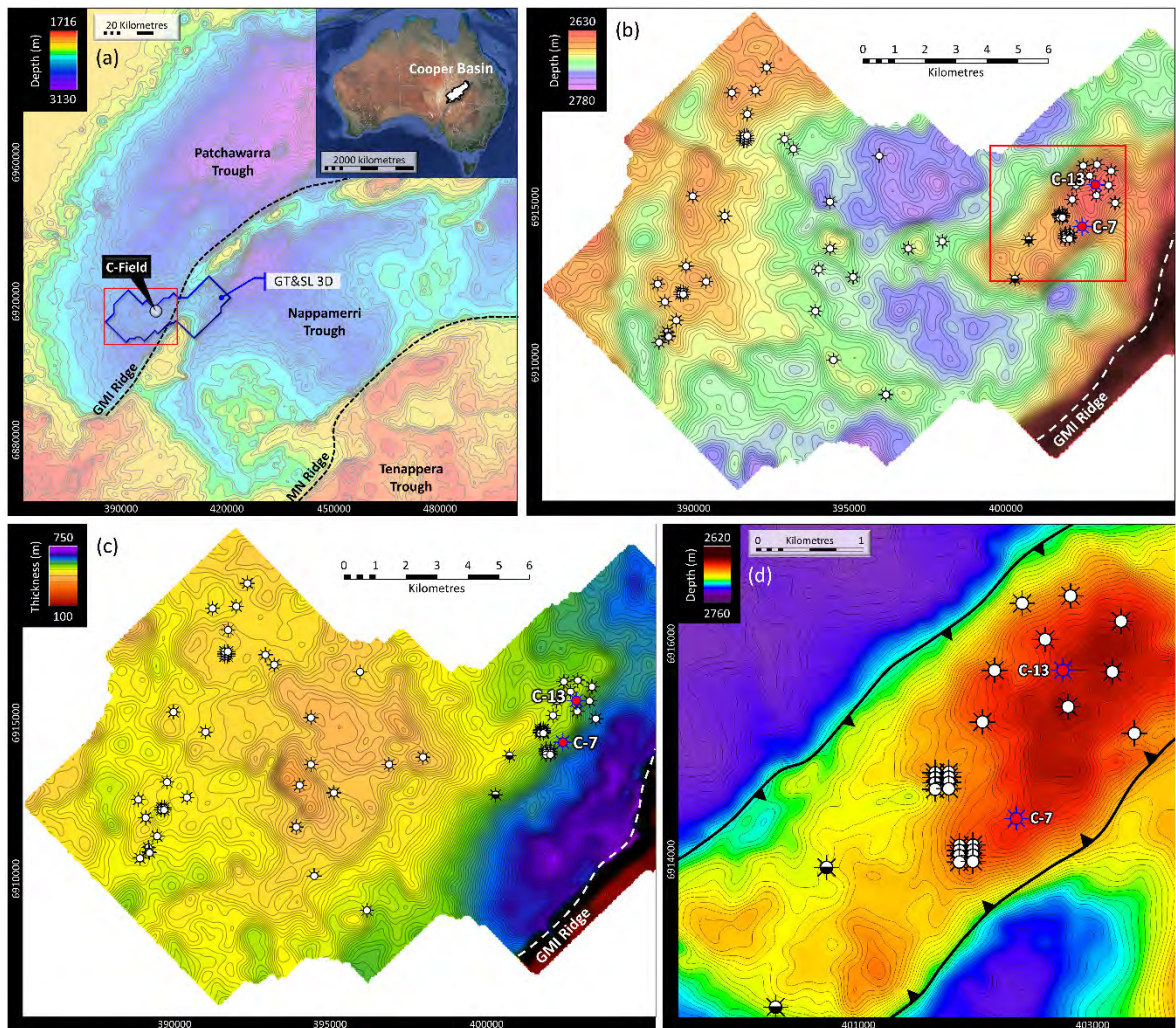


Figure 1. (a) Location of the study area (C-Field) within the GT&SL 3D seismic survey located in the South Australian portion of the Cooper Basin (inset map of Australia). Location of the Gidgealpa-Merrimelia-Innamickna (GMI) and Murteree-Nappacoongee (MN) ridges and Patchawarra, Nappamerri, and Tenaperra troughs shown. (b) Depth map to the top Patchawarra Formation with the location of C-7 and C-13 wells shown. See Fig. 1a for location. (c) Isopach map of the Patchawarra Formation with location of C-7 and C-13 wells shown. (d) Depth map of the top Patchawarra Formation within the C-Field. See Fig. 1b for location.

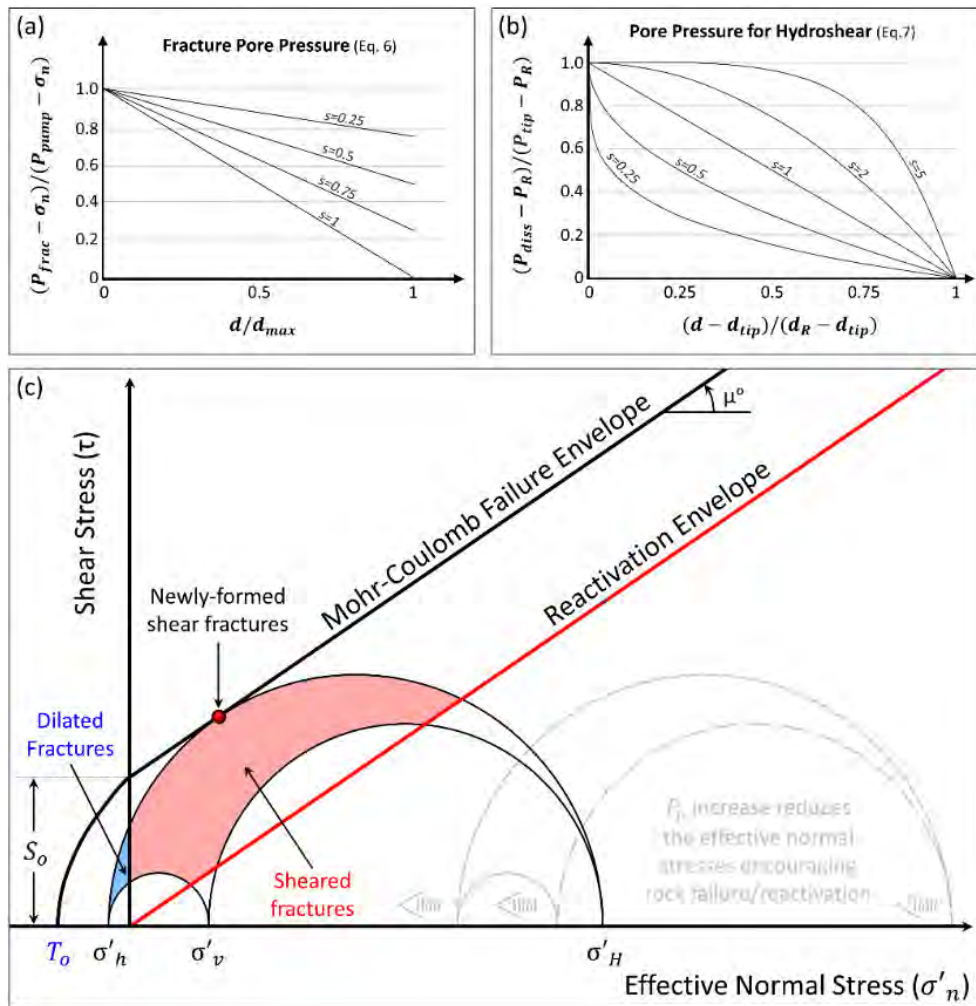


Figure 2. (a) The decrease in fracture pore pressure (P_{frac}) with increasing distance away from the well (d), with respect to the normal stress (σ_n), pumping pressure (P_{pump}) and maximum hydraulic fracture distance away from the well (d_{max}). A standard slope (s) of 0.5 was used for this study as no detailed information was available for the Cooper Basin (after Golder Associates Inc., 2015). (b) The pressure dissipation (P_{diss}) from inflated natural fracture into the reservoir and uninflated natural fractures with respect to the distance away from fracture tip. P_R is initial reservoir pressure, P_{tip} is pressure at inflated natural fracture tip, d is the path distance from injection point to the local point beyond the fracture tip, d_R is the distance from injection point to the point where reservoir pressure is unperturbed by the simulation and equal to P_R . A standard slope (s) of 3 was used for this study as no detailed information was available for the Cooper Basin (after Golder Associates Inc., 2015). (c) A theoretical Mohr-Coulomb circle construction illustrating the stress conditions required for dilation and shear reactivation, and new fracture development. The increase in pore pressure (P_p) during hydraulic fracturing reduces the maximum (σ'_H) minimum (σ'_h), and vertical (σ'_v) effective principal stress magnitudes shifting the Mohr's circle towards the failure and reactivation envelopes. T_o is the tensile rock strength, S_o is the cohesive shear strength, and μ is the angle of internal friction.

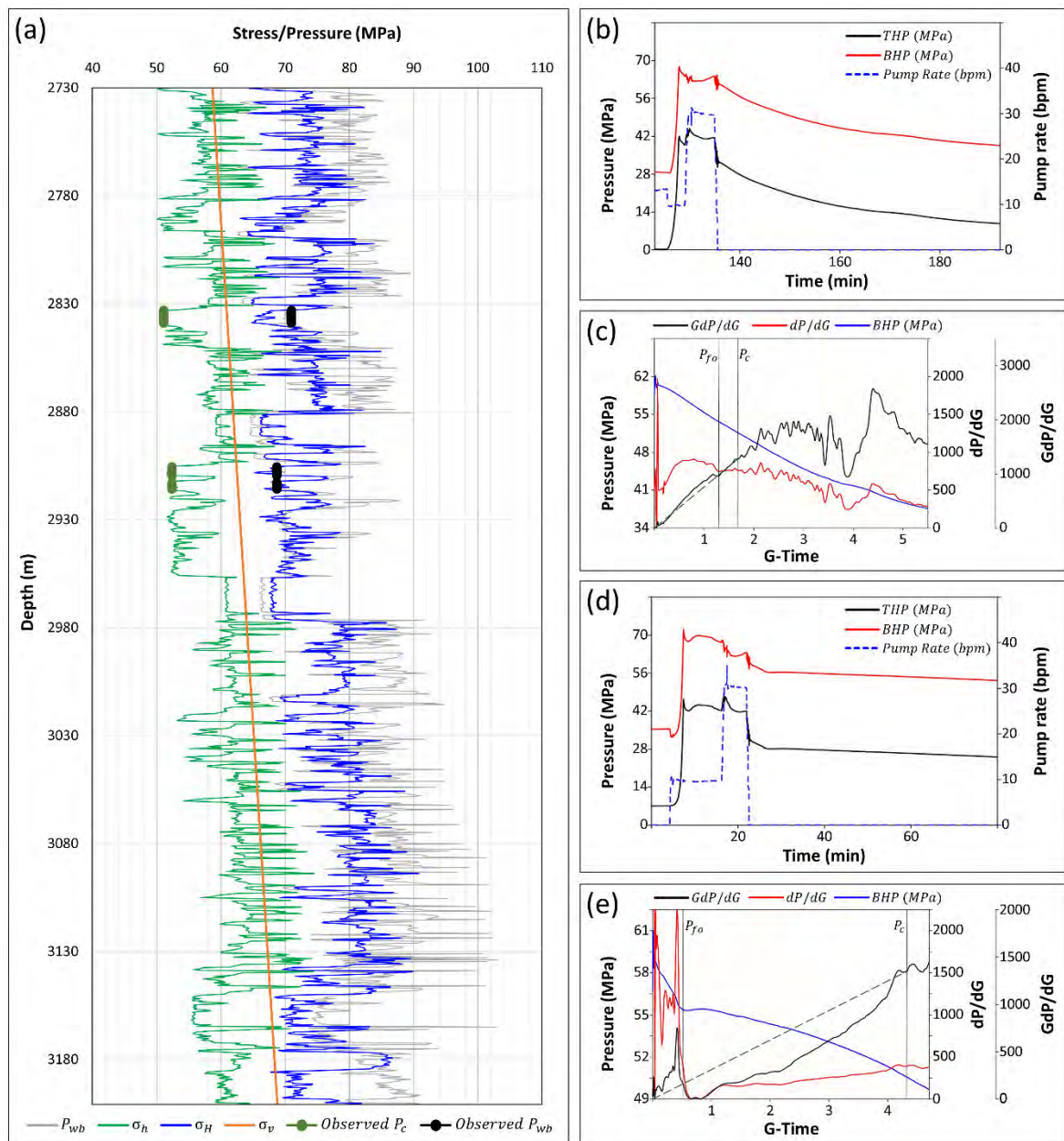


Figure 3. (a) Construction of the mechanical earth model in the C-7 well for the entire Patchawarra Formation interval. The observed closure (*Observed P_c*) and breakdown (*Observed P_{wb}*) pressures are compared with the calculated breakdown pressure (P_{wb}), maximum horizontal (σ_H), minimum horizontal (σ_h), and vertical stress (σ_v) magnitudes. (b) Diagnostic fracture injection test (DFIT) at 2920m depth. (c) G-function (dP/dG) and semi G-function (GdP/dG) analysis at 2920m depth. (d) DFIT at 2840m depth. (e) G-function (dP/dG) and semi G-function (GdP/dG) analysis at 2840m depth. Where THP is tubing head pressure, and BHP is the bottom hole pressure.

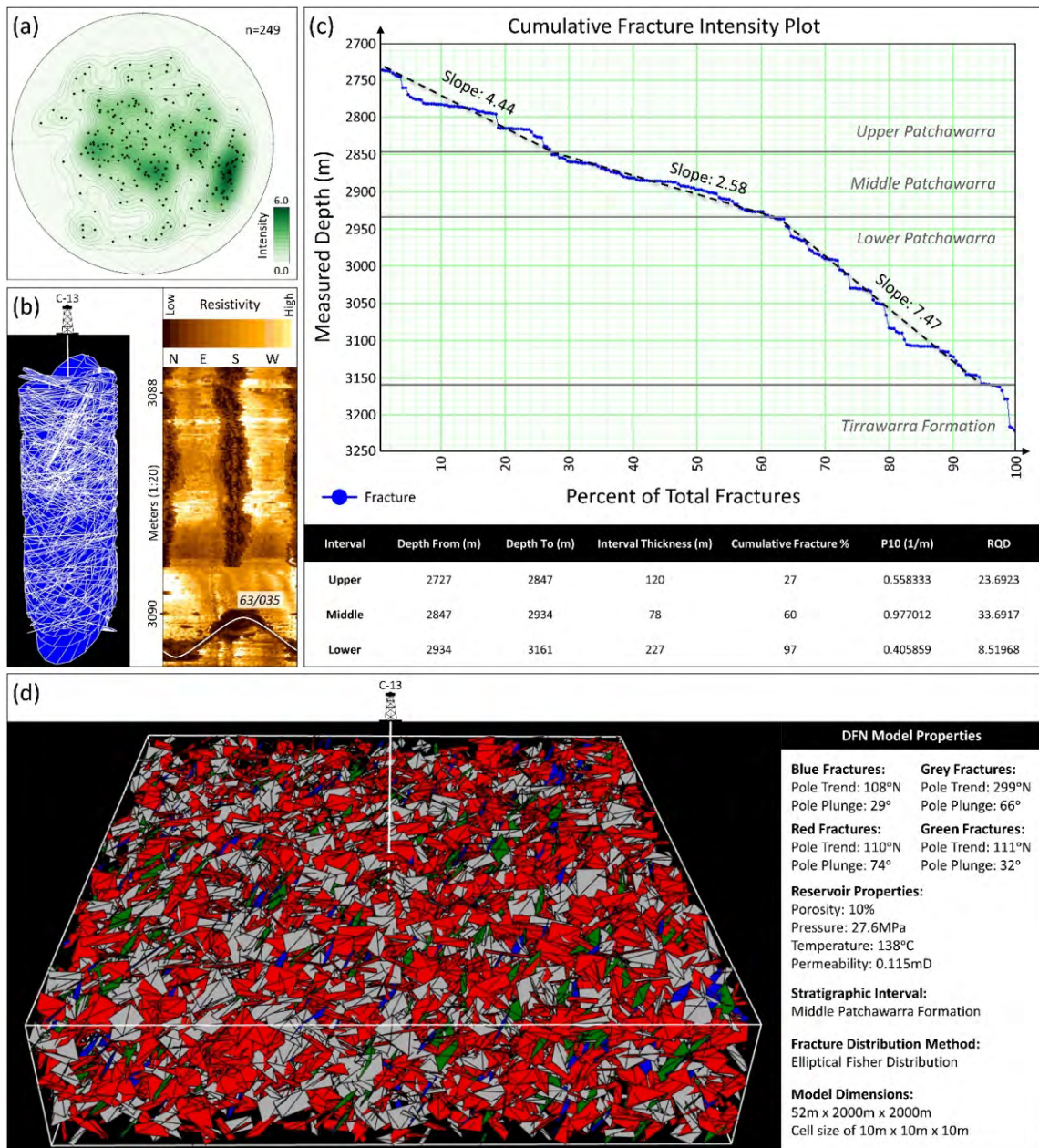


Figure 4. (a) Pre-existing natural fractures within the Patchawarra Formation interpreted from the C-13 borehole image log and projected onto an equal-area lower hemisphere stereonet (Grohmann and Campanha, 2010). (b) Natural fracture distribution on the C-13 well and an example of a natural fracturing in the borehole image log. (c) Natural fracture cumulative intensity analysis for the upper, middle, and lower Patchawarra Formation presenting the fracture intensity slope, fracture intensity per meter (P10), and rock quality designation (RQD). (d) The discrete fracture network (DFN) used for this analysis showing four different natural fracture sets within the Patchawarra Formation.

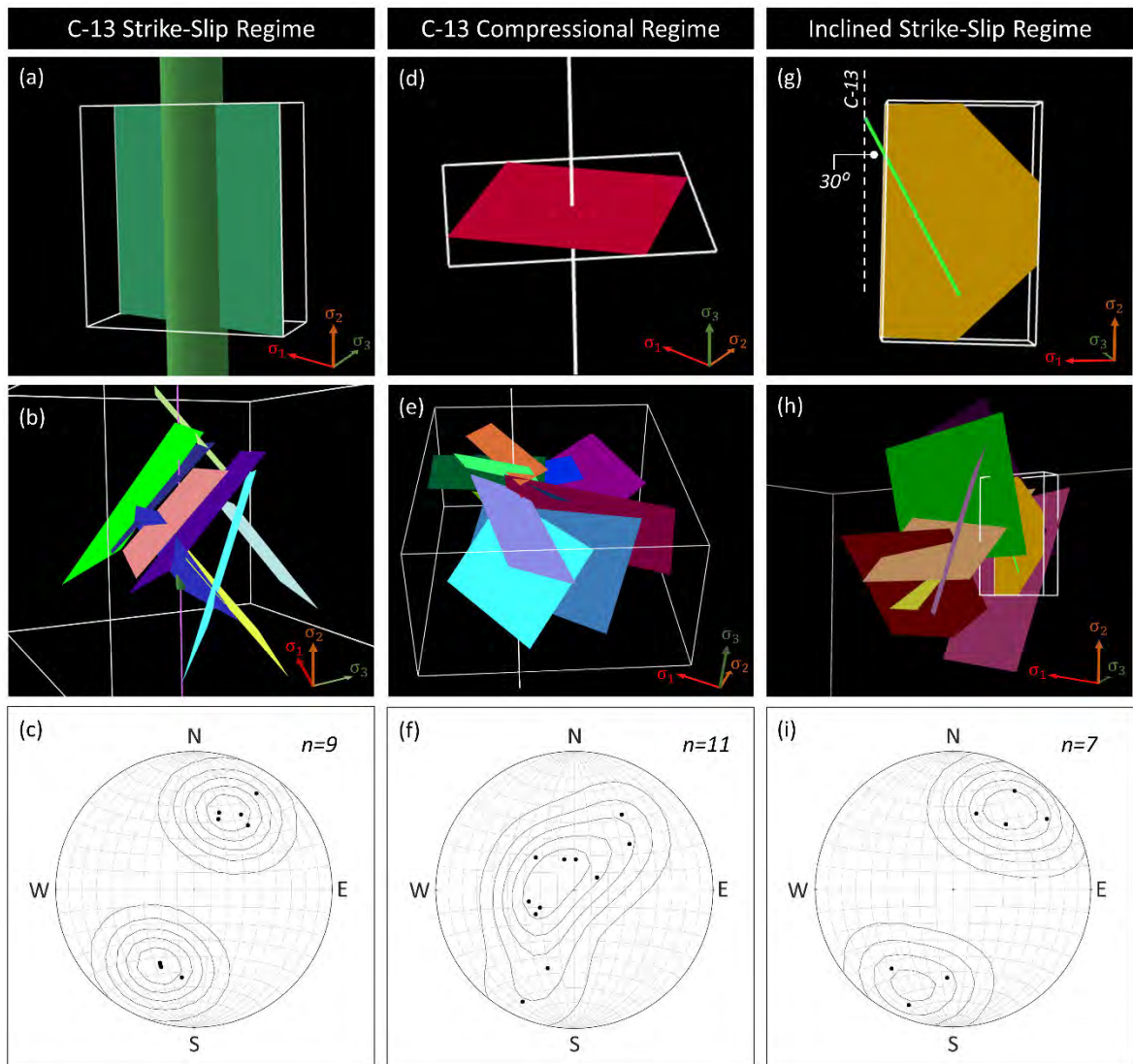


Figure 5. Hydraulic fracture simulation results. Using a strike-slip stress regime, the (a) induced hydraulic fracture, (b) interaction between the induced hydraulic fracture and pre-existing natural fractures, and (c) the pole to inflated pre-existing natural fractures is shown. Using a compressional stress regime, the (d) induced hydraulic fracture, (e) interaction between the induced hydraulic fracture and pre-existing natural fractures, and (f) the pole to inflated pre-existing natural fractures is shown. Using a strike-slip stress regime for the inclined well, the (g) induced hydraulic fracture, (h) interaction between the induced hydraulic fracture and pre-existing natural fractures, and (i) the pole to inflated pre-existing natural fractures is shown. σ_1 : maximum principal stress; σ_2 : intermediate principal stress; σ_3 : minimum principal stress.

**Chapter 7 : Design and Optimization of Multi-Stage Hydraulic
Fracturing in A Horizontal Well in A Shale Gas
Reservoir in Cooper Basin, South Australia**

Design and optimisation of multi-stage hydraulic fracturing in a horizontal well in a shale gas reservoir in the Cooper Basin, South Australia



Lead author
**Kunakorn
Pokalai**

K. Pokalai, Y. Fei, M. Ahmad, M. Haghighi and M.E. Gonzalez Perdomo

Australian School of Petroleum, The University of Adelaide
Level 2, Santos Petroleum Engineering Building (gate 6)
Frome Road
Adelaide, SA 5000
kunakorn.pokalai@adelaide.edu.au

ABSTRACT

Multi-stage hydraulic fracturing in horizontal wells is a well-known technology and is a key mechanism for gas recovery from extremely low permeable shale gas reservoirs. Since Australia's Cooper Basin has a more complex stress regime and higher temperatures when compared to US shale gas formations, the design and optimisation of this technology in the Cooper Basin has not been explored to the authors' knowledge.

The Murteree and Roseneath shale formations in the Cooper Basin are 8,500 ft in depth and have been targets for shale gas production by different oil and gas operators. Deeper zones are difficult to fracture, as fracture gradients are often above 1 psi/ft.

In this study, 1D vertical mechanical earth modelling using petrophysical log data was developed. Then, the stress profile was tuned and validated using the minimum horizontal stress from a mini-frac test taken along a vertical well. A 3D hydraulic fracture simulation in a vertical well was developed as a pilot to select the best locations for horizontal drilling. The selection criteria for the best location included the stress regime, gas flow rate and fracture geometry. Then a multi-stage fracture treatment in a horizontal well was designed.

A large number of cases were simulated based on different well lengths, stage spacing and the number of stages. The productivity index was selected as the objective function for the optimisation process. The best case finally was selected as the optimum multi-stage hydraulic fracturing in a horizontal well in the Cooper Basin.

KEYWORDS

Shale gas, Cooper Basin, horizontal well, multi-stage hydraulic fracturing.

INTRODUCTION

In low-permeability formations such as shale gas reservoirs, a well would be uneconomic unless a successful hydraulic fracturing treatment is designed. The first hydraulic fracturing treatment was carried out on a gas well in the Hugoton field in 1947 (Veatch et al, 1989). Hydraulic fracturing has been applied in the Cooper Basin since 1968 (McGowen et al, 2007).

Most of the hydraulic fracturing has been targeted in low-permeability reservoirs such as tight sand and coal seam gas reservoirs. Recently, exploration started in shale gas reservoirs

as well; however, up to now no published data is available on multi-stage hydraulic fracturing in a horizontal well in the Cooper Basin.

The first commercial shale gas well in the Cooper Basin is Moomba-191, which vertically targeted the Roseneath, Epsilon and Murteree (REM) Formation (Starkey et al, 2014). This well provided stabilised production of 2.7 MMscf/d; however, since previous shale gas targets have been drilled vertically, no sufficient information is available for horizontal drilling.

Understanding of shale properties, by adopting a technical review of the literature on US shale gas, is the key to finding the best location (sweet spot) to increase the productivity. These parameters depend on the hydrocarbon content, fracture barriers, mineralogy and structural geology of the basin (Schein and Mack, 2007). For successful fracture treatment, the stress orientation, depth of hydraulic fracturing and existence of natural fractures are also important parameters and can form a guideline for predicting potential fracture reactivation in a shale gas reservoir.

The 3D hydraulic fracturing simulator of Moomba-191 was previously generated based on different well logs to derive the mechanical rock properties and to estimate minimum horizontal stress (Barree et al, 2009). Furthermore, a study by Reynolds et al (2006) measured three principle stress magnitudes and concluded that reverse faulting and strike-slip stress regimes are the dominant trend in the Cooper Basin.

In this peer-reviewed paper, the first hydraulic fracturing in a vertical well is simulated as a pilot run to find the potential of the quality of the stimulation process and gas production estimation. Then a horizontal well is designed and a multi-stage hydraulic fracturing simulation is subsequently constructed. To optimise productivity, the sensitivity analysis was conducted by varying the lateral length and hydraulic fracturing stages.

GEOLOGICAL BACKGROUND

The Cooper Basin is located in central Australia. Sediments were deposited in a non-marine environment during the Late Carboniferous to Middle Triassic era and is up to 4.5 km thick (Hill and Gravestock, 1995). The overlying Eromanga Basin of Jurassic to Cretaceous age is separated by an unconformity at the top of the Cooper Basin (Apak et al, 1997), which varies in depth from 3,180–9,180 ft below sea level (Laws and Gravestock, 1998). This is depicted in Figure 1.

The SA sector of the Cooper Basin comprises a series of northeast to southwest trending ridges and troughs as shown in Figure 2. This sector has an area of 35,000 km², and has the greatest thickness of hydrocarbon-bearing Permian hybrid strata with fine to coarse sandstones, coal seams of various thicknesses and/or organic shale. Two major intrabasin highs separate the Patchawarra, Nappamerri and Tennapera troughs (Menpes et al, 2013). The Gidgealpa-Merrimelia-Innamincka (GMI) and Murteree-Nappacoongee ridges are the major depocentres. The largest amount of well data from thousands of oil and gas exploratory and production wells come from this part of the basin (Gravestock and Jensen-Schmidt, 1998).

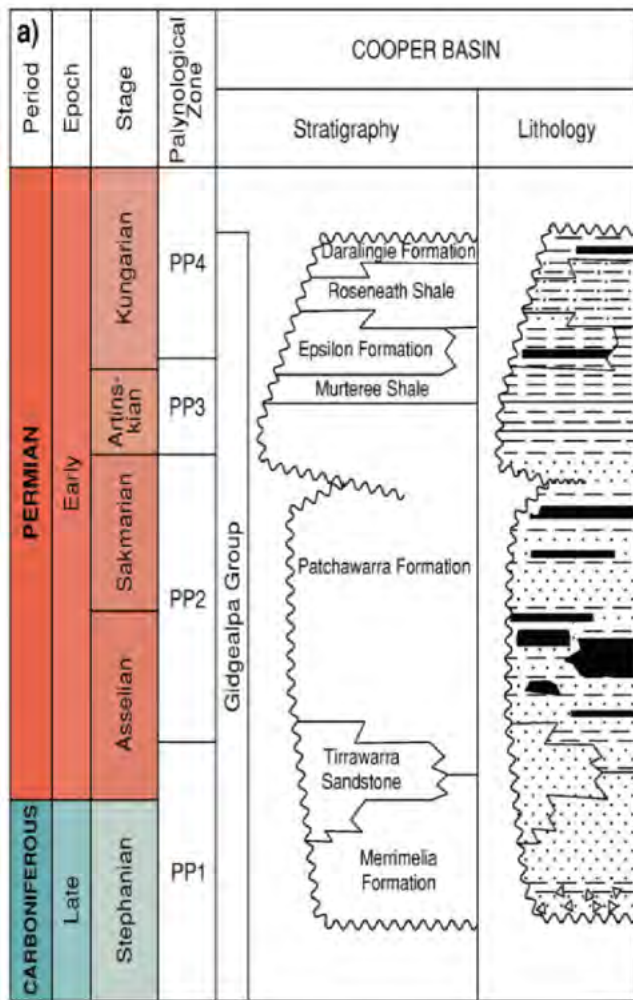


Figure 1. Stratigraphic column for the Cooper Basin and REM Interval—Roseaneath Shale, Epsilon Tight Sand and Murtree Shale (Radke, 2009).

The exploration and production data from numerous production wells indicate that Permian shale is the potential source rock. Recently, after rigorous exploration for unconventional gas, these shale reservoirs have been proven as pervasive unconventional shale gas plays, where the Roseaneath and Murteree formations are the most prolific shale gas reservoirs in the basin. Based on the same deposition, stratigraphy and lithological similarities, the Roseaneath and Murteree shales have the same geochemical, petrophysical and geomechanical characteristics. Previously considered as lean source rocks, the Murteree and Roseaneath shale formations are now considered to be organically rich and over-matured source rocks based on their latest geochemical analysis and total organic content (TOC) of 5.0 wt%, and it has attained a vitrinite reflectance maturity level of 3.0% (PIRSA, 2011).

The Roseaneath and Murteree source rocks are dominated by Type III kerogens derived from plant assemblages. X-ray diffraction (XRD) and quantitative evaluation of minerals by scanning electron microscopy (QEMSCAN) for mineralogical data indicate that the Roseaneath and Murteree carbonaceous shale plays consist of quartz, siderite and mainly illite clay (Ahmad et al, 2012), as shown in Table 1.

GEOMECHANICAL AND FRACTURE PROPERTIES

To produce gas from an ultra-low permeability reservoir, a detailed quantitative mineralogical and geomechanical analysis of the rock is necessary, which is usually obtained from wireline logs and laboratory measurements performed on the

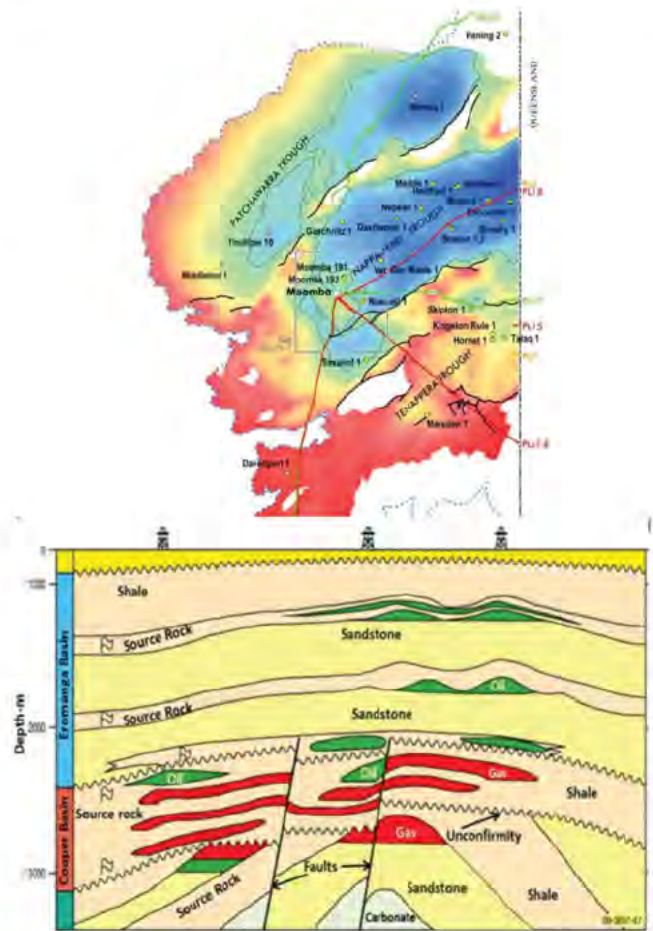


Figure 2. Schematic section showing typical petroleum traps in the Cooper and Eromanga basins (with modification from Menpes et al [2013] and Thornton [1979]).

rock sample. The type and amount of these minerals helps in the selection of completion targets, hydraulic fracturing fluids and proppant. Furthermore, to determine the in situ stress in a formation, and the mechanical properties such as Poisson's ratio and Young's modulus, petrophysical logs and mini-frac test data are used.

According to the multiple rock formation layers, the in situ stress is variable according to the local stress and properties of rock within each layer. The three principle stresses are the main factors that control the fracture azimuth and orientation, fracture growth and the selection of fluid and proppant treatment.

Reynolds et al (2005) reported 890 borehole breakout tests and 608 mini-frac tests, which indicates that the approximate maximum horizontal stress is oriented in the east to west direction at 101°N. In addition, results from Pitkin et al (2012) show the surface tiltmeter, measured from Holdfast-1 and Encounter-1 in Roseaneath, to be N12°W and N20°W, respectively. These are in contrast to the results from Reynolds et al (2005). When comparing the percentage value of fracture propagation between the vertical and horizontal directions, however, the fracture tends to propagate in the vertical direction. In this model, 90°N is selected to be the direction of maximum horizontal stress from east to west for the transverse fracture modelling.

In shale gas reservoirs, pre-existing natural fractures are very important because they have a potential to create a fracture network. This can be evaluated by fracture intensity. The borehole image log provides information about the intensity and orientation of the fractures as shown in Figures 3 and 4, respectively. Roseaneath Shale has the highest fracture intensity of 0.0765 fractures per feet when compared to the other formations. Moreover, the top of the Roseaneath Shale has a higher

Table 1. Distribution of minerals and their elastic properties—from a Murteree Shale sample—taken using the QEMSCAN automated mineralogy system (Ahmad and Haghghi, 2012).

Mineral phase	Mineral volume ^a (%)	Mineral volume ^b (%)	Elastic properties
Quartz	32.60	44.02	Brittle fraction with low Poisson's ratio and high Young's modulus values
Siderite	06.60	05.35	
Rutile	00.70	00.79	
Pyrite	00.00	00.02	
Kaolinite	16.50	14.32	Ductile fraction with high Poisson's Ratio and low Young's modulus values
Illite/Muscovite	40.09	28.37	
Other silicates/accessory minerals	03.51	04.54	

^aMineralogy of Roseneath Shale from Moomba-191 Well Completion Report (Tedesco, 2012).

^bMineralogy of Murteree Shale in core samples from Della-4 and Moomba-46 Well Completion Report (PIRSA, 1972).

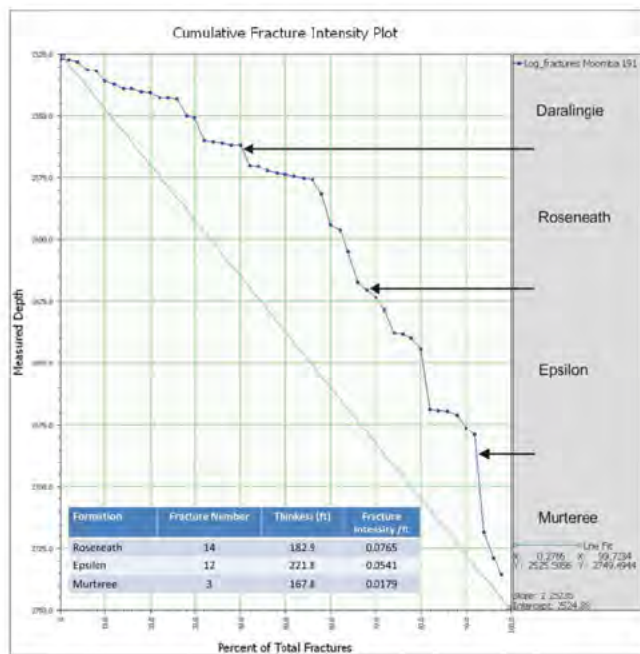


Figure 3. Cumulative fracture intensity versus depth in Moomba-191.

occurrence of fractures than the bottom. Fracture pole orientation shows the orientation of the fracture intensity in the south-westerly direction to be approximately at 195°N. This helps in the planning of horizontal well completion.

Mini-frac tests have been conducted on 24 wells in the Cooper Basin (Reynolds et al, 2006). The range of the minimum horizontal stress or closure pressure from 4,350 psi to 8,700 psi at the formation depth between 6,560–9,840 ft can be seen in Figure 5. In addition, Naslin (2013) reports the closure pressure to be between 7,600–8,600 psi in the Roseneath and Murteree shales.

The authors of this paper have used the minimum horizontal stress to tune and calibrate the hydraulic fracturing model, which was initially constructed by dipole sonic and density logs. The minimum horizontal stress was calculated using Equation 1, based on the uniaxial strain model (Barree et al, 2009).

$$\sigma_{Hmin} = \frac{\nu}{1 - \nu} (\sigma_v - \alpha_v P_p) + \alpha_h P_p + (\epsilon_h E + \sigma_t) \quad (1)$$

In Equation 1, the first term on the right-hand side implies that the effective vertical stress is converted to the effective horizontal stress due to the overburden stress and the pore pressure by Poisson's ratio. The second term is a horizontal stress that is created from the pore pressure. The final term is

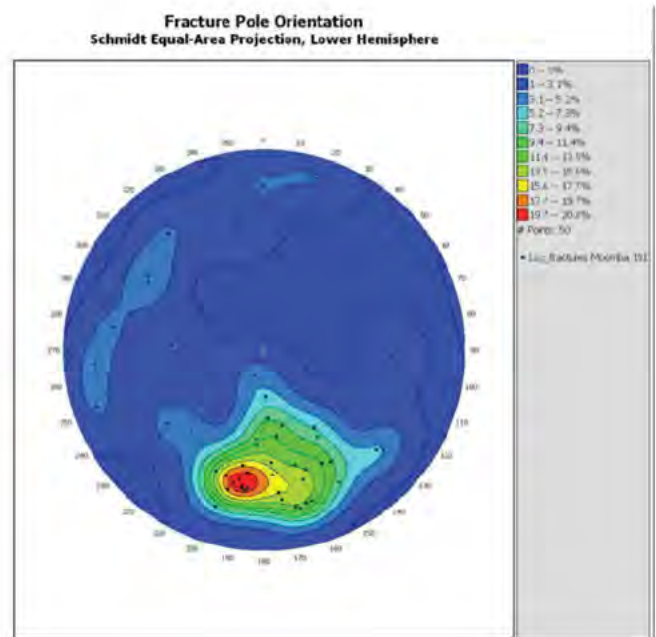


Figure 4. Fracture pole Orientation in Moomba-191.

attributed to the tectonic stress and tectonic strain, which is present due to the loading of Earth's crust.

Table 2 shows the summary of average elastic rock properties in the Roseneath and Murteree shales. The minimum horizontal stress in the Murteree Shale is around 350 psi higher than in the Roseneath Shale in spite of the fact that Poisson's ratio and Young's modulus are similar in both formations. The tectonic strain of 420 microstrains was used to tune the minimum horizontal stress in the Roseneath Shale.

Continued next page.

Continued from previous page.

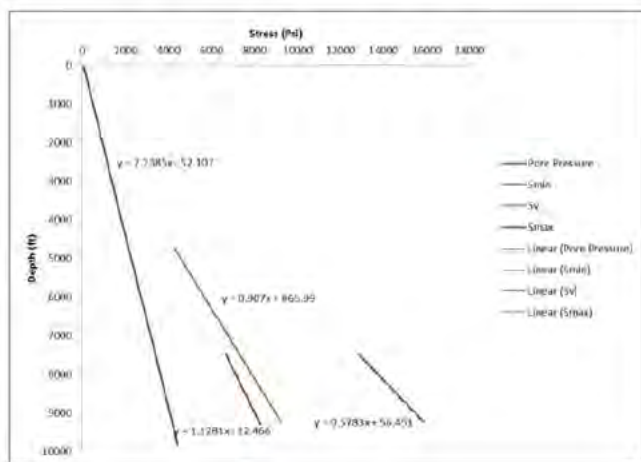


Figure 5. Stress versus depth plot for Dullingari North-8 adapted from Reynolds et al (2006).

Table 2. Summary of geomechanical properties in the Roseneath and Murteree shales.

Properties	Roseneath Shale	Murteree Shale
Poisson's ratio	0.27	0.27
Young's modulus (MMpsi)	3.8	3.9
Brittleness	0.4	0.4
Minimum horizontal stress (psi)	7,650	8,000
Stress anisotropy (psi)	7,096	7,096

MODEL CONSTRUCTION

A 3D fracture propagation model for the Moomba-191 well was developed under well-defined stress conditions by using GOHFER® (Barree, 1983). The model has the ability to decouple with the rock properties based on the assumption of linear elastically coupled materials.

The schematic of the model for the Roseneath Shale is shown in Figure 6. The grids are in Cartesian coordinates with a uniform size of 5 × 20 ft, and with top and bottom boundaries between 8,400 ft and 8,700 ft. The simulator default of an asymmetric perforation type was chosen.

A grid structure was generated first to calculate fluid/solid transportation, and the shape of the fracture was created to determine the height containment, and width and length of the fracture. Each grid point was assigned a proppant concentration, pressure and width in vertical and lateral directions. The grid points along the vertical direction were generated using petrophysical well logs; however, because of the lack of 3D seismic and production data, the true structural and local stratigraphy could not be developed for adequate lateral grid structure. Table 3 shows the input data for the hydraulic fracturing simulation.

The first step of the simulation was to collect data from well logs and cores to import and generate the elastic properties. Then the minimum horizontal stress was tuned by adjusting the pore pressure and the tectonic strain to validate the stress profile. Finally, a 3D hydraulic fracture model was generated. This modeling workflow can be seen in Figure 7.

The spectral gamma ray (GR_{spec}) logs are generated by using the sum of the concentration of Thorium (Th), Uranium (U) and Potassium (K) as shown in Equation 2 (Barree, 2009).

$$GR_{spec} (API) = 4Th (ppm) + 8U (ppm) + 14K (%) \quad (2)$$

In Figure 8, the spectral gamma ray response is higher than the gamma ray response. This is most likely due to the distinguished radioactive mineralogy in shale. These curves provide GR_{min} and GR_{max} values of 30 API and 201 API, respectively. Both the gamma ray and the spectral gamma ray deflect to the right consistently in the target zone, indicating the predominant fraction of lithology to be shale.

Based on Equation 1, the stress profiles are built under the assumption of strike-slip faulting ($\sigma_{Hmax} > \sigma_v > \sigma_{Hmin}$) as shown in Figure 9, which shows the minimum horizontal stresses of 7,650 psi in the Roseneath and 8,000 psi in the Murteree shales. The stress was determined and validated using the constraining stress by Reynolds et al (2006) and Naslin (2013).

Once the stress profile has been generated, the fracture treatment of a vertical well is simulated based on the report by Pitkin et al (2012). In this case study, hydrochloric (HCl) acid is pumped first to reduce the near well bore pressure loss (NWBPL)—as the Cooper Basin has been reported as having high NWBPL by Johnson et al (2002)—followed by water and linear gel. In the Roseneath Shale, 291,000 gallons of fracturing fluid with an average pumping slurry rate of 50 bpm, and 150,000 lbs of ceramic proppants were used. In the Murteree Shale, 300,000 gallons of fracturing fluid and 124,000 lbs of proppant was used, as shown in Figure 10.

To develop a horizontal well model, identification of the sweet spot and target depth are essential. In this model, the Roseneath Shale was first used for developing the model because it was estimated to have a higher gas production rate, larger reservoir thickness, and fracture intensity.

The well plan was targeted in the Roseneath Shale between 8,400–8,600 ft. The kick-off point started at 7,830 ft, with a deviation angle of eight degrees per 100 ft. These parameters are summarised in Table 4.

The variables in Table 5 show how to optimise the multi-stage hydraulic fracturing design at different lateral lengths and fracture stages. Miller et al (2011) indicate that if the number of perforation clusters per stage increases, the percentage of non-flowing perforation clusters increase. Based on these criteria, therefore, the authors of this paper selected the number of perforation clusters per stage to be six in this design.

The results from shale in the Eagle Ford Basin have been used for fracture treatment (Borstmayer et al, 2011). This design is suitable for brittle shale in both Roseneath and Murteree shales. The brittleness of these shale formations are approximately 40% based on Poisson's ratio and Young's modulus. The shale also has a high quartz content of 30%, showing a moderate brittleness. Rickman et al (2008) recommended the use of linear gel for moderately brittle shale; however, most cases from the US indicate that slick water is the desirable fracturing fluid (Fonseca and Farinas, 2013).

Continued next page.

Continued from previous page.

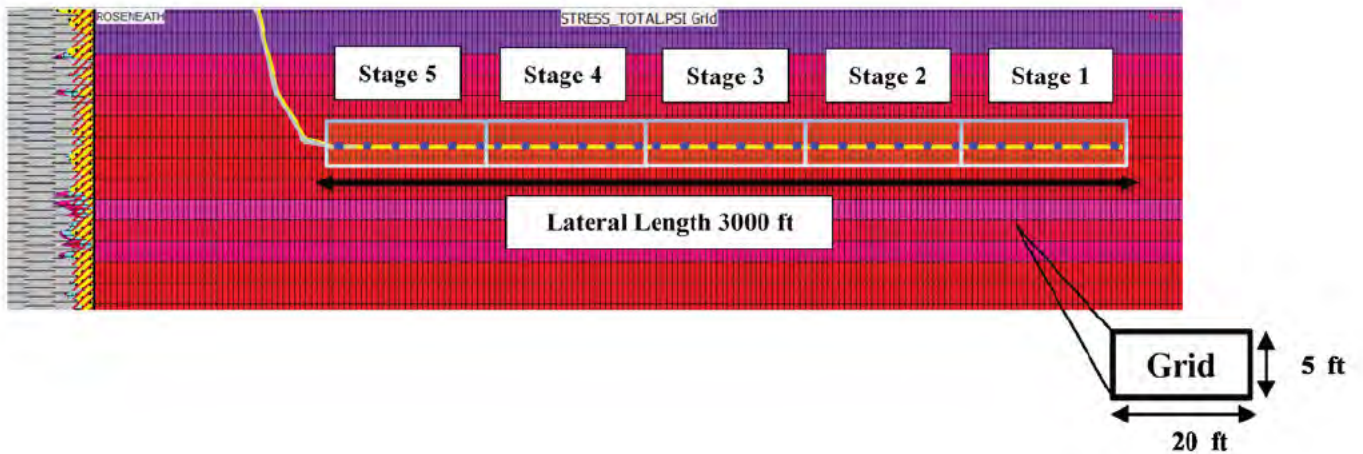


Figure 6. Schematic diagram of multi-stage hydraulic fracturing (lateral length is 3,000 ft with five stages).

Table 3. Input data for the hydraulic fracturing simulation.

Reservoir properties	Roseneath Shale	Murteree Shale
Measured depth (ft)	8,413–8,596	8,818–8,956
Thickness (ft)	182.9	167.8
Reservoir pressure (psi)	4,286	4,484
Reservoir temperature (F)	316	327
Permeability (mD)	4.47×10^{-5}	5.70×10^{-5}
Porosity (%)	2.1	1.7
Water saturation (%)	47.8	51.2
Gas saturation (%)	44.9	41.3
Grid properties	Roseneath Shale	Murteree Shale
Node size (height; ft)	5	5
Aspect ratio	4	4
Perforation type	Asymmetrical	Asymmetrical
Top-bottom boundary (ft)	8,400–8,700	8,700–9,000

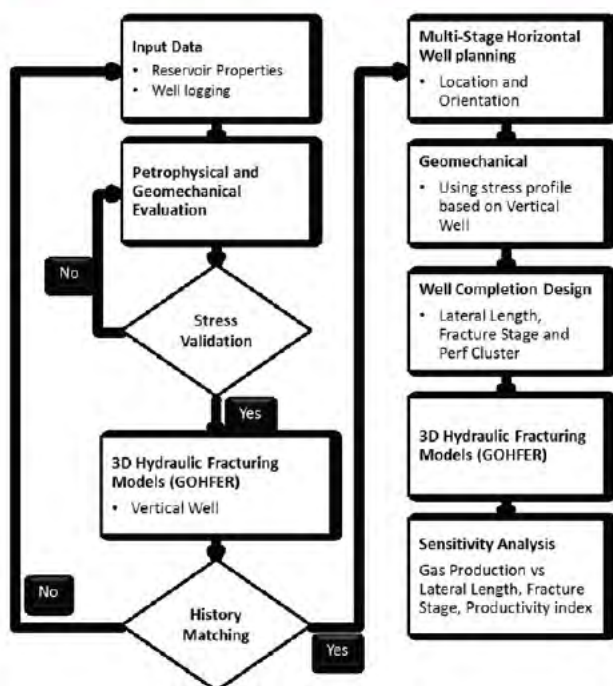


Figure 7. Workflow of the 3D hydraulic fracturing model.

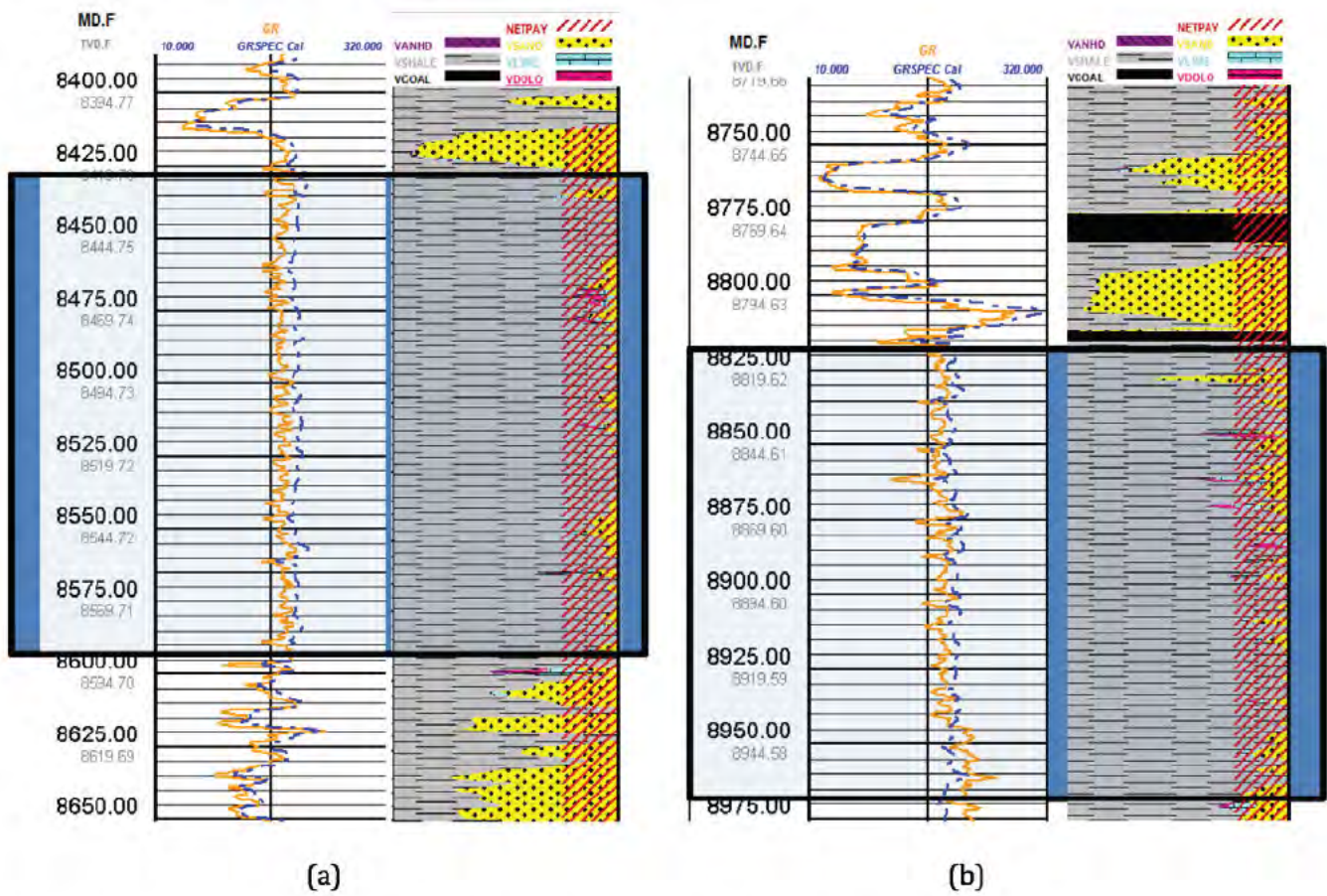


Figure 8. The gamma ray log (orange line) and the spectral gamma ray log (blue line) for the Roseneath (a) and Murteree (b) shales.

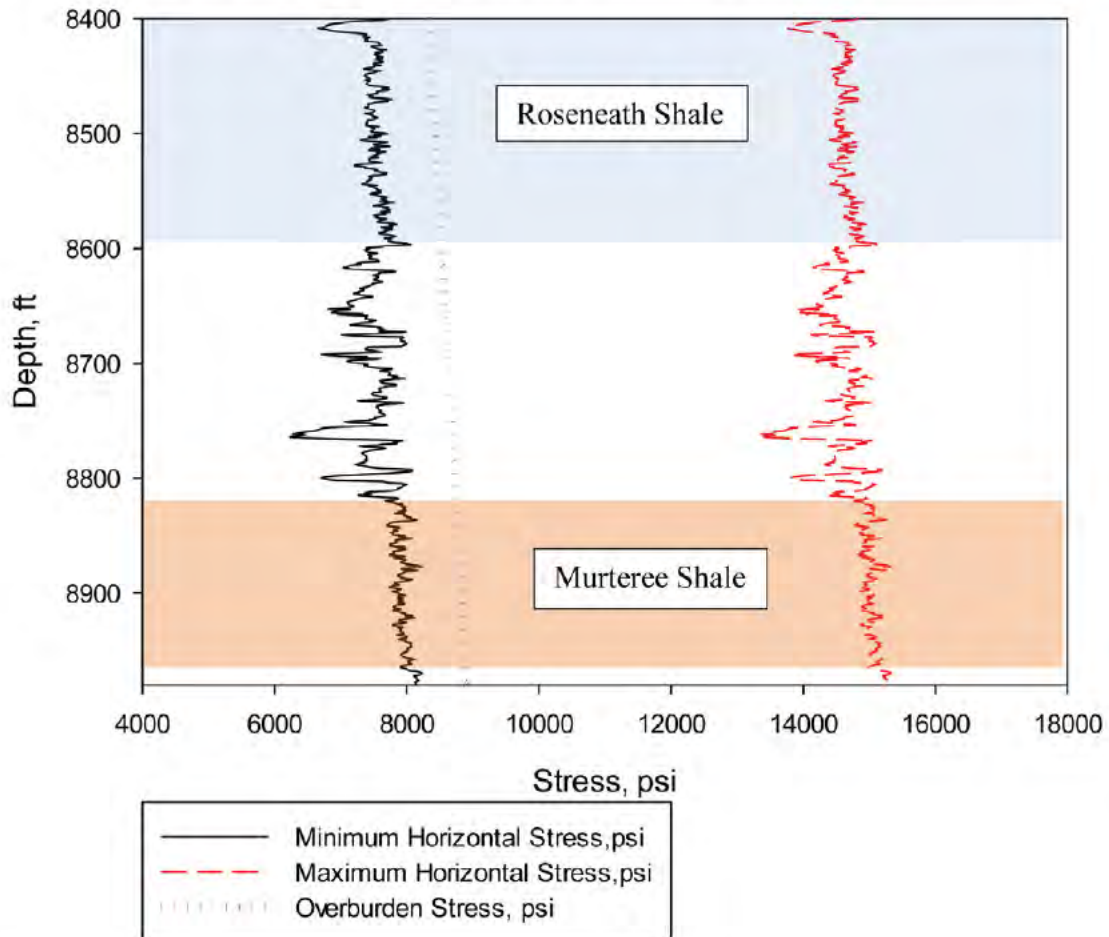


Figure 9. The stress profile for the Roseneath and Murteree shales, adapted from Reynolds et al (2006).

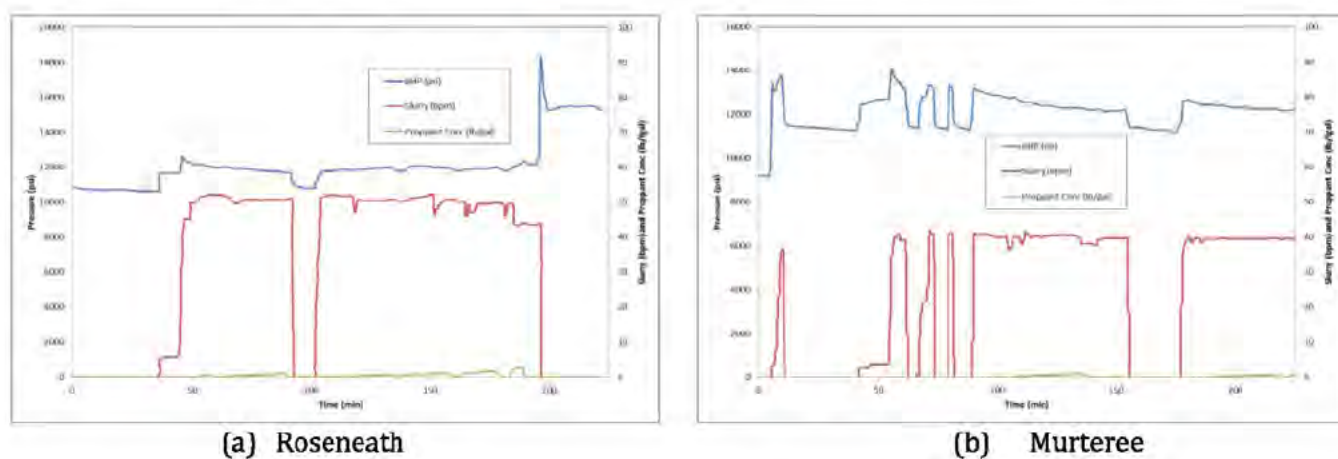


Figure 10. The pumping schedule for the Roseneath (a) and Murteree (b) shales, adapted from Pitkin et al (2012).

Table 4. Well design and fracturing treatment parameters of the horizontal well in the Roseneath Shale.

Well parameters	
Wellbore diameter (in)	4
Kick-off point	7,830
Deviation angle (degrees/100 ft)	8
Wellbore fluid (drilling mud)	2% KCl
Node size (ft)	5
Aspect ratio	4
Cluster number	6
Perforation density (spf)	8
Lateral length (ft)	1,000 and 3,000
Number of fracture stages	5, 10, 15 and 20
Fracturing treatment parameters	
Type fracturing fluid	Slick water
Fluid volume per stage (gal)	220,000
Type of proppant	White sand 100 mesh, ceramic 30/60
Proppant volume per stage (lb)	300,000

Table 5. Multi-stage hydraulic fracturing design.

Case	Lateral length (ft)	Fracture stage	Interval (ft)	Effective interval (ft)
1	1,000	5	200	180
2	1,000	10	100	90
3	1,000	15	67	60
4	1,000	20	50	45
5	3,000	5	600	540
6	3,000	10	300	270
7	3,000	15	200	180
8	3,000	20	150	135

RESULTS AND DISCUSSION

The simulation results from the Roseneath and Murteree shales are displayed in Table 6. As shown, the Roseneath Shale has the highest incremental reserves of 934 MMscf because the stimulated reservoir volume (SRV) is 5,000 ft³, which is larger in the Roseneath Shale compared to the Murteree Shale. Interestingly, the Murteree Shale shows a higher conductivity value of 3.4 md.ft, but it does not give a higher cumulative production when compared to the Roseneath Shale because this low-permeability reservoir preferably maximises the SRV rather than conductivity.

The results indicate that the fracture conductivity is very low when compared to the ceramic proppant conductivity that was measured in the laboratory under high-stress conditions of 8,000 psi. The proppant conductivity was measured to be 1,700 md.ft. Despite this, at the subsurface condition, the conductivity decreases due to the impact of the multiphase flow effect, high temperatures and gel damage. Saldungaray and Palisch (2012) reported a case study from the Barnett Shale where the well history match showed the realistic fracture conductivity was 2 md.ft.

Before developing the horizontal well model, production history matching with the pilot vertical well model is neces-

sary. This is required to validate reservoir properties such as permeability, pressure drawdown and skin factor. The results of a history match are shown in Figure 11. As time progresses, there is a better history matching of the real production data and the simulation data. Ultimately, at around 500 days, there is an exact match.

Figure 12 shows the maximum bottomhole pressure to be around 9,500 psi, with an injection slurry rate of 50 bpm. The pumping starts with injecting only fracturing fluids to create a pad, followed by the injection of low slurry concentrations with white sand 100 mesh. After that, the main slurry treatment with ceramic proppant 30/60 is injected. Finally, the flushing stage is performed. Five subsequent stages follow this process.

Figure 13 shows the proppant concentration of case 5 (five stages fracturing with 3,000 ft lateral length). The 30 transverse fractures have been generated with a total drainage area of 177 acres. The simulation shows the fracture growth downwards at the lower part of the Roseneath Shale and the high proppant accumulation at the lower zone. Some of the fractures do not connect to the well and up to 40% of the fractures are not connected within each perforation cluster due to the high-stress regime.

The designs of the sensitivity analysis are shown in Table 5.

Table 6. The results of hydraulic fracturing in vertical wells.

Properties	Roseneath Shale	Murteree Shale
Fracture height (ft)	85	70
Average fracture width (in)	0.2	0.3
Fracture half length (ft)	1,760	1,550
Fracture conductivity (md.ft)	1.6	3.4
Dimensionless fracture conductivity (FCD)	0.035	0.077
Average gas rate (MMscf/d)	1.9	1.8
Gas cumulative value at 500 days (MMscf)	934	916

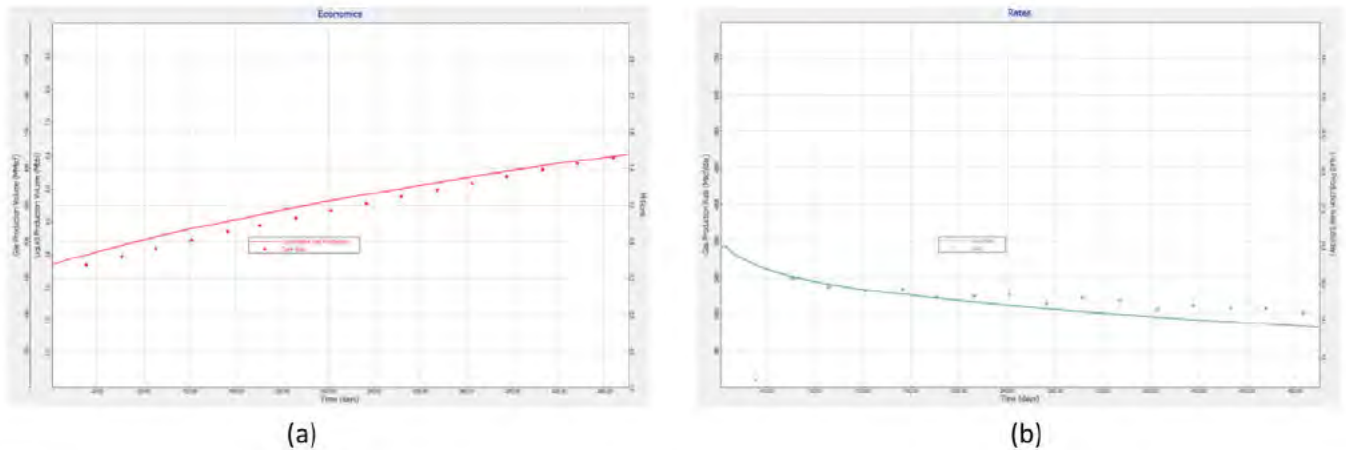


Figure 11. The results of Murteree Shale production: cumulative production versus time (a) and gas production rate versus time (b).

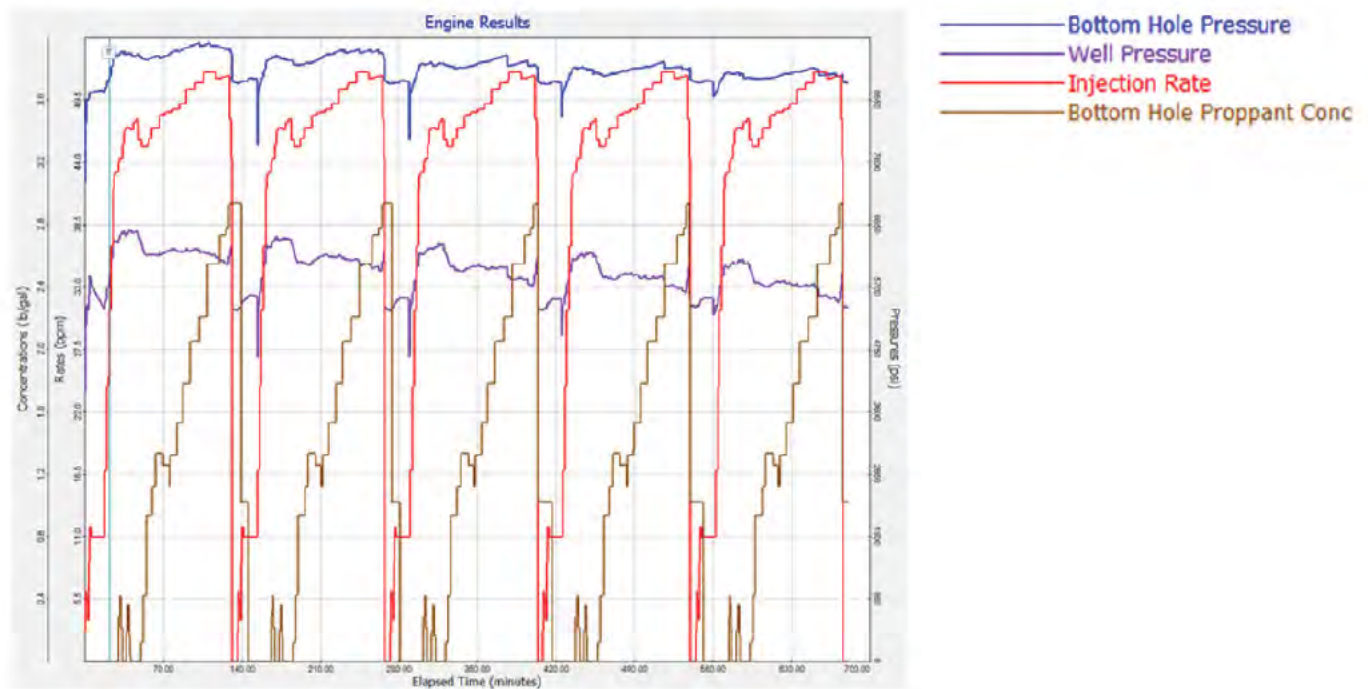


Figure 12. The output of pumping design for a horizontal well with 3,000 ft lateral length and five stages.

Continued next page.

Continued from previous page.

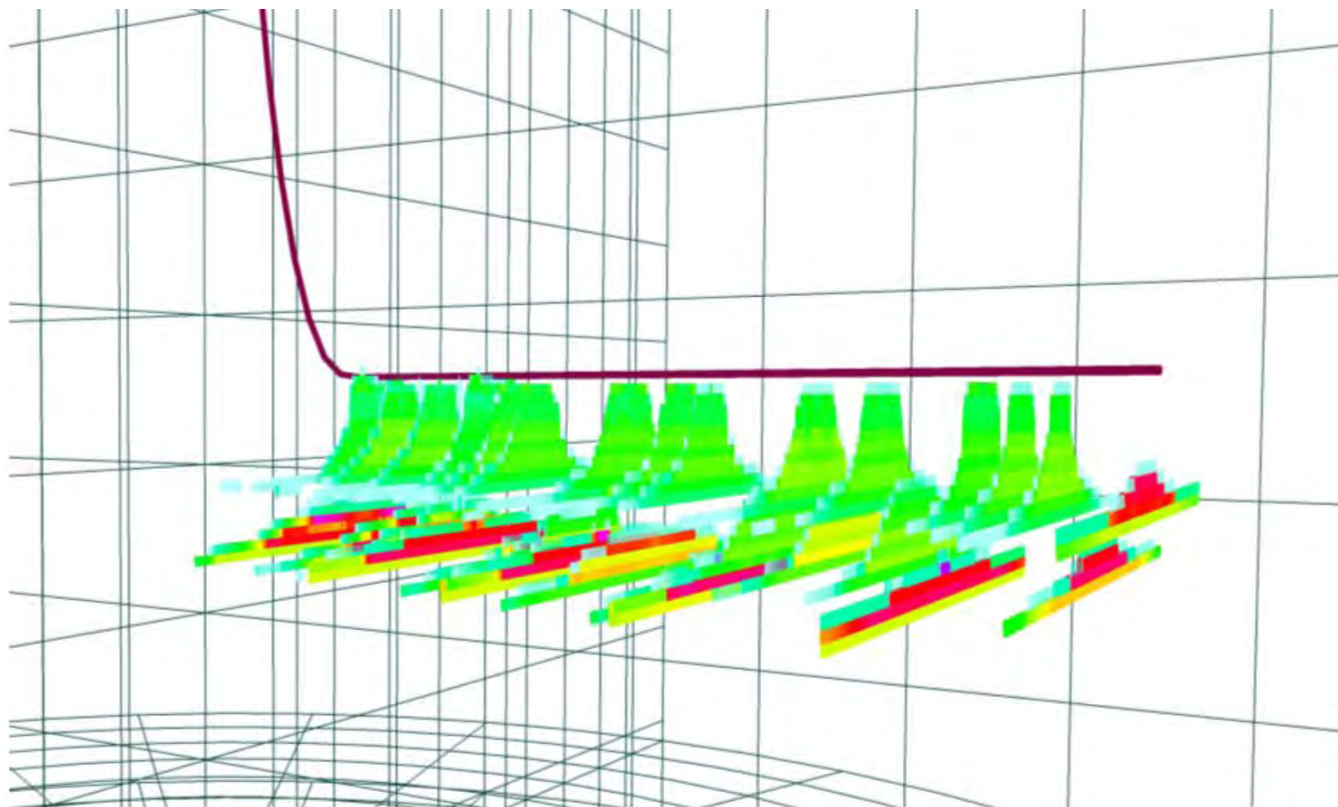


Figure 13. The proppant concentration of multi-stage hydraulic fracturing (lateral length is 3,000 ft with five stages).

The sensitivity of the lateral length is analysed by using a separation of 1,000 and 3,000 ft. In each lateral length, four different fracture stages were evaluated. The horizontal well provides the higher gas production rate when compared to the vertical well, as shown in Table 7. The fracture dimension of case 5 (3,000 ft lateral length and five stages) gives a fracture half-length longer when compared to case 1 (1,000 ft lateral length and five stages); however, case 1 provides a higher fracture height than case 5. Overall, the SRV in case 5 is 750 MMft³ whereas in case 1 it is only 330 MMft³. In terms of fracture conductivity, the higher conductivity value did not provide better cumulative gas production, as can be seen in case 2 and case 5. In terms of gas productivity, however, the gas production rate and cumulative production increases when the fracture stage increases, as shown in Figures 14 and 15. The fracturing design with a lateral length of 3,000 ft and 20 stages provided the highest production rate of 26.7 MMscf/d and cumulative production rate of 13.34 Bscf at 500 days.

The SRV has been defined as creating a hydraulic fracture volume in a low-permeability reservoir. Figure 16 presents a linear relationship between the SRV and the cumulative gas production in different lateral lengths. The creation of a large SRV provides the maximum well performance because it provides the ultimate drainage area. In this case, therefore, a lateral length of 3,000 provides a stronger relationship between the SRV and cumulative gas production, which indicates that at the same SRV the longer lateral length provides more cumulative gas production.

Figure 17 shows the productivity index of horizontal wells (α_h) in comparison with the productivity index of vertical wells (α_v). Case 8 (20 stages, 3,000 ft) provides the highest stimulation ratio (α_h/α_v) of 14.05 when compared with the five stages of cases 1 and 5. The authors also found that with the same amount of treatment volume (two million gallons),

the longer lateral length (case 5) gives almost three times the stimulation ratio when compared to case 1.

CONCLUSIONS

- The stress profile has been developed and adjusted at the top and bottom of the target formation to control the fracture geometry (height containment). Without controlling the stress contrast, the fracture could grow up to the Daralingie Formation, which may result in a large value for history matching of gas production.
- Roseneath Shale has good potential to develop, based on the identification of higher fracture intensity. Using a 3D fracturing model proved to be useful in designing multi-stage hydraulic fracturing in shale gas by integrating key parameters such as mineralogy, in situ stress, and fluid and proppant properties.
- The Roseneath and Murteree shales possess the same geomechanical properties such as Poisson's ratio, Young's modulus and brittleness due to similar lithology. The selection and design of a hydraulic fracturing fluid and proppants are equally applicable to any stimulation operation in the shale gas reservoirs of the Nappamerri Trough.
- For optimisation of gas productivity, a higher lateral length performs better due to possible natural fracture activation.
- In this model, slick water is considered to be a compatible fluid as it suits moderate to high brittle rock properties. It is, however, recommended to design the fracturing fluid in future studies. Optimum fracturing fluid could be identified by characterisation of fluid leak-off, rheology, and proppant transportation.
- To improve the fracture stages, amount of fracture treatment, and location of the perforation cluster, logging-while-drilling (LWD) is recommended for future horizontal well design.

Table 7. Results of hydraulic fracturing in vertical wells.

Properties	Fracture height (ft)	Fracture width (in)	Fracture half-length (ft)	SRV (MMft ³)	Fracture conductivity (md.ft)	Average gas rate (MMscf/d)	Gas cumulative rate at 500 days (Bscf)
Case 1	165	0.1	1,945	330	6.63	2.2	1.09
Case 2	-	-	-	660	6.63	4.4	2.18
Case 3	-	-	-	990	6.63	6.5	3.27
Case 4	-	-	-	1,320	6.63	8.7	4.36
Case 5	125	0.1	1,990	750	4.81	6.7	3.33
Case 6	-	-	-	1,500	4.81	13.3	6.67
Case 7	-	-	-	2,250	4.81	20.0	10.00
Case 8	-	-	-	3,000	4.81	26.7	13.34

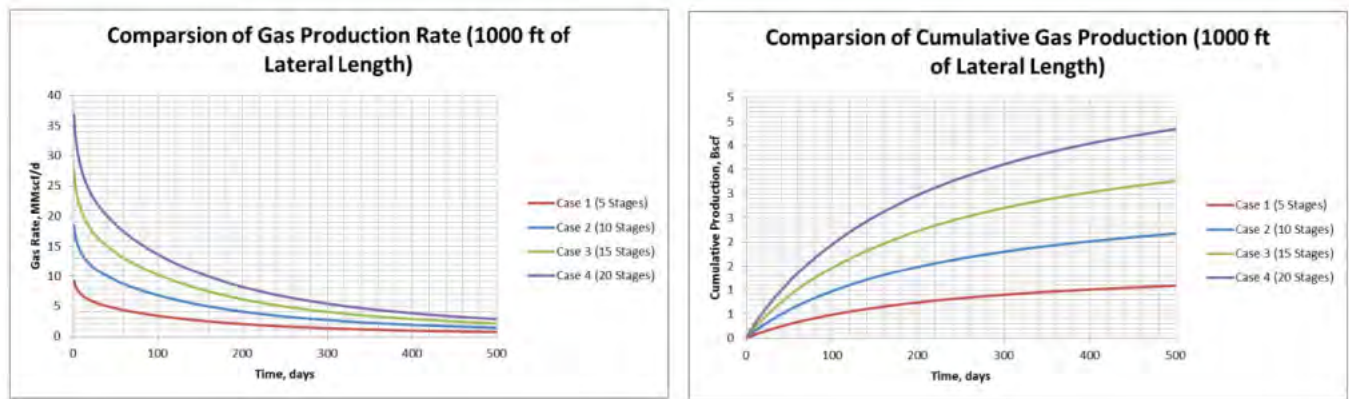


Figure 14. The gas production rate (MMscf/d) and gas cumulative production rate (Bscf/d) in a well with 1,000 ft lateral length.

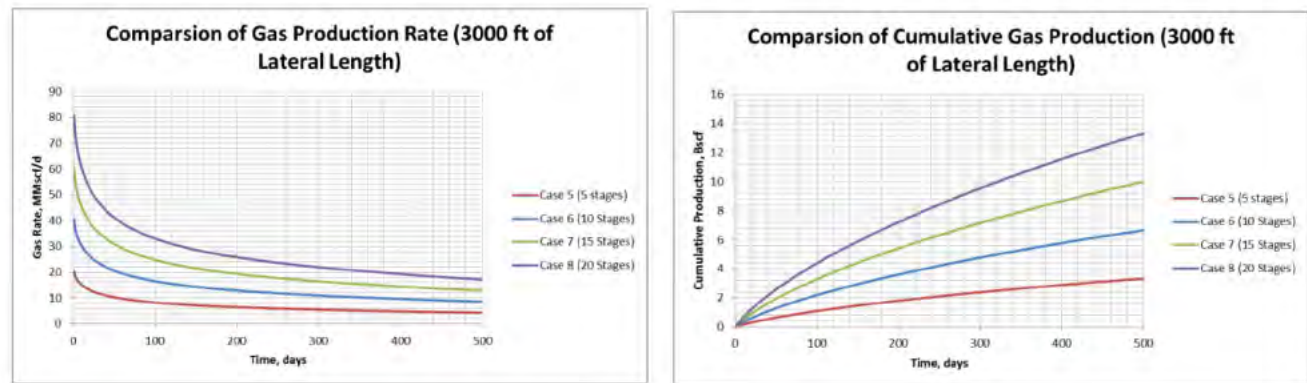


Figure 15. The gas production rate (MMscf/d) and gas cumulative production rate (Bscf/d) in a well with 3,000 ft lateral length.

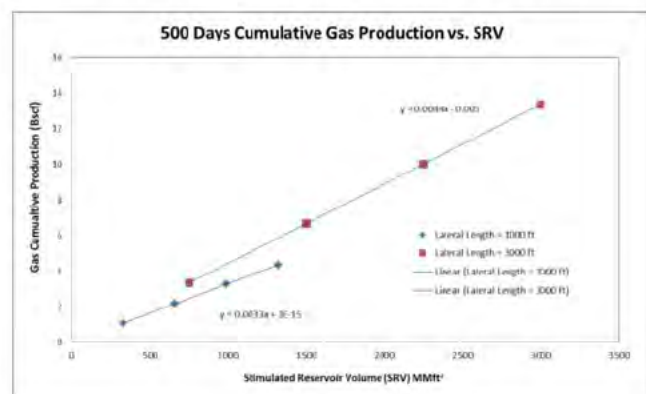


Figure 16. SRV versus the cumulative gas production rate.

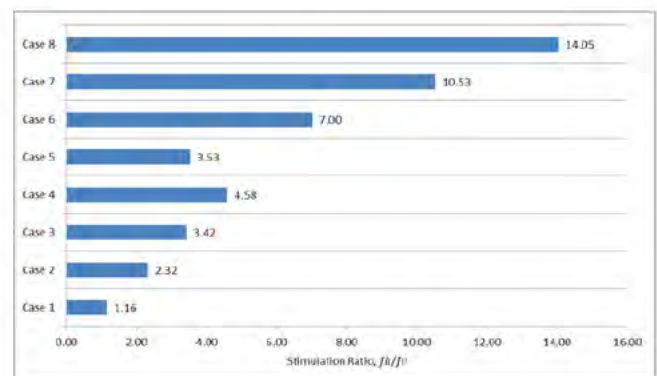


Figure 17. The productivity index of a horizontal well compared with the productivity index of a vertical well.

ACKNOWLEDGMENTS

The authors would like to express their thanks to Dr Hani Abul Khair, Dr Dennis Cook and Fathima Sajiah Mohamed for their suggestions and contributions towards this research paper.

NOMENCLATURE

σ_{hmin}	Minimum horizontal stress (psi)
σ_{Hmax}	Maximum horizontal stress (psi)
σ_v	Vertical horizontal stress (psi)
σ_t	Tectonic stress (psi)
ν	Poisson's ratio (dimensionless)
Pp	Pore pressure (psi)
ϵ_h	Horizontal tectonic strain (microstrains)
E	Young's modulus (MMpsi)
α_h	Horizontal poroelastic constant (dimensionless)
α_v	Vertical poroelastic constant (dimensionless)
GR _{spec}	Spectral gamma ray (API)
SRV	Stimulated reservoir volume

REFERENCES

- AHMAD, M., ALAMAR, A., KOO, R., NGUYEN, H. AND HAGHIGHI, M., 2012—Evaluation of free porosity in shale gas reservoirs (Roseneath and Murteree formations case study). *The APPEA Journal*, 52, 603–10.
- AHMAD, M. AND HAGHIGHI, M., 2012—Mineralogy and Petrophysical Evaluation of Roseneath and Murteree Shale Formations, Cooper Basin, Australia using QEMSCAN and CT Scanning. SPE Asia Pacific Oil and Gas Conference and Exhibition, Perth, Western Australia, 22–24 October, SPE-158461-MS.
- APAK, S.N., STUART, W.J., LEMON, N.M. AND WOOD, G., 1997—Structural evaluation of the Permian-Triassic Cooper Basin, Australia: relation to hydrocarbon trap styles. *AAPG Bulletin*, 81 (4), 533–55.
- BARREE, R.D., 1983—A Practical Numerical Simulator for Three-dimensional Fracture Propagation in Heterogeneous Media. SPE Reservoir Simulation Symposium, San Francisco, California, 15–18 November, SPE-12273-MS.
- BARREE, R.D., 2009—Mechanical properties log processing and calibration. PowerPoint slideshow. Lakewood, Colorado: Barree & Associates.
- BARREE, R.D., GILBERT, J.V. AND CONWAY, M., 2009—Stress and Rock Property Profiling for Unconventional Reservoir Stimulation. SPE Hydraulic Fracturing Technology Conference, The Woodlands, Texas, 19–21 January, SPE-118703-MS.
- BORSTMAYER, R., STEGENT, N., WAGNER, A. AND MULLEN, J., 2011—Approach optimizes completion design. *The American Oil & Gas Reporter*, August 2011, 7 pp.
- FONSECA, E.R. AND FARINAS, M.J., 2013—Hydraulic Fracturing Simulation Case Study and Post Frac Analysis in the Haynesville Shale. SPE Hydraulic Fracturing Technology Conference The Woodlands, Texas, 4–6 February, SPE-163847-MS.
- GRAVESTOCK, D.I. AND JENSEN-SCHMIDT, B., 1998—Structural setting. In: Gravestock, D.I., Hibbert, J.E. and Drexel, J.F. (eds.) *Petroleum Geology of South Australia, Volume 4: Cooper Basin*. Adelaide: Department of Primary Industries and Resources.
- HILL, A.J. AND GRAVESTOCK, D.I., 1995—Cooper Basin. In: Drexel J.F. and Preiss, W.V. (eds) *The Geology of South Australia, Volume 2, The Phanerozoic*. Bulletin 54. Adelaide: South Australian Geological Survey.
- JOHNSON JR., R.L., AW, K.P., BALL, D. AND WILLIS, M., 2002—Completion, Perforating and Hydraulic Fracturing Design Changes Yield Success in an Area of Problematic Frac Placement - the Cooper Basin, Australia. SPE Asia Pacific Oil & Gas Conference and Exhibition, Melbourne, Victoria, 8–10 October, SPE-77906-MS.
- LAWS, R.A. AND GRAVESTOCK, D.I., 1998—Introduction. In: Gravestock, D.I., Hibbert, J.E. and Drexel, J.F. (eds) *Petroleum Geology of South Australia, Volume 4: Cooper Basin*. Adelaide: Department of Primary Industries and Resources.
- MCGOWEN, J.M., GILBERT, J.V. AND SAMARI, E., 2007—Hydraulic Fracturing Down Under. Hydraulic Fracturing Technology Conference, College station, Texas, 29–31 January, SPE-106051-MS.
- MENPES, S., HILL, A. AND PEPICELLI, D., 2013—Characteristics of the Gidgealpa Group Composite Resource Play in the Cooper Basin, South Australia. Unconventional Resources Technology Conference Denver, Colorado, 12–14 August, SPE-168855-MS.
- MILLER, C.K., WATERS, G.A. AND RYLANDER, E.I., 2011—Evaluation of Production Log Data from Horizontal Wells Drilled in Organic Shales. SPE North American Unconventional Gas Conference and Exhibition The Woodlands, Texas, 14–16 June, SPE-144326-MS.
- NASLIN, L., 2013—From Petrophysics to Rock Mechanical Properties: A Support to Shale Gas Hydraulic Fracturing Program in Cooper Basin, Australia. Thirty-Seventh Indonesian Petroleum Association Annual Convention & Exhibition, Jakarta, Indonesia, 15–17 May, IPA13-G-144.
- PIRSA (PRIMARY INDUSTRIES AND RESOURCES SOUTH AUSTRALIA), 1972—PEL 5&6 Nappacoongee-Murteree Block, Cooper and Eromanga Basins, Della-4 Well Completion Report. Submitted by Delhi Petroleum Pty Ltd. Adelaide: PIRSA.
- PIRSA, 2011—PEL 218 South Australia, Cooper and Eromanga Basins. Encounter-1 Well Completion Report. Submitted by Beach Energy Limited Adelaide, July 2011. Adelaide: PIRSA.
- PITKIN, M.C., WADHAM, T.H., MCGOWEN, J.M. AND THOM, W.W., 2012—Taking the First Steps: Stimulating the Nappamerri Trough Resource Play. SPE Asia Pacific Oil and Gas Conference and Exhibition Perth, Western Australia, 22–24 October, SPE-160307-MS.
- RADKE, B., 2009—Hydrocarbon & Geothermal Prospectivity of Sedimentary Basins in Central Australia: Warburton, Cooper, Pedirka, Galilee, Simpson & Eromanga Basins. *Geoscience Australia Record 2009/25*. Canberra: Geoscience Australia.
- REYNOLDS, S.D., MILDREN, S.D., HILLIS, R.R. AND MEYER, J.J., 2006—Constraining stress magnitudes using petroleum exploration data in the Cooper-Eromanga Basins, Australia. *Tectonophysics*, 415 (1–4), 123–40.

REYNOLDS, S., MILDREN, S., HILLIS, R., MEYER, J. AND FLOTTMANN, T., 2005—Maximum horizontal stress orientations in the Cooper Basin, Australia: implications for plate-scale tectonics and local stress sources. *Geophysical Journal International*, 160 (1), 331–43.

RICKMAN, R., MULLEN, M.J., PETRE, J.E., GRIESER, W.V. AND KUNDERT, D., 2008—A Practical Use of Shale Petrophysics for Stimulation Design Optimization: All Shale Plays Are Not Clones of the Barnett Shale. *SPE Annual Technical Conference and Exhibition*, Denver, Colorado, 21–24 September, SPE-115258-MS.

SALDUNGARAY, P.M. AND PALISCH, T.T., 2012—Hydraulic Fracture Optimization in Unconventional Reservoirs. *SPE Middle East Unconventional Gas Conference and Exhibition*, Abu Dhabi, UAE, 23–25 January, SPE-151128-MS.

SCHEIN, G.W. AND MACK, D.J., 2007—Unconventional gas. In: Economides, M.J. and Martin, T. (eds) *Modern Fracturing: Enhancing Natural Gas Production*. Houston, Texas: Energy Tribune Publishing Inc.

STARKEY, A.P.J., KATELIS, Z.G. AND MCGHEE, P., 2014—The US Shale Gas “Revolution”: A Review of the Production Performance and Geology to Establish Potential Economic Benchmarks for Australia. *SPE Asia Pacific Oil & Gas Conference and Exhibition*, Adelaide, South Australia, 14–16 October, SPE-171463-MS.

TEDESCO, A., 2012—Moomba-191 Well Completion Report. Adelaide: Santos Limited.

THORNTON, R.C.N., 1979—Regional stratigraphic analysis of Gidgealpa Group, southern Cooper Basin, South Australia. *Geological Survey of South Australia Bulletin* 49. Adelaide: Department of Mines and Energy.

VEATCH JR., R.W., MOSCHOVIDLS, Z.A. AND FAST, C.R. 1989—An overview of hydraulic fracturing. In: Gidley, J.L., Holditch, S.A., Nierode, D.E. and Veatch Jr., R.W. (eds) *Recent Advances in Hydraulic Fracturing*. Houston, Texas: Society of Petroleum Engineers.

Authors' biographies next page.

THE AUTHORS



Kunakorn Pokalai is presently a PhD candidate in petroleum engineering at the University of Adelaide. He has a BEng in petrochemical engineering from Silpakorn University (Thailand), and completed a Graduate Certificate in Management and a Master's degree in petroleum engineering from the University of Adelaide.

Kunakorn's research interests are in the simulation of unconventional reservoirs and hydraulic fracturing. He mainly focuses on the issue of fracturing fluid flowback in the Cooper Basin.

Kunakorn was the recipient of the prestigious American Association of Petroleum Geologists (AAPG) Imperial Barrel Award in the Asia Pacific Region in 2014.

Member: Society of Petroleum Engineers (SPE) and AAPG.

kunakorn.pokalai@adelaide.edu.au



Yang Fei is presently undertaking a PhD in petroleum engineering at the Australian School of Petroleum (ASP). Before starting his PhD, Yang received his BEng (hons) in petroleum engineering from the University of Adelaide.

Previously, Yang has worked as a technical assistant at Santos Ltd for three years. Yang's area of expertise is in production engineering and optimisation, where he focuses on the development and maintenance of GAP/PROSPER/MBAL models of satellites from the Cooper Basin. In addition to that, he was providing support in running various scenarios to identify potential projects to fully optimise satellite performance.

Yang's PhD involves researching waterless hydraulic fracturing alternatives for Australian unconventional reservoirs.

Member: SPE, the Petroleum Exploration Society of Australia (PESA) and AAPG.

yang.fe@adelaide.edu.au



Maqsood Ahmad did his PhD in 2014 at ASP. His PhD was titled Petrophysical and mineralogical evaluation of shale gas reservoirs: a Cooper Basin case study.

After gaining a post-graduate degree in geology from The University of Punjab (Lahore, Pakistan), Maqsood was appointed as a research assistant for some projects funded by the Pakistan Science Foundation in the Institute of Geology in Lahore.

Later, Maqsood acquired his Master of Information Technology and Master of Engineering Science in Petroleum Engineering degrees from the Queensland University of Technology (Brisbane) and University of New South Wales (Sydney) in 2001 and 2010, respectively.

Maqsood's research interests include source rock evaluation for hydrocarbon generation potential and characterisation of source rocks as potential unconventional natural gas reservoirs using conventional and unconventional techniques.

After joining the ASP Maqsood has worked in fields such as the enhanced understanding in application of micro and nano CT scanning, FIB/SEM, QEMSCAN, high-pressure gravimetric analyser for sorption measurements, and application hydraulic fracturing techniques in shale gas, coal seam and tight gas reservoirs.

Member: SPE, PESA and AAPG.

maqsood.ahmad@adelaide.edu.au



Manouchehr (Manny) Haghighi is an Associate Professor of Petroleum Engineering. His research and teaching focus is on unconventional reservoirs, reservoir simulation, well testing and formation evaluation. Manouchehr has supervised more than 40 MSc and 10 PhD students.

Before joining the University of Adelaide in 2009, Manouchehr was an Associate Professor of Petroleum Engineering at the University of Tehran (Iran). During 2000–07 he was the Head of the Petroleum Engineering program at the University of Tehran.

In 2000, Manouchehr established Simtech, a consulting company for the integrated reservoir simulation in which he has been Project Director of several full field simulation projects for oil and gas reservoirs.

From 1995 to 2000 Manouchehr was working with the National Iranian Oil Company (NIOC) and was the director of a program for the training of NIOC staff at several universities in the US, UK, Canada, France, Australia and Norway. Manouchehr was a visiting professor at the University of Calgary from 2007–08.

Manouchehr has published more than 80 articles in peer-reviewed journals and presented in international conferences. He has served as a reviewer for different journals such as the Journal of Petroleum Science and Engineering.

Member: SPE.

manouchehr.haghighi@adelaide.edu.au



Mary Gonzalez is a Lecturer of Petroleum Engineering and the Engineering Honours Academic Coordinator for the ASP. Her research and teaching focus is on reservoir and production engineering, particularly for production enhancement and optimisation.

Mary joined the ASP in 2009 after several years of experience in the oil and gas industry, where she provided practical petroleum engineering consultancy services and solutions in the areas of subsurface and production engineering.

Mary is a collaborator for APPEA and has a BSc degree and a post graduate degree in petroleum engineering, and post graduate studies in higher education.

Member: SPE and PESA.

maria.gonzalezperdomo@adelaide.edu.au

THIS PAGE LEFT BLANK INTENTIONALLY.

Chapter 8 : Conclusions

In this section, from the results of different chapters in this thesis, the following conclusive remarks are presented.

- It was found that the complexity of an alternating reverse and strike-slip stress regime in the Cooper Basin is the main factor for failure of hydraulic fracturing processes.
- During the calibration of the hydraulic fracturing models, it was found that tectonic strain in the direction of the maximum horizontal stress is three times larger than in the direction of the minimum horizontal stress in the Cooper Basin.
- For optimizing hydraulic fracturing in the complex and high stress conditions of the Cooper Basin, directional drilling was proposed to intersect the maximum number of pre-existing natural fractures, which results in five times higher stimulated reservoir volume (SRV) compared to the vertical well case that natural fractures are not considered.
- A well trajectory with azimuth of 138° and inclination of 60° was found to be an optimized trajectory for intersecting higher number of fractures in the case study location while also maintaining wellbore stability.
- It was found that in our case study, high near wellbore pressure loss equal to around 600 psi significantly reduced proppant placement, which affected the pressure distribution in the fracture and reduced the effectiveness of hydrocarbon production.
- It was found that tortuosity was the main factor associated with high near wellbore pressure loss in the case study.
- Using an integrated approach, by coupling of 3D hydraulic fracturing modelling and reservoir simulation, the fracturing fluid recovery (flowback) improved hydrocarbon production.

- It was found that there is an optimized soaking time (the shut in time between hydraulic fracturing operation and the start of flowback) that was mainly controlled by the effects of gravity and capillary pressure.
- In modelling of multi-stage hydraulic fracturing in a horizontal well in a shale gas reservoir from the Cooper Basin, the relationship between different design parameters such as number of stages and the lateral length was found. Increasing the number of the fracturing stages from 5 to 20 stages and increasing lateral length from 1000 to 3000 ft, resulted in an increase of 3000 MMft³ stimulated rock volume, which increased the gas cumulative production twelve times compared to the base case.
- By using a mechanical earth model and 3D hydraulic fracturing simulation, it was found that gelled LPG fracturing fluid increases fracturing fluid recovery (flowback) up to 76% within 60 days in low permeability and high temperature reservoirs.
- It was found that the stability of foam based fracturing fluid is affected by both mechanisms of foam drainage and disproportionation.
- It was found that the stability of foam can be improved through the use of nanoparticles.

References

- Alexander, E.M., Gravestock, D.I., Cubitt, C. and Chaney, A., 1998. Lithostratigraphy and Environments of Deposition. In: D.I. Gravestock, J.E. Hibburb and J.F. Drexel (Editors), *The Petroleum Geology of South Australia*. Department of Primary Industries and Resources, South Australia.
- Anderson, E.M., 1905. The dynamics of faulting. *The Transactions of the Edinburgh Geological Society*: 387–402.
- Areias, P.M.A. and Belytschko, T., 2005. Analysis of three-dimensional crack initiation and propagation using the extended finite element method. *International Journal for Numerical Methods in Engineering*, 63(5): 760-788.
- Barree, D., Barree, L. and Craig, D., 2007. *Holistic Fracture Diagnostics*, SPE Rocky Mountain Oil & Gas Technology Symposium. Society of Petroleum Engineers, Denver, Colorado, U.S.A.
- Barree, R.D., 1983. A Practical Numerical Simulator for Three-Dimensional Fracture Propagation in Heterogeneous Media, SPE Reservoir Simulation Symposium. Society of Petroleum Engineers, San Francisco, California.
- Barree, R.D., 2015. *Stress Shadowing and Fracture Interference in GOHFER*, Barree & Associates.
- Barree, R.D., Barree, V.L. and Craig, D., 2009a. *Holistic Fracture Diagnostics: Consistent Interpretation of Prefrac Injection Tests Using Multiple Analysis Methods*. SPE Production & Operations: 396 - 406.
- Barree, R.D., Gilbert, J.V. and Conway, M., 2009b. *Stress and Rock Property Profiling for Unconventional Reservoir Stimulation*. Society of Petroleum Engineers.
- Barree, R.D., Gilbert, J.V. and Conway, M., 2009c. *Stress and Rock Property Profiling for Unconventional Reservoir Stimulation*, SPE Hydraulic Fracturing Technology Conference. Society of Petroleum Engineers, The Woodlands, Texas.
- Bellarby, J., 2009. *Well Completion Design*, 59. Elsevier, Oxford.
- Blyton, C.A.J., Gala, D.P. and Sharma, M.M., 2015. *A Comprehensive Study of Proppant Transport in a Hydraulic Fracture*, SPE Annual Technical Conference and Exhibition. Society of Petroleum Engineers, Houston, Texas, USA.
- Carter, R.D., 1957. Derivation of the general equation for estimating the extent of the fractured area. *Drilling and Production Practice*: 261-269.

- Castillo, J.L., 1987. Modified Fracture Pressure Decline Analysis Including Pressure-Dependent Leakoff, SPE Low Permeability Reservoirs Symposium. Society of Petroleum Engineers, Denver, Colorado.
- Chipperfield, S.T., Roberts, G.A., Miller, W.K., II and Vandersypen, R.S., 2000. Gel Slugs: A Near-Wellbore Pressure-Loss Remediation Technique for Propped Fracturing, the 2000 SPE/CERI Gas Technology Symposium Society of Petroleum Engineers, Calgary, Alberta Canada.
- Clark, J.B., 1949. A Hydraulic Process for Increasing the Productivity of Wells. *Journal of Petroleum Technology*, 1(1): 1-8.
- Cleary, M.P., 1980. Comprehensive Design Formulae For Hydraulic Fracturing, SPE Annual Technical Conference and Exhibition. Society of Petroleum Engineers, Dallas, Texas.
- Cotton, T.B., Scardigno, M.F. and Hibburt, J.E., 2007. Petroleum geology of South Australia. Volume 2: Eromanga Basin. , 2.
- Craig, D.P. and Brown, T.D., 1999. Estimating Pore Pressure and Permeability in Massively Stacked Lenticular Reservoirs Using Diagnostic Fracture-Injection Tests, SPE Annual Technical Conference and Exhibition. Society of Petroleum Engineers, Houston, Texas
- Dontsov, E.V. and Peirce, A.P., 2015. An enhanced pseudo-3D model for hydraulic fracturing accounting for viscous height growth, non-local elasticity, and lateral toughness. *Engineering Fracture Mechanics*, 142: 116-139.
- Economides, M.J. and Martin, T., 2007. Modern Fracturing: Enhancing Natural Gas Production. Energy Tribune Publishing.
- Fung, R.L., Vilayakumar, S. and Cormack, D.E., 1987. Calculation of Vertical Fracture Containment in Layered Formations. *SPE Formation Evaluation*, 2(04): 518 - 522.
- Gdanski, R.D. and Bryant, J.E., 2012a. Modeling Gel Filter Cake Recovery by Flow and Dilution Mechanisms, SPE Hydraulic Fracturing Technology Conference. Society of Petroleum Engineers, The Woodlands, Texas, USA.
- Gdanski, R.D. and Bryant, J.E., 2012b. Observation of Gel Filtercake Recovery by Dissolution in Flowback Fluids, SPE International Symposium and Exhibition on Formation Damage Control. Society of Petroleum Engineers, Lafayette, Louisiana, USA.
- Gdanski, R.D. and Funkhouser, G.P., 2011. Surfactant Modeling for Insight into Load-Recovery Enhancement for Fracturing Treatments, SPE International Symposium on Oilfield Chemistry. Society of Petroleum Engineers, The Woodlands, Texas, USA.

- Gdanski, R.D., Weaver, J.D., Slabaugh, B.F., Walters, H.G. and Parker, M.A., 2005. Fracture Face Damage - It Matters, SPE European Formation Damage Conference. Society of Petroleum Engineers, Sheveningen, The Netherlands.
- Geertsma, J. and De Klerk, F., 1969. A Rapid Method of Predicting Width and Extent of Hydraulically Induced Fractures. *Journal of Petroleum Technology*, 21(12): 1,571 - 1,581.
- Goldstein, B. et al., 2012. Roadmap for Unconventional Gas Projects in South Australia. In: I. Department for Manufacturing, Trade, Resources and Energy (Editor), Adelaide SA.
- Greenstreet, C., 2015. From play to production: the Cooper unconventional story—20 years in the making, 2015 APPEA Journal and Conference, Melbourne.
- Griffith, A.A., 1920. The Phenomena of Rupture and Flow in Solids. *Philosophical Transactions of the Royal Society of London A: Mathematical, Physical and Engineering Sciences*, 221(582-593): 163-198.
- Gu, H. et al., 2012. Hydraulic Fracture Crossing Natural Fracture at Nonorthogonal Angles: A Criterion and Its Validation. *SPE Journal of Petroleum Technology*, 27(01): 20 - 26.
- Hall, L.S. et al., 2016. Cooper Basin Petroleum Systems Analysis : Regional Hydrocarbon Prospectivity of the Cooper Basin, Part 3. In: G. Australia (Editor).
- Hillis, R., Morton, J., Warner, D. and Penney, R., 2001. Deep basin gas: A new exploration paradigm in the Nappamerri Trough, Cooper Basin, South Australia. *APPEA Journal*, 41: 185-200.
- Holditch, S.A., 1979. Factors Affecting Water Blocking and Gas Flow From Hydraulically Fractured Gas Wells. *Journal of Petroleum Technology*, 31(12): 1515 - 1524.
- Hubbert, M.K. and Willis, D.G., 1957. Mechanics of Hydraulic Fracturing. *Petroleum Transactions*, 210: 153-163.
- Jaeger, J., Cook, N.G.W. and Zimmerman, R.W., 2007. *Fundamentals of rock mechanics*. Malden, Mass, Oxford, Blackwell.
- Johnson, R.L., Jr., Aw, K.P., Ball, D. and Willis, M., 2002. Completion, Perforating and Hydraulic Fracturing Design Changes Yield Success in an Area of Problematic Frac Placement - the Cooper Basin, Australia, the SPE Asia Pacific Oil & Gas Conference and Exhibition. Society of Petroleum Engineers, Melbourne, Australia.
- Johnson, R.L., Jr. and Greenstreet, C.W., 2003. Managing Uncertainty Related to Hydraulic Fracturing Modeling in Complex Stress Environments with Pressure-Dependent Leakoff, The SPE Annual Technical Conference and Exhibition. Society of Petroleum Engineers, Denver, Colorado, US.

- Kapel, A.J., 1972. The geology of the Patchawarra area, Cooper Basin. *APPEA Journal*, 6: 71-75.
- Khristianovic, S.A. and Zheltov, Y.P., 1955. Formation of Vertical Fractures by Means of Highly Viscous Liquid, 4th World Petroleum Congress. World Petroleum Congress, Rome, Italy.
- Kresse, O., Weng, X., Gu, H. and Wu, R., 2013. Numerical Modeling of Hydraulic Fractures Interaction in Complex Naturally Fractured Formations. *Rock Mechanics and Rock Engineering*, 46(3): 555-568.
- Kulikowski, D. and Amrouch, K., 2017. Combining Geophysical Data and Calcite Twin Stress Inversion to Refine the Tectonic History of Subsurface and Offshore Provinces: A Case Study on the Cooper-Eromanga Basin, Australia. *Tectonics*, 36(3): 515-541.
- Lasdon, L.S., Warren, A.D., Jain, A. and Ratner, M., 1978. Design and Testing of a Generalized Reduced Gradient Code for Nonlinear. *ACM Transactions on Mathematical Software*, 4: 34-50.
- Leonov, L., 2009. Use of Pore Pressure Prediction Software in the Cowralli Field, University of Adelaide, 55 pp.
- Li, Q., Xing, H., Liu, J. and Liu, X., 2015. A review on hydraulic fracturing of unconventional reservoir. *Petroleum*, 1(1): 8-15.
- Mack, M.G. and Warpinski, N.R., 2000. Mechanics of Hydraulic Fracturing. In: M.J. Economides and K.G. Nolte (Editors), *Reservoir Stimulation*. John Wiley & Sons.
- Mahadevan, J. and Sharma, M.M., 2003. Clean-up of Water Blocks in Low Permeability Formations, SPE Annual Technical Conference and Exhibition. Society of Petroleum Engineers, Denver, Colorado.
- Mahadevan, J., Yortsos, Y.C. and Sharma, M.M., 2005. Evaporative Clean-Up of Water-Blocks in Gas Wells, SPE Production Operations Symposium. Society of Petroleum Engineers, Oklahoma City, Oklahoma.
- Mao, B., 2011. Special applications in formation stimulation and injection modeling, *Drilling and Completion in Petroleum Engineering. Multiphysics Modeling*. CRC Press, pp. 193-220.
- McGowen, J.M., Gilbert, J.V. and Samari, E., 2007. Hydraulic Fracturing Down Under, SPE Hydraulic Fracturing Technology Conference. Society of Petroleum Engineers, College Station, Texas USA.
- Mendelsohn, D.A., 1984. A Review of Hydraulic Fracture Modeling—II: 3D Modeling and Vertical Growth in Layered Rock. *Journal of Energy Resources Technology*, 106(4): 543-553.

- Menpes, S., Hill, A. and Pepicelli, D., 2013. Characteristics of the Gidgealpa Group Composite Resource Play in the Cooper Basin, South Australia, Unconventional Resources Technology Conference. Unconventional Resources Technology Conference, Denver, Colorado, USA
- Mueller, M.C., Boyd, A.J. and Esmersoy, C., 1994. Case Studies of the Dipole Shear Anisotropy Log, 1994 SEG Annual Meeting. Society of Exploration Geophysicists, Los Angeles, California.
- Nelson, E.J. et al., 2007. The relationship between closure pressures from fluid injection tests and the minimum principal stress in strong rocks. *International Journal of Rock Mechanics and Mining Sciences*, 44(5): 787-801.
- Nolte, K.G., 1986. A General Analysis of Fracturing Pressure Decline With Application to Three Models. *SPE Journal Paper*, 1(06).
- Nolte, K.G., Maniere, J.L. and Owens, K.A., 1997. After-Closure Analysis of Fracture Calibration Tests, SPE Annual Technical Conference and Exhibition. Society of Petroleum Engineers, San Antonio, Texas.
- Nolte, K.G. and Smith, M.B., 1981. Interpretation of Fracturing Pressures. *Journal of Petroleum Technology*, 33(09): 1767-1775.
- Nordgren, R.P., 1972. Propagation of a Vertical Hydraulic Fracture. *Society of Petroleum Engineers Journal*, 12(04): 306-314.
- Parekh, B. and Sharma, M.M., 2004. Cleanup of Water Blocks in Depleted Low-Permeability Reservoirs, SPE Annual Technical Conference and Exhibition. Society of Petroleum Engineers, Houston, Texas.
- Perkins, T.K. and Kern, L.R., 1961. Widths of Hydraulic Fractures. *Journal of Petroleum Technology*, 13(09): 937-949.
- Pitkin, M.C., Wadham, T.H., McGowen, J.M. and Thom, W.W., 2012. Taking the First Steps: Stimulating the Nappamerri Trough Resource Play, SPE Asia Pacific Oil and Gas Conference and Exhibition. Society of Petroleum Engineers, Perth, Australia.
- Pokalai, K., Haghghi, M., Sarkar, S., Tyiasning, S. and Cooke, D., 2015. Investigation of the Effects of Near-Wellbore Pressure Loss and Pressure-Dependent Leakoff on Flowback during Hydraulic Fracturing With Pre-Existing Natural Fractures, The SPE/IATMI Asia Pacific Oil & Gas Conference and Exhibition Nusa Dua, Bali, Indonesia.
- Prats, M., 1981. Effect of Burial History on the Subsurface Horizontal Stresses of Formations Having Different Material Properties. *Society of Petroleum Engineers Journal*, 21(06): 658-662.

- Reynolds, S.D., Mildren, S.D., Hillis, R.R. and Meyer, J.J., 2006. Constraining stress magnitudes using petroleum exploration data in the Cooper–Eromanga Basins, Australia. *Tectonophysics*, 415(1–4): 123-140.
- Roberts, G.A., Chipperfield, S.T. and Miller, W.K., 2000. The Evolution of a High Near-Wellbore Pressure Loss Treatment Strategy for the Australian Cooper Basin, The 2000 SPE Annual Technical Conference and Exhibition. Society of Petroleum Engineers, Dallas, Texas.
- Robinson, B.M., Holditch, S.A. and Whitehead, W.S., 1988. Minimizing Damage to a Propped Fracture by Controlled Flowback Procedures. *Journal of Petroleum Technology*, 40(6): 753-759.
- Sack, R.A., 1946. Extension of Griffith's theory of rupture to three dimensions. *Proceedings of The Physical Society*, 58(6): 729-736.
- Santos, 2015. South Australian Cooper Basin: Environmental Impact Report: Drilling, Completions and Well Operations, Adelaide, SA.
- Sharma, M.M., 2005. Advance Fracturing Technology for Tight Gas: An East Texas Field Demonstration, The University of Texas at Austin, Austin, Texas.
- Simonson, E.R., Abou-Sayed, A.S. and Clifton, R.J., 1978. Containment of Massive Hydraulic Fractures. *Society of Petroleum Engineers Journal*, 18(01): 27 - 32.
- Smith, M.B. and Montgomery, C.T., 2015. Frac Pressure Analysis, Hydraulic Fracturing. *Hydraulic Fracturing: Emerging Trends & Technologies in Petroleum Engineering*. CRC Press, Boca Raton, FL, pp. 221-334.
- Sneddon, I.N., 1946. The Distribution of Stress in the Neighbourhood of a Crack in an Elastic Solid. *Proceedings of the Royal Society of London A: Mathematical, Physical and Engineering Sciences*, 187(1009): 229-260.
- Sneddon, I.N., 1973. Integral transform methods. In: G. Sih (Editor), *Methods of analysis and solutions of crack problems*. Mechanics of fracture. Springer Netherlands, pp. 315-367.
- Sneddon, I.N. and Elliott, H.A., 1946. The Opening of A Griffith Crack Under Internal Pressure. *Quarterly of Applied Mathematics*, 4(3): 262-267.
- Tannich, J.D., 1975. Liquid Removal From Hydraulically Fractured Gas Wells. *Journal of Petroleum Technology*, 27(11): 1309-1317.
- Tiab, D. and Donaldson, E.C., 2011. *Petrophysics : theory and practice of measuring reservoir rock and fluid transport properties*. Gulf Professional, Oxford.
- Timoshenko, S. and Goodie, J.N., 1951. *Theory of elasticity*. McGraw-Hill.

- van Dam, D.B. and de Pater, C.J., 2001. Roughness of Hydraulic Fractures: Importance of In-Situ Stress and Tip Processes. *SPE Journal of Petroleum Technology*, 6(01): 4-13.
- Wang, J.Y., Holditch, S.A. and McVay, D., 2009. Modeling Fracture Fluid Cleanup in Tight Gas Wells, *SPE Hydraulic Fracturing Technology Conference*. Society of Petroleum Engineers, The Woodlands, Texas.
- Warpinski, N.R., Moschovidis, Z.A., Parker, C.D. and Abou-Sayed, I.S., 1994. Comparison Study of Hydraulic Fracturing Models—Test Case: GRI Staged Field Experiment No. 3. *SPE Production & Facilities*, 9(01): 7-16.
- Warpinski, N.R. and Smith, M.B., 1989. Rock Mechanics and Fracture Geometry. In: J.L. Gidley, S.A. Holditch, D.E. Nierode and R.W. Veatch Jr. (Editors), *Recent Advances in Hydraulic Fracturing SPE*, Richardson, TX U.S.A.
- Weng, X., 2015. Modeling of complex hydraulic fractures in naturally fractured formation. *Journal of Unconventional Oil and Gas Resources*, 9: 114-135.
- Whitehead, W.S., Hunt, E.R. and Holditch, S.A., 1987. The Effects of Lithology and Reservoir Pressure on the In-Situ Stresses in the Waskom (Travis Peak) Field, Low Permeability Reservoirs Symposium. Society of Petroleum Engineers, Denver, Colorado.
- Wills, H.A., Miskimins, J.L. and Kazem, H., 2009. Coupled 3D Numerical Investigation of Hydraulic Fracture Cleanup for Both Slickwater and Gelled Fluids, *SPE Annual Technical Conference and Exhibition*. Society of Petroleum Engineers, New Orleans, Louisiana.
- Yamamoto, K., Shimamoto, T. and Maezumi, S., 1999. Development of a True 3D Hydraulic Fracturing Simulator, *SPE Asia Pacific Oil and Gas Conference and Exhibition*. Society of Petroleum Engineers, Jakarta, Indonesia.
- Zhang, X., Jeffrey, R.G. and Thiercelin, M., 2009. Mechanics of fluid-driven fracture growth in naturally fractured reservoirs with simple network geometries. *Journal of Geophysical Research: Solid Earth*, 114(B12).
- Zhang, Z. and Li, X., 2016. The shear mechanisms of natural fractures during the hydraulic stimulation of shale gas reservoirs. *Materials*, 9(9).
- Zoback, M.D., 2007. *Reservoir Geomechanics*. Cambridge University Press, UK, 449 pp.

Appendix A: Petrophysics Properties

Cowralli 6 Stage1

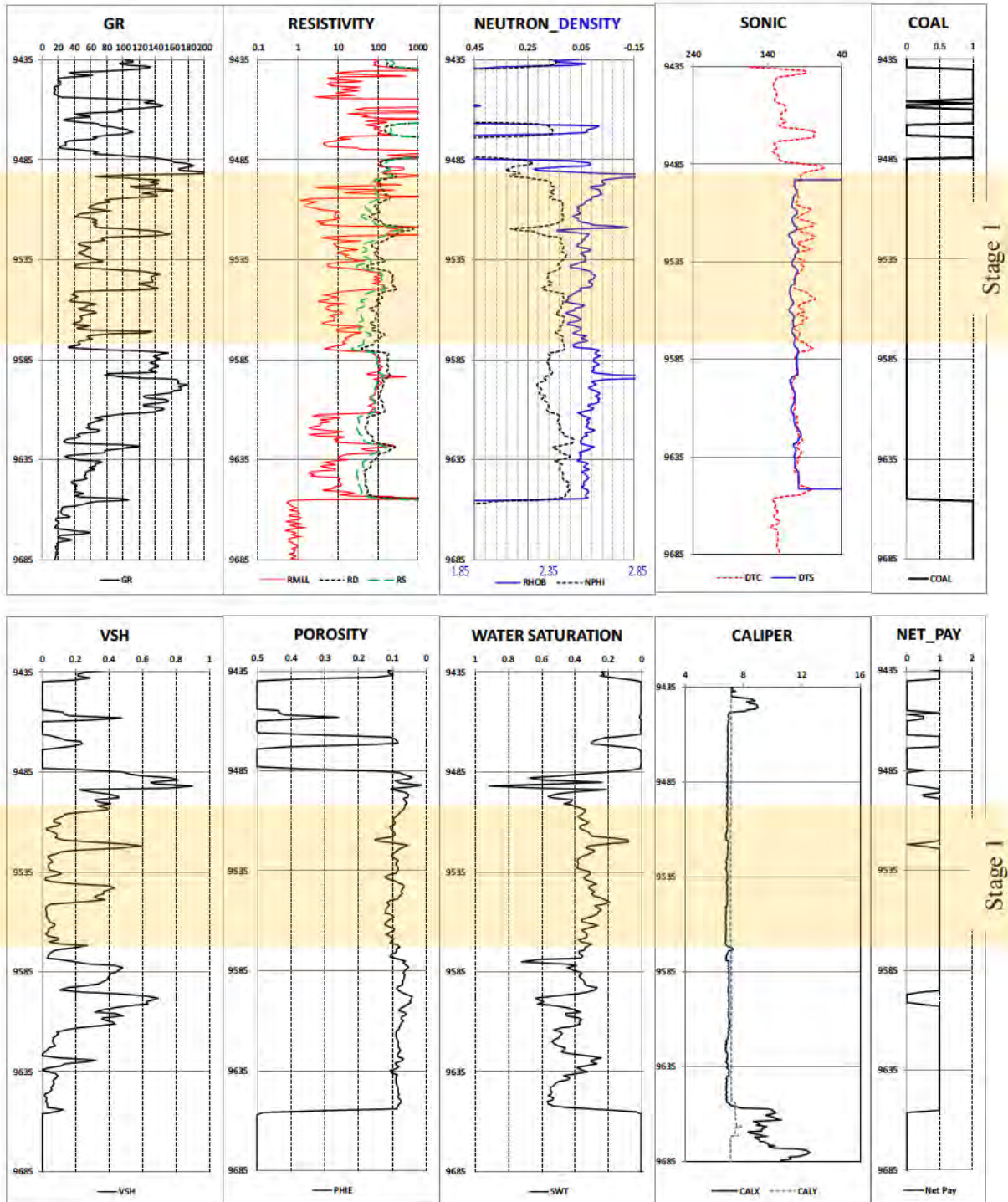


Figure A- 1 : Petrophysics Summary of Cowralli 6 Stage1

Cowralli 6 Stage 2

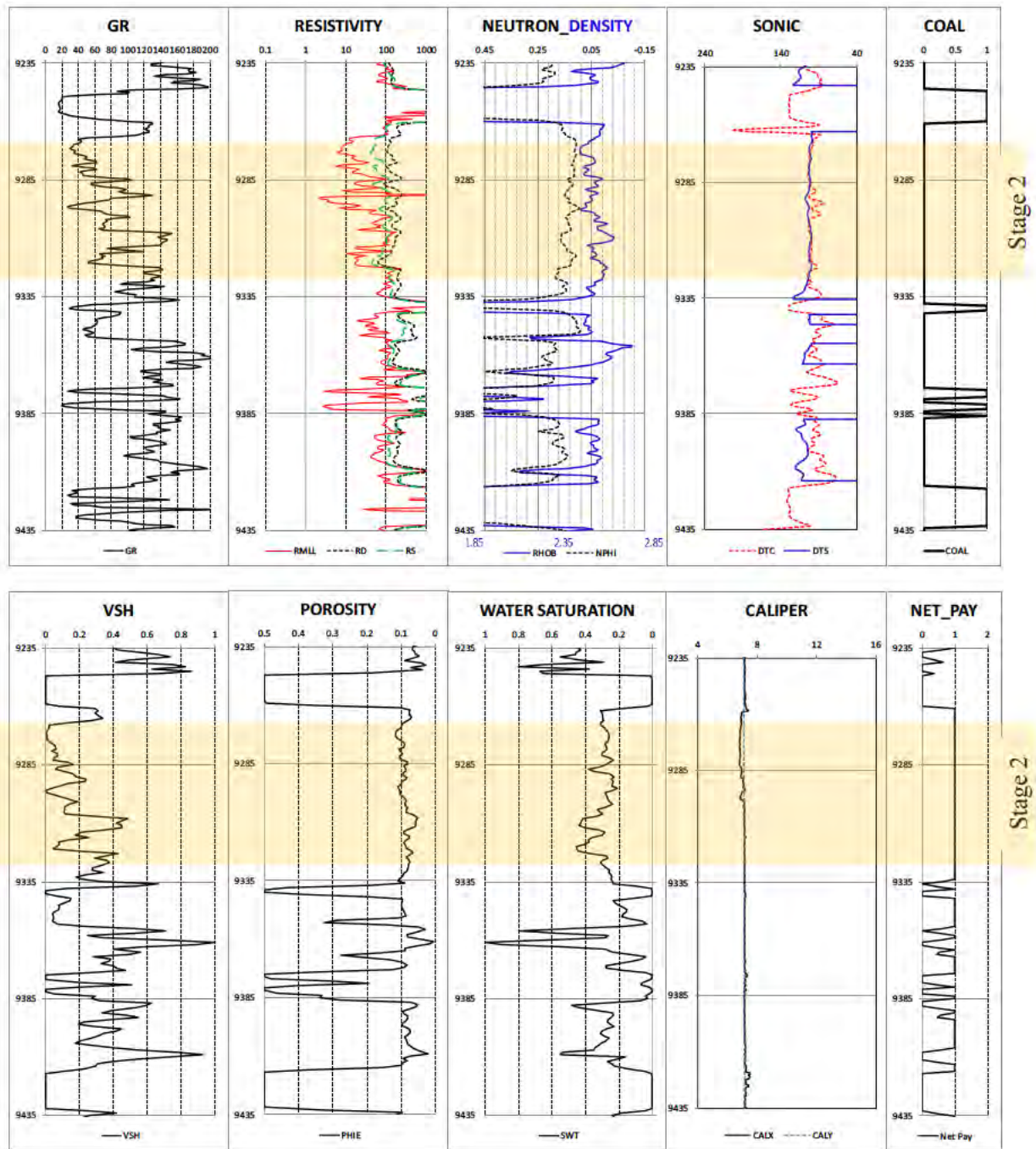


Figure A- 2 : Petrophysics Summary of Cowralli 6 Stage2

Cowralli 7 Stage 1

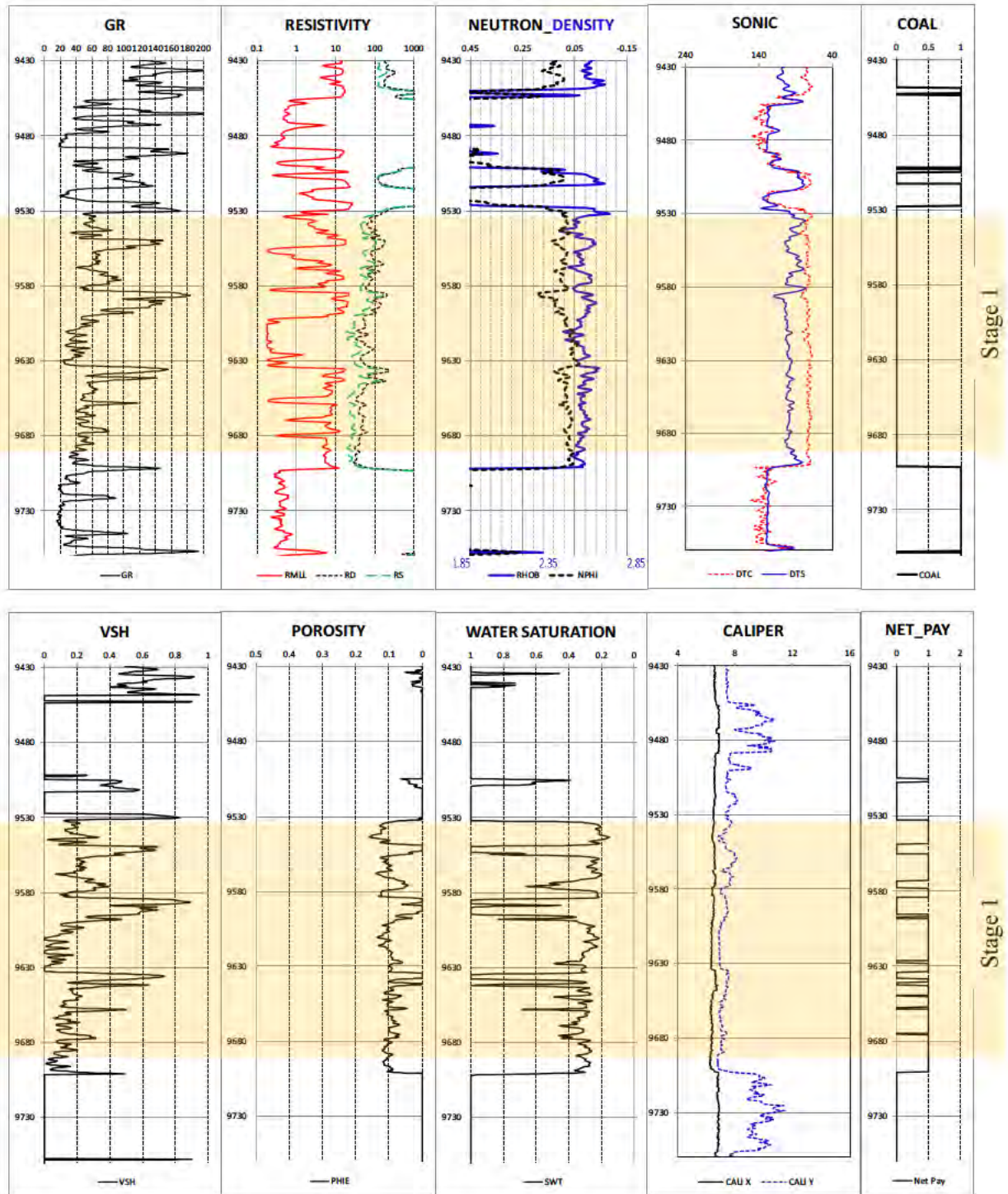


Figure A- 3 : Petrophysics Summary of Cowralli 7 Stage1

Cowralli 7 Stage 2

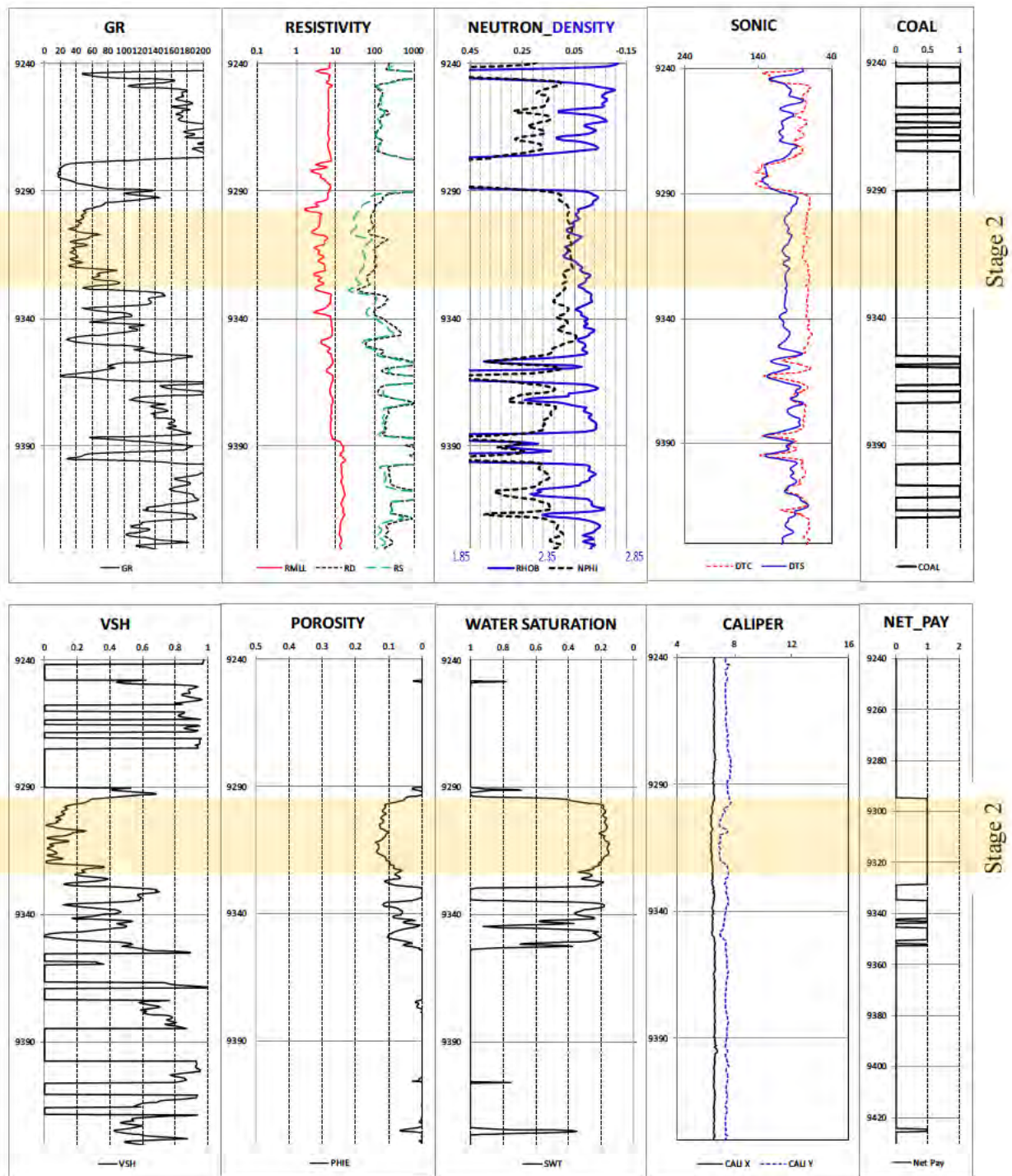


Figure A- 4 : Petrophysics Summary of Cowralli 7 Stage2

Cowralli 8 Stage 1

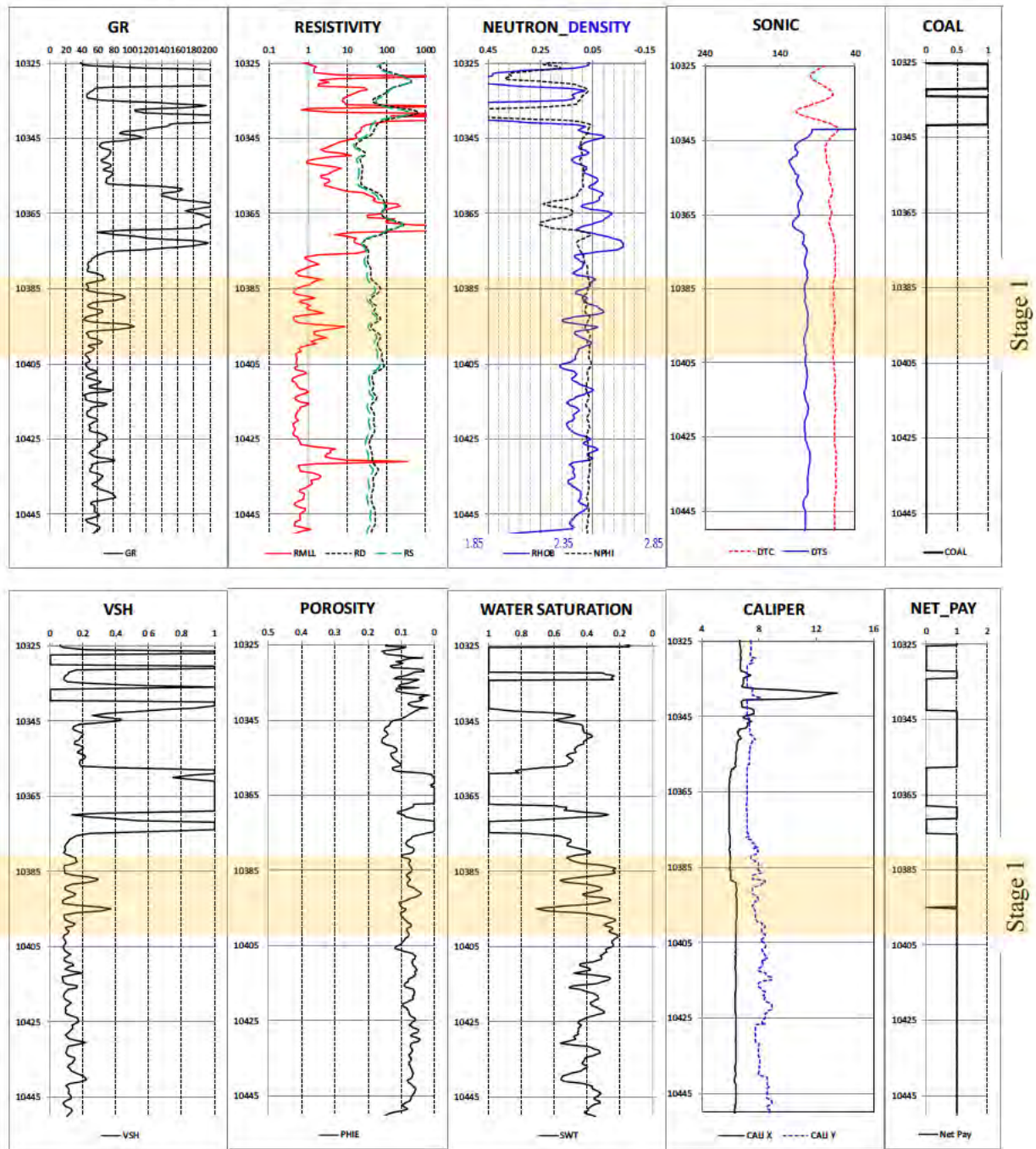


Figure A- 5 : Petrophysics Summary of Cowralli 8 Stage1

Cowralli 8 Stage 2

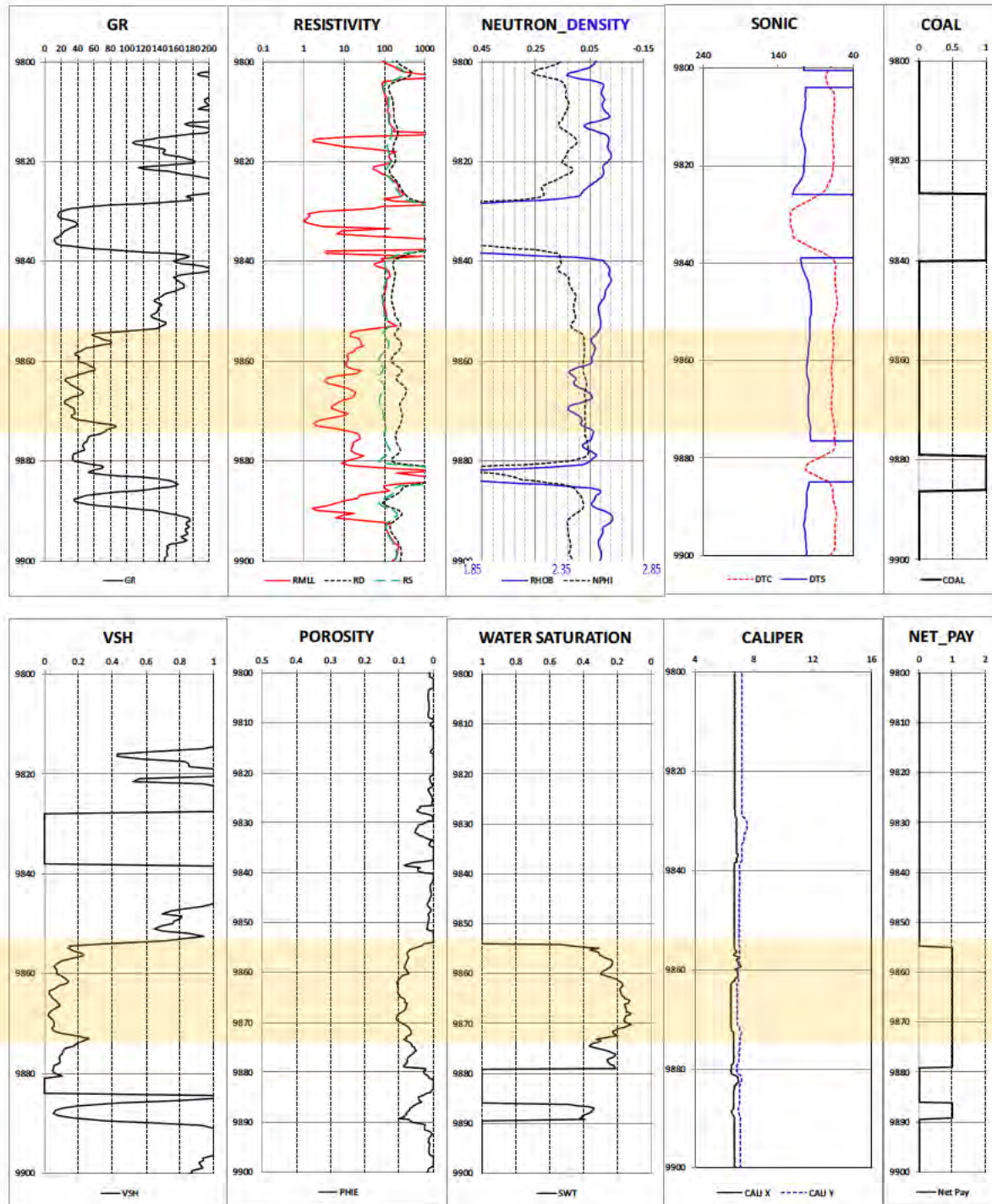


Figure A- 6 : Petrophysics Summary of Cowralli 8 Stage 2

Cowralli 8 Stage 3 and Stage 4

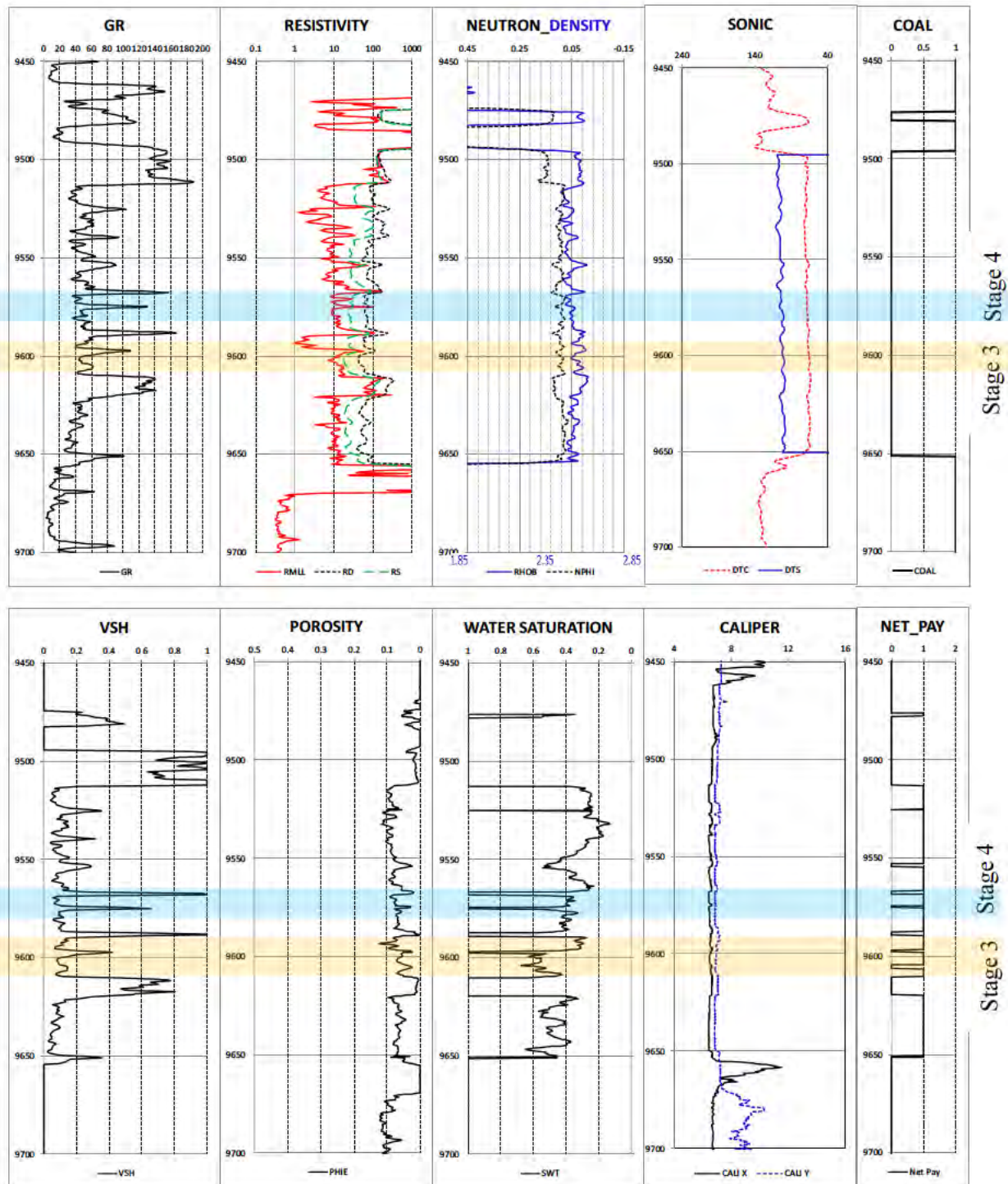


Figure A-7 : Petrophysics Summary of Cowralli 8 Stage 3 and Stage 4

Cowralli 8 Stage 5, 6 and 7

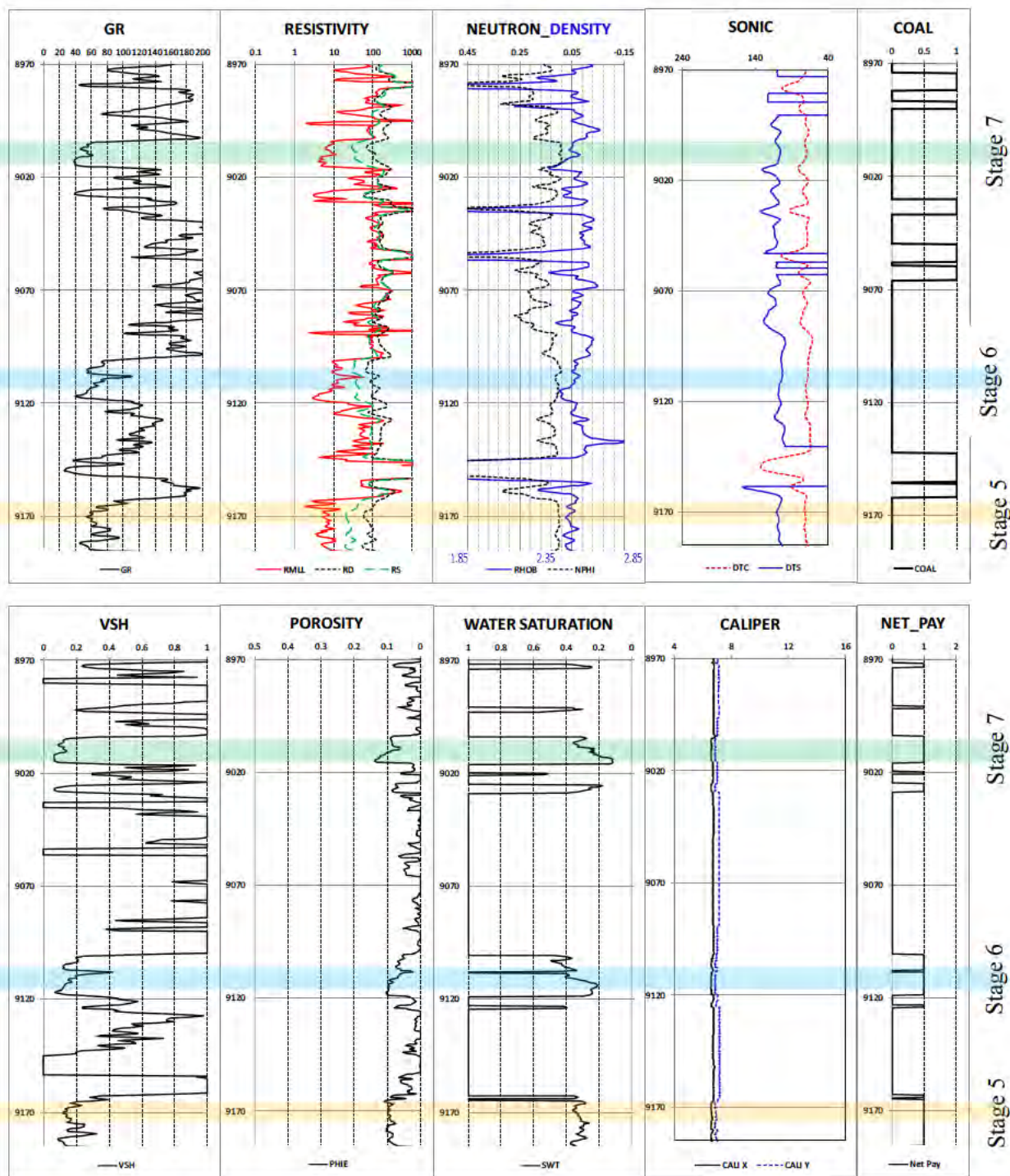


Figure A- 8 : Petrophysics Summary of Cowralli 8 Stage 5, 6 and Stage 7

Appendix B: Geomechanics Properties

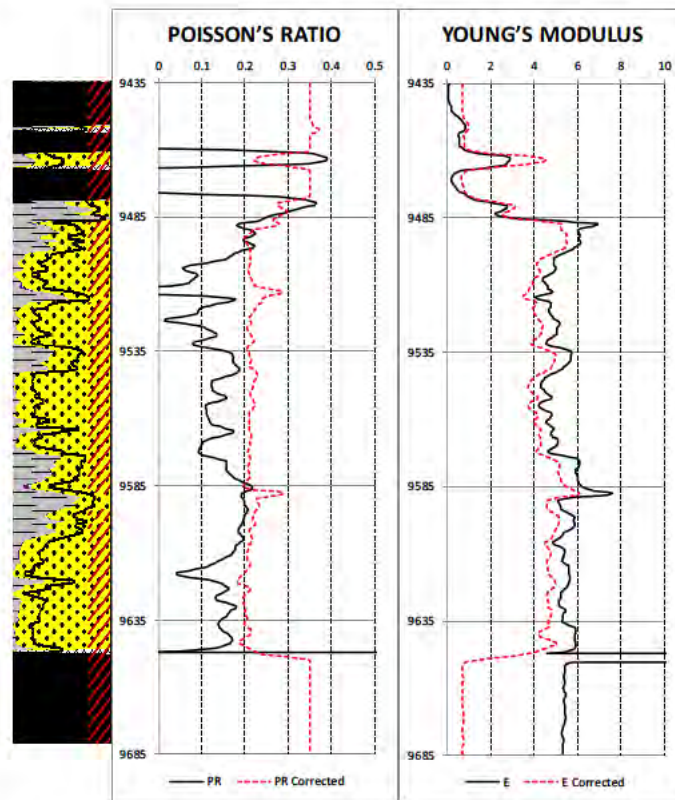


Figure B- 1 : Geomechanics Properties of Cowralli 6 Stage 1

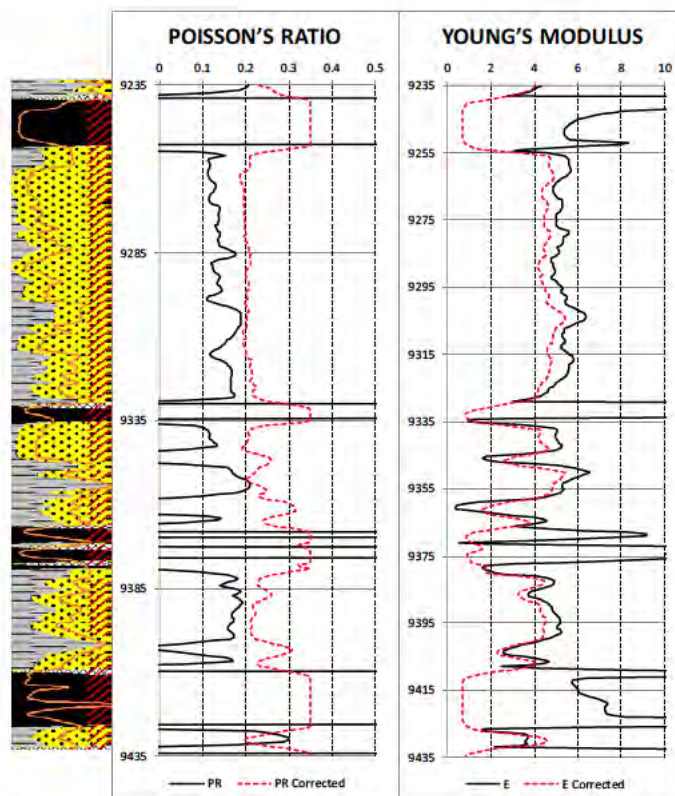


Figure B- 2 : Geomechanics Properties of Cowralli 6 Stage 2

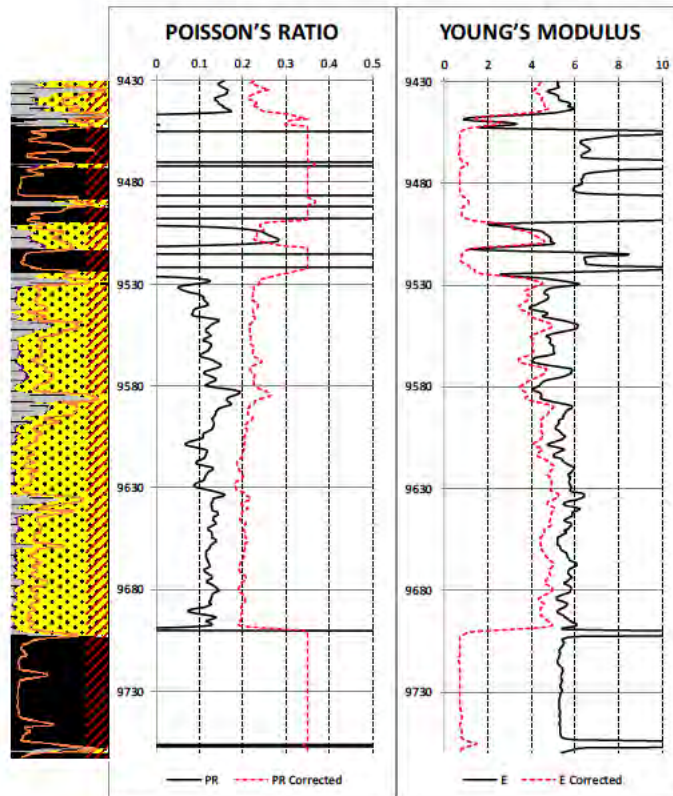


Figure B- 3 : Geomechanics Properties of Cowralli 7 Stage 1

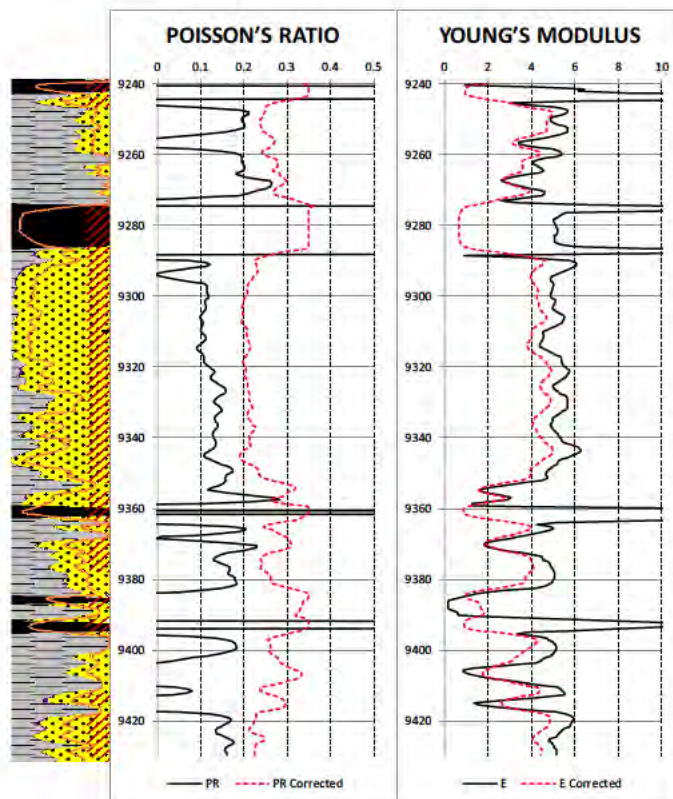


Figure B- 4 : Geomechanics Properties of Cowralli 7 Stage 2

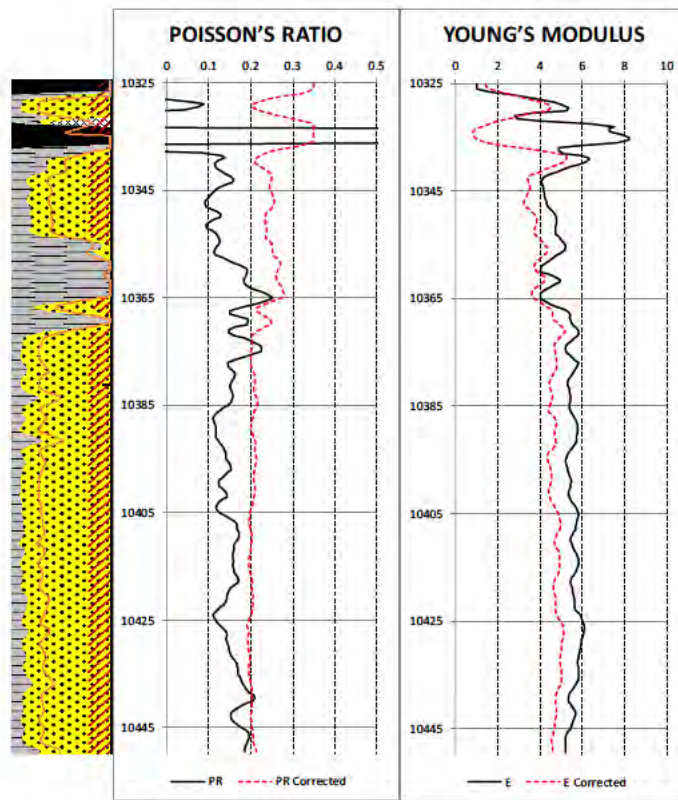


Figure B- 5 : Geomechanics Properties of Cowralli 8 Stage 1

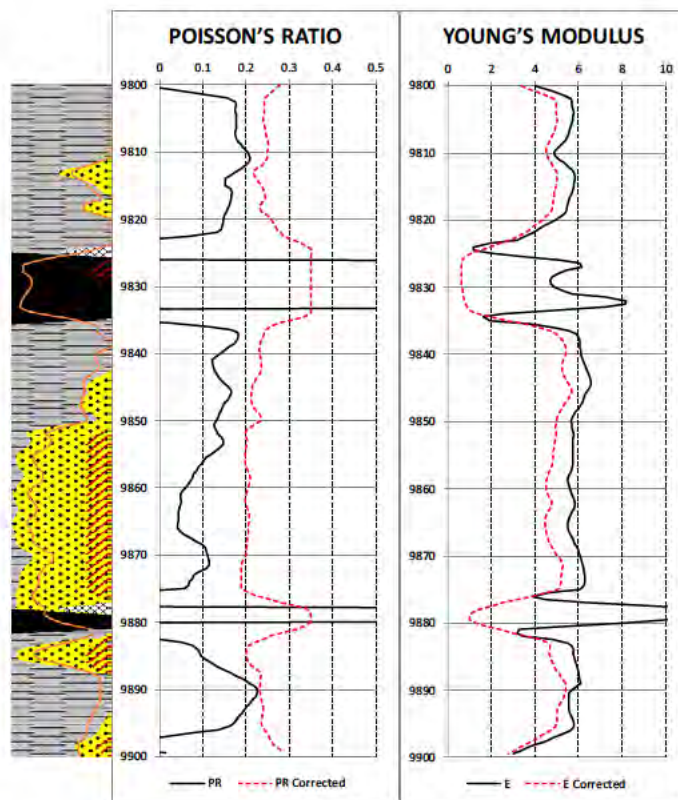


Figure B- 6 : Geomechanics Properties of Cowralli 8 Stage 2

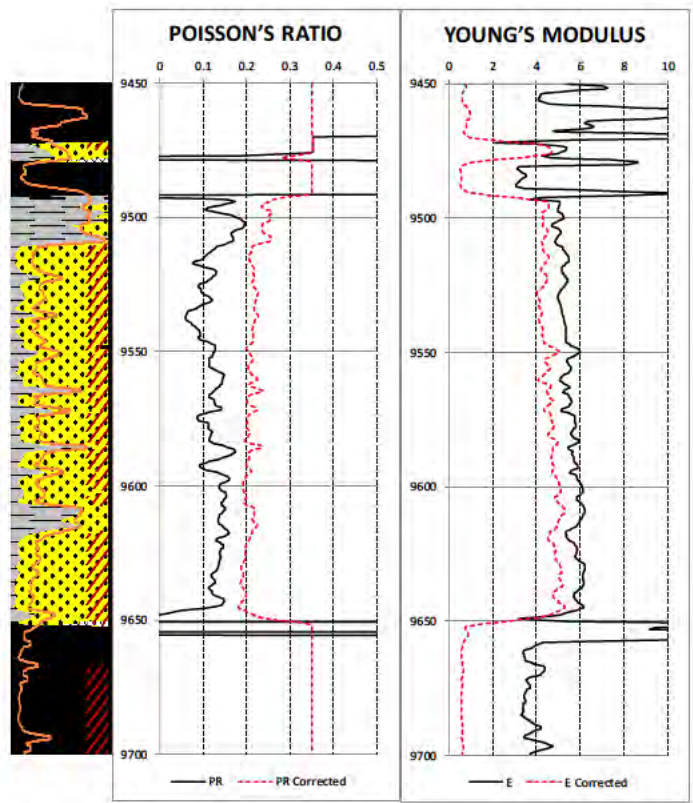


Figure B- 7 : Geomechanics Properties of Cowralli 8 Stage 3 and Stage 4

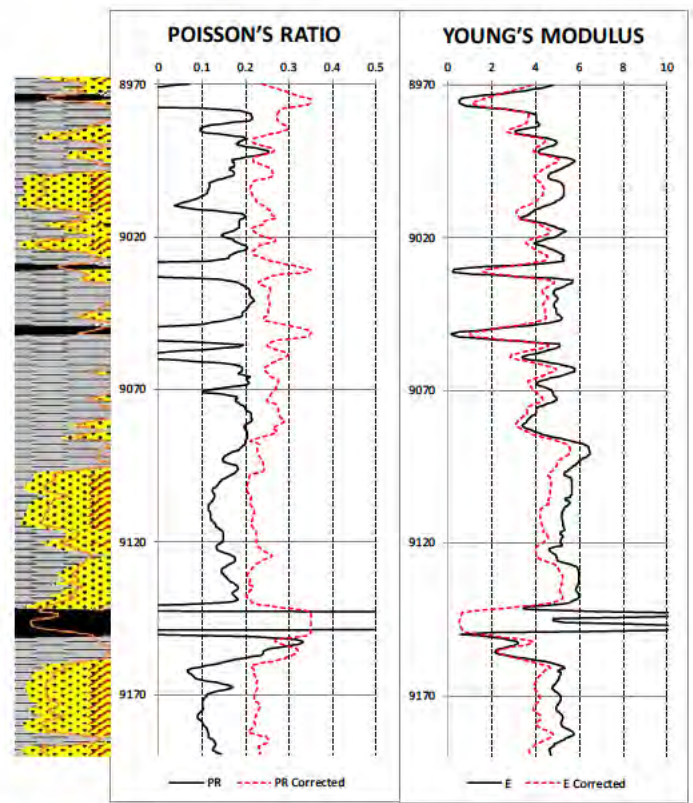


Figure B- 8 : Geomechanics Properties of Cowralli 8 Stage 5 Stage 6 and Stage 7

Appendix C: Diagnostics Fracture Injection Test Plots

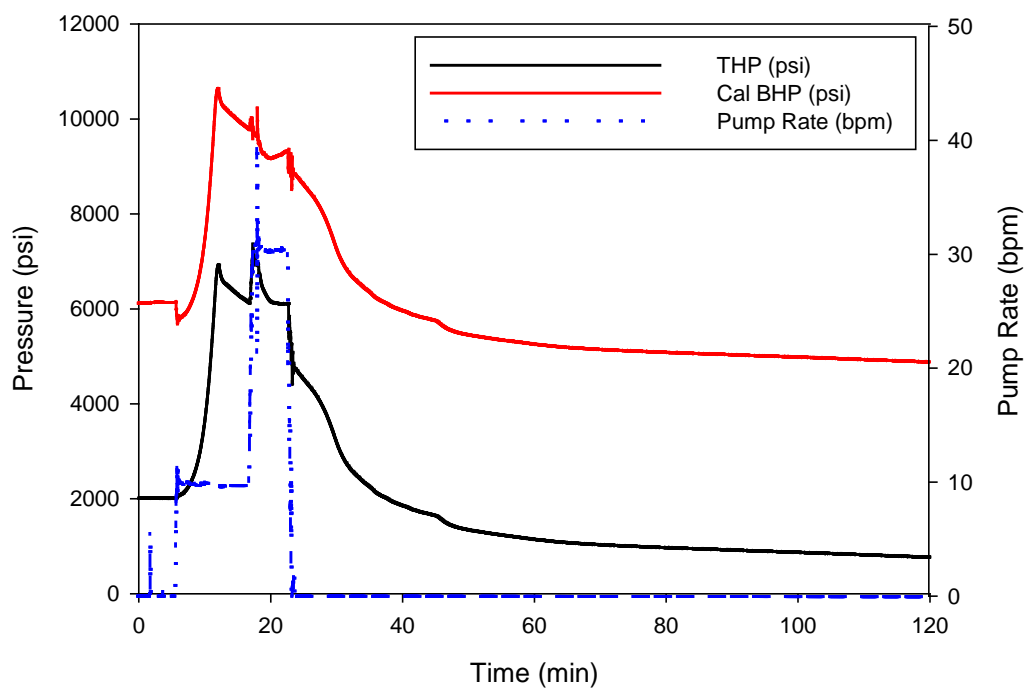


Figure C- 1 : Diagnostic fracture injection test plots in well Cowralli 6 Stage 1

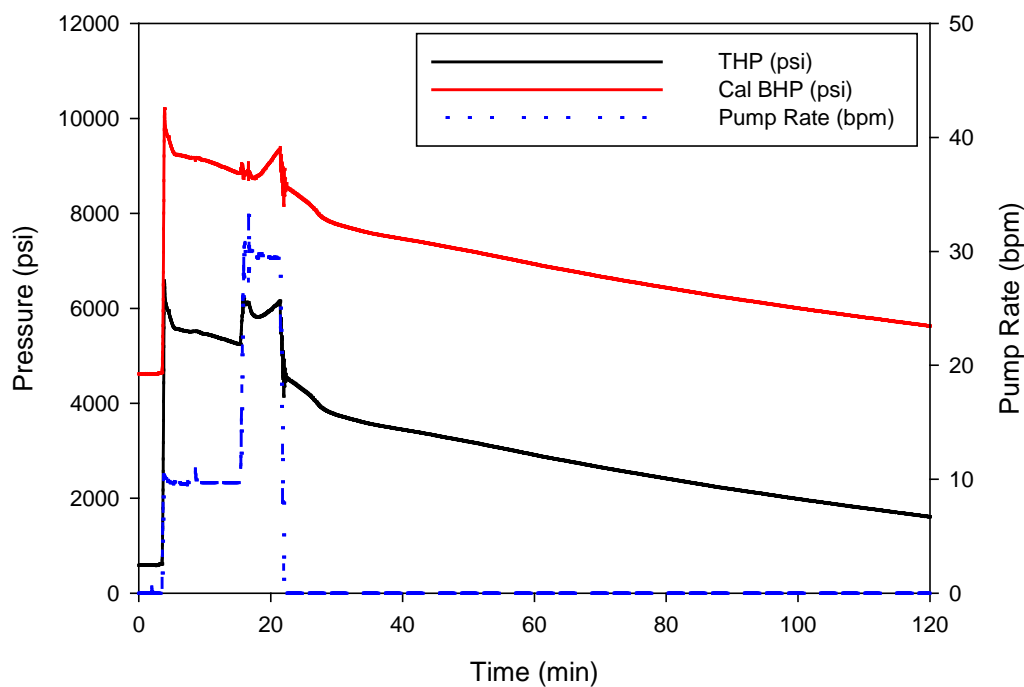


Figure C- 2 : Diagnostic fracture injection test plots in well Cowralli 6 Stage 2

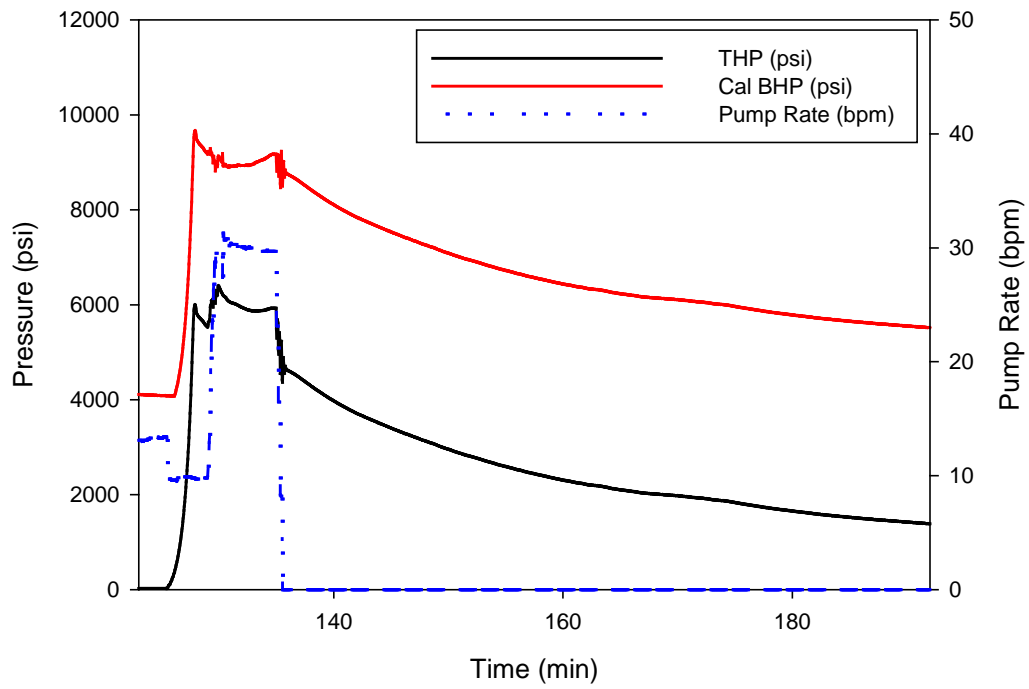


Figure C- 3 : Diagnostic fracture injection test plots in well Cowralli 7 Stage 1

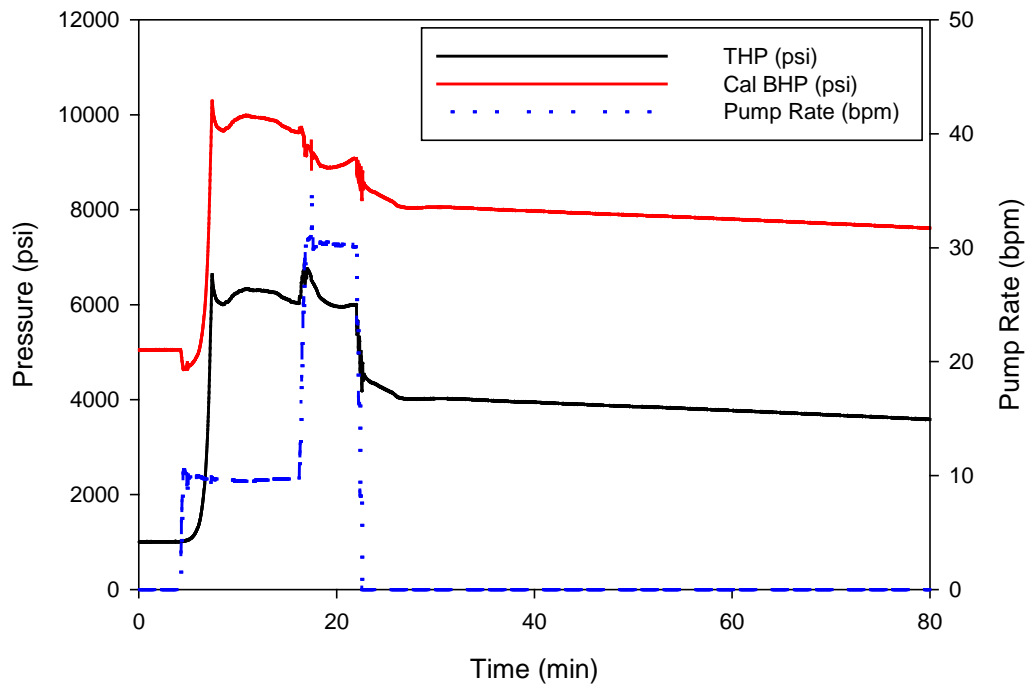


Figure C- 4 : Diagnostic fracture injection test plots in well Cowralli 7 Stage 2

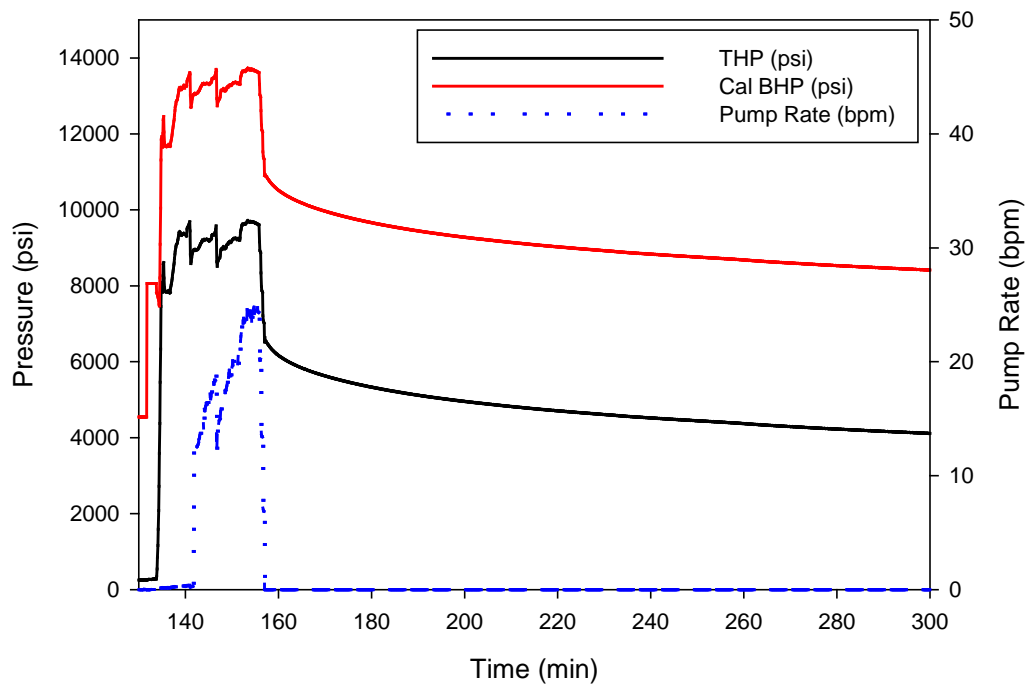


Figure C- 5 : Diagnostic fracture injection test plots in well Cowralli 8 Stage 1

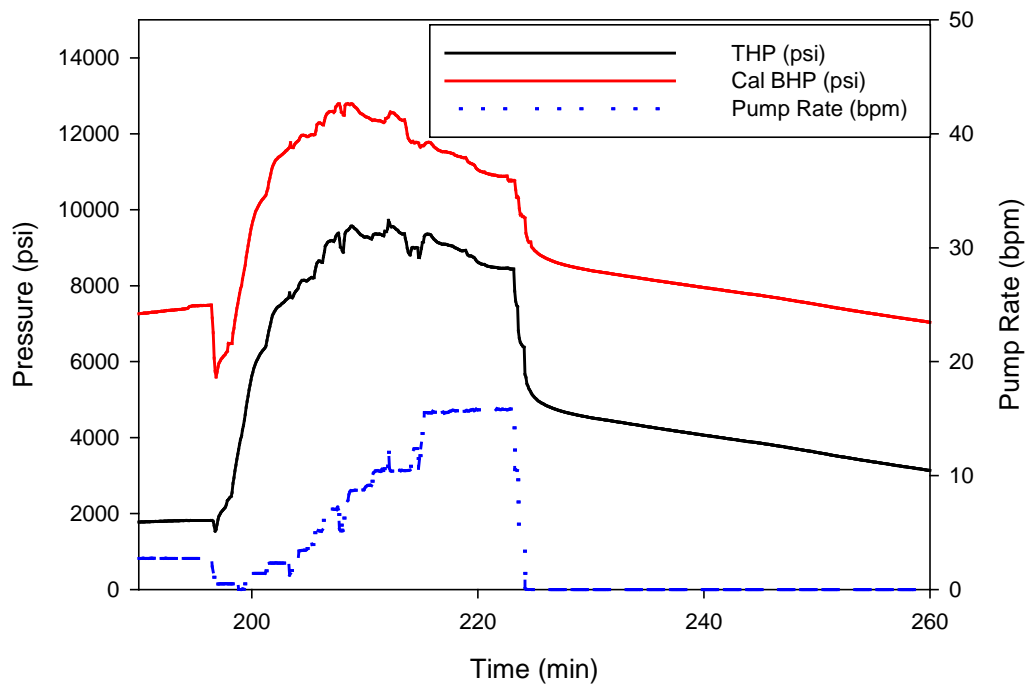


Figure C- 6 : Diagnostic fracture injection test plots in well Cowralli 8 Stage 2

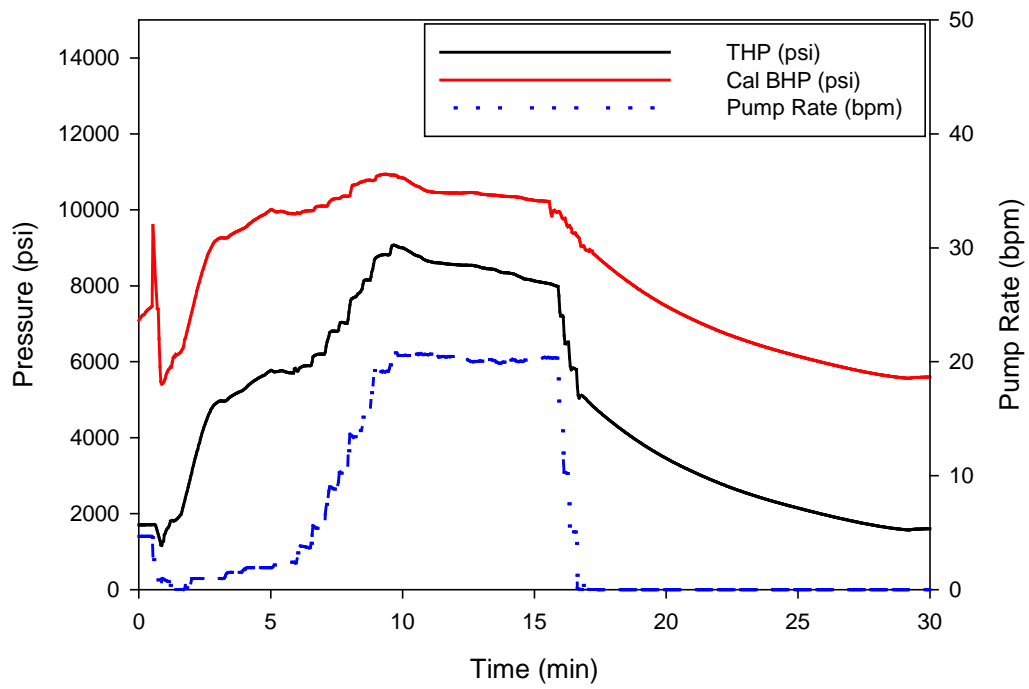


Figure C- 7 : Diagnostic fracture injection test plots in well Cowralli 8 Stage 3

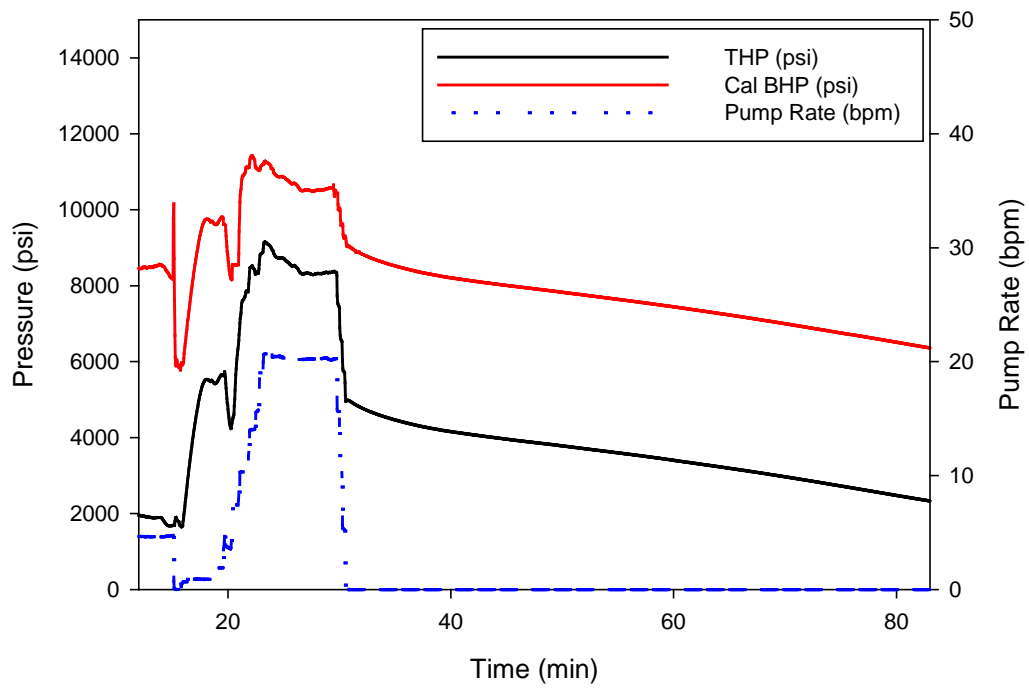


Figure C- 8 : Diagnostic fracture injection test plots in well Cowralli 8 Stage 4

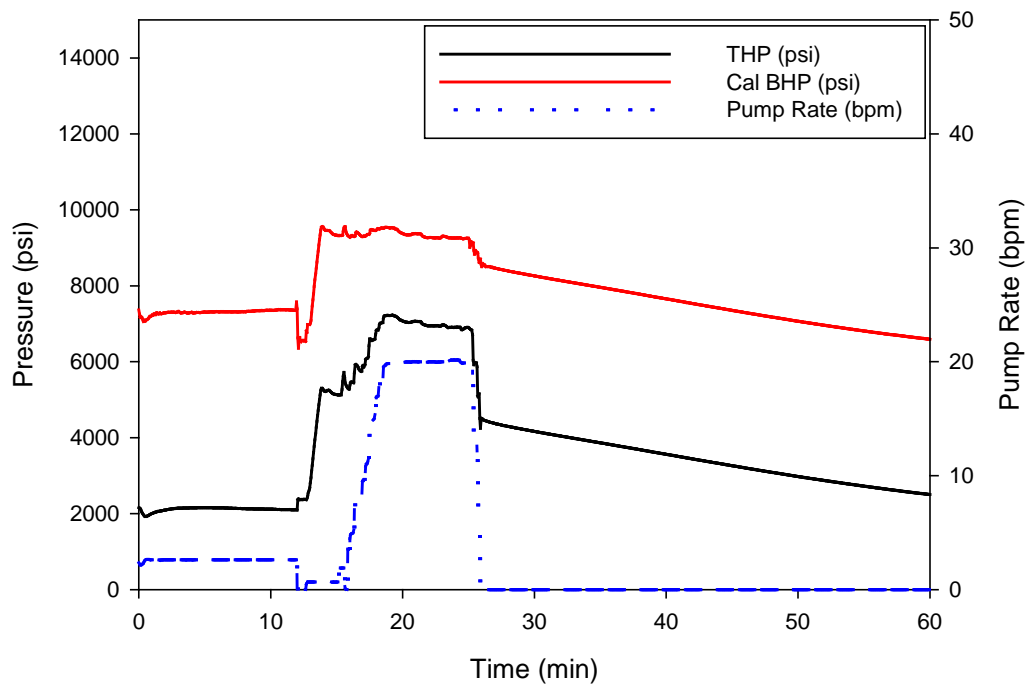


Figure C- 9 : Diagnostic fracture injection test plots in well Cowralli 8 Stage 5

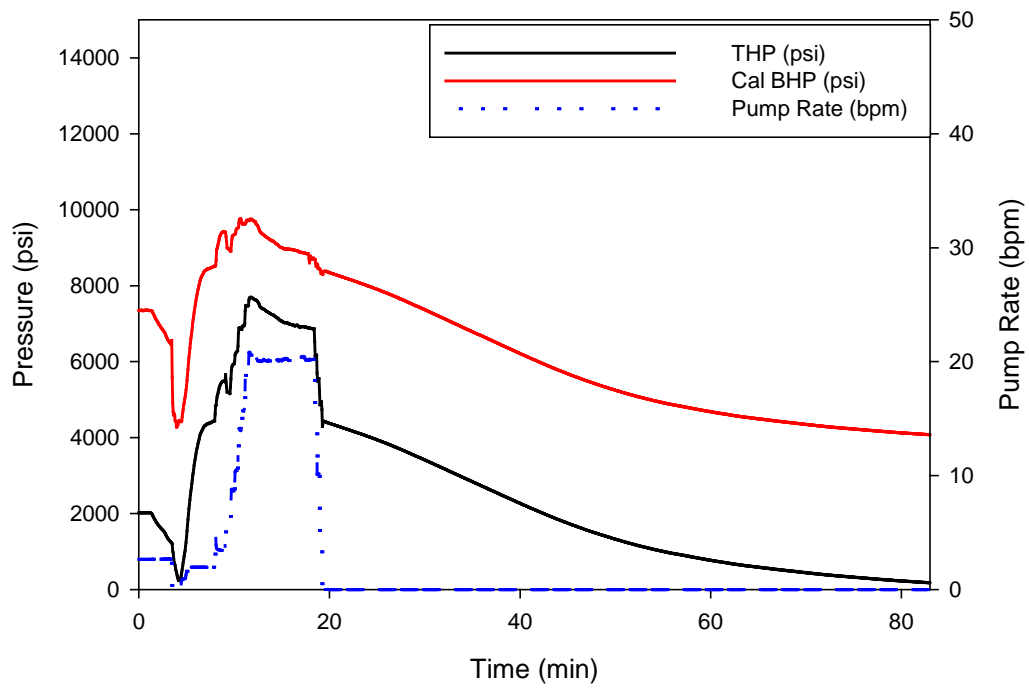


Figure C- 10 : Diagnostic fracture injection test plots in well Cowralli 8 Stage 6

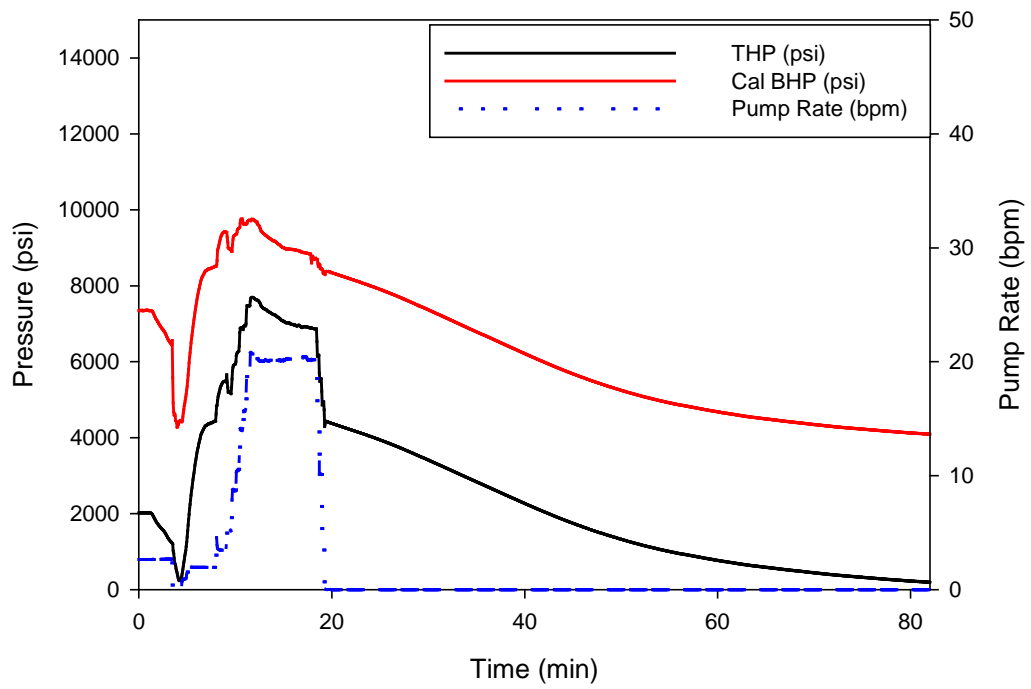


Figure C- 11 : Diagnostic fracture injection test plots in well Cowralli 8 Stage 7

Appendix D: Step Down Test Plots

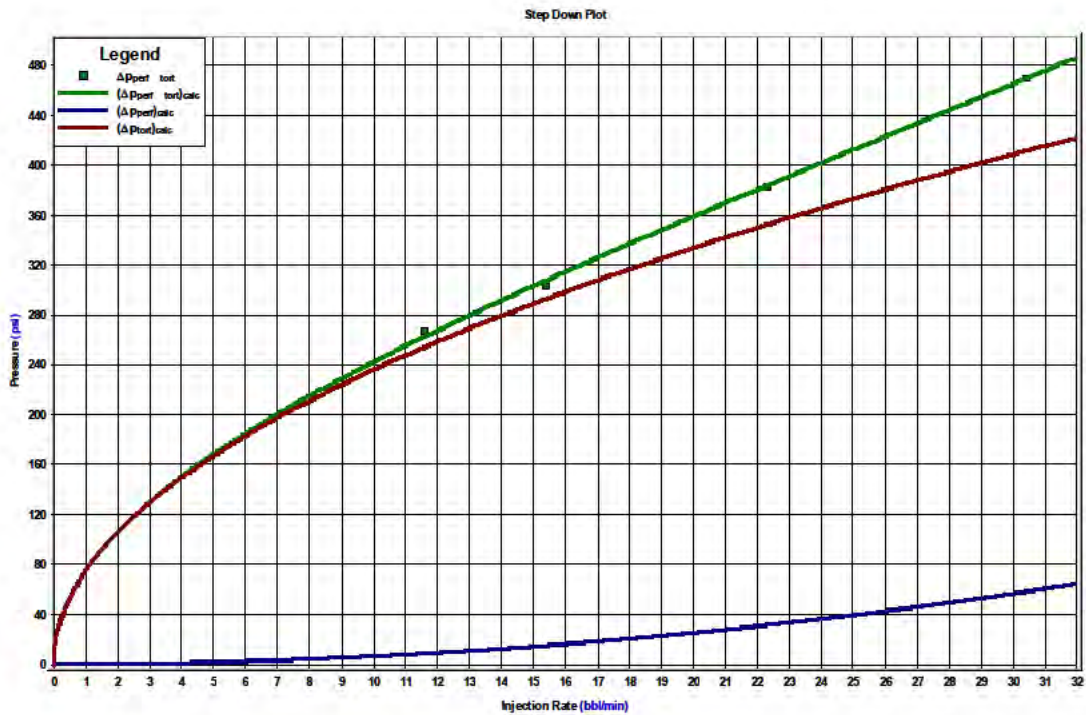
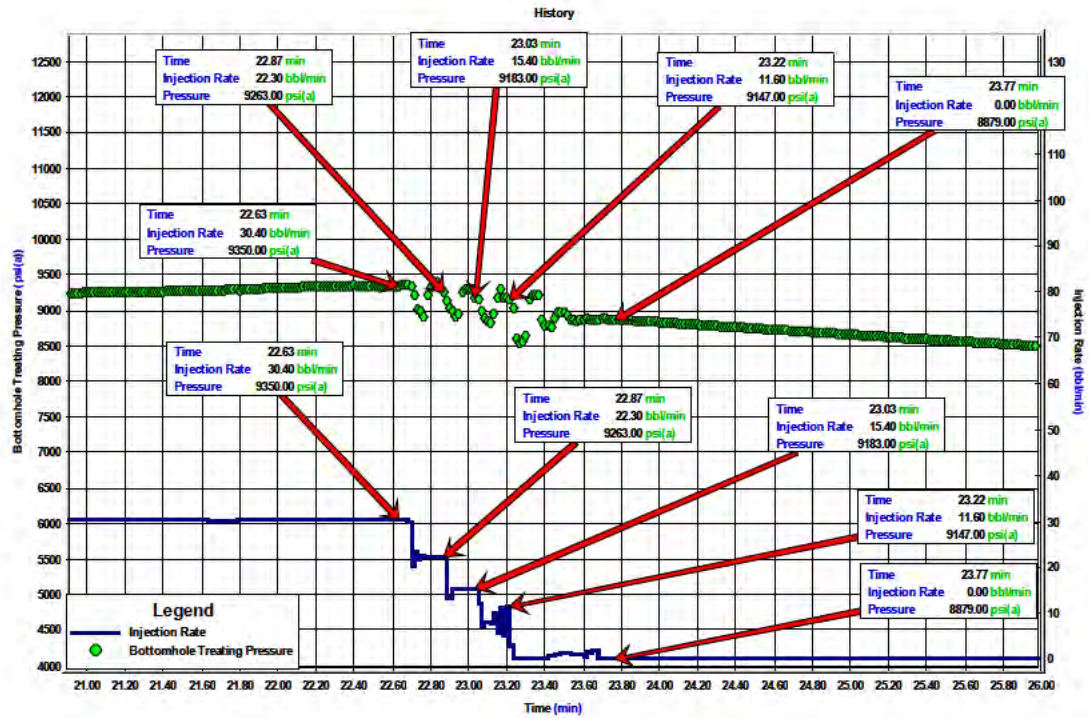


Figure D- 1 : Step Down Test Plot in well Cowralli 6 Stage 1

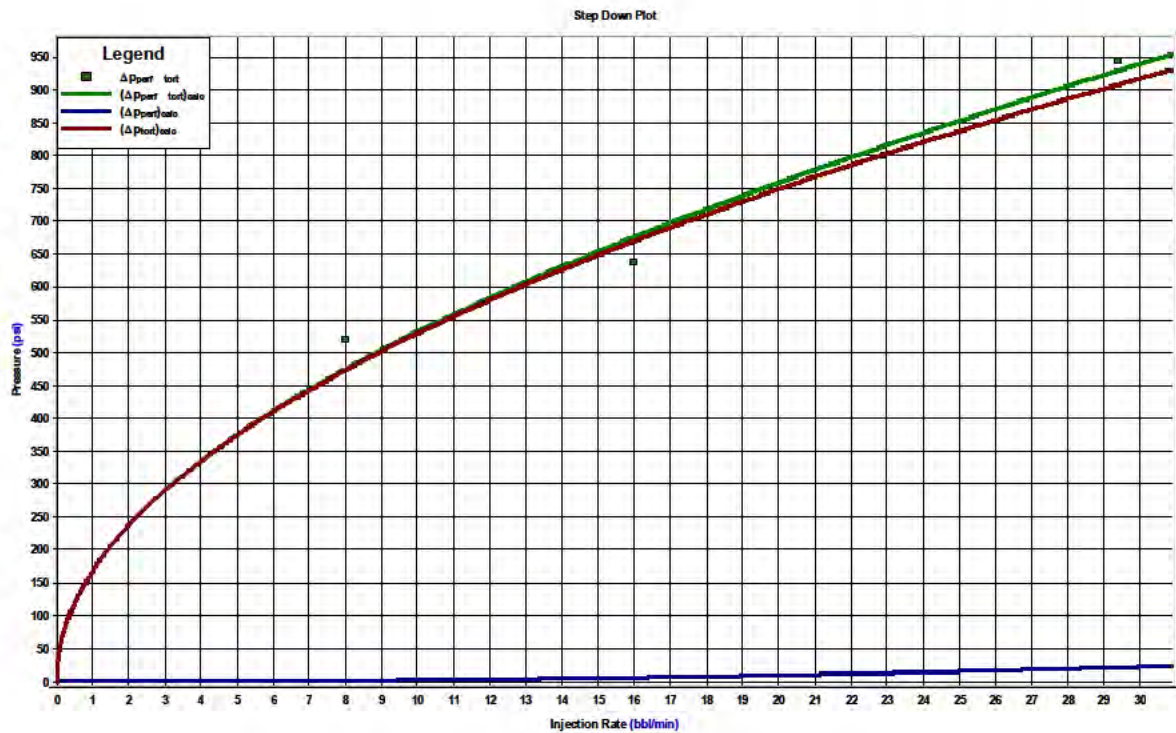
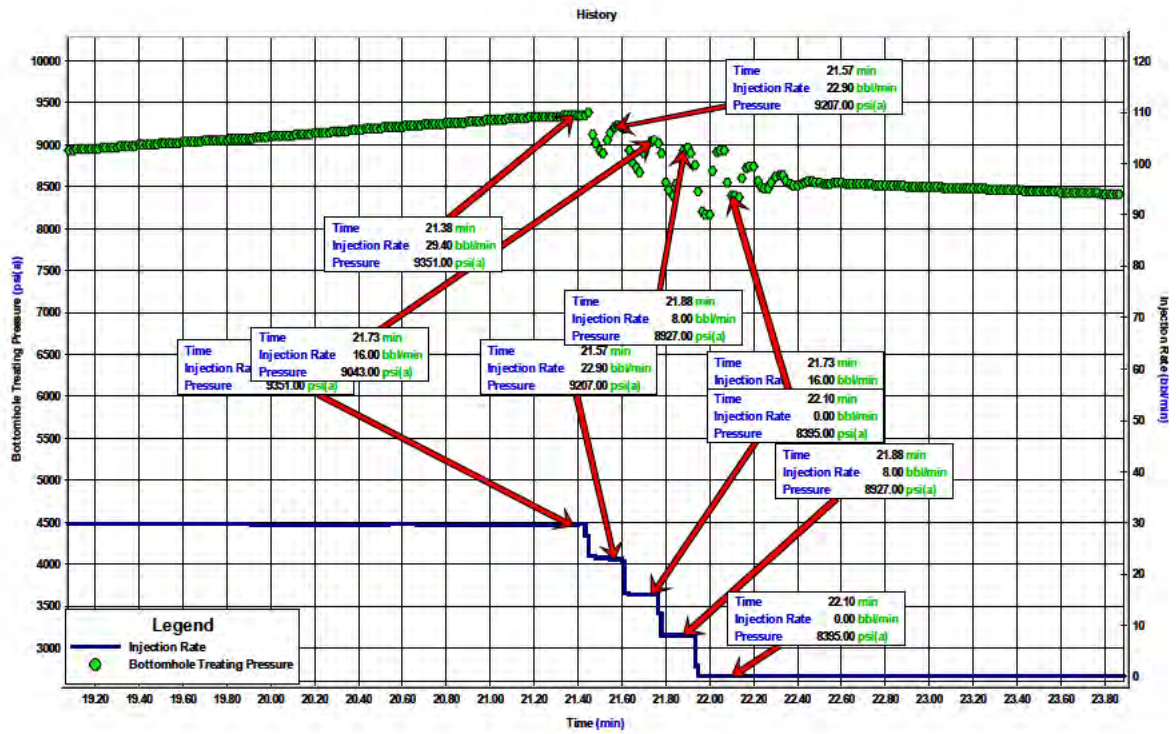


Figure D- 2: Step Down Test Plot in well Cowralli 6 Stage 2

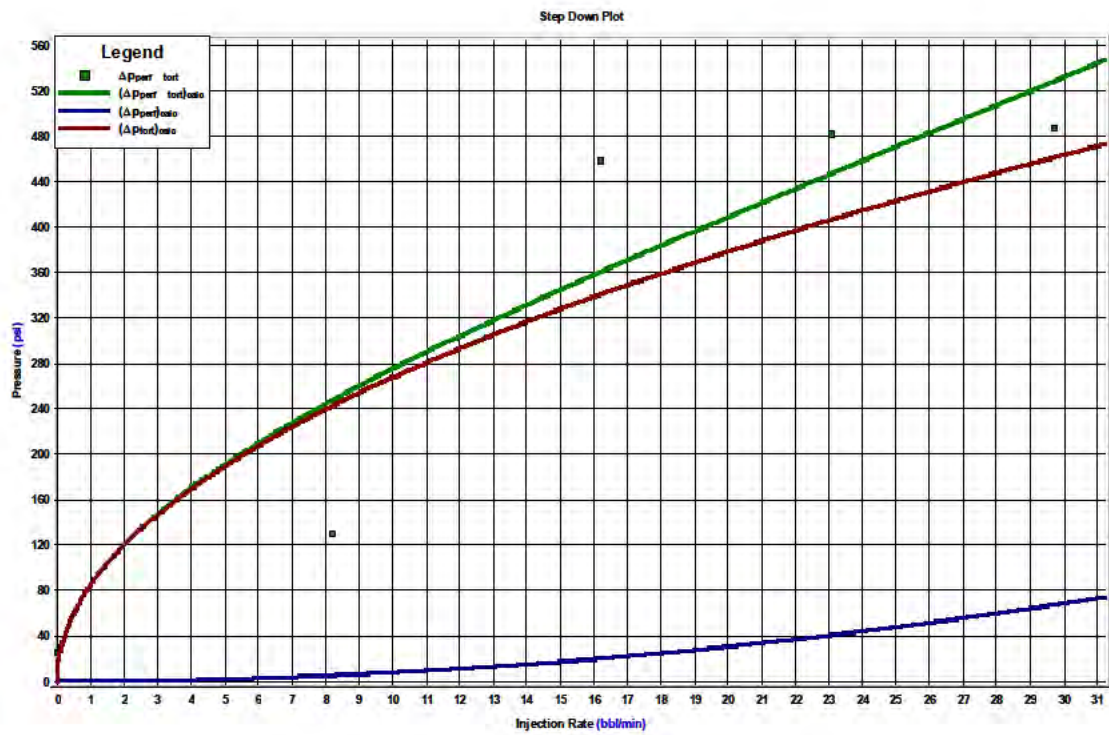
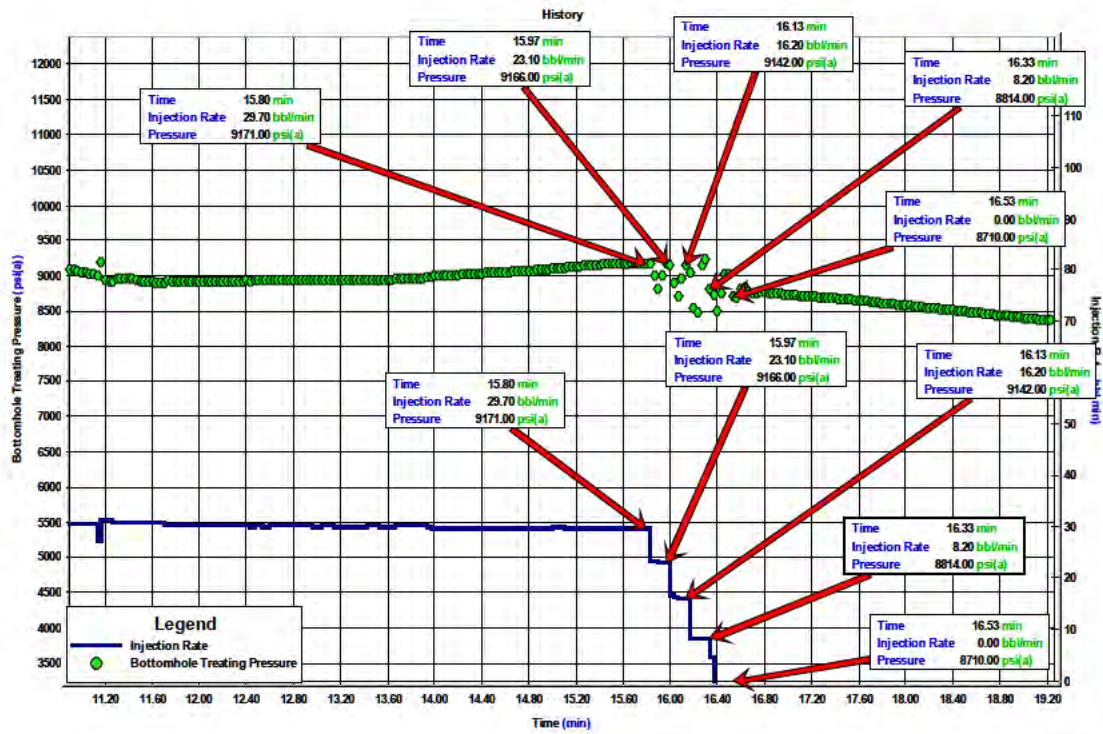


Figure D- 3 : Step Down Test Plot in well Cowralli 7 Stage 1

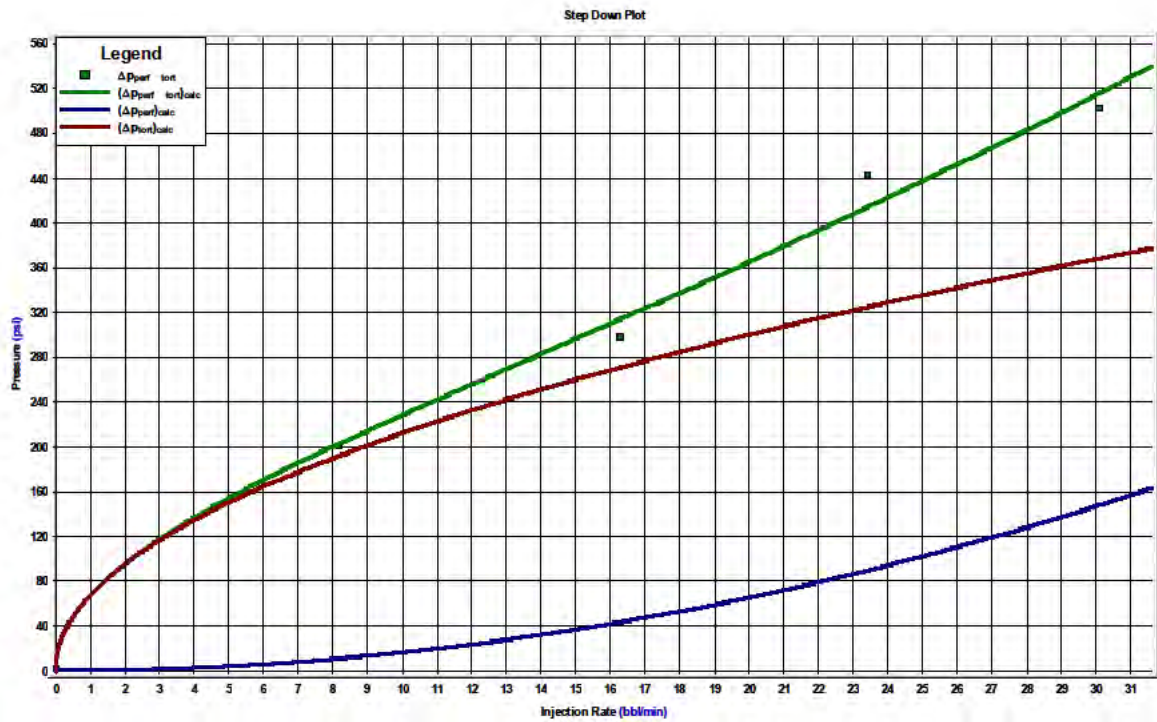
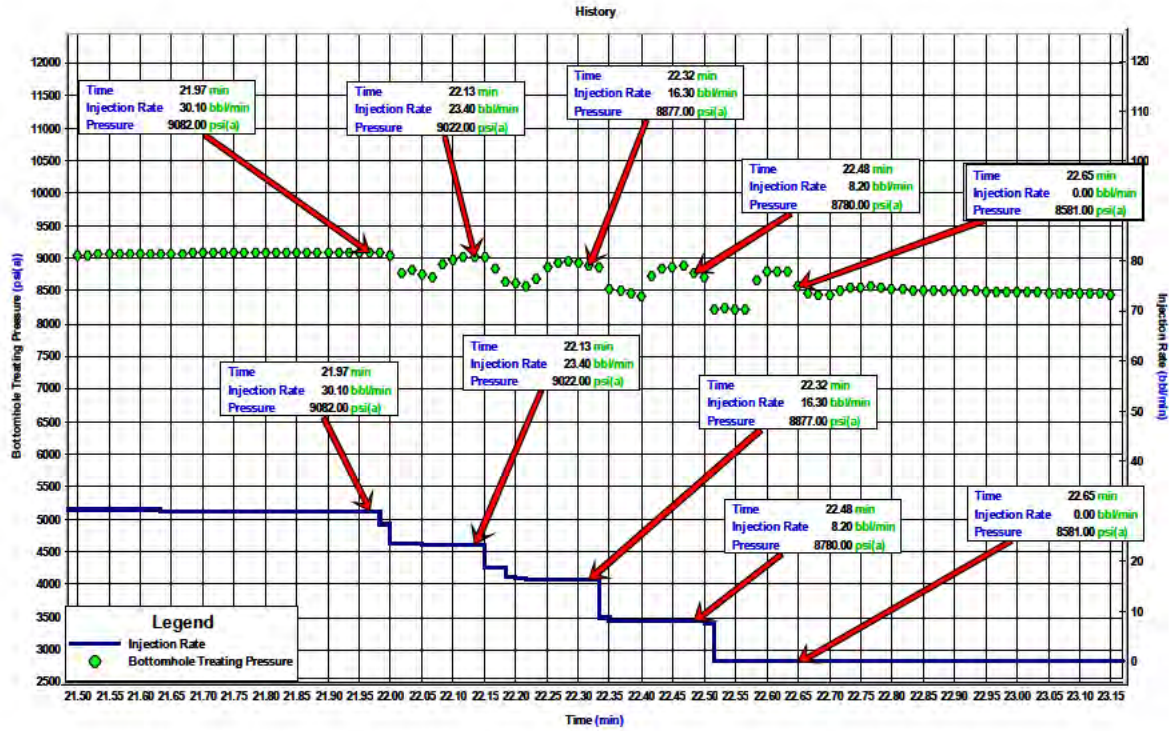


Figure D- 4 : Step Down Test Plot in well Cowralli 7 Stage 2

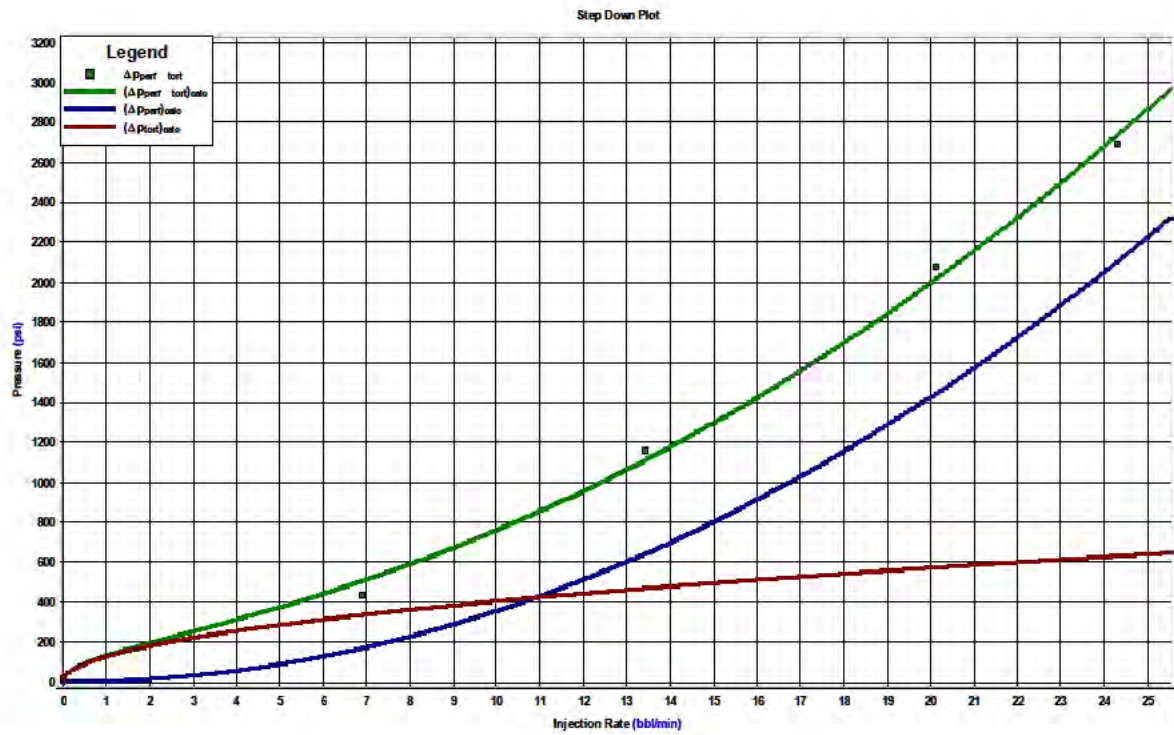
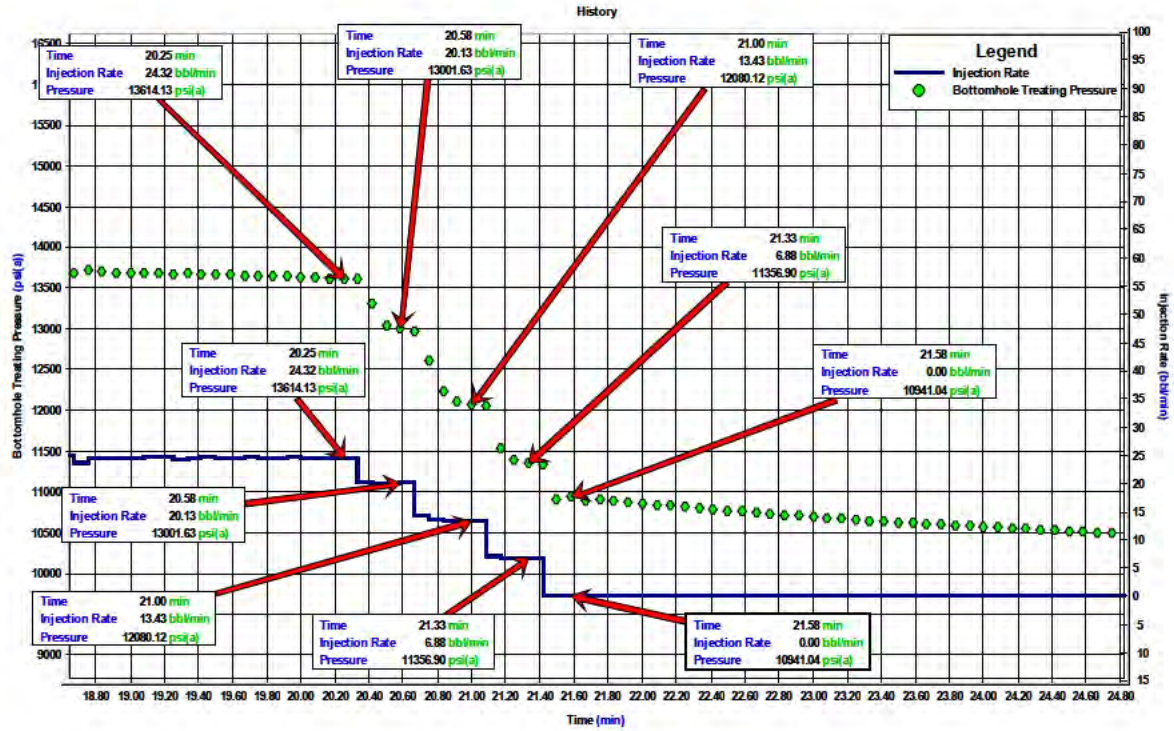


Figure D- 5 : Step Down Test Plot in well Cowralli 8 Stage 1

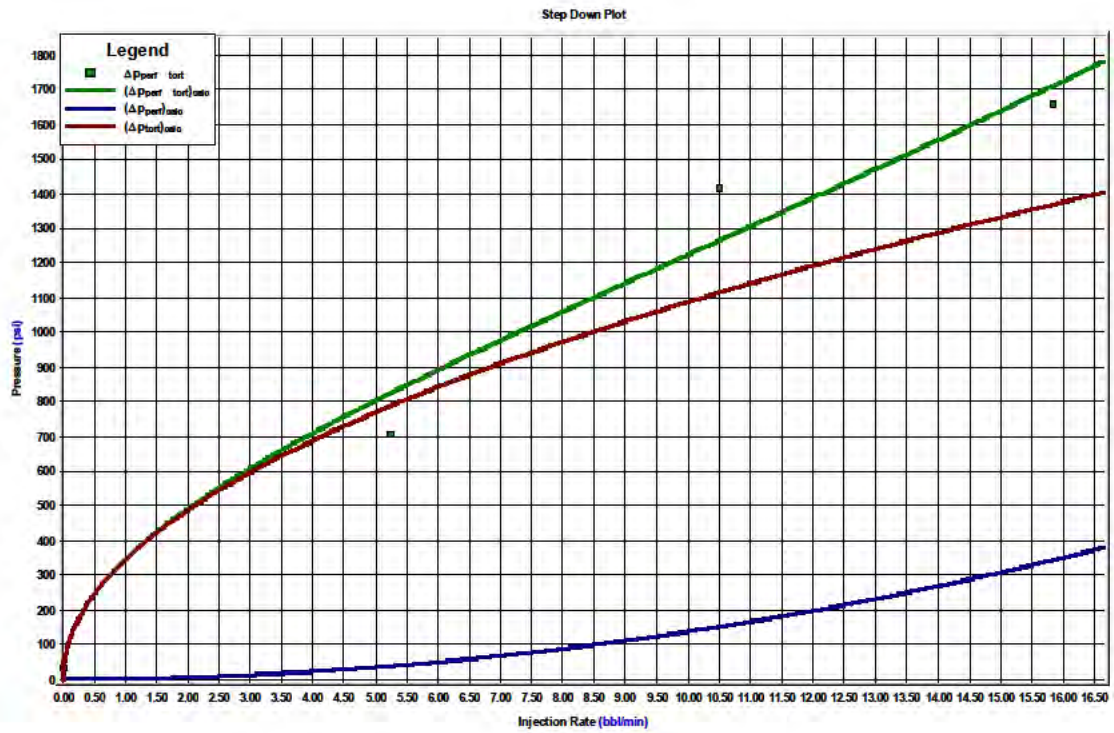
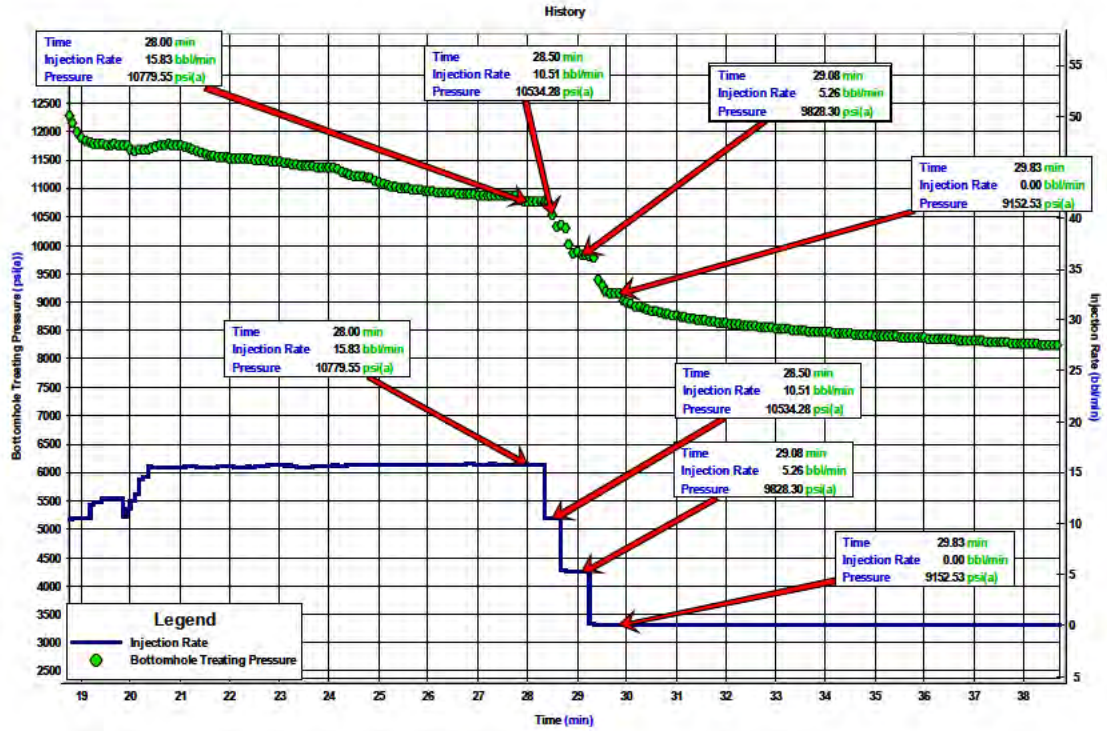


Figure D- 6 : Step Down Test Plot in well Cowralli 8 Stage 2

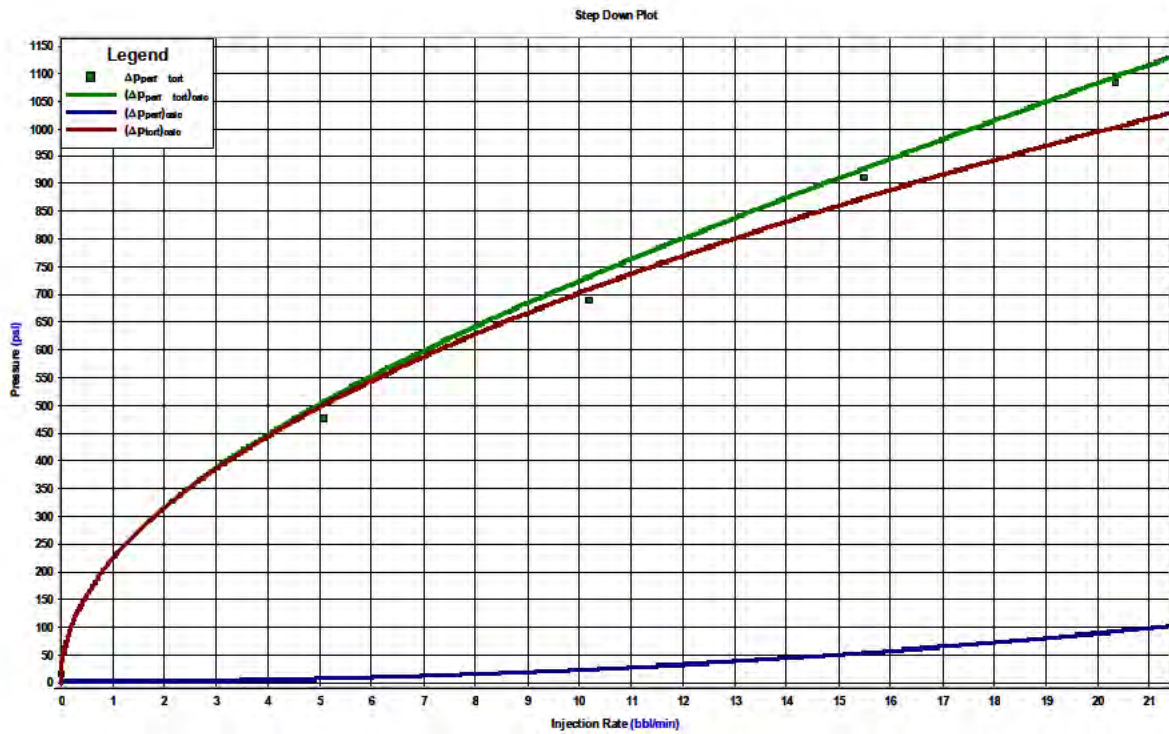
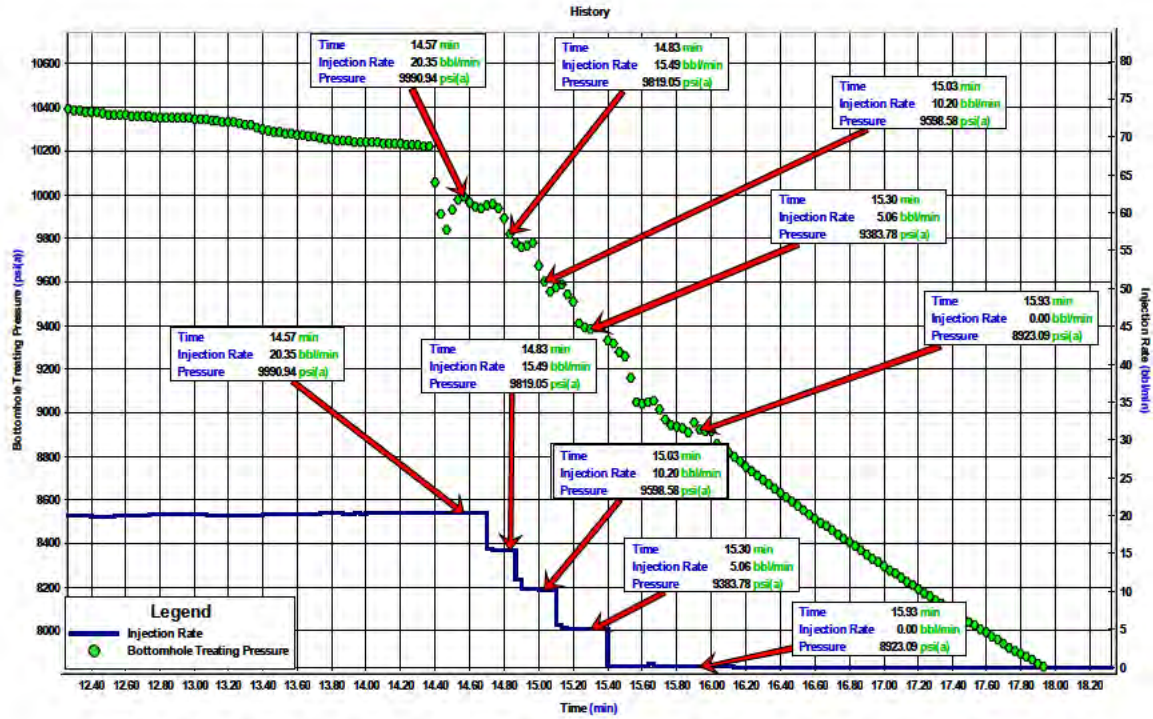


Figure D- 7 : Step Down Test Plot in well Cowralli 8 Stage 3

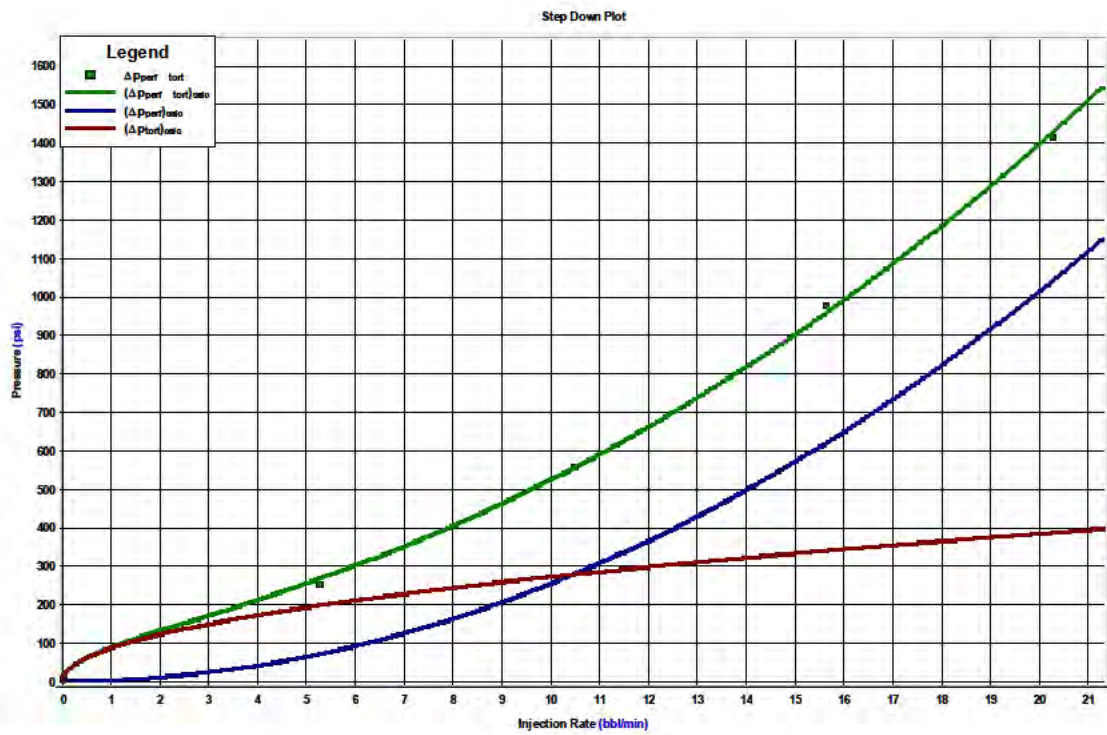
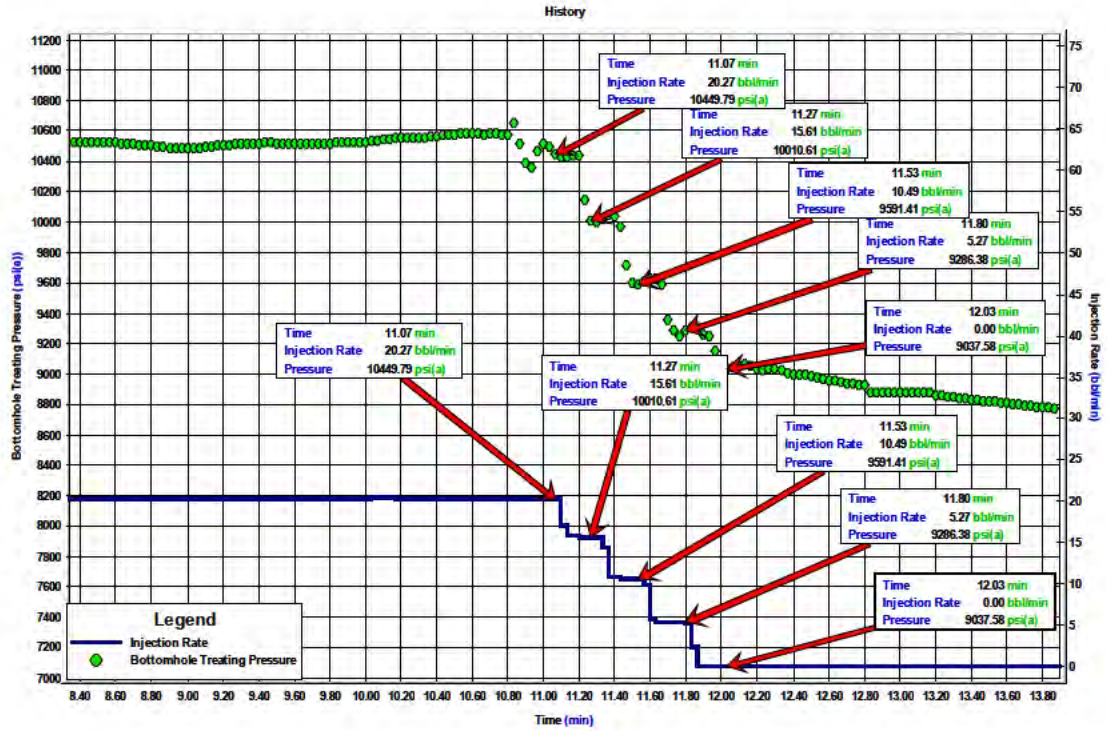


Figure D- 8 : Step Down Test Plot in well Cowralli 8 Stage 4

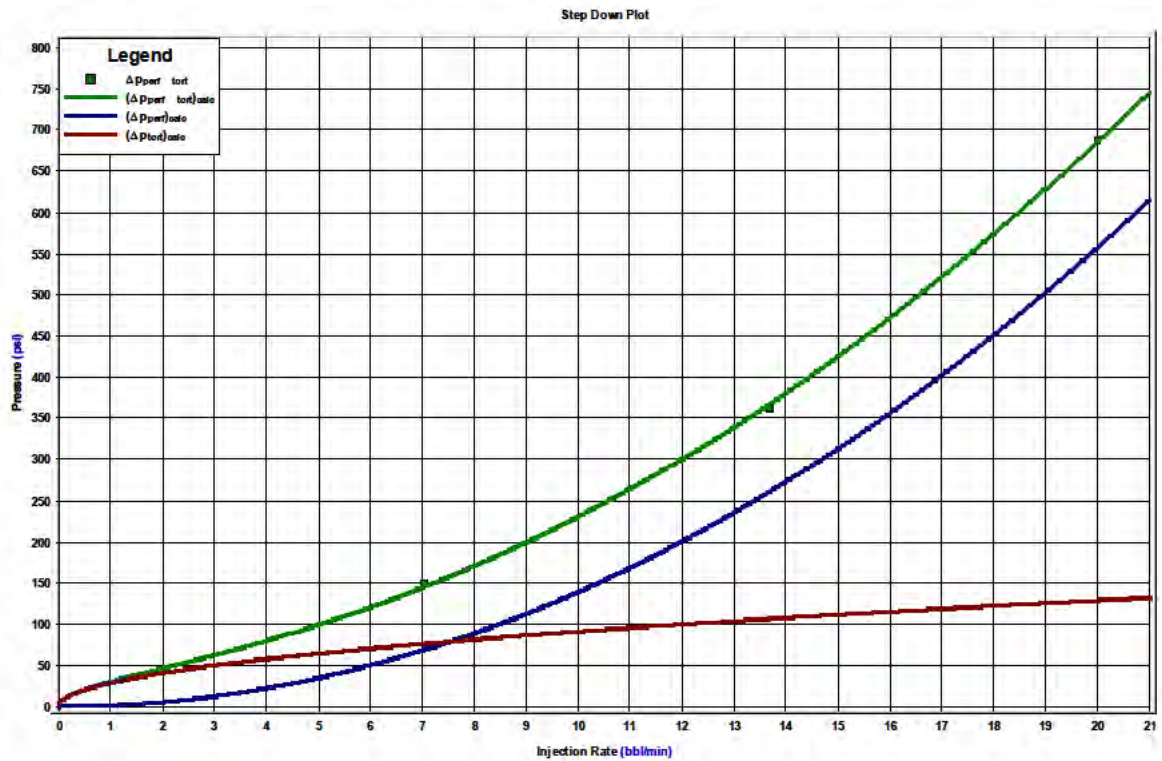
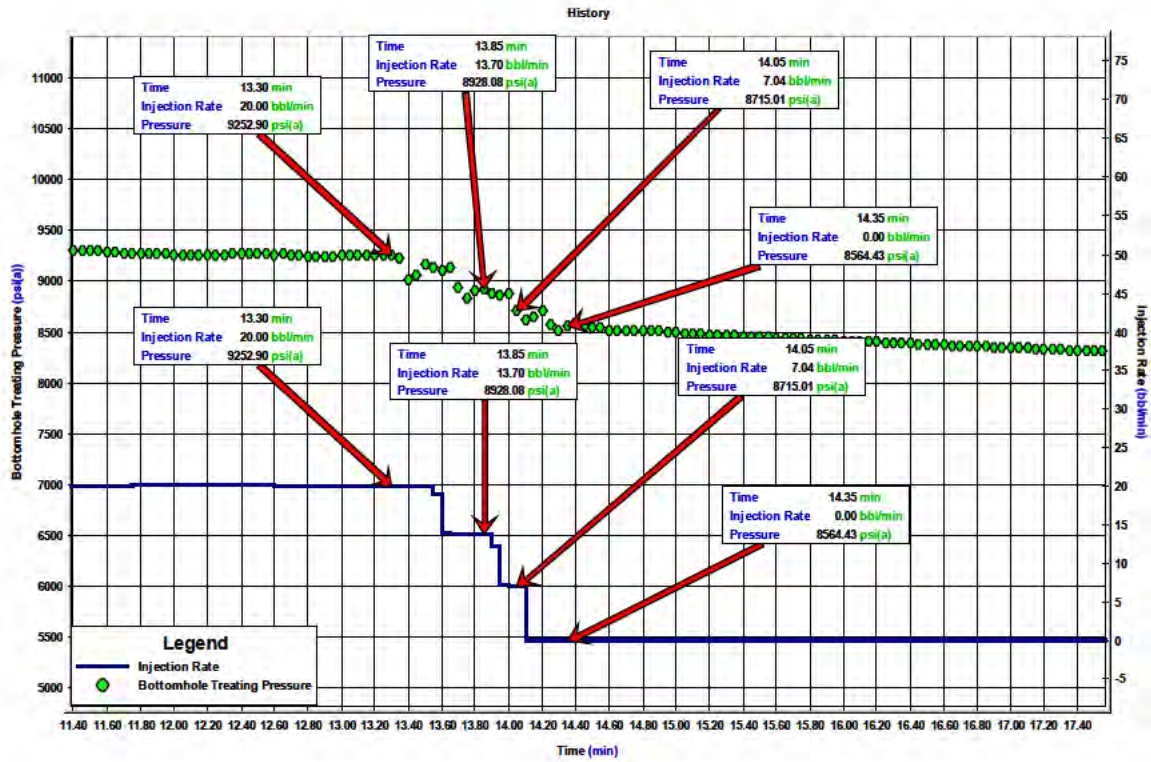


Figure D- 9 : Step Down Test Plot in well Cowralli 8 Stage 5

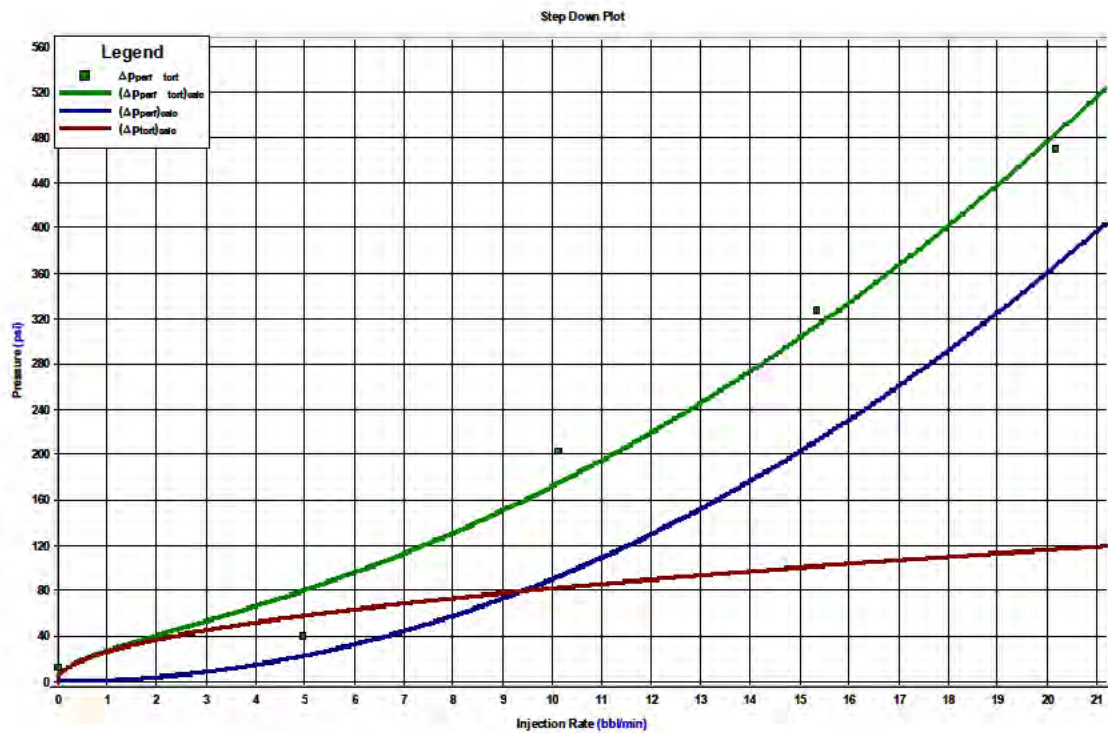
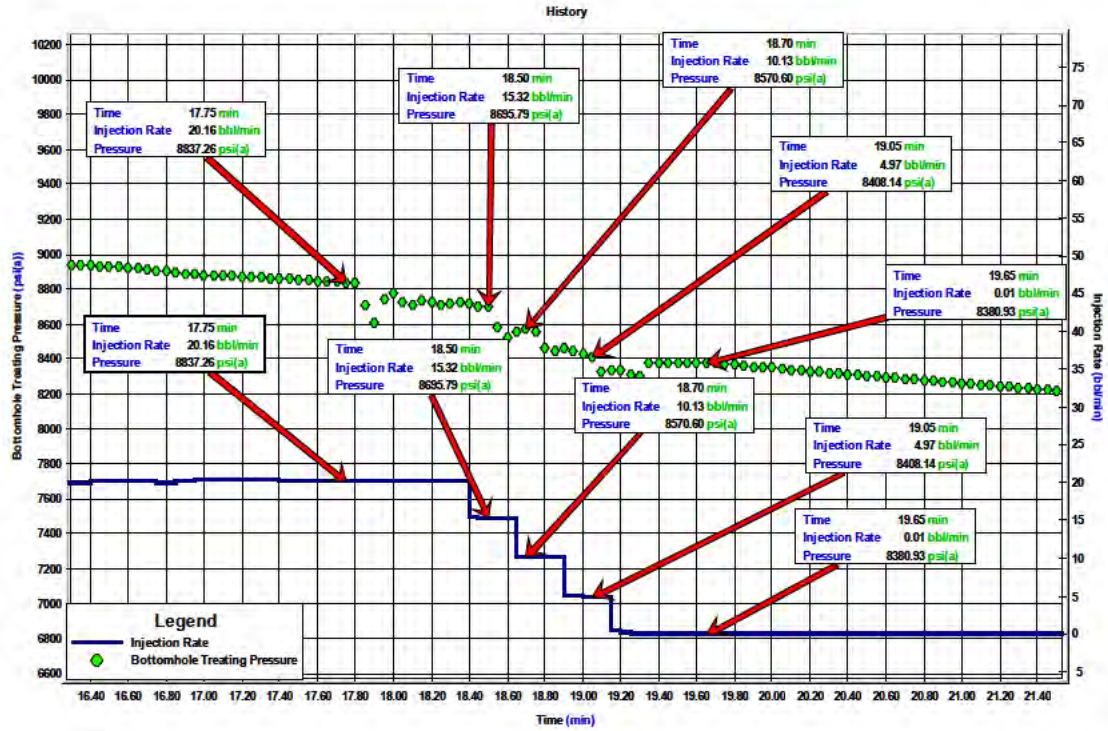


Figure D- 10 : Step Down Test Plot in well Cowralli 8 Stage 6

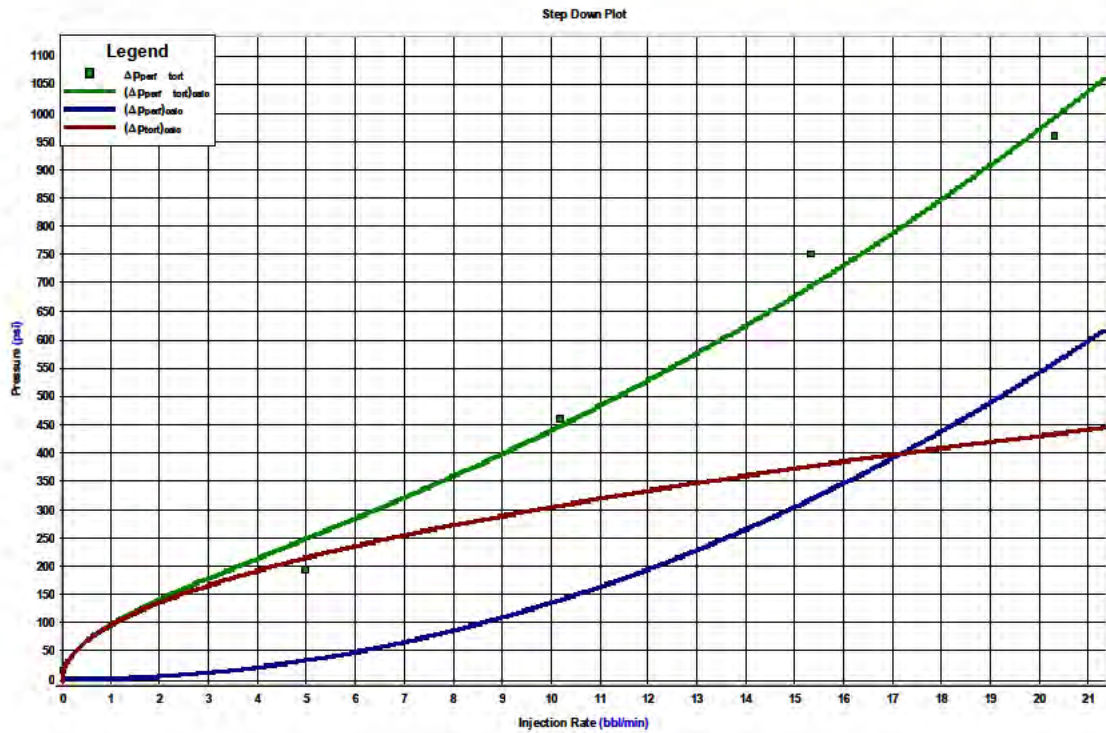
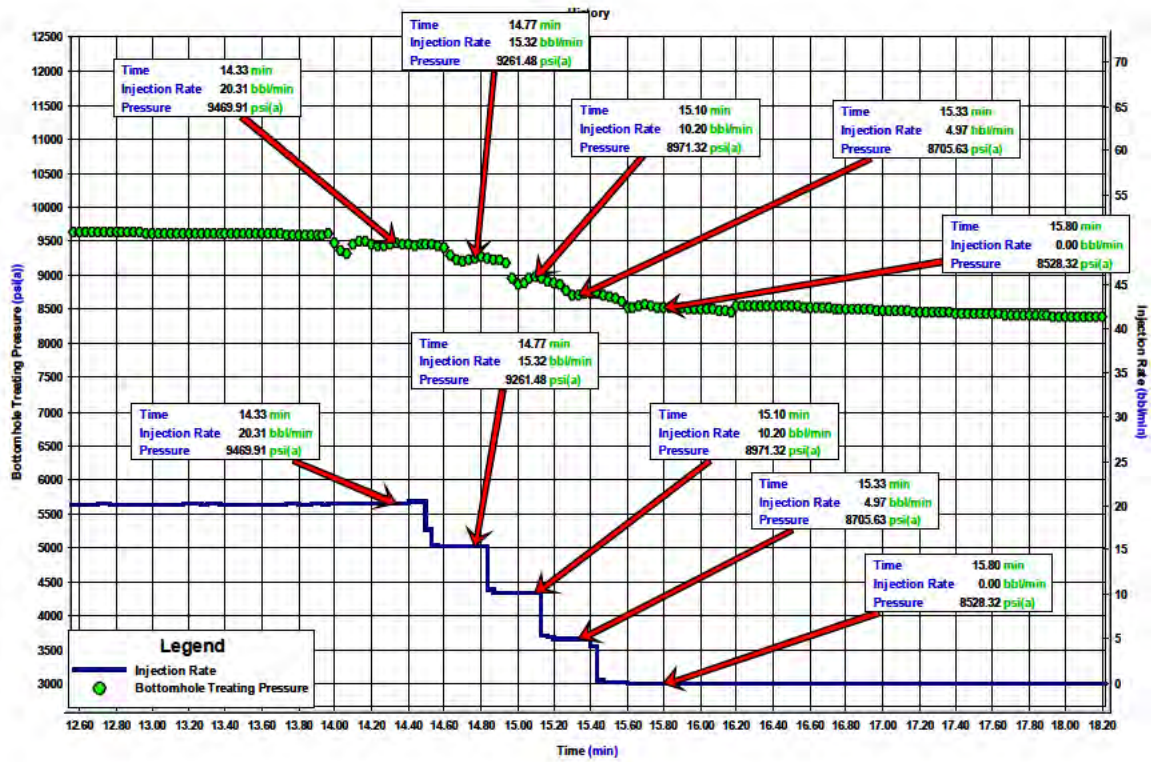
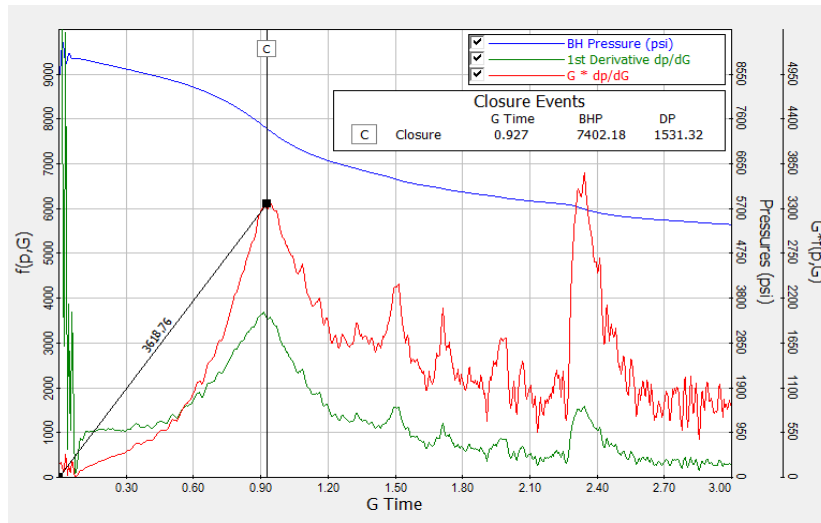
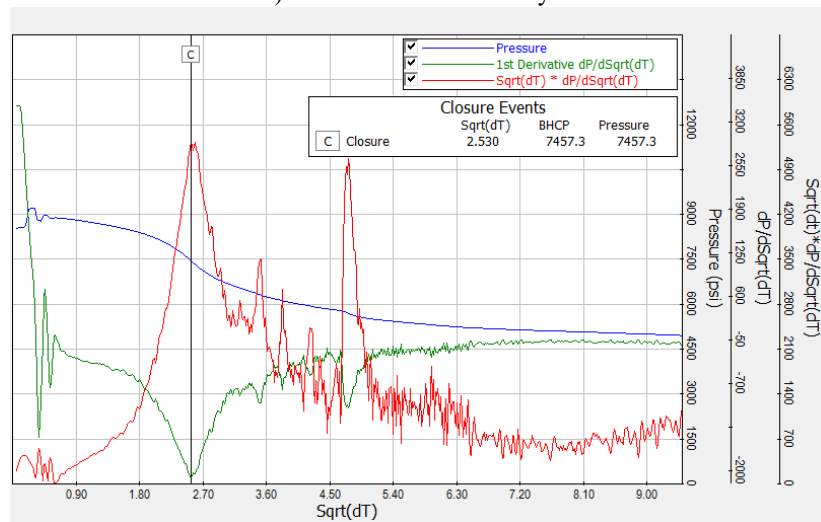


Figure D- 11 : Step Down Test Plot in well Cowralli 8 Stage 7

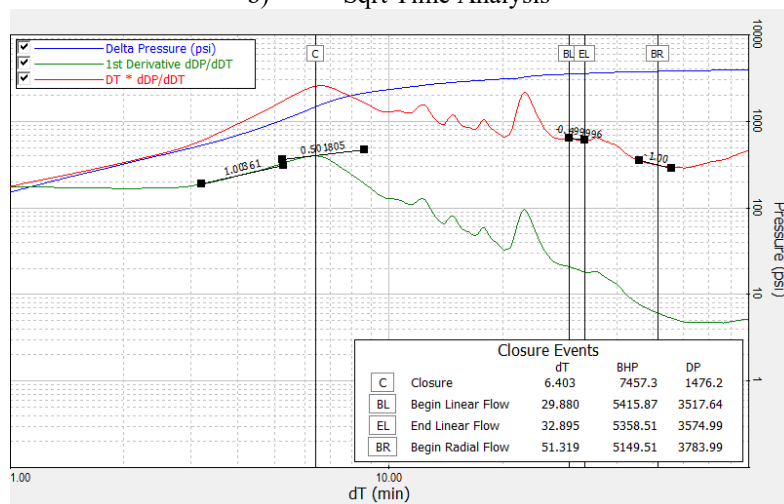
Appendix E: Pre-Closure Analysis Plots



a) G Function Analysis

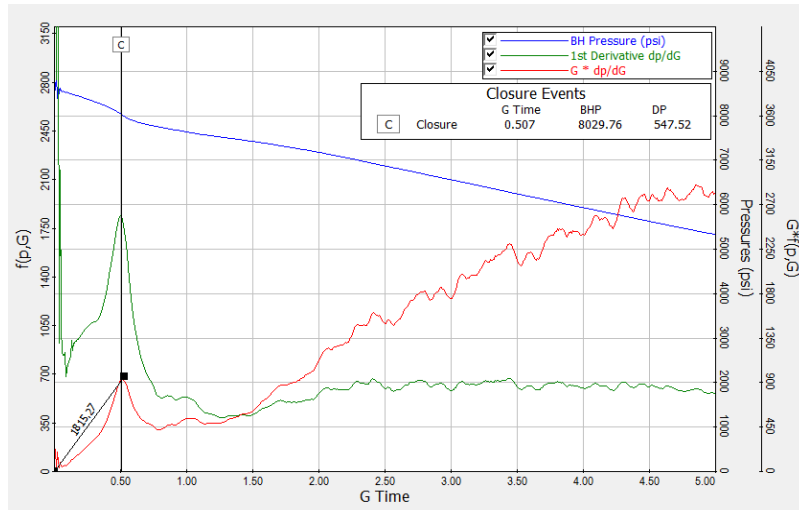


b) Sqrt Time Analysis

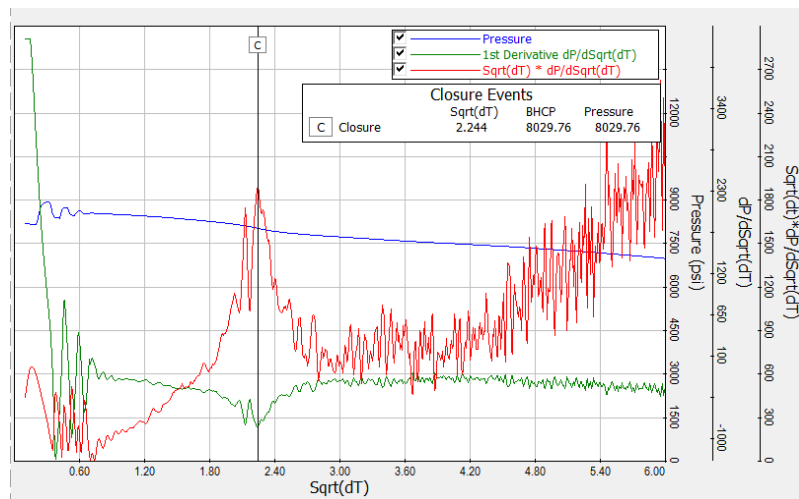


c) Log-Log Analysis

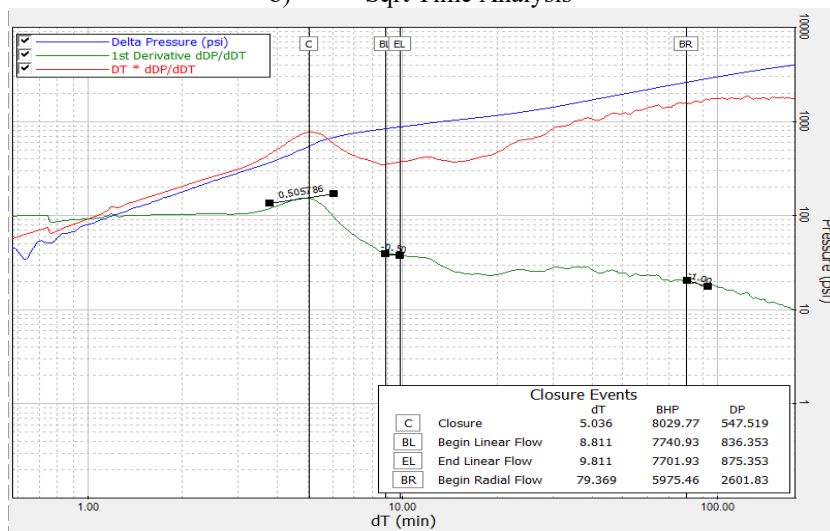
Figure E- 1 : Pre-Closure analysis plots in Cowralli 6 Stage 1



a) G Function Analysis

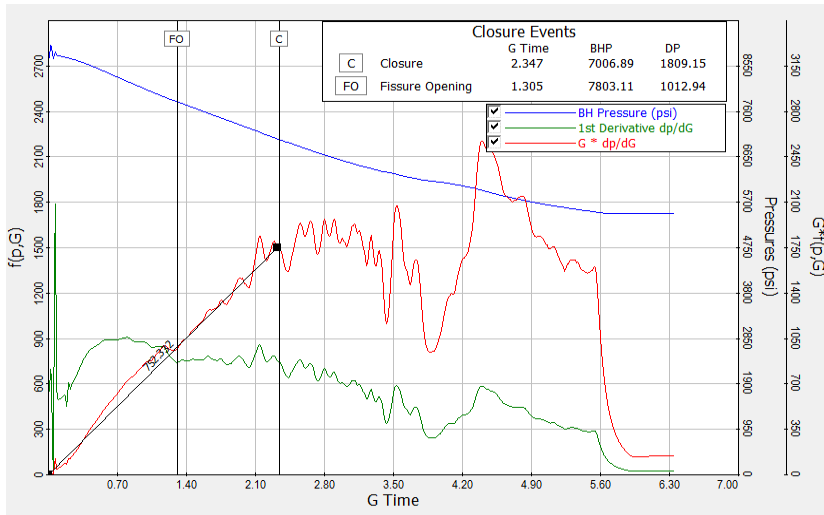


b) Sqrt Time Analysis

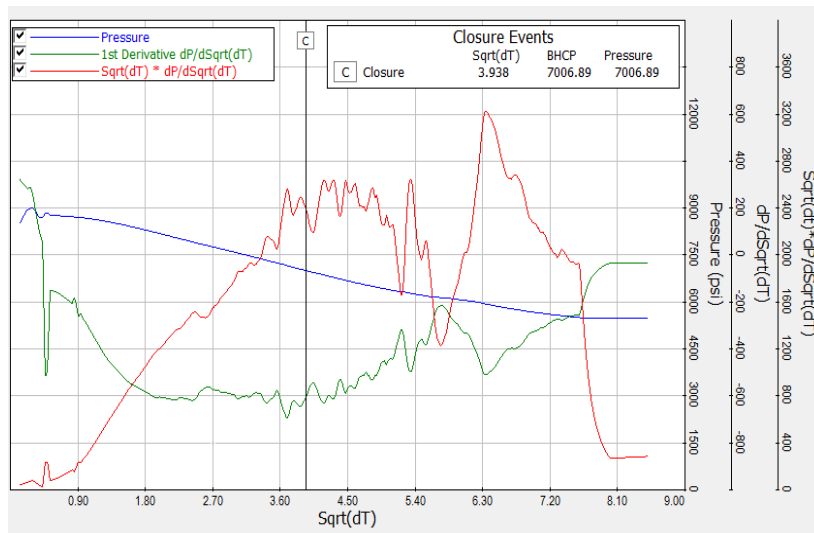


c) Log-Log Analysis

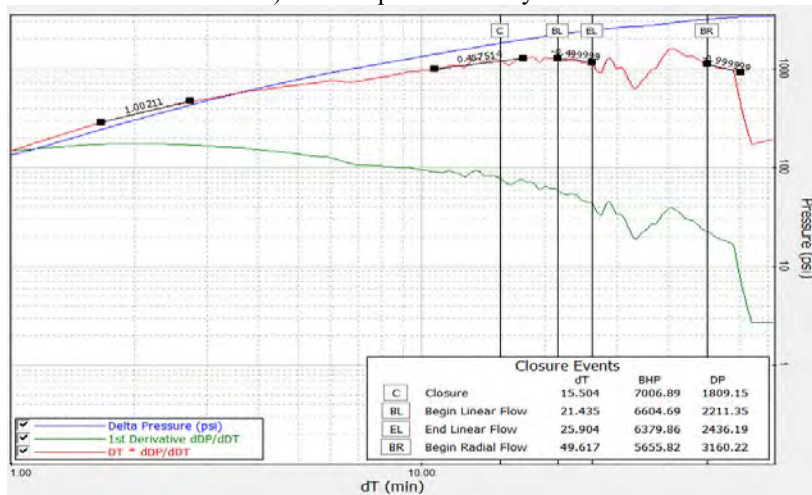
Figure E- 2 : Pre-Closure analysis plots in Cowralli 6 Stage 2



a) G Function Analysis

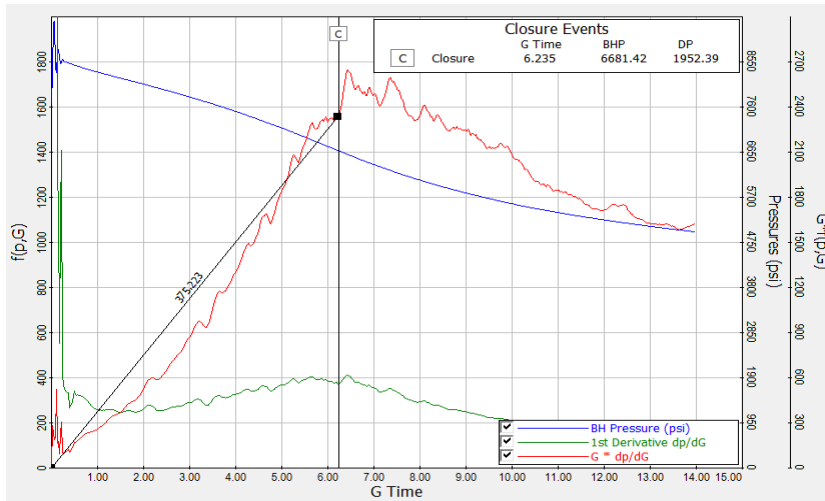


b) Sqrt Time Analysis

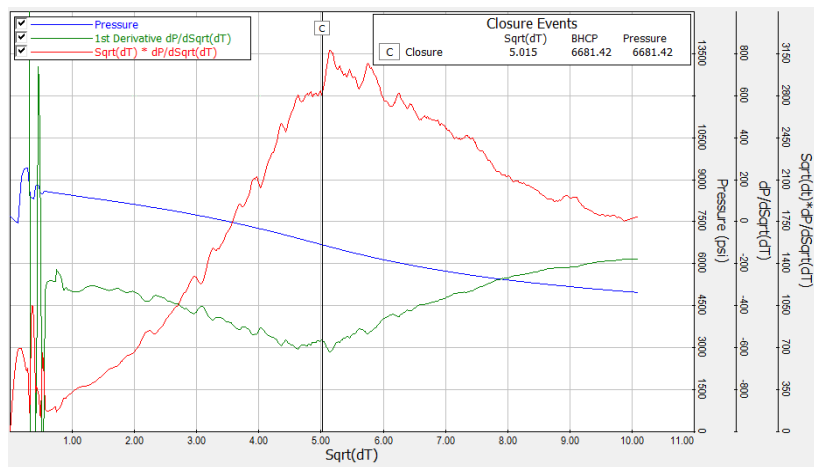


c) Log-Log Analysis

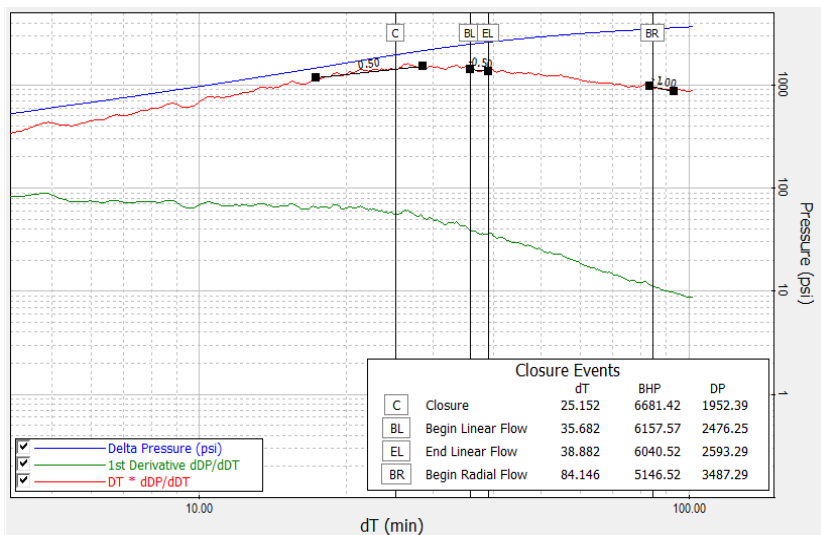
Figure F- 3 : Pre-Closure analysis plots in Cowralli 7 Stage 1



a) G Function Analysis

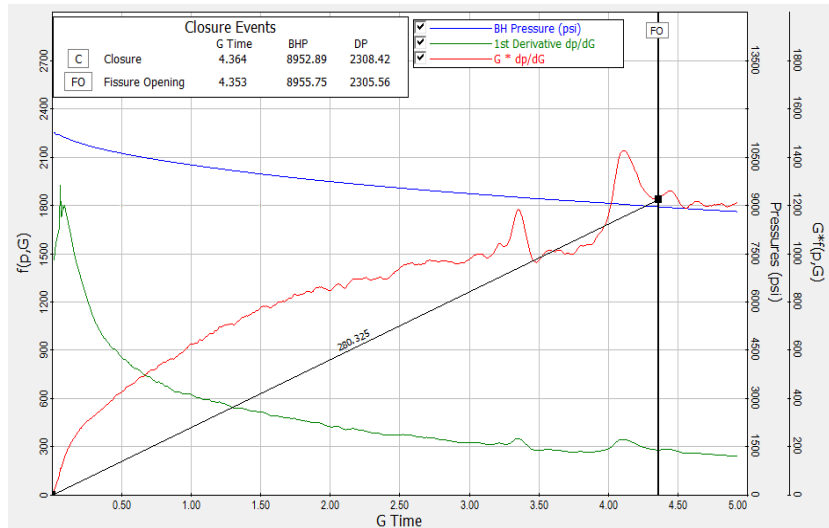


b) Sqrt Time Analysis

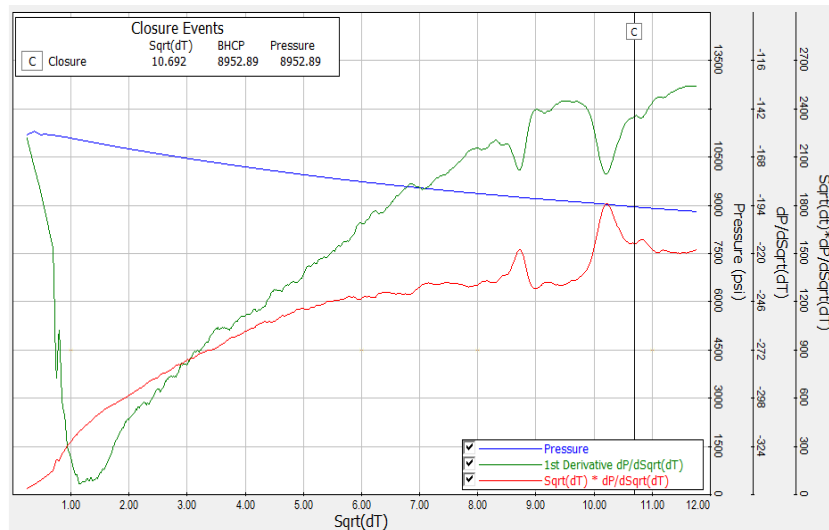


c) Log-Log Analysis

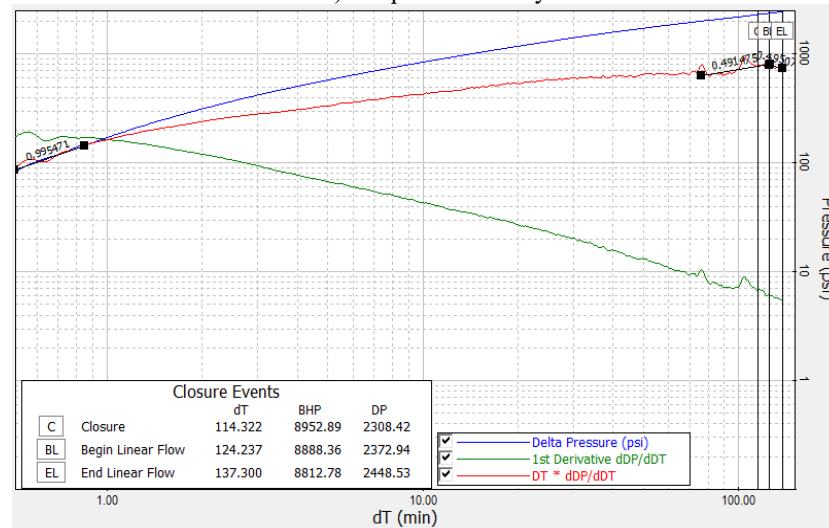
Figure E- 4 : Pre-Closure analysis plots in Cowralli 7 Stage 2



a) G Function Analysis

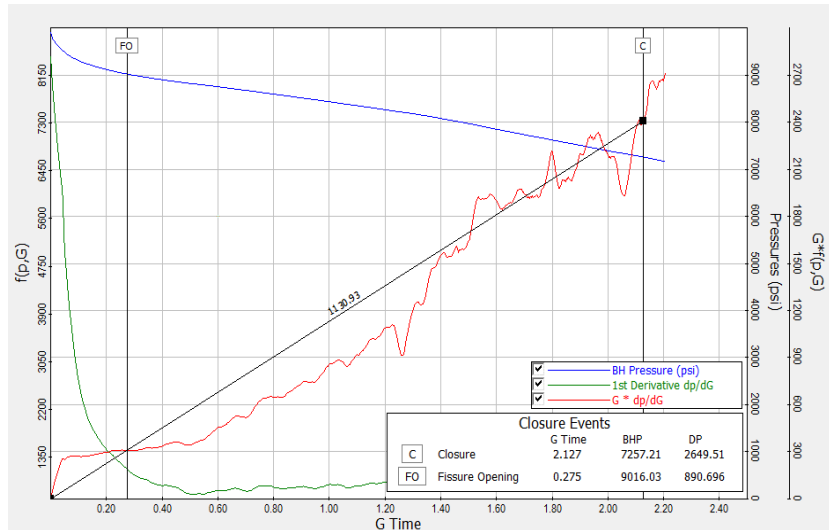


b) Sqrt Time Analysis

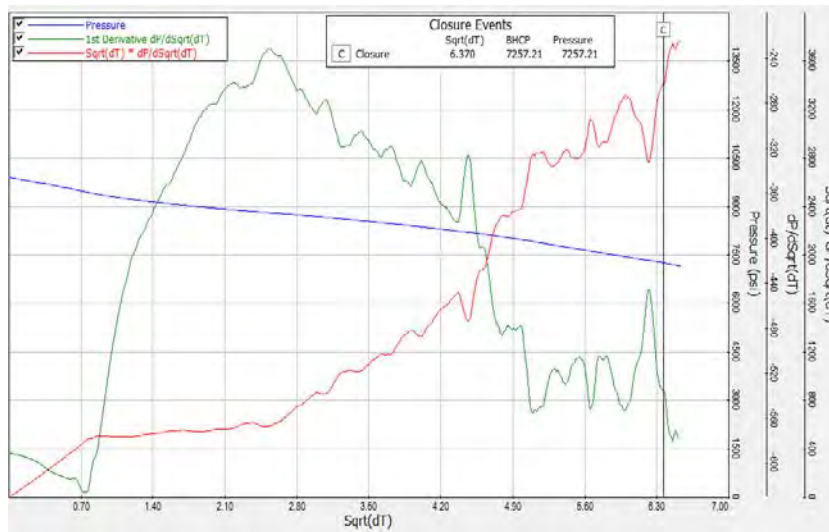


c) Log-Log Analysis

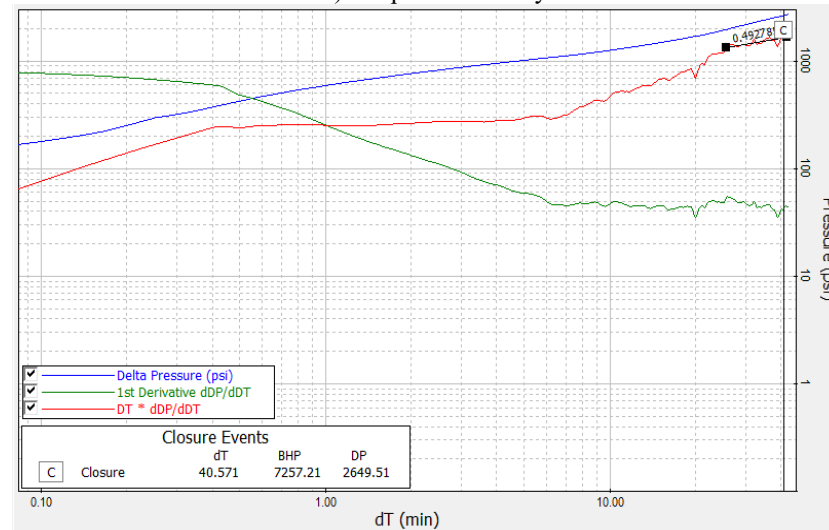
Figure E- 5 : Pre-Closure analysis plots in Cowralli 8 Stage 1



a) G Function Analysis

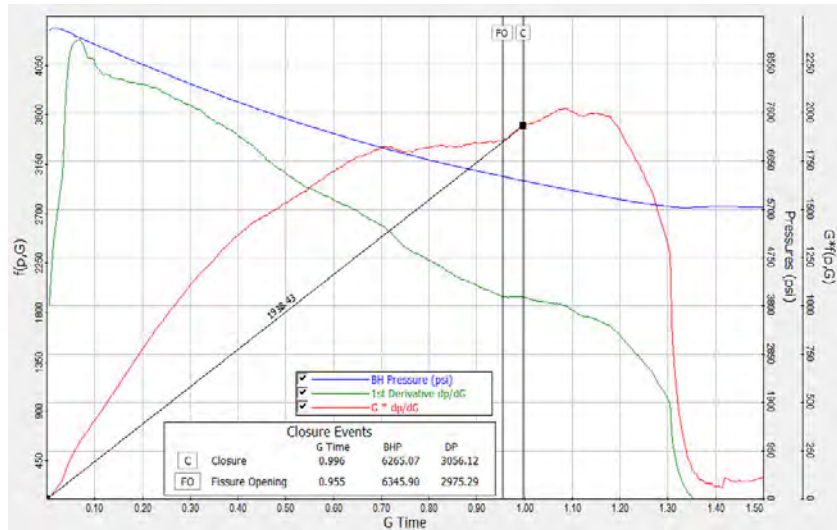


b) Sqrt Time Analysis

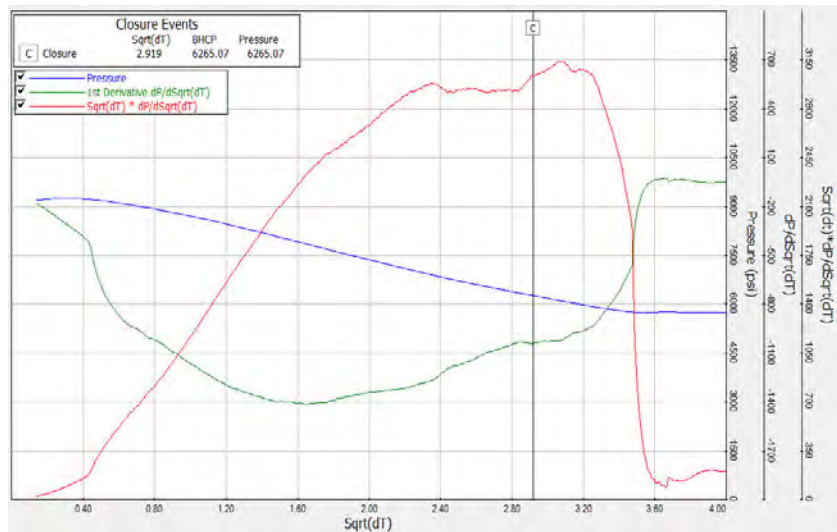


c) Log-Log Analysis

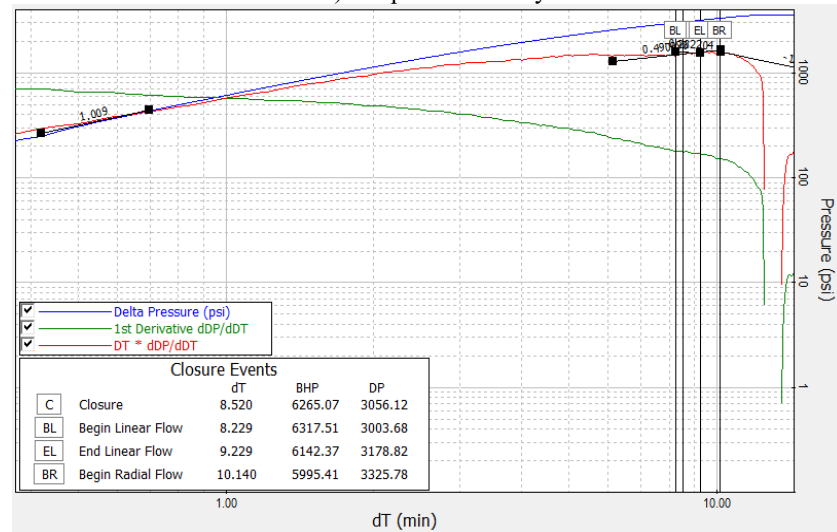
Figure E- 6 : Pre-Closure analysis plots in Cowralli 8 Stage 2



a) G Function Analysis

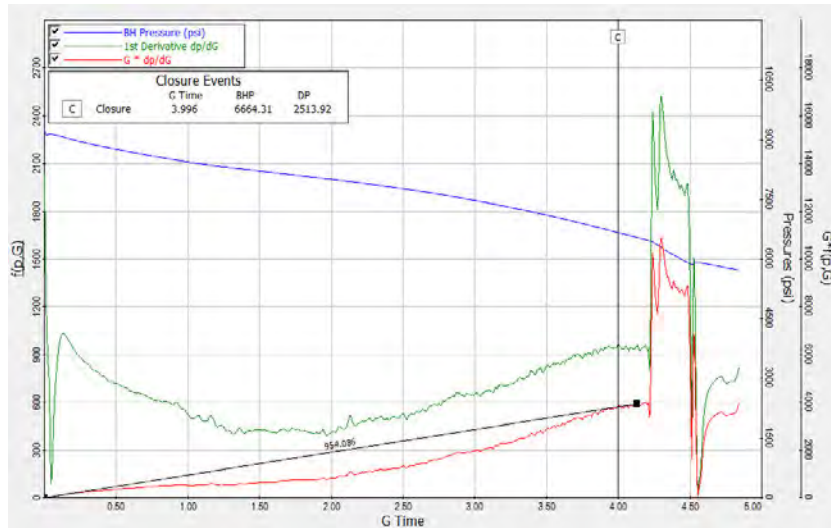


b) Sqrt Time Analysis

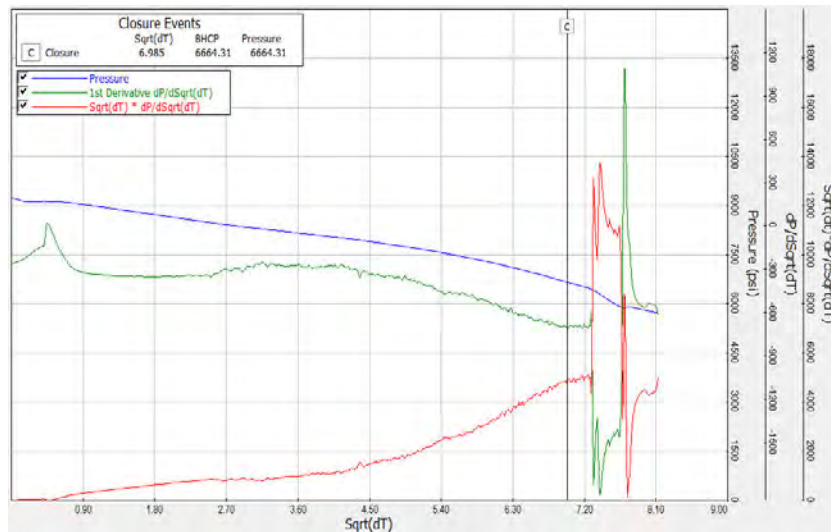


c) Log-Log Analysis

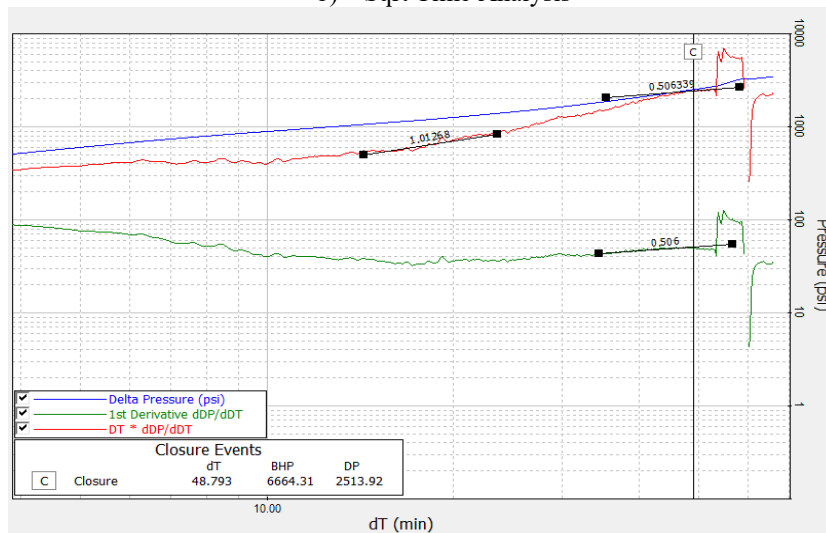
Figure E- 7 : Pre-Closure analysis plots in Cowralli 8 Stage 3



a) G Function Analysis

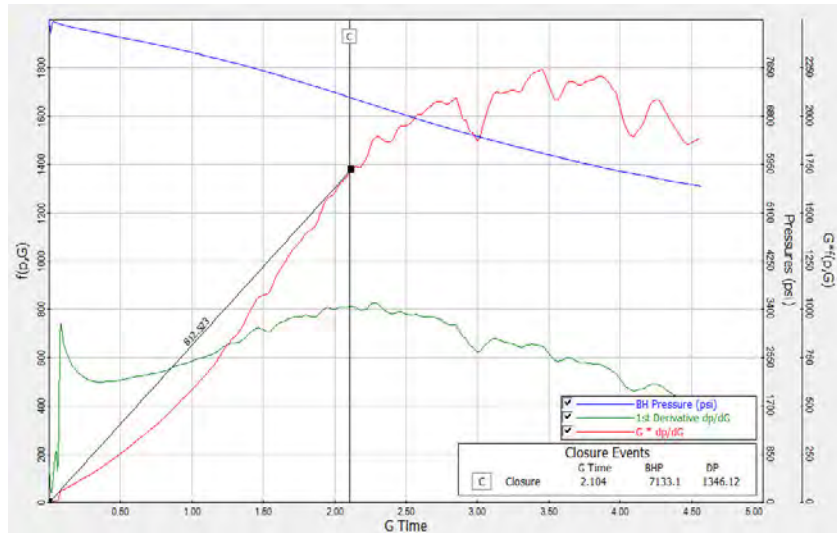


b) Sqrt Time Analysis

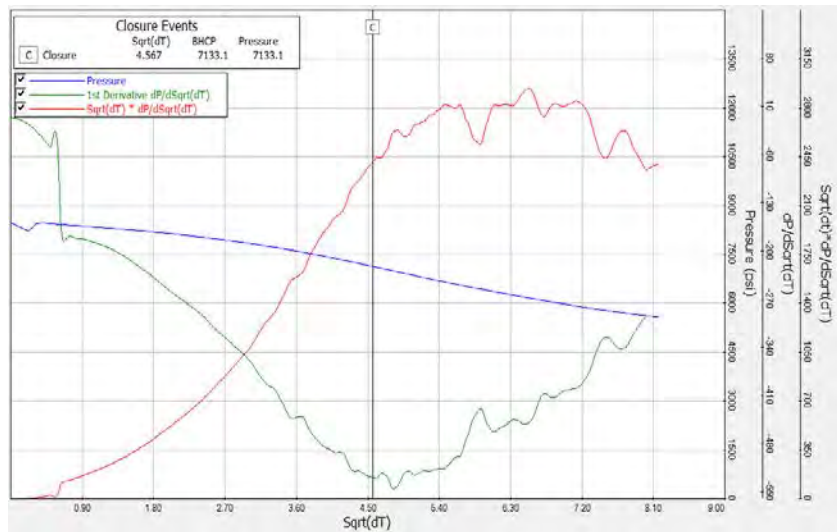


c) Log-Log Analysis

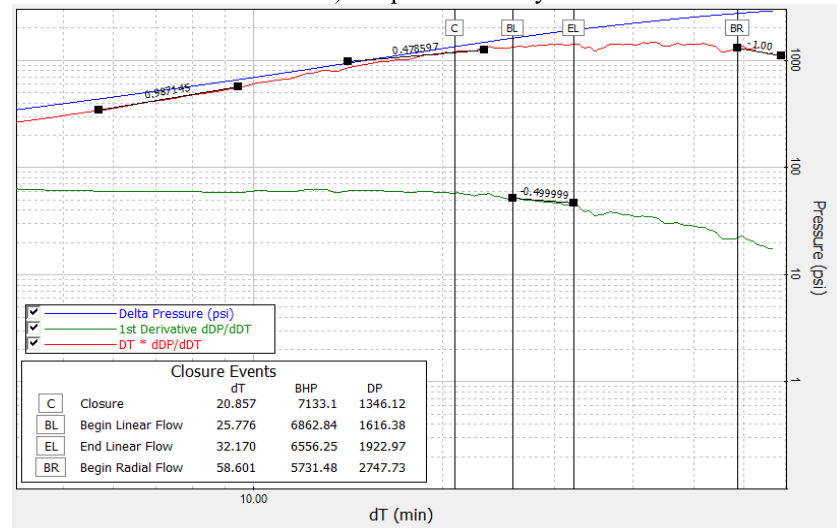
Figure E- 8 : Pre-Closure analysis plots in Cowralli 8 Stage 4



a) G Function Analysis

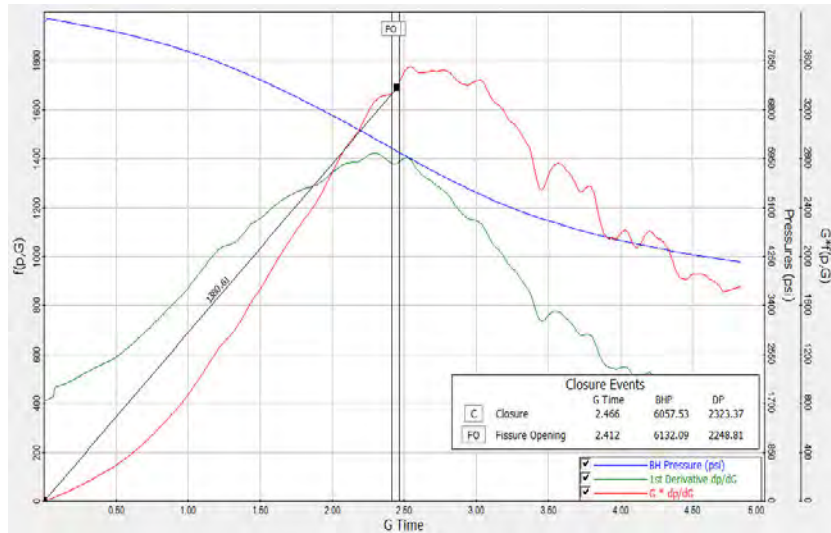


b) Sqrt Time Analysis

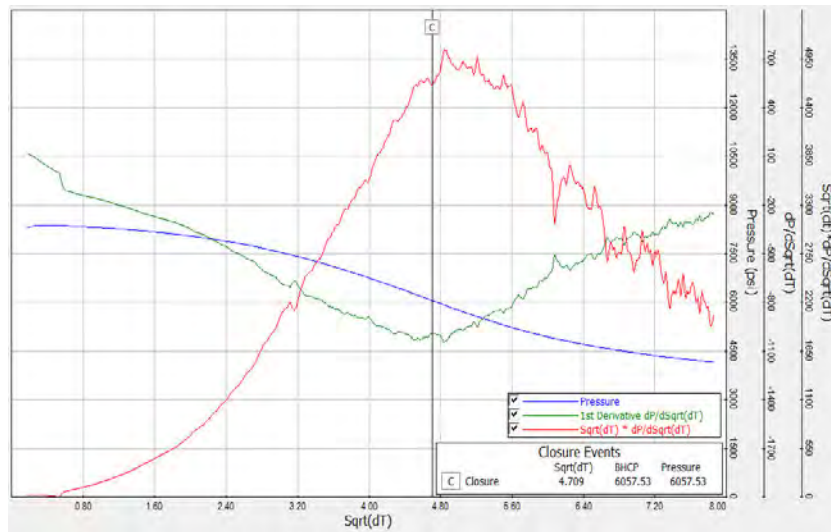


c) Log-Log Analysis

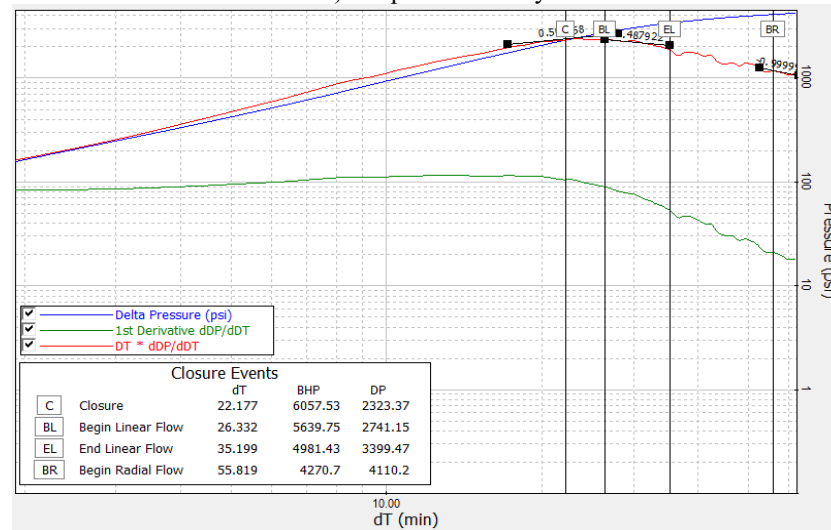
Figure E- 9 : Pre-Closure analysis plots in Cowralli 8 Stage 5



a) G Function Analysis

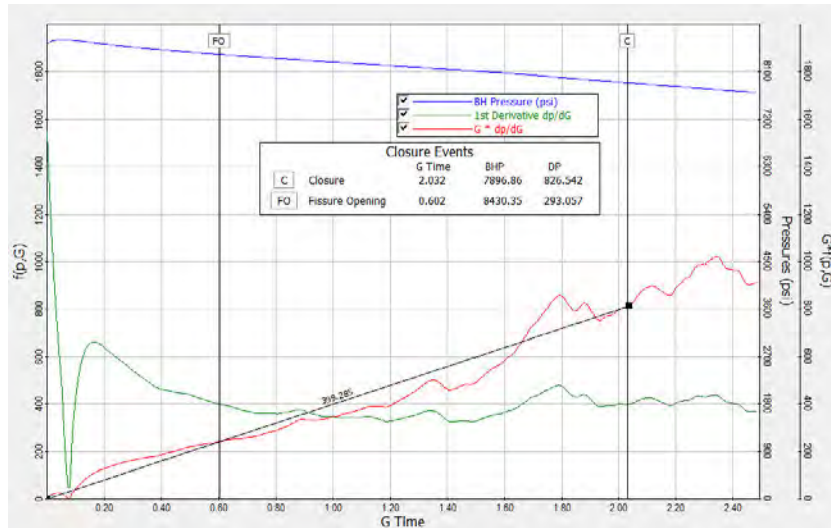


b) Sqrt Time Analysis

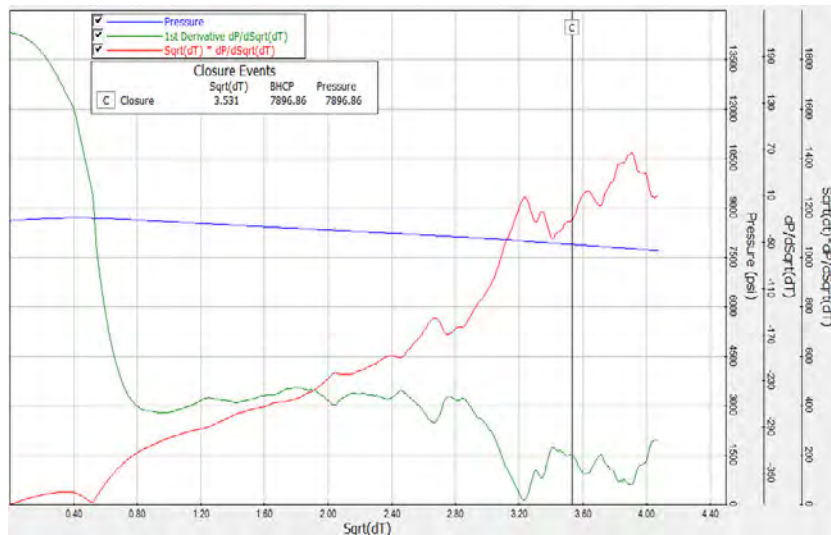


c) Log-Log Analysis

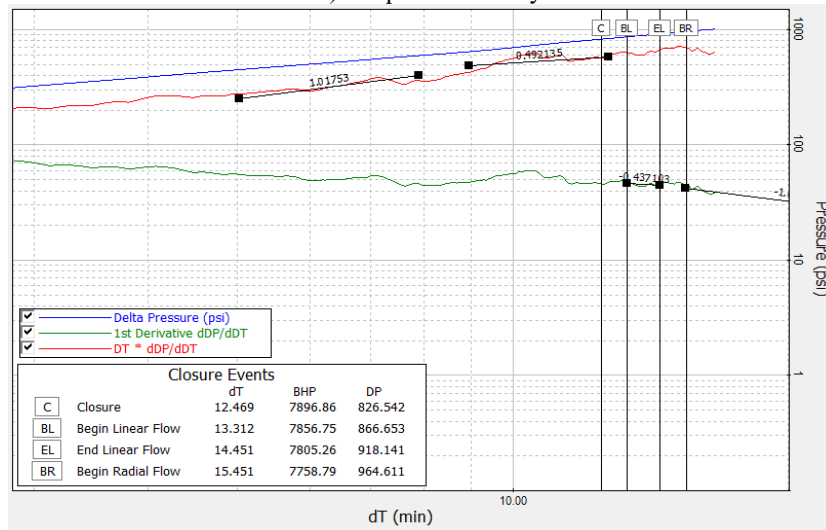
Figure E- 10 : Pre-Closure analysis plots in Cowralli 8 Stage 6



a) G Function Analysis



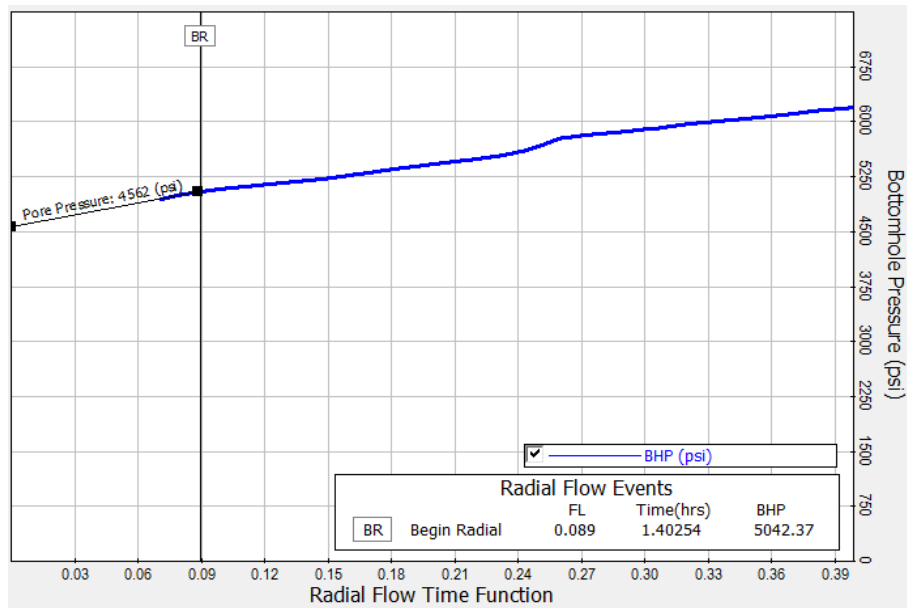
b) Sqrt Time Analysis



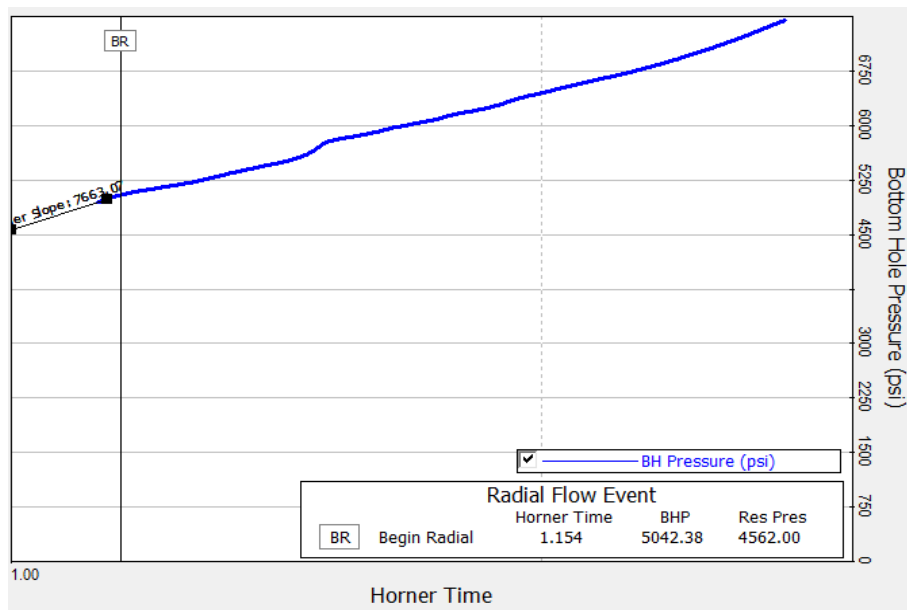
c) Log-Log Analysis

Figure E- 11 : Pre-Closure analysis plots in Cowralli 8 Stage 7

Appendix F: After Closure Analysis Plots

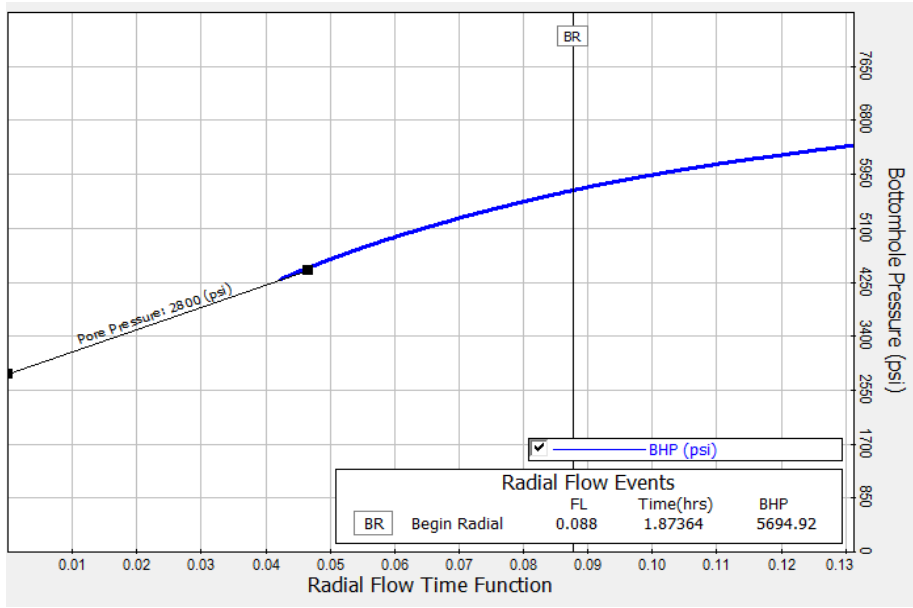


(a) Radial Flow Analysis

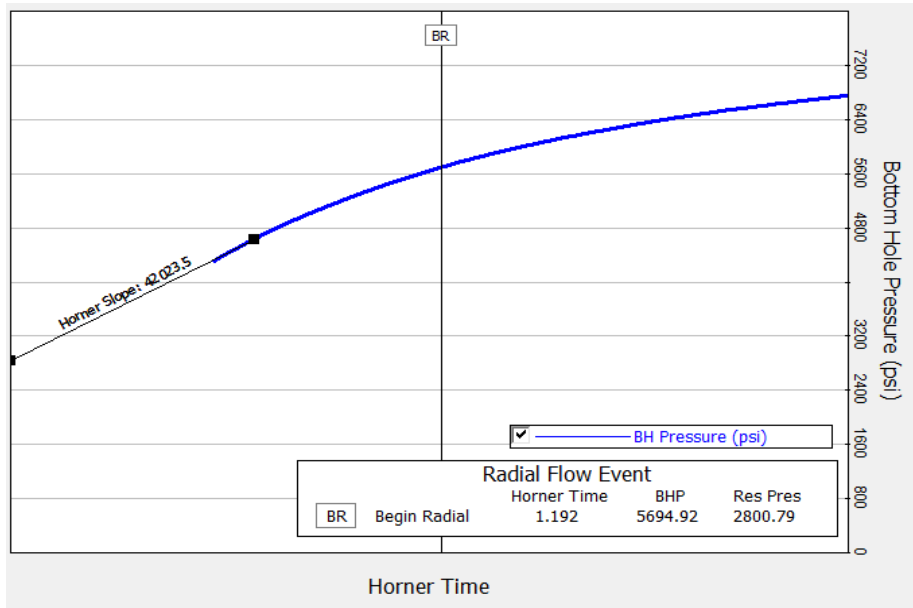


(b) Horner Plot Analysis

Figure F - 1 : After-Closure analysis plots in Cowralli 6 Stage 1

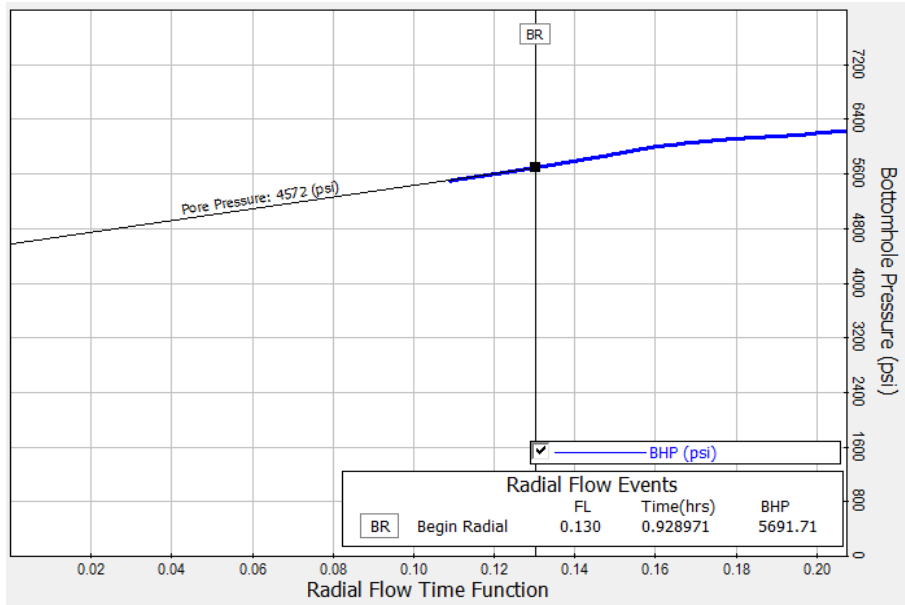


(a) Radial Flow Analysis

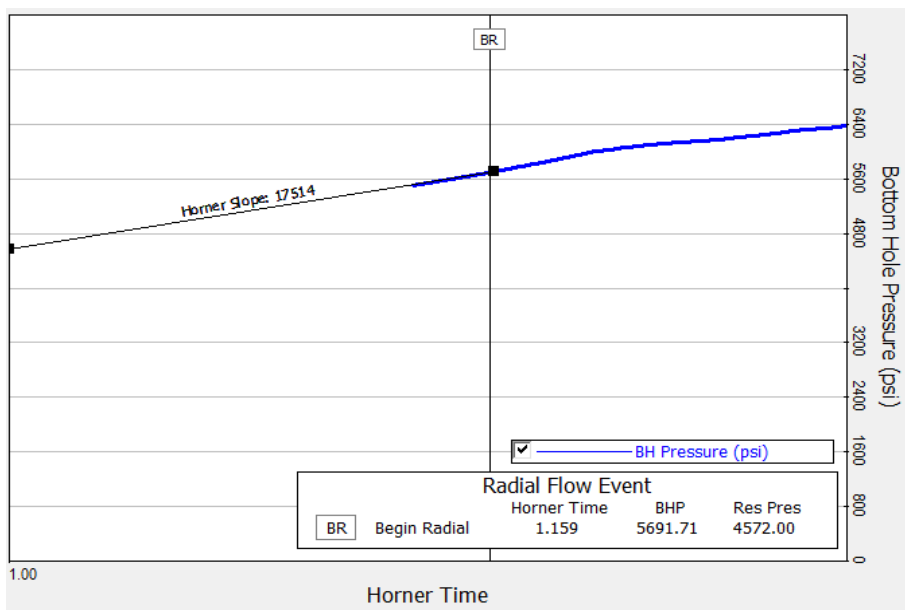


(b) Horner Plot Analysis

Figure F - 2 : After-Closure analysis plots in Cowralli 6 Stage 2

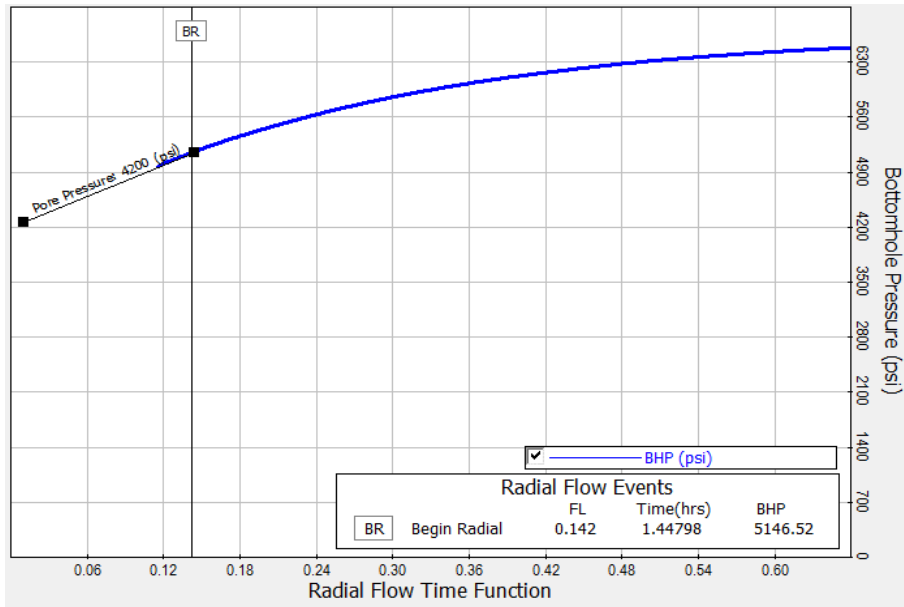


(a) Radial Flow Analysis

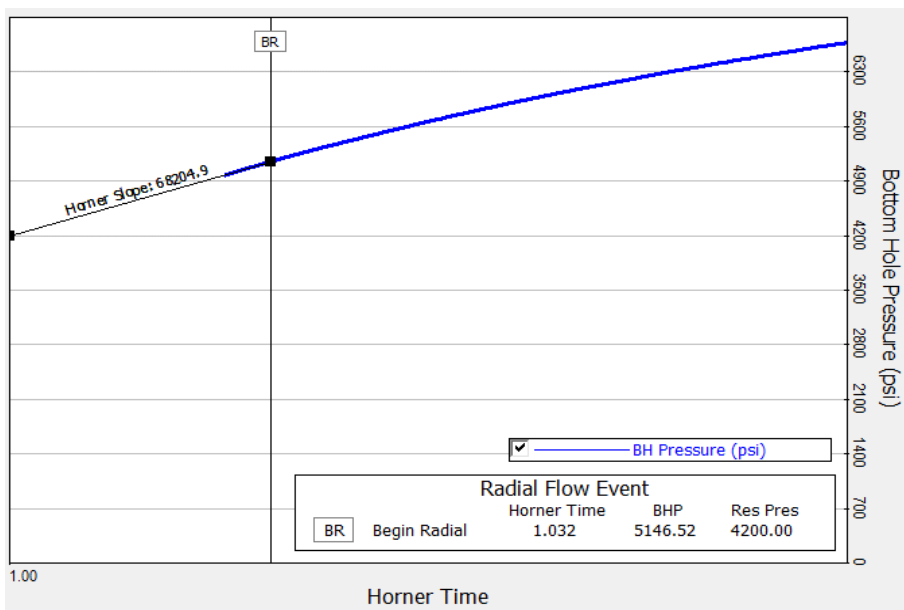


(b) Horner Plot Analysis

Figure F - 3 : After-Closure analysis plots in Cowralli 7 Stage 1

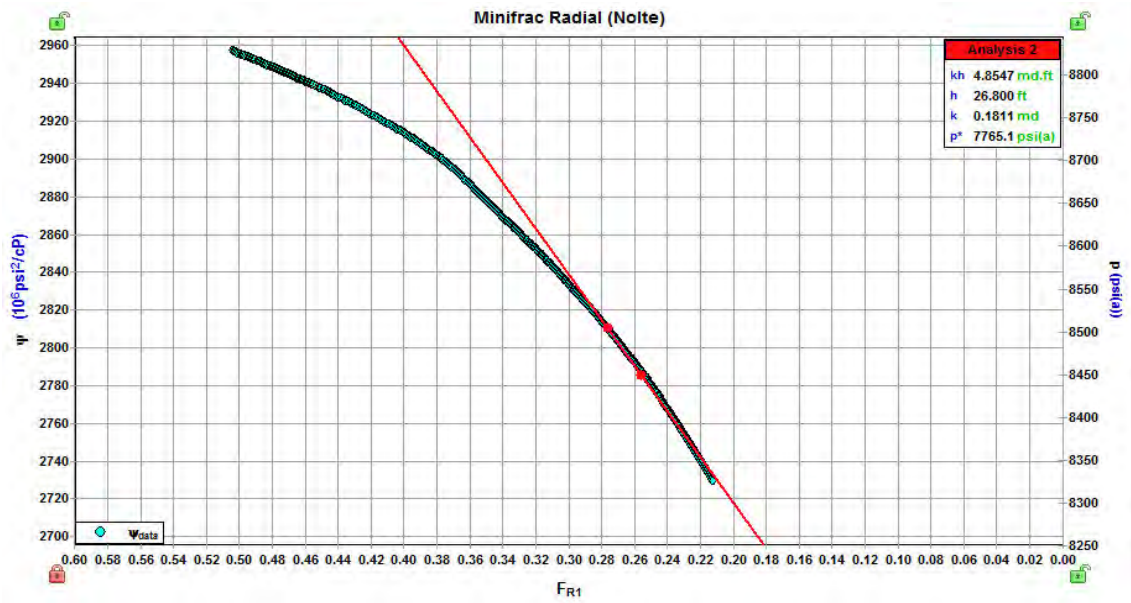


(a) Radial Flow Analysis

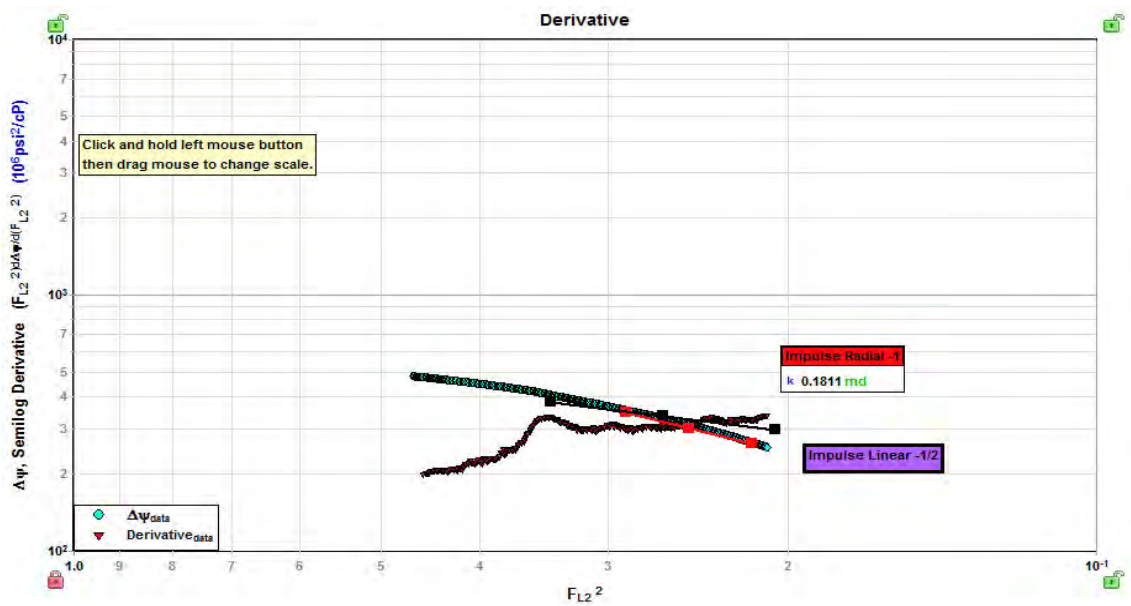


(b) Horner Plot Analysis

Figure F - 4 : After-Closure analysis plots in Cowralli 7 Stage 2

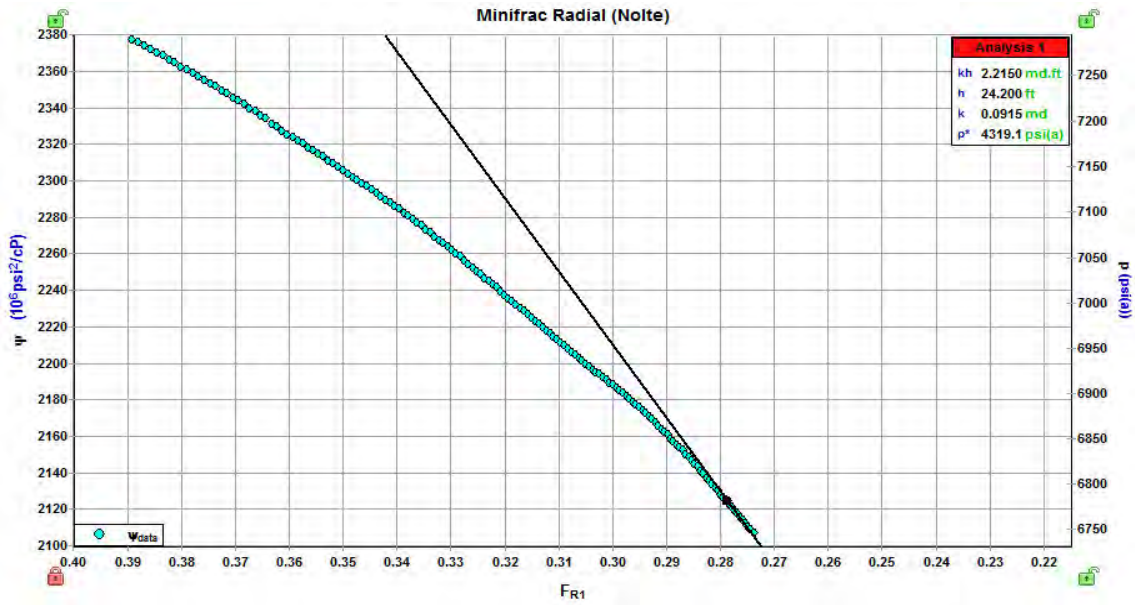


(a) Radial Flow Analysis (Nolte)

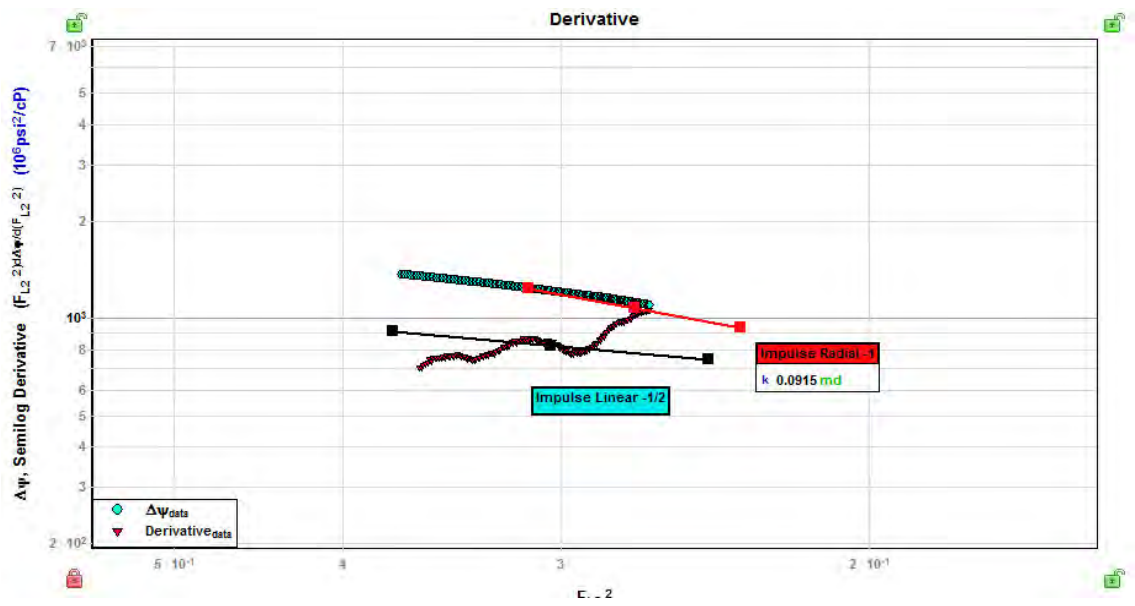


(b) Derivative Analysis (Nolte)

Figure F - 5 : After-Closure analysis plots in Cowralli 8 Stage 1

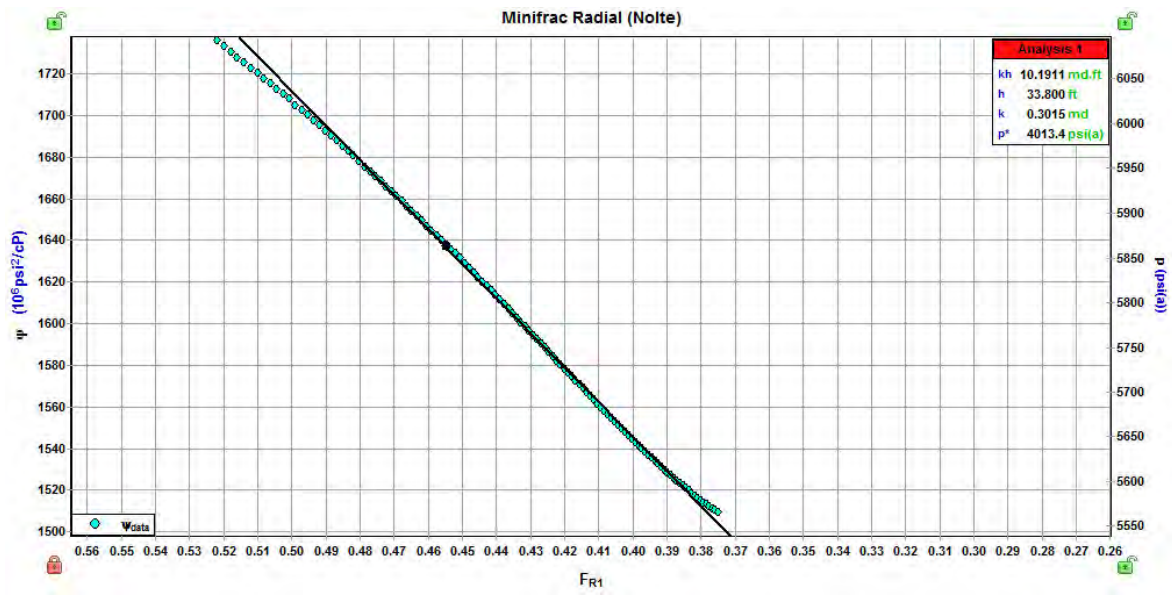


(a) Radial Flow Analysis (Nolte)

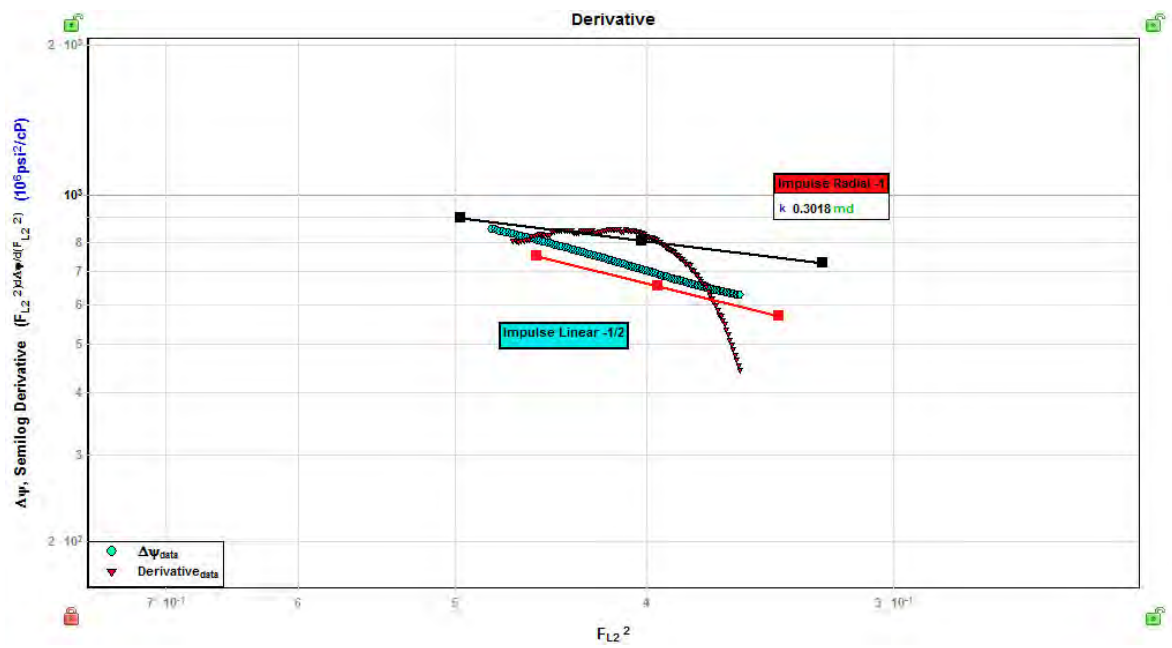


(b) Derivative Analysis (Nolte)

Figure F - 6 : After-Closure analysis plots in Cowralli 8 Stage 2

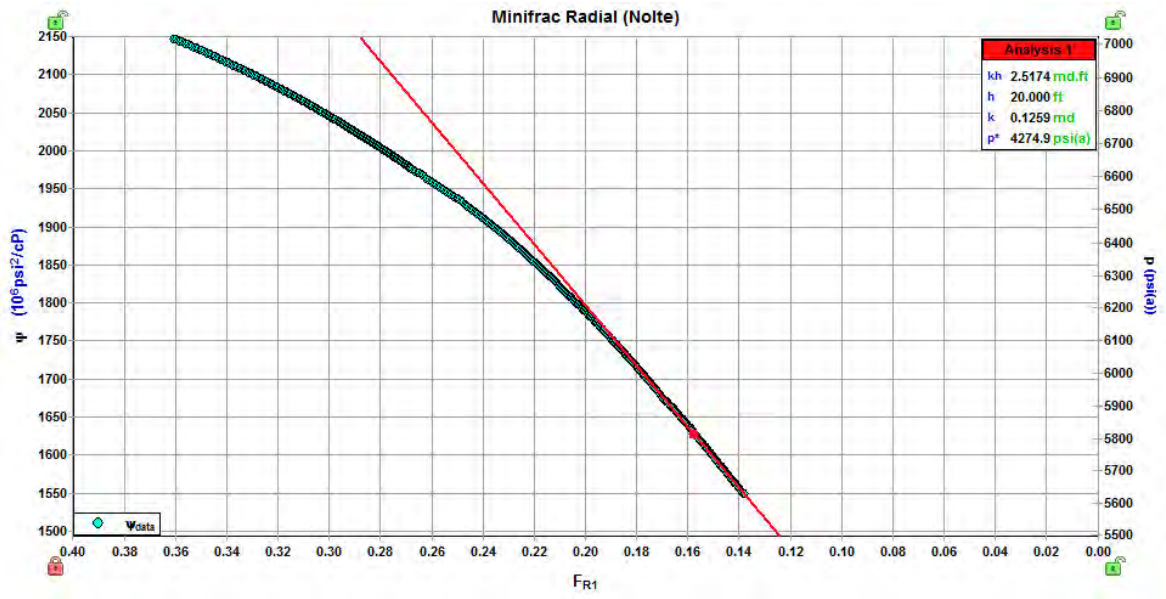


(a) Radial Flow Analysis (Nolte)

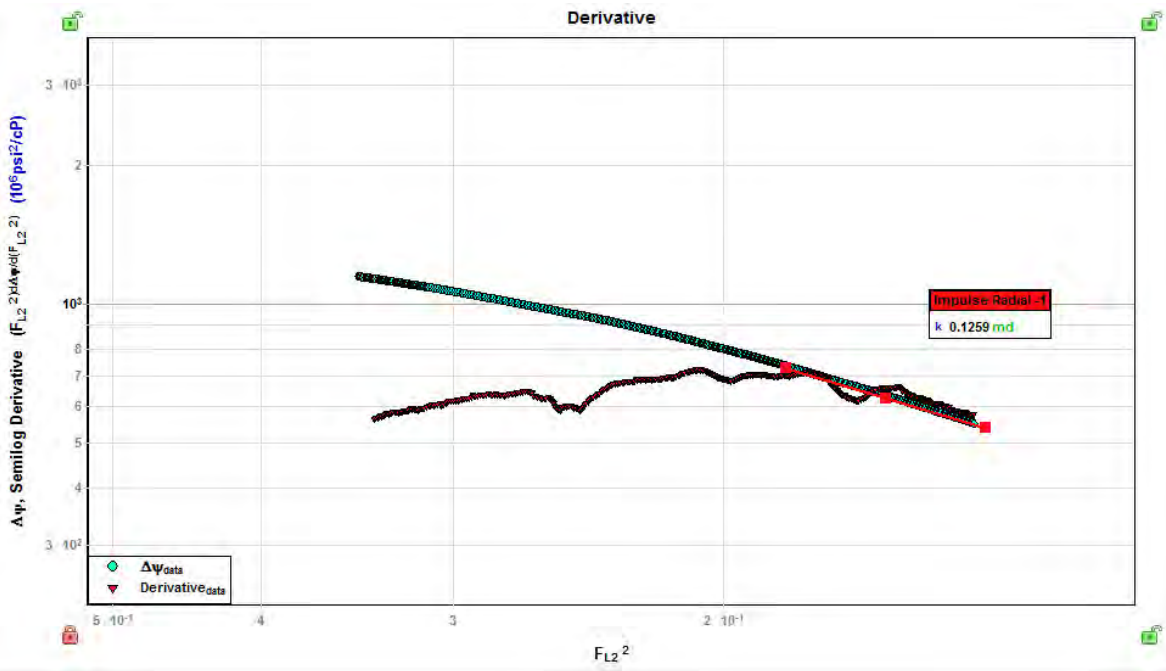


(b) Derivative Analysis (Nolte)

Figure F - 7 : After-Closure analysis plots in Cowralli 8 Stage 3

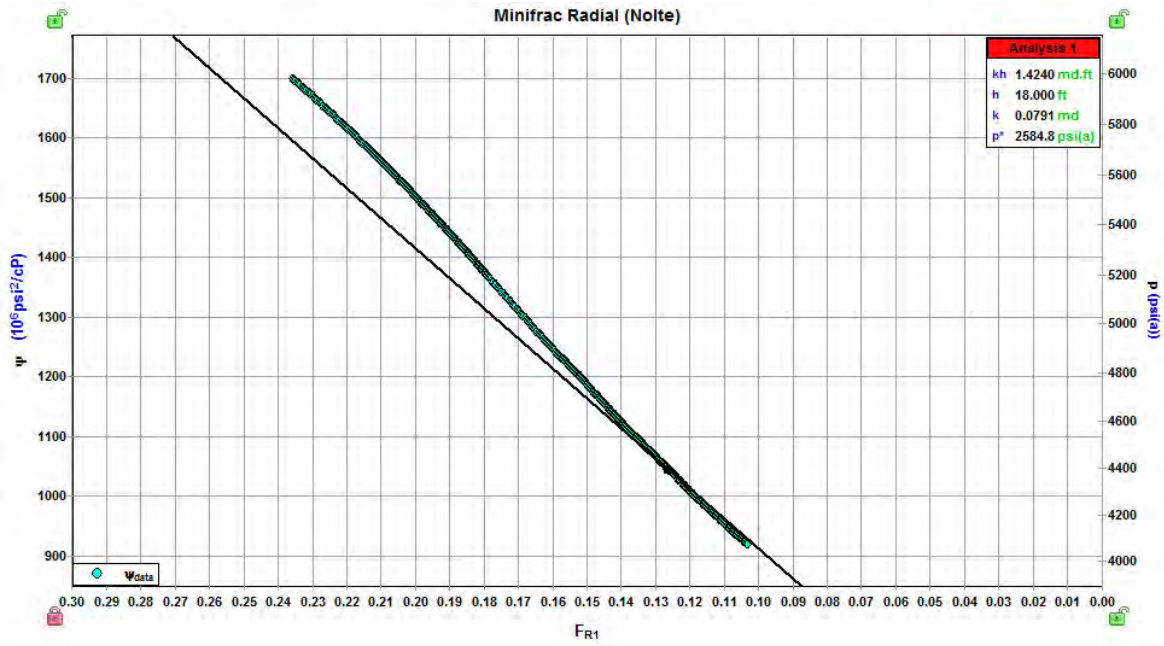


(a) Radial Flow Analysis (Nolte)

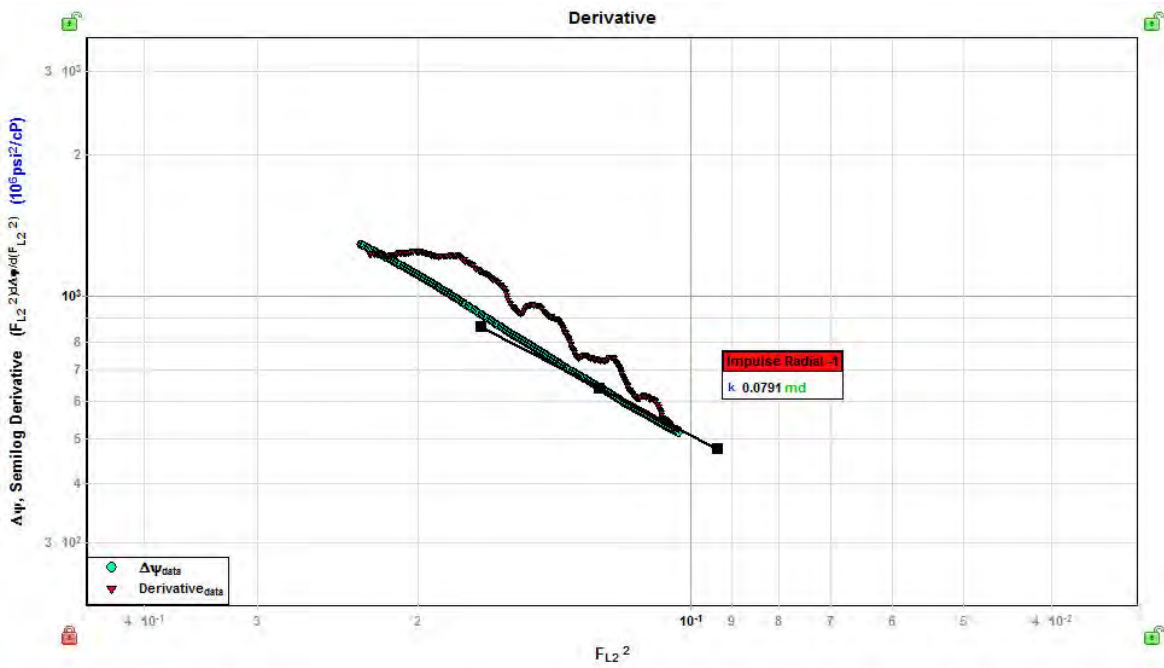


(b) Derivative Analysis (Nolte)

Figure F - 8 : After-Closure analysis plots in Cowralli 8 Stage 5

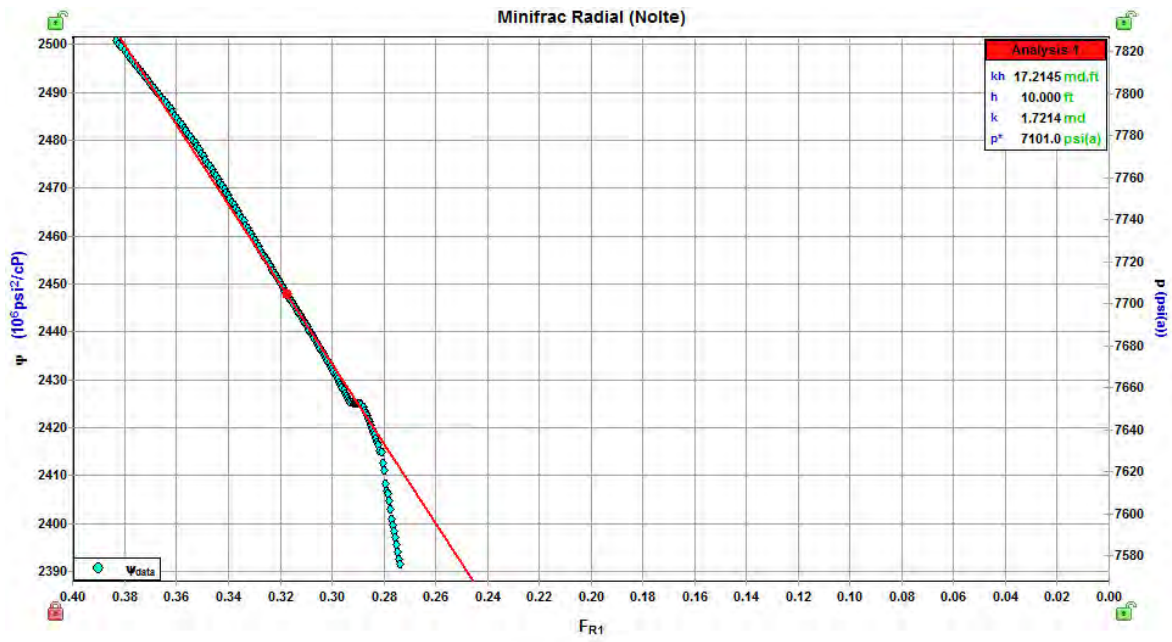


(a) Radial Flow Analysis (Nolte)

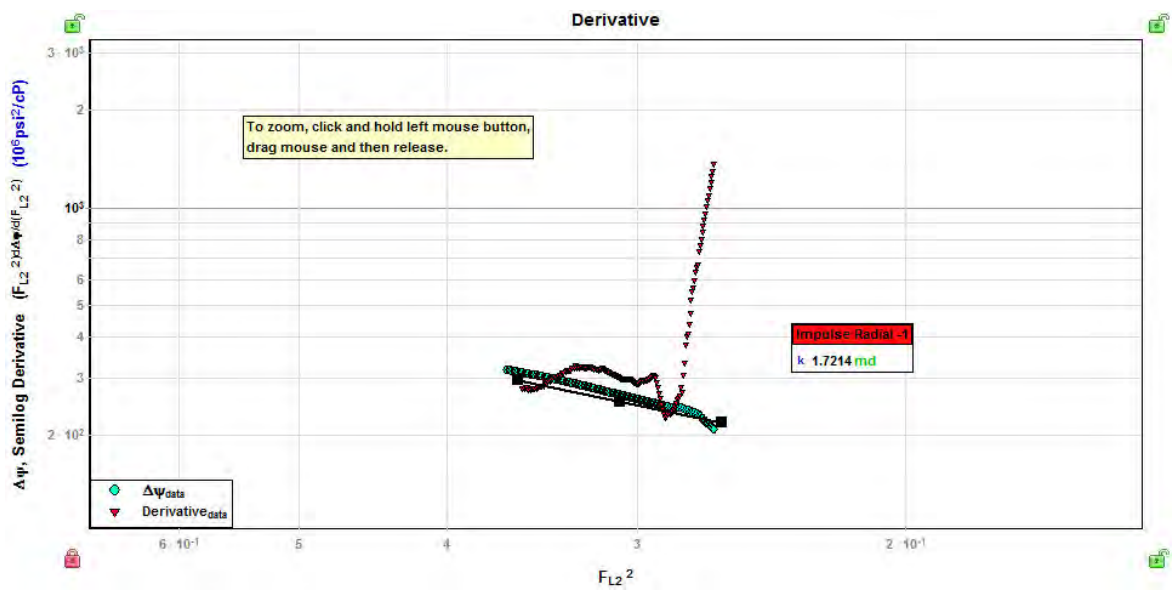


(b) Derivative Analysis (Nolte)

Figure F - 9 : After-Closure analysis plots in Cowralli 8 Stage 6



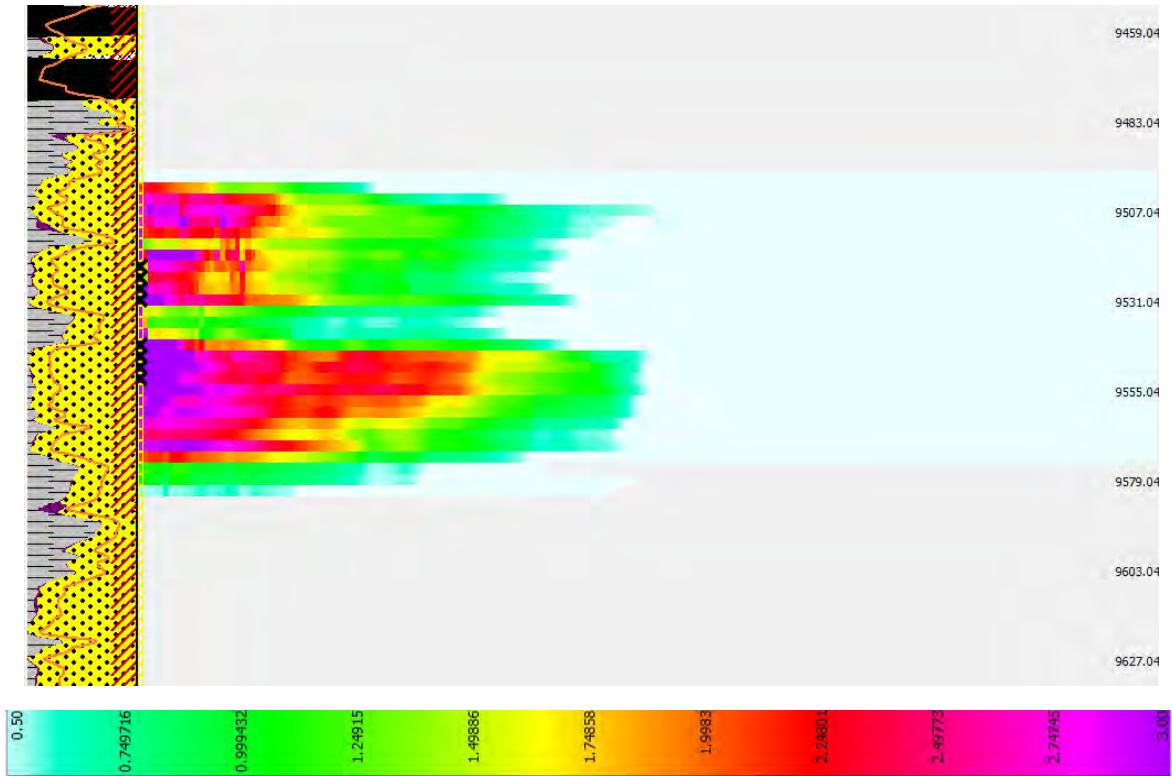
(a) Radial Flow Analysis (Nolte)



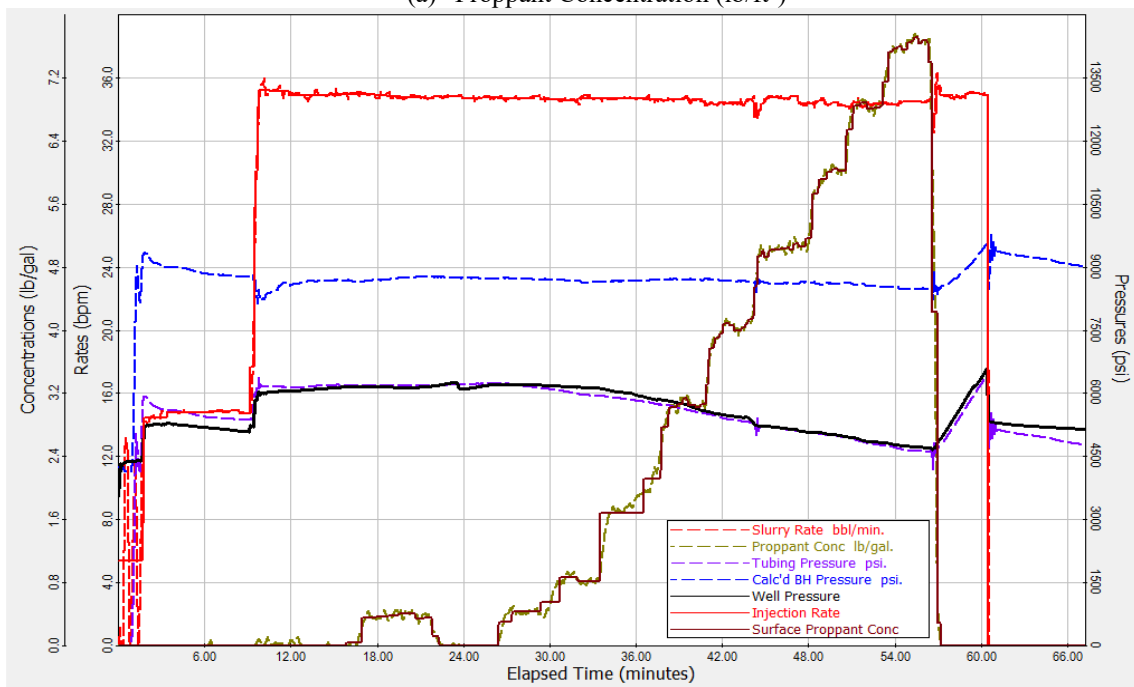
(b) Derivative Analysis (Nolte)

Figure F - 10 : After-Closure analysis plots in Cowralli 8 Stage 7

Appendix G: 3-D Hydraulic Fracturing Models

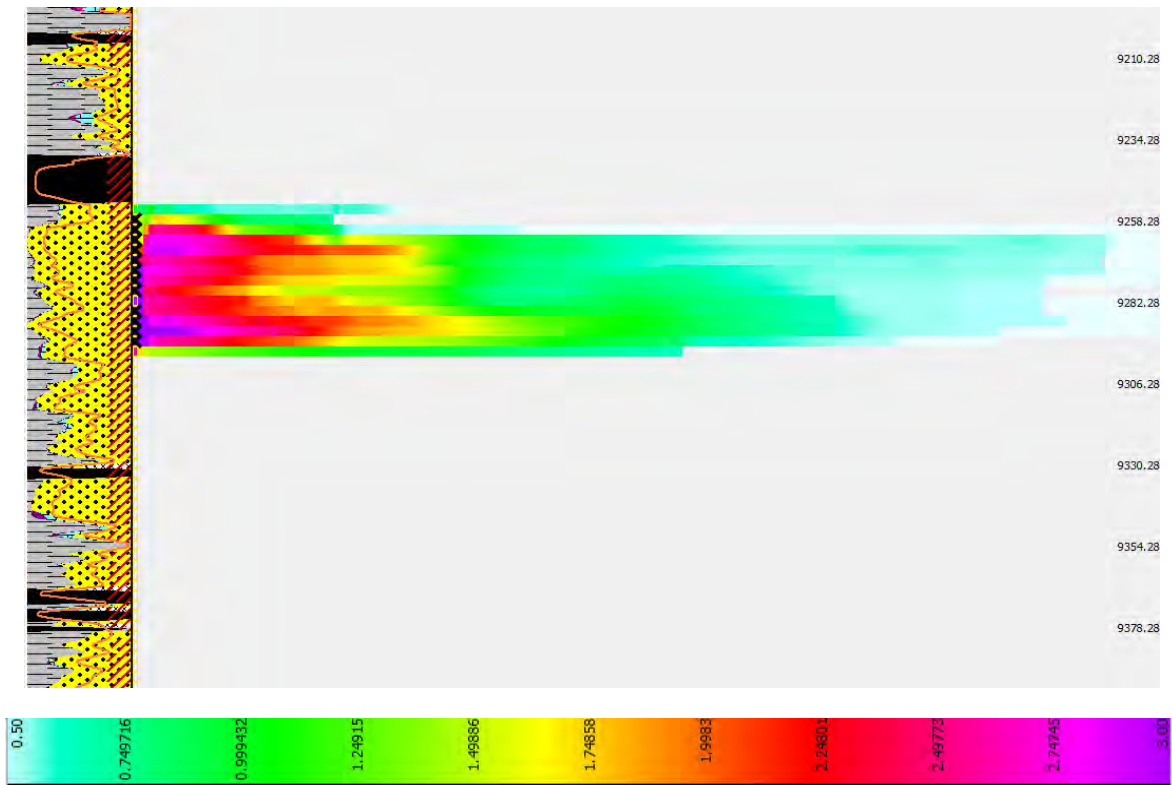


(a) Proppant Concentration (lb/ft²)

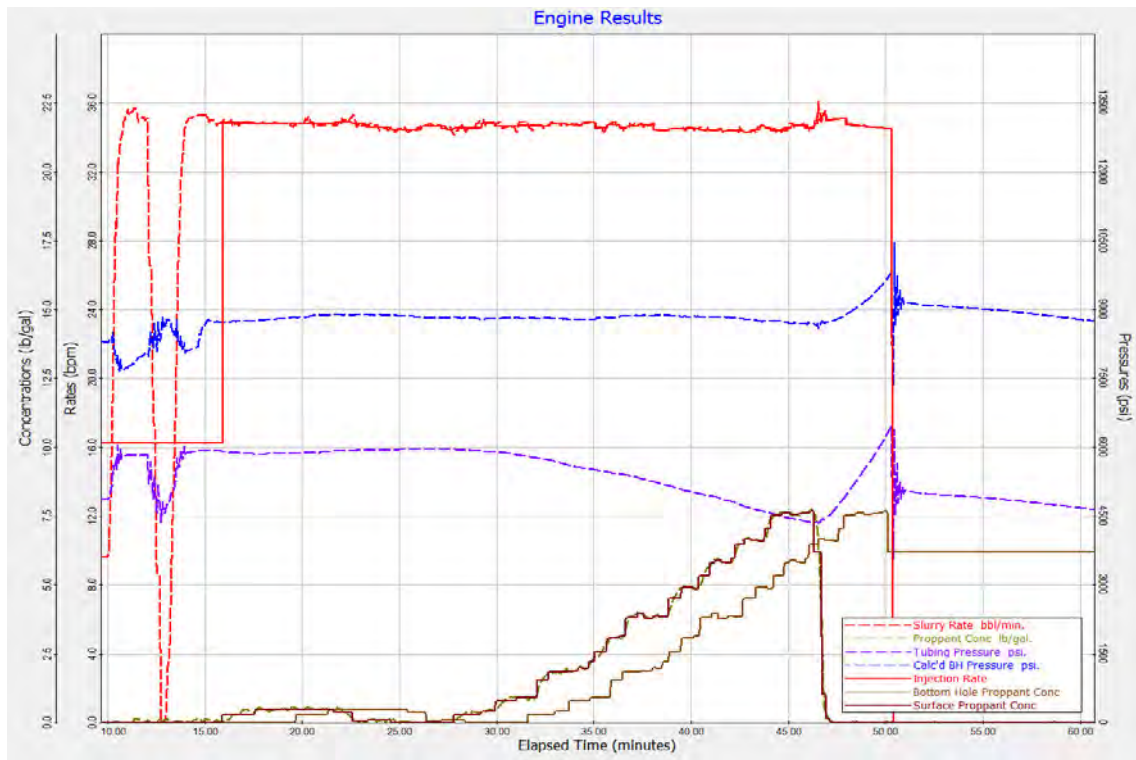


(b) Main Hydraulic Fracturing Treatment

Figure G- 1 : Hydraulic Fracturing Models in Cowralli 6 Stage 1

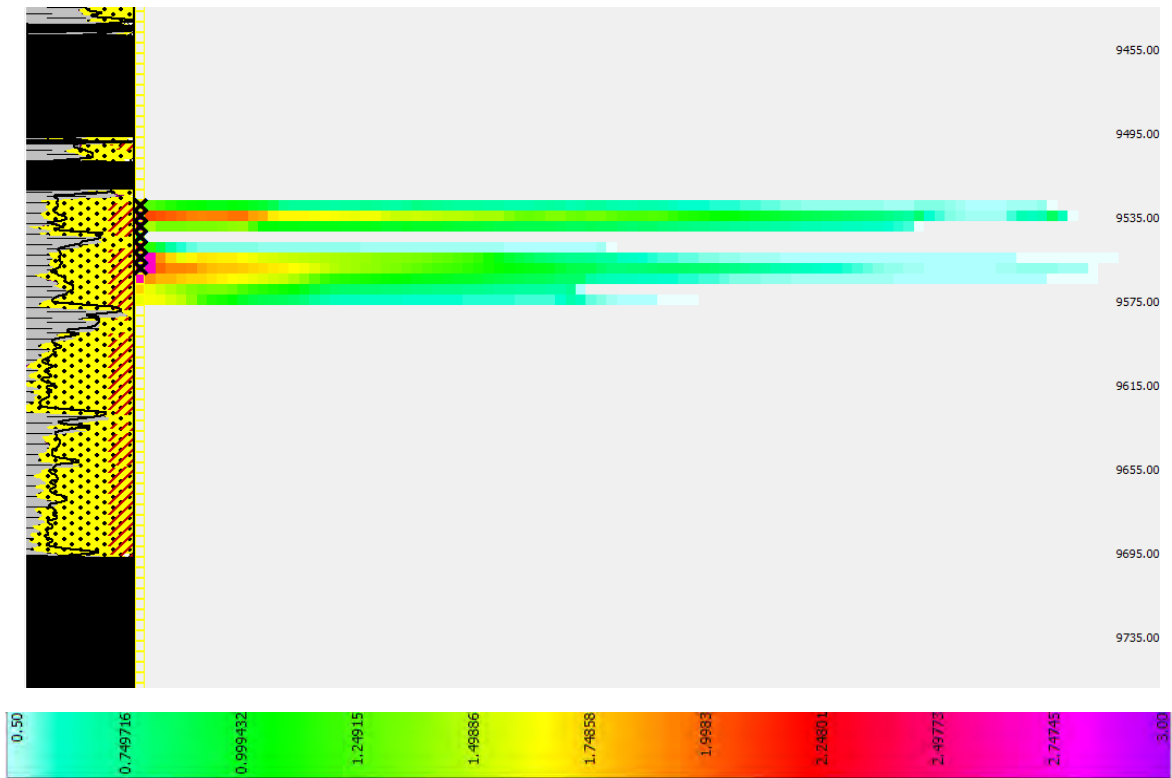


(a) Proppant Concentration (lb/ft²)

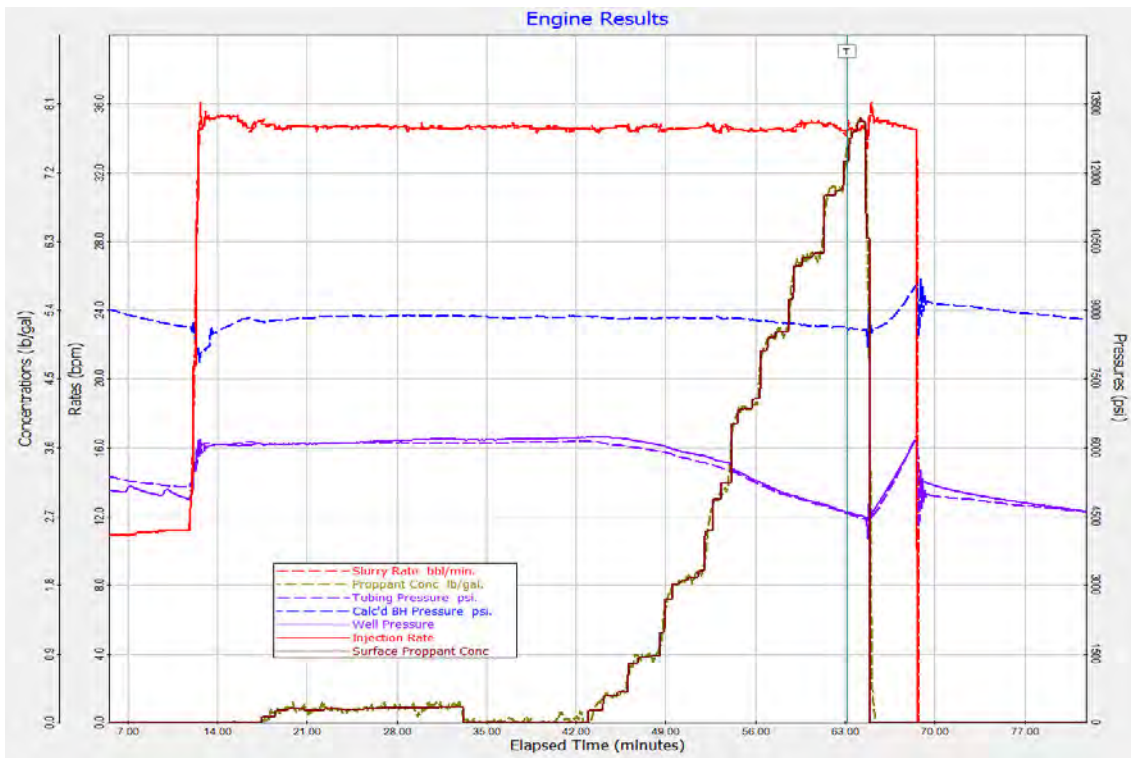


(b) Main Hydraulic Fracturing Treatment

Figure G- 2 : Hydraulic Fracturing Models in Cowralli 6 Stage 2

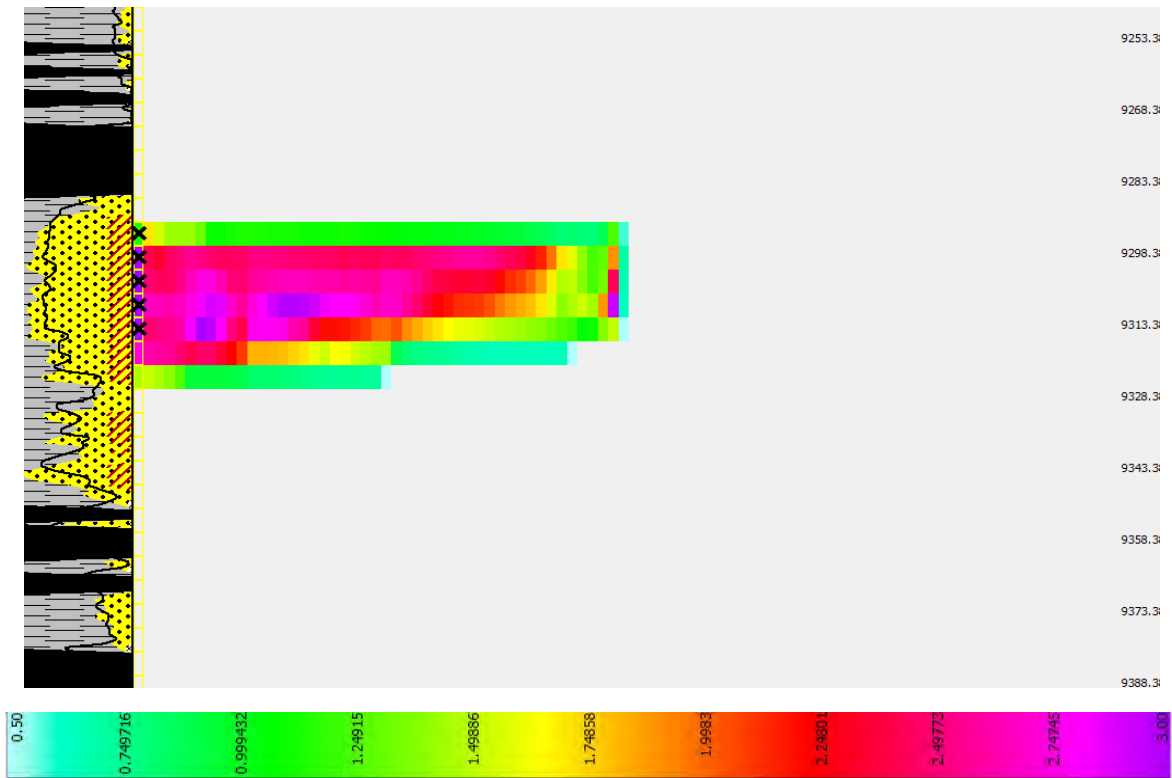


(a) Proppant Concentration (lb/ft²)

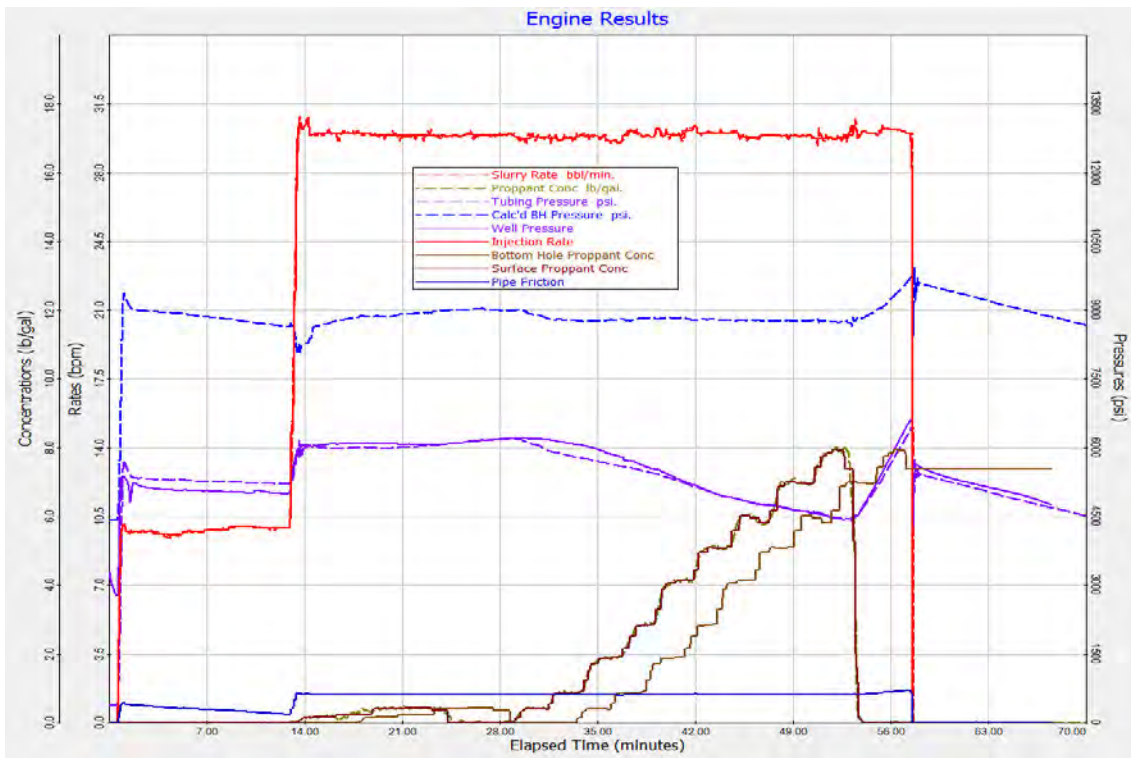


(b) Main Hydraulic Fracturing Treatment

Figure G- 3 : Hydraulic Fracturing Models in Cowralli 7 Stage 1

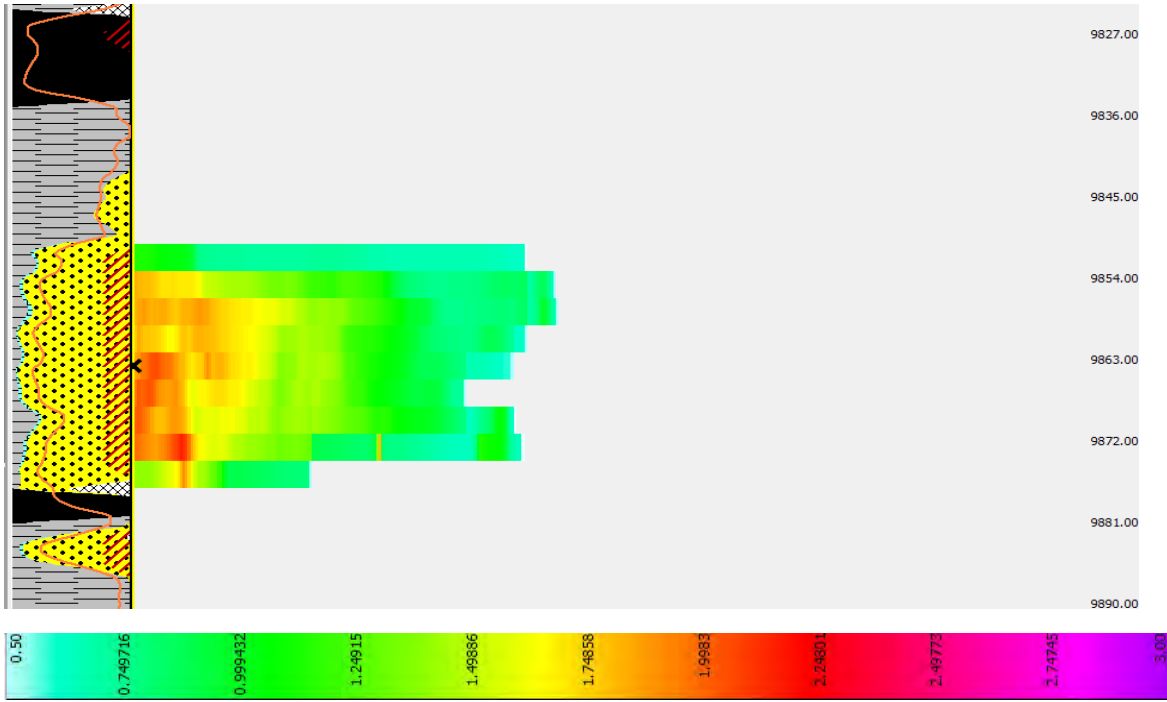


(a) Proppant Concentration (lb/ft²)

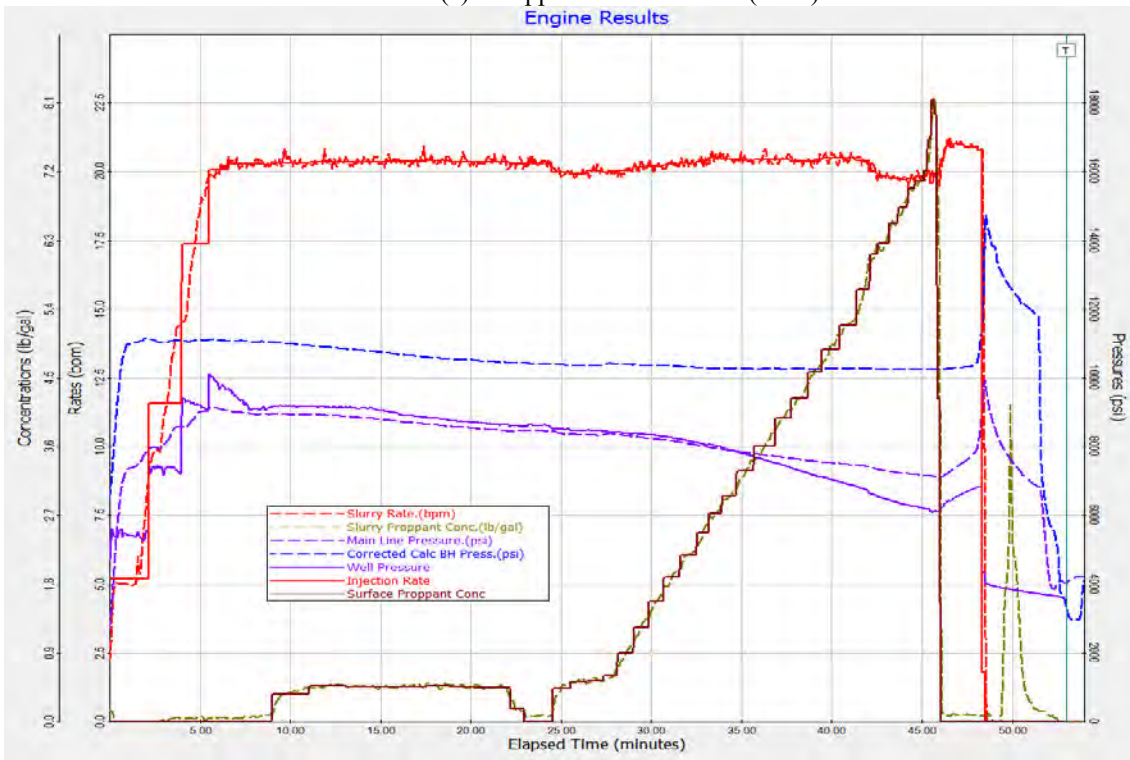


(b) Main Hydraulic Fracturing Treatment

Figure G- 4 : Hydraulic Fracturing Models in Cowralli 7 Stage 2



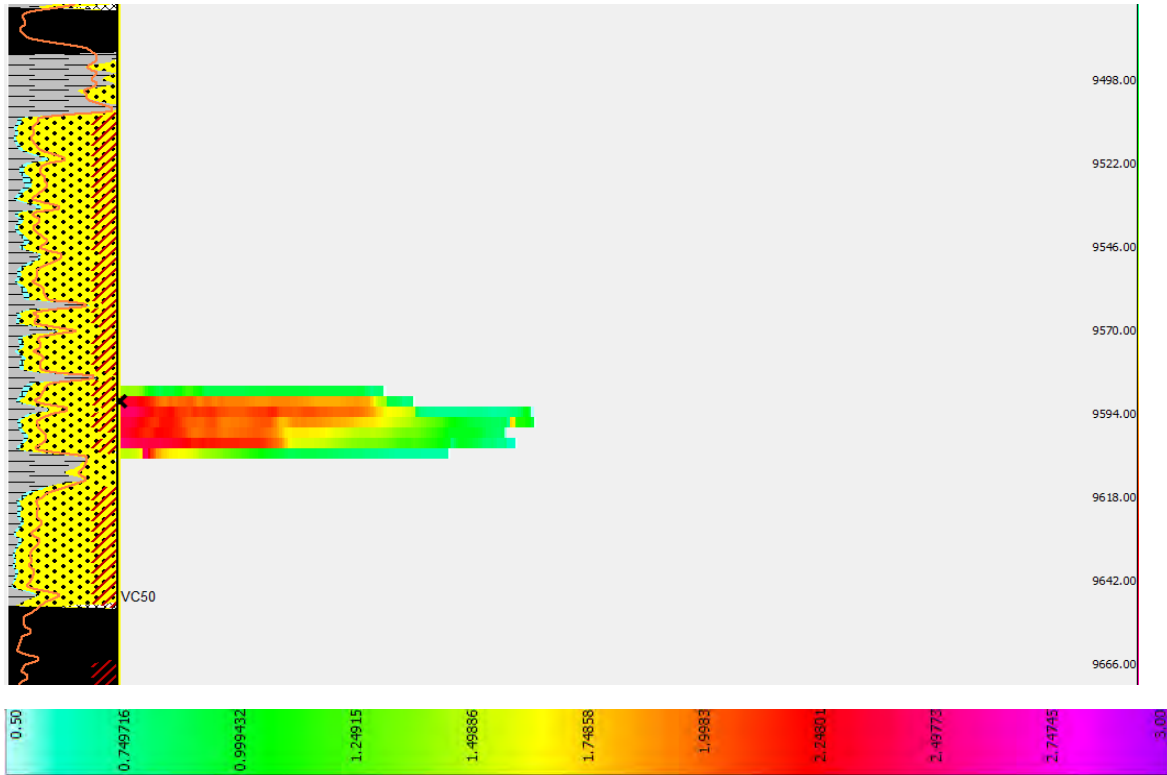
(a) Proppant Concentration (lb/ft²)
Engine Results



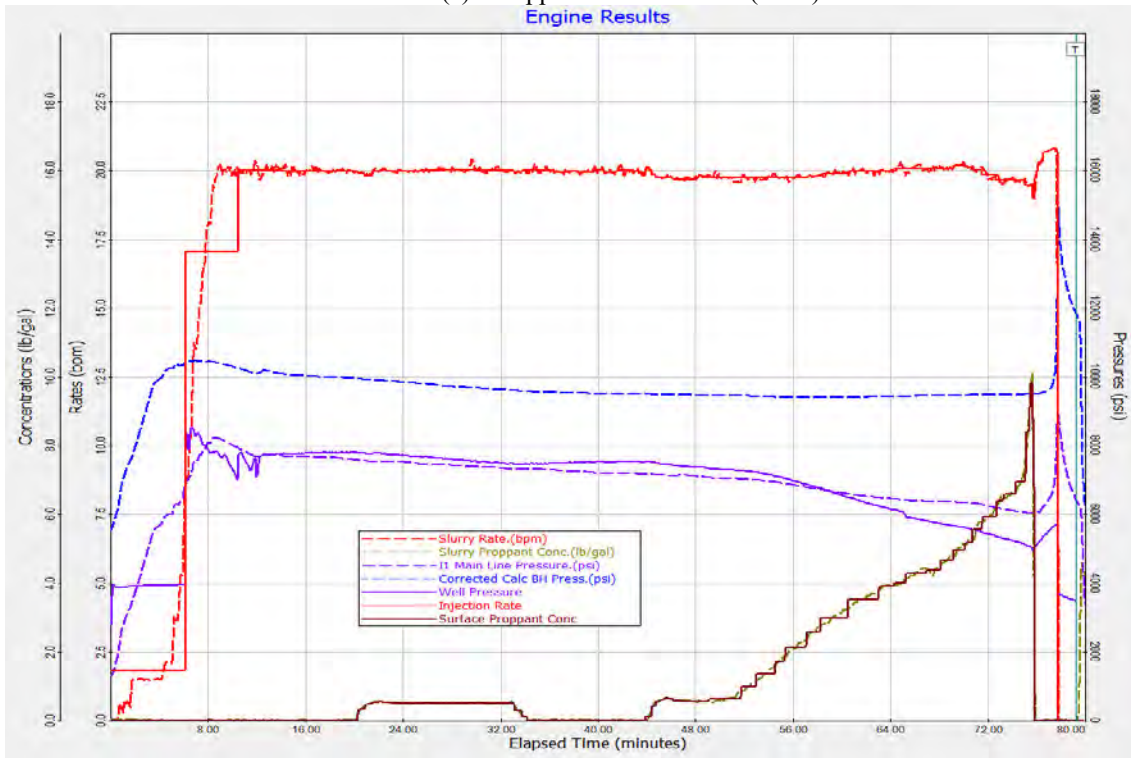
(b) Main Hydraulic Fracturing Treatment

Figure G- 5 : Hydraulic Fracturing Models in Cowralli 8 Stage 2

Notes: Since Cowralli 8 Stage 1 is located in the Tirrawarra Formation, 3D hydraulic fracture simulation was not investigated.

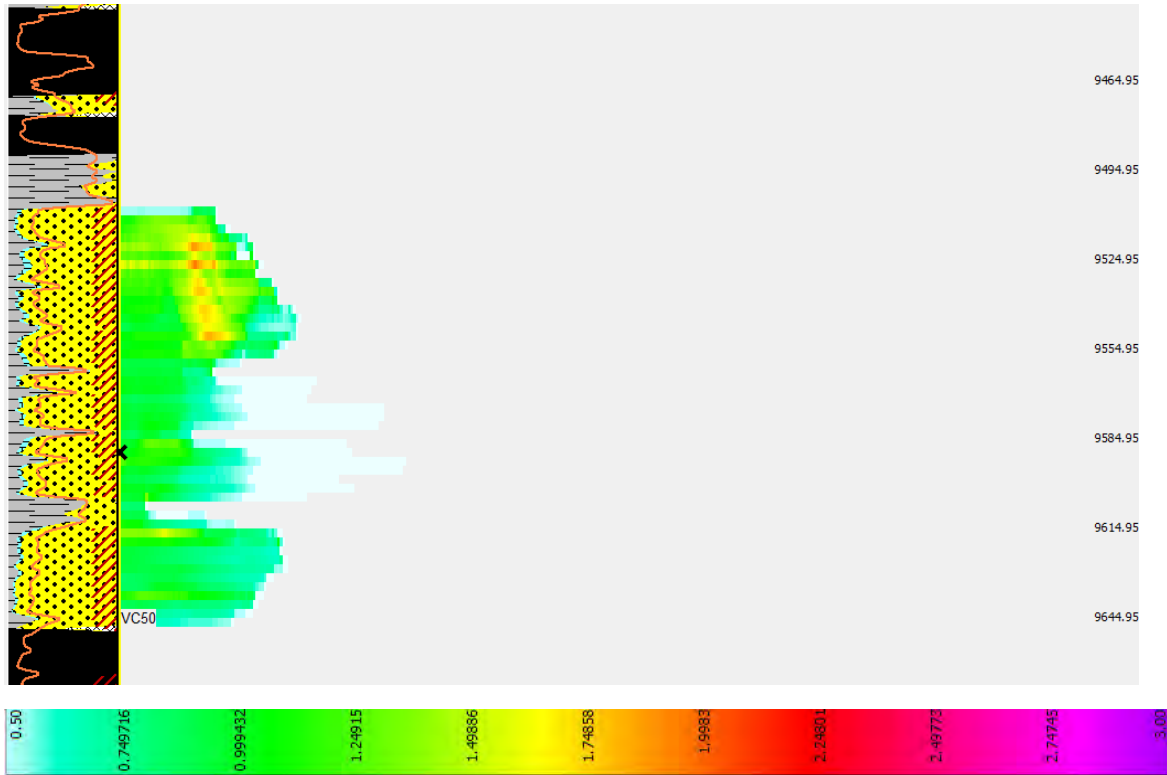


(a) Proppant Concentration (lb/ft²)

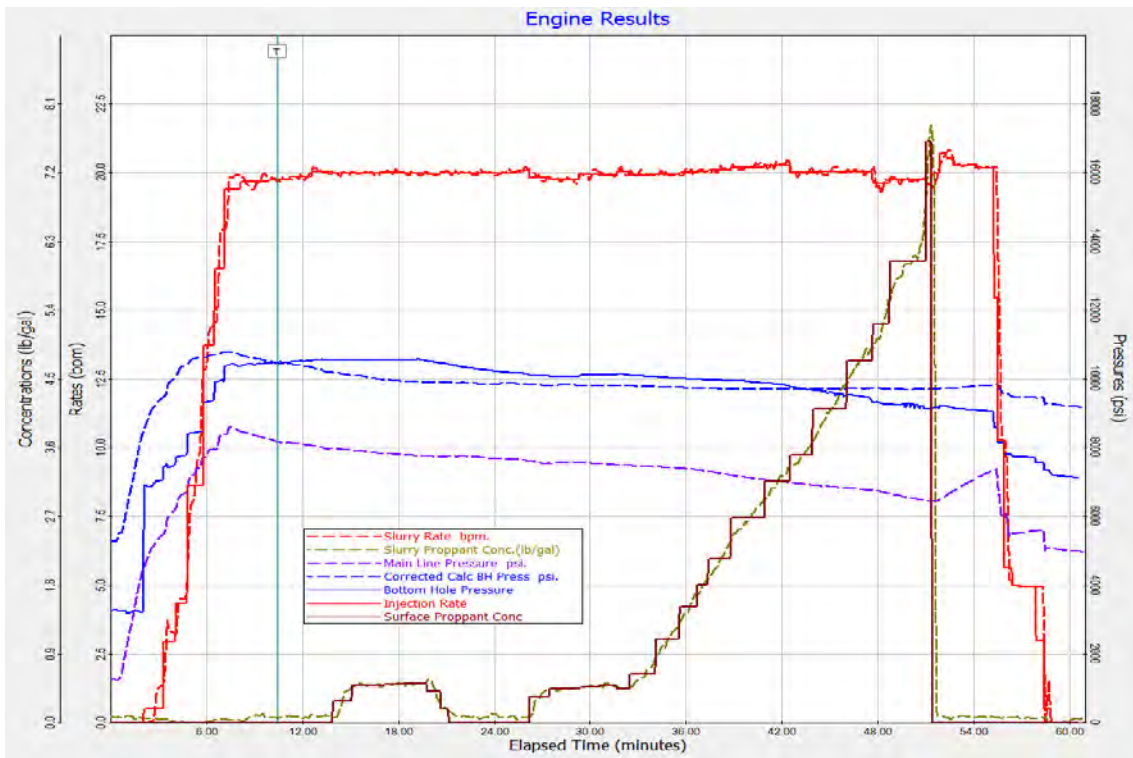


(b) Main Hydraulic Fracturing Treatment

Figure G- 6 : Hydraulic Fracturing Models in Cowralli 8 Stage 3

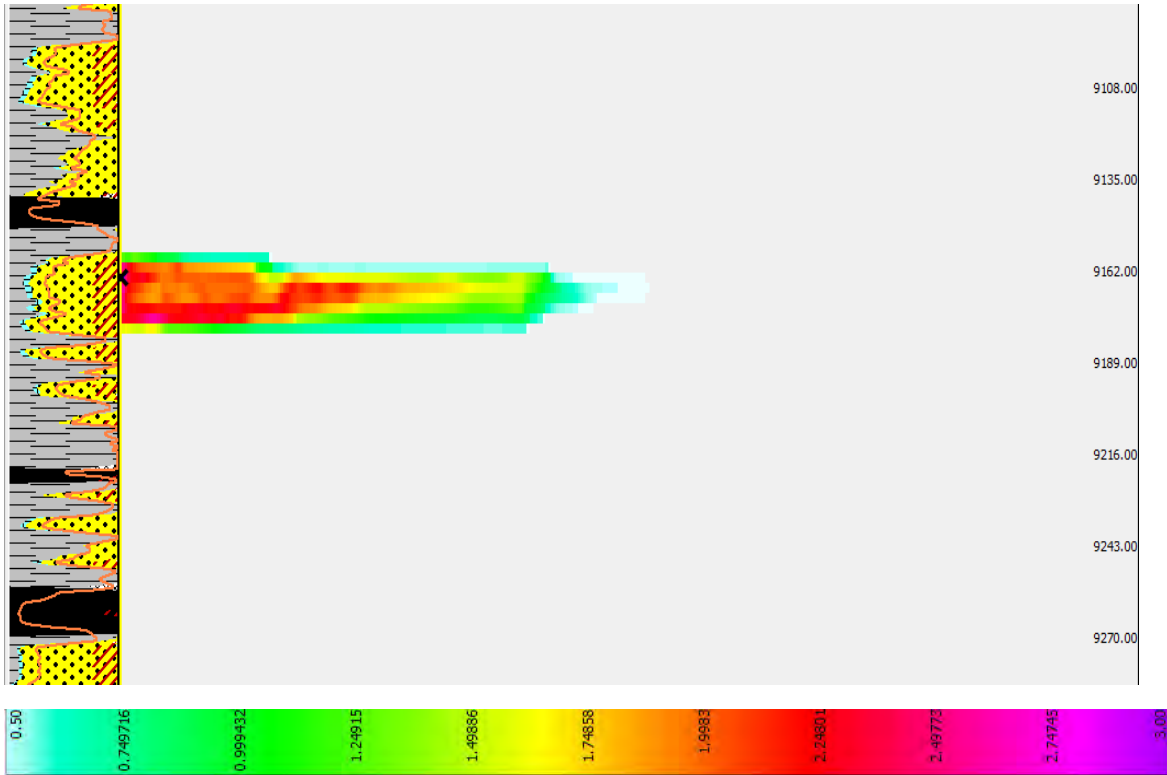


(a) Proppant Concentration (lb/ft²)

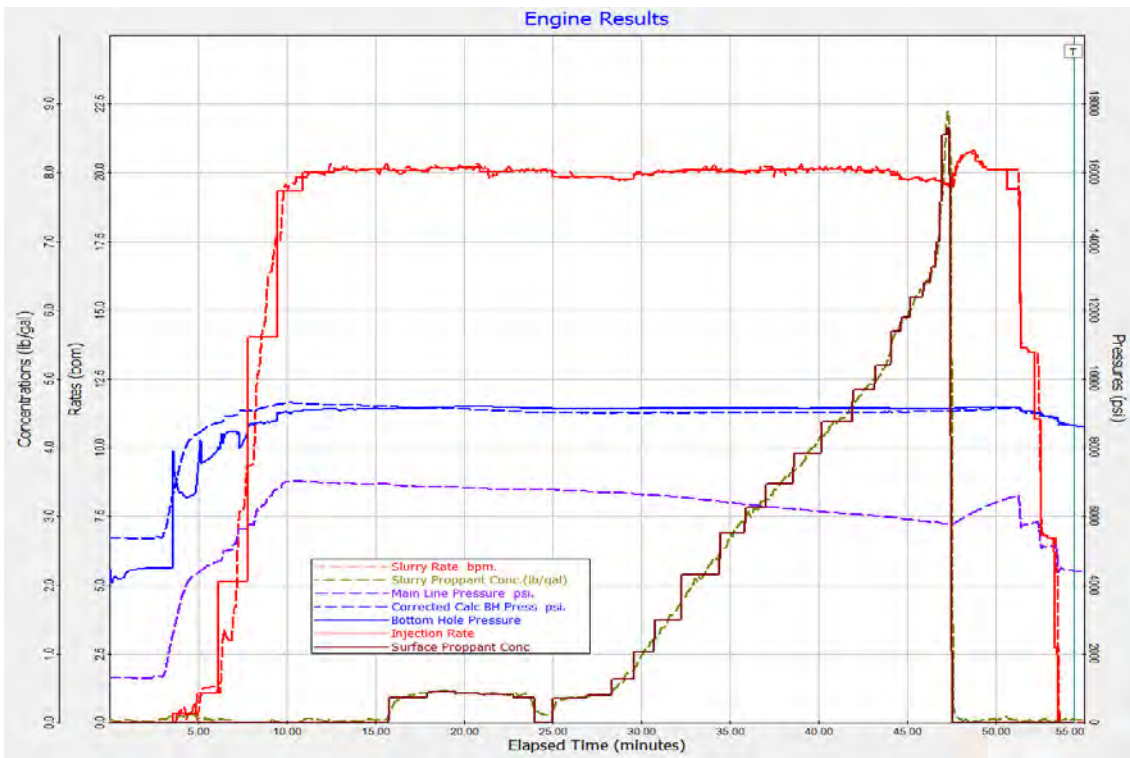


(b) Main Hydraulic Fracturing Treatment

Figure G- 7 : Hydraulic Fracturing Models in Cowralli 8 Stage 4

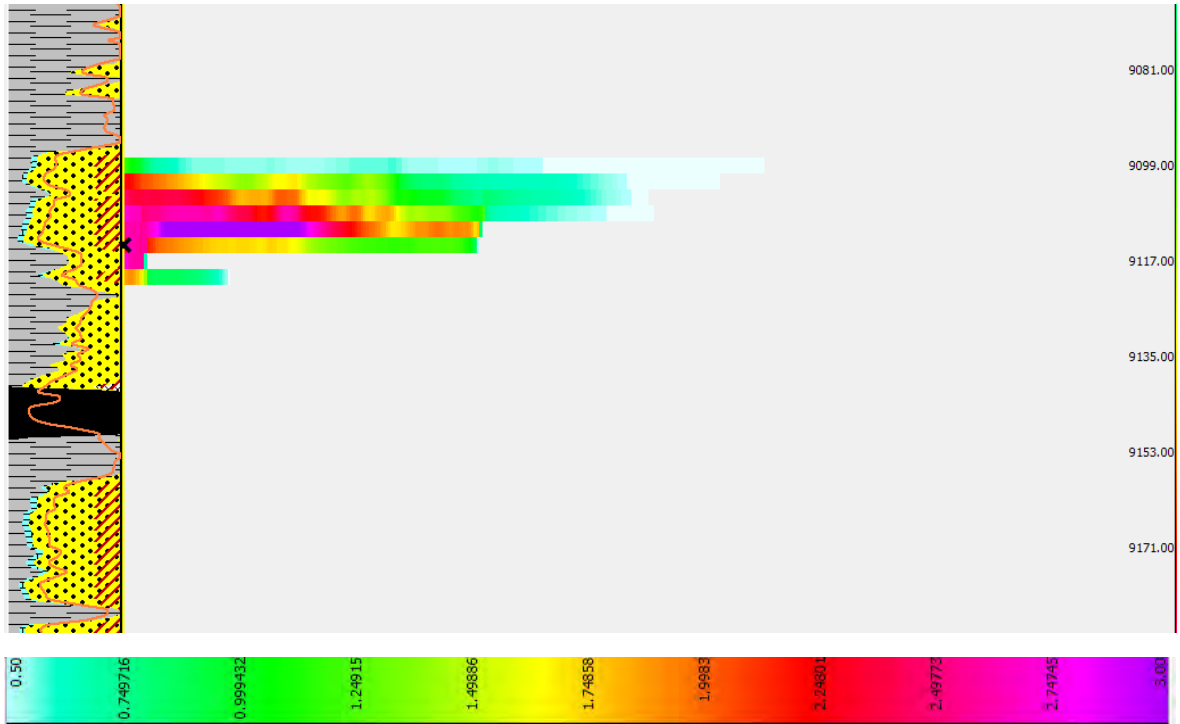


(a) Proppant Concentration (lb/ft²)

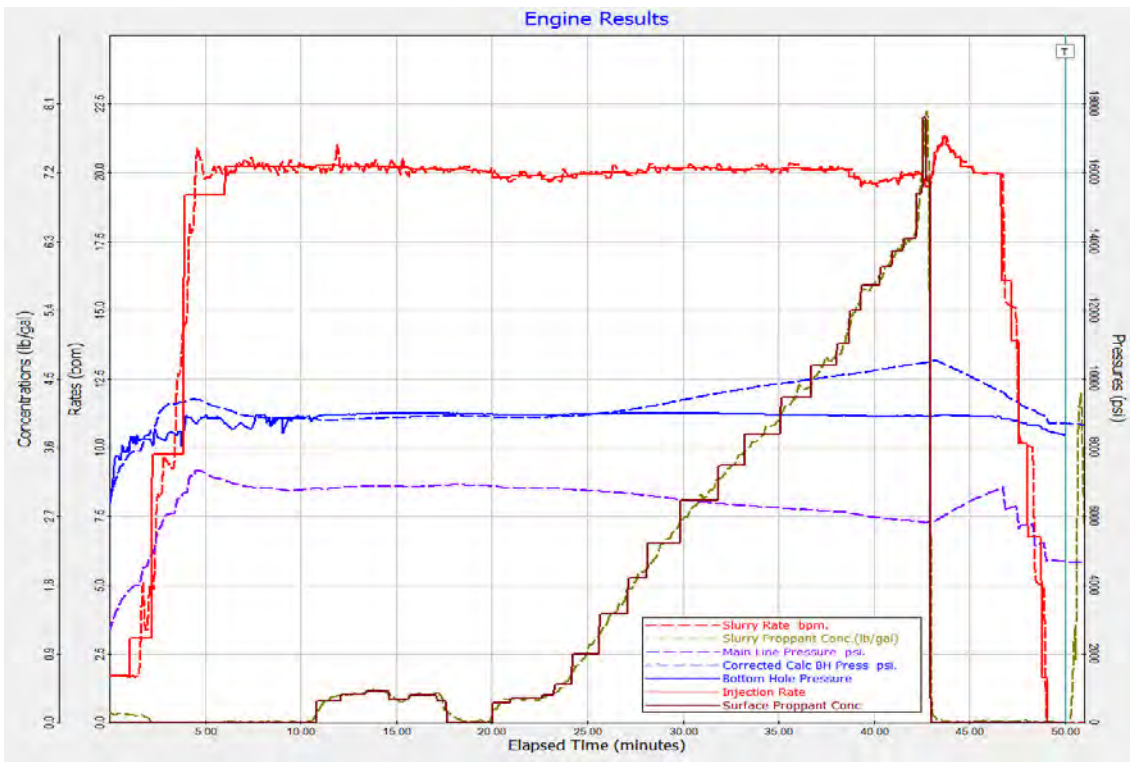


(b) Main Hydraulic Fracturing Treatment

Figure G- 8 : Hydraulic Fracturing Models in Cowralli 8 Stage 5

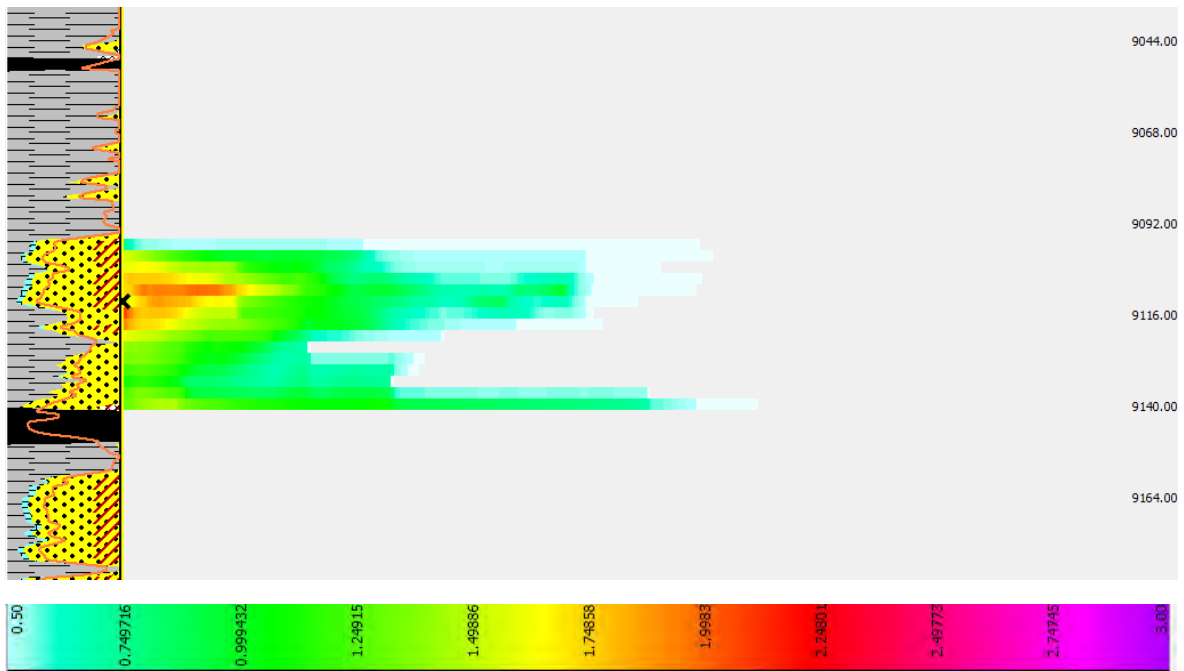


(a) Proppant Concentration (lb/ft²)

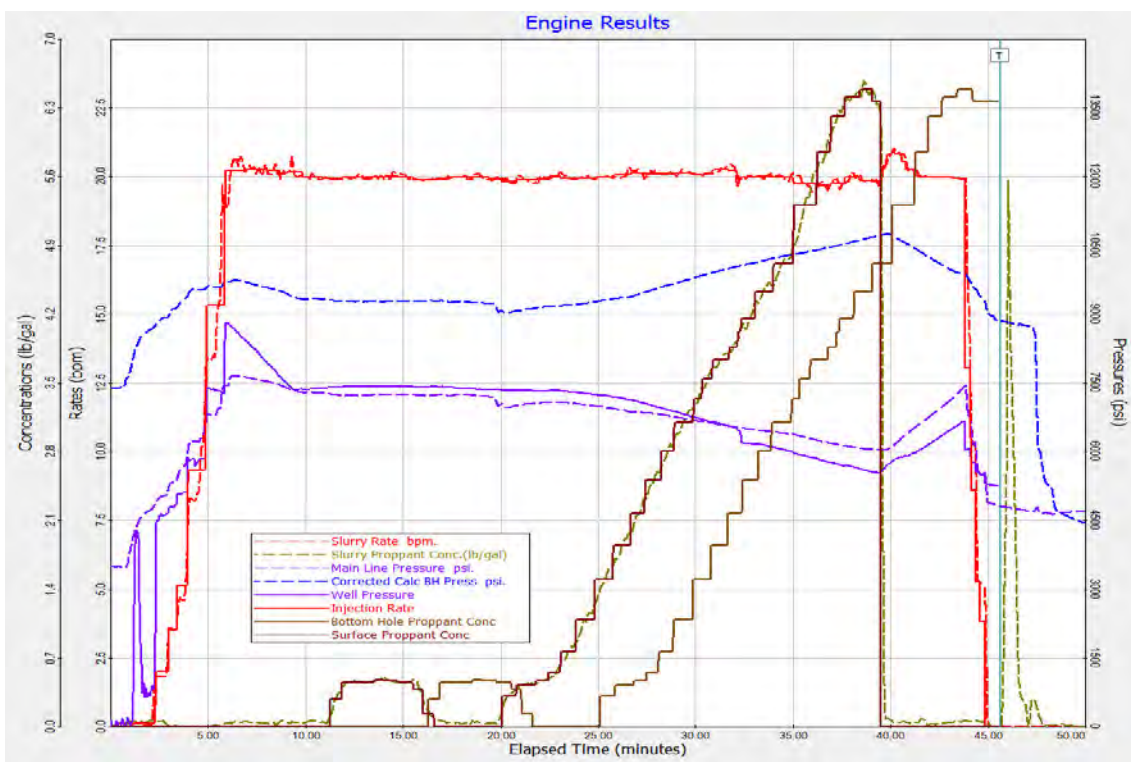


(b) Main Hydraulic Fracturing Treatment

Figure G- 9 : Hydraulic Fracturing Models in Cowralli 8 Stage 6



(a) Proppant Concentration (lb/ft²)



(a) Main Hydraulic Fracturing Treatment

Figure G- 10 : Hydraulic Fracturing Models in Cowralli 8 Stage 7

Appendix H: A Comprehensive Review of the Intracratonic Cooper and Eromanga Basins, Australia

David **Kulikowski**^a (david.kulikowski@adelaide.edu.au)

Khalid **Amrouch**^a (khalid.amrouch@adelaide.edu.au)

Kunakorn **Pokalai**^a (kunakorn.pokalai@adelaide.edu.au)

Michael E. **Gray**^a (michael.e.gray@adelaide.edu.au)

^aAustralian School of Petroleum, University of Adelaide, North Tce, 5005, Adelaide, AUS.

CORRESPONDING AUTHOR: David Kulikowski

KEY WORDS: Cooper Basin; Eromanga Basin; Tectonic; Seismic; Fault; Geophysics.

ABSTRACT

This review focuses on integrating old literature with present-day models to provide a modern summary of Australia's largest onshore hydrocarbon province, the Cooper-Eromanga Basin, with a focus on structural geology and geophysics. A rapid rise in cutting-edge research has been facilitated by exploration companies transitioning away from the nearly extinct anticlinal theory, to technically more challenging plays within the basin. The purpose of this review is to provide new and existing operating companies, and researchers, with a summary of the recent research developments, together with the fundamentals of the basin, to ensure that the tremendous unconventional hydrocarbon potential is effectively extracted. A modern tectonostratigraphic evolution model is presented alongside the stress magnitude, regime and orientation of the six events that have affected the province (N-S Carboniferous Alice Springs Event; SE-NW Mid-Permian Event; NE-SW Late Permian Daralingie Event; E-W Triassic Hunter-Bowe Event; E-W Late Cretaceous Event; N-S Paleogene Event). Integration of these complete paleo-stress tensors with geomechanical models has constrained the dynamic reactivation (shear and tensile) of faults through time to find that since the critical moment (90 Ma), N-S and E-W striking high angle (50-70°) faults were most likely to facilitate hydrocarbon migration. These form the major topics of discussion; however, the temporal and spatial distribution of natural fractures away from the wellbore, seismic time-to-depth conversion methods and accuracies, petroleum systems elements and processes, current and future exploration programs, common hydraulic fracturing and well surveillance programs, and recommendations for future research are also discussed. This review provides a knowledge platform that can be disseminated by new and existing operating companies to provide employees with a broad and up to date overview of this highly prospective basin. The methodologies, cutting-edge research and novel approaches presented here form a framework that can be applied to other hydrocarbon provinces around the world.

1. INTRODUCTION

The Cooper-Eromanga Basin is Australia's largest onshore hydrocarbon province (Fig. 1) and has been producing oil and gas from tight reservoirs since the first natural gas discovery at Gidgealpa in 1963 (Gravestock et al., 1998a; Radke, 2009; Mackie, 2015). The basin is oil and gas saturated and requires the simplest of structural traps, an anticline, for effecting accumulation and preservation (Apak et al., 1997; Gravestock et al., 1998b; Mackie, 2015). As such, much of the early research has focused on basic structural interpretation of sparse two-dimensional (2D) seismic data that remained in the time-domain, with the primary focus of identifying these anticlinal closures (e.g. Stuart, 1976; Veevers et al., 1982; Elliot, 1983; Kuang, 1985; Stanmore, 1989; Apak et al., 1997; Sun, 1997; Gravestock & Jensen-Schmidt, 1996). The lack of detailed research has been further compounded by the limited exposure of rocks at surface, particularly within the South Australian portion of the basin, which has ultimately restricted much of the research to wellbore derived data. However, recent advancements in seismic data acquisition and processing, coupled with novel software applications and approaches, have enabled researchers to better constrain the structural geology and tectonic evolution of the Cooper-Eromanga Basin. A detailed and modern synthesis of this prospective province, with a focus on the structural geology and geophysics, will provide fundamental and up to date understandings that will benefit future hydrocarbon exploration and development programs and highlight the present day research gaps that can be further investigated.

The significantly reduced seismic resolution below Permian coal measures has made research difficult in the past. As a result, the structural and stratigraphic evolution of the province has received conflicting arguments through time, evolving from original models that display normal faults (Kuang, 1985; Gravestock & Jensen-Schmidt, 1996), followed by researchers interpreting the same structures as reverse faults (Apak et al., 1997; Sun et al.,

1997), to most recent studies that have presented evidence for extensive, compressional, and strike-slip faulting (Radke, 2009; Grant-Wooley et al., 2014; Kulikowski et al., 2016c, 2017a; Kulikowski & Amrouch, 2017a, 2017b, 2017c). These models are discussed and integrated with recent research to provide a modern tectonostratigraphic evolution model, which includes paleo-stress orientations, magnitudes and stress regimes that have affected the province through time.

This transition of structural models can also be linked to the improvement, and the use, of seismic time-to-depth conversion methods, which can have a significant impact on: (1) the true measurable fault dip angle; (2) the presence or absence of shallow low relief structures; and (3) pseudo structures resulting from high or low velocity heterogeneities. To promote the use and accuracy of high resolution 3D seismic data in future research, we describe the most commonly used seismic time-to-depth conversion methods, discuss their individual limitations and accuracies, identify the key seismic reflector profiles, and highlight the importance of accurate seismic time-to-depth conversion for future hydrocarbon exploration and research purposes.

Similarly, the improvement of petrophysics, drilling, and hydraulic fracture stimulation technologies has fostered exciting new research on geomechanics, optimisation of drilling programs, and in modelling the intrinsic relationship between hydraulic fracture stimulations and pre-existing natural fractures and faults (Chipperfield et al., 2000; Roberts et al., 2000; Johnson et al., 2002; Johnson and Greenstreet, 2003; McGowen et al., 2007; Scott et al., 2013; Johnson et al., 2015; Pokalai et al., 2016, 2017). Understanding the growth of hydraulic fractures, both temporally and spatially away from the wellbore, has been a strongly debated topic within the province (Scott et al., 2013; Cooke et al., 2015). The high stress environment, the effect of pre-existing natural fractures, the influence of near wellbore pressure loss, and the complexity of intra-formational heterogeneity have contributed to

ineffective hydraulic fracture programs in the past (Scott et al., 2013; Cooke et al., 2015; Pokalai et al., 2016; 2017). These issues, together with current hydraulic fracturing practises and well surveillance programs, are discussed to provide fundamental background information for companies, both existing and new, that are investing in the basin.

This recent influx of high quality detailed research has been driven by the transition to a more technically challenging hydrocarbon exploration strategy. Few undrilled anticlinal traps remain within the basin, facilitating the shift to technically more challenging exploration that is focused on identifying new targets such as stratigraphic traps, basin centred gas, deep coals and polygonal fault related accumulations (Lowe-Young et al., 1997; Morton, 1998; Watterson et al., 2000; Hillis et al., 2001; Radke, 2009; Mackie, 2015). This paradigm shift has tremendous opportunities for new investors and existing companies targeting hydrocarbons within this prolific basin. To facilitate this transition, the purpose of this research is to collate and critically discuss published works and integrate the key findings into a single document that provides: (1) a modern tectonostratigraphic evolution model; (2) a summary of geomechanical modelling results that predict fault and fracture reactivation (tensile and shear) through time to better understand hydrocarbon migration pathways; (3) a synthesis of the petroleum system processes and elements; (4) the spatial and temporal distributions of permeable natural fracture networks; (5) common hydraulic fracturing and well surveillance programs contrast with the common difficulties and risks; (6) a discussion on the seismic time-to-depth conversion methods that are being used and their accuracies and limitations; (7) current and future hydrocarbon exploration and development targets; and (8) a discussion on the future research opportunities that can impact the success of future hydrocarbon programs.

This review paper collates and integrates previous research with modern understandings to form a knowledge platform that can be disseminated by new and existing operating

companies to provide employees with a broad and up to date overview of this highly prospective basin. The detailed methodologies, cutting-edge research and novel approaches form a framework that can be applied to other hydrocarbon provinces around the world.

Insert Fig. 1

2. MODERN TECTONOSTRATIGRAPHIC EVOLUTION MODEL

Unique to this province, the Silurian to Cambrian Warburton Basin, Triassic to Permian Cooper Basin, Cretaceous to Jurassic Eromanga Basin, and Paleogene to Quaternary Lake Eyre Basin are separated in time by regional unconformities that were developed through successive reactivation of pre-existing faults (Fig. 2) (Kantsler et al., 1984; Bradshaw, 1993; Apak, 1997; Gravestock & Jensen-Schmidt, 1998; Mavromatidis, 2006). These vertically stacked basins have unique spatial extents and unique stratigraphy and hydrocarbon potential. The Warburton Basin is considered basement within this region and consists of volcanic, shallow shelf, deltaic and prograding shoreline deposits (Gatehouse, 1986). The Cooper Basin is the most hydrocarbon-rich, with a large volume of Permian coals that cycle with intra-formational sandstone and shale (Kantsler et al., 1984; Apak et al., 1997; Alexander et al., 1998). The Cooper Basin consists mostly of sediments deposited by fluvial, lacustrine, and swamp conditions. The Eromanga Basin is also hydrocarbon-rich with many of the present day exploration programs targeting oil-rich Jurassic and Early Cretaceous sediments primarily along the western flank of the basin (Lowe-Young et al., 1997). The depositional environment during this time transitioned from fluvial, lacustrine, deltaic, shoreface marine, and open shallow marine (Lowe-Young et al. 1997). The Lake Eyre Basin is presently exposed at surface with no hydrocarbon potential.

The Permian coals are the major hydrocarbon source rock of the basin, and increase in thickness in the South Australian portion of the basin. As such, the major exploration and

development targets are located within South Australia (Reynolds et al., 2006). This portion of the basin contains two NE-SW striking ridges; the Gidgealpa-Merrimelia-Innaminka (GMI) Ridge and the Murteree-Nappacoongee (MN) Ridge (Fig. 3b) (Kuang, 1985; Apak et al., 1997; Gravestock & Jensen-Schmidt, 1998). These prominent ridges form the major hydrocarbon fields in the basin and also separate the NE-SW elongate Patchawarra, Nappamerri and Tenappera troughs (Fig. 3). In the following sections, the structural and stratigraphic evolution of this intra-cratonic region will be discussed, with emphasis on the most up-to-date research.

Insert Fig. 2

Insert Fig. 3

2.1 Pre-Cambrian Extension (650-575 Ma)

During the Late Proterozoic much of the world's landmass was submerged by ocean with a relatively small landmass exposed at surface, consisting of portions of Antarctica, India, South Africa, Congo, and the western portion of Australia (Fig. 4a) (Myers et al., 1996; Boger & Miller, 2003; Collins & Pisarevsky, 2005; Kulikowski and Amrouch, 2017). The ancient Australian landmass was in a similar geometry to present day; slightly rotated in a clockwise direction and bisected in an NNE-SSW direction by the paleo-tectonic plate boundary (Myers et al., 1996; Boger & Miller, 2003; Collins & Pisarevsky, 2005). This boundary is now referred to as the Tasman Line that separates the younger land mass in eastern Australia from the rest of the continent (Haines et al., 2002). Rifting within the Panthalassic Ocean, east of ancient plate, began in the Late Proterozoic (650 Ma) in an approximately SE-NW direction. This regional rifting event affected the then Centralian Superbasin as well as the Warburton Basin, developing SE-NW striking strike-slip faults and NE-SW striking normal faults within the Igneous Meta-sedimentary rocks named the

Willyama Supergroup (Veevers & Powell, 1984; Evan, 1988; Apak et al., 1997). These basin- to continent-scale SE-NW strike-slip faults are present within many other Australian provinces (Myers et al., 1996; Gibson et al., 2013).

Deep fault development during the Early Cambrian was concurrent with exhumation of the Mooracoochie Volcanics, which marks the base of the Warburton Basin stratigraphy (Gatehouse, 1986; Sun, 1997; Meixner et al., 2000). Continued extension developed accommodation space for the deposition of shallow shelf sediments that became the Diamond Bog Dolomite (~510 Ma), Coongie Limestone Member (~505-497 Ma), and Kalladeina Formation (~508-485 Ma) (Gatehouse, 1986). As relative sea levels rose, the depositional environment transitioned into low-stand fan, deltaic, and prograding shoreline, which deposited the Narcoonowie Formation (~490 Ma), Pando Formation (~488 Ma), and Innamincka Formation (~485-435 Ma) (Gatehouse, 1986; Rezaee & Sun, 2007). Regional erosion of the upper Innamincka Formation represents the unconformable boundary to the overlying Permian to Triassic Cooper Basin.

Insert Fig. 4

2.2 Carboniferous Alice Springs Event (450-300 Ma)

The Alice Springs Event (ASE) has had a significant influence on the tectonic development of central and northern Australia (Haines et al., 2002). Its effect has been recorded in a number of petroleum basins and structural provinces, including the Amadeus, Ngalia, Georgina, Wiso, Officer, and Warburton basins, as well as the Arunta and Musgrave inliers (Haines et al., 2002). Calcite twin, natural fracture and fault data from within the South Australian portion of the Warburton Basin has constrained this regional tectonic event to have occurred under a strike-slip stress regime with maximum principal stress in an N-S direction in this region (Fig. 4b) (Kulikowski & Amrouch, 2017a). The effective maximum

principal stress magnitude was also calculated (49 MPa) through calcite twin stress inversion (Fig. 4i) (Kulikowski & Amrouch, 2017c). Geomechanical modelling of fault reactivation under this paleo-stress tensor identified N-S and NE-SW striking high angle (50-70°), and SE-NW striking strike-slip faults to be the most likely to reactivate (Kulikowski & Amrouch, 2017c). A NNE-SSW and SE-NW striking vertical conjugate natural fracture set was developed during this event and is present only within the Warburton Basin stratigraphy (Kulikowski & Amrouch, 2017a).

As mentioned earlier, the stratigraphy of this region contains a regional unconformity that separates the Warburton and Cooper basins and is a result of basement fault reactivation, exhumation and erosion of upper Warburton Basin sediments. Carboniferous Big Lake Granodiorite was also exhumed during this event in local regions south of the GMI Ridge and provides elevated contemporary temperature gradients due to their high uranium content (Meixner et al., 2000; Kulikowski et al., 2016a). The Australian continent remained connected to Antarctica during this time and exposed to plate scale glaciation (Collins & Pisarevsky, 2000; Gray & Foster, 2004; Metcalfe, 2013).

As the continent began to escape glaciation during the Late Carboniferous to Early Permian, the glacial Merrimelia Formation (~290 Ma) was deposited onto the regional unconformity, marking the base of the Cooper Basin. The overlying Tirrawarra Formation (~287 Ma) was deposited under a postglacial outwash to braided fluvial depositional environment (Lowe-Young et al., 1997; Mavromatidis, 2006). The Tirrawarra Formation is produced for oil, albeit being deeper and under higher temperatures and pressures than the gas-rich middle to upper Permian and Triassic reservoirs (Gravestock et al., 1998a). The depositional environment transitioned into fluvio-deltaic, lacustrine and swamp during the middle Permian, and deposited repeated cycles of sandstone, shale, and coal to compose the

predominantly gas-rich Patchawarra Formation (~285-260 Ma) (Kantsler et al., 1984; Apak et al., 1997; Alexander et al., 1998).

2.3 Mid-Permian Event (290-270 Ma)

During deposition of the Patchawarra Formation, intra-formational on-lapping is observed from seismic data along paleo-structural highs, which are more often than not also the present day structures (Apak et al., 1997; Gravestock & Jensen-Schmidt, 1998). On-lap is observed between 273 and 270 Ma, inferring that structural highs were present during the Mid-Permian and limited the accommodation space (Apak et al., 1996; Kulikowski & Amrouch, 2017a, 2017b). Seismic interpretation aligns with stress inversion of calcite twin, natural fracture and fault data, which demonstrate a compressional SE-NW oriented event with an effective maximum principal stress magnitude of 56 MPa (Fig. 4i) (Kulikowski & Amrouch, 2017a, 2017c). The far-field stresses likely originated from the approximately NE-SW to N-S striking subduction line along the eastern margin of Australia (Fig. 4c). The paleo-stress conditions likely reactivated E-W, NE-SW and N-S striking high angle (50-70°) faults and developed a regional NE-SW striking low dip angle (30°) conjugate natural fracture set within the Patchawarra, Tirrawarra and Merrimelia formations and also within basement (Kulikowski & Amrouch, 2017a, 2017c).

As compression from the short lived Mid-Permian Event eased, the upper Patchawarra Formation became finer grained and more shale dominated (Apak et al., 1997). An east to west transgression ended the deposition of the Patchawarra Formation, transitioning into a shoreface and lacustrine dominated environment that deposited the Murteree Shale (~264 Ma), Epsilon Formation (~262 Ma), Roseneath Shale (~260 Ma), and Daralingie Formation (~258 Ma) (Bradshaw, 1993; Apak et al., 1997; Lowe-Young et al., 1997; Gravestock & Jensen-Schmidt, 1998; Mavromatidis, 2006). The Roseneath-Epsilon-Murteree (REM) stratal

unit represents the major shale gas play in the region with total organic carbon (TOC) values ranging between 1.0 and 4.1% (Jadoon et al., 2016).

2.4 Late Permian Daralingie Event (258 Ma)

Following the deposition of the Daralingie Formation, an erosional unconformity was first identified in 2D seismic data (Apak et al., 1996) and later confirmed through calcite twin stress inversion analysis (Kulikowski & Amrouch, 2017a). This SE-NW oriented strike-slip stress regime event recorded an effective maximum principal stress magnitude of approximately 56 MPa (Fig. 4i) that reactivated NE-SW striking high angle (50-70°) faults (Kulikowski & Amrouch, 2017c). This event is most notable along the NE-SW striking GMI and MN ridges, as a significant portion of the Daralingie Formation was eroded from these areas (Kuang, 1985; Apak et al. 1997; Mavromatidis, 2006). New fracture and fault development was absent during this time, with the stress preferentially accommodated along pre-existing faults (Kulikowski et al., 2017a). The far-field stress was likely related to the N-S striking subduction zone east of Australia during this time (Fig. 4d) (Kulikowski & Amrouch, 2017a).

2.5 Upper Triassic Hunter-Bowen Event (245-190 Ma)

Post-compressional flexural relaxation, or sag, followed the Daralingie Event and generated accommodation space for the deposition of the Toolachee Formation (~250 Ma) that consists of sands, shales and coals deposited under meandering fluvial to deltaic conditions (Kantsler et al. 1984; Apak et al. 1997; Lowe-Young et al., 1997). The depositional environment transitioned to a floodplain, lacustrine and fluvial channel system in the Triassic, depositing the Nappamerri Group, which includes the Callamurra Member (~245 Ma), Panning Member (~243 Ma), Wimma Sandstone Member (~241 Ma), Tinchoo Formation (~238 Ma), and the Cuddapan Formation (~210 Ma) (Kantsler et al. 1984; Apak et al. 1997; Lowe-young et al.,

1997; Alexander et al. 1998; Mavromatidis, 2006). The early Nappamerri Group was likely charged with oil and gas from the underlying Toolachee Formation, and perhaps along fault conduits from the deeper early Permian source rocks (Lowe-Young et al., 1997).

A regional erosional unconformity is carved into the upper Tinchoo Formation and the majority of the Cuddapan Formation, which is only present in local areas of the basin (Lowe-Young et al., 1997). This unconformity separates the Cooper and Eromanga basins and marks the timing of the Hunter-Bowen Event. The maximum principal stress was horizontal and in an E-W direction (Fig. 4e) (Kuang, 1985; Apak et al., 1997; Gravestock & Jensen-Schmidt, 1998; Kulikowski & Amrouch, 2017a). The regional erosional boundary was first interpreted from 2D seismic data (Kuang, 1985; Apak et al., 1997) and later confirmed through calcite twin stress inversion, and natural fracture and fault stress inversion (Kulikowski & Amrouch, 2017a). Calcite twin stress inversion results identified an E-W oriented compressional event with an effective maximum principal stress magnitude of 60 MPa (Fig. 4i) corresponding to the Hunter-Bowen Event (Kulikowski & Amrouch, 2017a, 2017c). Geomechanical modelling using this stress tensor identified that NE-SW striking high angle (50-70°) faults were most likely to shear reactivate at this time (Kulikowski & Amrouch, 2017c). Reactivation of predominantly this fault set exhumed and eroded up to 500 meters of Nappamerri Group sediments (Apak et al., 1997; Kantsler et al., 1983; Alexander et al., 1998; Mavromatidis, 2006).

2.6 Late Cretaceous Event (95-55 Ma)

As the Hunter-Bowen Event subsided, flexural relaxation generated accommodation space and a fluvial depositional environment transcended, which deposited the Poolowanna Formation (~200-180 Ma) onto the regional unconformity (Green et al. 1989; Hoffman, 1989; Lowe-Young et al. 1997). Tectonic quiescence continued with the deposition of the

braided fluvial Hutton Sandstone (~178-160 Ma), fluvial to lacustrine Birkhead Formation (~157 Ma), and braided fluvial to lacustrine Mooga Formation (~152 Ma) and Adori Sandstone (~152 Ma) (Green et al. 1989; Hoffman, 1989; Lowe-Young et al. 1997). The braided fluvial to lacustrine depositional environment continued within the region, depositing the Namur Sandstone (~152-140 Ma), Westbourne Formation (~150 Ma), Hooray Sandstone (~141 Ma), and the oil-rich Murta Member (~140 Ma) (Lowe-Young et al., 1997). Jurassic units contain abundant oil (and gas) reservoirs at a shallower depth than Permian reservoirs, and primarily targeted on the western flank of the Cooper Basin (Lowe-Young et al., 1997).

The depositional environment transitioned into fluvial to shallow marine conditions and deposited the Cadna-owie Formation (~140-126 Ma) (Lowe-Young et al., 1997). The overlying Wyandra Sandstone Member (~125 Ma) was deposited under deltaic to shoreface marine conditions and contains some oil and gas potential (Lowe-Young et al., 1997). Following this, the Bulldog Shale (~125-108 Ma) and Wallumbilla Formation (~125-104 Ma) were deposited in restricted open marine conditions, which transitioned into a shoreface depositional environment to deposit the Coorikiana Sandstone (~105 Ma) (Lowe-Young et al., 1997). Shallow open marine conditions developed and deposited the Oodnadatta Formation (~104-98 Ma), Toolebuc Formation (~103 Ma), and Allaru Mudstone (~100 Ma) (Lowe-Young et al., 1997). Finally, the Winton Formation (~97-93 Ma) and Mackunda Formation (~97 Ma) were deposited by fluvial-lacustrine conditions to mark the final period of sediment deposition within the Eromanga Basin (Lowe-Young et al., 1997). These Middle to Late Cretaceous marine sediments also host the regionally extensive polygonal fault system that may present a new target for future exploration (Watterson et al., 2000). The critical moment in the Cooper-Eromanga Basin hydrocarbon system, which marks the time of major hydrocarbon generation, migration, accumulation and preservation, occurred at 90 Ma (Lowe-Young, et al., 1997).

The Winton and Mackunda formations were significantly eroded following their exhumation by the E-W Late Cretaceous compressional Event (Fig. 4f) (e.g. Kuang, 1985; Green et al. 1989; Hoffman, 1989; Apak et al. 1997; Lowe-Young et al. 1997; Gravestock & Jensen-Schmidt, 1998; Mavromatidis, 2006; Kulikowski & Amrouch, 2017a, 2017b). Folding related to pre-existing NE-SW striking faults, rather than reactivation, facilitated the development of this erosional boundary, which separates the Eromanga and Lake Eyre basins (Fig. 2). An effective maximum principal stress magnitude of 59 MPa was measured from calcite twin stress inversion analysis (Fig. 4i) (Kulikowski & Amrouch, 2017c). N-S striking low angle (30°) conjugate natural fractures were developed during this time (Kulikowski & Amrouch, 2017a). Considering that this event occurred during and after the critical moment, understanding the dilation and shear tendency of faults is vital for accurate migration pathway modelling. Under these stress conditions, E-W and NE-SW striking high angle (60°) faults were the most likely to act as hydrocarbon conduits (Kulikowski & Amrouch, 2017c).

2.7 Paleogene Event (33-23 Ma)

During deposition of the Lake Eyre Basin, which is presently at surface, an N-S oriented Paleogene compressional event developed E-W striking low angle (30°) conjugate natural fractures throughout the stratigraphic column (Kulikowski & Amrouch, 2017a). This event is attributed to the northwards movement of the Australian plate (Fig. 4g). The effective maximum principal stress magnitude of this event was calculated from calcite twin stress inversion analysis and found to be 64 MPa (Fig. 4i) (Kulikowski & Amrouch, 2017c). Interestingly, this event does not appear to have reactivated or developed faults; however, N-S and NE-SW striking high angle (50-70°) faults are considered to have been likely to dilate and act as permeable hydrocarbon conduits (Kulikowski & Amrouch, 2017c).

3. PETROLEUM SYSTEM

3.1 Hydrocarbon Source Rocks

Hydrocarbons in the Cooper Basin are principally sourced from intra-formational Permian coals and Permian to Jurassic carbonaceous shales, and reservoired within fluvial sandstones (Fig. 5) (Boreham & Hill, 1998). The petroleum system is largely gas saturated with small volumes of liquids found in localised areas (Kantsler et al., 1984). As such, the isotopic composition of intra-formational coals and carboniferous shales indicates fresh water origin and dominated by high order plants (Kantsler et al., 1984; Boreham & Hill, 1998). The Toolachee, Daralingie, Epsilon and Patchawarra formations contain an average total organic content (TOC) of 3.9% and 6.9 kg/tonne of hydrocarbon (Smyth, 1983; Boreham and Hill, 1998). The most organic-rich source rock is within the Toolachee Formation, averaging 214 kg/tonne (Hydrogen index) across the Cooper Basin (Boreham & Hill, 1998). Liquid hydrocarbon yields are low in Permian reservoirs due to high vitrinite and inertinite (Type III kerogens) composition in shale and coal measures, and are absent within the over mature Nappamerri Trough, which contributes only dry gas (Kantsler et al., 1984; Boreham & Hill, 1998).

Insert Fig. 5

The hydrocarbon source for the overlying Eromanga Basin is more uncertain, and likely to be sourced from: (1) non-marine Jurassic aged rocks (Powell et al., 1989; Lowe-Young et al., 1997); (2) Permian shales and coals that migrated through reactivated faults (Heath et al., 1989; Lowe-Young et al., 1997); and (3) a combination of both Jurassic and Permian source rocks (Fig. 6c) (Kantsler et al., 1984; Gilby et al., 1989; Jenkins et al., 1989; Lowe-Young et al., 1997). Jurassic aged units contain oil and gas; however, only gas has been discovered in Cretaceous aged reservoirs in the Strzelecki, Packsaddle and Nappacoongee regions (Kantsler

et al., 1984). Permian aged source rocks are currently within the gas window, with Jurassic to Cretaceous source rocks currently at peak oil generation (Kantsler et al., 1984).

Insert Fig. 6

3.2 Hydrocarbon Generation

Permian and Triassic source rocks reached the hydrocarbon generation window as early as the Permian to Middle Triassic during maximum burial (Fig. 6), and peaked during a secondary sag period in the Middle Cretaceous (Deighton & Hill, 1998; Mavromatidis, 2006). Relatively minor hydrocarbon generation and expulsion commenced in the Permian to Middle Triassic, before peaking in the Middle to Late Cretaceous and potentially continues today (Fig. 6a & 6b) (Pitt, 1986; Duddy, 1987; Gallagher, 1988; Lowe-Young et al., 1997; Mavromatidis, 2006; Deighton & Hill, 2009). Minor volumes of hydrocarbons were also generated in the Nappamerri Trough during the Permian, and, given sufficient residual kerogen, the effect of Late Tertiary elevated temperatures and Tertiary deposition may have led to secondary (late-stage) hydrocarbon generation and expulsion in certain parts of the basin (Fig. 6b) (Deighton & Hill, 2009).

Although a rare phenomenon, the concentration of carbon dioxide (CO_2) within the Cooper-Eromanga Basin is significantly higher (10-30 v/v%) than typical sedimentary basins (Rigby & Smith, 1981; Kantsler et al., 1984; Wycherley et al., 1999). However, the origin remains somewhat questionable, but likely to be related to magmagenesis or metamorphic reactions, which is supported by the correlation between raised CO_2 levels and the presence of Carboniferous Uranium-rich Moomba-Big Lake Granodiorite (Gatehouse et al., 1995; Wycherley et al., 1999).

3.3 Hydrocarbon Migration

Hydrocarbon generation and expulsion is divided into three phases: (1) early expulsion between the Late Permian and Early Triassic; (2) primary expulsion within the Cretaceous; (3) and a possible secondary expulsion during the Late Cenozoic (Fig. 6) (Lowe-Young et al., 1997; Radke, 2009). These three phases of expulsion coincide with the timing of hydrocarbon migration (Fig. 6c) (Lowe-Young et al., 1997; Radke, 2009). Hydrocarbon generated from Permian source rocks migrated short distances to the vertically stacked overlying or underlying intra-formational reservoirs, or alternatively along deep seated and reactivated basement-involved faults into overlying Eromanga Basin reservoirs (Boreham & Hill, 1998; Gravestock et al., 1998; Radke, 2009). Tertiary hydrocarbon migration through stacked intra-formational seals into overlying reservoirs has also been discussed (Heath et al., 1989; Boulton et al., 1998; Gravestock et al., 1998; Hillis et al., 2001; Radke, 2009). Geomechanical modelling of fault reactivation (dilation and shear) through time highlighted the changing conduit potential of individual fault sets as stress conditions changed (Kulikowski et al., 2016c; Kulikowski & Amrouch, 2017c).

Secondary hydrocarbon migration from Permian source rocks into overlying Jurassic Eromanga Basin reservoirs has been suggested by numerous authors after observing oil compositions that were not consistent with a Jurassic origin (Heath et al., 1989; Hallmann et al., 2007). The origin of Jurassic oils has been found to be from either: (1) Permian source rocks; (2) Jurassic source rocks; or (3) a combination of the two (Smyth, 1983; Heath et al., 1989; Lowe-Young et al., 1997; Hallmann et al., 2007). In the case of Permian source rock origin, secondary migration of oil was through: (1) permeable fault conduits into shallow Eromanga Basin reservoirs; or (2) through a permeable carrier bed in the up-dip direction towards the western Cooper Basin flank, where overlying Triassic sealing units effectively pinch-out and allow the oil to migrate into directly overlying reservoir rocks (Heath et al., 1989; Lowe-Young et al., 1997; Borazjani et al., 2017a, 2017b). This western flank region

hosts many large producing oil fields (Heath et al., 1989; Lowe-Young et al., 1997; Borazjani et al., 2017a, 2017b). In these two migration pathway cases, the oil composition between source and reservoir has shown to be different due to the effects of deep bed filtration (Borazjani et al., 2017a, 2017b), or water-washing (Heath et al., 1989) of hydrocarbons.

The ability of a fault to act as a potential hydrocarbon conduit can be measured by calculating the Dilation Tendency, or the likelihood of faults to undergo tensile reactivation. Alternatively the likelihood of faults to shear reactivate can be measured by calculating Slip Tendencies. These likelihoods were calculated for four regional fault sets, which were modelled under six unique paleo-stress tensors (Alice Springs Event, Mid-Permian Event, Daralingie Event, Hunter-Bowen Event, Late Cretaceous Event, and Paleogene Event), as well as the present day stress conditions (Kulikowski et al., 2016c; Kulikowski & Amrouch, 2017c). The results of these studies found that early expulsion of hydrocarbons would have preferentially migrated along NE-SW striking high angle (50-70°) faults during the Late Permian and along E-W striking high angle (50-70°) faults during the Late Triassic. Since the critical moment (90 Ma) hydrocarbons would have preferentially migrated along E-W striking high angle (50-70°) faults during the Late Cretaceous and N-S striking high angle (50-70°) faults during the Paleogene. Hydrocarbons generated during the secondary phase, or present day, would likely be migrating along E-W striking high angle (50-70°) faults or SE-NW strike-slip faults. See Chapter 6.2 for more detail.

3.4 Hydrocarbon Seals and Trap Development

Intra-formational fluvial-lacustrine to lacustrine shales and coal measures form cyclically deposited impermeable seals to underlying reservoirs, while also acting as potential source rocks to overlying reservoirs (Bradshaw, 1993; Gravestock & Jensen-Schmidt, 1998). These vertically stacked intra-formational shales and coals have the highest influence on sealing

hydrocarbons within the four-way closing anticlinal traps that are present throughout the basin (Gravestock et al., 1998). The Murteree and Roseneath shales are highly efficient seals to the Patchawarra and Epsilon formations respectively; however, intra-formational shales hold back hydrocarbon to individual and compartmentalised intra-formational sandstone reservoirs (Gravestock et al., 1998). Cretaceous marine sediments and the Late Jurassic Birkhead Formation form regional seals for Jurassic to Early Cretaceous Eromanga Basin reservoirs (Gravestock et al., 1998; Radke, 2009).

The regional Murteree Shale and intra-formational Patchawarra Formation seals are eroded along the western margin of the basin contributing to the significant number of oil discoveries made along the western flank, as oil migrates from the deep sections of the Patchawarra Trough into shallow Eromanga Basin reservoirs (Radke, 2009). Low amplitude structural closures within the Eromanga Basin are sealed by the regional Birkhead and Wallumbilla formations, facilitating the accumulation of hydrocarbons (Radke, 2009; Kulikowski et al., 2016b, 2017c). A regional polygonal fault system is present within Cretaceous sediments and is observed to occasionally penetrate into the hydrocarbon-rich Murta Member (Fig. 7) (Watterson et al., 2000; Kulikowski et al., 2017a). Where these normal faults are approximately E-W striking and penetrate into the Murta Member, hydrocarbons may be migrating through permeable fault conduits into shallow reservoirs, possibly presenting a new exploration strategy (Watterson et al., 2000; Kulikowski et al., 2017a).

Insert Fig. 7

Structural trap development occurred as early as the Mid-Permian Event and Late Permian Daralingie Event, coinciding with the early phase of hydrocarbon generation and expulsion (Deighton & Hill, 1998; Kulikowski & Amrouch, 2017b). Key anticlinal traps were developed by two subsequent events; the E-W Hunter-Bowen Event and E-W Late

Cretaceous Event (Kulikowski & Amrouch, 2017a, 2017b). These two events reactivated basement-involved faults to create broad anticlinal domes within the Permian, and low amplitude anticlines within Cretaceous sediments prior to the primary phase of hydrocarbon generation and expulsion (Deighton & Hill, 1998). The N-S Paleogene Event (33-23 Ma) may have contributed to a late-stage of structural trap development; however, this occurred significantly after the critical moment in the hydrocarbon system and may have negatively influenced the preservation of existing hydrocarbon accumulations (Lowe-Young et al., 1997; Kulikowski & Amrouch, 2017b, 2017c). Although the majority of accumulations are trapped by anticlines, there does exist an opportunity to begin targeting higher risk stratigraphic pinch-out traps and on-lapping features that are common within the basin, particularly within the hydrocarbon-rich Patchawarra Formation (Apak et al., 1997; Kulikowski & Amrouch, 2017b).

3.5 Hydrocarbon Accumulation and Preservation

Hydrocarbons are primarily reseroired within the Tirrawarra Formation, Patchawarra Formation, Murteree Shale, Epsilon Formation, Roseneath Shale, Daralingie Formation, and Toolachee Formation of the Cooper Basin, and the Hutton Formation and Namur Sandstone of the Eromanga Basin (Kantsler et al., 1984; Alexander et al., 1998; Gravestock et al., 1998a; Mackie, 2015). Although these are the dominant oil and gas producers, with the Hutton Sandstone contributing greater than 50% of oil discoveries (by volume) in the Eromanga Basin, hydrocarbons can be found in virtually all reservoir-quality zones older than the Late Cretaceous (Kantsler et al., 1984; Lowe-Young et al., 1997; Radke, 2009). The majority of hydrocarbon discoveries are located within the South Australian portion of the Cooper Basin, reflecting the significantly greater volume of Permian source rocks (Kantsler et al., 1984; Reynolds et al., 2006). Primary hydrocarbon accumulation commenced during the Late Cretaceous critical moment (90 Ma), with existing fields withstanding the Late

Cretaceous Event (95-55 Ma), Paleogene Event (33-23 Ma), and the present day stress environment (Fig. 6c) (Kantsler et al., 1984; Lowe-Young et al., 1997; Mackie, 2015; Kulikowski & Amrouch, 2017a).

The preservation of accumulations appears to be unaffected by these three events, as seismic data shows that basement-involved faults were not reactivated; however, sub-seismic resolution faulting may be possible considering that resolution is not better than 15 m (Kulikowski et al., 2017a; Kulikowski and Amrouch, 2017c). Fault reactivation causing less than 15 m of displacement can be sufficient to cause seal breach and facilitate tertiary migration of hydrocarbons, particularly if fault geometries are optimally oriented to tensile reactivate (dilate). Geomechanical modelling of fault reactivation has shown that the most common fault set, NE-SW striking high angle (50-70°), was the most likely to shear reactivate during the four most recent (Daralingie Event, Hunter-Bowen Event, Late Cretaceous Event, Paleogene Event) tectonic events (Kulikowski & Amrouch, 2017c). Under contemporary stresses, SE-NW strike-slip faults are most likely to shear reactivate and must be accurately interpreted because of the high likelihood of interacting with, and complicating, hydraulic fracture stimulations (Pokalai et al., 2016, 2017; Kulikowski et al., 2016c).

4. GEOPHYSICS

4.1 Significant Seismic Reflectors

With the majority of hydrocarbons reservoired within Permian rocks, the top Toolachee Formation, top Patchawarra Formation, and VC Coal seismic reflectors are mostly commonly interpreted. The Cretaceous Cadna-owie Formation reflector (C-reflector) is an easily identifiable and regional strong amplitude reflector typically found at 1000-1500 m (Fig. 8a). Its interpretation provides the structural trap geometry for Jurassic and Cretaceous reservoirs, as well as providing broad insights into the underlying structures. This reflector also shows

intermittent normal displacement caused by polygonal faults extending from the Mackunda Formation (AM-reflector) into the deeper hydrocarbon-rich Murta Member (D-reflector) (Fig. 7). The top Nappamerri Group reflector (N-reflector) shows a similar characteristic to the Cadna-owie Formation reflector, although with variable amplitude due to the erosional boundary that it represents at 1500-2000 m (Fig. 8a). This reflector marks the boundary between the Cooper and Eromanga basins.

Insert Fig. 8

Top Permian stratigraphy is identified by an abrupt strong amplitude package at approximately 2000 m that represents the fluvial to deltaic Toolachee Formation (P-reflector) (Fig. 8a). The top Patchawarra Formation (V-reflector) is notoriously bland, attributed to the relatively more transitional boundary between the upper Patchawarra Formation and the Murteree Shale (U-reflector) that results in a low acoustic impedance boundary. As such, the stronger amplitude reflector immediately below the top Patchawarra Formation is typically interpreted (Fig. 8a). Within the Patchawarra Formation, the VC30 and VC50 coal measures produce strong amplitude (soft-kick) reflectors; however, the reflectors commonly split and merge (Fig. 8a). Middle Patchawarra Formation reflectors have been shown to on-lap onto paleo-structures correlating to the Mid-Permian Event (290-270 Ma) (Apak et al., 1997; Kulikowski & Amrouch, 2017b). Below the Permian coal measures, seismic resolution rapidly decays and the interpretation of reflectors and faults becomes difficult (Fig. 8a). The Tirrawarra and Merrimelia formation reflectors are absent in some parts of the basin and require high well control to be interpreted accurately.

Seismic interpretation of the basement (Z-reflector) is again difficult throughout the basin, commonly requiring phantom interpretation through significant fault shadow (Fig. 8a). Seismic resolution has been calculated to be upwards of 150 m, in contrast to Cretaceous

reflectors that can be between 15-20 m (Kulikowski et al., 2017a). Recently acquired 3D seismic surveys have much greater resolution below Permian coal measures, with broadband and full-azimuthal seismic data expected to significantly improve the resolution in the near future.

4.2 Seismic Time-to-Depth Conversion Methods

The seismic time-to-depth conversion process can incur large (10's of feet) errors caused by local velocity anomalies, incorrect well ties, or more commonly from a poor understanding of the near surface ground variation, or statics. Although errors cannot be removed entirely, selecting the most accurate depth conversion method for the given study area can have noticeable effects. For example, the presence of low relief hydrocarbon-rich structural traps within the Eromanga Basin can depend on the depth conversion method being used (Kulikowski et al., 2016b, 2017c). Additionally, fault analysis may lead to incorrect results if seismic data remains in the time-domain, as fault geometries will change once in the depth-domain (Fig. 8b & 8c).

Complete seismic volume time-to-depth conversion is often time consuming and not necessary for generating simply reflector maps. As such, time-to-depth conversion is often performed using gridding software, or horizon maths tools built into seismic processing and interpretation software. For the purpose of generating reflector maps, only the interpreted two-way-time (TWT) seismic reflector grid, rather than the seismic volume, is converted. In the simplest sense, the TWT grid is multiplied by a constant velocity to generate a depth grid. Three seismic time-to-depth conversion methods are commonly used within the Cooper-Eromanga Basin, including the: (1) average velocity method (Fig. 9a); (2) time-depth trend method (Fig. 9b); and (3) interval velocity method (Fig. 9c).

Insert Fig. 9

4.2.1 Average (Pseudo) Velocity Method

The average (pseudo) velocity (V_a) method is one of the more simple, yet most commonly used, seismic time-to-depth conversion methods within the Cooper-Eromanga Basin. This simple approach does not explicitly consider velocity anomalies. Rather, for any given well location and for any given reflector, the true depth (Δz : depth in feet) is obtained from well data and the interpreted time (Δt : one-way-time in seconds) obtained from seismic data (Fig. 9a). The ratio of the two measured values provides the V_a at the well location, such that;

$$V_a = \frac{\sum_{k=1}^n z_k}{\sum_{k=1}^n t_k} = \frac{\Delta Z (ft)}{\Delta t (s)}$$

Where k is the k^{th} reflector measured from n well locations. The time-to-depth conversion process involves multiplying the resultant V_a with the seismic data (one-way-time: OWT in seconds), to give true depth (ft), such that;

$$True\ Depth = V_a * OWT$$

For seismic data that contains an abundance of well control, the V_a for each well location can be summed to determine the overall mean V_a of the entire survey. Alternatively, the V_a values at each well location can be gridded to produce a spatial contour map of V_a , which can take into account spatial velocity anomalies. The V_a from the surface to the Upper Cretaceous, Cadna-owie Formation, and Top Permian seismic reflectors was measured from 12 3D seismic surveys (Fig. 3b) to give a basin wide V_a value (Fig. 9d). The basin wide V_a from the surface to the: (1) Upper Cretaceous reflector is 2,280 m/s, (2) Cadna-owie Formation reflector is 2,375 m/s; and (3) Top Permian reflector is 2,740 m/s (Fig. 9d). Although simplistic, this method has been found to be one of the most accurate in the Cooper-Eromanga Basin (Rady, 2006; Kulikowski et al., 2016b, 2017c).

4.2.2 Time-Depth Trend Method

The time-depth (T-D) trend method utilises the relationship between the TWT and true depth values for a given reflector, hence is closely related to the average velocity method. The T-D pairs at a given well location for a given seismic reflector are plotted on a two-way graph and a linear ($y = mx + c$), or occasionally exponential ($y = ax^2 + bx + c$), trend is defined, where y is depth, x is time, m is slope, and a , b , and c are constants (Fig. 9b). The T-D trend equation that defines the distribution is used to directly convert the TWT seismic data to depth. The T-D Trend (Fig. 9e) from the 12 3D seismic surveys (Kulikowski et al., 2017a) was found to be approximately;

$$Depth (m) = 280.5 * (TWT)^2 + 847.97 * (TWT)$$

Where TWT is two-way-time measured in seconds. Not all T-D pairs will plot precisely on this trend, and may create poor well ties. Therefore, when performing a time-to-depth conversion on a gridded reflector, the resultant depth grid must be tied to the well control precisely by firstly gridding the error between the true depth and the time-to-depth converted grid, and secondly subtracting the resultant error correction grid from the time-to-depth converted grid (Kulikowski et al., 2016b, 2017c).

This method of time-to-depth conversion is a commonly used method in the Cooper-Eromanga Basin, with early work utilising check-shot data and continuous velocity logs to calibrate seismic data. Continuous velocity logs can provide direct input data for velocity models and T-D pairs for key stratigraphic markers. Check-shot data for time-to-depth conversion has somewhat become outdated, with advancements in technology providing more accuracy through vertical seismic profile (VSP) acquisition (Jolly, 1953; Levin & Lynn, 1958; Ganley & Kanasewich, 1980; Hauge, 1981; Balch et al., 1982; Balch & Lee, 1984; Gajewski & Psencik, 1990). Check-shot and VSP data are obtained in a similar fashion to

seismic data, where a P-wave travel time is measured from the surface to a receiver (Stainsby & Worthington, 1985). In the case of check-shot and VSP data, the receiver is lowered through the borehole to a key stratigraphic marker. However, the resolution of VSP data is significantly higher, as the number of borehole receivers can be as dense as every 25 m, in contrast to check-shot data that is only collected at key stratigraphic intervals.

4.2.3 Interval (Layer-Cake) Velocity Method

The interval velocity (V_i) method is used to represent the abrupt changes in velocity evident across significant stratigraphic packages. A look at continuous velocity logs and synthetic seismograms shows that velocities are not constant and can abruptly increase or decrease depending on the rock composition (Al Chalabi, 1974). The more basic interval velocity model divides the subsurface into key stratigraphic packages that have unique velocities (V_i), such that the depth can be calculated by;

$$Depth = \sum_{j=1}^n V_i(t_{j+1} - t_j)$$

Where n is the number of intervals (layers) bound by the j^{th} reflectors, which are measured in the time-domain, t (one-way-time), at a given well location.

High velocity cemented calcite zones (CCZ) are present within the Eromanga Basin and can distort the true subsurface image when not incorporated into velocity models (Kulikowski et al., 2016). Precises interval velocity modelling can include these high velocity zones for more accurate seismic depth conversion. Interval velocity models are also used when anomalous velocities are present within a specific stratal-unit, which can be caused by overpressures, cementation, or the presence of faults and fractures.

4.3 Seismic Time-to-Depth Conversion Accuracy

The accuracy of converting post-stack seismic data from the time-domain to the depth-domain has been a significant topic of conversation within the Cooper-Eromanga Basin. Inaccurate seismic depth conversion has significant implications for a number of key processes, which include: (1) drilling low amplitude Jurassic to Cretaceous pseudo-structures that appear in depth converted seismic data due to velocity anomalies; (2) overlooking low amplitude Jurassic to Cretaceous structural traps that do not appear in depth converted seismic data due to inaccurate velocity modelling; (3) inaccurate economic estimates of new wells that, if depth is underestimated, may require drilling additional 10's of feet that may change the economic feasibility; (4) coring the wrong intervals while drilling; (5) inaccurate reserves calculations that could be under or overestimated; and (6) errors with geomechanical modelling of fault reactivation, as fault geometries will change and could influence the sealing potential of fault bound accumulations (Hillis et al., 1995; Lowe-Young et al., 1997; Kulikowski et al., 2016).

The historical inaccuracy of seismic depth conversions can be attributed to a number of factors ranging from: (1) known high velocity calcite cemented zones (CCZ); (2) the regional system of Cretaceous polygonal faults that can influence the spatial and temporal velocity; (3) velocity characteristics of fluvially deposited channel sands; and (4) the near surface 'statics' attributed to changes in surface conditions (rocky, regolith, etc.) (Hillis et al., 1995; Lowe-Young et al., 1997; Kulikowski et al., 2016b, 2017c). The effect of statics on seismic depth conversion is difficult to constrain, but can be slightly mitigated through up-hole seismic refraction surveys that deliberately drill shallow wells to target the velocity of the near surface (Igboekwe & Ohaegbuchi, 2011). This technique can accurately measure the velocity at the wellbore, but, as with most wellbore derived data, must be extrapolated to the wider and often kilometre-scale field, which is a large assumption that can influence accuracy. To entirely mitigate the large effect of statics in seismic depth conversion accuracy

within the Cooper-Eromanga Basin, a method of velocity acquisition targeting the near surface must be investigated.

At this present moment, much of the work on seismic time-to-depth conversion accuracy in the basin appears to be kept behind closed doors by operating companies. Literature provides only two studies in the Cooper-Eromanga Basin that are focused on this topic (Hillis et al., 1995; Kulikowski et al., 2017c), with Hillis et al. (1995) choosing to focus on a small local dataset. The only regional study assessing the depth conversion accuracy in the basin used a statistical approach testing the accuracy of the four most commonly used methods (average (pseudo) velocity, time-depth trend, kriging with external drift using TWT, and kriging with external drift to tie stacking velocities to average well velocities) by employing a cross-validation, or blind-well test, method (Kulikowski et al., 2017c). An automated looping script was developed to manage their large dataset, comprising of 13 3D seismic volumes, 73 interpreted TWT grids, and 729 wells (Kulikowski et al., 2017c). Their results found that although the average (pseudo) velocity method was the most accurate at a high-level (± 24.9 ft), the accuracy of methods changes by 10's of feet depending on the unique dataset and the combination of significant variables (Kulikowski et al., 2017c).

The significant variables to the accuracy of depth conversion were the distance between the well that is being predicted and an existing well control, the spatial location within the basin, the reflector of interest, and the location of the well that is being predicted relative to the existing well data envelope (Kulikowski et al., 2017c). Interestingly the number of well controls had a negligible effect on accuracy, but rather the proximity of well controls to the well that is being predicted (Kulikowski et al., 2017c). The regional study (Kulikowski et al., 2017c) reiterates the argument that depth conversion accuracy in the Cooper-Eromanga Basin is a complicated issue that must be further investigated.

4.4 Seismic Data Analysis

Analysis of seismic data through the use of seismic attributes, amplitude versus offset (AVO) analysis, spectral decomposition, and seismic inversion modelling can unlock hidden details that may not be obvious within the amplitude volume. These techniques have become a common tool for exploration and development programs around the world and would be highly beneficial in the fluvially dominated Cooper-Eromanga Basin (Fig. 10). Incoherency (coherency or similarity) is a seismic attribute that was first introduced by Bahorich and Farmer (1995) and further developed by Gersztenkorn and Marfurt (1999) and is used to visually emphasise the discrepancy (typically faults) between adjacent seismic traces along a horizon or time-slice (Neves et al. 2004; Mai et al. 2009; Backé et al. 2011; Basir et al. 2013). This attribute has been shown to be particularly beneficial when interpreting basement and polygonal faults (Fig. 10b) from the low resolution seismic data typical to the Cooper-Eromanga Basin (Kulikowski et al., 2017a). Curvature is another structural attribute that is defined as the rate of change of the direction of a curve (Roberts, 2001), where significant curvature values are often associated with reflector displacement such as those caused by fractures or faults (Roberts, 2001; Al-Dossary and Marfurt, 2006; Backe et al., 2011; King et al., 2011; Abul Khair et al., 2012; Kulikowski et al., 2017b). This attribute has the potential to constrain the distribution of natural fracture sweet-spots away from the wellbore (Kulikowski et al., 2017b).

Considering that hydrocarbons are predominantly reservoired within fluvial sandstones in the Cooper-Eromanga Basin, displaying the spatial distribution of amplitude along a reflector surface can aid in detecting these strong amplitude reservoirs (Fig. 10a), particularly if associated with characteristic amplitude versus offset (AVO) responses. In some cases, these reservoirs can verge on being at a sub-seismic resolution scale and can be overlooked in seismic data. The application of spectral decomposition on the seismic volume can assist in

detecting these thin fluvial beds (Fig. 10d) and can also provide a more visual representation of small scale faults (Partyka et al., 1999). Another issue facing explorationists is the discrimination between the signature of thin gas reservoirs and coals in stacked seismic data. Owing to the significant difference in Poisson's ratio between sandstone and coal, the application of AVO analysis to Cooper-Eromanga Basin seismic data has provided evidence to suggest that such discrimination is possible and most effective when using a rotated extended elastic impedance attribute in the presence of tuning (Fig. 10c) (Tyiasning and Cooke, 2015).

Insert Fig. 10

5. CONTEMPORARY STRESS TENSOR

Contemporary stress tensors are well constrained in the basin, calculated from borehole breakouts and drilling induced tensile fractures, diagnostic fracture injection tests, and leak off tests (e.g. Hillis et al., 1999; Hillis & Reynolds, 2000, 2003; Reynolds et al., 2002, 2003, 2004, 2005, 2006; Sandiford et al., 2004; Nelson et al., 2006, 2007; Muller et al., 2012; Pokalai et al., 2016, 2017). The far-field origin of in situ stresses has been explained by Reynolds et al. (2003) to originate from the Tonga-Kermadec subduction zone and the New Zealand collisional boundary. These tectonic stresses are transferred through the upper crust of eastern Australia to give an approximately ESE-WNW maximum horizontal stress within the Cooper-Eromanga Basin. The stress regime is dominantly strike-slip, but can transition to a compressional stress regime with increased depth, as the overpressures will decrease the effective vertical stress magnitude more than the effective horizontal stress magnitudes (Reynolds et al., 2006; Cooke et al., 2015). Alternatively, depletion of hydrocarbon reservoirs can reduce pore pressure, which in turn increases the effective vertical stress magnitude (Teufel, 1991). Given that the effective vertical stress magnitude can become larger than both effective horizontal stress magnitudes through reservoir depletion, the in situ stress can transition into an extensional stress regime (Teufel, 1991). This transition between regimes will have implications for late-stage development programs incorporating hydraulic fracturing and infill drilling, as the unexpected stress regime can impact the effectiveness of those programs.

For the majority of the basin a strike-slip stress regime is present, with an ESE-WNW oriented maximum principal stress (Fig. 11a); however, local stress perturbations caused by faults can cause stress rotation (Fig. 11b). The magnitude of maximum horizontal stress has been constrained to approximately 41 MPa/km based on a combination of frictional limit theory (Sibson, 1974), drilling induced tensile fractures, and the use of tensile strength and

knowledge of horizontal fabrics at the wellbore wall (Reynolds et al., 2005; Nelson et al., 2005; 2007). The vertical principal stress magnitude is dependent on the overburden rock thickness and density, as well as the local pore pressure (Fig. 11c). The range of magnitudes present within the basin for the vertical stress is between approximately 17 and 20 MPa/km (Reynolds et al., 2006; Nelson et al., 2007; Pokalai et al., 2016, 2017). As mentioned earlier, a decrease in the pore pressure caused by depletion can increase the effective magnitude of the vertical principal stress. Minimum horizontal stress magnitudes are typically calculated from leak off tests or obtained from the minimum closure pressure during a mini-frac test (Fig. 11c). Within the Cooper-Eromanga Basin, the minimum horizontal stress magnitude can vary significantly between approximately 12 and 27 MPa/km and can depend on the interpretation technique used to read closure pressures (Nelson et al., 2007).

Insert Fig. 11

Equally as important as the principal stress magnitude, the pore pressure gradient can influence the reactivation and development of natural fractures and faults. Increases in pore pressure effectively shift the Mohr's circle to the left, closer to the failure and reactivation envelopes. This effect can be induced by hydraulic fracture stimulation treatments and through gas and water injection wells. Pore pressure within the basin remains at a hydrostatic gradient (0.433 psi/ft) until depths of between 8000 and 8800 ft, where overpressure is first observed and is largely depended on the location (van Ruth & Hillis, 2000; Kulikowski et al., 2016a). A recent study within the basin calculated the effective tectonic strain to be between approximately 400 and 500 microstrains, with strain in the maximum horizontal stress direction being three times greater than that in the minimum horizontal stress direction (Pokalai et al., 2016, 2017).

6. GEOMECHANICAL MODELLING OF FAULT REACTIVATION

6.1 Theory

Reactivation refers to the movement of faults and fractures under present day stress conditions and can be analysed by creating a geomechanical model and measuring the shear or tensile (dilation) reactivation potential. Therefore, a poor understanding of the local and regional geomechanical conditions has tremendous implications for hydrocarbon migration pathway models, hydraulic fracture stimulation treatments, reservoir development, and seal integrity. Faults that are optimally oriented to undergo tensile reactivation, or dilate, can provide permeable conduits for hydrocarbon migration. An increase in pore pressure, through hydraulic fracture stimulation or water/gas injection wells, can facilitate shear or tensile reactivation along pre-existing faults and fractures. Geomechanical models have also been shown to effectively predict the shear and tensile reactivation potential of faults under paleo-stress conditions, which becomes most beneficial when incorporated with hydrocarbon migration pathway modelling (Kulikowski & Amrouch, 2017c).

The Dilation Tendency (T_d) measures the likelihood that faults and fractures will tensile reactive and is governed by the orientation and magnitude of the effective normal stress, σ_n' , acting on a fault plane. The T_d is normalised to the differential stress to give values between zero (low likelihood) and one (high likelihood), where σ_1' is the maximum effective stress and σ_3' is the minimum effective stress (Ferrill et al., 1999; Jolie et al., 2015), such that;

$$T_d = \frac{\sigma_1' - \sigma_n'}{\sigma_1' - \sigma_3'}$$

Fracture Stability is a measure of the pore pressure required to effectively shift the Mohr's circle to the left and intersect the failure or reactivation envelope for a given fault plane. The

relationship between an increase in pore pressure (ΔP_p) and the change in horizontal stress magnitude (ΔS_{Hor}) is such that (Hung and Wu, 2012);

$$\Delta S_{Hor} = \alpha \left(\frac{1 - 2\nu}{1 - \nu} \right) \Delta P_p$$

Where α is Biot's coefficient that describes the difference between the total and effective stresses, and ν is the Poisson ratio. This equation shows the direct relationship between increasing pore pressure to an increase in the horizontal stress magnitudes. Therefore, the Fracture Stability results are provided as the pore pressure increase required to induce shear reactivation. The Slip Tendency of faults provides a normalised scale of the Fracture Stability, where zero (0) has a low likelihood, and one (1) has a high likelihood of shear reactivating.

The likelihood of faults and fractures to act as conduits can also be measured through the Leakage Factor equation that relates the pore pressure (P_p) with the difference between the normal stress (σ_n) and shear stresses (τ) acting on a given fault plane, such that;

$$Leakage\ Factor = \frac{P_p}{\sigma_n - \tau}$$

The structural stability is assessed for three groups of structural data common to the Cooper-Eromanga Basin: (1) Basement Faults; (2) Polygonal Faults; and (3) Natural Fractures.

6.2 Basement Faults

6.2.1 SUMMARY

The majority of the basement-involved faults developed during the early tectonic development of the Australian-Mawson Block (Fig. 4a), where a Pre-Cambrian (650-575 Ma) SE-NW oriented extensional stress regime event created NE-SW striking normal faults and SE-NW strike-slip faults throughout much of Australia (Kuang, 1985; Haines, 2002; Apak et

al., 1997; Gibson et al., 2013; Kulikowski and Amrouch, 2017a). These two dominant fault sets are present throughout the Cooper-Eromanga Basin and form close relationships with anticlinal hydrocarbons traps (Fig. 12) and the NE-SW striking GMI and MN ridges (Fig. 3b). Through time, these pre-existing basement-involved faults were repeatedly reactivated by subsequent compressional and strike-slip stress regime events (Apak et al., 1997; Gravestock & Jensen-Schmidt, 1998; Kulikowski & Amrouch, 2017a, 2017b; Kulikowski et al., 2017a). Repeated reactivation of pre-existing faults is supported by multiple erosional unconformities and the negligible distribution of low angle compressional faults, albeit up to four compressional events (Mid-Permian Event, Hunter-Bowen Event, Late Cretaceous Event, and Paleogene Event) had affected the region (Kulikowski & Amrouch, 2017a). Under Andersonian faulting theory (Anderson, 1951), such compressional events would develop low angle (30°) faults; however, due to the abundance of high angle (60°) normal faults, it would be more stress economic to reactivate existing faults rather than develop new faults (Kulikowski & Amrouch, 2017a).

Insert Fig. 12

The original NE-SW striking normal faults, which are present throughout the basin (Fig. 13a & 13b), are now observed to positively displace reflectors (Apak et al., 1997; Gravestock & Jensen-Schmidt, 1998; Radke, 2009; Kulikowski & Amrouch, 2017a, 2017b; Kulikowski et al., 2017a). Their stratigraphic distribution is often limited to terminating within basement or Middle Permian stratigraphy, and rarely penetrating into younger units (Apak et al., 1997; Gravestock & Jensen-Schmidt, 1998; Radke, 2009; Kulikowski & Amrouch, 2017b). Due to the poor seismic resolution below Permian coal measures, detailed fault growth studies (e.g. Giba et al., 2012; Jackson and Rotevatn, 2013; Robson et al., 2017) have not been possible and their interpretation becomes more difficult with depth. The difficulty is also exaggerated when developing fault models from seismic data that remains in the time-domain, as the true

fault angle is not being captured (Fig. 8b & 8c). The difference in basement-fault geometry between the time and depth-domains has proven to be problematic for previous researchers that used sparse 2D seismic data, as their work interpreted purely extensional faults, which were later re-interpreted as compressional faulting, and which are now known to be a combination of inverted normal faults, compressional faults and strike-slip faults (e.g. Kuang, 1985; Stanmore & Johnstone, 1988; Apak et al., 1997; Sun, 1997; Gravestock & Jensen-Schmidt, 1998; Radke, 2009; Grant-Woolley et al., 2014; Kulikowski & Amrouch, 2017b; Kulikowski et al., 2017a).

Insert Fig. 13

The SE-NW strike-slip faults are present throughout the region and have been attributed to reducing reservoir performance through cataclasis, compartmentalisation of reservoirs, and potentially complicating hydraulic fracture stimulation treatments (Grant-Woolley et al., 2014; Kulikowski et al., 2016c). These strike-slip faults appear predominantly within basement and can extend into the hydrocarbon-rich Patchawarra Formation (Apak et al., 1997; Radke, 2009; Kulikowski & Amrouch, 2017b; Kulikowski et al., 2017a). This fault set can easily be overlooked in cross-section due to the seismic resolution at basement and must be investigated in time-slice (or depth-slice) views to observe lateral displacements or linear features. A series of large basin-scale en echelon NNE-SSW strike-slip faults are present in the Patchawarra Trough (Fig. 3a) and form pop-up or positive flower structures that have been developed into highly economic fields. Their presence elsewhere in the basin may be equally as fruitful; however, are yet to be discovered!

6.2.2 REACTIVATION POTENTIAL UNDER PALEO-STRESSES

A new approach for assessing the reactivation and dilation potential of faults through time was presented by Kulikowski & Amrouch (2017c), using the Cooper-Eromanga Basin as a

case study. This approach utilises complete paleo-stress tensors for six events that were obtained through calcite twin stress inversion analysis (Kulikowski & Amrouch, 2017a). Complete paleo-stress tensors were integrated with geomechanical models to simulate the stress conditions present during each of the six key stages of basin evolution. Results found that after the critical moment in the Cooper-Eromanga Basin petroleum system (90 Ma), E-W (Late Cretaceous Event) and N-S (Paleogene Event) striking high angle (50-70°) faults were most likely to be dilated and acting as permeable hydrocarbon conduits (Fig. 13c). The critical moment defines the major period of hydrocarbon generation, migration and entrapment. This provides critical information that improves hydrocarbon migration pathway models that previously considered faults to have static 2D mechanical properties.

The history of basement fault reactivation is often constrained through fault growth analysis using 3D seismic data (e.g. Williams et al., 1989; Childs et al., 1996; Baudon & Cartwright, 2008); however, this cannot be performed in regions that have poor seismic resolution. For such regions, including the Cooper-Eromanga Basin, the Slip Tendency of faults is calculated using paleo-stress tensors and geomechanical modelling to provide insights into the 4D evolution of fault reactivation. Kulikowski & Amrouch (2017c) measured the Slip Tendency of four major fault sets modelled using the paleo-stress tensors during six tectonic events (Fig. 13d). The results showed that N-S striking high angle (50-70°) faults were most likely to reactivate during the Alice Springs Event, and E-W striking high angle (50-70°) faults likely reactivated during the Mid-Permian Event (Fig. 13d). Since these two events NE-SW striking high angle (50-70°) faults were most likely to shear reactivate under the subsequent Daralingie Event, Hunter-Bowen Event, Late Cretaceous Event and Paleogene Event (Fig. 13d). This is in line with other research suggesting considerable exhumation and erosion along the major NE-SW striking GMI and MN ridges (Kuang, 1985; Apak et al., 1997;

Gravestock & Jensen-Schmidt, 1998; Mavromatidis, 2006, 2007; Kulikowski & Amrouch, 2017b).

6.2.3 REACTIVATION POTENTIAL UNDER CONTEMPORARY STRESSES

A case study on the Swan Lake 3D and Dullingari 3D seismic surveys, located adjacent to the GMI and MN ridges, respectively, investigated the reactivation potential of basement-involved faults under contemporary stresses by measuring the Slip Tendency, Dilation Tendency, and Fracture Stability (Kulikowski et al., 2016c). The study analysed four unique fault sets modelled using hydrostatic pressure, in situ stress, and typical rock mechanics parameters from the Cooper Basin.

Results from Kulikowski et al. (2016c) showed that E-W striking faults have the highest Dilation Tendency (0.900) and thus most likely to act as permeable hydrocarbon conduits under the present day stress (Fig. 13c). The study also identified SE-NW strike-slip faults within both 3D seismic surveys and found that they are most likely to shear reactivate (Fig. 13d). A pore pressure increase of between only 0.5 and 5.0 MPa is required for this fault set to intersect the reactivation curve. Shear reactivation can compartmentalise the reservoir, reduce reservoir properties through cataclasis, complicate hydraulic fracture propagation, and facilitate tertiary migration of hydrocarbons. Therefore, precise seismic interpretation, particularly in depth-slice to observe lateral offsets, must focus on the identification of SE-NW striking strike-slip faults in order to incorporate their presence with the development of hydraulic fracture stimulation and drilling programs.

6.3 Cretaceous Polygonal Fault System

6.3.1 SUMMARY

Layer bound polygonal faults are present within Cretaceous Eromanga Basin marine sediments across the entire basin (Heath et al., 1989; Watterson et al., 2000; Kulikowski et al., 2017a; Kulikowski & Amrouch, 2017b). These faults were first identified from 2D seismic data (Rumph, 1982; Moore & Pitt, 1984; Newton, 1986; Gilby & Mortimore, 1989;

Scholefield, 1989; Gorter et al., 1989; Young et al., 1989; Longley, 1989), with the 3D distribution and regional extent only recently discovered in literature (Oldham & Gibbins, 1995; Watterson et al., 2000; Kulikowski et al., 2017a). A detailed analysis of polygonal faults within the Lake Hope 3D seismic survey suggests that their development is linked to a density inversion, where a low density and overpressured stratal unit was buried and de-watered by overlying normally pressured and higher density sediments (Watterson et al., 2000). The planar normal faults are mostly contained within the Mackunda Formation, Coorikiana Sandstone, Bulldog Shale and Wallumbilla Formation; however, larger faults are found to penetrate into the underlying and oil-rich Murta Member (Fig. 7). Maximum throw was found within the Coorikiana Sandstone. The dip angle of faults remains constant along a given fault plane and can range between 44° and 61° (Watterson et al., 2000). This polygonal fault system may present a new hydrocarbon exploration opportunity targeting shallow oil that has migrated from Lower Cretaceous oil-rich reservoirs through permeable polygonal faults (Fig. 7) (Watterson et al., 2000).

The normal displacement across polygonal faults can tilt shallow reservoirs such that low relief structural traps are developed and potentially fault sealing. Low relief structures that are bound by deeply penetrating faults can facilitate the accumulation of oil in shallow reservoirs. This play has yet to be truly tested in this region, but is analogous to the polygonal fault system associated with Tertiary hydrocarbon-rich shales in the North Sea (Cartwright & Lonergan, 1997; Lonergan et al., 1998). The presence of faults within hydrocarbon reservoirs can have tremendous implications for effective production and development, such as compartmentalisation of the reservoir, tertiary hydrocarbon migration, and complications with hydraulic fracture stimulation treatments. Considering that Lower Cretaceous and Jurassic hydrocarbon reservoirs are currently being explored and developed, an

understanding of the geometry, intensity and reactivation potential of the Cretaceous polygonal fault system is highly beneficial.

6.3.2 REACTIVATION POTENTIAL UNDER CONTEMPORARY STRESSES

This potential new play type was first suggested by Watterson et al. (2000), who suggested the possibility that these faults may be facilitating the tertiary migration of hydrocarbons from known reservoirs to shallow sedimentary rocks. Little literature has since appeared in relation to this exploration opportunity, with the regional extent of this system only recently discovered (Kulikowski et al., 2017a). The Leakage Factor and Dilation Tendency of this regional polygonal fault system were modelled to determine the optimum fault geometry required for fluid flow (Kulikowski et al., 2017a).

The results show that high dip angle (50-90°) polygonal faults striking 080-260°N and 125-305°N have the largest Leakage Factor, and fault planes with high dip angle (50-90°) striking 105-285°N have the largest Dilation Tendency (Kulikowski et al., 2017a). These fault planes are therefore most likely to facilitate the tertiary migration of hydrocarbons from Lower Cretaceous hydrocarbon-rich reservoirs into shallow structures, given that they penetrate below the Cadna-owie Formation into the hydrocarbon-rich Murta Member.

6.4 Natural Fractures

6.4.1 SUMMARY

Natural fractures can provide highly permeable pathways for hydrocarbon production if the local and regional fracture set geometries are known. The strike and dip angle of fracture sets are equally as important for optimising hydrocarbon recovery. Six regionally pervasive conjugate natural fracture sets (Fig. 14a) are present in the Cooper-Eromanga Basin (Kulikowski & Amrouch, 2017a). The timing of their development, stratigraphic distribution, and spatial intensity has been well constrained (Kulikowski et al., 2016a; Kulikowski &

Amrouch, 2017a). Extrapolation of wellbore derived natural fractures to the wider reservoir has also been investigated by a number of authors (Backe et al., 2011; Abul Khair et al., 2012; King et al., 2011; Kulikowski et al., 2017b), suggesting that upwards of 70% of wellbore fractures are represented in seismic curvature results.

Insert Fig. 14

6.4.2 NATURAL FRACTURES AT THE WELLBORE

Low dip angle (30°) conjugate fracture sets striking E-W and N-S are present throughout the stratigraphic column and associated with the Paleogene Event, and the Upper Cretaceous and Hunter-Bowen events, respectively. A third low dip angle conjugate fracture set is present only within the Patchawarra, Tirrawarra, Merrimelia and Basement formations striking NE-SW and associated with the Mid-Permian Event. A vertical conjugate natural fracture set striking NNE-SSW and SE-NW is present only within Basement and developed during the Alice Springs Event. Two additional conjugate natural fracture sets are present throughout the stratigraphic column, striking NE-SW and SE-NW with high dip angles (50-70°), and most likely associated with periods of post-compressional flexural relaxation, or basin sag (Abul Khair et al., 2016; Kulikowski & Amrouch, 2017a). The majority of interpreted fractures have high dip angles (50-70°) making the true wellbore fracture intensity of vertical wells difficult to constrain. A comparison between the fracture intensity interpreted from vertical, horizontal and inclined wells would provide more meaningful and representative fracture intensities.

A robust natural fracture study was performed for the Warburton Basin (Sun, 1999) using core, borehole image logs, and dip meter logs. The conclusions present a number of fracture sets; however, their methods relied too heavily on the strike of fractures and did not consider that slight changes in dip angle (20°) can have a different interpretation (Anderson, 1951).

For this reason the use of seismic attributes, such as most positive and most negative curvature, can be misleading by only providing the strike of possible fractures and faults. Fracture sets with similar strike direction but different dip angles cannot be distinguished from these seismic trending methods.

Horizontal fractures have also been proposed to exist in the basin, and likely associated with periods of significant exhumation and erosion (Flottmann et al., 2004; Tyiasning & Cooke, 2016; Cooke et al., 2016). Significant erosion can reduce the vertical stress magnitude and create local compressional stress regimes that can develop tensile horizontal fractures. These horizontal fractures can complicate hydraulic fracture stimulation treatments by preferentially reactivating and causing rotation of hydraulic fractures into the horizontal plane, which is a common phenomenon in the Cooper-Eromanga Basin (Cooke et al., 2016; Pokalai et al., 2016, 2017).

6.4.3 NATURAL FRACTURES AWAY FROM THE WELLBORE

A common assumption within the petroleum industry is that wellbore data can be extrapolated to the wider reservoir, which assumes that stress conditions, structural data, pore pressures, reservoir properties and characteristic, and other important criteria remain constant. If incorrect, this assumption can lead to obvious implications for exploration and development programs. As the Cooper-Eromanga Basin contains low permeability reservoirs, the presence of permeable fracture networks can add great economic value to prospects; however, much of the existing work assumes that borehole data is representative of the wider kilometre-scale fields (Kulikowski et al., 2017b). Recent advancements in seismic acquisition and processing have enabled the use of seismic attributes to provide information away from the wellbore that is otherwise overlooked in the original amplitude volumes.

Curvature analysis is a seismic attribute that has been shown to correlate well with wellbore derived fracture and fault data (e.g. Murray, 1968; Lisle, 1995; Stewart & Podolski, 1999; Hakami et al., 2004; Al-Dosary & Marfurt, 2006; Chopra & Marfurt, 2007; King et al., 2011; Abul Khair et al., 2012; Kulikowski et al., 2017b). The value for curvature is defined as the rate of change of the direction of a curve (Roberts, 2001), such that for any point (P) the curvature (K) is defined as the rate of change of the dip angle ($d\omega$) with respect to the arc length (dS) (Roberts, 2001). The arc length (dS) is obtained from the osculating circle that has a common tangent to P and makes the greatest possible contact with the curve (Roberts, 2001). The radius of the osculating circle forms the radius of curvature (R); such that in two-dimensions the value for K is defined as (Roberts, 2001);

$$K = \frac{d\omega}{dS} = \frac{2\pi}{2\pi R} = \frac{1}{R}$$

Curvature analysis has previously been performed within the Cooper-Eromanga Basin (Backe et al., 2011; King et al., 2011; Abul Khair et al., 2012; Kulikowski et al., 2017b) showing a close relationship with fractures measured at the wellbore (Fig. 14b & 14c). The spatial and temporal distribution of permeable fracture networks away from the wellbore using curvature analysis has shown that high angle E-W and SE-NW striking fractures are highly pervasive and most likely to be permeable under contemporary stresses (Kulikowski et al., 2017b). These E-W and SE-NW striking fracture sets are present in each of the five 3D seismic surveys analysed by Kulikowski et al. (2017b) and were found to increase in intensity along E-W elongate anticlinal structures, which may present an exploration target for future programs. The use of curvature analysis for field development programs that target fracture networks appears invaluable, as it can provide the spatial and temporal distributions of permeable fracture networks in the subsurface away from the wellbore.

6.4.4 REACTIVATION POTENTIAL UNDER CONTEMPORARY STRESSES

Understanding the distribution, geometry, and intensity of permeable fracture networks is an important aspect of development programs in the low permeability Cooper-Eromanga Basin. The likelihood of fractures to reactivate and be open to fluid flow is primarily controlled by the contemporary stress conditions relative to the fracture geometry. The contemporary stress in the Cooper-Eromanga Basin has an approximately E-W oriented maximum horizontal stress and is under a strike-slip stress regime, but the orientation can vary by up to 20° and the regime can alternate between a compressional stress regime (Fig. 11c) (Nelson et al., 2007; Reynolds & Hillis, 2000; Reynolds et al., 2004; King et al., 2008, 2011; Abul Khair et al., 2012; Pokalai et al., 2016, 2017). This variation of in situ stress has a profound influence on: (1) reactivation potential of fractures and faults; (2) hydraulic fracturing; and (3) infers that geomechanical modelling performed on the basin-scale may not be representative of the field-scale.

King et al. (2011) and Abul Khair et al. (2012) measured the fracture susceptibility of natural fractures on a basin-scale assuming an E-W oriented maximum horizontal stress that alternates between a strike-slip and compressional stress regime. Their study found that NE-SW and SE-NW striking fractures with moderate dip angles are most prone to reactivation (Fig. 14d & 14e). Understanding the shear reactivation potential is important; however, measuring the likelihood of tensile reactivation is equally as important. Kulikowski et al. (2017b) measured the Dilation Tendency of 454 fractures to show that E-W and SE-NW striking high angle (60°) fractures are optimally oriented to dilate and act as potential hydrocarbon conduits under contemporary stresses (Fig. 14f). These sets are regionally pervasive away from the wellbore within the Patchawarra Formation and would form ideal fracture sweet-spots given sufficient intensity (Fig. 14b & 14c).

7. HYDRAULIC FRACTURE STIMULATION AND WELL SURVEILANCE

Hydraulic fracturing has been performed in the Cooper Basin since 1969 (McGowen et al., 2007). The majority of hydraulic fracturing treatments are focus on the predominately Permian sandstone reservoirs, especially in the tight sand Patchawarra Formation. This formation has low (milliDarcy) permeability and requires multistage hydraulic fracturing to optimise production and be economically feasible. There is significant gas potential to explore and develop in this area; however, the stress complexity and high pressure and temperature conditions are challenging to effectively execute hydraulic fracturing programs.

During injection and fracture propagation a considerable pressure loss can be observed near the wellbore. This near-wellbore pressure loss (NWBPL) was first discussed by Chipperfield et al. (2000) and Roberts et al. (2000), who stated that the causes of NWBPL are related to pressure loss within the perforations, and tortuosity within the induced fracture path near the wellbore. Johnson et al. (2002) and Johnson and Greenstreet (2003) discussed pressure dependent leak-off (PDL) and NWBPL in the Cooper Basin and showed the significant impact it can have on production performance. NWBPL is caused by frictional pressure loss at the wellbore and closely related to tortuosity. Four different types of fracture propagation can result from high tortuosity including fracture turning, fracture twisting, multiple fracturing and fracture migration. High NWBPL can therefore complicate the hydraulic fracture process and result in a lower percentage of proppant being placed within the target reservoir (Pokalai et al., 2015a, 2015b).

When pre-existing natural fractures are present within a reservoir the near-wellbore pressure loss is considerably higher due to the complex interactions that create multiple fractures with tortuous paths. This tortuous path will shear and tensile reactivate pre-existing natural fractures to create a large amount of pressure dependent leak-off. Therefore, pressure dependent leak-off can have both positive and negative impacts. It can increase rock permeability by increasing the stimulated rock volume, while at the same time causing a high

near-wellbore pressure drop. However, to have better proppant placement and to maximise the flowback of fracturing fluid, near-wellbore pressure needs to be reduced.

The majority of the Patchawarra Formation consists of thick sand intervals that cycle between coal measures and shale, and is currently exposed to high pressure, high stress, and high temperature conditions. Therefore, the fracturing fluid system and proppant need to be selected in order to suit these conditions. Fracturing fluid is commonly a water-based fluid system within the Cooper-Eromanga Basin comprising of either a Linear Gel or a Borate Crosslink Gel that is injected during the pad stage, slurry stage and the flushing stage. Proppant is typically 100 mesh sand and is pumped into the target zone to reduce NWBPL and to bridge-off the PDL. This is followed by the injection of ceramic proppant to provide high fracture conductivity. The perforations that the hydraulic fracture is pumped into are typically made by lowering expendable hollow carrier (EHC) or link guns down the wellbore to perforate the casing completion at the target location. The style of perforating guns is primarily dependant on well completion, with EHC guns commonly used in monobore completions to mitigate rat-hole loss, and link guns are used in conventional completion designs.

Once perforations and hydraulic fracture stimulations are complete and the well begins producing hydrocarbons, there is a significant need for well surveillance and intervention programs due to the harsh subsurface conditions within the Cooper-Eromanga Basin. These can range from high temperatures, high pressures, and high CO_2 concentrations, to liquid loading (water in the wellbore) issues that can lead to reduced production (Rigby & Smith, 1981; Wycherley et al., 1999; McGowen et al., 2007; Winterfield et al., 2014). Hydrocarbon production can also be inhibited by the development of scale (halite and calcite) within the perforations, where pressure and temperature rapidly decrease causing solutes to precipitate. The CO_2 concentration within the Cooper-Eromanga Basin is significantly higher (10-30

v/v%) than the average sedimentary basin (Rigby & Smith, 1981; Wycherley et al., 1999), contributing to the need to mitigate calcite scale through acid treatments, re-perforation, and regular wireline drift and broach intervention programs (Pitkin et al., 2012). Salts (NaCl) have also been found to precipitate within perforations originating from salty groundwater invading the reservoir.

Other than causing scale build-up, the invasion of groundwater into the wellbore can also increase the production rate required to lift, and unload, the liquids to surface and can cause liquid loading within the wellbore to effectively stop production (Winterfield et al., 2014). Mitigation techniques for this may include artificial lifts (nitrogen injection), compressor installation to reduce back-pressure, plunger lift systems, injection of foaming agents via micro-strings, installation of siphon strings (or recompletion to small diameter tubing) to reduce the minimum rate to lift liquids, well cycling (pressure build-up), and producing the well to atmospheric pressures for a short period of time to unload liquids (McGowen et al., 2007; Winterfield et al., 2014).

8. EXPLORATION AND DEVELOPMENT

8.1 Current Programs

Current exploration programs are somewhat simplistic and have remained inline with the original anticlinal theory; identify and drill an anticlinal closure (Apak et al., 1997; Lowe-young et al., 1997; Morton, 1998; O'Neil, 1998). This approach has generated in excess of 6.5 trillion cubic feet (TCF) of sales gas, with 1.6 TCF remaining to be produced (Mackie, 2015). Oil exploration, now primarily targeting the Jurassic Eromanga Basin reservoirs, has also become highly profitable, generating 520 million barrels (mmbbls) from Jurassic to Cretaceous reservoirs, with 150 mmbbls of recoverable reserves remaining (Mackie, 2015). The largest discovered oil producer is the Early Permian Tirrawarra Formation (braided delta

and braided stream sandstone), particularly within the Tirrawarra Field where more than 80% of Cooper-Eromanga Basin oil is reservoired (Gravestock et al., 1998a). Taking into account the number of exploration wells drilled versus new Permian gas field discoveries, the success rate for current exploration programs is approximately 40% (Mackie, 2015). The success of Mesozoic oil exploration wells grew from 12% to 45% after the introduction of 3D seismic data acquisition, illustrating the significance of geophysical advancements in discovering new fields and new play types (Mackie, 2015).

There are currently two major plays in the province; targeting the Jurassic Eromanga Basin oil reservoirs, and persisting with the anticlinal theory in the oil and gas saturated Cooper Basin (Lowe-Young et al., 1997; Radke, 2009; Scott et al., 2013; Mackie, 2015). The central portion of the Eromanga Basin oil play overlies the South Australian portion of the Cooper Basin and forms Australia's most prolific oil province (Lowe-Young et al., 1997). The majority of Jurassic oil is reservoired within the Birkhead Formation, Hutton Sandstone, and Poolowanna Formation given that a structural trap exists (Lowe-Young et al., 1997; Kulikowski et al., 2016b, 2017c). It is important to note, however, that the presence of these typically low-relief structural traps can depend on the seismic time-to-depth conversion method being used, as the conversion errors can be greater than the structural closure (Lowe-Young et al., 1997; Radke, 2009; Kulikowski et al., 2016b, 2017c). The source of Jurassic oil in the central portion of the play has been attributed to Permian source rocks migrating vertically through leaky seals or along fault conduits (Lowe-Young et al., 1997; Radke, 2009). Recently, the Eromanga Basin oil play has been extended to the western flank of the Cooper Basin, where major oil exploration and production is currently taking place (Lowe-Young et al., 1997). The western flank oil play targets low amplitude anticlinal traps within the Jurassic Eromanga Basin reservoirs that are also charged by Permian source rocks (Lowe-Young et al., 1997; Rake, 2009).

The anticlinal closures common to the basin are often associated with reactivated basement-involved faults that develop broad structures in the overlying stratigraphy, but they can also be associated with positive flower (pop-up) features that are common in the Patchawarra Trough, or as fault-bound anticlines where large basement-involved faults have reactivated and penetrated through overlying units (Apak et al., 1997; Lowe-Young et al., 1997; Radke, 2009; Scott et al., 2013; Mackie, 2015; Kulikowski et al., 2017a). The case of fault-bound anticlines is most common along the GMI and MN ridges where the large NE-SW striking high angle (50-70°) faults have shown evidence of relatively more recent reactivation (Apak et al., 1997; Gravestock et al., 1998; Kulikowski and Amrouch, 2017b). These anticlinal traps allow for the accumulation of oil and gas within all reservoir quality sandstones in both the Cooper and Eromanga basins (Kantsler, 1984; Lowe-Young et al., 1997; Alexander et al., 1998; Morton, 1998; Radke, 2009; Scott et al., 2013).

8.2 Future Research and Exploration Programs

As the humble anticline becomes entirely exploited in this province, companies will transition into the next phase of hydrocarbon exploration targeting technically more challenging plays, such as the basin centred gas play, deep coal measure play, stratigraphic plays, polygonal fault play, and potentially fractured basement play that is juxtaposed to Permian source rocks. Each of these relatively unconventional plays will require a more thorough understanding of the basin. Therefore, as exploration within the Cooper-Eromanga Basin becomes more challenging, the collaboration between academic researchers and explorationists will become more integral to exploration success. Much of the regional structural, stratigraphic, and stress framework for the basin has been well constrained in recent times (e.g. Apak et al., 1997; Gravestock & Jensen-Schmidt, 1998; Hillis et al., 1999, 2001, 2008; Reynolds et al., 2002, 2003, 2004, 2005, 2006; Mavromatidis, 2006, 2007; Nelson et al., 2006, 2007a, 2007b; Radke, 2009; Pokalai et al., 2015a, 2015b, 2016, 2017;

Kulikowski & Amrouch, 2017a, 2017b, 2017c; Kulikowski et al., 2016a, 2017a); however, there does remain a large volume of research that can directly impact the success of future hydrocarbon exploration and development programs. Additionally, exploration and production companies play an important role in the effective exploitation of Australia's largest onshore hydrocarbon province by testing new concepts and acquiring new data that will promote further research in the basin.

A complete 2D reconstruction of the basin has not yet been completed and would provide valuable information on the fault growth through time. Detailed fault growth analyses are not possible in the basin given the poor seismic resolution at basement; however, with continued improvement in seismic acquisition and processing techniques, a fault growth study may be possible in the future. This may ultimately lead to a complete structural and stratigraphic 3D reconstruction of the basin and provide a 3D view of the temporal and spatial distribution of the four overlying basins. The spatial extent of major unconformities would also be useful, particularly as oil migration from Permian sources to Eromanga Basin reservoirs relies on the presence of unconformities that have effectively removed regional seals (Lowe-Young et al., 1997). The distribution and magnitude of overpressure has previously been investigated (Hillis et al., 2001; van Ruth et al., 2000, 2003; Kulikowski et al., 2016a); however, the mechanism for overpressure generation in the basin remains questionable and may be investigated by integrating reservoir pressure, vertical stress magnitude, and sonic velocity data (Tingay et al., 2007). The degree of stress perturbation caused by pre-existing faults should also be investigated in more detail, as local stress rotation does exist (Fig. 11b).

To accurately interpret seismic data, the amplitude volume must be converted from the time-domain to the depth-domain using an appropriate depth conversion method (Kulikowski et al., 2016b, 2017c). The errors associated with seismic depth conversion can be attributed to a number of factors, but an understanding of the near surface velocity variation (statics) has

not been explored. Mapping the spatial variation of statics in a form that can be incorporated into velocity modelling would provide more accurate results. Considering that the contemporary stress alternates between a strike-slip and compressional stress regime (Fig. 11c), an understanding of the spatial variation in vertical stress magnitudes (calculated from density logs) would be highly beneficial and, if in a gridded map format, could be used to predict stress regimes across the basin.

Rock mechanics data does exist for key parts of the region but is selectively sampled and not representative of heterogeneities, and can contradict with other works (Abul Khair et al., 2013; Nelson et al., 2007; Pokalai et al., 2015). A detailed study focused on constraining the complete and representative rock mechanics data for the Warburton, Cooper and Eromanga basins would provide more certainty on geomechanical and hydraulic fracture stimulation models. Ideally, future hydraulic fracture stimulation models would incorporate the certain interaction between induced fractures and naturally occurring fractures and faults, with particular attention to SE-NW strike-slip faults that are most likely to reactivate under contemporary stresses (Kulikowski et al., 2016c). These SE-NW strike-slip faults are difficult to interpret in low resolution seismic data, but can reduce reservoir properties through cataclasis, can compartmentalise the reservoir, and contribute to tertiary hydrocarbon migration if reactivated (Grant-Woolley et al., 2014; Kulikowski et al., 2016c). A study investigating the possible relationship between well and reservoir performance with distance to these SE-NW strike-slip faults would provide a better understanding on their effect on production.

Finally, although not directly applicable to academic researchers, operating companies may discover new opportunities and hydrocarbon reserves by testing such concepts as the: (1) fracture basement play; (2) basin centred gas play; (3) hydraulic fracturing of deep coal; (4) polygonal fault system play; (5) targeting stratigraphic traps; (6) cutting-edge use of seismic

data (direct hydrocarbon indicators); and (7) cost effective alternatives to optimise production (pad drilling, deviated wells from existing wellbores, deepening old shallow oil wells to target Permian reservoirs, and perforating thin (1-2 feet) gas saturated and pressurised reservoirs that were initially dismissed).

9. CONCLUSIONS

This review forms a robust synthesis of recent developments within Australia's largest onshore hydrocarbon province, the Cooper-Eromanga Basin. New technologies and software application have armed researchers with cutting edge analysis techniques and applications that have generated a recent increase in information that was previously not available. The purpose of this study is to provide readers with a holistic insight into the province that includes: (1) a detailed tectonic and stratigraphic evolution; (2) a summary of geomechanical modelling results that predict fault and fracture reactivation (tensile and shear) through time to better understand hydrocarbon migration pathways; (3) a synthesis of the petroleum system processes and elements; (4) the spatial and temporal distributions of permeable natural fracture networks through wellbore and seismic data analysis; (5) common hydraulic fracturing and well surveillance programs contrast with a discussion on the common difficulties and risks; (6) a discussion on the seismic time-to-depth conversion methods that are being used and their individual accuracies and limitations; (7) current and future hydrocarbon exploration and development targets; and (8) a discussion on the future research opportunities that can directly impact the effectiveness of exploration and development programs.

Reviewing the province has highlighted opportunities for future exploration and identified possible research topics that will be fundamental to the success of future exploration and development programs. These future programs will begin to target technically more

challenging plays as the humble anticline becomes entirely exploited and will require a thorough understanding of the province. The methodologies and approaches summarised within this review forms a research framework that can be applied to other hydrocarbon provinces to better understand the dynamic structural geology, tectonic evolution and application of geophysics.

10. ACKNOWLEDGEMENTS

The authors appreciate the financial contribution made by the GeoFrac Consortium, which includes the sponsoring companies: Santos, Beach Energy, Chevron, Halliburton and BG Group (QGC). DUG Insight software (v.4.0, 2016) was used for seismic visualisation, interpretation and analysis. Conflict of interest: none.

11. REFERENCES

- Abul Khair, H.A., Cooke, D., King, R., Hand, M., Tingay, M. (2012). Preliminary workflow for subsurface fracture mapping using 3D seismic surveys: A case study from the Cooper Basin, South Australia. In: Geothermal Research Council Conference, Reno, Nevada, 36, 339-350.
- Abul Khair H., Cooke D., Hand M. (2013). The effect of present day in situ stresses and paleo-stresses on locating sweet spots in unconventional reservoirs, a case study from Moomba-Big Lake fields, Cooper Basin, South Australia. *Journal of Petroleum Exploration and Production Technology*, 3, (4), 207-221.
- Abul Khair H., Cooke D., Hand M. (2015). Seismic mapping and geomechanical analyses of faults within deep hot granites, a workflow for enhanced geothermal system projects. *Geothermics*, 53, 46-56.
- Al-Chalbi, M. (1974). An analysis of stacking, RMS, average, and interval velocities over a horizontally layered ground. *Geophysical Prospecting*, 22(3), 458-475.
- Alexander, E.M., Gravestock, D.I., Cubitt, C., Chaney, A. (1998). Lithostratigraphy and environments of deposition. In: Gravestock, D.I., Hibburt, J.E., Drexel, J.F., (Eds), *The Petroleum Geology of South Australia. Vol. 4: Cooper Basin, South Australia*. Department of Primary Industries and Resources. Report Book, 98/9, 69-116.
- Anderson, E.M. (1951). *The Dynamics of Faulting and Dyke Formation with Applications to Britain*, Oliver and Boyd, Edinburgh.
- Apak, S.N., Stuart, W.J., Lemon, N.M., Wood, G. (1997). Structural evolution of the Permian-Triassic Cooper Basin, Australia: Relation to hydrocarbon trap styles. *AAPG Bulletin*, 81, 533-555.

- Backe, G., Abul Khair, H., King, R., Holford, S. (2011). Fracture mapping and modelling in shale-gas target in the Cooper basin, South Australia. *The APPEA Journal*, 51, 397-410.
- Balch, A.H., Lee, M.W., Miller, J.J., Ryder, R.T. (1982). The use of vertical seismic profiles in seismic investigations of the earth. *Geophysics*, 47(6), 906-918.
- Balch, A.H., Lee, M.W. (1984). *Vertical Seismic Profiling: Techniques, Applications, and Case Histories*. International Human Resources Development Corporation, Boston, 488 p.
- Baudon, C., Cartwright, J. (2008). The kinematics of reactivation of normal faults using high resolution throw mapping. *Journal of Structural Geology*, 30(8), 1072–1084.
- Borazjani, S., Kulikowski, D., Amrouch, K., McCabe, P., Bedrikovetsky, P. (2017a). Composition changes of hydrocarbons during secondary petroleum migration. *The APPEA Journal*, extended abstract, accepted.
- Borazjani, S., Kulikowski, D., Amrouch, K., McCabe, P., Bedrikovetsky, P. (2017b). Deep bed filtration of hydrocarbons during secondary petroleum migration. *Geofluids*, under review.
- Boreham C. J., Hill A. J. (1998). Source rock distribution and hydrocarbon geochemistry. In: *The petroleum geology of South Australia. Vol. 4: Cooper Basin* (eds. D.I. Gravestock, J.E. Hibburt and J.F. Drexel), pp 129-142. South Australia. Department of Primary Industries and Resources. Report Book, 98/9.
- Bradshaw, M.T., (1993). Australian petroleum systems. *PESA Journal* 21, 43-53.
- Childs, C., Nicol, A., Walsh, J.J., Watterson, J. (1996). Growth of vertically segmented normal faults. *Journal of Structural Geology*, 18(12), 1389-1397.
- Cooke, D., Tyiasning, S., Abul Khair, H. (2016). Unexpected behaviors of stimulated fractures in the high-stress Cooper Basin. *The Leading Edge*, 35(1), 78-84.
- Deighton, I., Hill, A.J., 1998. Thermal and Burial History. In: *The petroleum geology of South Australia. Vol. 4: Cooper Basin* (eds. D.I. Gravestock, J.E. Hibburt and J.F. Drexel), pp 143-156. South Australia. Department of Primary Industries and Resources. Report Book, 98/9.
- Elliott, L.G. (1993). Post-Carboniferous tectonic evolution of eastern Australia. *APEA Journal*, 33, 215-215.
- Evans, P.R. (1988). The formation of petroleum and geological history of Australia. In: *Petroleum in Australia: the first century*. APEA Journal, Special Publication, 26-47.
- Flottmann, T., Campagna, D.J., Hillis, R., Warner, D. (2004). Horizontal microfractures and core discing in sandstone reservoirs, Cooper Basin, Australia. In: *Eastern Australasian basins symposium II: Petroleum Exploration Society of Australia Special Publication* (pp. 689-694).
- Gajewski, D., Pšenčík, I. (1990). Vertical seismic profile synthetics by dynamic ray tracing in laterally varying layered anisotropic structures. *Journal of Geophysical Research: Solid Earth*, 95(B7), 11301-11315.
- Ganley, D.C., Kanasewich, E.R. (1980). Measurement of absorption and dispersion from check shot surveys. *Journal of Geophysical Research: Solid Earth*, 85(B10), 5219-5226.
- Giba, M., Walsh, J.J., Nicol, A. (2012). Segmentation and growth of an obliquely reactivated normal fault. *Journal of Structural Geology*, 39, 253-267.

- Gravestock, D.I., Jensen-Schmidt, B. (1998). Structural setting. In: Gravestock, D.I., Hibburt, J.E., Drexel, J.F., (Eds), *The Petroleum Geology of South Australia. Vol. 4: Cooper Basin, South Australia*. Department of Primary Industries and Resources. Report Book, 98/9, 47-68.
- Gray, M.E, Daniel, R., Kaldi, J., Kulikowski, D. (2017). Determining the Accuracy of Pseudo-Capillary Pressure Curves Generated from Nuclear Magnetic Resonance (NMR) Data: The Cooper Basin, Australia. *Australian Journal of Earth Sciences*, submitted.
- Green, P.M., Brain, T.J., John, B.H. (1989). Possible stratigraphic controls on hydrocarbon distribution within the Jurassic-Early Cretaceous rocks, Eromanga Basin, southern Queensland. In: *The Cooper and Eromanga Basins, Australia* (ed. B.J. O'Neil), pp. 251-264. Petroleum Exploration Society of Australia, Society of Petroleum Engineers, Australian Society of Exploration Geophysicists (S.A. Branches), Adelaide (Proceedings of Cooper and Eromanga Basins Conference).
- Haines, P.W., Hand, M., Sandiford, M. (2001). Palaeozoic synorogenic sedimentation in central and northern Australia: A review of distribution and timing with implications for the evolution of intracontinental orogens. *Australian Journal of Earth Sciences*, 48, 911-928.
- Hardage, B.A. (1985). Vertical seismic profiling. *The Leading Edge*, 4(11), 59-59.
- Hauge, P.S. (1981). Measurements of attenuation from vertical seismic profiles. *Geophysics*, 46(11), 1548-1558.
- Heath, R., McIntyre, S., Gibbins, N. (1989). A Permian origin for Jurassic reservoir oil in the Eromanga Basin. In: *The Cooper and Eromanga Basins, Australia* (ed. B.J. O'Neil), pp. 405-416. Petroleum Exploration Society of Australia, Society of Petroleum Engineers, Australian Society of Exploration Geophysicists (S.A. Branches), Adelaide (Proceedings of Cooper and Eromanga Basins Conference).
- Hillis, R.R., Macklin, T.A., Siffleet, P. (1995). Regional depth-conversion of mapped seismic two-way-times in the Cooper-Eromanga Basins. *Exploration Geophysics*, 26(2/3), 412-418.
- Hoffmann, K.L. (1989). The influence of pre-Jurassic tectonic regimes on the structural development of the southern Eromanga Basin, Queensland. In: *The Cooper and Eromanga Basins, Australia* (ed. B.J. O'Neil), pp. 315-328. Petroleum Exploration Society of Australia, Society of Petroleum Engineers, Australian Society of Exploration Geophysicists (S.A. Branches), Adelaide (Proceedings of Cooper and Eromanga Basins Conference).
- Igboekwe, M.U., Ohaegbuchi, H.E. (2011). Investigation into the weathering layer using up-hole method of seismic refraction. *Journal of Geology and Mining Research*, 3(3), 73-86.
- Jackson, C.A.L., Rotevatn, A. (2013). 3D seismic analysis of the structure and evolution of a salt-influenced normal fault zone: a test of competing fault growth models. *Journal of Structural Geology*, 54, 215-234, doi:10.1016/j.jsg.2013.06.012.
- Jadoon, Q.K., Roberts, E., Blenkinsop, T., Raphael, A.J., Shah, S.A. (2016). Mineralogical modelling and petrophysical parameters in Permian gas shales from the Roseneath and Murteree formations, Cooper Basin, Australia. *Petroleum Exploration and Development*, 43(2), 277-284.
- Johnson, Jr., R.L., Abul Khair, H., Jeffrey, R.G., Meyer, J.J., Stark, C., Tauchintz, J. (2015). Improving fracture initiation and potential impact on fracture coverage by implementing optimal well planning and drilling methods for typical stress conditions in the Cooper Basin, Central Australia. *The APPEA Journal and Conference Proceedings*, 55, extended abstract.

Kantsler, A.J., Prudence, T.J.C., Cook, A.C., Zwigulis, M. (1984). Hydrocarbon habitat of the Cooper/Eromanga basin, Australia. In: Petroleum geochemistry and basin evolution (eds. G. Demaison and R. J. Murriss), pp 373-390. American Association of Petroleum Geologists Memoir 35.

King, R., Abul Khair, H., Bailey, A., Backe, G., Holford, S., Hand, M. (2011). Integration of In-Situ Stress Analysis and Three-Dimensional Seismic Mapping to Understand Fracture Networks in Australian Basins. In: Proceedings from the Australian Geothermal Energy Conference, 16-18 November, Melbourne, Australia, 129-134.

Kuang, K.S. (1985). History and style of Cooper-Eromanga Basin structures. *Exploration Geophysics*, 16, 245-248.

Kulikowski, D., Cooke, D., Amrouch, K. (2016a). Constraining the distribution and relationship between overpressure, natural fracture density and temperature in the Cooper Basin. *The Australian Petroleum Production and Exploration Association Journal*, 56, 11-28, doi:10.1071/AJ15002.

Kulikowski, D., Hochwald, C., Cooke, D., Amrouch, K. (2016b). A Statistical Approach to Assessing Depth Conversion Uncertainty on a Regional Dataset: Cooper-Eromanga Basin, Australia. ASEG-PESA-AIG 2016 Conference, Adelaide. Extended Abstract #200, 484-490, doi:10.1071/aseg2016ab200.

Kulikowski, D., Amrouch, K., Cooke, D. (2016c). Geomechanical Modelling of Fault Reactivation in the Cooper Basin, Australia. *Australian Journal of Earth Sciences*, 63(3), 295-314, doi:10.1080/08120099.2016.1212925.

Kulikowski, D., Amrouch, K. (2017a). Combining Geophysical Data and Calcite Twin Stress Inversion to Refine the Tectonic History of Subsurface and Offshore Provinces: A Case Study on the Cooper-Eromanga Basin, Australia. *Tectonics*, 36(3), 515-541, doi:10.1002/2016TC004366.

Kulikowski, D., Amrouch, K. (2017b). 3D Seismic Analysis Investigating the Relationship Between Structural Activity and Stratigraphic Architecture in the Intracratonic Cooper and Eromanga Basins, Australia. *Marine and Petroleum Geology*, submitted.

Kulikowski, D., Amrouch, K. (2017c). 4D Modelling of Fault Reactivation using Complete Paleo-Stress Tensors from the Cooper- Eromanga Basin, Australia. *Australian Journal of Earth Sciences*, submitted.

Kulikowski, D., Amrouch, K., Cooke, D., Gray, M.E. (2017a). Basement Structural Architecture and Hydrocarbon Conduit Potential of Polygonal Faults in the Cooper-Eromanga Basin, Australia. *Geophysical Prospecting*, in press, doi:10.1111/1365-2478.12531.

Kulikowski, D., Amrouch, K., Burgin, H.B. (2017b). Mapping Permeable Subsurface Fracture Networks: A Case Study on the Cooper Basin, Australia. *Journal of Structural Geology*, Submitted.

Kulikowski, D., Hochwald, C., Amrouch, K. (2017c). An automated cross-validation method to assess seismic time-to-depth conversion accuracy: A case study on the Cooper-Eromanga Basin, Australia. Unsubmitted.

Lowe-Young, B.S., Mackie, S.I., Heath, R.S. (1997). The Cooper-Eromanga petroleum system, Australia: Investigation of essential elements and processes. *Indonesian Petroleum*

Association. Proceedings of the Petroleum Systems of SE Asia and Australasia Conference, Jakarta, 199-211.

Mackie, S. (2015). History of Petroleum Exploration and Development in the Cooper and Eromanga Basins. AAPG/SEG International Conference and Exhibition, Melbourne, Australia, Search and Discovery Article #10814.

Mavromatidis, A. (2006). Burial/exhumation histories for the Cooper-Eromanga Basins and implications for hydrocarbon exploration, Eastern Australia. *Basin Research*, 18, 351-373.

Muller, R.D., Dyksterhuis, S., Rey, P. (2012). Australian paleo-stress fields and tectonic reactivation over the past 100 Ma. *Australian Journal of Earth Sciences*, 59, 13-28.

Nelson, E.J., Meyer, J.J., Hillis, R.R., Mildren, S.D. (2005). Transverse drilling-induced tensile fractures in the West Tuna area, Gippsland Basin, Australia: implications for the in situ stress regime. *International Journal of Rock Mechanics and Mining Sciences*, 42(3), 361-371.

Othman, A.A., Fathy, M., Maher, A. (2016). Use of spectral decomposition technique for delineation of channels at Solar gas discovery, offshore West Nile Delta, Egypt. *Egyptian Journal of Petroleum*, 25(1), 45-51.

Partyka, G., Gridley, J., Lopez, J. (1999). Interpretational applications of spectral decomposition in reservoir characterization. *The Leading Edge*, 18(3), 353-360.

Pokalai, K., Fei, Y., Ahmad, M., Haghghi, M., Gonzalez, M. (2015a). Design and optimisation of multi-stage hydraulic fracturing in a horizontal well in a shale gas reservoir in the Cooper Basin, South Australia. *The Australian Petroleum Production and Exploration Association Journal*, 55, 1-14.

Pokalai K., Haghghi M., Sarkar S., Tyiasning S., Cooke D. (2015b). Investigation of the Effects of Near-Wellbore Pressure Loss and Pressure Dependent Leakoff on Flowback during Hydraulic Fracturing with Pre-Existing Natural Fractures. SPE/IATMI Asia Pacific Oil and Gas Conference and Exhibition, Nusa Dua, Bali, SPE-176440.

Pokalai, K., Kulikowski, D., Johnson, Jr., R.L., Haghghi, M., Cooke, D. (2016). Development of a new approach for hydraulic fracturing in tight sand with pre-existing natural fractures. *The Australian Petroleum Production and Exploration Association Journal*, 56, 225-238.

Pokalai, K., Kulikowski, D., Amrouch, K., Haghghi, M., Johnson, Jr., R.L. (2017). Integrated 3D modelling of hydraulic fracturing in tight reservoirs with pre-existing natural fractures and complex stress conditions: A case study from the Cooper Basin, Australia. *Journal of Petroleum Science and Engineering*, submitted.

Radke, B. (2009). Hydrocarbon and Geothermal Prospectivity of Sedimentary Basins in Central Australia; Warburton, Cooper, Pedirka, Galilee, Simpson and Eromanga Basins. *Geoscience Australia Record* 2009/25.

Reynolds, S.D., Mildren, S.D., Hillis, R.R., Meyer, J.J., Flottmann, T. (2005). Maximum horizontal stress orientations in the Cooper Basin, Australia. implications for plate-scale tectonics and local stress sources. *Geophysical Journal International*, 160, 332-343.

Reynolds, S.D., Mildren, S.D., Hillis, R.R., Meyer, J.J. (2006). Constraining stress magnitudes using petroleum exploration data in the Cooper-Eromanga Basins, Australia. *Tectonophysics*, 415, 123-140.

- Rezaee, M.R., Sun, X. (2007). Fracture-Filling Cements in the Palaeozoic Warburton Basin, South Australia. *Journal of Petroleum Geology*, 30(1), 79-90.
- Roberts, G.A., Chipperfield, S.T., Miller, W.K. (2000). The evolution of a high near-wellbore pressure loss treatment strategy for the Australian Cooper Basin. In SPE Annual Technical Conference and Exhibition. Society of Petroleum Engineers.
- Robson, A.G., Holford, S.P., King, R.C., Kulikowski, D. (2017). Structural evolution of horst and half-graben structures proximal to a transtensional fault system using a 3D seismic dataset from the Shipwreck Trough, offshore Otway Basin, Australia. *Marine and Petroleum Geology*, in press, doi: 10.1016/j.marpetgeo.2017.10.028.
- Senior, B.R., Galloway, M.C., Ingram, J.A., Senior D. (1968). The geology of the Barrolka, Eromanga, Durham Downs, Thargomindah, Tickalara and Bulloo 1:250,000 Sheet areas, Queensland. Bureau of Mineral Resources.
- Stainsby, S.D., Worthington, M.H. (1985). Q estimation from vertical seismic profile data and anomalous variations in the central North Sea. *Geophysics*, 50(4), 615-626.
- Stanmore, P.J. (1989). Case studies of stratigraphic and fault traps in the Cooper Basin, Australia. In *The Cooper and Eromanga Basins, Australia. Proceedings of the Cooper and Eromanga Basins Conference*, Adelaide (pp. 361-369).
- Stuart, W.J. (1976). The genesis of Permian and lower Triassic reservoir sandstones during phases of southern Cooper Basin development. *APEA Journal*, 16(1), 27-48.
- Sun, X. (1997). Structural style of the Warburton Basin and control in the Cooper and Eromanga Basins, South Australia. *Exploration Geophysics*, 28(3), 333-339.
- Tyiasning, S., Cooke, D. (2015). A comparison of competing amplitude variation with offset techniques applied to tight gas sand exploration in the Cooper Basin of Australia. *Interpretation*, 3(3), SZ15-SZ26.
- Tyiasning, S., Cooke, D. (2016). Anisotropy signatures in the Cooper Basin of Australia: Stress versus fractures. *Interpretation*, 4(2), SE51-SE61.
- Veevers, J.J., Jones, J.G., Powell, C.M. (1982). Tectonic framework of Australia's sedimentary basins. *APEA Journal*, 22(1), 283-300.
- Veevers, J.J., Powell, C.M. (1984). Uluru and Adelaidean regimes, in J. J. Veevers, ed., *Phanerozoic earth history of Australia*: Oxford, Clarendon Press, p. 329-339.
- Watterson, J., Walsh, J., Nicol, A., Nell, P.A.R., Bretan, P.G. (2000). Geometry and origin of a polygonal fault system. *Journal of the Geological Society*, 157(1), 151-162.
- Williams, G.D., Powell, C.M., Cooper, M.A. (1989). Geometry and kinematics of inversion tectonics. *Geological Society, London, Special Publications*, 44(1), 3-15.

12. FIGURES

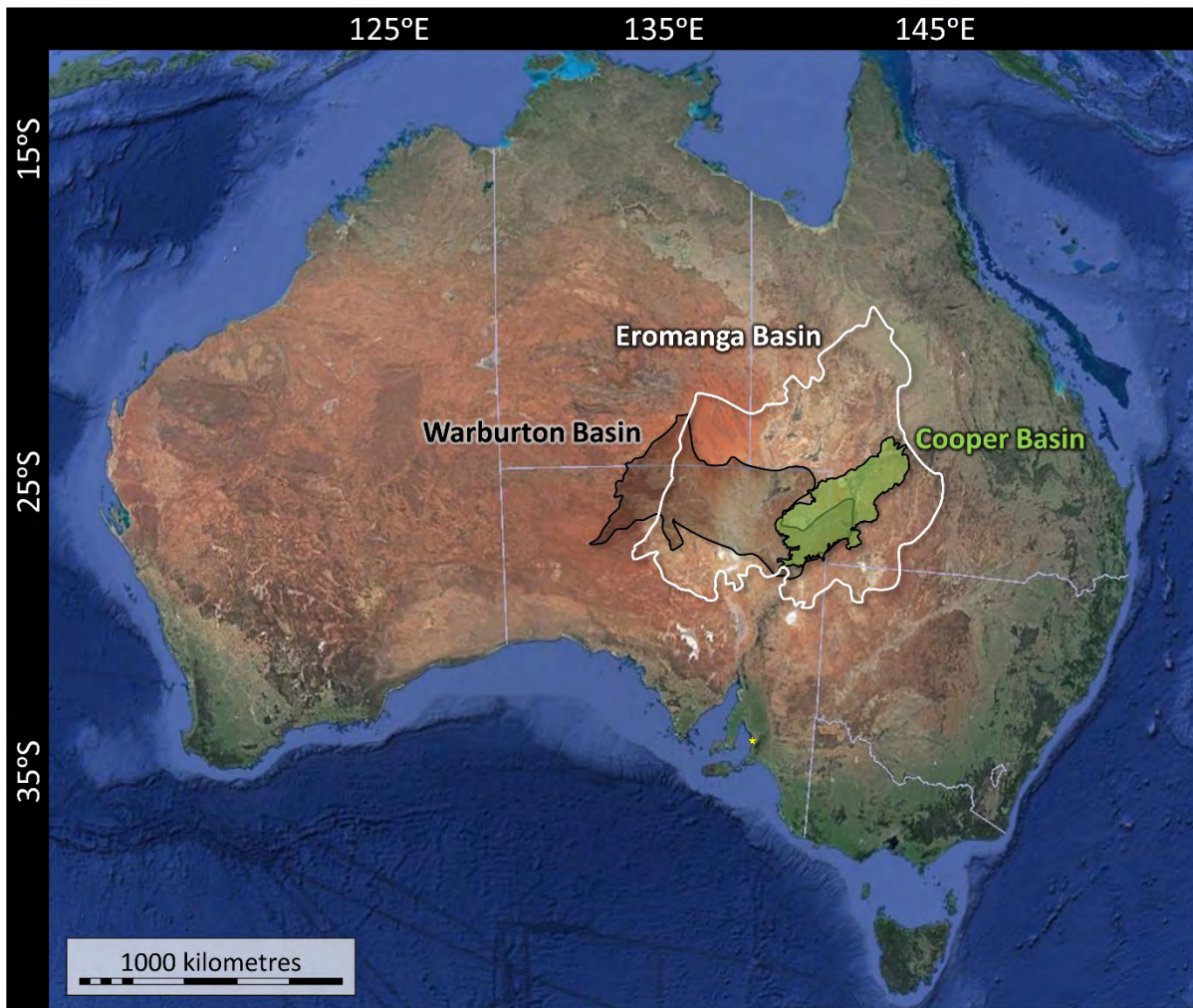


Figure 1. Location of the Warburton, Cooper, and Eromanga basins (after Kulikowski et al., 2016c).

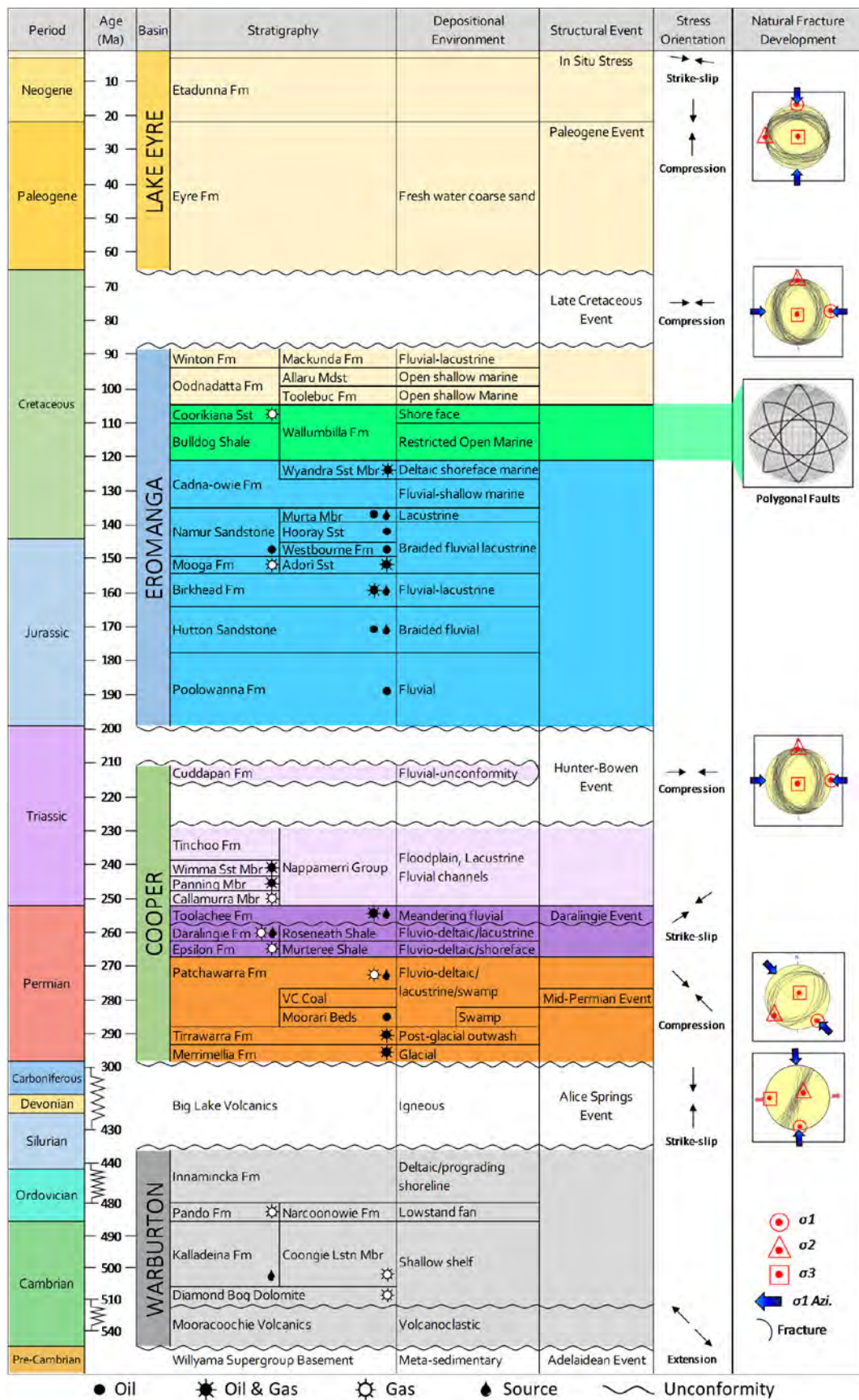


Figure 2. Tectonostratigraphy of the Cooper-Eromanga Basin (after Kulikowski & Amrouch., 2017a).

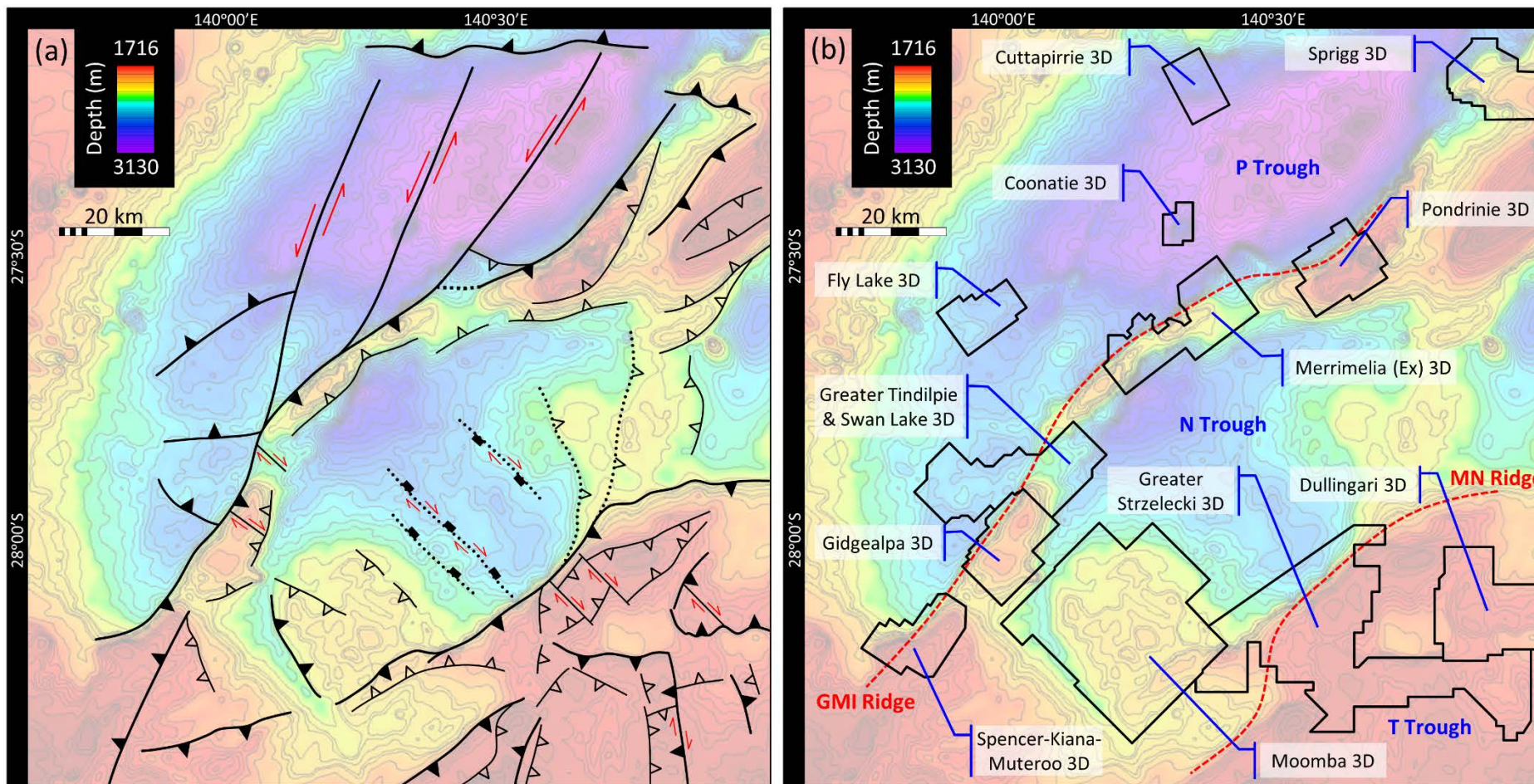


Figure 3. (a) Fault map of the South Australian Cooper-Eromanga Basin (after Kulikowski et al., 2017a). (b) Location of 12 3D seismic surveys commonly used for research. The location of the Gidgealpa-Merrimelia-Innaminka (GMI) and Murteree Nappacoongee (MN) ridges, and the Patchawarra (P Trough), Nappamerri (N Trough), and Tenappera (T Trough) troughs are shown (after Kulikowski et al., 2017a).

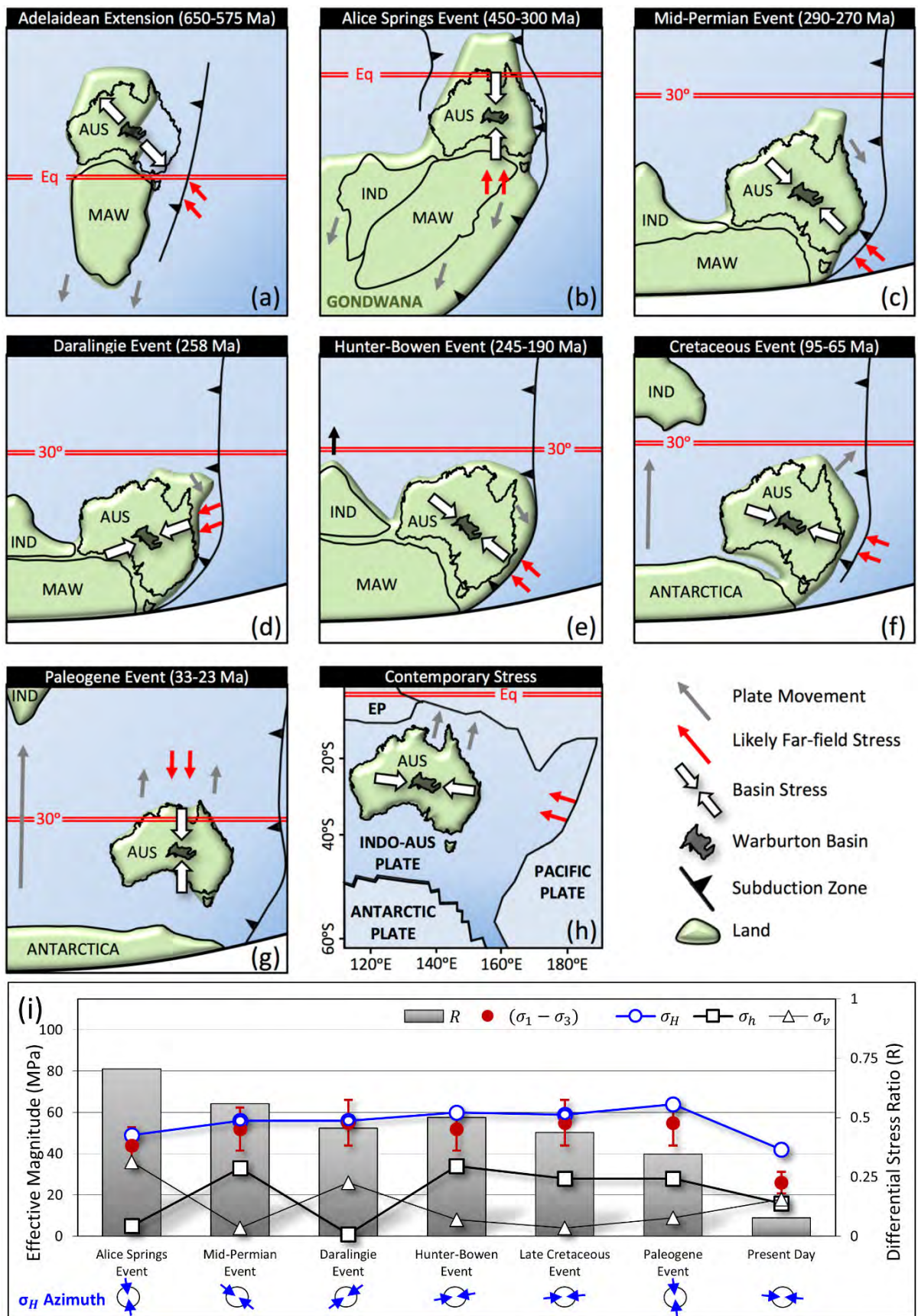


Figure 4. (a)→(h) Geodynamic evolution of Australia with Cooper-Eromanga Basin derived stresses through time. (i) Evolution of principal stresses (after Kulikowski & Amrouch, 2017a, 2017c).

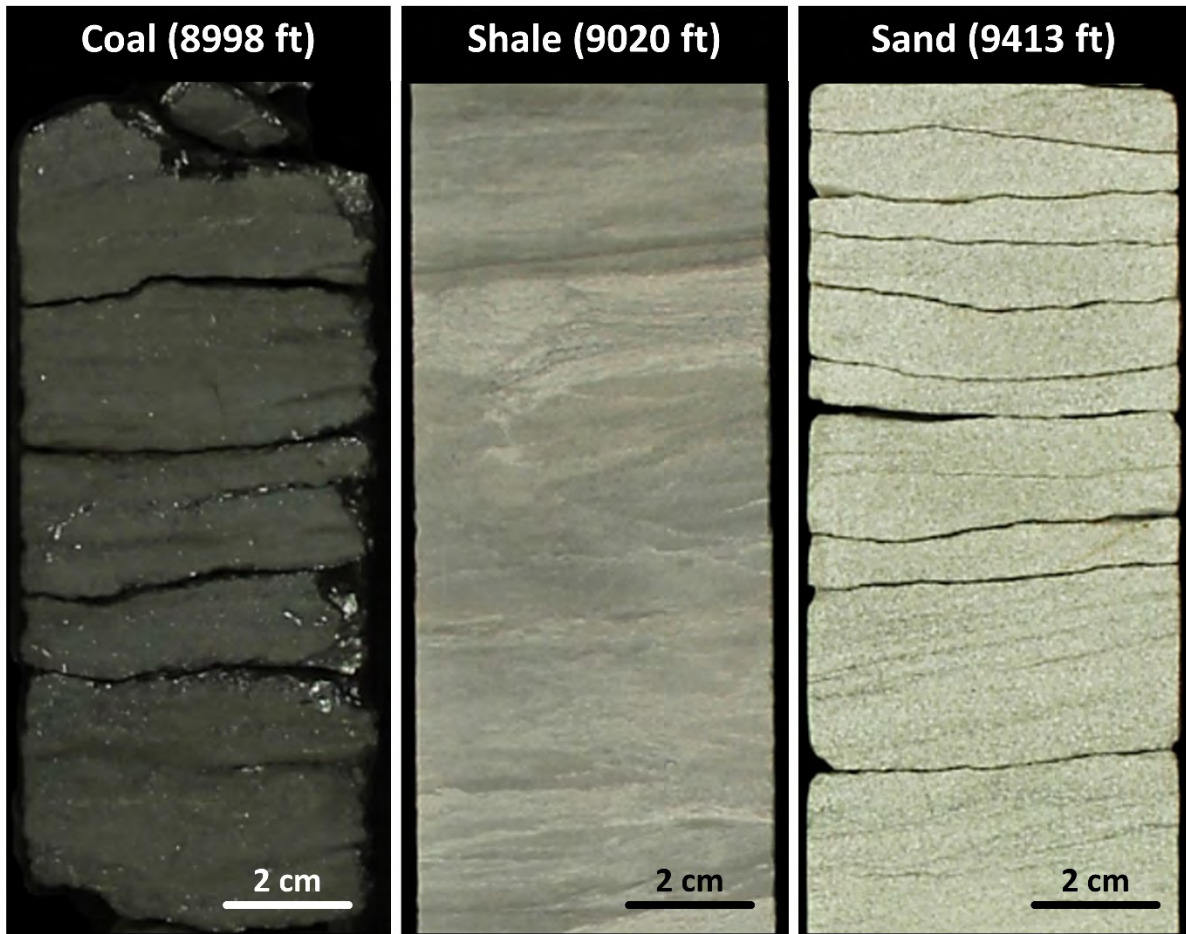


Figure 5. Cyclic lithology variation within the Patchawarra Formation (Core images obtained from Tindilpie 11 well completion report).

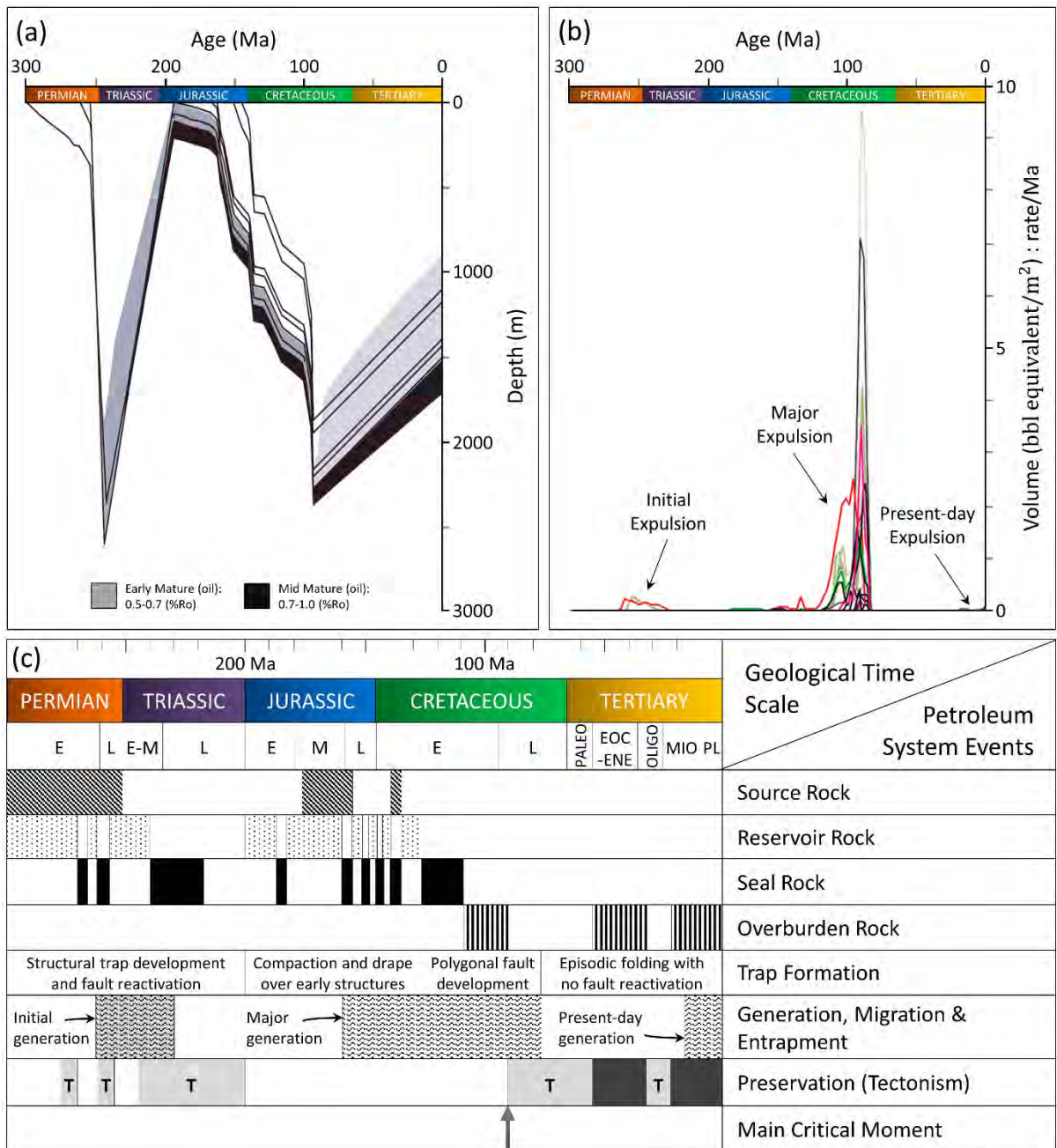


Figure 6. (a) Burial history of Cooper-Eromanga Basin sediments (after Mavromatidis, 2006). (b) Gas (per well) and oil expulsion through time (after Deighton & Hill, 2009). (c) Timing of key petroleum system processes (after Lowe-Young et al., 1997).

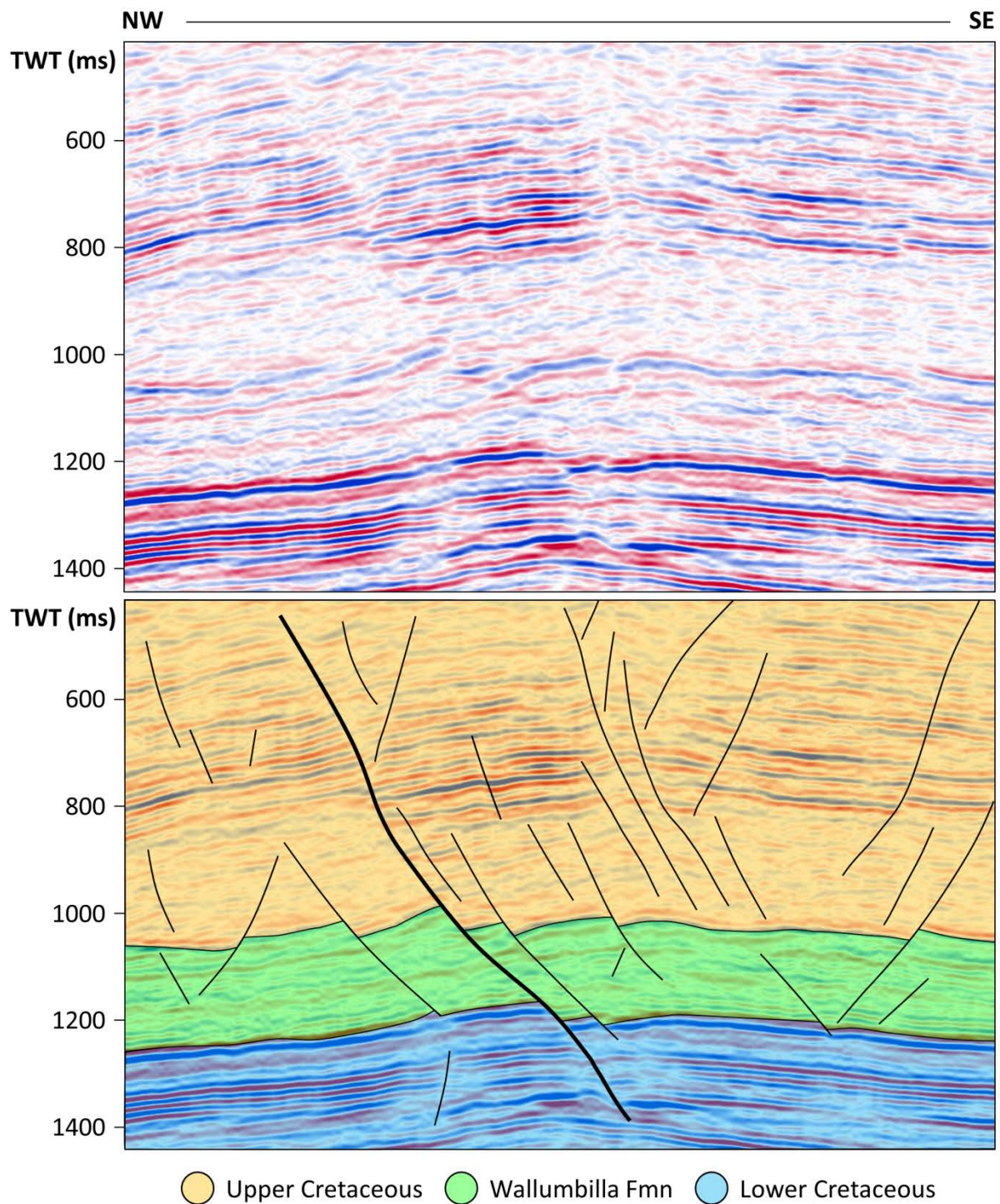


Figure 7. Cross-section from the Spencer-Kiana-Murteree 3D seismic survey (Inline 640) showing the polygonal fault system with large normal faults observed to displace the Cadnaowie Formation reflector and extend into oil-rich Lower Cretaceous reservoirs (Kulikowski et al., 2017a). See Figure 3b for seismic survey location.

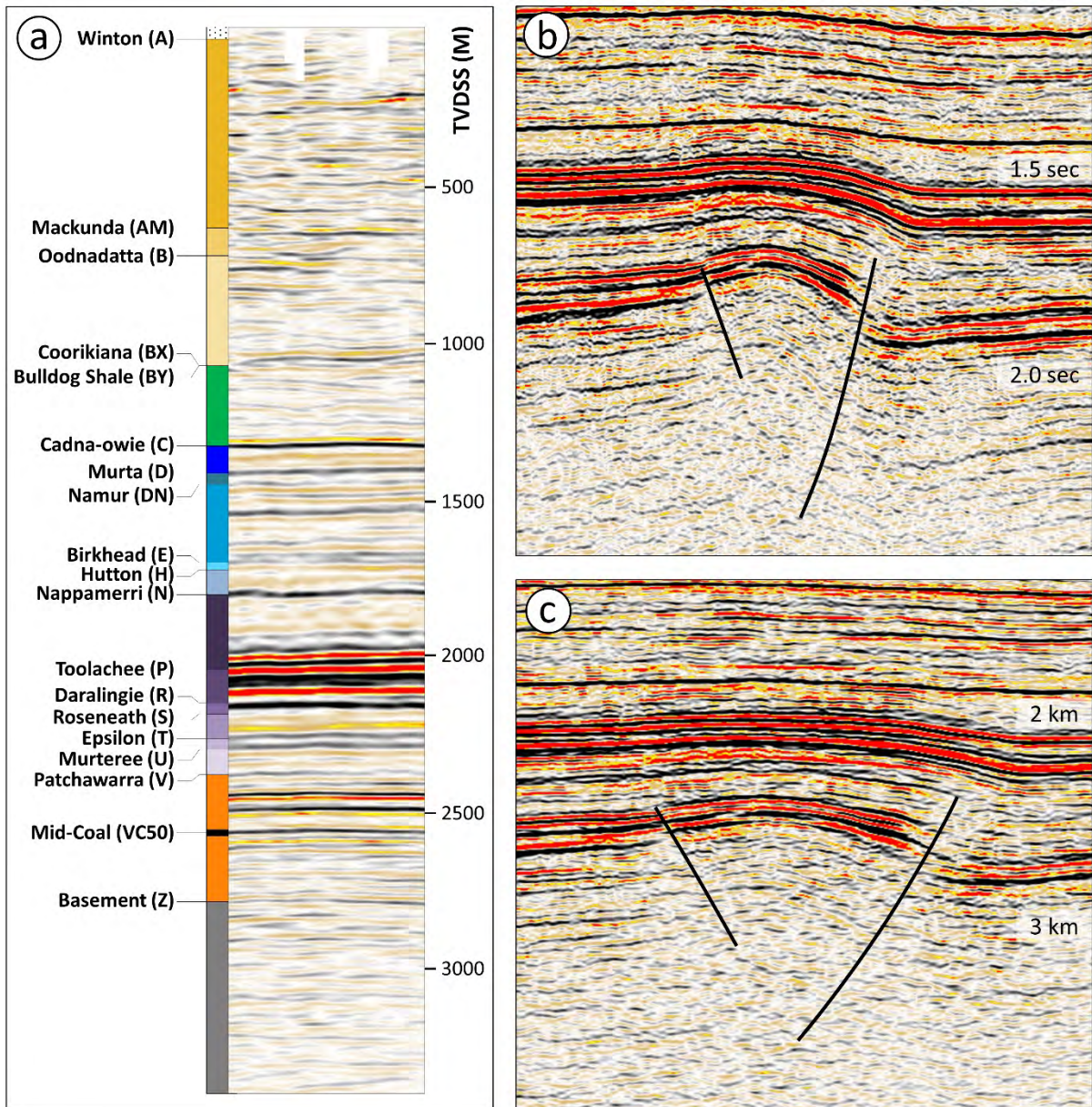


Figure 8. (a) Typical seismic reflection profile showing stratigraphic and seismic markers. The difference in fault geometry when seismic data is in: (b) the time-domain; and (c) the depth-domain.

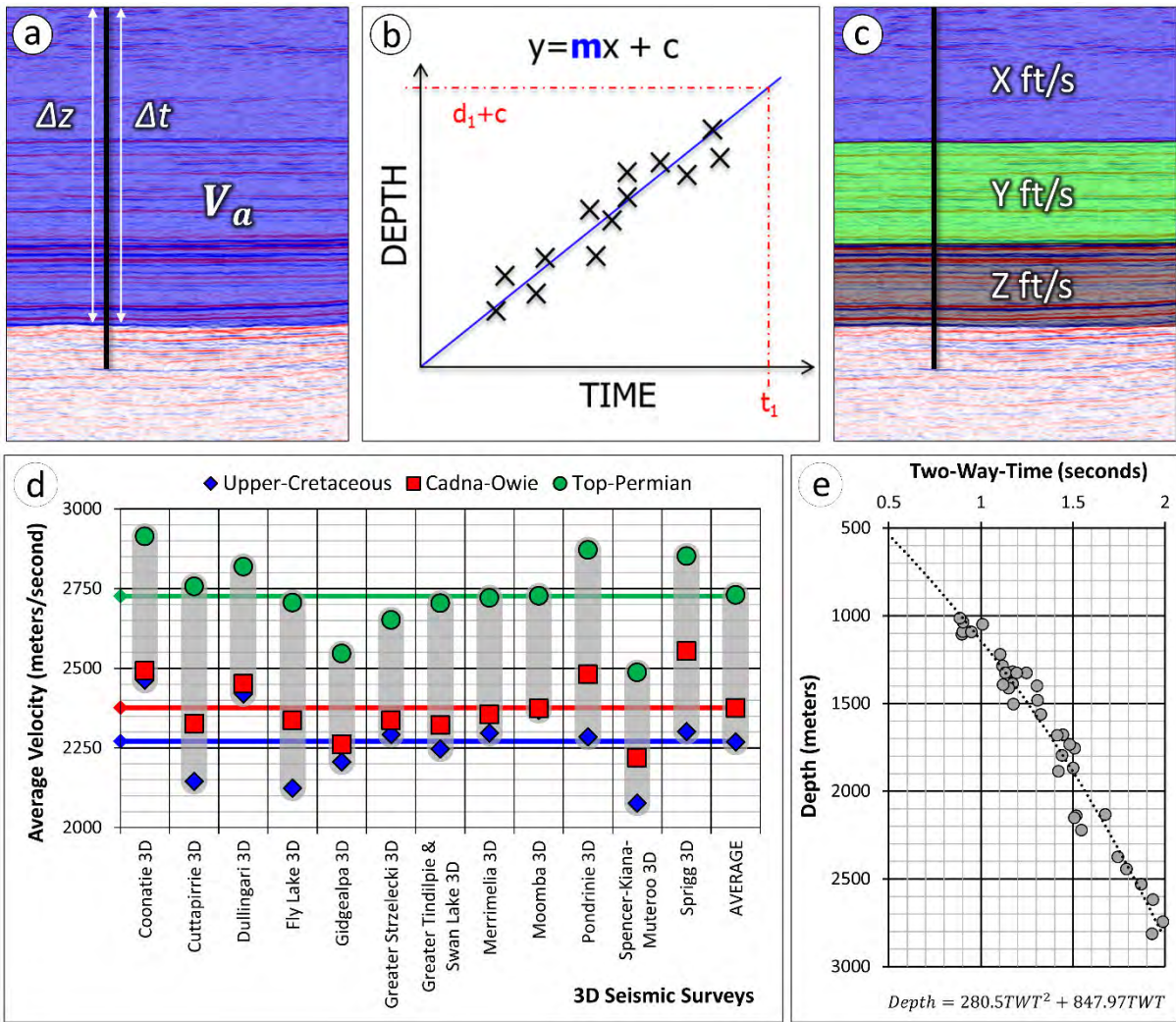


Figure 9. Common seismic time-to-depth conversion methods. (a) Average velocity (V_a) method uses the ratio between depth (from well) and time (from seismic data) for a reflector. (b) Time-depth trend method fits a trend for the time-depth pair data. (c) Interval velocity, or layer-cake, method divides the seismic survey into key stratal units and applies different velocities to those layers. (d) Average Velocities for key seismic reflectors. (e) Time-Depth trend obtained from 12 3D seismic surveys (after Kulikowski et al., 2016b, 2017a). See Figure 3b for seismic survey location.

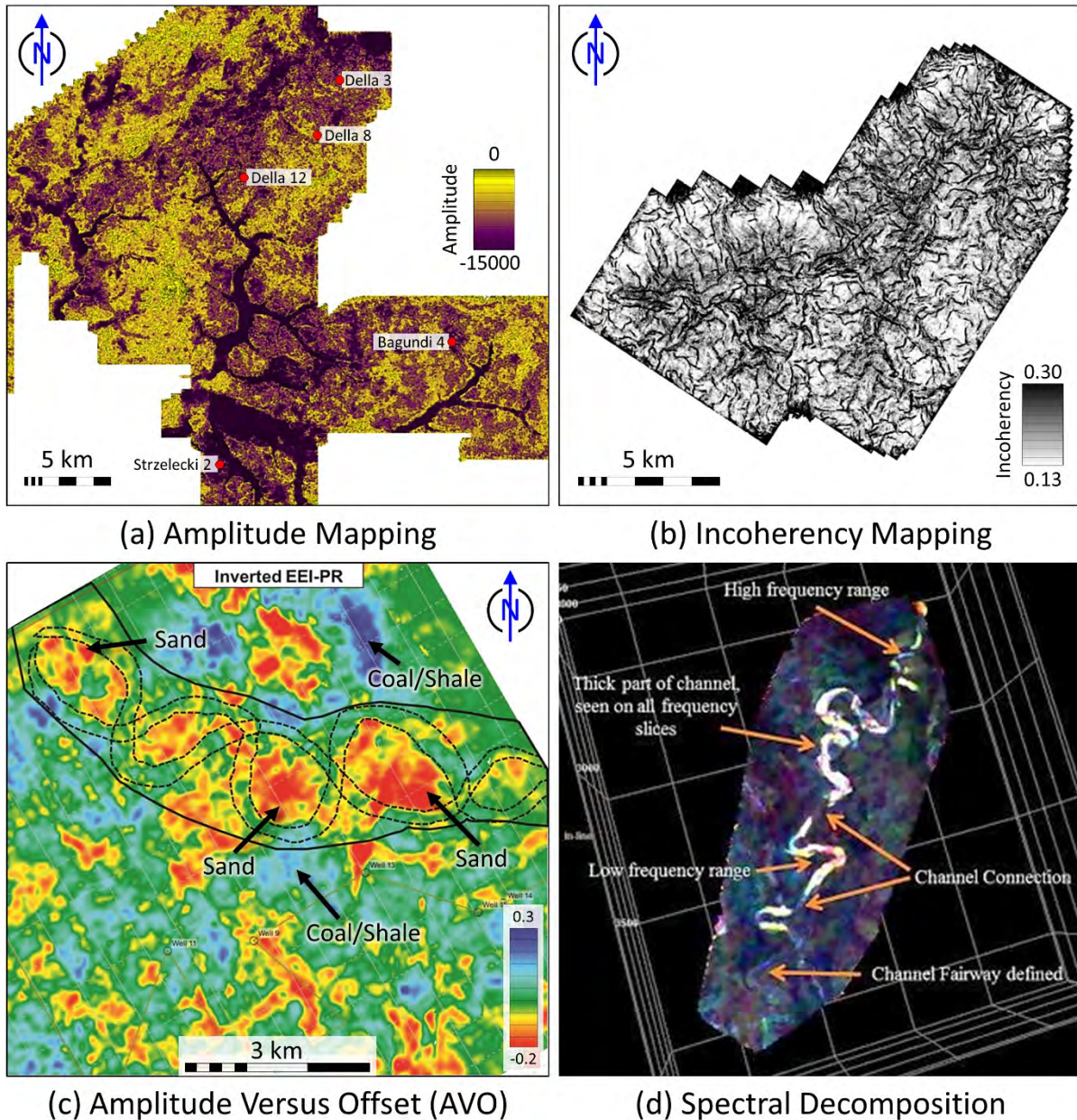


Figure 10. Seismic data analysis techniques beneficial to the fluvial dominated Cooper-Eromanga Basin. (a) Amplitudes extracted along reflector surfaces to locate channel systems. Example from Greater Strzelecki 3D showing a large regional channel system (after Kulikowski and Amrouch, 2017); (b) Incoherency analysis along a reflector to identify subtle faults. Example from Spencer-Kiana-Muteroo 3D showing the distribution of polygonal faults along the Upper Cretaceous reflector (after Kulikowski and Amrouch, 2017b); (c) Application of amplitude versus offset (AVO) to differentiate between sandstone and coal measures. The example shows the distribution of sandstone (red-yellow) and shale/coal (green-blue) in the Cooper Basin (after Tyiasning and Cooke, 2015); and (d) A spectral decomposition analysis used to delineate the geometry of a fluvial channel in the West Nile Delta, Egypt (Othman et al., 2016).

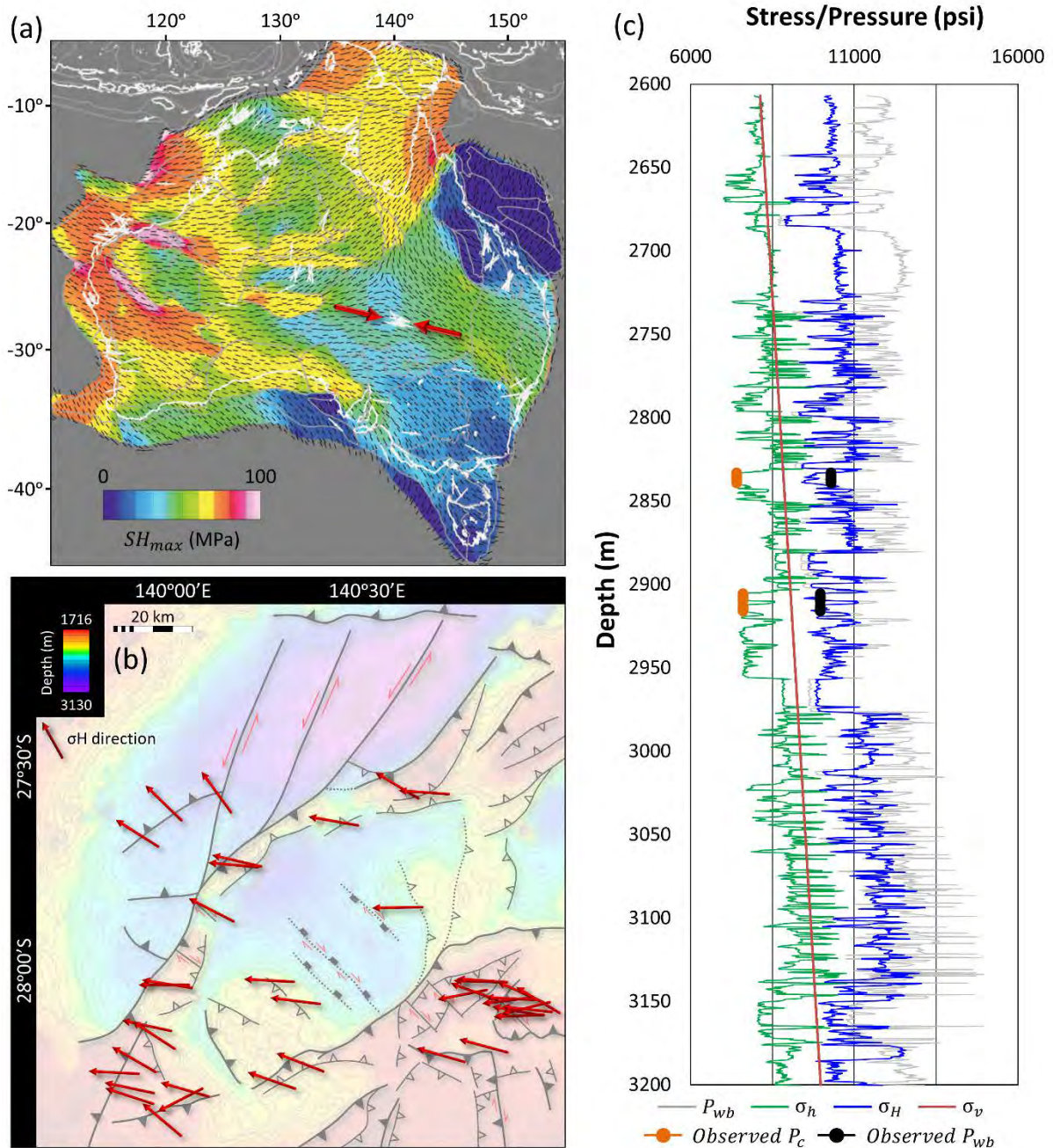


Figure 11. Orientation of the maximum horizontal stress orientation across: (a) Australia (after Muller et al., 2012); and (b) the Cooper-Eromanga Basin (after Kulikowski et al., 2017a). (c) A typical mechanical earth model for the Patchawarra Formation showing the minimum (σ_h) and maximum (σ_H) horizontal stresses, vertical stress (σ_v), breakdown pressure from logs (P_{wb}) and well test data (observed P_{wb}), and closure pressure (observed P_c) (after Pokalai et al., 2017). See Figure 4i for the origin of far-field stresses.

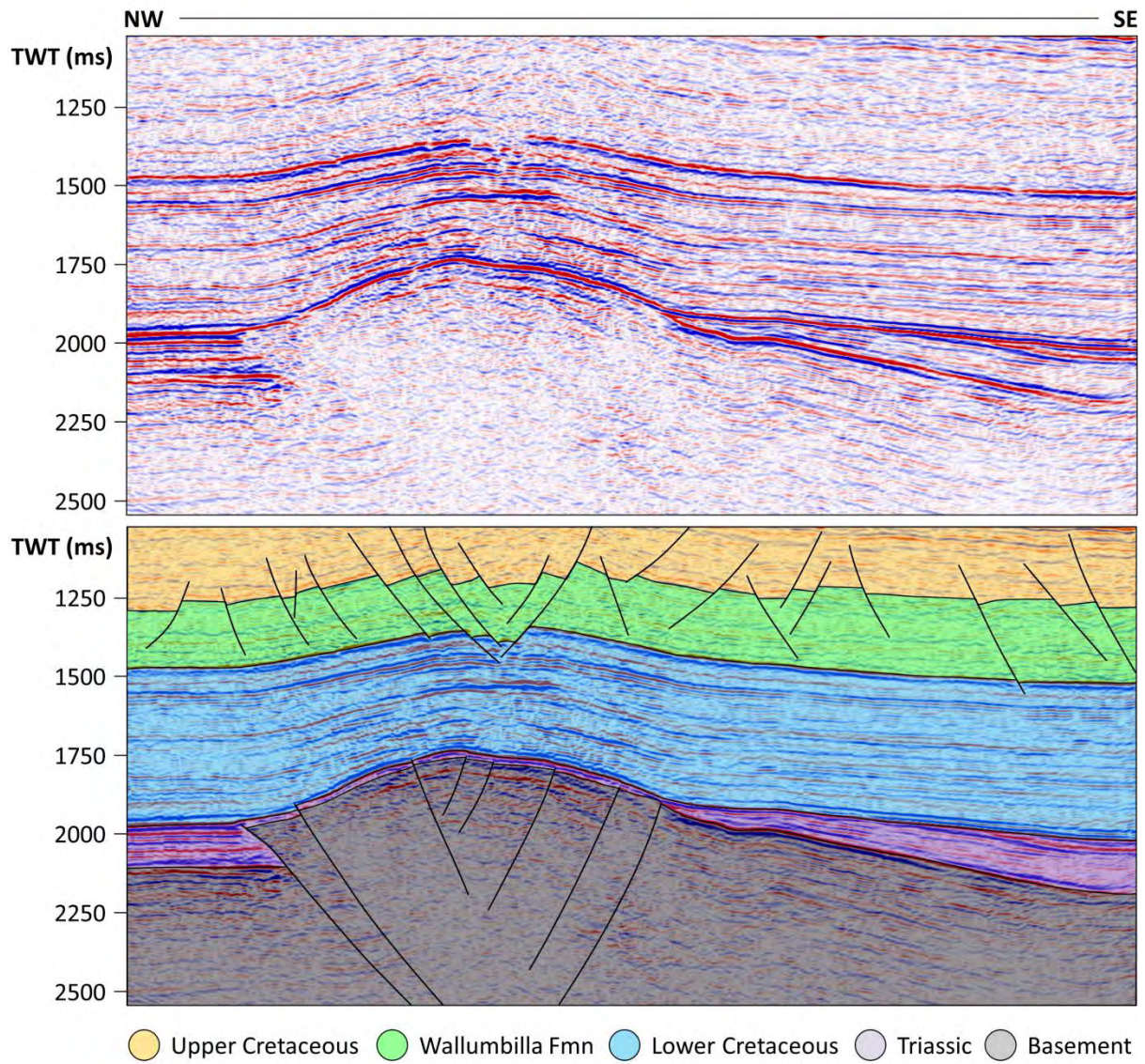


Figure 12. Basement and polygonal faults in the Merrimelia (Extension) 3D seismic survey interpreted along Inline 4295 (Kulikowski et al., 2017a). See Figure 3b for seismic survey location.

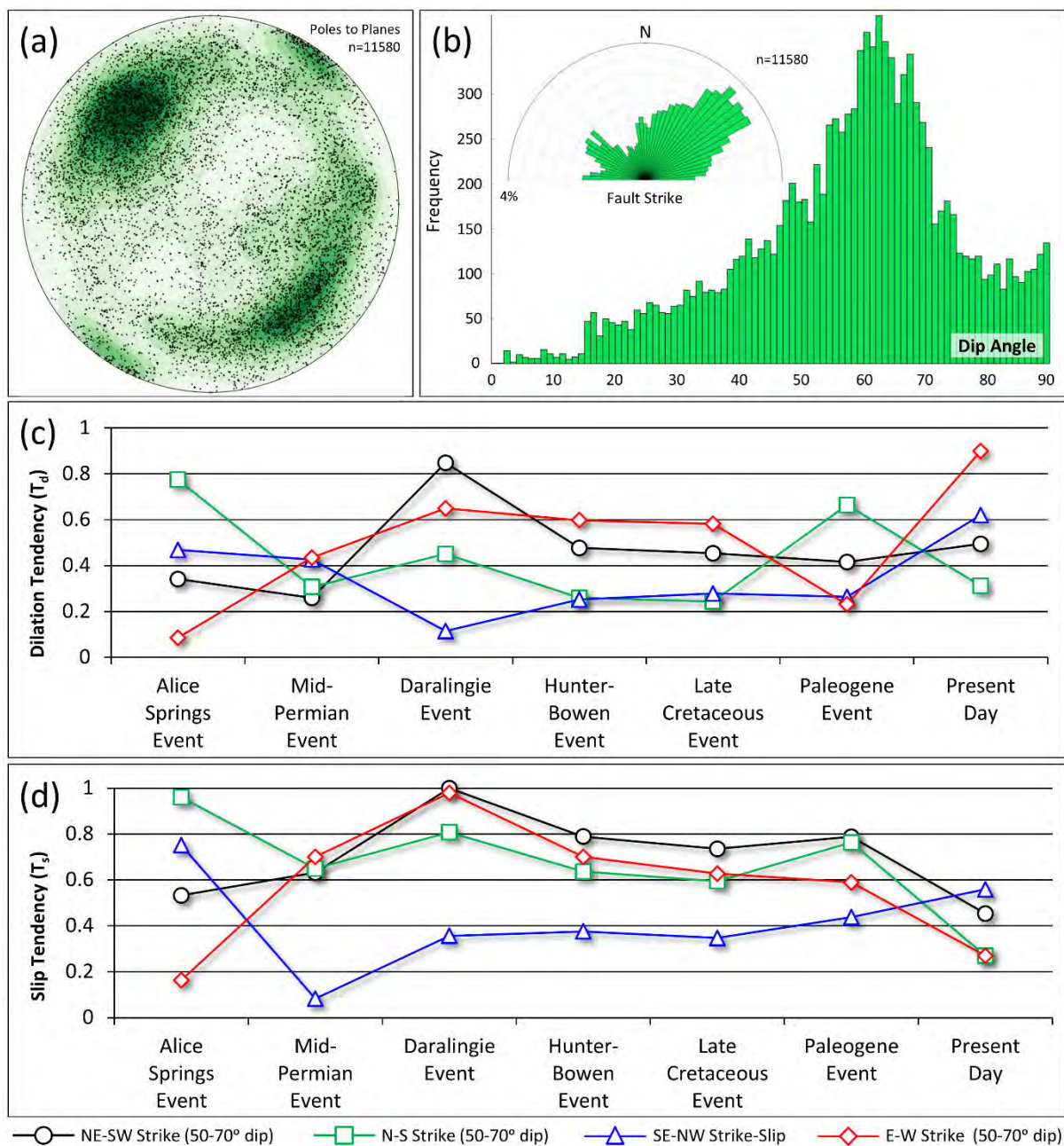


Figure 13. Fault geometry from six 3D seismic surveys (Dullingari 3D, Greater Tindilpie & Swan Lake 3D, Gidgealpa 3D, Greater Strzelecki 3D, Merrimelia (Ext) 3D, and Fly Lake 3D) presented as: (a) poles to planes; and (b) dip and strike (after Kulikowski & Amrouch, 2017a). Reactivation potential of the four most common fault sets measured using the: (c) Dilation Tendency; and (d) Slip Tendency (after Kulikowski & Amrouch, 2017c). See Figure 3 for location of 3D seismic surveys.

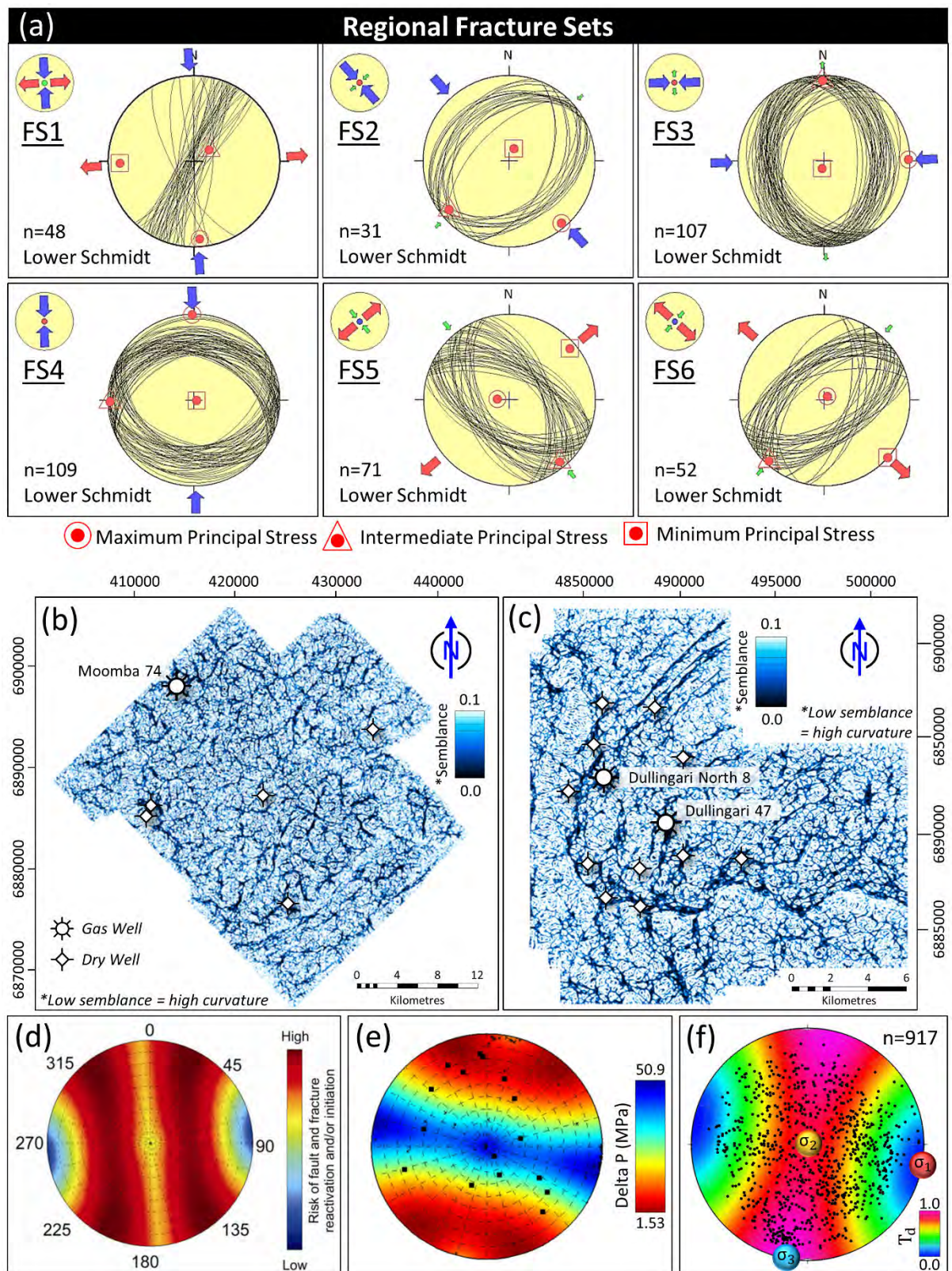


Figure 14. (a) Regional natural fracture sets (Kulikowski & Amrouch, 2017a). Most positive curvature processed into semblance in: (b) Moomba 3D; and (c) Dullingari 3D (Kulikowski et al., 2017b). In situ stress showing: (d) Fracture susceptibility (King et al., 2011); (e) Structural Permeability (Abul Khair et al., 2013); and (f) Dilation Tendency (T_d) (Kulikowski et al., 2017a). See Figure 3b for location.

Appendix I: Cooper Basin Simulation Study of Flow-back after Hydraulic Fracturing in Tight Gas Wells

A Cooper Basin simulation study of flow-back after hydraulic fracturing in tight gas wells



Lead author
**Sume
Sarkar**

**S. Sarkar, M. Haghghi, M. Sayyafzadeh, D. Cooke,
K. Pokalai and F. Mohamed Ali Sahib**

The University of Adelaide
Adelaide, SA 5005
sume.sarkar@adelaide.edu.au

ABSTRACT

After fluid injection (slickwater) during hydraulic fracturing, the flow-back of fracture fluid is necessary before gas production starts. A review of fracture treatments indicates that the incomplete return of treating fluids is a reason for the failure of hydraulic fracturing and is associated with poor gas production. The aim of this study is to investigate the parameters that limit flow-back in low permeability gas wells in the Cooper Basin.

The authors used numerical simulation to find the critical controlling parameters to introduce the best practice for maximising the flow-back in the Cooper Basin. Several 3D and multiphase flow simulation models were constructed for three wells in the Patchawarra Formation during fracture fluid injection, soaking time and during flow-back. All models were validated using history matching with the production data.

The results show that the drainage pattern is distinctly different in the following directions: vertically upward, vertically downward, and horizontal along the fracture half-length and along the matrix. The lowest recovery is observed during the upward vertical displacements due to poor sweep efficiency. Furthermore, it is observed that drawdown does not influence the recovery significantly for upward displacements. Surface tension reduction, however, can improve sweep efficiency and improve recovery considerably. Also, the wettability of the rocks has a significant impact on ultimate recovery when the effect of gravity is dominant. The authors conclude that a significant amount of injected fluid is trapped in the formation because of poor sweep efficiency and formation of gas fingers, which results from low mobility ratio and gravity segregation.

KEYWORDS

Tight gas reservoirs, flow-back, numerical modelling.

INTRODUCTION

Hydraulic fracturing is a wellbore stimulation process to produce gas from unconventional reservoirs. Water-based fracture fluid is injected into the formation during this stimulation process. It is required to return the injected fluid (flow-back) before gas production starts. When the fracture fluid is injected into the formation, the gas is displaced. After shut-in, this fluid imbibes to the rock matrix and displaces the gas from the matrix due to counter-current imbibition. In this shut-in time, the gas is accumulated in the fracture. During flow-back, the gas in the matrix cannot come to the fracture due to the water blockage.

Past research shows that inefficient fracture fluid recovery kills gas wells, leaving a significant amount of gas in the reservoir, which makes this technique economically not viable. Tannich (1975) shows that a significant amount of fracture fluid trapped in the fractures or imbibed into the rock matrix reduces the potentiality of fracture conductivity and results in fracture face damage (Fletcher et al, 1992; Ghalambor and Guo, 2010).

Mobility ratio and capillary pressure are the two primary factors that may govern the fracture cleanup during the flow-back. The high viscosity of displacing fluids results in low mobility ratio, which forms flow instability such as fingering or channelling in the formation. It causes early breakthrough of non-wetting fluid, which in turn decreases the areal sweep efficiency (Tidwell and Parker, 1996; Benham and Olson, 1963). It is believed that poor sweep efficiency is the reason for low fracture fluid recovery. Correspondingly, capillary pressure increase is due to the crushing of proppant, which ultimately results in repeated stresses because of shut-in and high production gas rates (Cheng, 2012). Due to the increase of capillary pressure, the displacement efficiency decreases the relative permeability of water and subsequently results in low recovery of the fracture fluid.

Gravity can also influence sweep efficiency. Figure 1 shows that fractures generate above and below the well perforation in vertical wells. It can be seen that drainage is in the gravity's direction for fractures above the well perforation and against gravity's direction for below the well perforation. Laboratory experiments conducted on gas/water drainage against and in gravity's direction show that drainage against gravity is very unstable and results in fingering (Glass et al, 2000; Ji et al, 1993).

A recent study shows that bottom well placement in the formation has better fracture fluid cleanup because of the gravity effects during flow-back, which indicate the governing role of gravity in fracture cleanup (Taylor et al, 2011). Results from Sharma and Agrawal's (2013) research suggests that capillarity and the fracture itself hold some fluid during the drainage of fracture fluid due to gravity.

Previous studies mainly focused on the role of viscous and capillary forces and the resultant instability during drainage in porous media. Very limited research has been conducted on the displacement mechanism in terms of instability after hydraulic fracture during flow-back against gravity's direction in multi-phase porous media. Most of the studies carried out numerically do not consider the effect of gravity. Some numerical research, taking gravity into consideration, were not focused on studying the factors that influence flow-back such as fracture dimensions, drawdown, surface tension and wettability with the heterogeneity of the reservoir.

In this paper, the displacement mechanism, critical velocity and instability phenomena for the gas-water system are first explained. Then, the details about the case study are described. The numerical modelling is then explained with an integrated workflow and algorithm. In the next step, validated models are used for several numerical experiments such as gravity, surface tension and wettability to observe the con-

trolling parameters for flow-back in low permeable heterogeneous tight sand gas wells. Drainage instability and sweep efficiency has also been addressed. Some experimental results are shown. Finally, results from the sensitivity analysis are discussed with some concluding remarks.

THEORETICAL BACKGROUND

Displacement mechanism in the gas-water system of multi-layered porous media may have similarities with the gas-water system in fractured porous media. Consider a displacement process where fluid one displaces fluid two in a system of dip angle (α) by simplifying Darcy's equation. The following expression (Eq. 1) is obtained for the fraction of water flowing.

$$f_w = \frac{1 + \frac{kk_{r1}A}{q\mu_1} \left(\frac{\partial P_{cov}}{\partial x} - \Delta\rho g \sin\alpha \right)}{1 + \frac{k_{r1}}{\mu_1} \frac{\mu_2}{k_{r2}}} \quad (1)$$

Capillary pressure will contribute to a higher fractional flow (see Eq. 1), and thus to a less efficient displacement.

Incomplete fracture fluid recovery occurs in gas wells when the gas phase does not give sufficient energy for the continuous removal of fluids from the fracture and matrix during drainage. An additional back pressure imposes on the formation due to the accumulation of the fracture fluid near the fracture, which ultimately gives resistance to the flow of gas and reduces the well productivity. The optimum velocity required to lift the gas in an upward direction against gravity is, therefore, called critical velocity, where fluid one is displaced by fluid two. Turner's theory can be used to calculate the critical velocity for a gas-water system for vertical gas wells. Turner et al (1969) analysed two physical models for the removal of gas well liquids—the liquid droplet and the liquid film models. Equation 2 shows Turner et al's (1969) correlation.

$$V_c = \frac{1.912\sigma^{\frac{1}{4}}(\rho_1 - \rho_2)^{\frac{1}{4}}}{\rho_1^{\frac{1}{2}}} \quad (2)$$

In Equation 2, V_c is critical velocity (ft/sec), σ is interfacial tension (dynes/cm), ρ_1 is liquid-phase density (lbm/ft³), and ρ_2 is gas-phase density (lbm/ft³). Fluid displacement is related with surface properties; by changing surface properties the velocity of the gas and lift of the gas from the matrix against high capillary pressure can be changed. Sharma and Agrawal (2013) use Turner's theory for a gas-water hydraulic fracture system to explain liquid loading mechanism after fracture operation.

Instability was described by Chouke's theory (Chouke et al, 1959). For displacement of fluid one by fluid two, the system is unstable for all displacement velocities (V) greater than the critical displacement velocity (V_c).

$$V_c = \frac{(\rho_1 - \rho_2)g\cos\alpha}{\left(\frac{\mu_2}{k_2} - \frac{\mu_1}{k_1} \right)} \quad (3)$$

From Equation 3, it can be deduced that the displacement direction relative to gravity's direction plays a vital role in de-

termining the stability of the system. For vertical displacement of fluid one by fluid two against gravity ($\alpha = 00$), an increase in the density of the displaced fluid (fluid one) decreases the critical velocity. This, in turn, increases the instability of the system. This means that $V > V_c$ is the necessary sufficient condition for a fluid lift from the formation. This research investigates the effect of gravity and capillarity on flow-back.

CASE STUDY

Application of these concepts is applied to three wells (A, B and C) in a field where the key reservoirs are the Permian Patchawarra and Tirrawarra formations in the Cooper Basin, SA (Fig. 2). The Patchawarra Formation comprises fluvial sandstones with interbedded siltstone and coal (Fig. 3). The Tirrawarra Sandstone is massive sandstone. The sandstones are typically clear, translucent, fine to coarse-grained, moderately strong siliceous cement, trace white argillaceous matrix and moderately hard with tight to poorly inferred porosity. The Tirrawarra Sandstone was formed as glacial outwash. The Patchawarra Formation conformably overlies the Tirrawarra Sandstone. The Patchawarra Formation is the thickest and most widespread Permian unit. The formation in the field is subdivided into Upper/Middle, Lower and Basal Patchawarra. The Upper/Middle Patchawarra sands retain better permeability and are hence more productive than the Lower and Basal Patchawarra.

The reservoirs in the Patchawarra Formation have a porosity range of 6–12% and a permeability range of 0.004–4 mD (overburden and Klinkenberg corrected). The rock properties degrade with depth due to increased depth of burial, and diagenetic effects and inefficient fracture fluid recovery during flow-back leads to non-economic results (Anantawati and Bulganda, 2013). The details of conventional pay are summarised in Table 1. In this case study, fracture stimulation was undertaken in two stages for wells A and B, and seven stages for well C (Santos, 2003a, 2003b, 2007).

NUMERICAL MODELLING

In this project, the fracture propagation model is coupled with reservoir simulation. Figure 4 shows the integrated workflow. As can be seen, the first stage is the building of the static model, and then the geomechanical properties are analysed. Next, the pre-fracture analysis is undertaken, followed by fracture propagation modelling, which incorporates a reservoir flow model. As an integrated workflow is required to build the fracture model, the methodology is started from the static model with the integration of geomechanics. To build the static model, inherent permeability and porosity is evaluated from core data. Before developing the fracture propagation model, the hydraulic fracturing process is analysed. Next, a 3D fracture propagation model is developed by using a commercial simulator that is based on the finite difference method. The hydraulic fracture propagation modelling workflow starts with the well logging data and generates geomechanical properties followed by injection-fall-off testing and fracture propagation modelling. Pokalai et al (2015) provide a detailed description of fracture modelling for tight gas reservoirs. The models are validated with the measured closure pressure, treating pressure and gas production rate. The validation properties are tortuosity and after closure pressure. Afterwards, this fracture model incorporates in the multiphase flow simulator, which is also based on the finite difference method. Later, this dynamic model validates with production data for further investigation (Figs 4 and 5). Coupling of the multi-stage hydraulic fracturing model with multi-phase flow simulation for a vertical well by following the integration approach has been discussed previ-

ously (Sarkar et al, 2015). A numerical model for every stage for the three wells was developed to investigate the fluid flow behavior during injection, after injection, and during flow-back.

A 3D hydraulic fracture propagation model is first developed for vertical well A, well B and well C as per the aforementioned methodology (Fig. 6). The multi-stage hydraulic fracture propagation model is then coupled with the finite difference reservoir flow simulator. In this research, a 3D gas-water black oil reservoir simulator is coupled with the 3D hydraulic fracture propagation model following a one-way coupling methodology. First, a single, planar hydraulic fracture for heterogeneous media in a vertical wellbore is developed for the three wells (Fig. 7). A Cartesian block-centered grid is used to develop these models. To map the water saturation and pressure after fracture operation, two different models were built. The authors needed to predict initial water saturation to simulate hydraulic fracture stimulation process in reservoir simulation; therefore, the simulation was run for three different periods:

1. the injection period (to create initial water saturation distribution for flow-back);

2. the shut-in period (soaking time investigation); and,
3. the production period.

The model is based on single porosity modelling, whereas porosity and permeability of the reservoir are recorded from the well log data analysis.

The reservoir properties used are provided in Tables 2 and 3, and are based on real field data; some correlation is also used to develop PVT modelling from the gas composition. Fine-scale gridding is used near the fracture face along the vertical wellbore to monitor the fluid behavior in the matrix and the fracture accurately. Relative permeability is calculated from laboratory data that is based on the steady state method. The details of the input data for relative permeability and capillary pressure is presented in Figures 8 and 9. After simulating numerous cases for the 11 stages in the three wells and conducting history matching, good matches were found and moved to further studies for this phenomenon (Figs 10-12). The validation parameters used to determine good were fracture permeability and stimulated reservoir volume.

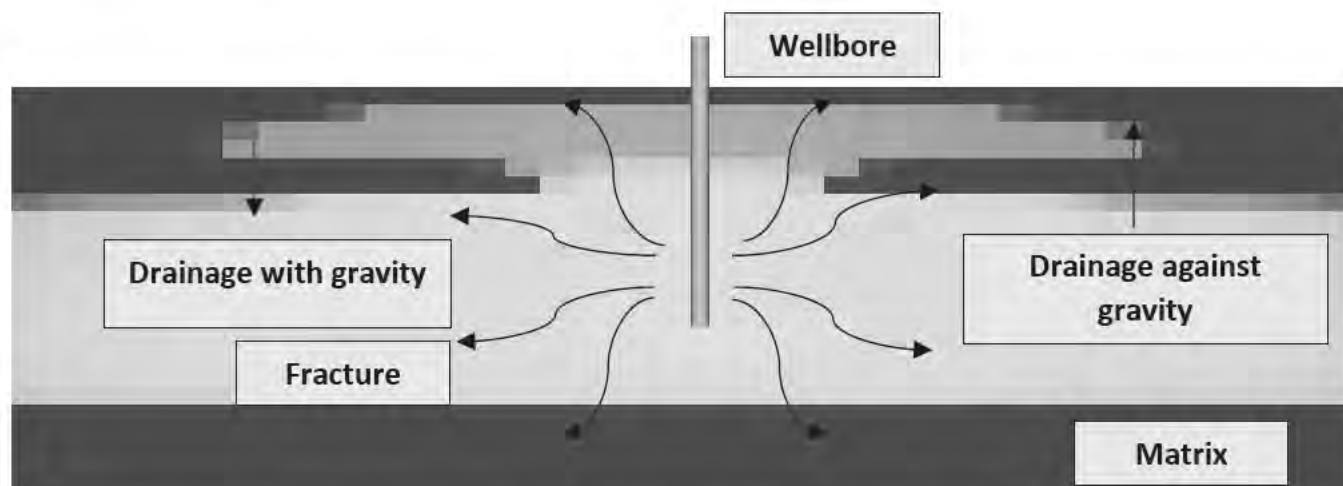


Figure 1. A conceptual model showing water drainage in a vertical well. Water drains with gravity in fractures above the wellbore perforation and against gravity in fractures below the wellbore perforation.



Figure 2. Location map of the study area, Cooper Basin, Australia.

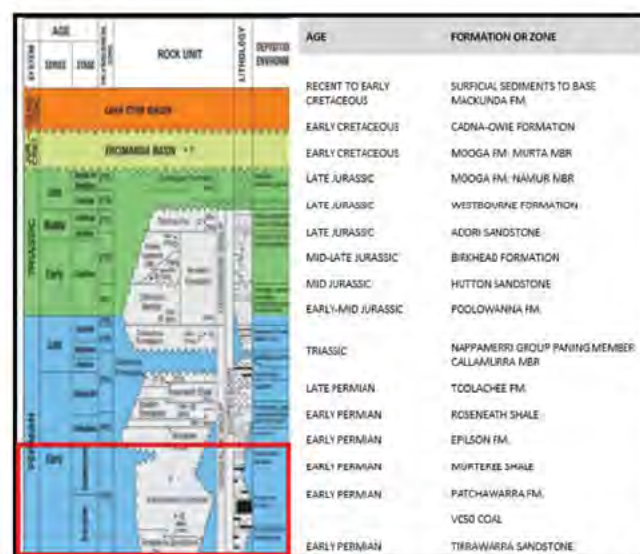


Figure 3. Stratigraphic chart of the Cooper Basin (Anantawati and Bulgauda, 2013).

Continued next page.

Continued from previous page.

Table 1. Conventional pay summary for the three wells.

Well	Formation	Sand interval (ft)	Gross sand (ft)	Net sand (mD)	Average porosity (%)	Net pay (ft)	Wt. average Sw (%)
A	Patchawarra Fm.	8,933–9,150	44.5	11.5	9.6	11.5	41
	Patchawarra VC 20	9,150–9,245	19.5	9	9.6	9	40
	Patchawarra VC 30	9,245–9,655	175	92	10.3	91.5	33
	Patchawarra VC 50	9,655–9,951	74.5	32	9.4	32	35
	Patchawarra VC 70	9,951–10,382	140.5	61.5	10.4	59.5	35
	Tirrawarra Fm.	10,382–10,511	85	31.5	8.9	18.5	63
B	Patchawarra Fm.	8,940–9,176	56.5	27.2	10.2	27.2	31
	Patchawarra VC 20	9,176–9,278	9.8	6	9.4	5.8	45
	Patchawarra VC 30	9,278–9,702	214.8	157.5	10.7	157	38
	Patchawarra VC 50	9702–10,014	49.8	17.8	9.2	17.5	30
	Patchawarra VC 70	10,014–10,452	114	61.5	10.8	60	34
	Tirrawarra Fm.	10,452–10,575	59.8	4.2	8.7	3.8	50
C	Patchawarra Fm.	8,924–10,375	791.2	256	10.4	210.5	26
	Tirrawarra Fm.	10,375–10,457	81.8	15.8	8.8	15.8	41

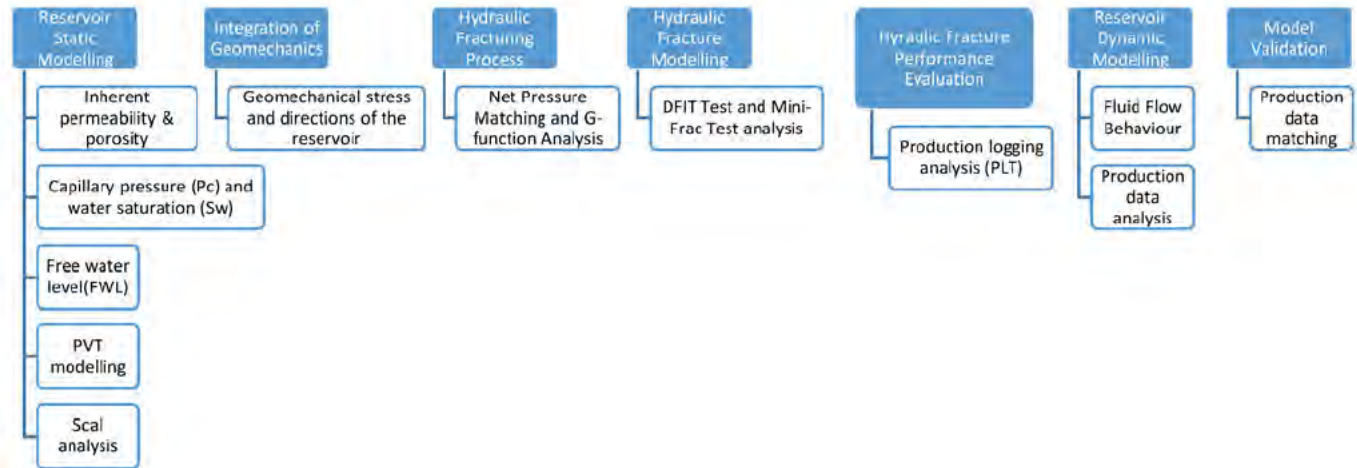


Figure 4. Integrated hydraulic fracturing modelling workflow.

Continued next page.

Continued from previous page.

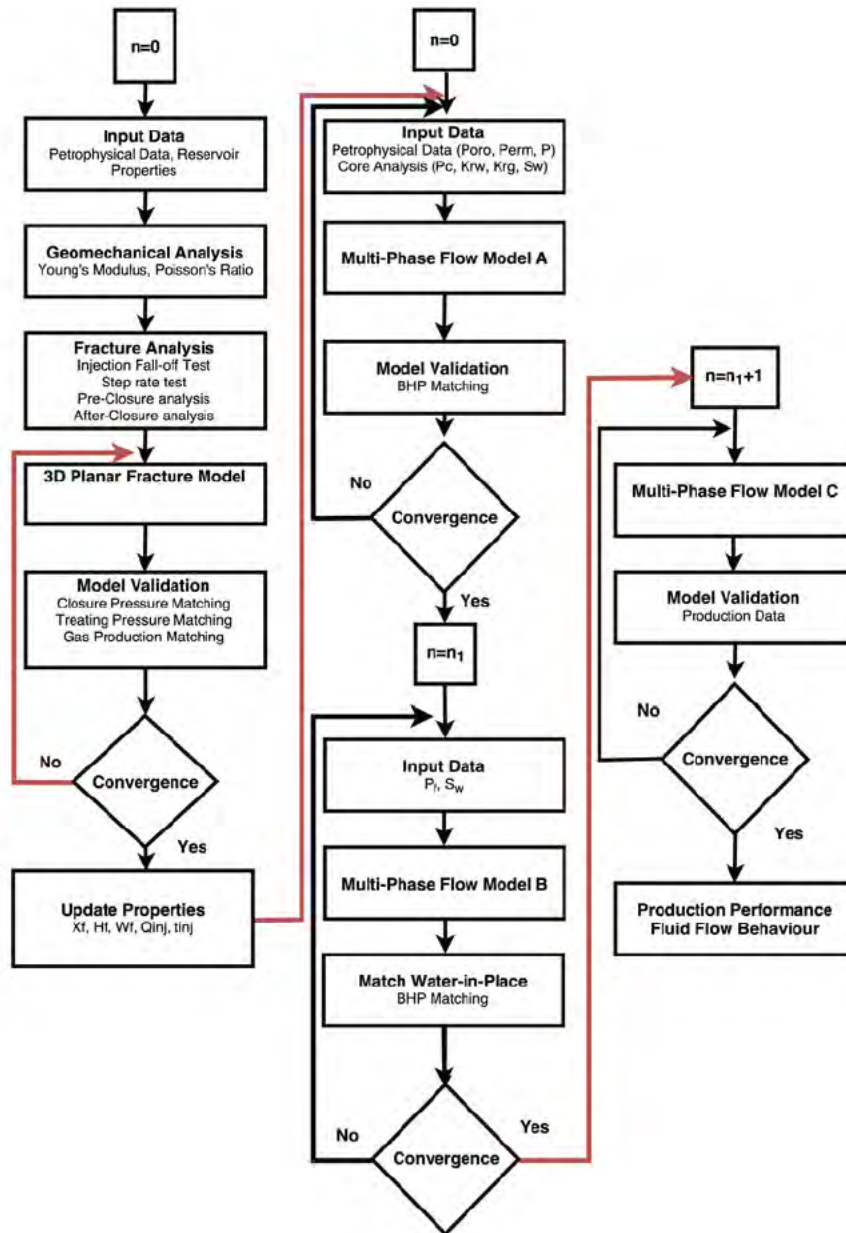


Figure 5. Workflow diagram for hydraulic fracture modelling.

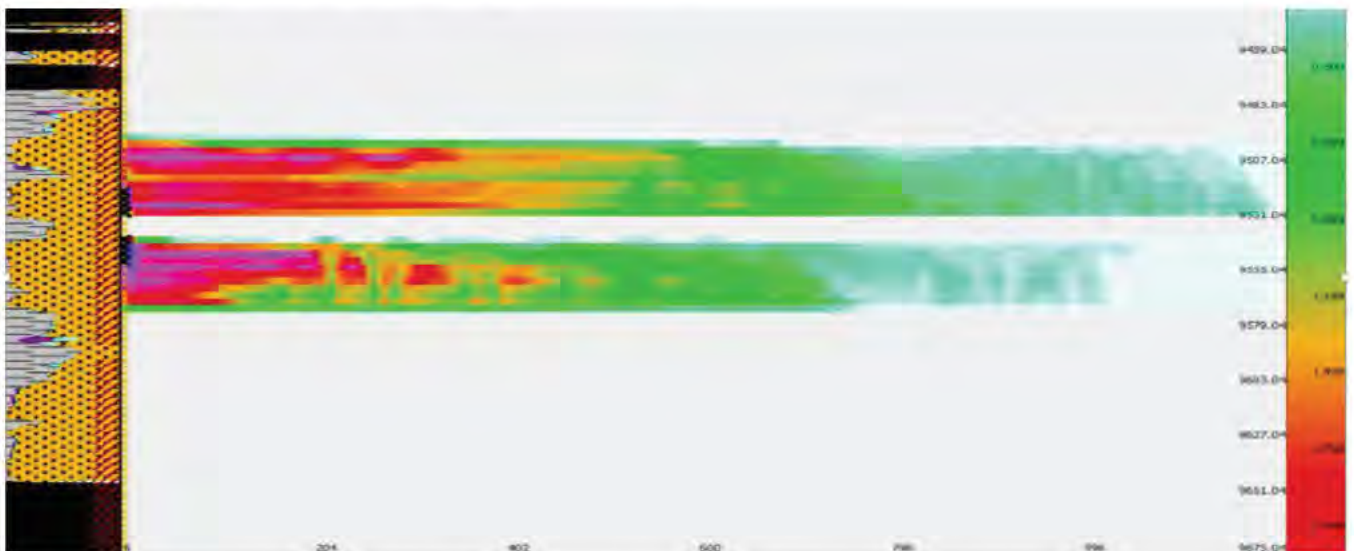


Figure 6. Propellant concentration (lb/ft³) of well C6 Stage 1. A 3D planar hydraulic fracture model.

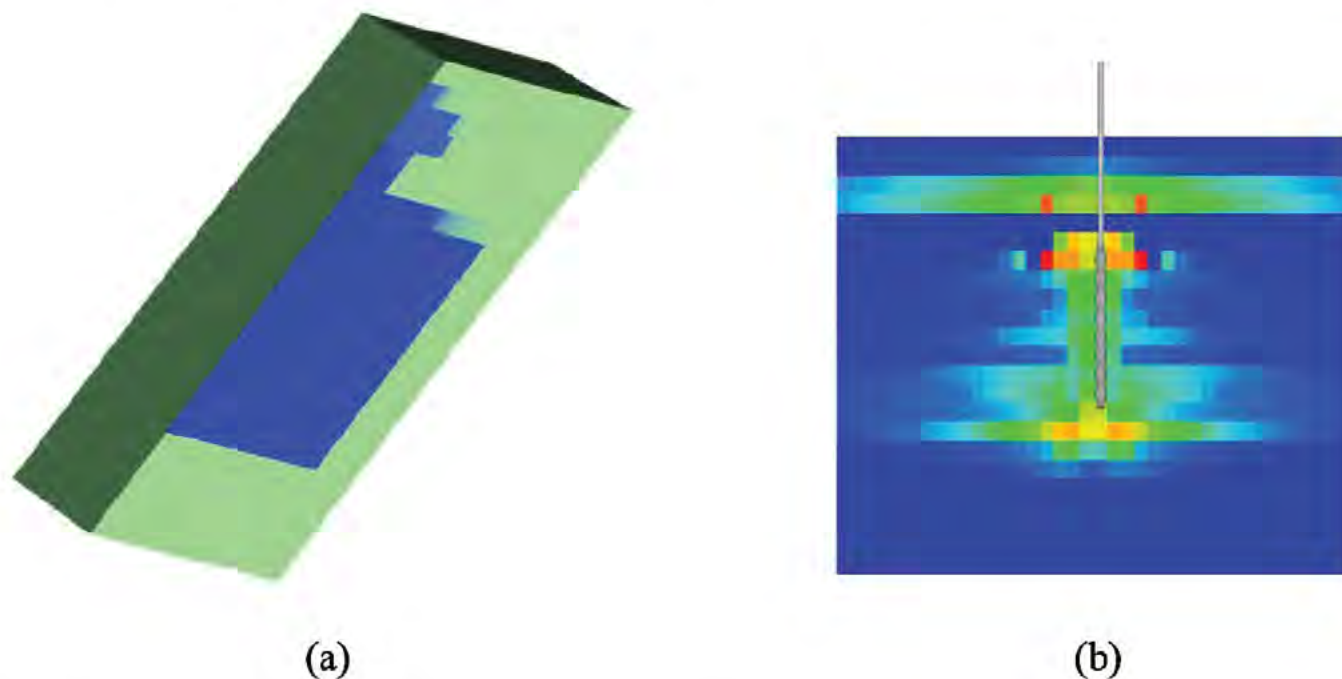


Figure 7. (a) A single planar hydraulic fracture model for a gas-water system. (b) Permeability distribution.

Table 2. Input parameters for the model of Wells A and B (base case).

Property/parameter	Well A		Well B	
	Stage 1	Stage 2	Stage 1	Stage 2
Fracture stage	Stage 1	Stage 2	Stage 1	Stage 2
Number of cells	47 × 88 × 36	47 × 76 × 25	47 × 36 × 29	47 × 48 × 27
Drainage area (ft ²)	211,200	182,400	86,400	115,200
Reservoir thickness (ft)	108	75	87	81
Initial reservoir pressure (psi)	4,195.6	2,634.5	4,203.3	4,092.6
Matrix permeability (mD)	0.00415–0.0552	0.00355–2.5	0.00173–2.5	4.30 × 10 ⁻⁶ –2.5
Matrix porosity (%)	8.7	16.5	14	13.7
Fracture permeability (mD)	2,993–135,328	9,698–314,455	6,876.97–390,024.51	5,540–76,500
Average fracture width (in)	0.2	0.4	0.1	0.4
Fracture half length (ft)	234	198	78	114
Fracture height (ft)	78	45	57	51
Fluid injection (STB)	2,385.97	1,834.57	2,650.16	1,807.08

Table 3. Input parameters for the model of Well C (base case).

Property/parameter	Well C						
	Stage 1	Stage 2	Stage 3	Stage 4	Stage 5	Stage 6	Stage 7
Fracture stage	Stage 1	Stage 2	Stage 3	Stage 4	Stage 5	Stage 6	Stage 7
Number of cells	47 × 12 × 26	47 × 94 × 33	47 × 100 × 17	47 × 50 × 57	47 × 166 × 18	47 × 120 × 18	47 × 50 × 25
Drainage area (ft ²)	96,000	225,600	240,000	120,000	398,400	288,000	120,000
Reservoir thickness (ft)	130	99	51	171	54	54	75
Initial reservoir pressure (psi)	4,195	4,095	4,026.7	3,091	4,205	3,014	4,084
Matrix permeability (mD)	0.00327–17.995	0.0566–0.0943	0.6	7.58 × 10 ⁻⁶ –13.653	4.70 × 10 ⁻⁶ –1.747	2.61 × 10 ⁻⁶ –2.265	4.26 × 10 ⁻⁶ –2.154
Matrix porosity (%)	7.5	3.2	5.4	5.8	5.46	3.3	3
Fracture permeability (mD)	0.5–11,793	42–3,124	32–10,950	9,135–30,635	1,038–20,222	25,060–192,652	11,839–52,397
Average fracture width (in)	0.1	0.3	0.5	0.1	0.3	0.4	0.2
Fracture half length (ft)	20	252	270	120	468	330	120
Fracture height (ft)	65	27	21	141	24	24	45
Fluid injection (STB)	3,689.4	1,171.62	1,812.98	1,294.92	1,128.95	1,143.02	1,009.56

Relative Permeability vs Water Saturation

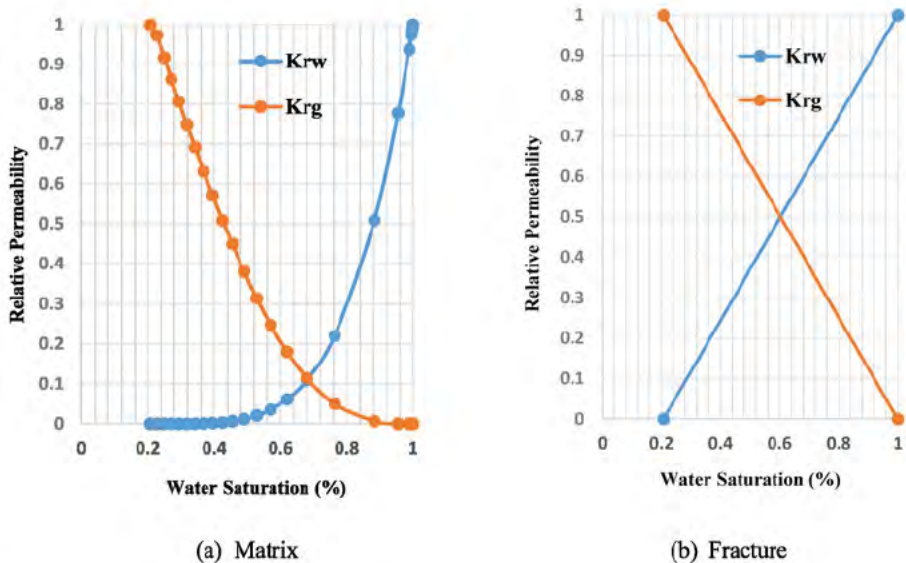


Figure 8. Relative permeability for base study; (a) matrix, and (b) fracture.

Capillary Pressure vs Water Saturation

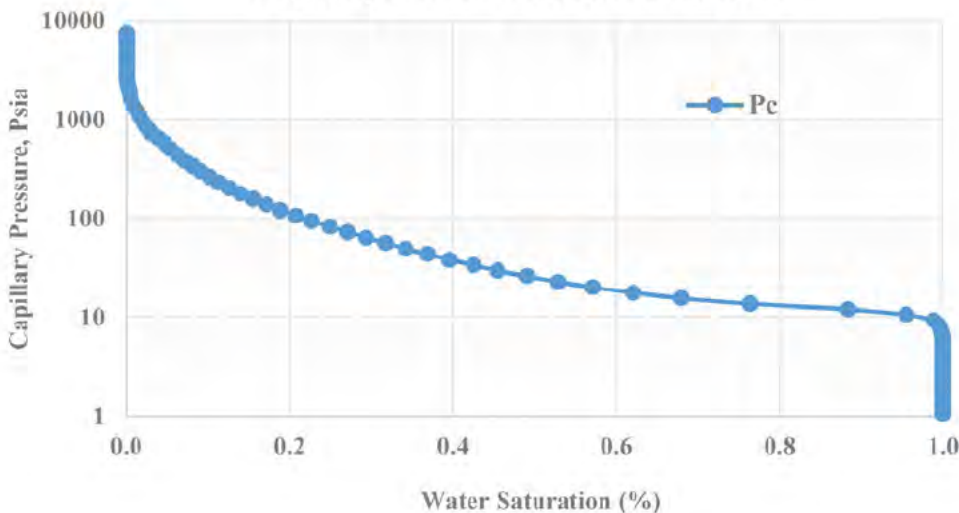


Figure 9. Capillary pressure for base case.

Output from Hydraulic Fracture Propagation Model

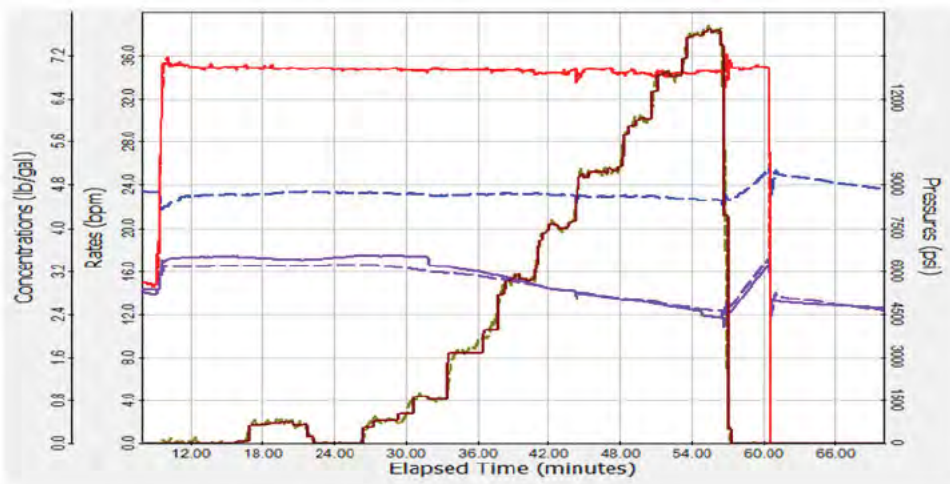


Figure 10. Surface treating pressure matching in Well A, stage 1.

(a) Gas Production Rate, (b) Gas Production Volume vs Time – Output from HF Model

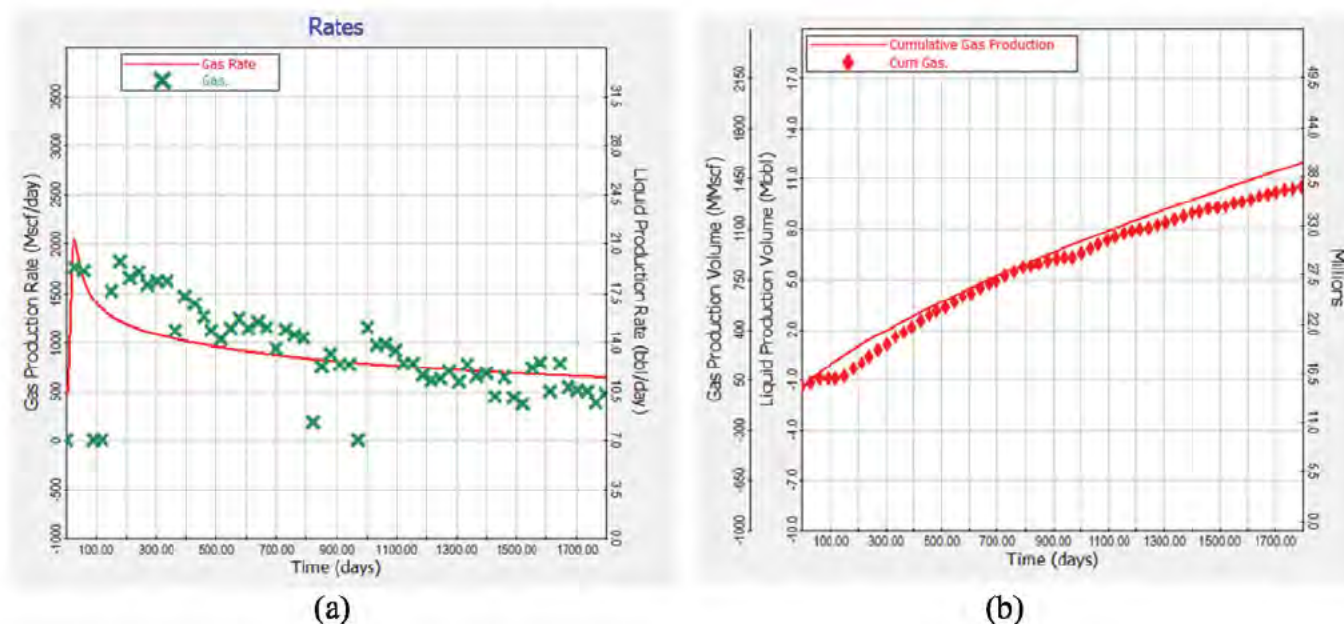


Figure 11. Gas production rate and cumulative gas production in Well A, Stage 1.

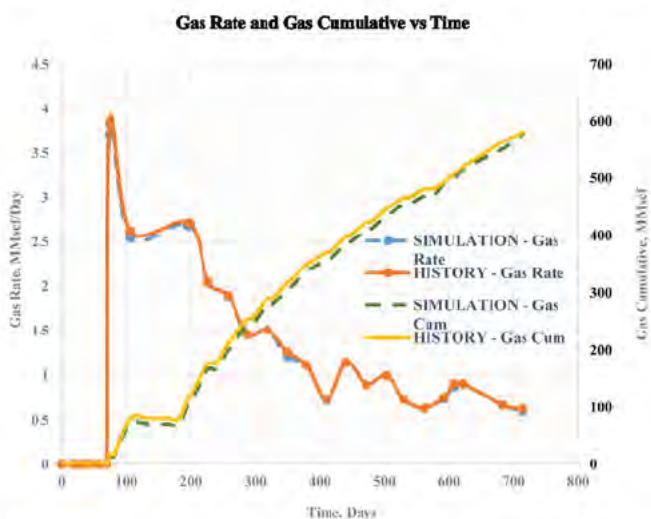


Figure 12. Gas production rate and cumulative gas production in Well A, Stage 2.

RESULTS AND DISCUSSION

For each well, the fluid recovery versus time is shown in Figure 13. Correspondingly, gas rate and cumulative gas production versus time for well C are presented in Figure 14. The water saturation profiles at different time steps are used to study the role of gravity drainage, capillary pressure, sweep efficiency and fingering on fluid recovery. The water saturation profiles during injection, soaking period and production are compared to study the displacement pattern. The water saturation profile versus dimensionless distance for different time steps is also plotted (Fig. 15c).

Effect of gravity

DISPLACEMENT IN BOTTOM PARTS OF THE RESERVOIRS

Displacement of gas by fracture fluid has been investigated after the immediate injection period to study the effect of grav-

ity. For this reason, simulations were run during soaking time and production from the top of the perforation of a vertical well. In this scenario, the flow will be down-dip towards gravity's direction during injection and up-dip against gravity's direction during production. Figures 15–17 compare the displacement images taken from different periods of injection, soaking and production, respectively, for well B. The plot of saturation profile versus dimensionless distance shows the gravity effect across time more clearly.

Figure 15 illustrates the saturation profiles after one minute and one hour of injection. In this period, fracture fluid displaces gas and gas moves into the formation. The fluid front progresses, and the fracture fluid is moving towards gravity. The dark-blue colour represents the area saturated by fracture fluid while the light-green colour represents the area saturated with gas. The darker the color, the higher the water saturation. It is evident from the images that the fluid front during injection is stable, and almost all gas displaces from the fracture zone. Also, the saturation plot shows that nearly 10% higher saturation between the two periods of time is maintained in the matrix before suddenly dropping to residual water saturation.

Figure 16 shows the displacement pattern where the well was shut-in (soaking) for 45 days after the fracture stimulation. During the soaking time, the fracture fluid imbibes into the matrix due to high capillary pressures and gas comes to the fracture for counter-current imbibition. As can be seen, the fluid in the top of the fracture is displaced by gas, however, due to the gravity effect, there is still some fluid remaining in the fracture. Figures 15 and 16 show that the displacement pattern is different, and also, the flow is unstable. During soaking periods, fingers are found, which grow in number with time. Most of the gas flow paths identified are at the bottom. Formation of this fingering is detrimental to fracture fluid recovery since a significant portion of the porous media is occupied by fracture fluid. The areal sweep efficiency is low in this case. Also, the figure shows that even after a long time a significant amount of water will remain in the fracture. This simulation study is repeated for wells A and B, and the results were unchanged. The saturation plots were consistent, which is more apparent from the saturation profile. The peak in the plot for time step

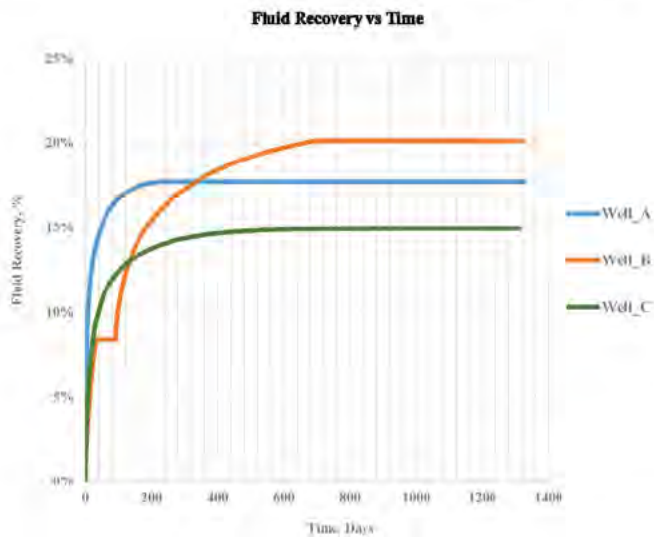


Figure 13. Fluid recovery for Wells A, B and C.

45 days shows that a significant amount of fluid remained before starting production. This phenomenon can be explained more briefly from the horizontal direction.

For further investigation, the saturation profile was plotted against dimensionless time during the production period. In this period, fluid is coming in the vertically upward direction. Figures 17a and 17b shows that some amount of fluid remains in the formation after two years. During this period, the fracturing fluid and gas are draining against gravity; therefore, high suction pressure is needed to clean-up the fluid from the bottom part of the fracture. Figure 17c indicates that the flow is unstable after 46 days and one year after of hydraulic fracture, and the saturation amount goes up to 52% and 25.5%, respectively. It is clear from this picture that a significant amount of fracturing fluid is trapped in the formation. Approximately 1.9% water saturation increased from the initial water saturation of the matrix (Fig. 17d). In this scenario, the fluid recovery is lower due to the unstable gravity.

DISPLACEMENT IN TOP SECTION OF THE RESERVOIRS

In the previous section, the authors discussed different displacement patterns in the different directions. It is also noted that a low recovery is found against gravity. For further investigation, saturation images and plots are studied in the top of the reservoirs for three periods. In this case, well perforation is below the study area. Figures 18–20 compare the displacement mechanism for three periods of operation.

Figures 18a–18c show that stable fluid front progresses instantaneously in the fracture and front thickness decreases significantly after one hour of injection at the top of the formation. In this case, gas is displaced by fracturing fluid against gravity. Due to the gravity force, the front thickness is lower at the top. It is also observed from the saturation plot that the front during injection is very stable up to a certain distance but after that, it is slightly unstable because high capillarity helps fluid to imbibe to the matrix. It, therefore, creates some paths that impede the flow stability. Nearly 20% higher saturation between two periods of time is maintained at a particular distance, which fluctuated later on.

Fluid front observed during soaking time are shown in Figures 19a–19c. There is a noticeable fluid front after one day of fracture operation. Almost 33% of the fluid is displaced by the gas within one day. Before starting production, all fracturing fluid imbibes to the matrix due to the strong gravity force and

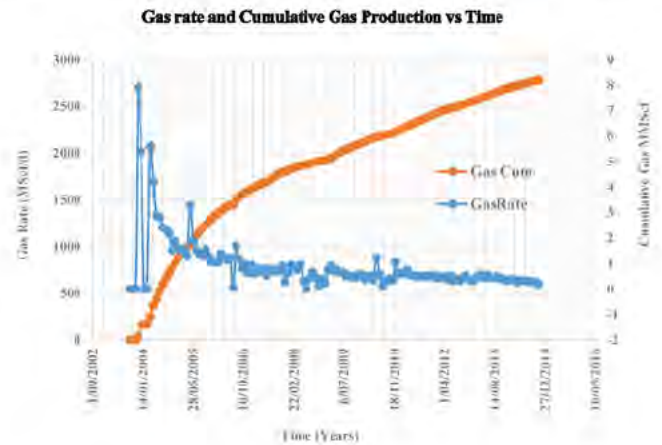


Figure 14. Drainage rate for Well C.

capillarity. In this case, fracturing fluid displacement is towards gravity's direction. During this period, a high density of fracturing fluid goes down-dip and also imbibes to the matrix. On the other hand, lower density fluid and gas imbibe to the fracture region.

Figures 20a–20g show the displacement pattern for 46 days (after soaking time when production starts after 45 days shut-in), 47 days, one year and two years after the production period. Figures 19b and 20a compare a small amount of fracture fluid that comes to the fracture during production. In this case, the well perforation is below this study area. Gas is, therefore, displacing towards gravity again. Also, Figure 20g displays some instability after 46 days, so the displacement starts from the centre. Instability in this direction is clearer from the gas saturation (Fig. 20d and 20e). In the next step, it drains efficiently (after 47 days) due to good vertical sweep efficiency. There is, therefore, a good agreement for the recovery of gas and fracturing fluid in the downward direction as all operations are going on in the direction of gravity except during the injection period.

DISPLACEMENT ALONG THE PROPPED FRACTURE LENGTH

For further investigation, saturation profiles are depicted along the propped fracture length. Saturation curves are plotted against dimensionless distance for the different layers for injection, soaking, and production periods (Figs 21–23). In this case, the flow is in the horizontal direction.

The fluid front is altered for different layers (Fig. 21a–21d). Also, the peak of the fracturing fluid is changed by a vertical distance. It depends on the fracture half-length and permeability of the formation. The fluid front is different for each layer due to the gravity segregation. After one hour of injection, the front is neutral near the matrix zone.

Figures 22a–22d illustrate that the saturation is very unstable along the horizontal direction. During shut-in, multiple fingers of flow paths are generated. The fracturing fluid is imbibing to the matrix, and due to the counter-current imbibition, the gas is occupied in the fracture. Most of the gas fills on the top layer of the fracture. The gravity effect can be seen more clearly in Figures 22c and 22d. The bottom layer has more fluid than the top layer (Fig. 22d) and fingering is observed in the middle. Figure 22c represents the various fronts for different layers, which indicates that the flow is unstable due to the imbibition process. Due to the good vertical sweep efficiency of gas, the top layer of the fracture is displaced by gas after 45 days of shut-in, but the fluid creates multiple paths when it imbibes to the matrix. It can, therefore, be claimed that vertical sweep efficiency is

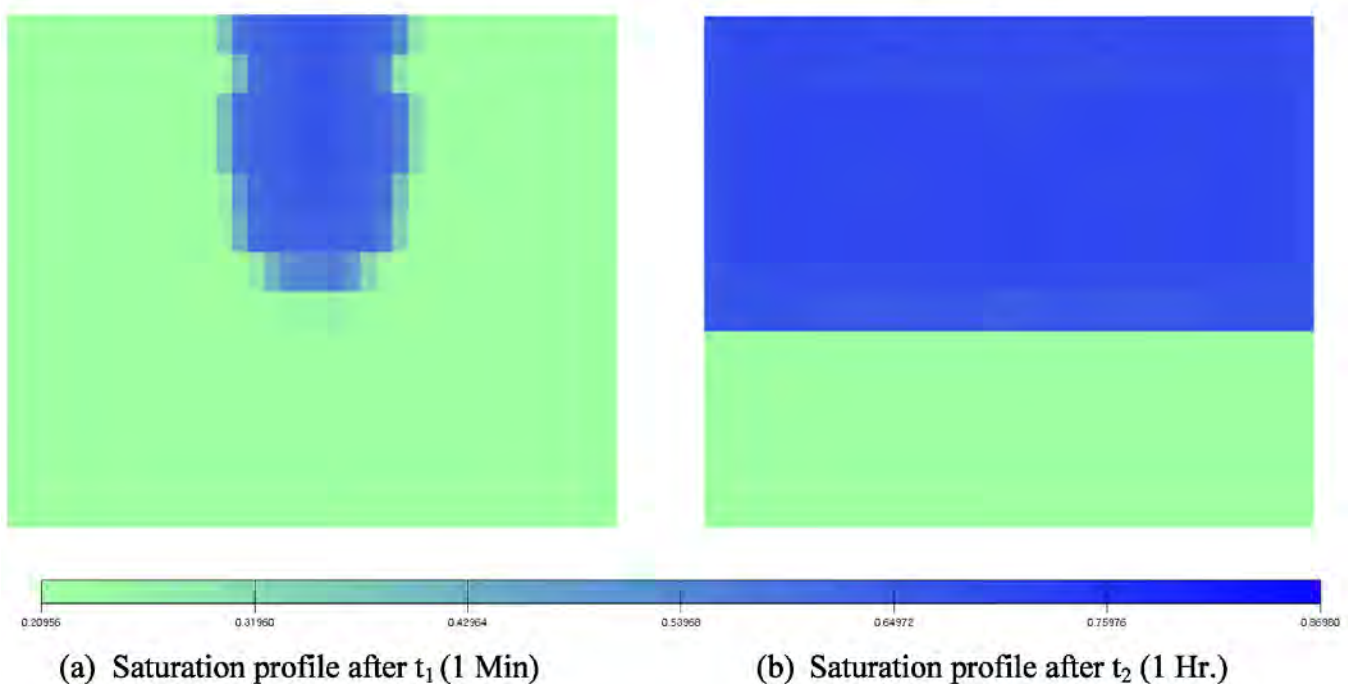
more in this direction, which has an adverse impact on fluid recovery. Figures 23a-23c show that fracturing fluid remains in the bottom part of the fracture after two years of production, which is an indication of gravity's effect.

to the fracture face and decreases the productivity of the tight gas well. Surface properties such as the interfacial tension between rock and fluid reduction and wettability alteration can, however, change the scenario and increase flow-back from the tight sand reservoirs.

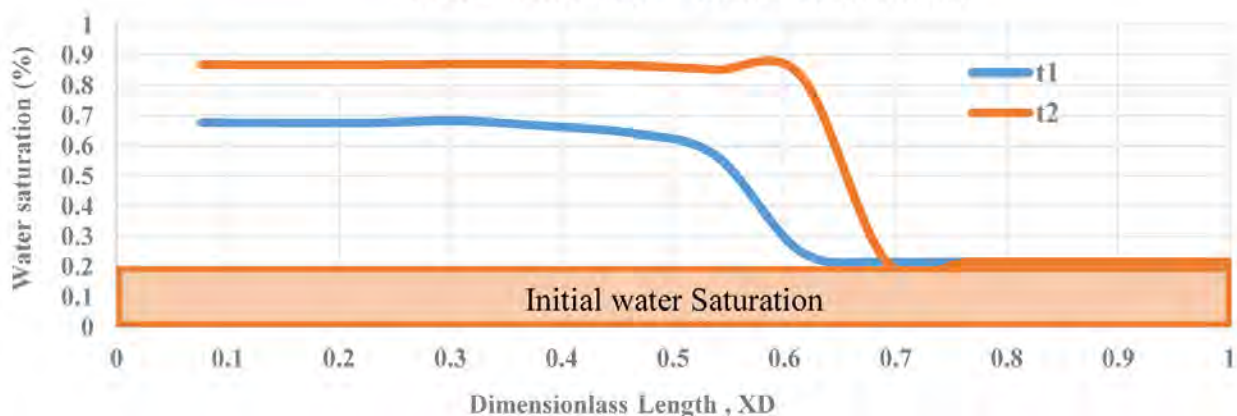
DISPLACEMENT ALONG THE MATRIX

Figure 24 illustrates the saturation maps along the matrix direction for a different period. It is apparent from the saturation profile that a significant amount of fracturing fluid imbibes to the matrix after the fracturing operation. A noticeable amount of fracturing fluid remains in the formation after two years of production, which creates the boundary for gas to come

Water Saturation Profile during Fracture Fluid Injection



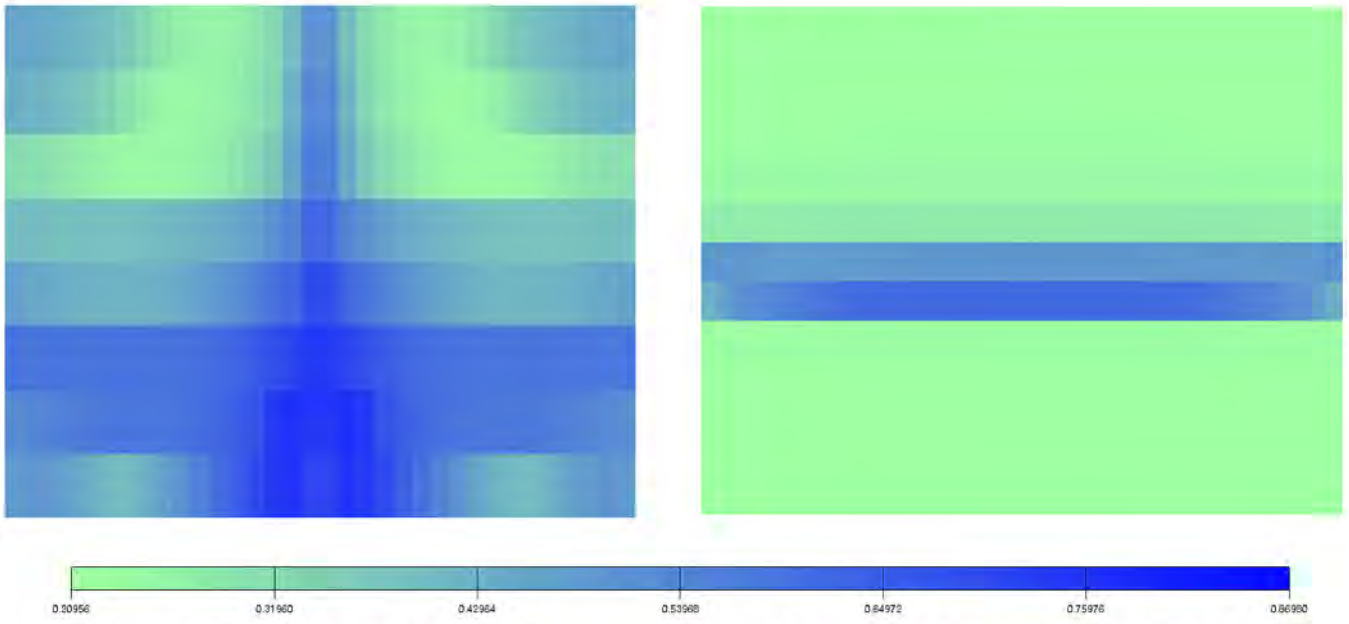
Water Saturation vs Dimensionless Time



(c) Saturation profile after 1 min and 1 hr. of injection in the vertically downward direction from the top of the well perforation.

Figure 15. Fracturing fluid saturation distribution during injection period in a vertical well (displacement vertically downward).

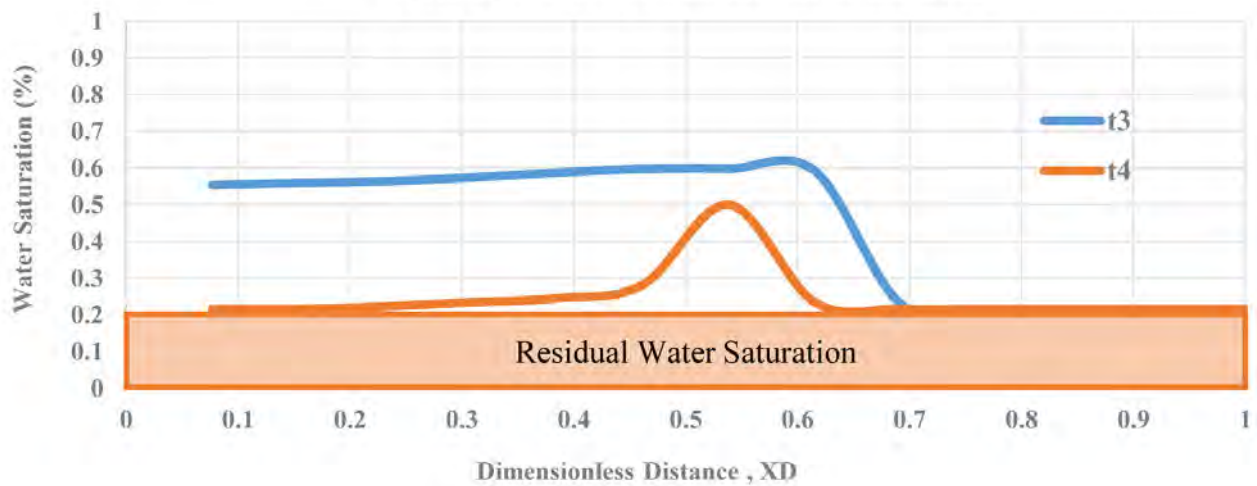
Water Saturation Profile during Soaking Time



(a) Saturation profile after t_3 (1 Day)

(b) Saturation profile after t_4 (45 Days)

Water Saturation vs Dimensionless Distance



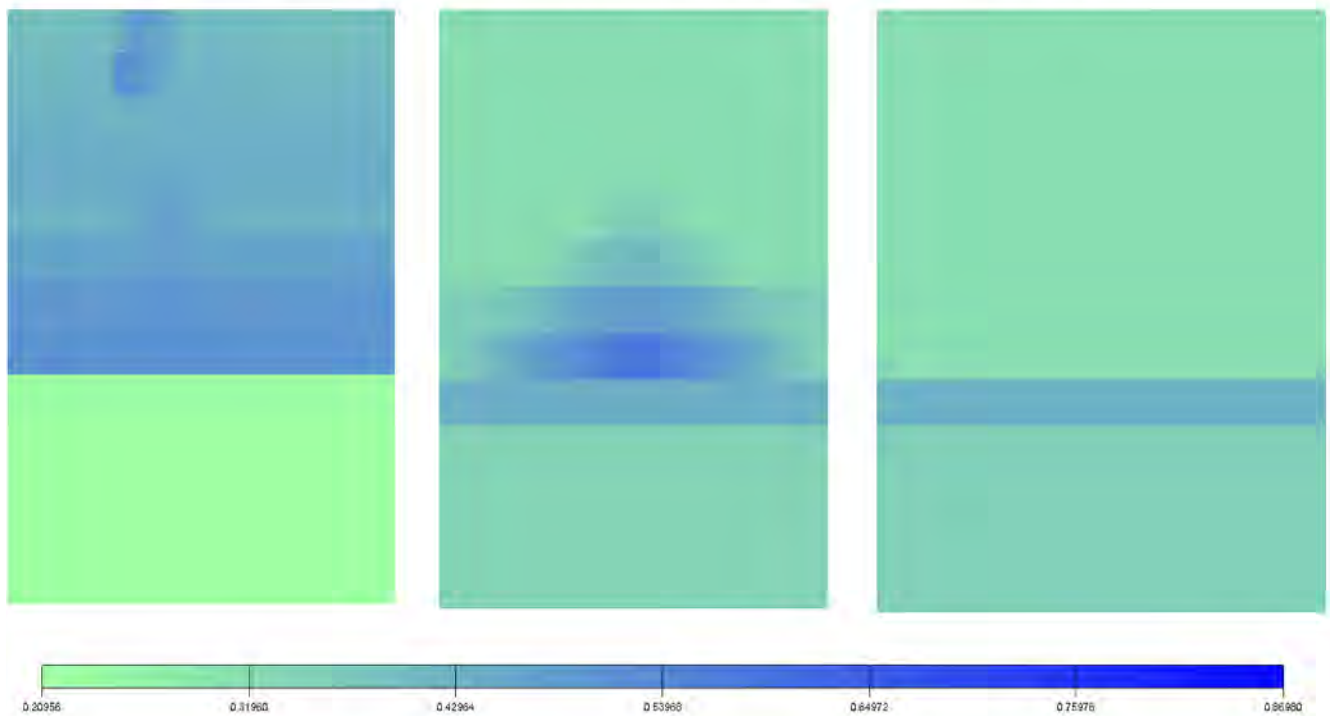
(c) Saturation profile after 1 Day and 45 Days during shut-in the well

Figure 16. Fracturing fluid saturation distribution during shut-in period in a vertical well (soaking time period).

Continued next page.

Continued from previous page.

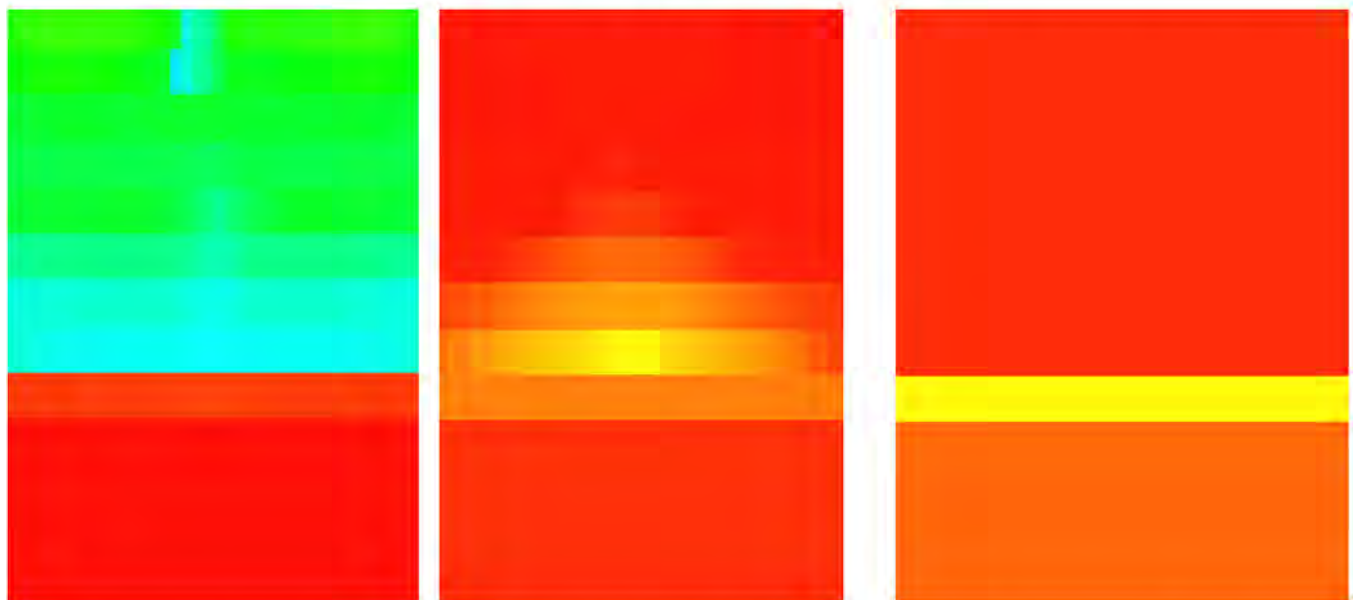
Water and Gas Saturation Profile during Production Period



(a) Water saturation after 46 Days

(b) Water saturation after 1 Year

(c) Water saturation after 2 Years



(d) Gas saturation after 46 Days

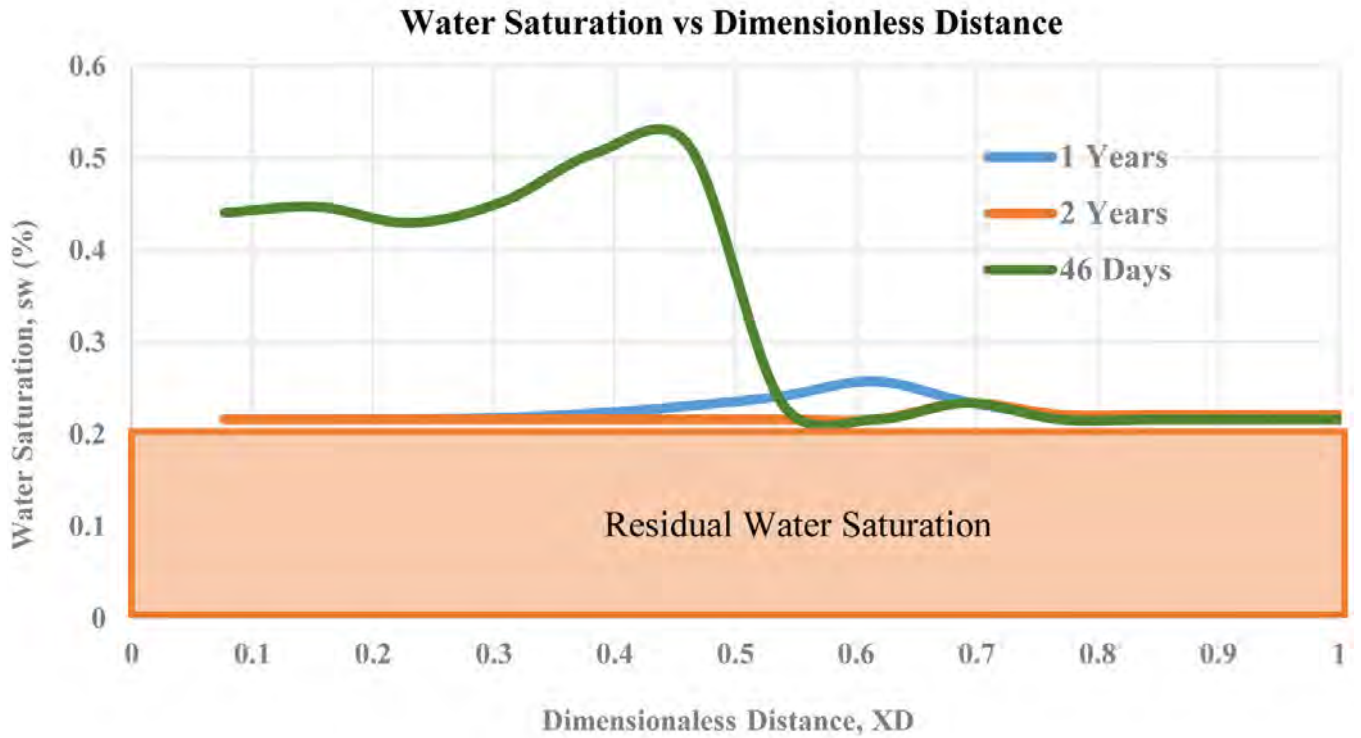
(e) Gas saturation after 1 Year

(f) Gas saturation after 2 Years

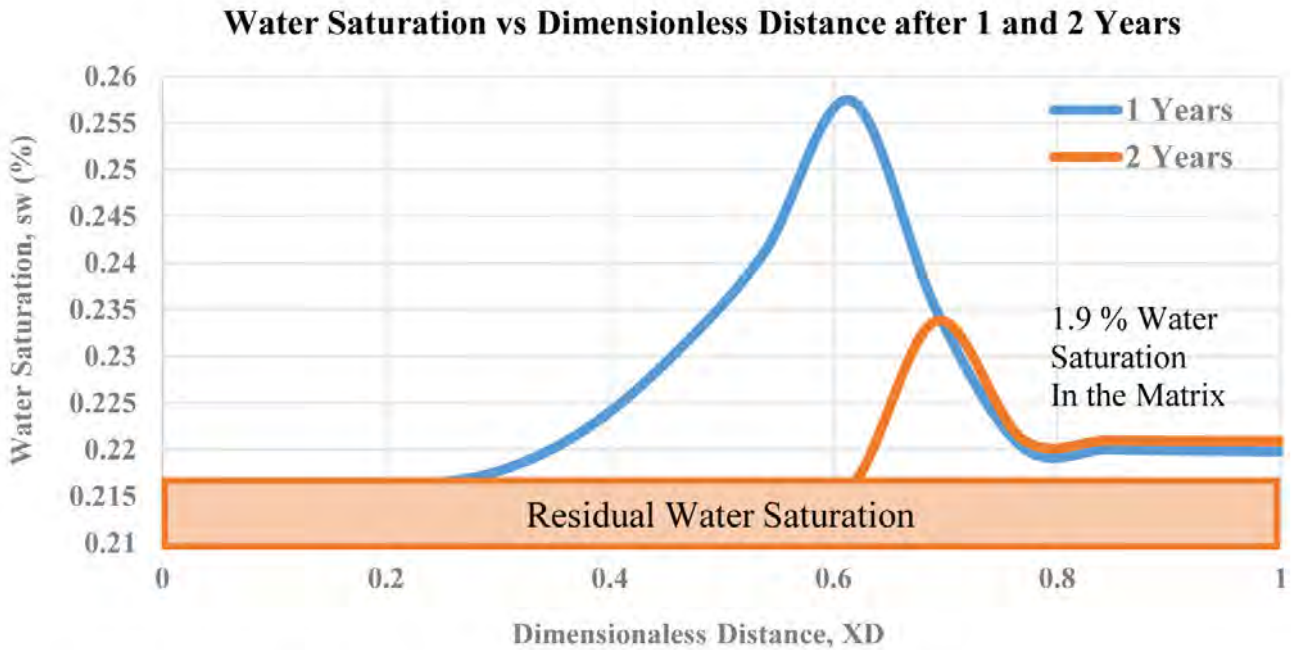
Figure 17. Fracturing fluid and gas saturation distribution during production period in a vertical well. (Figure continued next page.)

Continued next page.

Continued from previous page.



(g) Saturation profile during production period when displacement towards the gravity.



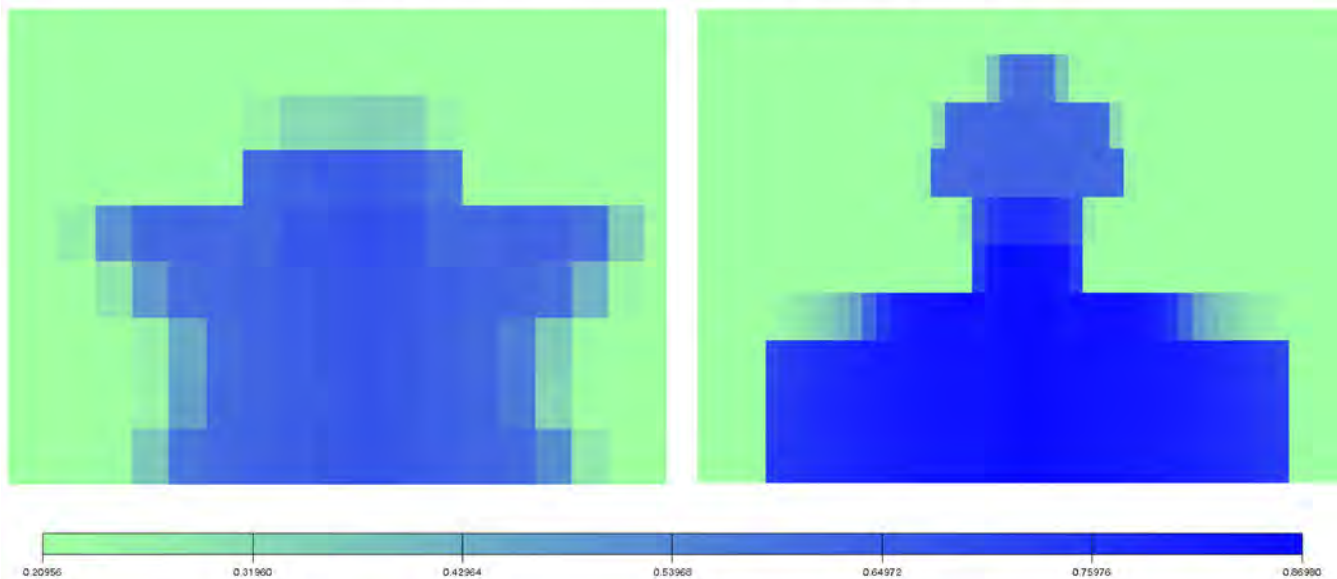
(h) Saturation profile during production period when displacement towards the gravity.

Figure 17. Fracturing fluid and gas saturation distribution during production period in a vertical well. (Figure continued from previous page.)

Continued next page.

Continued from previous page.

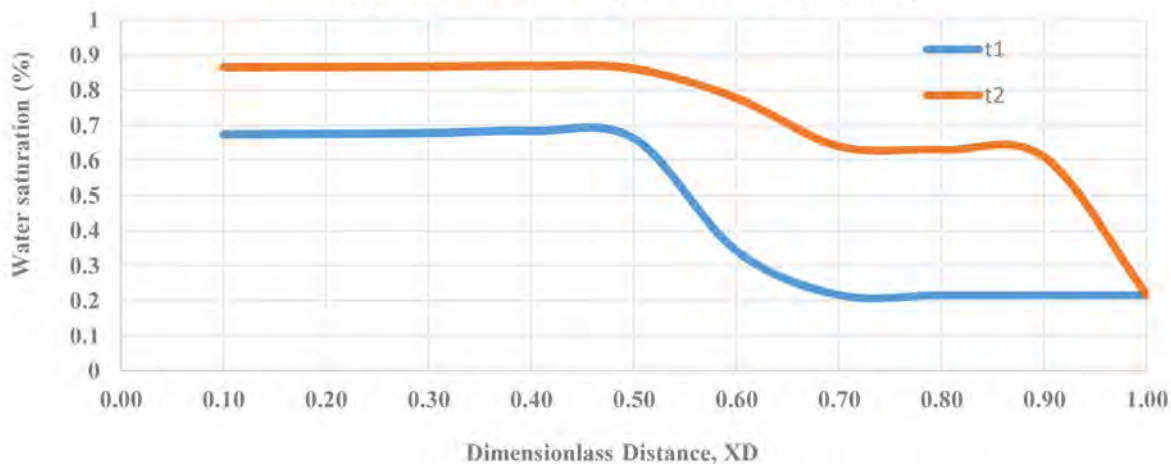
Water Saturation Profile during Injection Period



(a) Saturation profile after t_1 (1 Min)

(b) Saturation profile after t_2 (1 Hr.)

Water Saturation vs Dimensionless Distance



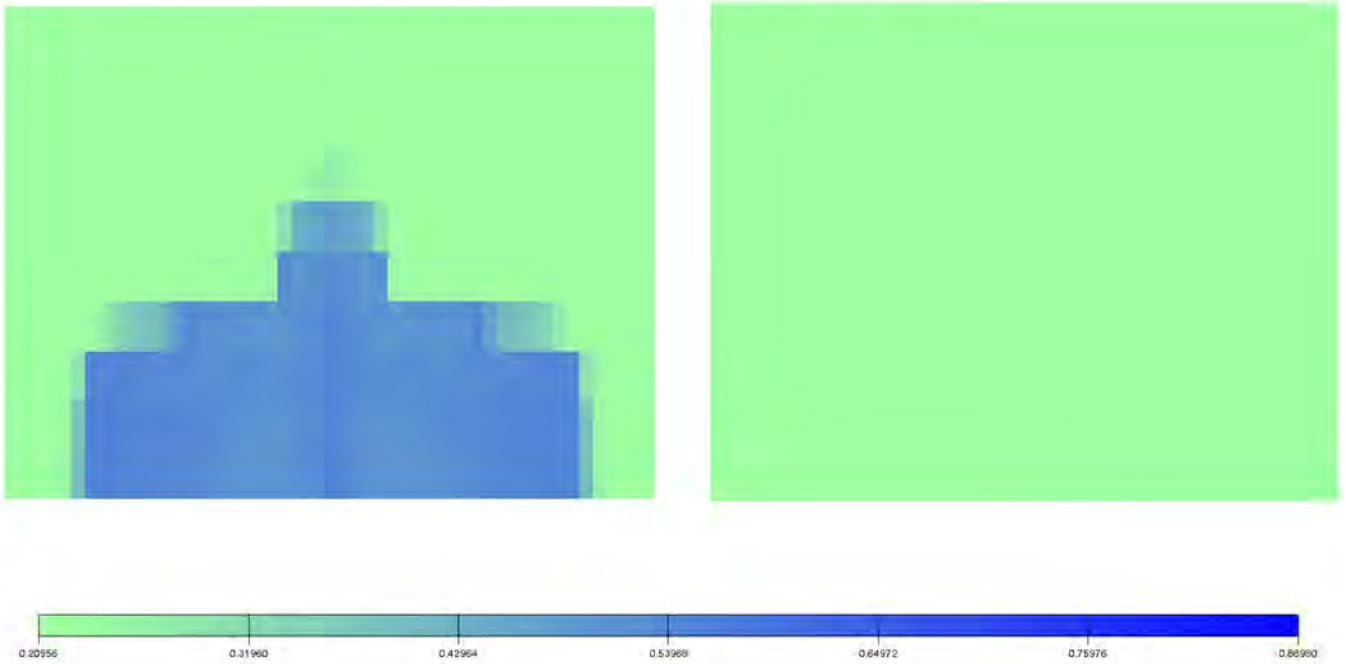
(c) Saturation profile with dimensionless distance in vertically upward direction against the gravity direction.

Figure 18. Fracturing fluid saturation distribution during injection period in a vertical well (displacement vertically upward direction).

Continued next page.

Continued from previous page.

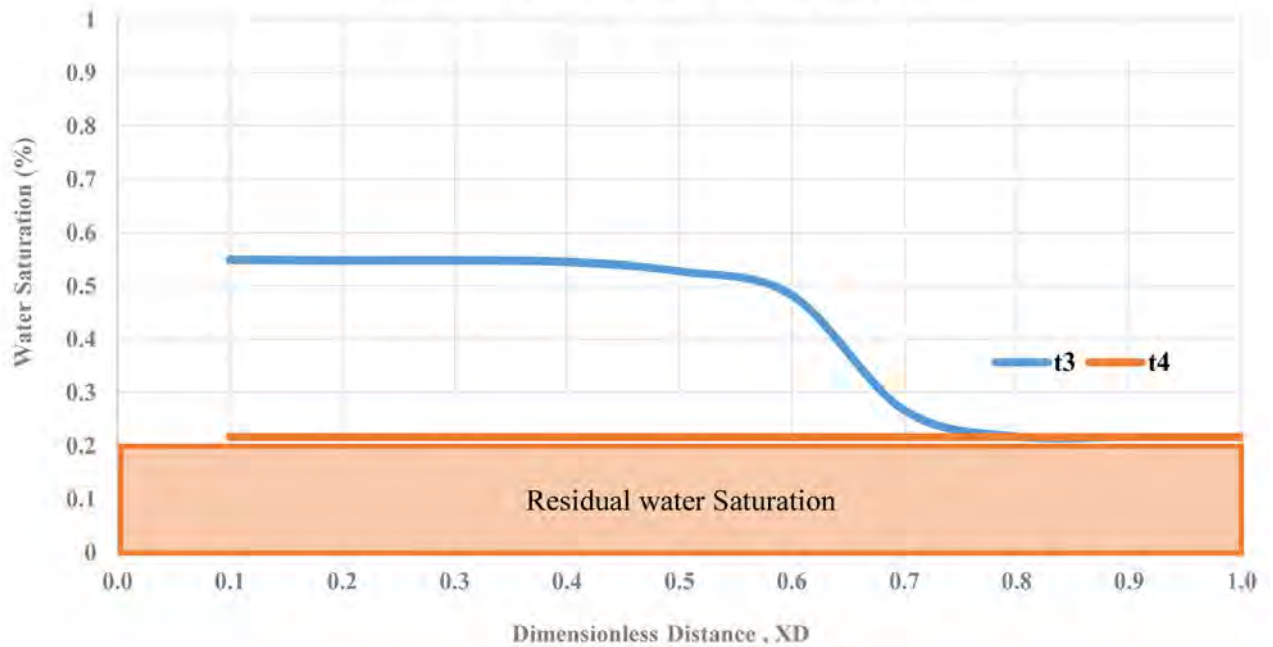
Water Saturation Profile during Soaking Time



(a) Saturation profile after t_3 (1 Day)

(b) Saturation profile after t_4 (45 Days)

Water Saturation vs Dimensionless Distance



(c) Saturation profile with dimensionless distance in vertically upward direction against the gravity direction

Figure 19. Fracturing fluid saturation distribution during shut-in period in a vertical well (soaking time period).

Continued next page.

Continued from previous page.



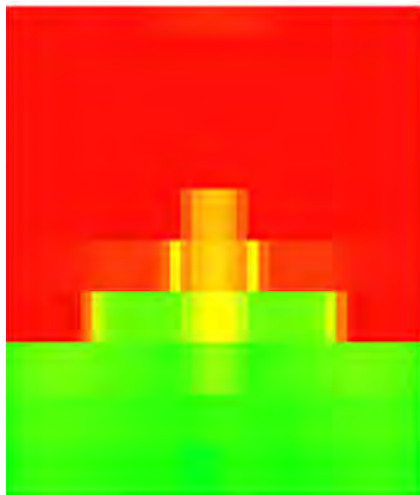
(a) Water saturation profile during production ($t_1 = 46$ Days)



(b) Water saturation profile during production ($t_1 = 1$ Year)



(c) Water saturation profile during production ($t_1 = 2$ years)



(d) Gas saturation profile during production ($t_1 = 46$ Days)



(e) Gas saturation profile during production ($t_1 = 1$ Year)

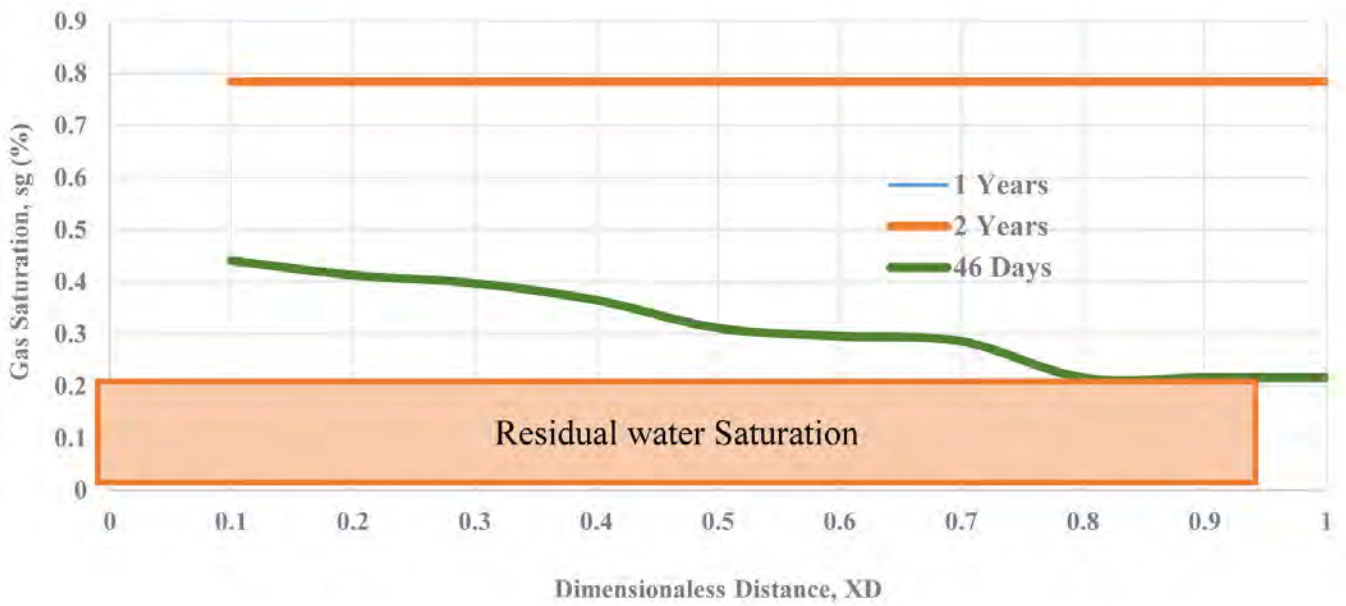


(f) Gas saturation profile during production ($t_1 = 2$ years)

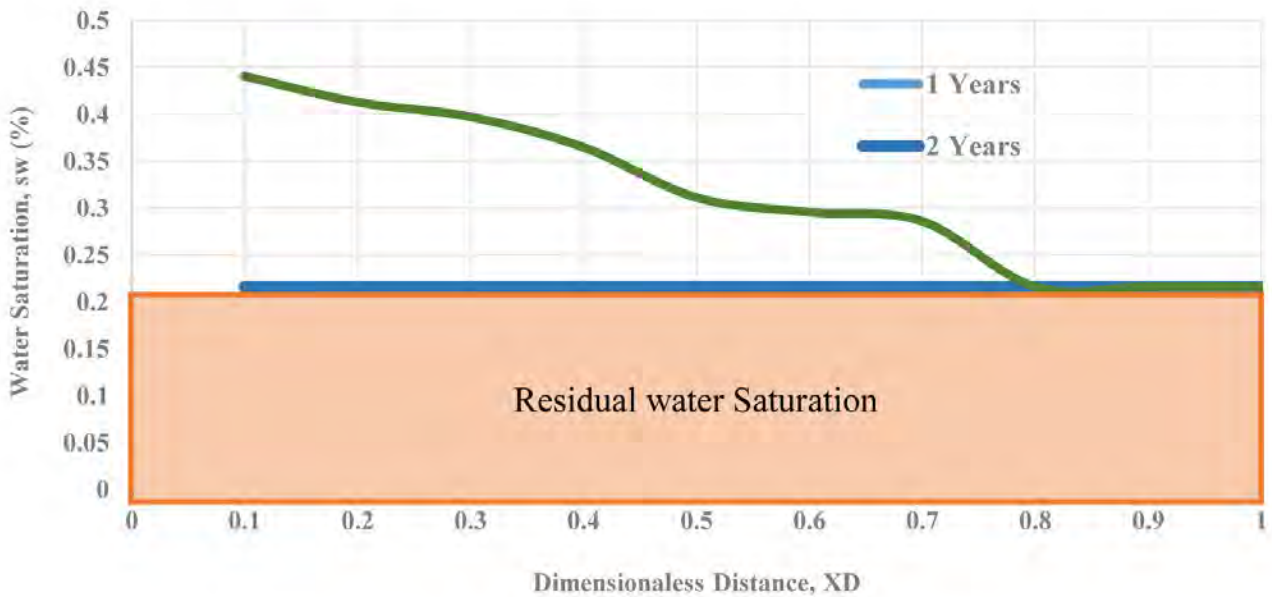
Figure 20. Fracturing fluid and gas saturation distribution during production period in a vertical well. (Figure continued next page.)

Continued next page.

Continued from previous page.



(g) Water saturation distribution towards the gravity during production period.



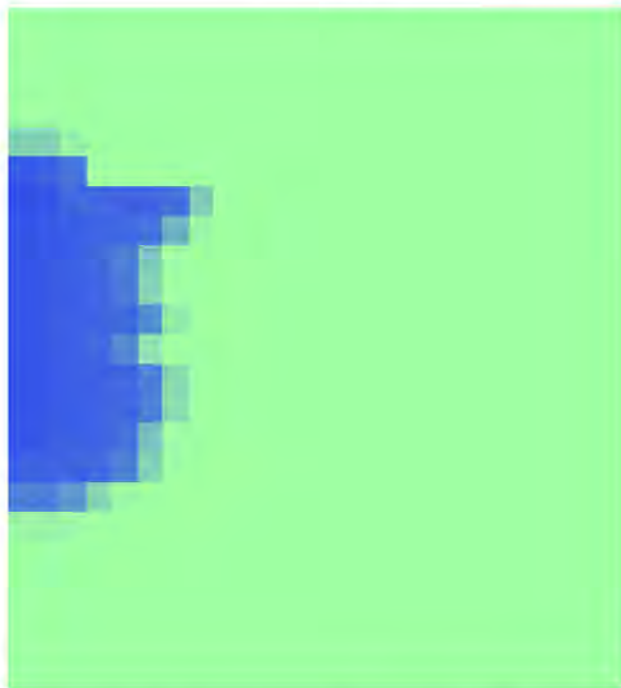
(h) Gas saturation distribution towards the gravity during production period.

Figure 20. Fracturing fluid and gas saturation distribution during production period in a vertical well. (Figure continued from previous page.)

Continued next page.

Continued from previous page.

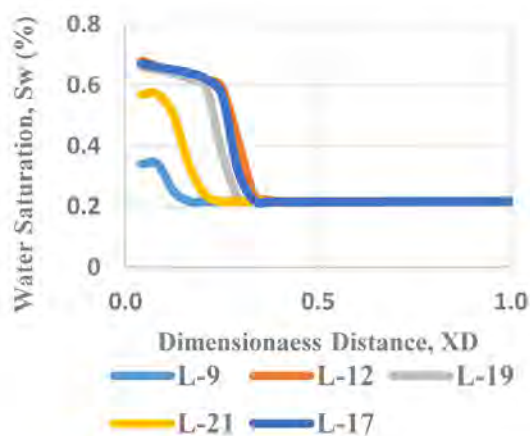
Water Saturation Profile along the Fracture Half-Length



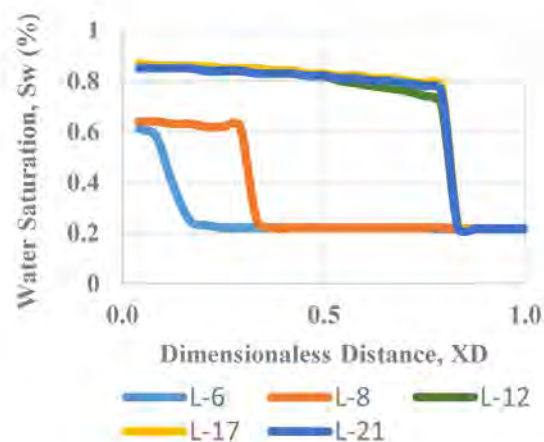
(a) Saturation mapping after 1 Min injection



(b) Saturation mapping after 1 hr. injection



(c) Saturation distribution along the fracture half-length in different layers after 1 Min



(d) Saturation distribution along the fracture half-length in different layers after 1 Hr.

Figure 21. Fracturing fluid saturation distribution during Injection along the horizontal direction.

Continued next page.

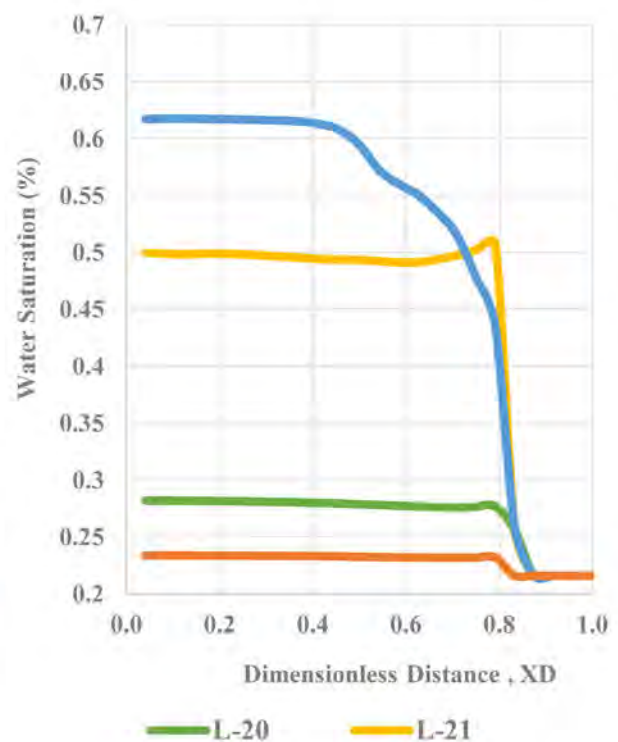
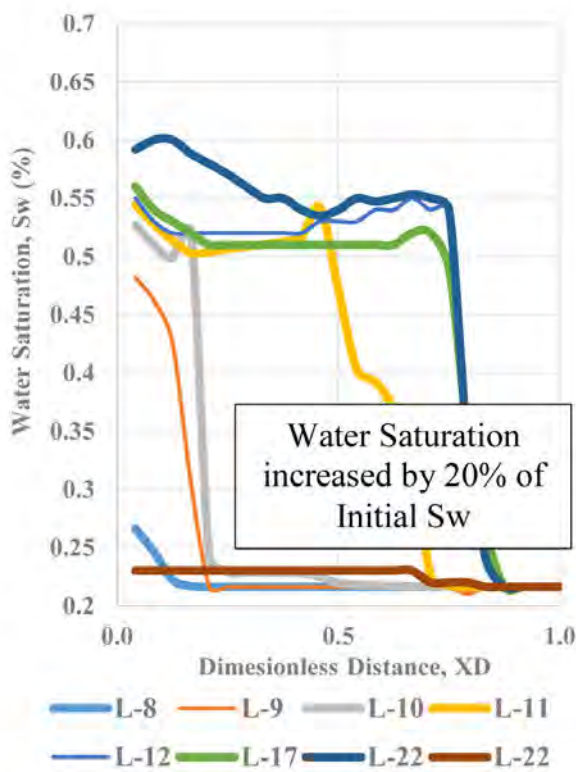
Continued from previous page.

Water Saturation Profile during Soaking Time



(a) Saturation mapping during soaking time along the horizontal direction (1 Day).

(b) Saturation mapping during soaking time along the horizontal direction (45 days).



(c) Saturation vs. dimensionless distance along the horizontal direction for different layers after 1 day.

(d) Saturation vs. dimensionless distance along the horizontal direction for different layers after 45 days.

Figure 22. Fracturing fluid saturation profile after injection period (during soaking time).

Water Saturation Profile during Production along the Fracture Half-Length

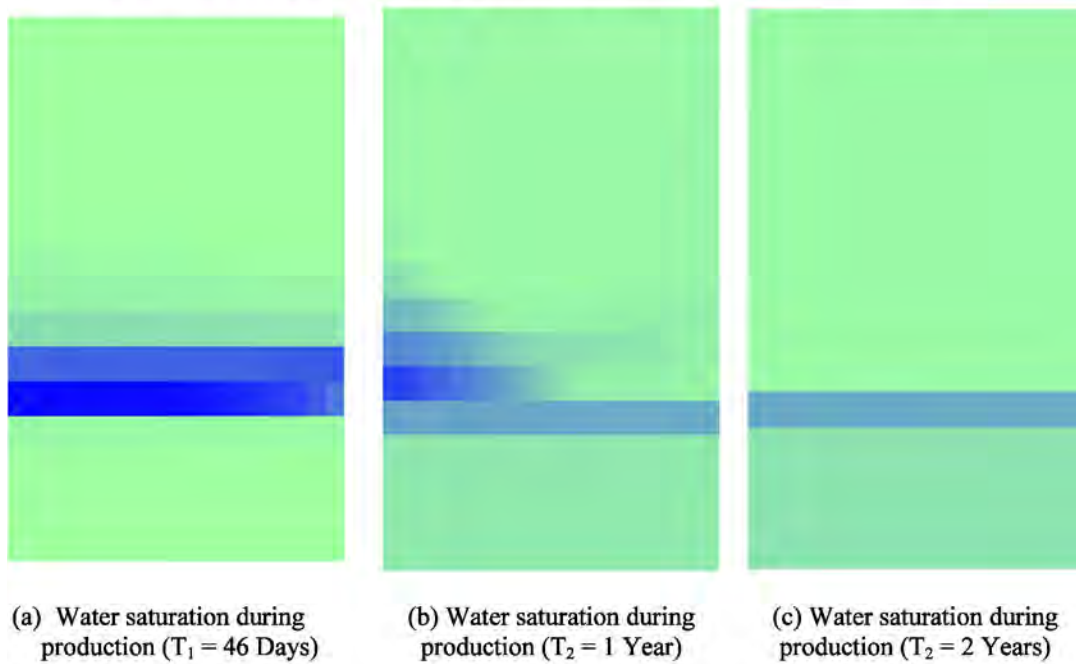


Figure 23. Fracturing fluid and gas saturation distribution along the propped fracture half-length during production period in a vertical well.

Water saturation along the Matrix

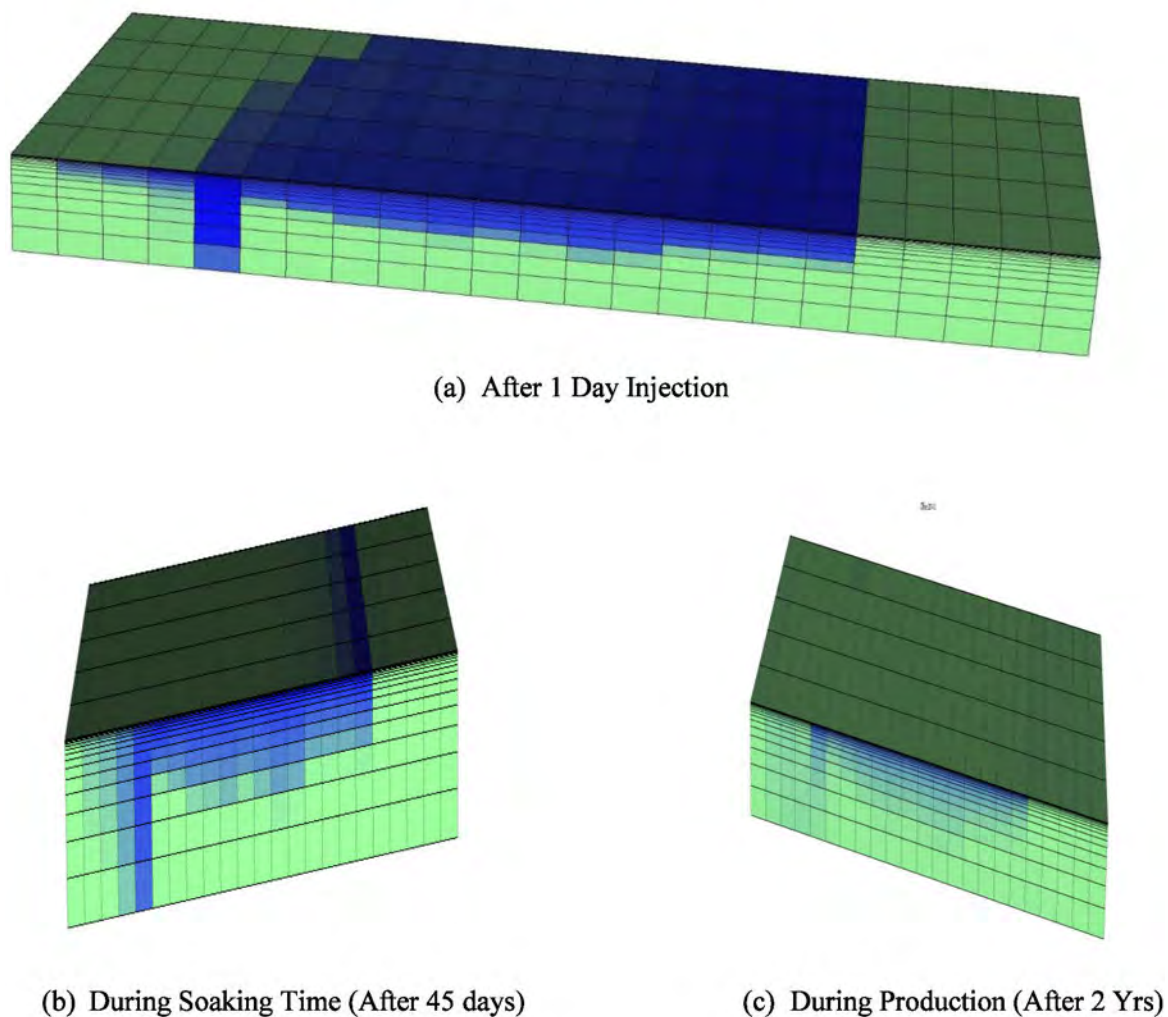


Figure 24. Images taken from the fluid displacement along the matrix show an unstable displacement and poor areal sweep efficiency.

Effect of capillary pressure

To study the effect of surface properties the authors changed the interfacial tension and wettability of the fracturing fluid. Talc and polytetrafluoroethylene (PTFE) were used to see the impact on fracturing fluid recovery. A laboratory experiment was conducted to measure the contact angle, while the surface tension value was taken from literature. The details of the case studies are listed in Table 4. The recovery rate is compared to explore the effect of all surface properties (Fig. 25). Gas cumulative is plotted in Figure 26 to explain the effect of PTFE for three wells.

INTERFACIAL TENSION

Figure 25 compares the recovery curves for PTFE and talc with 100% water as a fracture fluid, along with other circumstances. Table 4 shows the details of the case studies. As can be seen from the comparison, the ultimate recovery of PTFE is almost 7% higher than that of water, while it is 1% higher for talc. It is evident that both cases have greater recovery than other situations, which results from low surface tension. More water imbibes into the formation and increases vertical sweep efficiency, even in the direction against gravity, due to the reduction of surface tension.

CONTACT ANGLE

Figure 27 shows the contact angle for the two chemicals. It was 50° for talc and 1,04° for PTFE. The contact angle was measured to investigate the effects of wettability in the laboratory. Details of these experiments are explained by Mohamed et al (2015). The system is hydrophobic with a contact angle greater than 90° for PTFE. Figure 26 illustrates that the ultimate recovery of fracture fluid from the hydrophobic system (40%) is more than two times that from the hydrophilic system (19%).

The combined effect of interfacial tension and surface tension is observed in cases 5 and 6. Table 4 lists the input parameters for this study. As shown in Figure 26, water recovery—in this instance—is higher than that in others, but it is the same as for case 4. Also, it indicates that wettability is the prime factor than interfacial tension to increase the flow-back, but it is required to lessen the surface tension. Figure 26 summarises the results of all case studies for the three wells and shows that cumulative gas production is increased 2–5% for three wells for PTFE.

CONCLUSIONS

The results of this study can be used to explain the low fracture fluid recovery observed during hydraulic fracture flow-back operations. In multi-stage hydraulic fracture programs some vertical fractures are created below the well perforation in vertical wells. In these fractures, fracture fluid drainage is against gravity, which suggests a poor fluid clean-up. Results also suggest that water recovery from these frac-fluids can be improved by modifying the surface properties. From this numerical simulation output, the following can be concluded:

- Drainage patterns are distinctly different in the following directions: vertically upward, vertically downward, and horizontal along the fracture half-length and the matrix.
- Three distinct clusters of gravity stable, gravity neutral, and unstable gravity behaviors are observed. There are a strong gravity and imbibition effects during injection, soaking time, and production.

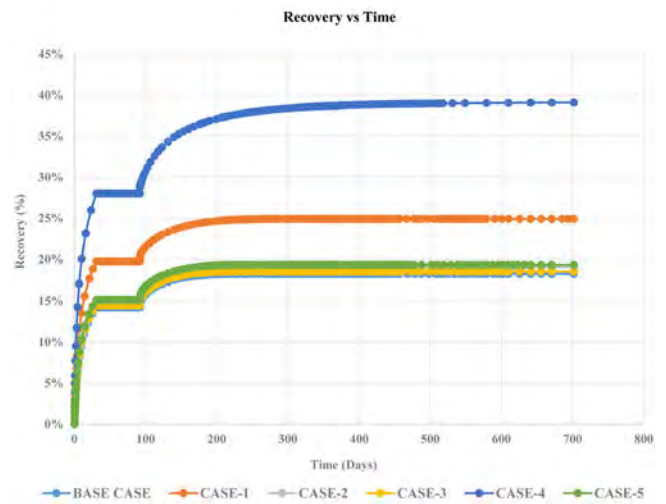


Figure 25. Effect of surface properties on water recovery for Well B, stage 2.

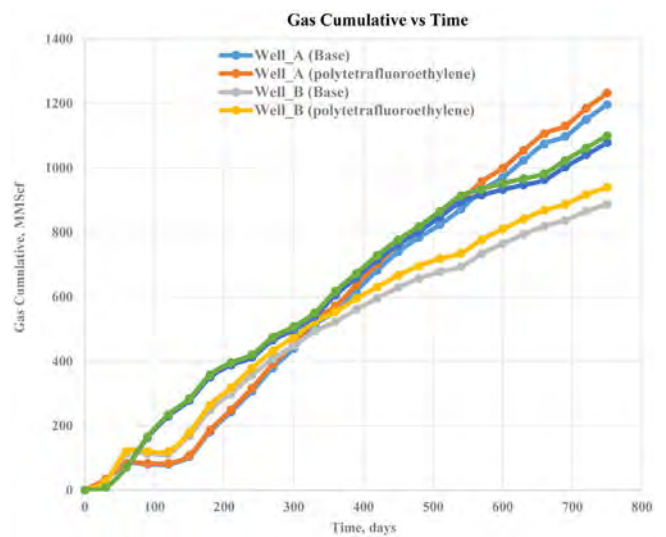


Figure 26. Effect of capillary pressure on gas cumulative for Wells A, B and C.

- It can be concluded that upward displacement, in which gas drains the fracture fluid against gravity in a porous medium, is unstable.
- Fingering increases along the horizontal direction and results in poor sweep efficiency and thus low fracture fluid recovery.
- For upward displacements during soaking time and production, it is observed that gravity does not influence the water recovery significantly, however, using PTFE in frac-fluid resulted in an almost 20% increase in ultimate water recovery.
- Changing the wettability of porous media from hydrophilic to hydrophobic doubled the water recovery. Changing the wettability resulted in the formation of wider fingers and thus higher sweep efficiency and ultimate water recovery.

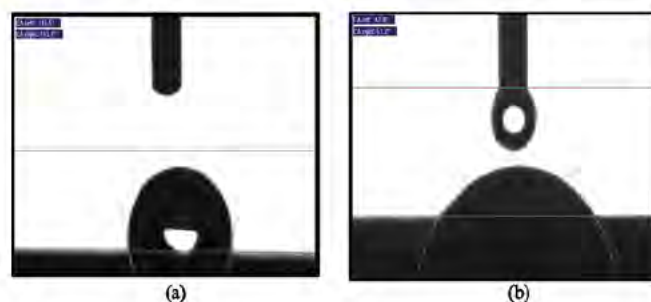
It is well known that surfactants and hydrophobic proppants can improve the recovery by reducing the capillary pressure; however, this study shows that PTFE and hydrophobic proppant can also improve the areal sweep efficiency in propped hydraulic fractures.

Continued next page.

Continued from previous page.

Table 4. Input parameters for the case studies.

Property/parameter	Case 1	Case 2	Case 3	Case 4	Case 5
Type of fracturing fluid	100% water	TALC	PTFE	PTFE	TALC
Surface tension	72 dynes/cm	45 dynes/cm	20.4 dynes/cm	20.4 dynes/cm	45 dynes/cm
Viscosity of gas	0.01657 cp	0.01657 cp	0.01657 cp	0.01657 cp	0.01657 cp
Density of gas	2.72×10^{-3} gm/cm ³	2.72×10^{-3} gm/cm ³	2.72×10^{-3} gm/cm ³	2.72×10^{-3} gm/cm ³	2.72×10^{-3} gm/cm ³
Proppant size	16/30	16/30	16/30	16/30	16/30
Wettability	Hydrophobic	Hydrophilic	Hydrophilic	Hydrophilic	Hydrophilic

**Figure 27.** Contact angle for (a) PTFE ($>90^\circ$), and (b) TALC ($<90^\circ$).

NOMENCLATURE

α	Dip angle
μ_1	Fluid 1 viscosity (cp)
μ_2	Fluid 2 viscosity (cp)
ρ_1	Fluid 1 density (lbm/ft ³)
ρ_2	Fluid 2 density (lbm/ft ³)
σ	Interfacial tension (dynes/cm)
A	Area (ft ²)
$\frac{dx}{dt}$	Velocity (ft/sec)
f_w	Fraction of water in the flowing stream passing any point in the rock (i.e. the water cut)
g	Acceleration due to gravity (ft/sec ²)
k	Formation permeability (mD)
k_1	Effective permeability to fluid 1 (mD)
k_2	Effective permeability to fluid 2 (mD)
k_{r1}	Relative permeability to fluid 1 (mD)
k_{r2}	Relative permeability to fluid 1 (mD)
P_{cow}	Capillary pressure (psi)
q	Total fluid flow rate (B/D)
V_c	Critical velocity (ft/sec)
x_{Sw}	Distance travelled by a particular S_w contour (ft)

ACKNOWLEDGMENTS

This work was supported by Santos Ltd, Australia. The authors would like to thank Simon Chipperfield, Steve Roberts and Joost Herweijer from Santos Ltd for their data and funding. Special thanks also goes to Schlumberger and GOHFER for their software support.

REFERENCES

ANANTAWATI, M. AND BULGAUDA, S., 2013—Prediction of Mobile Water in a Tight Gas Sandstone Reservoir using NMR and Fractional Flow Model. SPE Asia Pacific Oil and Gas Conference and Exhibition, Jakarta, Indonesia, 22–24 October, SPE-165766.

BENHAM, A.L. AND OLSON, R.W., 1963—A model study of viscous fingering. Society of Petroleum Engineers Journal, 3 (2), 138–44.

CHENG, Y., 2012—Impact of water dynamics in fractures on the performance of hydraulically fractured wells in gas-shale reservoirs. Journal of Canadian Petroleum Technology, 51 (2), 143–51.

CHUOKE, R.L., VAN MEURS, P. AND VAN DER POEL, C., 1959—The instability of slow, immiscible, viscous liquid-liquid displacements in permeable media. Petroleum Transactions, AIME, 216, 188–94.

FLETCHER, A.J.P., LAMB, S.P. AND CLIFFORD, P.J., 1992—Formation damage from polymer solutions: factors governing injectivity. SPE Reservoir Engineering, 7 (2), 237–46.

GHALAMBOR, A. AND GUO, B., 2010—How Much Can Fracturing Fluid Damage Productivity of Oil Wells? SPE International Symposium and Exhibition on Formation Damage Control, Lafayette, Louisiana, 10–12 February, SPE-125905.

GLASS, R.J., CONRAD, S.H. AND PEPLINSKI, W., 2000—Gravity-destabilized nonwetting phase invasion in macroheterogeneous porous media: experimental observations of invasion dynamics and scale analysis. Water Resources Research, 36 (11), 3,121–37.

JI, W., DAHMANI, A., AHLFELD, D.P., LIN, J.D. AND HILL, E., 1993—Laboratory study of air sparging: air flow visualization. Ground Water Monitoring & Remediation, 13 (4), 115–26.

MOHAMED, F., AL HINAI, M., AL NABHANI, H., YU, S., SARKAR, S. AND HAGHIGHI, M., 2015—Wettability Alteration in Hydraulically Fractured Tight Sand for Flow-back Improvement. Abu Dhabi International Petroleum Exhibition and Conference, Abu Dhabi, UAE, 9–12 November, SPE-177893.

POKALAI, K., HAGHIGHI, M., SARKAR, S., TYIASNING, S. AND COOKE, D., 2015—Investigation of the Effects of Near-Wellbore Pressure Loss and Pressure Dependent Leakoff on Flowback during Hydraulic Fracturing with Pre-Existing Natural Fractures. SPE/IATMI Asia Pacific Oil and Gas Conference and Exhibition, Nusa Dua, Bali, 20–22 October, SPE-176440.

SANTOS, 2003a—Well A well completion report. Adelaide: Santos Ltd.

SANTOS, 2003b—Well B well completion report. Adelaide: Santos Ltd.

SANTOS, 2007—Well C well completion report. Adelaide: Santos Ltd.

SARKAR, S., HAGHIGHI, M., POKALAI, K. AND SAYYAFZADEH, M., 2015—Coupling of multi-stage hydraulic fracture propagation model with multi-phase flow model in tight gas reservoirs with pre-existing natural fractures (case study, Cooper Basin, Australia). Unpublished.

SHARMA, M. AND AGRAWAL, S., 2013—Impact of Liquid Loading in Hydraulic Fractures on Well Productivity. SPE Hydraulic Fracturing Technology Conference, The Woodlands, Texas, 4–6 February, SPE-163837.

TANNICH, J.D., 1975—Liquid removal from hydraulically fractured gas wells. *Journal of Petroleum Technology*, 27 (11), 1,309–17.

TAYLOR, R.S., BARREE, R.D., AGUILERA, R., HOTCH, O. AND STOROZHENKO, K.K., 2011—Why Not to Base Economic Evaluations on Initial Production Alone. Canadian Unconventional Resources Conference, Calgary, Alberta, 15–17 November, SPE-148680.

TIDWELL, V. AND PARKER, M., 1996—Laboratory Imaging of Stimulation Fluid Displacement from Hydraulic Fractures. SPE Annual Technical Conference and Exhibition, Denver, Colorado, 6–9 October, SPE-36491.

TURNER, R.G., HUBBARD, M.G. AND DUKLER, A.E., 1969—Analysis and prediction of minimum flow rate for the continuous removal of liquids from gas wells. *Journal of Petroleum Technology*, 21 (11), 1,475–82.

THE AUTHORS



Sume Sarkar is a PhD candidate at the Australian School of Petroleum. She has experience in petroleum sector regulation in a south Asian context. She holds a MSc degree in petroleum engineering with specialisation in reservoir engineering from the Norwegian University of Science and Technology, and a BSc degree in chemical engineering from Bangladesh University of Engineering and Technology. Sume is conducting research on two major areas for unconventional reservoirs in the Cooper Basin: fracturing fluid flow-back modelling, and geomechanical modelling for multi-stage hydraulic fracture operations.

sume.sarkar@adelaide.edu.au



Manouchehr (Manny) Haghighi is an associate professor of petroleum engineering. His research and teaching focus is on unconventional reservoirs, reservoir simulation, well testing, and formation evaluation. He has supervised more than 40 MSc and 10 PhD students. Before joining the University of Adelaide in 2009, Manouchehr was associate professor of petroleum engineering at the University of Tehran (Iran). During 2000–07, he was the head of the petroleum engineering program at the University of Tehran. In 2000, Manouchehr established Simtech, a consulting company for integrated reservoir simulation in which he has been project director of several full-field simulation projects for oil and gas reservoirs.

From 1995 to 2000 Manouchehr worked with the National Iranian Oil Company (NIOC) and was the director of a program for the training of NIOC staff at several universities in the US, UK, Canada, France, Australia and Norway. Manouchehr was a visiting professor at the University of Calgary from 2007–08.

Manouchehr has published more than 80 articles in peer-reviewed journals or presented in international conferences. He has served as a reviewer for various journals including the *Journal of Petroleum Science and Engineering*. Member: SPE.

manouchehr.haghighi@adelaide.edu.au

Authors' biographies continued next page.

Authors' biographies continued from previous page.

THE AUTHORS



Mohammad Sayyafzadeh is a Lecturer at the Australian School of Petroleum. He holds a PhD in petroleum engineering from the University of Adelaide, and a MSc degree in reservoir engineering and a BSc degree in chemical engineering from Tehran Polytechnic.

Mohammad conducts research in two major areas. The first is numerical mathematics and theoretical computer science, with an emphasis on applications in the fields of reservoir engineering, such as probabilistic inverse modelling and uncertainty quantification, evolutionary computation algorithms for history matching and well placement optimisation, dimensionality reduction methods for heterogeneous reservoir characterisation, and surrogate-modelling techniques. The second area is reservoir engineering with an emphasis on unconventional resources such as modelling and simulation of enhanced coalbed methane (ECBM) recovery, simulation of CO₂ sequestration in coal seams, simulation of flow-back after hydraulic fracturing in tight-sand reservoirs, pore-scale simulation of two-phase flow in naturally-fracture rocks, and well-placement optimisation in coal seam plays.

Mohammad has co-authored several papers that have been published in various journals, and serves as a reviewer for a few prestigious journals and conferences.

mohammad.sayyafzadeh@adelaide.edu.au



Kunakorn Pokalai is presently a production engineering PhD candidate at the University of Adelaide. He has a BEng in petrochemical engineering from Silpakorn University (Thailand), and completed a Graduate Certificate in Management, and a master's in petroleum engineering from the University of Adelaide.

Kunakorn's research interests are in the simulation of unconventional reservoirs and hydraulic fracturing. He mainly focuses on the issue of fracturing fluid flowback in the Cooper Basin. He was the recipient of the prestigious AAPG Imperial Barrel Award in the Asia Pacific Region in 2014. Member: SPE and AAPG.

kunakorn.pokalai@adelaide.edu.au



Dennis Cooke has a PhD in geophysics from the Colorado School of Mines, and more than 25 years of experience in oil and gas exploration and development. He is a past-president of the Australian Society of Exploration Geophysicists (ASEG), and a former vice president of the Society of Exploration Geophysicists (SEG).

Dennis owns and operates ZDAC Geophysical Technology, which provides technology and services for seismic inversion and reservoir characterisation. He is an Adjunct Assistant Professor at the University of Adelaide's Australian School of Petroleum.

dennis.cooke@adelaide.edu.au



Fathima Mohamed is presently a PhD candidate in petroleum engineering and management at the Australian School of Petroleum, The University of Adelaide. She received a BE degree in petroleum engineering from the same institution. Her research interests, among others, include flow back enhancement in gas wells, alternative fracturing fluids, and wettability alteration.

fathima.mohamed@adelaide.edu.au

Appendix J: Alternative Fracturing Fluid Systems

J1: Simulation of Hydraulic Fracturing with Propane-Based Fluid using a Fracture Propagation Model Coupled with Multiphase Flow Simulation in the Cooper Basin, South Australia

Simulation of hydraulic fracturing with propane-based fluid using a fracture propagation model coupled with multiphase flow simulation in the Cooper Basin, South Australia



Lead author
Yang
Fei

Y. Fei, M.E. Gonzalez Perdomo, V.Q. Nguyen, Z.Y. Lei, K. Pokalai, S. Sarkar and M. Haghighi

Australian School of Petroleum
The University of Adelaide
Adelaide, SA 5005
yang.fe@adelaide.edu.au

ABSTRACT

In many unconventional reservoirs, gas wells do not perform to their potential when water-based fracturing fluids are used for treatments. The sub-optimal fracture productivity can be attributed to many factors such as effective fracture length loss, low load fluid recovery, flowback time, and water availability. The development of unconventional reservoirs has, therefore, prompted the industry to reconsider waterless fracturing treatments as viable alternatives to water-based fracturing fluids.

In this paper, a simulation approach was used by coupling a fracture propagation model with a multiphase flow model. The Toolachee Formation is a tight sand in the Cooper Basin, around 7,200 ft in depth, and has been targeted for gas production. In this study, a 3D hydraulic fracture propagation model was first developed to provide fracture dimensions and conductivity. Then, from an offset well injection fall off test, the model was tuned by using different calibration parameters such as fracture gradient and closure pressure to validate the model. Finally, fracture propagation model outputs were used as the inputs for multiphase flow reservoir simulation.

A large number of cases were simulated based on different fracturing fluids and the concept of permeability jail to represent several water-induced damage effects. It was found that LPG was a successful treatment, especially in a reservoir where the authors suspected the presence of permeability jails. The authors also observed that total flowback recovery approached 76% within 60 days in the case of using gelled LPG. Modelling predictions also support the need for high-quality foam, and LPG can be expected to bring long-term productivity gains in normal tight gas relative permeability behaviour.

KEYWORDS

Tight gas, Cooper Basin, LPG fracturing fluid.

INTRODUCTION

Unconventional hydrocarbon reservoirs such as tight gas, shale gas and coalbed methane are becoming important resources for existing and future oil and gas supply; however, because of the low-permeable nature of unconventional reservoirs, they need hydraulic fracturing treatment. In this operation, a large volume of fracturing fluid is injected at high rates into the wellbore to overcome the rock and to induce fractures around the wellbore in the targeted formation. During a hydraulic fracture operation some of the fracturing fluid will

leak-off from the fracture and invade the reservoir. In tight sand reservoirs the invaded water-based fracturing fluid may cause damage (water blockage) to reservoir permeability and fracture conductivity. Consequently, the use of water-based fracturing fluids in tight gas reservoirs may limit the potential of well productivity and result in longer flow-back times (Lestz et al, 2007).

Typically, water-based fluids are the simplest and most cost-effective solution to induce a fracture in a rock formation; however, alternatives to water-based fluids have significantly outperformed water treatments in many reservoirs. For instance, in 1970 foams were extensively used in various depleted reservoirs in which water fractures were not effective (Economides and Martin, 2007). More recently, the development of many unconventional reservoirs has prompted the industry to reconsider waterless fracturing treatments as viable alternatives to water-based fracturing fluids. In these reservoirs, the interactions between the rock formation and the fracturing fluids may be detrimental to hydrocarbon production (Ribeiro and Sharma, 2013).

The LPG fracking technique has been commercially applied in unconventional reservoirs in North America. Gandossi (2013) reported that between 2008 and 2013, more than 2,000 LPG fracturing operations were carried out by a Canadian service company in North America. The LPG fluid's properties such as density, viscosity and surface tension with complete solubility in formation hydrocarbons are very beneficial (Gupta, 2009). In a field application, LPG is gelled before fracturing to allow transport of the proppant into the fracture (Leblanc et al, 2011).

In this paper, a diagnostics fracturing injection test (DFIT) was studied to validate instantaneous shut in pressure (ISIP), closure pressure, type of leak-off, and reservoir permeability. Then, based on mechanical rock properties from log data, minimum horizontal stress was estimated and a 3D hydraulic fracturing propagation model was developed (Pokalai et al, 2015). Eventually the results of the fracture dimension and conductivity were provided in a multiphase flow model to simulate the flowback and gas production of the fractured wells.

Since a hydraulic fracturing operation has already been carried out in well Merrimelia-62, the authors used nitrogen foam as a base case. After matching and validation with actual field flowback and history production, the new concept of permeability jail was investigated by a sensitivity analysis for three different fluid formulations: slickwater, N₂ foam, and LPG.

Conventional fracturing fluids include water-based and polymer-containing fluids. Unconventional fracturing fluids include non-polymer-containing fluids such as viscoelastic surfactant fluids, methanol-containing fluids, liquid CO₂-based fluids, and LPG-based fluids.

The ideal fracturing fluid should have:

1. compatibility with the formation to minimise formation damage;
2. sufficient viscosity to create a fracture and transport the proppant; and,
3. rapid viscosity breakdown after the proppant is placed to maximise fracture conductivity (Economides and Martin, 2007).

Figure 1 describes the significance of the fracturing fluid properties in hydraulic fracturing treatment (Economides and Martin, 2007; Economides and Nolte, 2000; Fink, 2013; Gidley et al, 1989; Valko and Economides, 1996).

The following are a few issues that need to be considered when using water-based fracturing fluids:

1. effective fracture length loss (Taylor et al, 2010);
2. low load fluid recovery (Economides and Martin, 2007);
3. flowback time (Al-Kanaan et al, 2013); and,
4. water availability.

Taylor et al (2010) suggested that the reason for phase trapping (fluid retention) is due to the high capillary threshold pressure. Values of the threshold pressure can be estimated using the Laplace-Young equation (Chalbaud et al, 2006) (Eq. 1).

$$P_c^{th} = P_{non-wetting} - P_{wetting} = \frac{2\gamma \cos \theta}{r} \quad (1)$$

In Equation 1, P_c^{th} is capillary threshold pressure (psi), γ is surface tension (dyn/cm), θ is the contact angle (degree), and r is pore radius (microns).

When pressure dropdown between reservoir pressure and flowing buttonhole pressure are not large enough to overcome the capillary threshold pressure, the fluids remain in the formation (Holditch, 1979). Taylor et al (2010) reported that capillary pressures of 1,450–2,900 psig, or much higher, can be present in low-permeability formations at low-water saturation levels. In addition, Economides and Martin (2007) presented that injecting water-based fracturing fluids into high-capillarity reservoirs results in creation of high water saturation in the near-wellbore. The relative permeability of gas will be dramatically reduced by the increasing water saturation (see Fig. 2).

Furthermore, the rock formation reacts both chemically and mechanically with the injected fluid. Clays may swell when placed in contact with water, but clays do not interact significantly with CO₂, N₂ and LPG. Many unconventional rock formations lose some of their mechanical integrity when placed in contact with water. As the rock becomes softer, the rock further closes on the proppant, thereby promoting proppant embedment (Ribeiro and Sharma, 2013).

LPG AS A FRACTURING FLUID

Hurst (1972) introduced a new stimulation technique using liquid gas. It is a fracturing treatment using an absolutely water-free fluid system. LPG gases are a mixture of petroleum natural gases (e.g. propane and butane) existing in a liquid state at ambient temperatures and moderate pressure (less than 200 psi). It behaves as other liquids do as long as they are under adequate pressure and below their critical temperature.

In field conditions, cold LPG at moderate pressure is frequently blended with proppant, gellant and breaker before being pumped into the formation for fracture. After pumping, the LPG changes phase behaviour as it converts to a gas phase due to reservoir conditions (increased pressure and temperature) and mixing with the reservoir gas (Lestz et al, 2007). Figure 3 demonstrates that with increasing the methane and propane mixture ratio, the saturation curve tends towards to the left. If the formation temperature is 160°F, with an initial 100% propane as fracturing fluid being pumped into the formation, the 100% liquid phase propane converts to a gas phase when the methane mixture ratio reaches 40%.

Leblanc et al (2011) presented a successful case for the application of a LPG-based fracturing fluid in the McCully gas field, in Canada. The results of using LPG, in comparison with a water-based fracturing fluid, show significant improvement in the McCully field, including:

1. the removal of water handling issues;
2. 100% of the propane was recovered within two weeks of the fracture treatment; and,
3. propane yielded an effective average fracture half-length that was double to that achieved by a water fracture.

In addition, laboratory tests have been conducted in the Montney Gas Reservoir in Canada, the results of which show that LPG is one of the best fracturing fluids and provides superior performance of regained methane permeability in comparison to all other conventional fluids (Taylor et al, 2010).

Gandossi (2013) demonstrated a comprehensive overview of hydraulic fracturing for shale gas production and presented a summary of the potential advantages and disadvantages of the LPG fracturing technique (see Table 1). One major disadvantage of LPG is that it is flammable and explosive; hence, it requires being carefully handled and pumped. Furthermore, nitrogen is usually mixed in either the pumping system or the fracturing fluid itself to prevent an explosion (Soni, 2014).

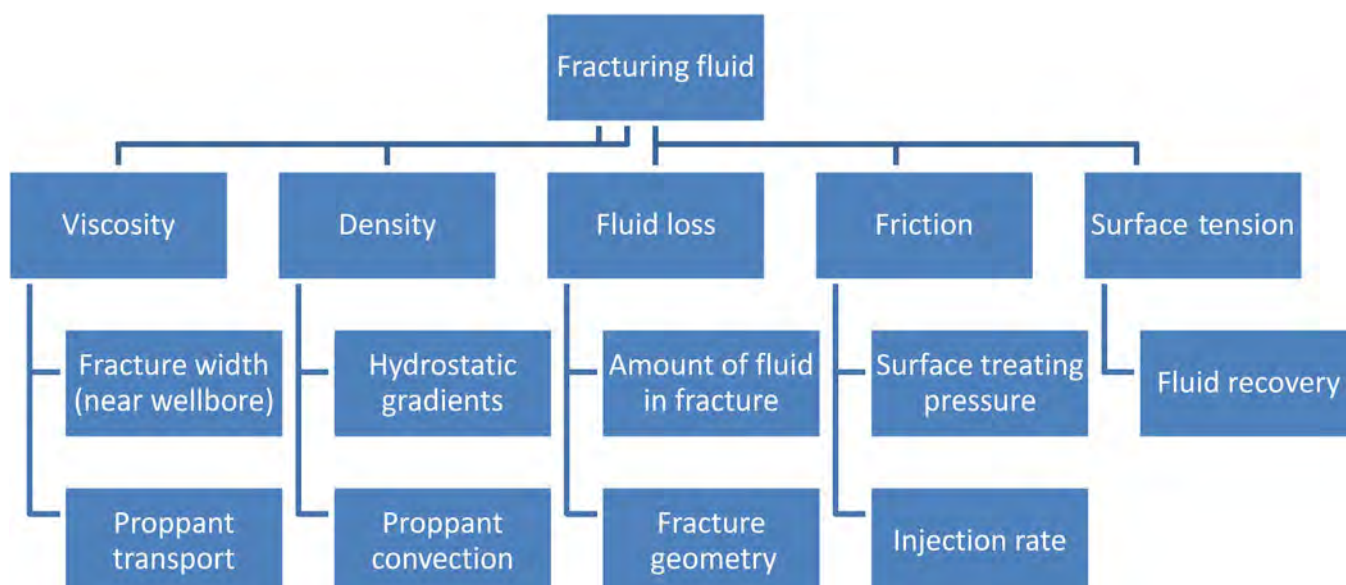


Figure 1. Physical and chemical properties of hydraulic fracturing fluid.

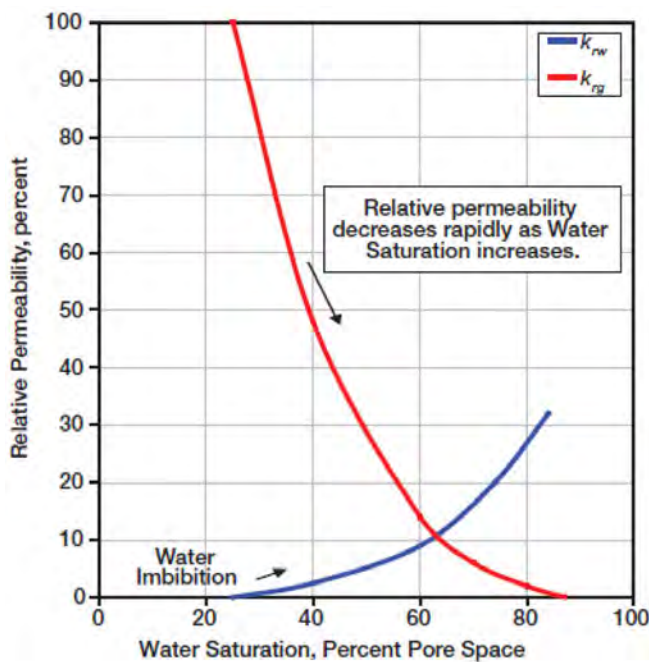


Figure 2. Effect of water imbibition on relative permeability change (Economides and Martin, 2007).

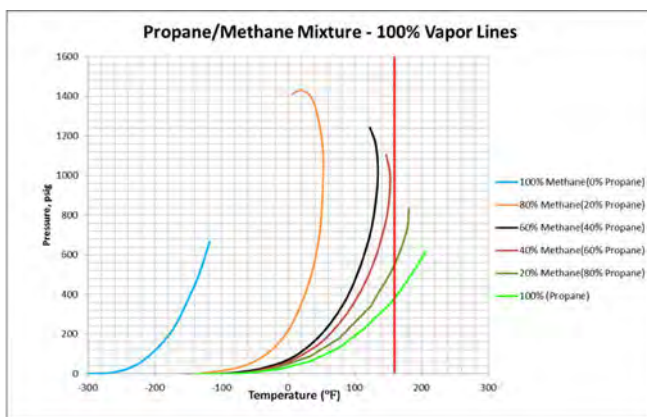


Figure 3. Propane-methane mixtures at formation conditions (Leblanc et al, 2011).

Table 1. Summary of potential advantages and disadvantages for LPG fracturing techniques (Gandossi, 2013).

Potential advantages	Potential disadvantages
<ul style="list-style-type: none"> Water usage much reduced or completely eliminated. Fewer or no chemical additives are required. Flaring is reduced. Truck traffic is reduced. LPG is an abundant by-product of the natural gas industry. Increases the productivity of the well. Lower viscosity, density and surface tension of the fluid, which results in lower energy consumption during fracturing. Full fluid compatibility with shale reservoirs (phase trapping virtually eliminated). No fluid loss, recovery rates (up to 100%) possible. Very rapid clean up. 	<ul style="list-style-type: none"> Involves the manipulation of large amounts of flammable propane, hence is potentially riskier than other fluids. Higher investment costs. Success relies on the formation's ability to return most of the propane back to surface to reduce the overall cost.

GEOLOGY AND HYDRAULIC FRACTURING IN THE COOPER BASIN

The Cooper Basin is a late Carboniferous to Middle Triassic, non-marine sedimentary basin in eastern-central Australia, spanning more than 130,000 km². The basin straddles the border of SA and Queensland, as illustrated in Figure 4. The Cooper Basin is the most significant onshore oil and gas province in Australia and is the primary onshore source for natural gas production (Gravestock and Jensen, 1998). Since the late 1960s significant volumes of oil, gas and LPG have been produced from more than 190 separate gas fields and 115 oil fields within the Cooper Basin (Santos, 2015). The primary fracture targets in the Cooper Basin tight gas are the Tirrawarra, Patchawarra and Toolachee formations. This paper's target formation is described in further detail below. The stratigraphic column of the Cooper Basin is shown in Figure 5.

The Toolachee Formation has large amounts of channels and crevasse splay deposits, with an average channel thickness of 15 ft and total gross thickness of 200–300 ft. The Toolachee Formation is widespread throughout the Cooper Basin and contains 25 of the basin's gas reserves (McGowen et al, 2007). There are two units within the Toolachee; the lower is carbonaceous shale with interbedded coal and sandstone, while the upper is sandstone with interbedded coals and shale. The reservoir permeability varies between 0.5 and 50 mD. Hydraulic fracturing in the Toolachee Formation accounts for 30% of all fracture treatments within the Cooper Basin.

Hydraulic fracturing has been used since 1968 to stimulate the Cooper Basin's oil and gas reservoirs. As of 2013, 700 wells in the Cooper Basin have been fracture stimulated and more than 1,500 individual fracture stimulation stages have been pumped (Braddeley, 2013). Figure 6 illustrates the increase in popularity of hydraulic fracturing in the Cooper Basin.

The main issues with hydraulic fracturing in the Cooper Basin have included high fracture gradients, high tortuosity and high pressure dependent leakoff (PDL) (Scott et al, 2013). Fracture gradients commonly range from 0.9–1.3 psi/ft because reservoir quality reduces or formation depth increases. High tortuosity is most likely caused by fracture tuning where the fracture remain principally vertical but is forced to counteract the maximum horizontal stress in the near wellbore region as it reorients after initiating from an unfavourable direction (Chipperfield and Britt, 2000). Lastly, McGowen et al (2007) reported that more than 65% of treatments in the Cooper Basin have observed high PDL. The typical fracturing fluids in the Cooper Basin that have been used are friction-reduced water (slickwater) and borate-crosslink gel. 100-mesh sand has been used throughout the basin to help reduce near wellbore pressure loss (NWBPL) and 20/40 to 40/70 mesh sands are the most commonly selected proppant (Pitkin et al, 2011). Special core analysis has, however, not been commonly conducted in this basin, so the relative permeability condition in most of the reservoirs remains unknown, which could potential cause low productivity and low flowback recovery by induced water-based fracturing fluid.

Merrimelia is a mature oil and gas producing field located approximately 45 km north of Moomba on the Gidgealpa-Merrimelia-Innaminka Ridge. This major positive structural feature runs the length of the SA sector of the Cooper/Eromanga Basin and separates the Patchawarra Trough from the Nappamerri Trough. Merrimelia-62 was drilled in mid-2011 as a gas development well in the Merrimelia field in SA (Fig. 7). The Toolachee was the primary target formation and the Callamurra Member was the secondary objective for Merrimelia-62. Hydrocarbon was indicated by the wireline logs. A total of 40 ft of net gas pay with a porosity of 11.6% was predicted for the Toolachee Formation. The Callamurra Member was prognosed to have 30 ft of net gas pay with a porosity of 11.9% (Santos, 2012).



Figure 4. Cooper Basin location (blue) and overlying Eromanga Basin (green).

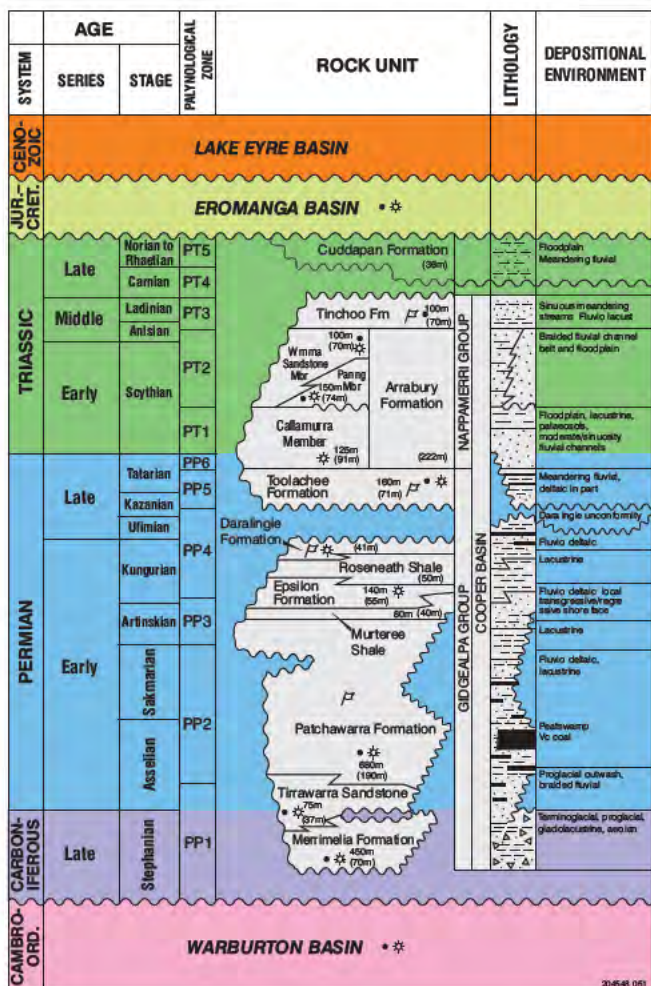


Figure 5. Stratigraphic summary of the Cooper Basin, SA (Alexander, 1998).

METHODOLOGY

In this paper, the authors used a fracture propagation model coupled with reservoir simulation. Figure 8 shows the details of the workflow.

First, the key reservoir properties—such as geomechanical stress and rock strength—that control the growth of hydraulic fracture needed to be determined from log data. IHS WellTest software was selected to simulate DFIT data due to its ability to model DIFT after-closure pressure without a full-scale fracture simulator. The

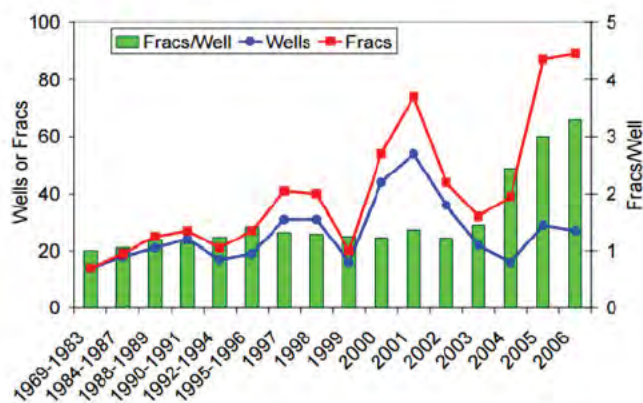


Figure 6. Fracture treatment in the Cooper Basin (McGowen et al, 2007).

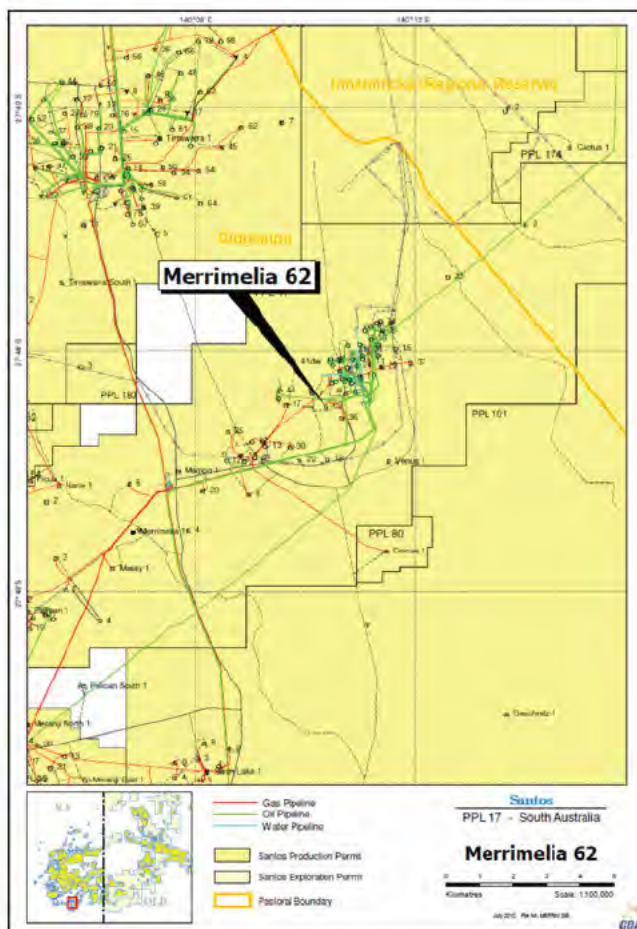


Figure 7. Location map of Merrimelia-62 (Santos, 2012).

result of pre-closure analysis are ISIP and closure pressure, which are the input parameters of the 1D mechanical earth model. Reservoir permeability and reservoir pressure are the after-closure analysis results, which are input into the fracture model. The pre-closure and after-closure results are summarised in Table 2.

Then, GOHFER (Grid-Orientated Hydraulic Fracture Extension Replicator) was used to model the fracture propagation to determine the fracture dimensions and conductivities. The actual pumping schedule for Merrimelia-62 is shown in Table 3. In this model, LPG fracturing fluid is generated from the viscosity versus time plot in the McCully field case study by Leblanc et al (2011). The temperature range is up to 150°F. As GOHFER can only generate the rheology curve based on a constant temperature, the viscosity data points on the graph are referring to this temperature. The viscosity is recorded to be 300 cP at a reference shear rate of 100 s⁻¹ and a base fluid in the GOHFER database is selected with similar initial viscosity.

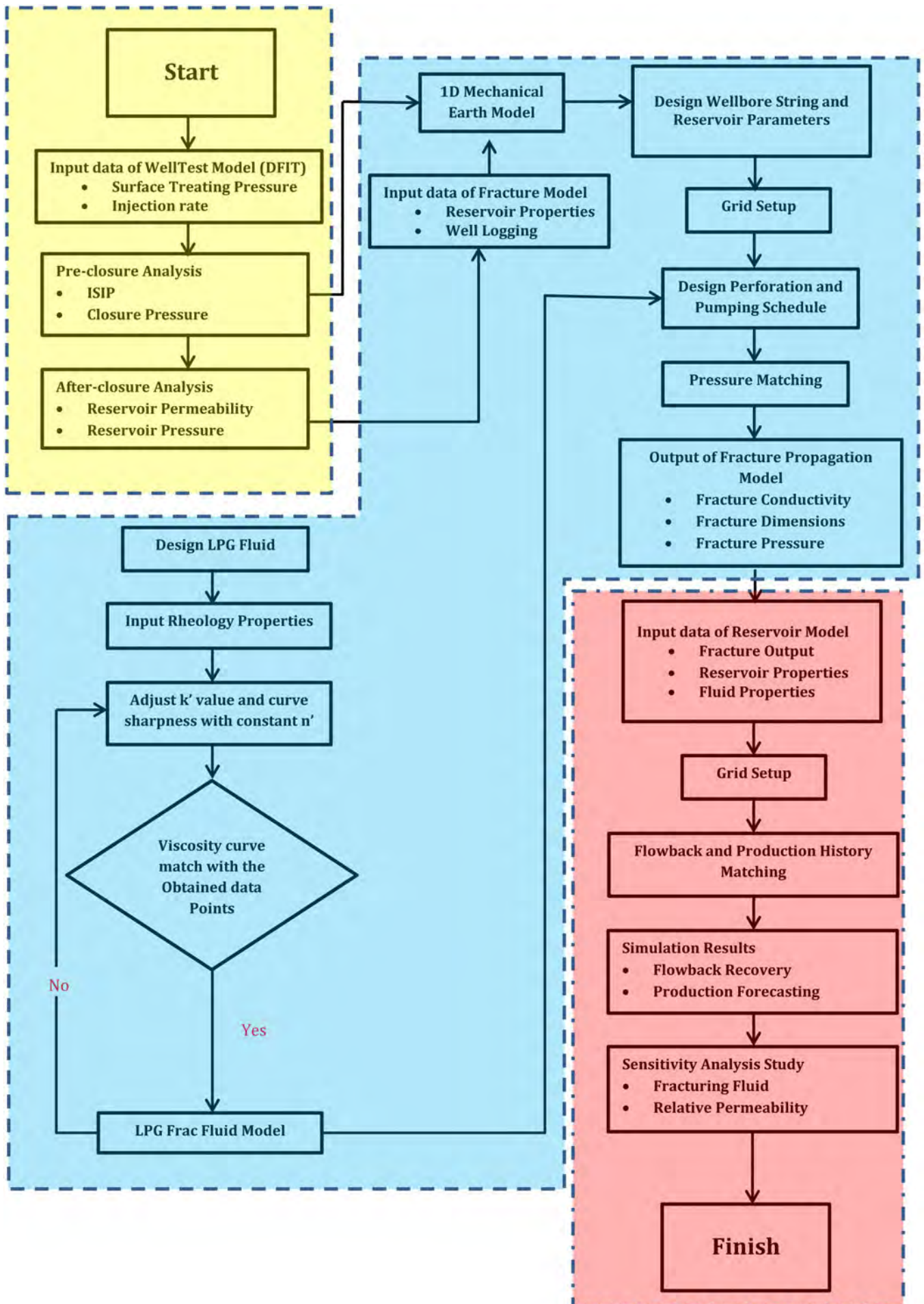


Figure 8. Workflow of the model development. Yellow indicates the IHS model process, blue indicates the GOHFER process, and red indicates the Eclipse process.

Table 2. Summary of Merrimelia–62 (stage 1) well injection fall off test results.

Pre-closure analysis	ISIP (psi)	4,871.87
	Closure pressure (psi)	4,091.79
	Closure gradient (psi/ft)	0.559
	Type of leak-off	Height recession
Nolte's after closure analysis	Permeability (mD)	0.1
	Flow capacity (mD.ft)	0.3079
	Fracture half-length (ft)	2.28
	Pore pressure (psi)	1,869

Table 3. Actual pumping schedule for Merrimelia–62 N₂ treatment.

Stage	1	2	3
Description	Pad	Slurry	Flush
Fluid type	HyborH_40	HyborH_40	Linear gel
Clean volume (gallons)	13,064	11,637	3,542
Breaker type	–	Vicon	Vicon
Start BH proppant concentration (ppg)	0	0.5–12	–
Proppant type	None	CarboProp 20/40	–
BH total rate (bpm)	26.7	26.7	26.7
N₂ foam quality (%)	50	50	50

Then the new rheology curve could be matched with the input data points by adjusting the n' and k' parameters. The simulator based on model inputs predicts the amount of proppant concentration, fracture half-length and fracture width. These key outputs (fracture conductivity, fracture dimensions and fracture pressure) are required for production modelling using Eclipse.

Finally, a reservoir simulator is used to model multiphase flow within the reservoir and the well production. In the actual field case, Merrimelia–62 has been fractured by 50% N₂ foam (base case). Eclipse was used to model the effect of fracture stimulation upon the productivity from Merrimelia–62. The reservoir properties of Merrimelia–62 are the main input parameters of Eclipse, as shown in Table 4. Pressure, volume, temperature (PVT) and relative permeability data was not available in the Merrimelia field so analogous data was required. Pressure, viscosity and formation volume factor data were sources from the Patchawarra Formation in the nearby Della field, while relative permeability (see Fig. 9a) and capillary pressure were provided from the Cowralli field. Flowback and history matching have been conducted to valid the model. The hydraulic fracturing results from GOHFER were used in Eclipse to model flowback recovery and production forecasting. Sensitivity analysis, which involves types of fracturing fluids and various relative permeability curves has also been studied in regards to gas productivity.

RESULTS AND DISCUSSION

From simulation of the fracture propagation model, the surface treating pressure has been matched with the post-job report (Fig. 10). The average pumping rate is 20 bpm, which

Table 4. Reservoir properties of the Merrimelia–62 well.

	Value	Unit
Measured depth	7,325	ft
Thickness	77	ft
Reservoir pressure	1,844.8	psi
Reservoir temperature	296	F
Permeability	0.01	mD
Porosity	10.1–13.7	%
Water saturation	50	%
Gas saturation	50	%

has been injected into the Toolachee Formation at a depth of 7,000 ft. The breakdown pressure indicated 6,700 psi, and propagation pressure 5,700 psi. Then, the coupled simulation was run for the base case. Figure 11 shows good matching for the true production with the model results, and the history matching parameters and results are summarised in Table 5.

Relative permeability curves are one of the major reservoir parameters controlling well productivity and, therefore, fracturing fluid selection. In some tight gas formations, water ceases to flow at a critical water saturation that is substantially greater than connate water saturation. Apart from phase trapping, the high effective stresses in the rock may impact the permeability to fluids so severely that classical theories for multiphase flow are no longer applicable (Shaoul et al, 2011). The relative permeabilities to both water and gas can be so low that neither phase has significant relative permeability across some range of saturations. This phenomenon is called permeability jail by Shanley et al (2004). In addition, numerous authors (Cluff and Byrnes, 2010; Shanley et al, 2004; Shaoul et al, 2011) also discuss the existence of a permeability jail in tight gas reservoir rocks where the water is trapped by the high capillary pressure, thereby reducing the permeability to gas significantly. The sensitivity study will investigate this phenomenon as part of the post-fracture production analysis of tight gas reservoirs. The relative permeability curves presented in Figure 9 are in accordance with the theory described by Shanley et al (2004) and data from Cluff and Byrnes (2010). The relative gas permeability formula (Eq. 2) is (Shanley et al., 2004):

$$k_{rg} = (1 - S_w)^2 \left[1 - S_w^{\left(\frac{2+3\lambda}{\lambda} \right)} \right] \quad (2)$$

In Equation 2, k_{rg} is the relative permeability of gas (fraction), S_w is water saturation (percentage), and λ is the slope (dimensionless). Figure 9 shows four examples of relative permeability curves. The first scenario (a) is the base case. The second scenario (b) is named the weak permeability jail and is based on low but finite fluid mobility in the jail saturation range. The third and fourth scenarios (c and d) are named the median and strong permeability jails, where the relative permeability curves of the fluids do not intersect and where within a region with a width of 0–0.2 (in water saturation) no fluids are mobile at all. The sensitivity of the relative permeability jail concept is analysed based on these four scenarios. In each scenario, three different types of fracing fluids were evaluated, as shown in Table 6.

Figure 12 shows the simulation results of flowback by different fracing fluids with original reservoir conditions. In Figure 12a, it can be seen that water production rates for both cases of 50% N₂ foam and LPG are about two to three times higher than slickwater. This is mainly due to the water trap-

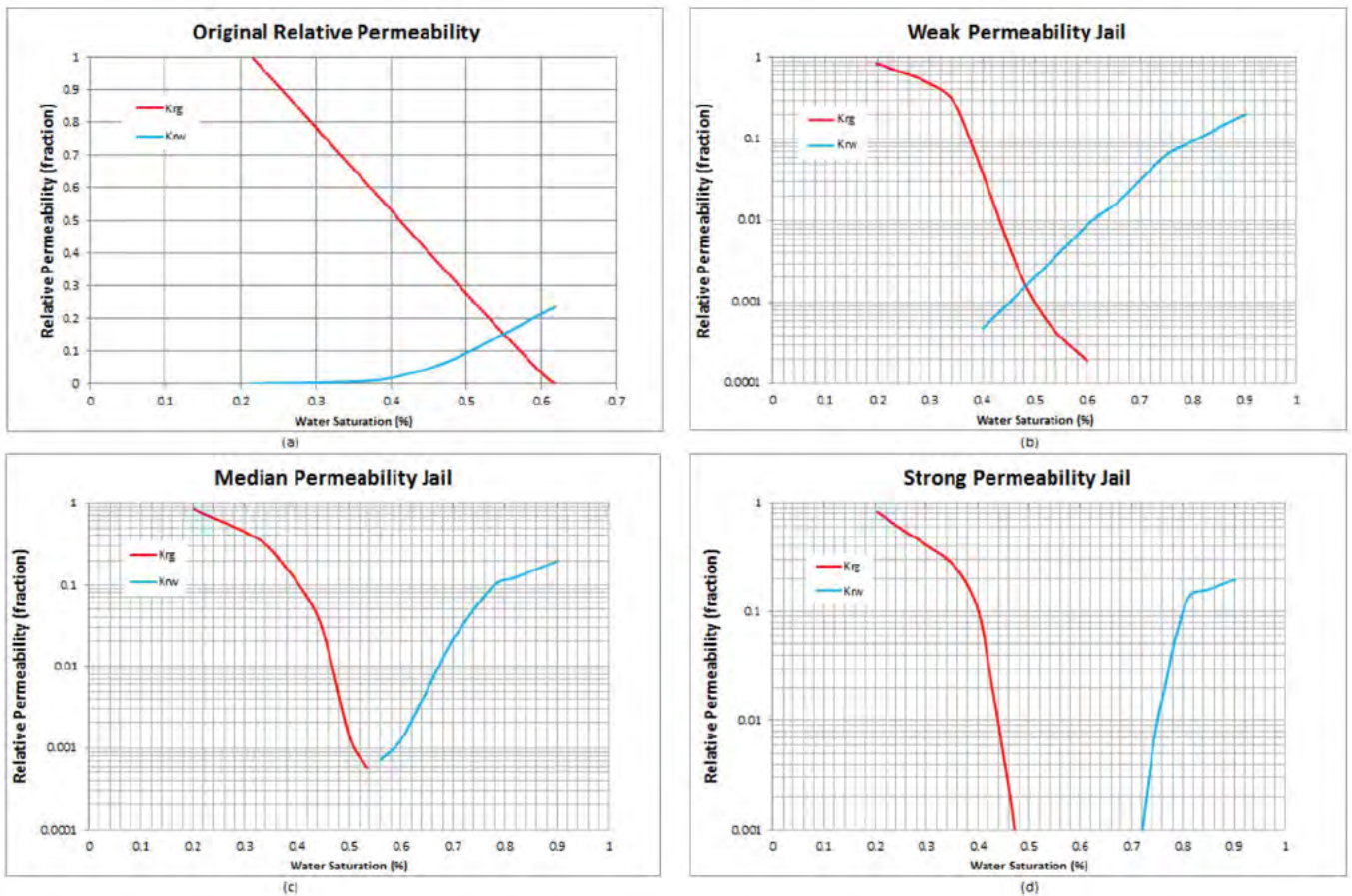


Figure 9. Sensitivity study of different relative permeability (rel-perm) curves. a) Original rel-perm curve for base case. b) Rel-perm curve for weak rel-perm jail. c) Rel-perm curve for median rel-perm jail. d) Rel-perm curve for strong rel-perm jail. (Shaoul et al, 2011.)

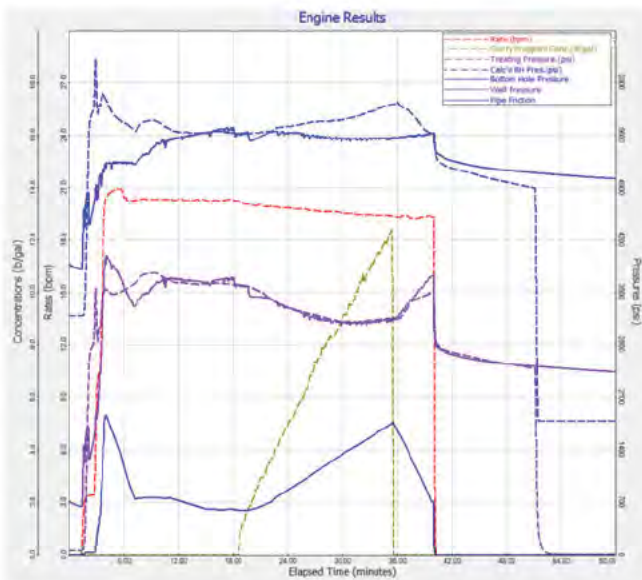


Figure 10. Surface treating pressure matching.

ping phenomenon. The average conductivity of slickwater in the fracturing zone is 2,007 md-ft, whereas in the case of LPG the average conductivity is 2,598 md-ft. The lower conductivity contributed to higher capillary pressure, which would cause liquid retention at a low reservoir pressure environment. Furthermore, the stabilised fracturing pressure of LPG has 5,315 psi, whereas the fracturing pressure of the slickwater case only has 4,821 psi. This is because of the expansion mechanism from energised fluids that converts to gas in the formation, and the additional expansion energy at 500 psi

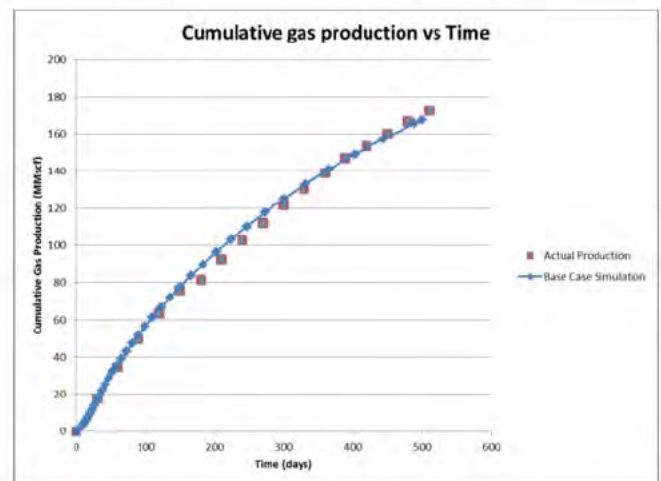


Figure 11. Production history matching of base case simulation.

would contribute to higher flowback. When comparing N_2 foam with LPG, LPG has a slightly better flowback rate in the initial stage (up to 50 days). This is because LPG is completely converted to the gas phase when it reaches the formation under reservoir conditions, and therefore less residual gel remains in the formation. Thus, the total flowback recovery was significantly enhanced to 76% within 60 days by using gelled LPG fracture stimulation. In addition, Figure 12b presents the cumulative water production with three fracturing fluids within 60 days. It can be seen that LPG has the highest total water production (509 STB), compared to 50% N_2 foam (433 STB) and slickwater (213 STB). The gas production rate as shown in Figure 13a shows that LPG reaches maximum gas production

Table 5. History matching results.

	Value	Unit
Permeability	1.9	mD
Porosity	0.08	Fraction
Drainage area	200	Acre
Clean-up time	50	Days
Skin	10	Dimensionless
Fluid efficiency	82.37	%
Retain permeability	68	%

Table 6. Sensitivity analysis of fluid type.

Rel-perm/ fluid type	50% N ₂ foam	Slickwater	LPG
Original reservoir	Base case	Case 1	Case 2
Weak rel-perm	Case 3	Case 4	Case 5
Median rel-perm	Case 6	Case 7	Case 8
Strong rel-perm	Case 9	Case 10	Case 11

almost one day after the fracturing treatment, while N₂ foam and slickwater require 40–50 days, which also proves that LPG performs with a much faster flowback time. The total injection volume is 673 STB. The load of recoveries are 76% for LPG, 64% for 50% of N₂ foam, and 32% for slickwater.

Figure 13b shows cumulative gas production after a fracture treatment for three types of fracturing fluids, which are the same data as presented in Figure 13a. It can be seen that cumulative gas production will be higher if there is less water in the fracturing fluid. The cumulative gas production, however, does not differ much between N₂ foam and LPG. Also, if the fracture treatment uses slickwater, the cumulative gas production will decrease 50% in one year, which is about 0.8 Bscf for one well in a 200 acre spacing. Thus, proper selection of the fracturing fluid is critical to the success of the fracture treatment and long-term gas production.

The results of the sensitivity analysis are shown in Figures 14–16, and are summarised in Table 7. Figure 14 shows cumulative gas production for the weak relative permeability jail scenario. It can be seen that cumulative gas production of LPG presents higher gas production (137 MMscf), followed by N₂ foam (110 MMscf) and slickwater (51 MMscf) at 230 days. In the median relative permeability jail scenario, Figure 15 shows the cumulative gas production of LPG (107 MMscf) remains the highest gas production, followed by N₂ foam (79 MMscf) and slickwater (51 MMscf). Similarly, with the weak and median cases, the strong case in Figure 16 also shows that LPG performs better than other fracturing fluids.

Figure 17 shows the results of reservoir simulation of cumulative gas production with different fracturing fluids at various reservoir scenarios. Case 2 (LPG, original rel-perm) pro-

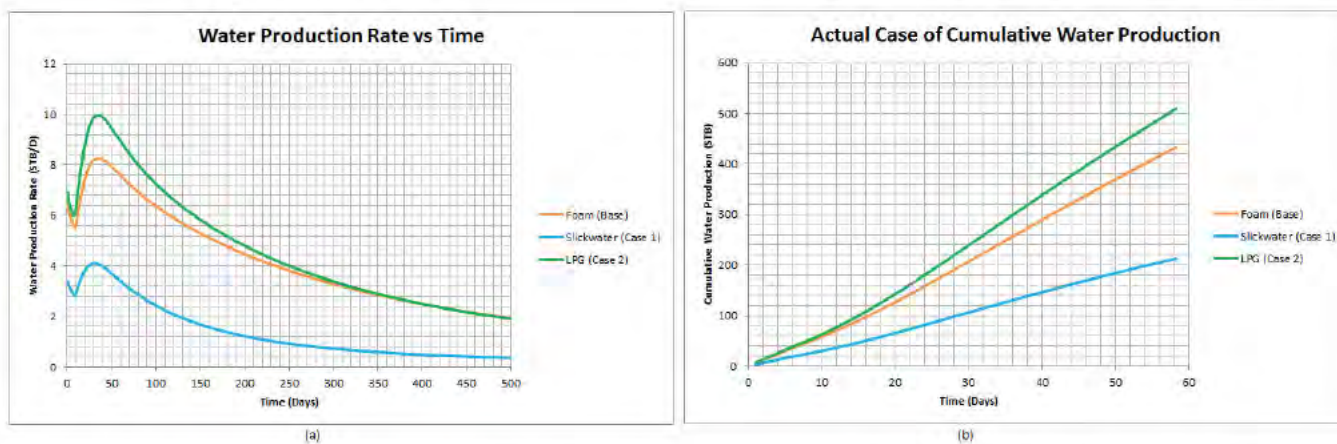


Figure 12. Effect of different fluid types on original reservoir condition. a) Water production rate versus time. b) Cumulative water production versus time.

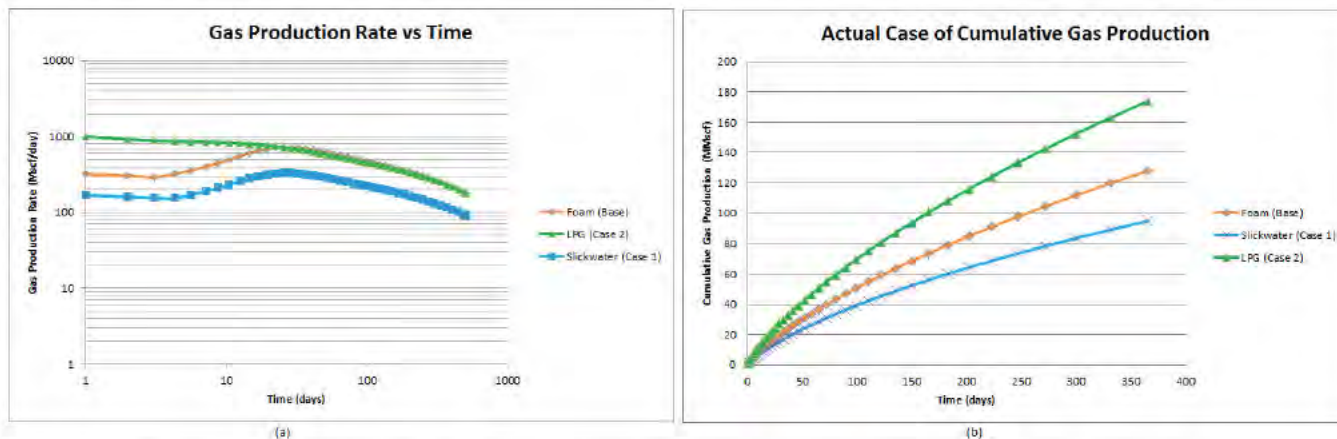


Figure 13. Effect of different fluid types on original reservoir condition. a) Gas production rate versus time. b) Cumulative gas production versus time.

vides the highest gas production of 170.9 MMscf compared to the base case (50% of N_2 foam, original rel-perm) and case 1 (slickwater, original rel-perm). The authors found that with more severe liquid sensitive formations (from original to strong rel-perm), the cumulative gas production of all the fracing fluid would decrease to 47%. Comparing between case 2 and case 1, if no water trapping was assumed in LPG (case 2), slickwater (case 1) could cause 53% of water blocking in the original rel-perm formation. This is also true at other reservoir scenarios when comparing with slickwater, which consequently induce 53% effective fracture half-length loss. The authors also found that when comparing with 50% N_2 foam, the results of LPG show that in the case of normal relative permeability behaviour, there is no significant benefit on the post-fracing production. In the case of the weak relative permeability jail, however, there is a benefit to be gained in the early-time production during the clean-up period that lasts several months.

CONCLUSIONS

LPG fracturing has the potential to eliminate all issues associated with water use and disposal, which is a key challenge in conventional hydraulic fracturing. Also, there are many advantages in using liquefied petroleum gases for hydraulic fracturing if it can be done safely. This paper introduced a fracture propagation model coupled with a multiphase flow model for an unconventional reservoir in the Cooper Basin by using actual field data. The simulation demonstrated the effectiveness of liquid retention and gas productivity enhancement under a low-pressure, high-temperature environment. The permeability jail has a negative impact on gas production. In a highly liquid sensitive formation (from original to strong rel-perm), the cumulative gas production of all the fracing fluids would decrease to 47%.

In the model, the resulting water production rates of foam and LPG are about two to three times higher than slickwater due to additional fracturing pressure. When comparing N_2 foam to LPG, LPG has slightly better flowback rates in the initial stage (up to 50 days). Thus, the total flowback recovery was significantly enhanced to 76% within 60 days by using gelled LPG fracture stimulation. In a normal tight relative permeability case, the results show that there is a potential of getting up to 53% of effective fracture half-length loss by slickwater. When looking at the possibility of removing the water phase completely (gelled LPG fracing), there is a potential of obtaining up to 53% of incremental gain comparing with slickwater in all the cases. In the case of 50% N_2 foam, however, the results show that there is no significant benefit on the post-fracing production under this permeability behaviour. Thus, higher quality foam is recommended in a low pressure water sensitivity formation. The permeability jail concept needs to be explored further with core testing in the Cooper Basin. Laboratory experiments are necessary to verify the presence of a permeability jail in low permeability sandstones. Moreover, to further validate the fracturing model, rheology experimental laboratory tests are recommended.

NOMENCLATURE

k	Formation permeability (mD)
k_{rg}	Relative permeability of gas (dimensionless)
μ	Viscosity (cP)
P_c^{th}	Capillary threshold pressure (psi)
r	Pore radius (microns)
θ	Contact angle (degree)
S_w	Water saturation (percentage)

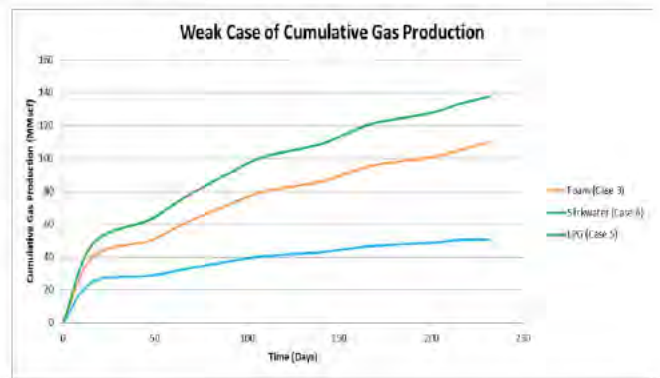


Figure 14. Effect of different fluid types on gas production (weak case).

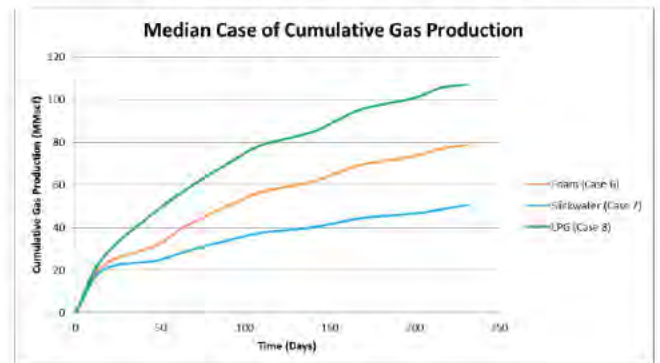


Figure 15. Effect of different fluid types on gas production (median case).

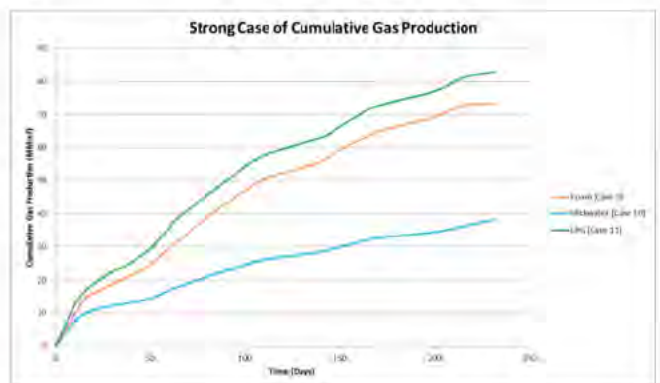


Figure 16. Effect of different fluid types on gas production (strong case).

Table 7. Results of sensitivity analysis.

Properties	Fracing fluid type	Rel-perm type	Gas cumulative at 230 days (MMscf)
Base case	N_2 foam	Original reservoir	167.5
Case 1	Slickwater	Original reservoir	80.7
Case 2	LPG	Original reservoir	170.9
Case 3	N_2 foam	Weak perm jail	110.2
Case 4	Slickwater	Weak perm jail	50.7
Case 5	LPG	Weak perm jail	137.7
Case 6	N_2 foam	Median perm jail	78.5
Case 7	Slickwater	Median perm jail	50.6
Case 8	LPG	Median perm jail	106.9
Case 9	N_2 foam	Strong perm jail	73.5
Case 10	Slickwater	Strong perm jail	38.2
Case 11	LPG	Strong perm jail	83.2

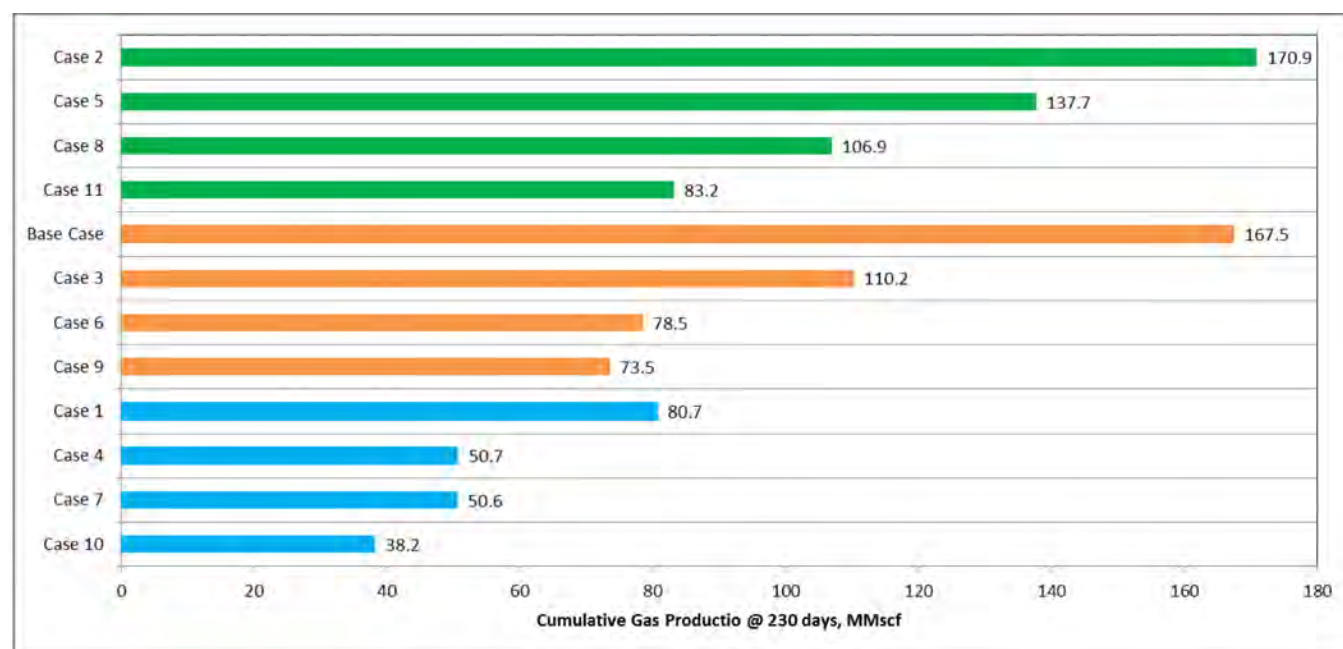


Figure 17. Cumulative production for reservoir simulation with various scenarios. The green colour represents LPG fluid, orange represents 50% N₂ foam, and blue represents slickwater.

REFERENCES

ALEXANDER, E.M., 1998—Lithostratigraphy and environments of deposition. In: Gravestock, D.I. and Jensen, S.B. (eds) *The Petroleum Geology of South Australia*, volume 4. Adelaide: Primary Industries and Resources South Australia.

AL-KANAAN, A., RAHIM, Z. AND AL-ANAZI, H., 2013—Selecting Optimal Fracture Fluids, Breaker System, and Proppant Type for Successful Hydraulic Fracturing and Enhanced Gas Production - Case Studies. SPE Unconventional Gas Conference and Exhibition, Muskat, Oman, 28–30 January, SPE-163976.

BADDELEY, T., 2013—Parliamentary inquiry into the implications for Western Australia of hydraulic fracturing for unconventional gas. Letter from Santos, 4 October 2013. Perth: Santos.

CHALBAUD, C.A., ROBIN, M. AND EGERMANN, P., 2006—Interfacial Tension Data and Correlations of Brine-CO₂ Systems under Reservoir Conditions. SPE Annual Technical Conference and Exhibition, San Antonio, Texas, 24–27 September, SPE-102918.

CHIPPERFIELD, S.T. AND BRITT, L.K., 2000—Application of after-closure analysis for improved fracture treatment optimisation: a Cooper Basin case study. SPE Rocky Mountain Regional/Low-Permeability Reservoirs Symposium and Exhibition, Denver, Colorado, 12–15 March, SPE-60316.

CLUFF, R.M. AND BYRNES, A.P., 2010—Relative Permeability In Tight Gas Sandstone Reservoirs - The “Permeability Jail” Model. SPWLA 51st Annual Logging Symposium, Perth, Western Australia, 19–23 June, SPWLA-2010-58470.

ECONOMIDES, M.J. AND MARTIN, T., 2007—Modern fracturing: enhancing natural gas production. Houston: Energy Tribune Publishing Inc.

ECONOMIDES, M.J. AND NOLTE, K.G., 2000—Reservoir stimulation. Chichester, West Sussex: John Wiley & Sons.

FINK, J.R., 2013—Hydraulic fracturing chemicals and fluids technology. Oxford: Elsevier.

GANDOSI, L., 2013—An overview of hydraulic fracturing and other formation stimulation technologies for shale gas production. Joint Research Centre of the European Commission report. Report EUR: 26347. Luxembourg: Publications Office of the European Commission.

GIDLEY, J.L., HOLDITCH, S.A., NIERODE, D.E. AND VEATCHJR, R.W., 1989—Recent advances in hydraulic fracturing. Richardson, Texas: Society of Petroleum Engineers.

GRAVESTOCK, D.I. AND JENSEN, S.B., 1998—The petroleum geology of South Australia, volume 4. Adelaide: Primary Industries and Resources South Australia.

GUPTA, D.V.S., 2009—Unconventional Fracturing Fluids for Tight Gas Reservoirs. SPE Hydraulic Fracturing Technology Conference, Woodlands, Texas, 19–21 January, SPE-119424.

HOLDITCH, S.A., 1979—Factors affecting water blocking and gas flow from hydraulically fractured gas wells. *Journal of Petroleum Technology*, 31 (12), 1,515–24

HURST, R.E., 1972—Gas Frac - A New Stimulation Technique Using Liquid Gases. SPE Rocky Mountain Regional Meeting, Denver, Colorado, 10–12 April, SPE-3837.

LEBLANC, D.P., MARTEL, T., GRAVES, D.G., TUDOR, E. AND LESTZ, R., 2011—Application of Propane (LPG) Based Hydraulic Fracturing in the McCully Gas Field, New Brunswick, Canada. North American Unconventional Gas Conference, Woodlands, Texas, 14–16 June, SPE-144093.

LESTZ, R.S., WILSON, L., TAYLOR, R.S., FUNKHOUSER, G.P., WATKINS, H. AND ATTAWAY, D., 2007—Liquid petroleum gas fracturing fluids for unconventional gas reservoirs. *Journal of Canadian Petroleum Technology*, 46 (12), 68–72.

MCGOWEN, J.M., GILBERT, J.V. AND SAMARI, E., 2007—Hydraulic Fracturing Down Under. SPE Hydraulic Fracturing Technology Conference, College Station, Texas, 29–31 January, SPE-106051.

POKALAI, K., FELI, Y., AHMAD, M., HAGHIGHI, M. AND GONZALEZ, M., 2015—Design and optimisation of multi-stage hydraulic fracturing in a horizontal well in a shale gas reservoir in the Cooper Basin, South Australia. *The APPEA Journal*, 55, 1–14.

RIBEIRO, L. AND SHARMA, M., 2013—Fluid Selection for Energized Fracture Treatments. SPE Hydraulic Fracturing Technology Conference, Woodlands, Texas, 4–6 February, SPE-163867.

SANTOS, 2012—Merrimelia 62 well completion report. Adelaide: Santos Ltd.

SANTOS, 2015—Cooper Basin (overview). Accessed December 2015. <<https://www.santos.com/what-we-do/activities/south-australia/cooper-basin/>>.

SCOTT, M.P., STEPHENS, T., DURANT, R., MCGOWEN, J., THOM, W. AND WOODROOF, R., 2013—Investigating hydraulic fracturing in tight gas sand and shale gas reservoirs in the Cooper Basin. SPE Unconventional Resources Conference and Exhibition—Asia Pacific, Brisbane, Queensland, 11–13 November, SPE-167073.

SHANLEY, K.W., CLUFF, R.M. AND ROBINSON, J.W., 2004—Factors controlling prolific gas production from low permeability sandstone reservoirs: implications for resource assessment, prospect development, and risk analysis. *AAPG Bulletin*, 88 (8), 1,083–121.

SHAOU, J.R., VAN ZELM, L.F. AND DE PATER, C.J., 2011—Damage mechanisms in unconventional gas well stimulation—a new look at an old problem. *SPE Production & Operations*, 26 (04), 388–400.

SONI, T.M., 2014—LPG-Based Fracturing: An Alternate Fracturing Technique in Shale Reservoirs. IADC/SPE Asia Pacific Drilling Technology Conference, Bangkok, Thailand, 25–27 August, SPE-170542.

TAYLOR, R.S., FYTEN, G., ROMANSON, R., MCINTOSH, G., LI-TUN, R., MUNN, D., BENNION, B., PLWOWAR, M. AND HOCH, O., 2010—Montney fracturing-fluid considerations. *Journal of Canadian Petroleum Technology*, 49 (12), 28–36.

VALKÓ, P. AND ECONOMIDES, M.J., 1996—Hydraulic fracture mechanics. Chichester, West Sussex: John Wiley & Sons.

THE AUTHORS



Yang Fei is presently undertaking a PhD in petroleum engineering at the Australian School of Petroleum (ASP). Before starting his PhD, Yang received his BE (Hons) in petroleum engineering from the University of Adelaide. Previously, Yang worked as a technical assistant at Santos Ltd for four years.

Yang's area of expertise is in production engineering and optimisation, where he focuses on the development and maintenance of GAP/PROSPER/MBAL models of satellites from the Cooper Basin. In addition to that, he provided support in running various scenarios to identify potential projects to fully optimise satellite performance. Yang's PhD involves researching waterless and foam-based hydraulic fracturing alternatives for Australian unconventional reservoirs. Member: SPE, PESA and AAPG.

yang.fe@adelaide.edu.au



Mary Gonzalez Perdomo is a lecturer of petroleum engineering, and the Engineering Honours Academic Coordinator for the ASP. Her research and teaching focus is on reservoir and production engineering, particularly production enhancement and optimisation.

She joined the ASP in 2009 after several years of experience in the oil and gas industry, where she provided practical petroleum engineering, consultancy services and solutions in the areas of subsurface and production engineering.

Mary has collaborated on APPEA papers, and has BSc and a post-graduate degrees in petroleum engineering, and post-graduate studies in higher education. Member: SPE and PESA.

maria.gonzalezperdomo@adelaide.edu.au

Authors' biographies continued next page.

Authors' biographies continued from previous page.

THE AUTHORS



Viet Quoc Nguyen is undertaking a Bachelor of Petroleum Engineering degree at the ASP. Viet's area of interest is in reservoir stimulation by using hydraulic fracturing. He is focusing on the benefits of applying LPG as a fracturing fluid in the Cooper Basin as a project for his final-year thesis. In Viet's work, hydraulic fracturing and reservoir production models are developed and incorporated with each other using IHS Welltest, GOHFER and Eclipse. Member: SPE.

vietquoc.nguyen@student.adelaide.edu.au



Zhongyu Lei is a recent graduate in the Bachelor of Petroleum Engineering (Honours) degree at the ASP, and has completed a three-month internship with Petro-China, researching and commissioning hydraulic fracturing in 2014. The title of Zhongyu's thesis, completed for her honour project, was Enhanced gas recovery using LPG fracturing fluid in tight/shale gas reservoirs (Cooper Basin). She focuses on simulating and researching the viability of using LPG as a hydraulic fluid for tight gas reservoirs in the Cooper Basin. In addition to that, Zhongyu is presently assisting Yang Fei with his PhD project involving research about waterless and foam-based hydraulic fracturing alternatives for Australian unconventional reservoirs. Member: SPE.

a1613566@student.adelaide.edu.au



Kunakorn Pokalai is presently a PhD candidate of petroleum engineering at the University of Adelaide. He has a BE in petrochemical engineering from Silpakorn University (Thailand), and completed a Graduate Certificate in Management and Masters in petroleum engineering from the University of Adelaide.

Kunakorn's research interests are in the simulation of unconventional reservoirs and hydraulic fracturing. He mainly focuses on the issue of fracturing fluid flowback in the Cooper Basin. Kunakorn was the recipient of the prestigious AAPG Imperial Barrel Award in the Asia Pacific Region in 2014. Member: SPE and AAPG.

kunakorn.pokalai@adelaide.edu.au



Sume Sarkar is a PhD candidate at the ASP. She has experience in petroleum sector regulation in a south Asian context. She holds a MSc degree in petroleum engineering with specialisation in reservoir engineering from Norwegian University of Science and Technology, and a BSc degree in chemical engineering from Bangladesh University of Engineering and Technology. Sume is conducting research on two major areas for unconventional reservoirs in the Cooper Basin: fracturing fluid flowback modelling, and geomechanical modelling for multi-stage hydraulic fracture operations.

sume.sarkar@adelaide.edu.au



Manouchehr (Manny) Haghighi is an associate professor of petroleum engineering. His research and teaching focus is on unconventional reservoirs, reservoir simulation, well testing, and formation evaluation. He has supervised more than 40 MSc and 10 PhD students. Before joining the University of Adelaide in 2009, Manouchehr was associate professor of petroleum engineering at the University of Tehran (Iran). During 2000–07, he was the head of the petroleum engineering program at the University of Tehran. In 2000, Manouchehr established Simtech, a consulting company for integrated reservoir simulation in which he has been project director of several full-field simulation projects for oil and gas reservoirs.

From 1995 to 2000 Manouchehr worked with the National Iranian Oil Company (NIOC) and was the director of a program for the training of NIOC staff at several universities in the US, UK, Canada, France, Australia and Norway. Manouchehr was a visiting professor at the University of Calgary from 2007–08.

Manouchehr has published more than 80 articles in peer-reviewed journals or presented in international conferences. He has served as a reviewer for various journals including the Journal of Petroleum Science and Engineering. Member: SPE.

manouchehr.haghighi@adelaide.edu.au

J2: 3D Simulation of Hydraulic Fracturing by Foam Based Fluids Using a Fracture Propagation Model Coupled with Geomechanics in an Unconventional Reservoir the Cooper Basin, South Australia

3D Simulation of Hydraulic Fracturing by Foam Based Fluids Using a Fracture Propagation Model Coupled with Geomechanics in an Unconventional Reservoir the Cooper Basin, South Australia

Y. Fei^{a*}, M.E Gonzalez Perdomo^b, K. Pokalai^c and M. Haghghi^d

^a University of Adelaide, Adelaide, Australia

yang.fei@adelaide.edu.au

^b University of Adelaide, Adelaide, Australia

maria.gonzalezperdomo@adelaide.edu.au

^c University of Adelaide, Adelaide, Australia

kunakorn.pokalai@adelaide.edu.au

^d University of Adelaide, Adelaide, Australia

manouchehr.haghghi@adelaide.edu.au

Abstract

Energized fluids have been previously used in hydraulic fracture treatment in depleted and low permeable gas reservoirs and have proven to be highly efficient to aid well cleanup as well as to minimize liquid retention effect and clay swelling. On the other hand, the Australian Cooper Basin has a very complex stress regime where high fracture gradients, high tortuosity induced fractures and high pressure dependent leakoff are commonly observed. Therefore, the application and optimisation of this technology in unconventional reservoirs of the Cooper Basin which needs to be adapted to counter these and reservoir effects.

The Murteree and Roseneath shale formations in the Cooper Basin are 8,500 ft in depth and have been targets for shale gas production by different oil and gas operators. In this paper, petrophysical evaluation of shale gas potential (Total Organic Carbon) from the Permian Murteree formation has been studied. Next, a geomechanical evaluation was carried out by generating a 1D vertical mechanical earth modelling (MEM) to define the stress regime and the principle stresses variation which requires full-wave sonic logs and a diagnostic fracture injection test (DFIT) to construct and calibrate the model. A 3D hydraulic fracture simulation in a vertical well was developed and validated with postfrac production data. Then, a sensitivity analysis was performed using a selection of different fracturing fluid treatments.

In the fracture propagation model, a large number of cases were simulated based on different types of fracturing fluids. It was found that the foam quality could contribute to a higher fracture pressure. This is because higher viscosity of foam contributes to higher net pressure in the fracture by improved leakoff control, with greater proppant carrying capacity comparing with slickwater to increase fracture conductivity. Based on our reservoir inputs, the simulation results indicated that the optimum scenario is a foam quality of 70% for both N₂ and CO₂ as it generates the maximum gas productivity. Modelling predictions support the expectation of long term productivity gains through the use of foams fracturing fluid. It is concluded that the use of foam results in a more rapid clean-up of the fracture itself and inside the wellbore, which is expected to provide higher productivity.

Keywords: *Foam, fracturing fluids, 1D MEM, Shale gas, Cooper Basin*

Introduction

Unconventional hydrocarbon reservoirs such as tight gas, shale gas and coalbed methane, are becoming important resources for the current and future oil and gas supply; however, because of the low permeable nature of unconventional reservoirs, they need hydraulic fracturing treatments to be economic. In this operation a large volume of fracturing fluid is injected at high rate into the wellbore in order to overcome the rock and to induce fractures around the wellbore in the targeted formation. In shale gas reservoirs the invaded water based fracturing fluid may cause damage (water blockage) to the reservoir permeability and fracture conductivity.

Typically, water-based fluids are the simplest and most cost-effective solution to induce a fracture in a rock formation; however, there are a couple of issues that need to be considered when using water-based fracturing fluids as compared to foamed fluids including: effective fracture length loss (Taylor et al., 2010); poorer load fluid recovery (Economides and Martin, 2007); increase flowback time (Al-Kanaan et al., 2013); and increased water usage. Clays may swell when placed in contact with water. For example, very clay-rich unconventional rock formations lose some of their mechanical integrity when placed in contact with water; as ductile rock becomes softer, the rock further closes on the proppant, thereby promoting proppant embedment (Ribeiro and Sharma, 2013).

The first commercial shale gas well in the Cooper Basin was Moomba 191, which vertically targeted the Roseneath, Epsilon and Murteree (REM) formation (Starkey et al., 2014). This well provided stabilised production of 2.7 MMscf/d. This paper describes the integration of geomechanics with a fracture propagation model, in the evaluation of several types of fracturing fluids on fracture conductivity and therefore total enhanced productivity.

Geological Background

The Cooper Basin is the most significant onshore oil and gas province in Australia and is the primary onshore source for natural gas production (Gravestock and Jensen, 1998). Every shale gas has different reservoir properties because they are unique depositional environments and the provenance. The early Permian Roseneath, Epsilon and Murteree formations interval is the most prolific unconventional shale gas play identified in the Cooper Basin (Ahmad and Haghighi, 2012). Commercial hydrocarbon bearing Roseneath and Murteree shale formations are being explored extensively as future unconventional shale gas reservoirs while the Epsilon formation is considered as a good tight sand gas reservoir due to the of lack of organics and low clay content (PIRSA, 1972). In addition, based on the same environment of deposition, stratigraphical, and lithological similarities, the Roseneath and Murteree formations share many geochemical and geological characteristics (Gravestock and Jensen, 1998), this can be shown in **Table 1**. For simplification, Murteree formation has been selected as the main target in this study.

Table 1: XRD mineralogy quantification for 8 selected Roseneath and Murteree shale samples (Ahmad and Haghighi, 2012)

Core Depth (M)	Quartz (%)	Carbonate (%)	Clay (%)	Toc (%)	Porosity (%)
Roseneath					
3167.03	34	10	40	3.97	2.46
3283.05	28	9	57	1.63	4.07
3290.10	40	13	41	0.97	3.05
3317.00	41	15	39	1.13	2.74
Murteree					
3421.50	40	12	42	4.69	4.78
3505.35	38	14	31	1.93	0.93
3516.80	44	5	54	1.68	3.71
3539.94	35	10	51	2.04	4.00

Foam as Fracturing Fluid

Water based fluids are the most widely used fracturing fluid because they have low cost, high performance and are easy to handle (Economides and Martin, 2007). However, from a productivity standpoint, a number of advantages can be achieved by foam fracturing fluid: (1) Limiting the formation damage caused by swelling clays and water blocking, (2) less gel is required to thicken the water so the potential for gel damage is reduced, (3) the amount of flowback fracturing fluid is reduced. One of the major productivity benefits of energised foams is faster and more complete fracture fluid clean up (Economides and Nolte, 2000); (Ribeiro and Sharma, 2013). There are also a number of operational advantages of using energised foams. By lowering the amount of water used for a fracture treatment, the cost of acquiring, handling and disposing of the water is reduced as well as the negative environmental impact of water use (Mack and Harrington, 1990). Foams were introduced as fracturing fluid in the early-1970s, and they have been extensively used in various depleted reservoirs in which water fractures were not effective (Economides and Martin, 2007). There are many papers in the literature of CO₂ or N₂ foams being used successfully in the United States, Canada and Europe to improve flowback and well productivity from low permeability gas formations (Craft et al., 1992; Goelitz and Evertz, 1982; Wamock et al., 1985). In addition, foam is generally considered to be a superior fracturing fluid than water based fracturing fluids except where their use is limited by higher costs or surface pressure limitations. They were commonly used in tight gas sands with ≤ 0.1 md permeability, low reservoir pressure and water sensitive clays throughout the 1980s to 1990s. They have been successfully implemented at depths 2,900 to 14,000 ft, reservoir pressures of 1000 to 13,000 psi and temperatures of 120 to 370 F (Wamock et al., 1985). It has been commonly reported that the foams can achieve faster clean-up, higher production and lower decline rates than with use of water based fracturing fluids (Garbis and Taylor, 1986); (Goelitz and Evertz, 1982); (Toney and Mack, 1991); (Craft et al., 1992); (Burke et al., 2011). Other reported benefits include a lower water consumption (Burke et al., 2011), lower surface treating pressure requirements (Garbis and Taylor, 1986) and reduced swabbing (Blauer and Kohlhaas, 1974); (Gaydos and Harris, 1980). Drawbacks of some foams can be increased costs; high gas losses, transportation and storage costs in remote locations; increased surface treating pressures depending on gas quality; reduced viscosity and higher near wellbore pressure loss (NWBPL) in tortuous fractures; and in some cases reductions in sand carrying

capacity due to higher base fluid sand loadings at high foam qualities (e.g., 70% quality foam creates 20lbm/gal proppant loading in the base fluids at an overall 6 lbm/gal foam sand loading).

Methodology

Modelling unconventional well assets is a challenging task. Large uncertainty exists and integration of the various domains, including geology, geomechanics, completion and reservoir engineering is needed to estimate the possible ranges for fracture geometry and more importantly fracture propagation. Too often, analysis is performed in a basin with idealized or synthetic data while ignoring some basic assumptions in log processing, properties calculations and fracture simulation. In this paper, the authors used a 1D mechanical earth model coupled with a fracture propagation model. **Figure 1** shows the details of the workflow (Fei et al., 2016).

First, a 1D MEM has been constructed to evaluate the geomechanical properties. A 1D MEM is a numerical representation of the rock mechanical properties and in-situ stress state of the subsurface. The rock properties, including density, Poisson's Ratio, Young's Modulus, pore pressure and earth stresses are the primary inputs for hydraulic fracturing modelling and evaluation (Pokalai, 2015; Pokalai, 2016). An accurate MEM including constraints or uncertainty on stress magnitudes and orientations, and mechanical rock properties are essential to understanding reservoir response for stimulation and production, particularly in low permeability reservoirs. **Eq. [1]** and **Eq. [2]** have been used mainly for the stress validation by using the effective tectonic strain.

$$\sigma_{hmin} = \frac{\nu}{1-\nu}(\sigma_v - \alpha_v p_p) + \frac{E}{1-\nu^2}\epsilon_h + \frac{E\nu}{1-\nu^2}\epsilon_H + \alpha_h p_p \quad [1]$$

$$\sigma_{Hmax} = \frac{\nu}{1-\nu}(\sigma_v - \alpha_v p_p) + \frac{E}{1-\nu^2}\epsilon_H + \frac{E\nu}{1-\nu^2}\epsilon_h + \alpha_h p_p \quad [2]$$

Then, a fully-3D hydraulic fracture simulator was used to model the fracture propagation to determine the fracture dimensions and conductivities. The initial step of the simulation was validated the 1D MEM results. Then, reservoir properties and stimulation properties were included in the model. In this study, a polymer gel fluid was selected as base case. After validation of the surface pressure and postfrac production, sensitivity analysis of different fracturing fluid has been performed.

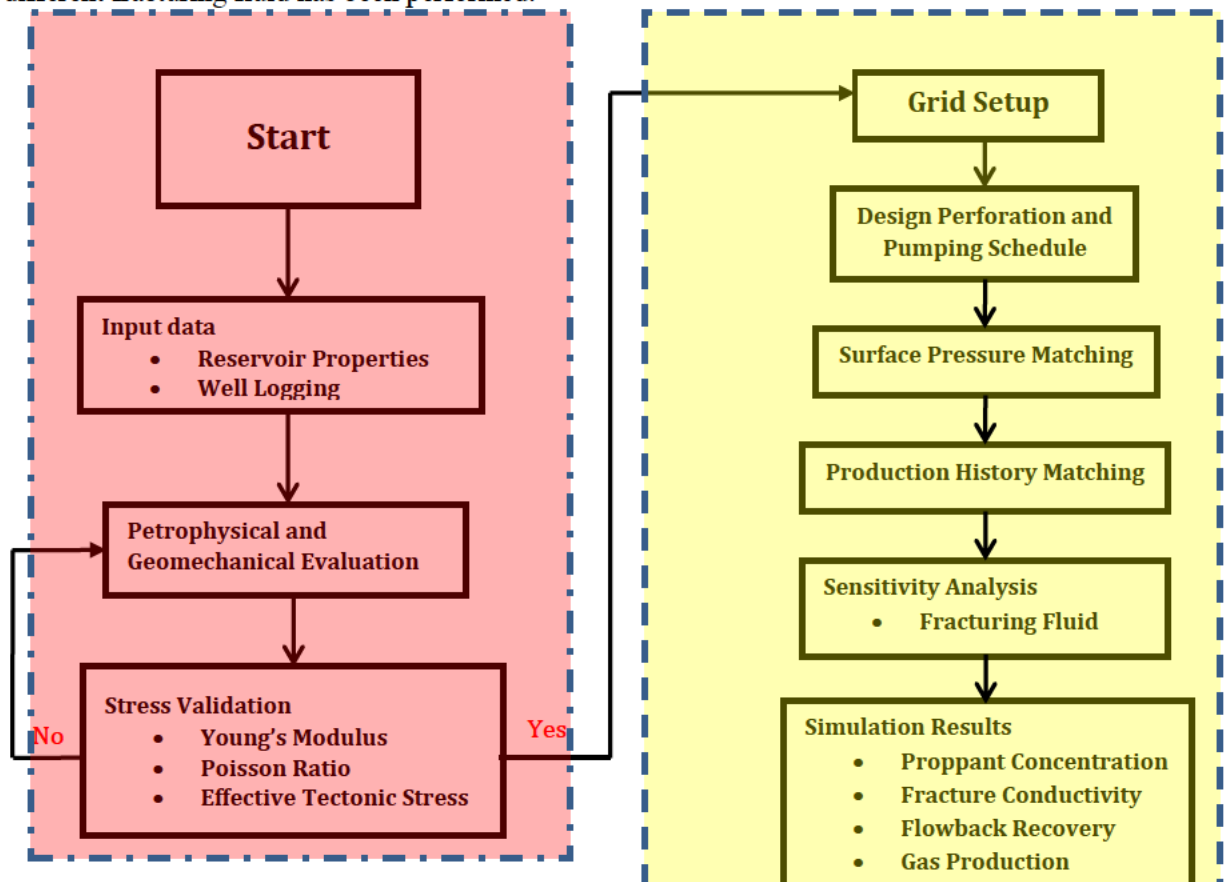


Figure 1. Workflow of the model development. Yellow indicates the 1D MEM process, and red indicates the fracture propagation model process. Modified from (Fei et al., 2016)

Results and Discussion

An accurate mechanical earth model which includes the constraints on stress magnitudes and mechanical rock properties need to be deeply understood. The results from the 1D MEM are shown in **Figure 2**. Young's modulus, Poisson ratio and effective tectonic strains were calibrated to match the simulated breakdown pressure with the observed pressure from a diagnostic fracture injection test (DFIT). A strike-slip fault can be observed in the Murteree formation ($S_{Hmax} > S_{vertical} > S_{hmin}$) in this study.

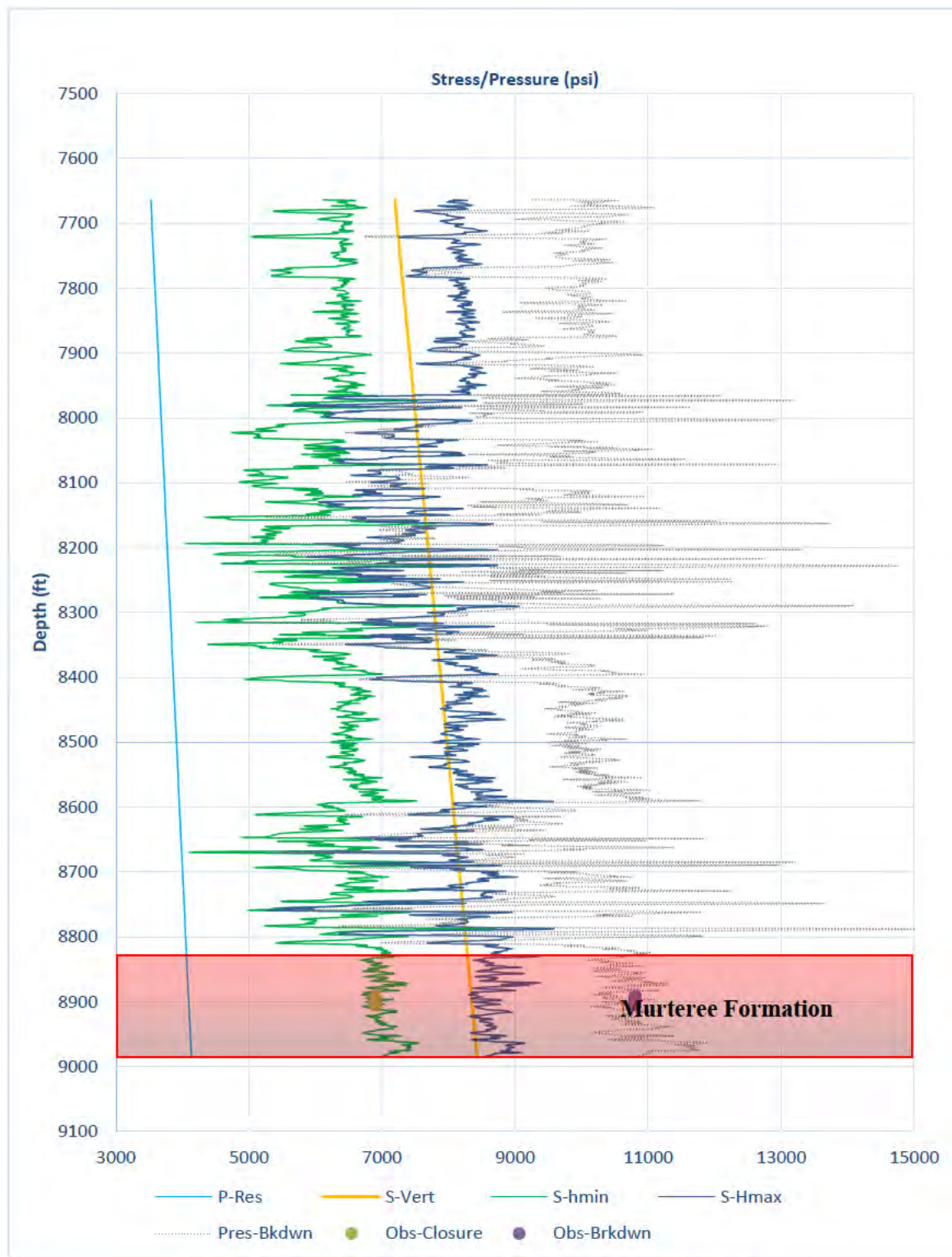


Figure 2. Principal stress versus depth profile for Moomba 191

In addition, production history matching is essential before performing a sensitivity analysis for the different fracturing fluids. This is required to validate reservoir properties such as permeability, pressure drawdown and skin factor. The results of the history match are shown in **Figure 3**. The quality of matching data is between +/- 3%. With average gas production rate 1.5 MMscf/day over 3 years.

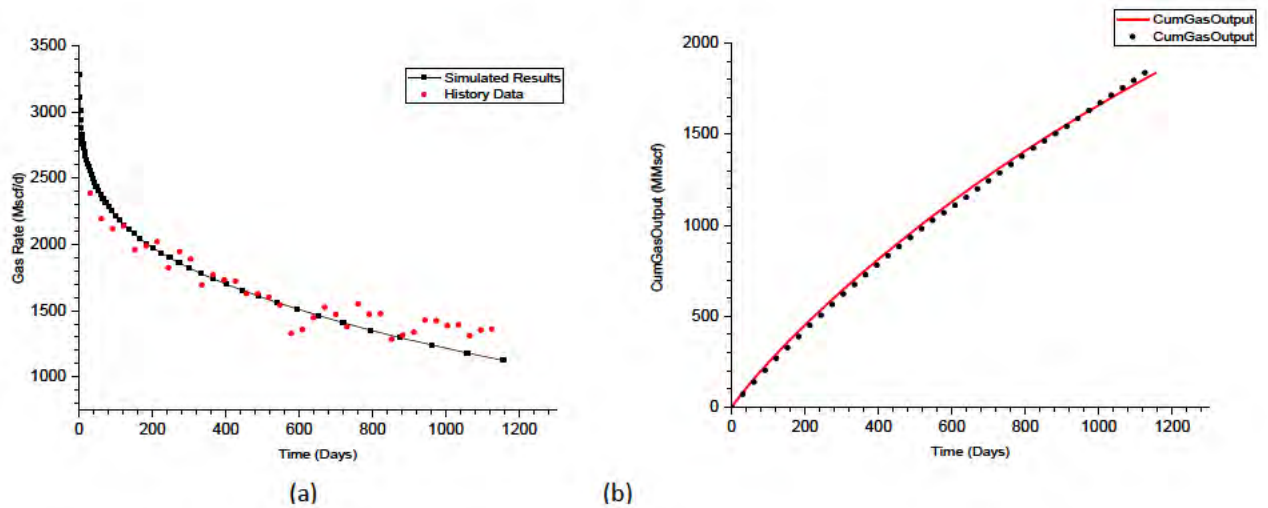


Figure 3: Results for Murteree shale production: gas production rate versus time (a) and cumulative production versus time

Then, the different types of fracturing fluids have been investigated in this study. Those fluids are: linear gel, slickwater, 50% N₂ foam, 70% N₂ foam, 50% CO₂ foam and 70% CO₂ foam. The first simulation aims to compare the fracture conductivity as it impacts how fast in the stimulated reservoir volume can be produced. This parameter can be controlled by numerous factors, such as proppant size, total proppant volume and fracturing fluid properties, as well as fluid residue damage and fluid efficiency. In order to minimize uncertainty, the simulation used a 40-70 mesh proppant size, a total amount of proppant (254,000 lbs) in all the cases, and the cut-off conductivity was set at 1 md-ft.

Linear gel, slickwater and a 50% of CO₂ foam in this conductivity study have been selected for the comparison purpose and the results are displayed in **Figure 4**. It has been observed that the conductivity in 50% CO₂ foam is the highest (**Figure 4a**), follow by linear gel (**Figure 4b**) and slickwater (**Figure 4c**). Unlike to fracture conductivity, proppant cut-off length from high to low exhibits better performance of the slickwater (550ft), followed by 50% CO₂ foam (450ft) and then linear gel (260ft). This implies that, although foam-based fluid generates comparatively shorter length fractures, the fractures created are greater and have better distributed proppants. In addition, foam-based fracturing fluids enhance conductivity and therefore productivity in a vertical well because it covers the whole thick shale interval as can be seen in **Figure 4a**. On the other hand, slickwater creates a longer fracture and give more accurate proppant settling at the perforation interval, this is good for a multi-stage frac job because it can reduce the stress shadow or stress interference which impact the nearby fracture conductivity.

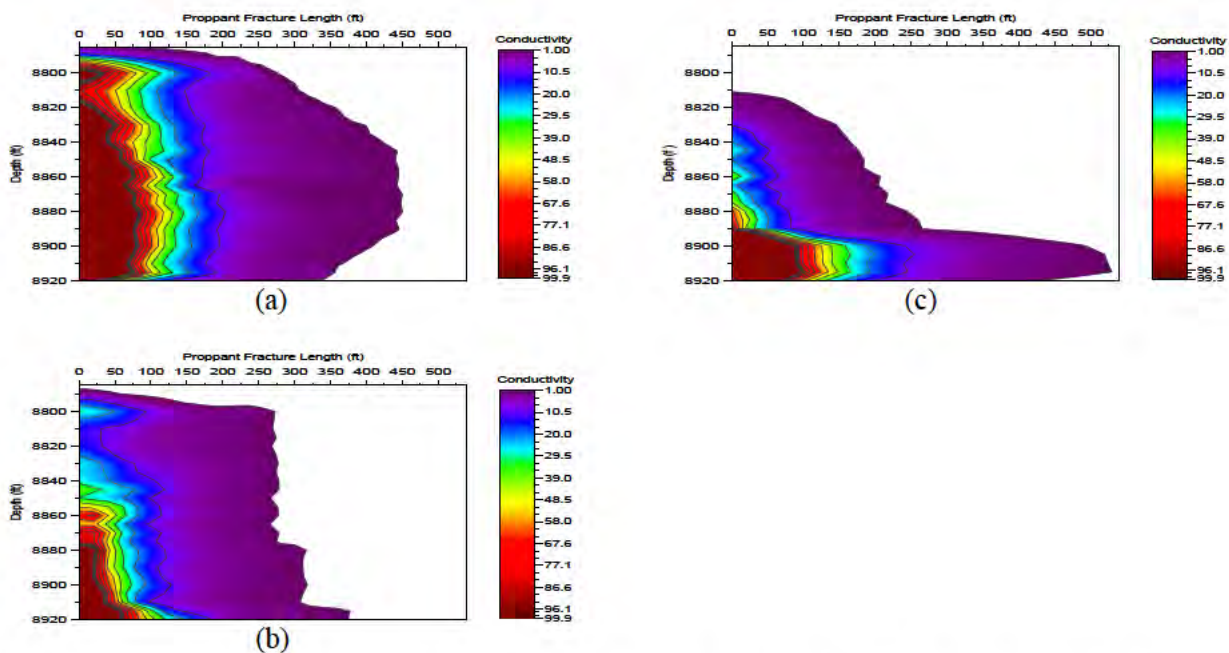


Figure 4. Result of Fracture conductivity of fracturing fluids. (a) 50% CO₂ foam; (b) Linear gel; (c) Slickwater

The proppant concentration can be compared with the fracture conductivity at different fracture lengths in **Figure 5-6**, in order to understand its correlation and to estimate how much proppant need to be placed to achieve desired conductivity.

In the case of 50% CO₂ foam, when fracture half-length is 0 ft (near wellbore), the maximum proppant concentration is between 1.2 to 2 lb/ft² and fracure conductivity can be up to 1000 md-ft. This is because gas solution come out from the foam during the frac treatment, which creates an additional energy to increase the fracture dimension in the fracture and in the invaded zone to allow more proppant to fill in. Increasing the proppant concentration results in the development of multiple layers of proppant and an increase in the fracture conductivity. In addition, with fracture half length increasing from 0 ft to 400 ft , a smaller fracture area would be created due to net pressure decreasing. Then, less amount of proppant could be filled in and hence reduce its conductivity. The proppant concentration in **Figure 5** shows a slight drop from average of about 1.6 lb/ft² to 1 lb/ft², which indicates the foam has an adequate viscosity to carrying the proppant along the fracture length.

Another case study is the use of slickwater, it can be observed that in this case the proppant concentration remains below 0.5 lb/ft² (**Figure 6**). This low proppant concentration results in conductivity reduction along the fracture length. The slickwater has less viscosity which creates a narrower fracture width, with reduced amount of proppant to be transported through the fracture. Thus, the less number of proppant layers would be developed.

The above results give an indication of foam as fracturing fluid performing better in terms of proppant transportation with higher corresponding fracture conductivity than water based fracturing fluids. The next step is to compare different foam quality and type of foam and how they impact the proppant concentration and fracture conductivity along the fracture length. The conductivity results are shown in **Figure 7**. As shown, CO₂ foam performs slightly better than N₂ foam in general potentially because of the different rheological behaviour. Furthermore, a 70% foam quality performs better in terms of proppant concentration and conductivity than 50% foam quality due to the further incremental of fluid viscosity. However, after the fracture half-length has reached over 150 ft, the conductivity would most likely be the same.

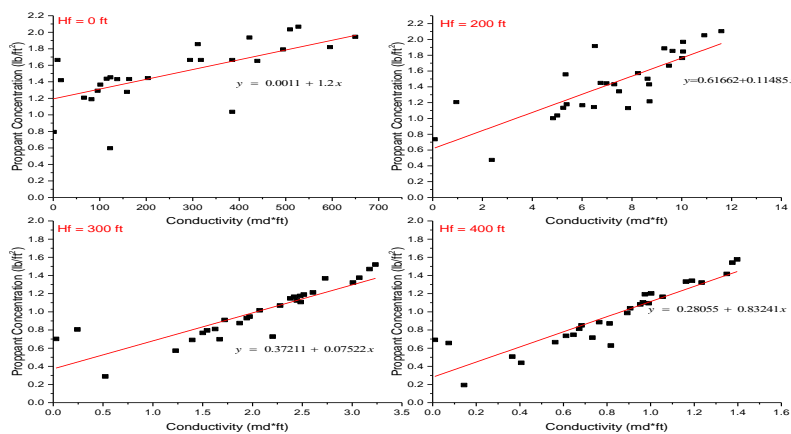


Figure 5. Fracture conductivity and proppant concentration for a 50% CO₂ foam at different fracturing lengths.

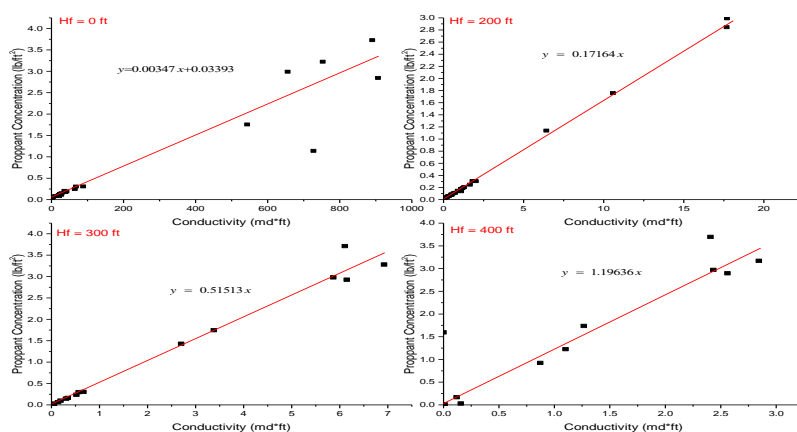


Figure 6. Fracture conductivity and proppant concentration for slickwater at different fracturing lengths.

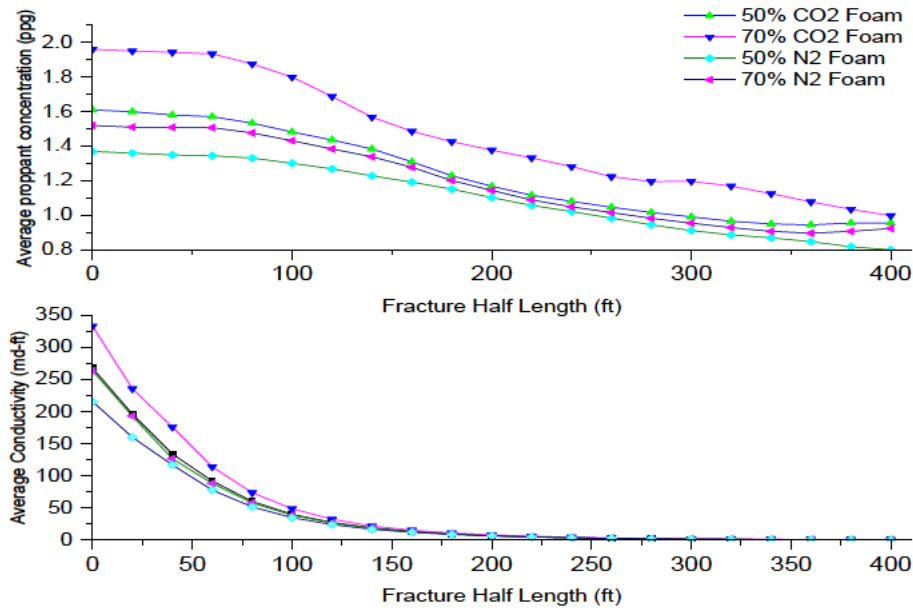


Figure 7. Fracture conductivity and proppant concentration for different quality of N₂ and CO₂ foam

Dimensionless fracture conductivity (F_{CD}) in the range of 10-20 has generally been accepted as an optimum range (Economides and Nolte, 2000). In this study (shown in Figure 8), all the foam cases have satisfied the criteria although linear gel and slickwater are below the optimum value. The main limitation for slickwater is viscosity and for linear gel are high gel residue and low retained permeability.

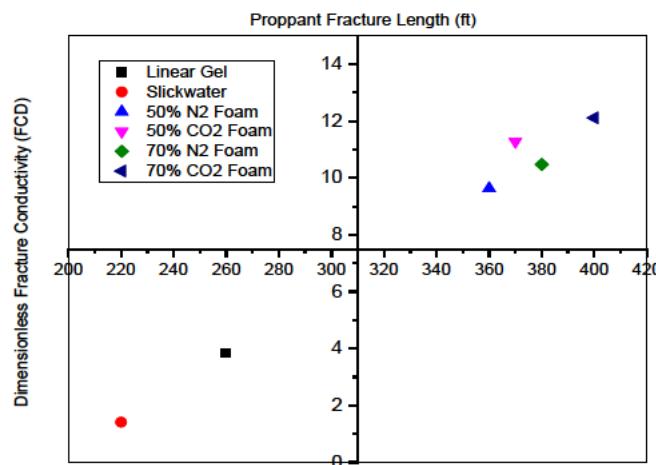


Figure 8. Dimensionless fracture conductivity versus proppant fracture length for different fracturing fluids

The ultimate objective of this study was to compare the flowback and gas production among the different fracturing fluids used for the hydraulic fracturing treatment. Figure 9 shows the simulation results of flowback using different frac fluids. It can be seen that the flowback recovery for both cases of 70% N₂ & CO₂ foam have achieved the best performance. A flowback recovery of up to 70-80% could be observed after 30 days, which is more than 2 times the flowback recovery of 50% N₂ & CO₂ foam (30-35% flow back recovery). The linear gel and slickwater shows about 5% of the flowback recovery after 30 days. The production results of the sensitivity analysis are illustrated in Figure 10. In this sensitivity analysis all the foam cases exhibit a higher gas production rate when compared to slickwater and linear gel, particularly at an initial period of 20 days. This is because of the expansion of the gas, which provides an additional energy to remove the fracturing fluid from the fracture and the invaded zone. This accelerates the clean-up of the well, so peak production from the well can begin sooner. Also since a greater amount of fracturing fluid is removed, the damage associated with retained fracturing fluid is reduced and the productivity of the well is increased.

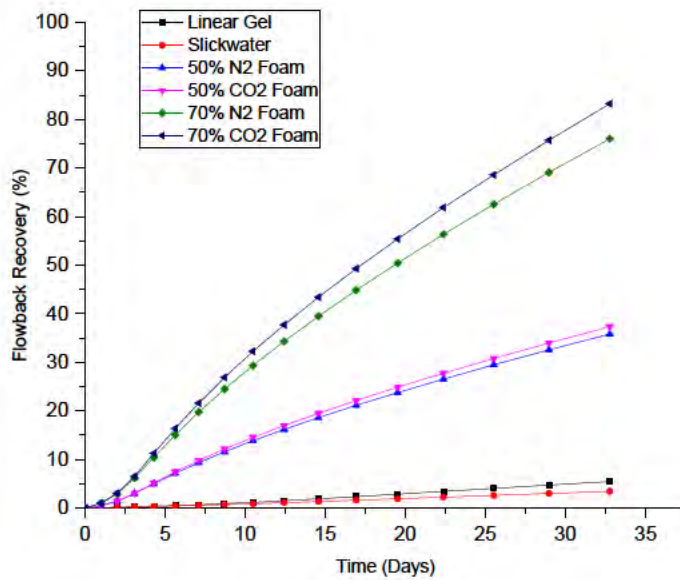


Figure 9. The effect of different fluid types on flowback recovery

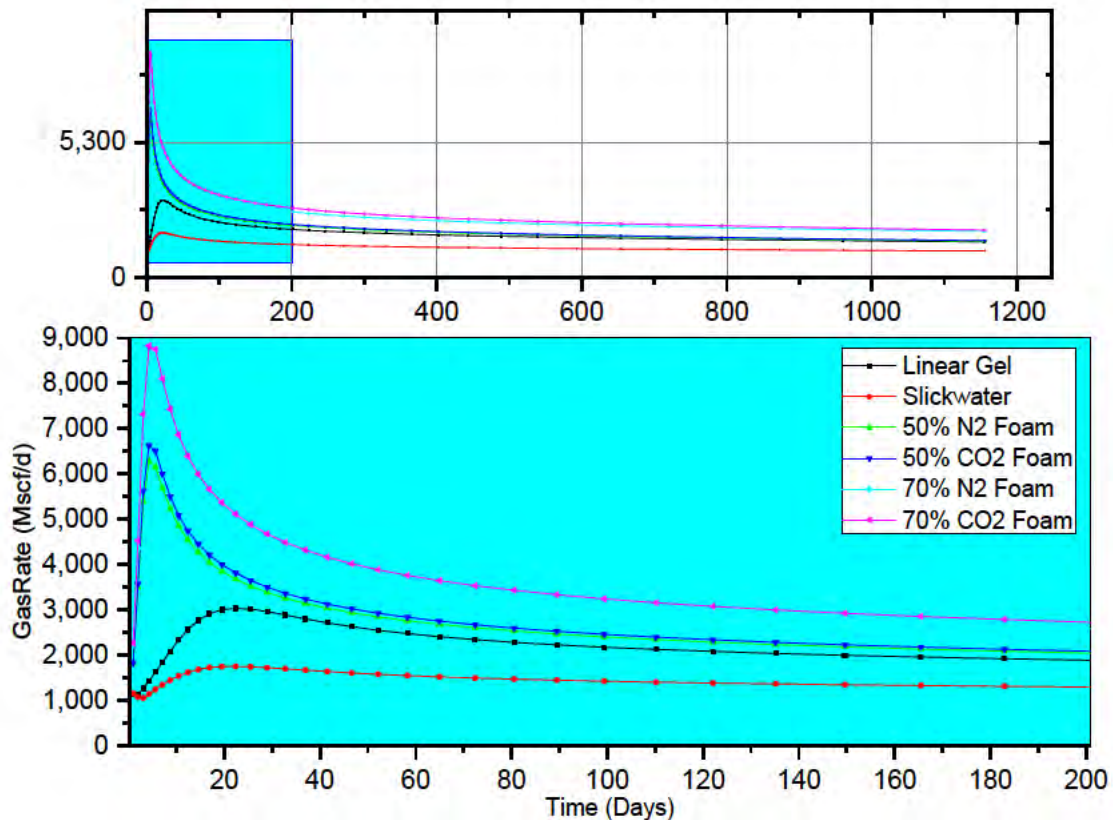


Figure 10. The effect of different fluid types on gas production

Conclusions

The 1D mechanical earth model (MEM) provided a reliable stresses profile so as to accurately predict the stress regimes, which has an impact on the fracture complexity. Based on the targeted zone, it shows highest stresses among the nearby formations. The model also observed that the Murteree formation in this field is predominantly influenced by strike-slip fault ($\sigma_H > \sigma_v > \sigma_h$).

In this study a range of fracturing fluid types were simulated; foam has proved to be an effective fracturing fluid for vertical wells as the fracture dimension cover all the targeted zone. Higher fracture conductivity, less water usage and higher retained permeability would accelerate the cleanup rate and enhance the gas production. CO₂ foam provides higher fracture conductivity than N₂ foam in general, potentially because of the different rheological behaviour. The mainly difference between N₂ foam and CO₂ foam in terms of

conductivity is a fracture half-length below 150 ft. In addition, the flowback recovery can be significantly enhanced by using foam as the liquid to gas expansion ratio provides additional energy. A 70% foam quality in this study provides the highest gas productivity.

Foam-based fracturing fluids have some limitations including: rheology of current frac fluid formulations (e.g. viscoelastic surfactant system, delay crosslink gels); high capital costs associated with gas production facilities required including equipment and space; logistics, supply considerations, and industrial competition; and potential damage to the environment. Foam stability is naturally limited by high temperature, the use of nanoparticle instead of guar gel and synthetic polymers as foam stabilizer with reduction of formation damage will be the focus of future research.

Acknowledgements

The authors would like to express their thanks to Dr Ray Johnson for his suggestions and contributions towards this research paper.

Nomenclature

σ_{hmin} : Minimum horizontal stress, psig
 σ_{Hmax} : Maximum horizontal stress, psig
 ν : Poisson ratio, dimensionless
 E : Young's modulus, MMpsi
 ε_h : Horizontal tectonic strain, microstrains
 p_p : Pore pressure, psi
 α_h : Horizontal poroelastic constant, dimensionless
 α_v : Vertical poroelastic constant, dimensionless

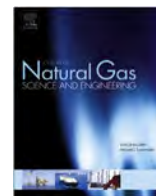
References

- Ahmad, M. and Haghghi, M., 2012. Mineralogy and Petrophysical Evaluation of Roseneath and Murteree Shale Formations, Cooper Basin, Australia Using QEMSCAN and CT Scanning. Society of Petroleum Engineers.
- Al-Kanaan, A., Rahim, Z. and Al-Anazi, H., 2013. Selecting Optimal Fracture Fluids, Breaker System, and Proppant Type for Successful Hydraulic Fracturing and Enhanced Gas Production - Case Studies, SPE Unconventional Gas Conference and Exhibition. Society of Petroleum Engineers, Muskat, Oman.
- Blauer, R.E. and Kohlhaas, C.A., 1974. Formation Fracturing with Foam. Society of Petroleum Engineers.
- Burke, L.H., Nevison, G.W. and Peters, W.E., 2011. Improved Unconventional Gas Recovery With Energized Fracturing Fluids: Montney Example. Society of Petroleum Engineers.
- Craft, J.R., Waddell, S.P. and McFatridge, D.G., 1992. CO₂ -Foam Fracturing With Methanol Successfully Stimulates Canyon Gas Sand.
- Economides, M.J. and Martin, T., 2007. Modern Fracturing: Enhancing Natural Gas Production. Energy Tribune Publishing Inc., Houston, TX.
- Economides, M.J. and Nolte, K.G., 2000. Reservoir Stimulation.
- Fei, Y. et al., 2016. Simulation of hydraulic fracturing with propane-based fluid using a fracture propagation model coupled with multiphase flow simulation in the Cooper Basin, South Australia. APPEA Journal.
- Garbis, S.J. and Taylor, J.L., III, 1986. The Utility of CO₂ as an Energizing Component for Fracturing Fluids.
- Gaydos, J.S. and Harris, P.C., 1980. Foam Fracturing: Theories, Procedures And Results. Society of Petroleum Engineers.
- Goelitz, R. and Evertz, G.E., 1982. Foam Fracturing In The Uinta Basin - A Field Study Of The Dakota And Wasatch Formations. Society of Petroleum Engineers.
- Gravestock, D.I. and Jensen, S., B., 1998. The Petroleum Geology of South Australia, 4. Primary Industries and Resources SA
- Mack, D.J. and Harrington, L.J., 1990. New Foams Introduce New Variables to Fracturing. Oil and Gas Journal.
- PIRSA, 1972. PEL 5 & 6 Nappacoongee-Murteree Block, Cooper and Eromanga Basins, Della#4 Well Completion Report, Open File Envelope No. 2047, Primary Industries and Resources South Australia
- Pokalai, K., Fei, Y., Ahmad, M., Haghghi, M. and Gonzalez, M, 2015. Design and optimisation of multi-stage hydraulic fracturing in a horizontal well in a shale gas reservoir in the Cooper Basin, South Australia. The APPEA Journal, 55.
- Pokalai, K., Kulikowski, D., Johnson, Jr, R.L., Haghghi, M., Cooke, D, 2016. Development of a new approach for hydraulic fracturing in tight sand with pre-existing natural fractures. The APPEA Journal, 56.
- Ribeiro, L. and Sharma, M., 2013. Fluid Selection for Energized Fracture Treatments, SPE Hydraulic Fracturing Technology Conference. Society of Petroleum Engineers, Woodlands, Texas, USA.
- Starkey, A.P.J., Katelis, Z.G. and McGhee, P., 2014. The US Shale Gas "Revolution": A Review of the Production Performance and Geology to Establish Potential Economic Benchmarks for Australia, Asia Pacific Oil & Gas Conference and Exhibition. Society of Petroleum Engineers, Adelaide, South Australia.
- Taylor, R.S. et al., 2010. Montney Fracturing-Fluid Considerations. Journal of Canadian Petroleum Technology.

Toney, F.L. and Mack, D.J., 1991. The Next Generation of Foam: A Field Study of Northwestern Oklahoma Foam Fracturing. Society of Petroleum Engineers.

Wamock, W.E., Jr., Harris, P.C. and King, D.S., 1985. Successful Field Applications of CO₂-Foam Fracturing Fluids in the Arkansas-Louisiana-Texas Region.

J3: Experimental and Simulation Study of Foam Stability and the Effects on Hydraulic Fracture Proppant Placement



Experimental and simulation study of foam stability and the effects on hydraulic fracture proppant placement



Yang Fei^{*}, Kunakorn Pokalai, Ray Johnson Jr., Mary Gonzalez, Manouchehr Haghighi

Australian School of Petroleum, University of Adelaide, South Australia, Australia

ARTICLE INFO

Article history:

Received 29 March 2017

Received in revised form

14 August 2017

Accepted 15 August 2017

Available online 4 September 2017

Keywords:

Foam stability

Hydraulic fracturing

Proppant placement

Drainage

ABSTRACT

Foam has previously been used as fracturing fluid; however, there have not been enough study on foam stability and its effectiveness on proppant placement during hydraulic fracturing. In this paper, an experimental study was performed using free drainage method at 90 °C. Then, the rheological characterization of foam was produced based on dynamic foam quality change during foam drainage experiments and also based on viscosity breakdown by disproportionation. Subsequently, a 3 D hydraulically fracturing simulation was developed to evaluate the foam performance as a fracturing fluid using different vertical well scenarios. The results show that foam stability is dependent not only on the overall treatment time but also to fracture closure on proppant. For example, longer closure time accelerate proppant settling and accumulation at the bottom of the fracture, lowering propped area, and reducing productivity. The simulation results indicate that this lower productivity can be attributed to the final propped area, proppant distribution confirming the relationship between foam stability, foam rheology, proppant transport and fracture effectiveness.

© 2017 Elsevier B.V. All rights reserved.

1. Introduction

Foams were introduced as fracturing fluid in the early 1980s, and they have been extensively used in various liquid sensitive and depleted reservoirs where water based fluids were less effective (Craft et al., 1992; Goelitz and Evertz, 1982; Wamock et al., 1985). It has been commonly reported that foams can achieve faster clean up, low leak off and less formation damage than conventional water based fracturing fluids (Burke et al., 2011; Garbis and Taylor, 1986; Goelitz and Evertz, 1982; Harris, 1985; Toney and Mack, 1991). Other reported benefits include lower water consumption and reduced swabbing (Blauer and Kohlhaas, 1974; Gaydos and Harris, 1980). Increasing transportation costs in remote locations, storage costs and high surface pumping requirement have been identified as limitation of field application (Wanniarachchi et al., 2015). However, the main issue of using foam in hydraulic fracture treatments is foam stability, particularly in high temperature conditions that foam becomes more unstable (Fei et al., 2017). Because the ability of a foam to induce fracture and carry proppant, it is essential to maintain foam stability at high

shear rates while pumping and low shear rates while fracture is closing. The failure of maintaining foam stability results in proppant screen out either in the fracture or at the wellbore or inadequate proppant distribution in the targeted interval at fracture closure, based on inadequate foam stability and proppant redistribution during closure (Johnson, 1995).

In this paper, the workflow of different tasks is discussed in the next section. Then, different mechanisms of foam stability are reviewed followed by the details of the experimental procedure and results. Furthermore, foam characterization and rheological modelling are discussed followed by the results of 3 D simulation. Finally some conclusive remarks are presented.

2. Methodology

This study involved 3 major tasks; 1 Foam stability experiments; 2 Foam rheological characterization and 3 3D hydraulically fracture simulation. The details of the workflow are shown in Fig. 1. First, a foam stability experiment was performed to record liquid drainage rate and foam collapsing time of sample. Those results provide guideline to develop dynamic foam rheology curve. Then, the corresponding foam rheological properties were calculated based on an existing rheological correlation from literature (Khade and Shah, 2004). The rheological properties of the base,

^{*} Corresponding author.

E-mail address: yang.fe@adelaide.edu.au (Y. Fei).

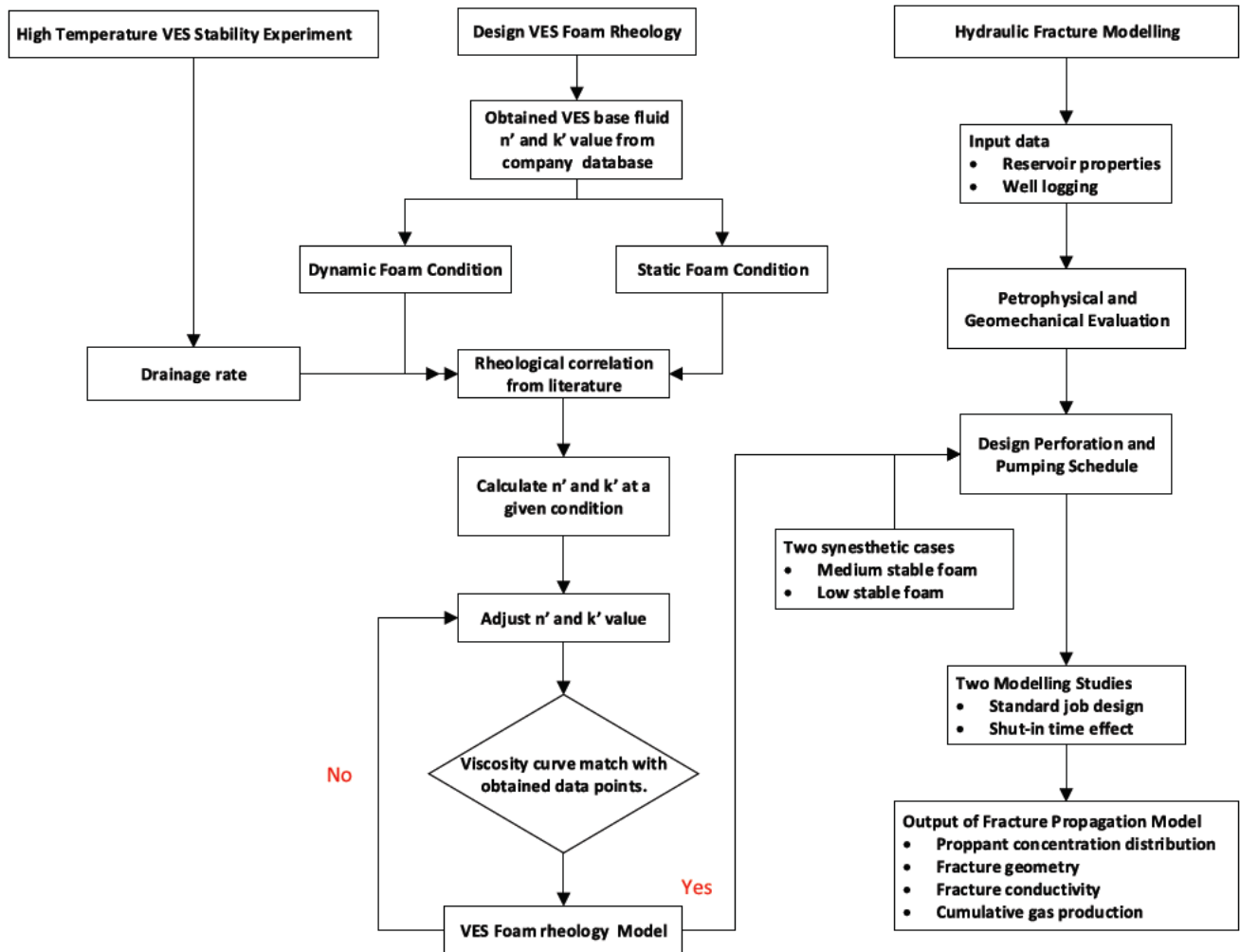


Fig. 1. Workflow of experiment and model development.

micellar fluid system were obtained from fracturing fluid database. For dynamic conditions, liquid drainage rates obtained from experiments to adjust foam quality changes with time. Eventually, a rheology curve was created that matched the observed input data points by adjusting rheological parameters in the correlation.

Next, a planar, fully 3D hydraulic fracture simulator was developed to model the fracture propagation and proppant transport (Barree, 1983). The details of the model development have been described in previous papers (Fei et al., 2016; Pokalai et al., 2015). In the simulator, the developed foam rheology model is integrated into the designed pumping schedule which recalculates the rheological properties on a grid by grid basis and predicts proppant distribution and conductivity. As aforementioned, there are a total of four differing cases: Case 1, constant foam quality (static case) assuming foam is entirely stable during the fracture progress with no gas fractional changes; Case 2, variable foam quality (dynamic case) where foam quality is based on experimental drainage rate observations and gas fractional changes with time; and Cases 3, and 4 as less stable foams based on duration to the critical time to analyse the influence of a stability factor on the treatment outcome.

3. Mechanism of foam stability

After foam is formed by injection of gas into a liquid solution, it

needs to be stabilized during fracturing and carrying the proppants. Foam stability can be divided into three mechanisms (Saint Jalmes, 2006; Wang et al., 2016): drainage, disproportionation and coalescence. Foam drainage is caused by liquid gravity segregation (Angarska et al., 2007; Koehler et al., 2000); disproportionation is caused by the gas transfer between bubbles induced by capillary pressure differences (Maestro et al., 2014); and bubble coalescence which is caused by the rupture of liquid films between neighbouring bubbles. (Saye and Sethian, 2013). During foam drainage, the foam quality increases with time, which influences the foam's rheology (Hohler and Cohen Addad, 2005; Weaire, 2008). During disproportionation, the bubble size increases causing the bubble to become more "fragile", affecting the rheology and increasing proppant settling in the fracture. The inter relationship of foam drainage and disproportionation determine the foam quality, proppant carrying capacity and foam volume (i.e., bulk deformation of bubbles), thereby controlling the fracturing fluid effectiveness.

3.1. Foam drainage

Foam drainage is the flow of liquid through the channels (plateau borders) and nodes between bubbles of the foam whilst experiencing a resistance due to viscous friction from the walls (Bhakta and Ruckenstein, 1995; Leonard and Lemlich, 1965; Magrabi et al., 2001). The drainage can be described as a complex

hydrodynamic process governed by gravity and capillary pressure (Hutzler et al., 2005; Koehler et al., 2004; Neethling et al., 2002). Fig. 2 shows a schematic of “free drainage”, which represent the common understanding of foam drainage. For example, consider a foam sample of initial foam height H_0 and initial uniform liquid fraction ϵ_0 at $t = 0$ in a cylinder with a closed base. Over time, the downward flow of the liquid dries the foam and the liquid accumulates at the base of the cylinder. The interface between the foam and the accumulated liquid over time is labelled L_t .

Drainage rate is crucially important for foam stability and rheology as it increases the foam quality (Q) as a function of time as follows:

$$Q_g^t = Q_g^0 + v_d t \quad (1)$$

Where Q_g^0 is initial foam quality, Q_g^t is foam quality after drained certain time t and v_D is foam drainage rate.

3.2. Disproportionation

Disproportionation is also known as Ostwald Ripening and is a process involving the diffusion of gas from smaller to larger bubbles. The driving force for this process is the Laplace pressure, or the pressure difference between bubbles of different sizes (Fig. 3):

$$P_A = P + 2\sigma/r_A \quad (2)$$

$$P_B = P + 2\sigma/r_B \quad (3)$$

$$P_{capillary} = P_A - P_B = 2\sigma \left(\frac{1}{r_A} - \frac{1}{r_B} \right) \quad (4)$$

where σ is the surface tension and r_A and r_B are the radius of bubble A and bubble B. The capillary pressure coupled with gas solubility in the aqueous phase initiates gas diffusion, leading to the growth of larger bubbles whilst smaller ones are shrinking. The mechanism of diffusive disproportionation in foams has been reviewed both theoretically and experimentally in terms of foam film permeability (Farajzadeh et al., 2008).

3.3. Foam rheology

Fig. 4, shows an example on how foam viscosity typically varies

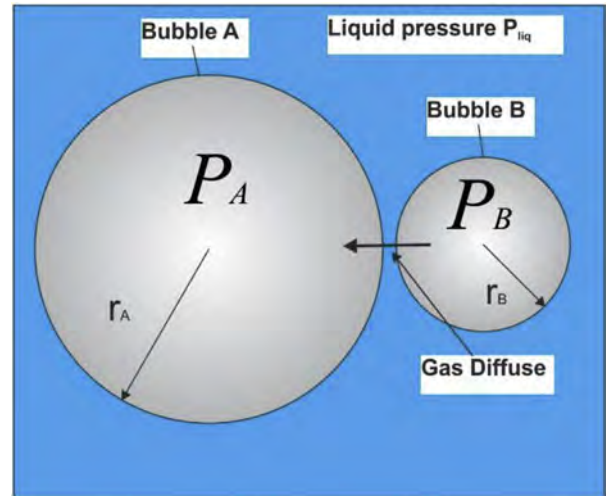


Fig. 3. Schematic of Ostwald ripening. Bubble A, growth from gas diffuse of bubble B by capillary pressure driving force, reproduced from Stevenson (2010).

as a function of foam quality. When foam is relatively wet (i.e., a low foam quality), the dispersed bubbles do not interact significantly, because the majority of the liquid content still exists in the plateau border and both film and gas diffusion rate are still low. However, as free drainage occurs, the friction between individual bubbles increases the foam viscosity non linearly with respect to time (Gu and Mohanty, 2015; Safouane et al., 2006). When foams become relatively dry (i.e., at higher foam quality), the bubbles interact significantly, a condition in which bubbles cannot maintain stability, leading to a sharp reduction in foam viscosity. Also the foam quality increases the proppant carrying capacity increases too and the maximum will be reached at the critical time. This proppant capacity is shown in Fig. 4 by the number of grey circles.

4. Experiments

Gelled foam samples were prepared by mixing a foaming agent with water in the presence of zwitterionic surfactant. During the experiments, the free drainage volume (V_f), foam bulk volume (V_0) and time (t) were recorded, resulting in the drainage rate and foam volume decay ratio. The calculated drainage rate can be used to calibrate the gas fractional change and determine the time when

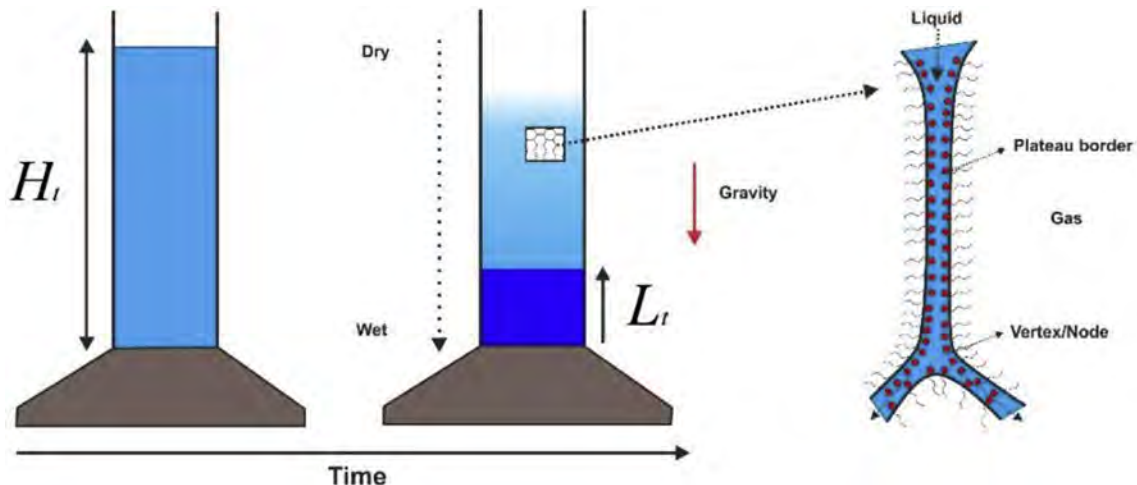


Fig. 2. Schematic of a free drainage experiment.

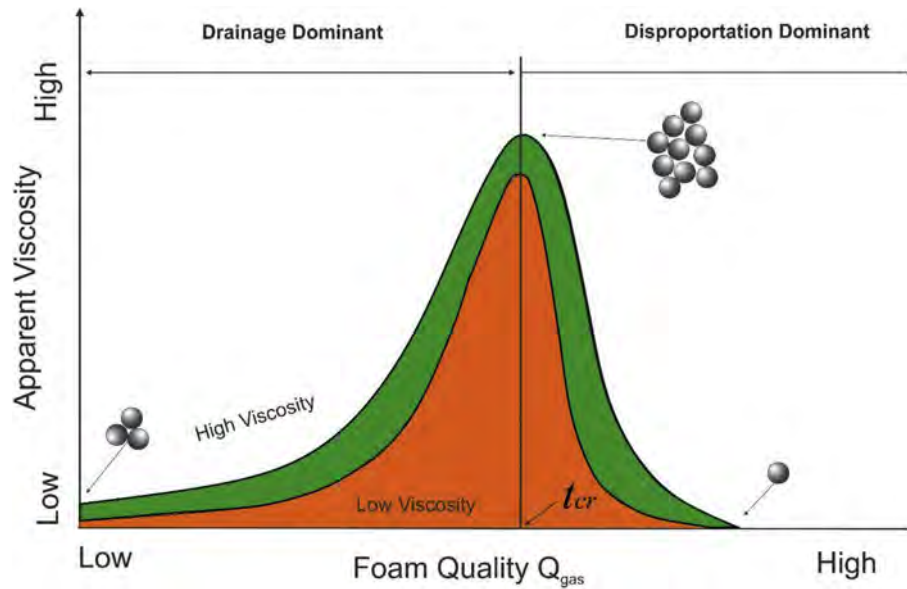


Fig. 4. A schematic of apparent foam viscosity as a function of foam quality.

the foam structure collapse. These data influence foam fluid rheological properties in the hydraulic fracturing modelling used to evaluate hydraulic fracture effectiveness in terms of projected productivity.

4.1. Materials

The Sodium Dodecyl Sulfate (SDS) and Sodium Dodecyl Benzene Sulfonate (SDBS) were 95 wt% active content powders, provided by Chengdu Kelong Co., Ltd, China. While EAPB is a zwitterionic surfactant of the betaine type, as shown by its chemical structure. This was manufactured by “Winsono New Material Technology” (China, Shanghai). All of these chemicals were used without further purification. Deionized water was used in all of the experiment. All working solutions were prepared immediately before each experiment at 25 ± 1 °C temperature.

4.2. Sample preparation

Case 2 sample was prepared using a mixture of anionic surfactant of 0.05 wt% sodium dodecyl sulphate [SDS] and 0.05 wt% sodium dodecyl benzene sulfonate [SDBS]. Those foaming agents were added into 100 mL of deionized water using a glass rod to dissolve the powder with gentle rotating speed to avoid bubble formation. Then, 1–5 wt% of EAPB was added as co-surfactant with continuous rod rotating. Once all additives were completely mixed, a high speed homogenization of the chemical mixture at 8000 rpm for 1 min entrained air was performed to produce fine foam. After the mixing was completed, the foam was immediately transferred to a 500 ml measurable cylinder in a pre-heated 90 °C oven. During the experiments, free drainage volume and foam total volume were recorded.

4.3. Results and discussions

The first observation is the effect of EAPB surfactant concentration on foam generation. The initial foam volume is inversely proportional to EAPB concentration and is presented in Fig. 5a. The effect of EAPB on foam generation is significant, in one case reducing the foam volume from 525 ml to 170 ml (i.e., foam quality of 37.5%). As the viscosity of a foaming solution increases with the

addition of EAPB, it is more difficult to diffuse gas into the solution at the same mixing rate (e.g., rotational speed of Warning blender), thereby reducing the foam volume. This observation also explains the difficulty of generating high foam qualities when high concentration of viscosifiers is employed to achieve better proppant transportation in hydraulic fracturing. For foam drainage and rupture test, 3% EAPB was used as experimental case study to trade off between foam quality and stability. Field practitioners have used delayed crosslinking of natural gums to achieve more stability in foamed fracturing fluids in order to transport higher concentrations of sand and limit detrimental effects of crosslinking on foam generation (Freeman et al., 1986; Johnson, 1995).

After the foam formation, several processes occur, each of them leading to foam destruction. To have a further stability analysis, the trend of drainage profile for 3% EAPB samples is studied. Fig. 5b displays the normalized drained liquid ($V(t) / V_{(10)}$) versus time. $V(t)$ is the foam volume that has been drained out of the foam, and $V_{(10)}$ is the total volume of liquid in the foam at $t = 0$. As it can be seen that drainage half time (τ) of 3% EAPB foam is 65 min; however, this study has found that drainage half life is not a key parameter to foam stability, particularly as it pertains to hydraulic fracture treatment simulation. Instead, the foam critical time (80 min) is a key parameter defining foam stability, which is the intersection of drainage trend (from 30 min to 80 min) and disproportionation trend (90 min–140 min).

In addition, Fig. 5c shows the ratio of remaining foam volume to total volume, illustrating that the foam volume decreases gradually during the first 90 min then sharply declines until no foam remains at 140 min. This is consistent with the drainage profile behaviour; thus, before the critical time, the samples are still in the drainage dominated regime (still contain sufficient film thickness) and bubble diffusion remains a minimum. After critical time, the foam ruptures quickly as the capillary suction pressure is more dominated than the disjoining pressure. Fig. 5d presents the volume change of the 3 wt% EAPB sample under 90 °C. At 90 min, it can be seen that most of liquid drains to the bottom whereas correspondingly the bubble size grows significantly. The coupling effect of drainage and disproportionation eventually cause the foam rupture. The experiment presents the entire lifetime of foam: from drainage, to disproportionation and eventually to coalescence. The remaining question is how much foam stability is required for a

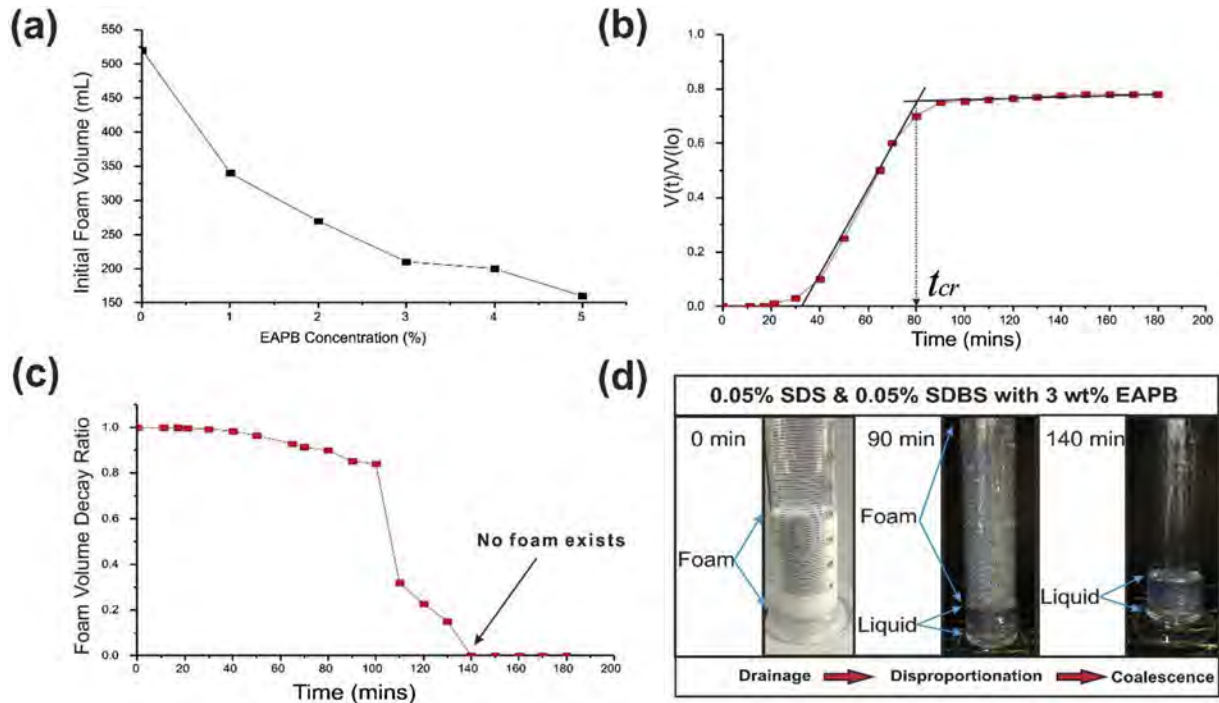


Fig. 5. Foam stability varies with EAPB concentration under 90 °C based on: (a) foamability, (b) foam drainage, (c) foam rupture, and (d) foam life-time visualisation.

foam fracturing fluid and what would be the effects on postfrac productivity.

5. Foam characterization and rheological modelling

Modelling of stability coupled with rheology of foam during a hydraulic fracturing treatment is complex issue in this work. The time dependence of non Newtonian foam is modelled by predicting the variance of two primary base fluid (power law) parameters: n_{Liquid} and k_{Liquid} , then coupled with the gas concentration to approximate the parameters for the foamed system: n_{Foam} and k_{Foam} . Published experimental correlations (Khade and Shah, 2004) have found to analogously predict the consistency and flow behavior index of foam fluids as a function of foam quality (Q_g):

$$\frac{n_{Foam}}{n_{Liquid}} = 1 - 0.6633Q_g^{5.168} \quad (5)$$

$$\frac{k_{Foam}}{k_{Liquid}} = e^{(0.4891Q_g + 5.6203Q_g^2)} \quad (6)$$

In this study a planar, fully 3 D hydraulic fracturing model known as GOHFER (Barree, 1983) was built. This model uses a Carreau rheological model to describe the time dependent fluid properties as a function of position in the hydraulic fracture, shear rate, temperature and sand concentration. The Carreau model relies on much of the same data as a power law model, based on a foam power law exponent (n_{Foam}) and fluid consistency index (k_{Foam}). In addition, values of zero shear viscosity (μ_0) (Asadi et al., 2002), high shear viscosity (μ_∞), and slurry rheology exponent (a) are required to determine the apparent viscosity (μ_{app}) as follows:

$$\mu_{app} = \mu_\infty + \frac{S_f \mu_0 \mu_\infty}{\left(1 + \left(\frac{S_f \gamma}{\gamma_l}\right)^2\right)^{\frac{1}{2} n_{foam}}} \quad (7)$$

$$\gamma_l = \left(\frac{U_o k_{foam}}{47879}\right)^{\frac{1}{n_{foam}}} \quad (8)$$

$$s_f = \left(1 - \frac{C_v}{C_{vmax}}\right)^{-a} \quad (9)$$

Where γ_l is the curve fit low shear transition, γ is the shear rate, C_v the volume of fraction solids, S_f sand factor, and each parameter is time dependent and change with temperature and breaker reactivity affecting μ_0 and μ_∞ .

The foam quality of static case is constant all the time during the treatment, the apparent viscosity could only be controlled by the time dependency of n_{Foam} and k_{Foam} . In the experiment, the model was run with dynamic foam quality based on the drainage observation. Thus, the apparent viscosity of the dynamic foam is controlled by an additional time dependent foam quality variable Q_g^t . The results calculated are summarized in Table 1. From $t = 0$ mins to $t = 30$ mins, there is almost no liquid drainage in the experiment; the viscosity between dynamic and static foam is the same. From $t = 30$ mins to $t_{cr} = 80$ mins, the viscosity of the dynamic foam increases by the effect of drainage. From $t_{cr} = 80$ mins to $t_{rup} = 140$ mins, the viscosity of dynamic foam decreases by disproportionation, then after $t_{rup} = 140$ mins, the foam totally collapses and no single structure remains. Following disassociation the fluid becomes characterised by the base fluid rheology, which is assumed to be completely degraded by breakers added to the foam or the viscosity of water (1cp).

Using the above results, the apparent viscosity vs time can be plotted (see Fig. 6a) as increasing from an initial base fluid viscosity to three fold static foam viscosity (based on $Q_g = 52\%$) as a result of the foam structure. The static and dynamic foam do not differ in the first 30 min, a period where the foam is completely stable. After 30 min, the foam drainage starts to increase, then the viscosity of the dynamic foam increases until it reaches a critical time, then the foam viscosity decreases as the foam structure collapses. This behaviour from the static and dynamic foam studies were matched

Table 1
Rheological Properties of static foam and dynamic foam.

Time (mins)	Constant foam quality (Static)		Variable foam quality (Dynamic)		
	Foam Quality (%)	Apparent Viscosity (cP)	Foam Drainage Ratio	Foam Quality (%)	Apparent Viscosity (cP)
1	52.381	234.778	0	52.381	234.778
10	52.381	234.778	0	52.381	234.778
20	52.381	234.778	0.01	52.632	237.737
30	52.381	230.214	0.03	53.140	239.152
40	52.381	199.670	0.1	55.000	228.091
50	52.381	166.624	0.25	59.459	241.290
60	52.381	124.648	0.425	65.672	256.768
70	52.381	96.162	0.6	73.333	311.331
80	52.381	75.496	0.7	78.571	331.151
90	52.381	59.524	0.75	81.481	307.620
100	52.381	44.280	0.755	81.784	230.997
140	52.381	1.000	0.78	83.333	1.000

to the Carreau rheological model as noted in Fig. 6b and (c).

In addition to the above models an additional two synthetic cases were created to illustrate the effect of foam stability on

hydraulic fracturing outcome. These cases were created by horizontally shifting the apparent viscosity of dynamic curve ($t_{cr} = 80 \text{ mins}$) to critical time $t_{cr} = 20 \text{ mins}$ (medium stability) and to critical time $t_{cr} = 3 \text{ mins}$ (low stability), as illustrated in Fig. 7. Then the same process of curve matching was performed to the Carreau rheological model.

6. Hydraulic fracture modelling

A 3D hydraulic fracturing simulation was developed using GOHFER (Barree, 1983). After running four different stability scenarios, the relationship between foam stability and fracture properties was obtained. The reservoir properties and the treatment parameters assumed based on a typical tight sand reservoir in the simulation and are listed in Table 2.

As discussed previously, first we modelled the created fracture geometry and resulting proppant distribution within the hydraulic fracture at standard job design in industry (Table 2) and based on the degree of foam stability (Figs. 6 and 7).

Second, sensitivity study of the shut in time is performed. Longer or shorter shut in periods affect the foam stability which

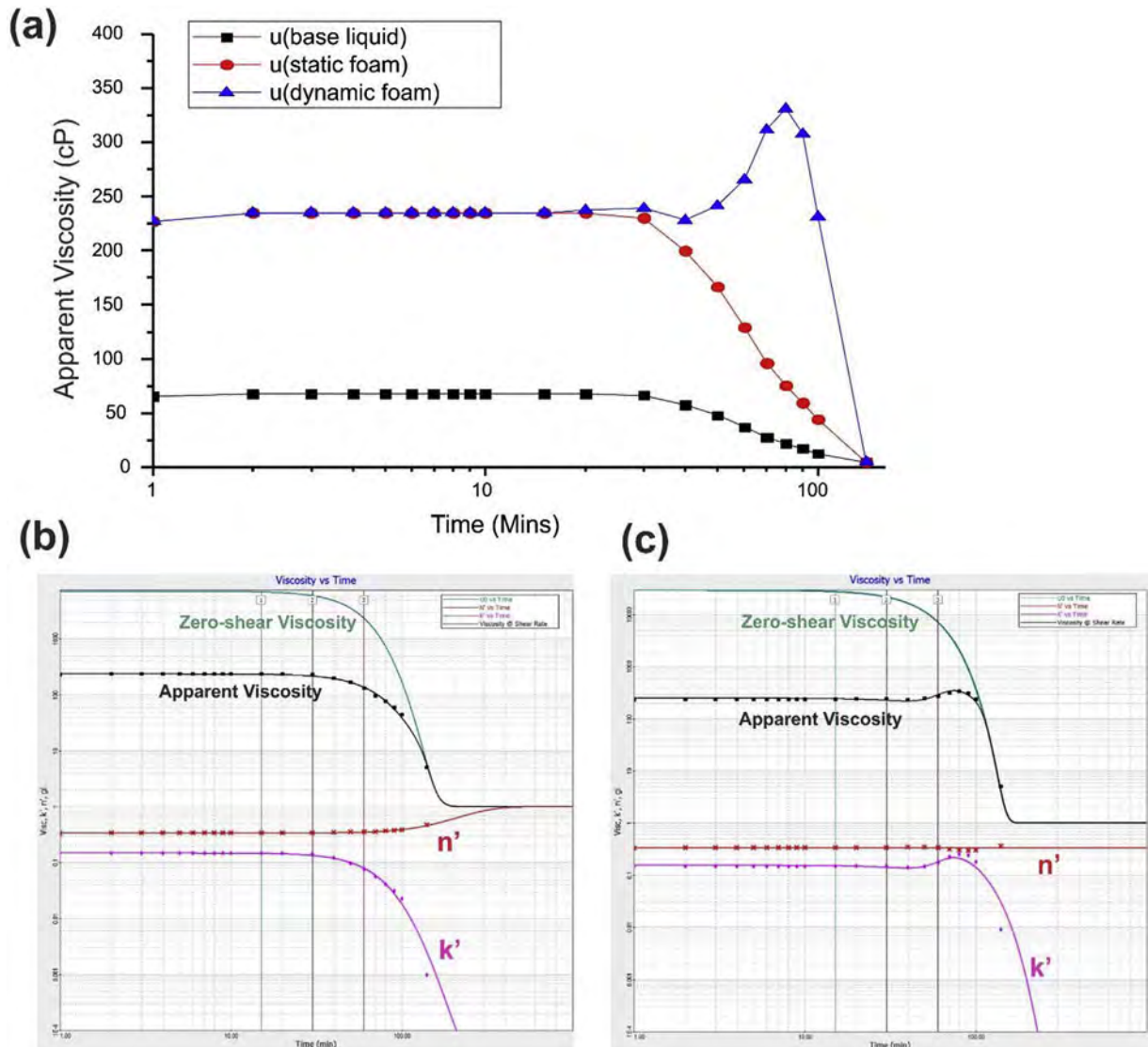


Fig. 6. The rheological properties of base fluid, static foam and dynamic foam quality (a). Carreau rheological model matching with obtained data point of the static foam quality (b) and dynamic foam quality (c).

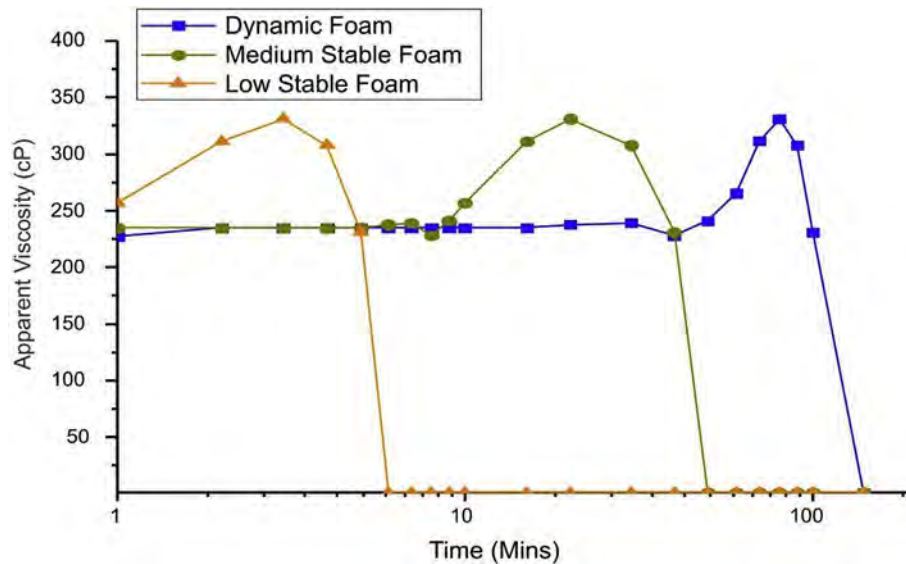


Fig. 7. Development of the synesthetic (medium and low stable) rheology curve from the reference curve (dynamic).

Table 2

Input data for standard treatment condition.

Well Parameters	Value
Measured depth, ft	7325
Thickness, ft	77
Reservoir pressure, psi	1857
Permeability, mD	0.17
Porosity, %	10
Water saturation, %	50
Gas saturation, %	50
Fracturing Treatment Parameters	
Type Fracturing Fluid	Foam
Clean volume, gallon	46,000
Proppant Type, mesh	Ceramic 20/40
Proppant amount, lbs	135000
Initial foam quality, %	52
Total pumping time, mins	60
Shut in time, mins	30
Pumping rate, bpm	20

subsequently has an influence on the proppant distribution, conductivity and post treatment production. Foam rheology at any point of the treatment depends on foam stability as shown in Fig. 8. The rheology profile can be split into two main parts: a stable region during pumping, where experimental data matches the static data, and an unstable region outside the stable envelope where foam drainage and disproportionation affect rheological properties. The shut in period varied from 0 to 1000 min is investigated in this study, with fixed pumping time at 60 min.

The following models show: (1) the relationship between foam stability and fracture properties under the standard treatment conditions. (2) The relationship between shut in time and production performance. This includes fracture geometry and proppant distribution impacted by the shut in time, when considering significantly shorter or longer than foam life. Consequently, overall well production are affected as a result of foam behaviour during both pumping and shut in periods.

6.1. Foam stability study

In the standard treatment condition, it can be seen that larger

propped areas are created and proppant is placed homogeneously in the static and dynamic cases (Fig. 9). This is because the job time (60 min pumping and 30 min shut in) is not significantly longer than the critical time for the dynamic foam (80 min). This indicates good foam stability results and good proppant transportation capabilities. In the medium stable case, the proppant carrying capacity decrease by foam stability, which causes postfrac production more discontinuity. In the low stable case, lower viscosity fluid and net pressure leads to a narrower aperture and hence longer penetration distance according to the total mass balance. This behaviour is caused due to an early rupture of the foam film during the treatment; which causes the apparent viscosity to drop significantly and to promote proppant settling, therefore leading to poor proppant placement. Therefore, for the unstable foam, there was a tendency to develop excessive and undesirable fracture length as it could not be able to transport the proppant to a further distance into the fracture.

Besides the fracture geometry, the fracture conductivity is another important treatment output which has a direct impact in the fracture productivity. Table 3 shows the summary of fracture geometries, average proppant concentration and conductivity for different foam stability. Generally speaking, relative stable foam provides better proppant transportation, higher propped area and higher conductivity. However, the average fracture conductivity of low stable case is the highest. This is because proppant accumulates in the near wellbore area due to poor transportation.

Fig. 10 shows that in the 1st year cumulative gas productions created by the four cases. The static and dynamic foam cases exhibit the best productivity, their curves are almost the same (overlap). While the low stable foam provides a higher production during the initial 120 days compared with the medium foam case due to higher fracture conductivity; it yields the worst cumulative production due to the limitation of propped area. This phenomenon can be much more significant in ultra low permeability reservoirs.

6.2. Shut in conditions study

After reviewing the above results, it is concluded that the foam stability is one of the essential parameters to be considered when design a foam fracturing treatment.

From the results shown in Fig. 11, it can be seen that the static

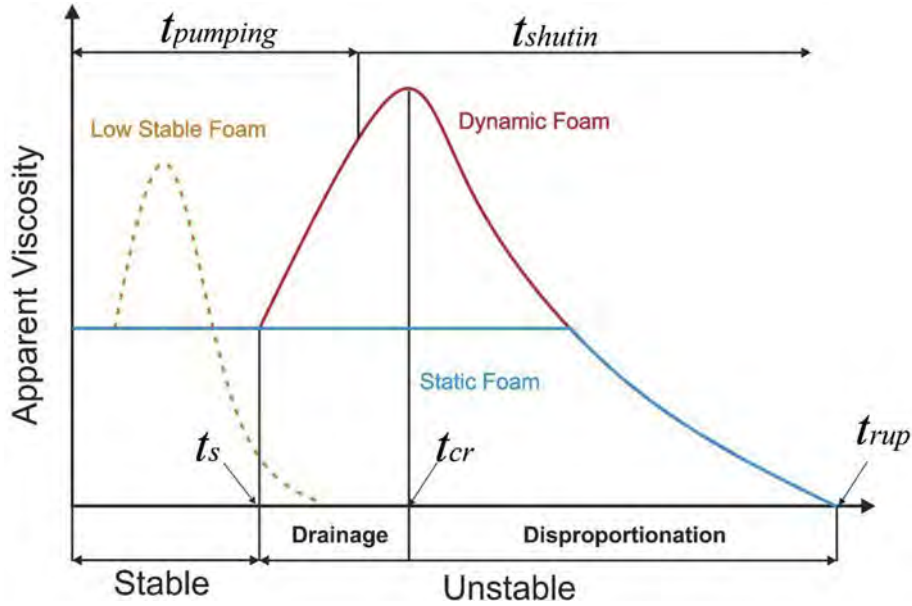


Fig. 8. Generic foam rheology vs. foam stability under frac treatment time.

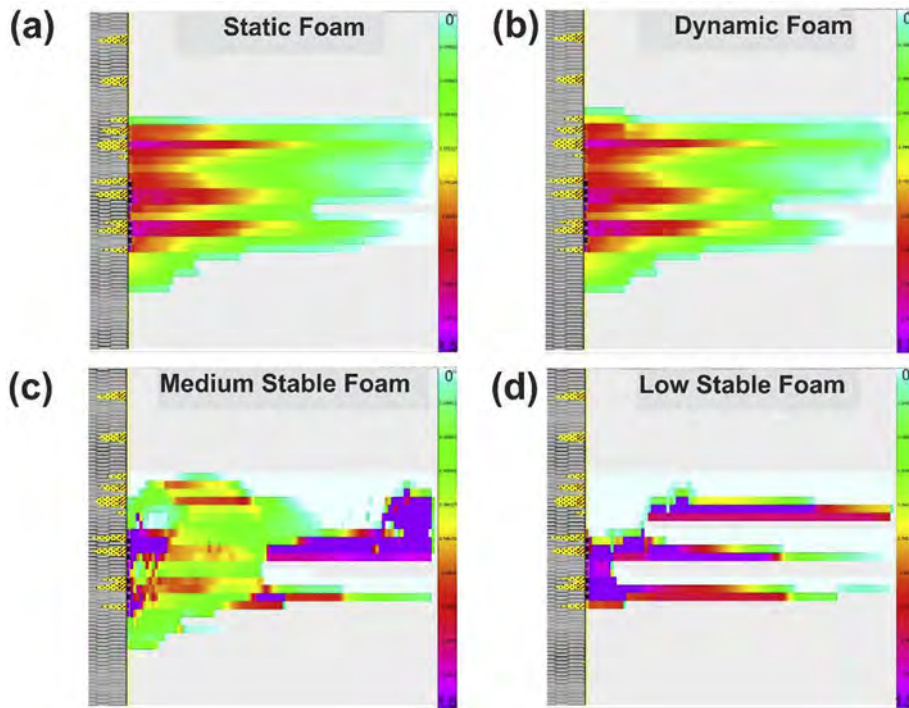


Fig. 9. Proppant concentration distribution for four different scenarios. Proppant concentration is scaled from 0 lb/ft² (light green) to 1.5 lb/ft² (purple). (For interpretation of the references to colour in this figure legend, the reader is referred to the web version of this article.)

and dynamic foam exhibit almost the same frac productivity at the first 80 min s shut in. The initial 140 min (60 min s from pumping and 80 min from shut in) is consistent with foam rupture time ($t_{rup} = 140mins$) from the experiment stability result. When the foam structure is completely ruptured, only base fluid remains, resulting to leakoff increase and proppant tends to drop at the bottom of the fracture, the total propped area decrease. Thus, the production significantly decreases. Interestingly, the dynamic foam shows 5 MMscf of cumulative production, which is higher than the static case after 80 min s shut in. We believe that this is because the

designed pumping time ($t_{pumping}$) ranges between stable time (t_s) and critical time (t_{cr}). The proppant transportation in the fracture is improved by the drainage effect. For the low stable case, the foam critical time is much less than pumping time, the loss of apparent viscosity during proppant placement leads to less propped area and productivity. From these observations, it can be seen that foam drainage in some extent improves fracturing productivity which depend on the location of pumping time between foam stable time and foam critical time (See pumping time example on dynamic foam in Fig. 8). The issue of long shut in time leads foam completely

Table 3
Results of hydraulic fracturing for different foam stability.

Properties	Static	Dynamic	Med Stable	Low Stable
Fracture Height, ft	110	115	100	60
Average Fracture Width, in	0.28	0.28	0.21	0.16
Propped Half Length, ft	285	270	210	285
Propped area, ft ³	1463	1449	735	456
Average Proppant Concentration, lb/ft ²	0.86	0.87	0.20	0.16
Average Fracture Conductivity, md*ft	369	370	312	872

coalescence, the remaining low viscous liquid can be detrimental to the final propped area and conductivity while the formation still in the period of closure. For visualisation of stability effect on proppant redistribution, please refer to the video. Hence, it is recommended that the design pumping time is just less than the foam critical time and shut in before foam could be ruptured.

Supplementary video related to this article can be found at <http://dx.doi.org/10.1016/j.jngse.2017.08.020>.

6.3. Model challenge

In the simulation model, the proppant settling (Harris et al., 2009) is mainly based on classical Stokes law whereas ignoring the effect of microstructure of liquid foam. In a microscopic study, we can explain the settling mechanism by the amount of net force on a proppant during drainage and gas diffusion process. Generally, as illustrated in Fig. 12, there are three different forces of (g) gravity, (F_p) pressure force and (F_n) pulling network force that exert on each proppant. The network force and the pressure force are the two main force components against proppant settling. This can be analysed by the quasi static “surface evolver” method (Brakke, 1992; Davies and Cox, 2009; Jing et al., 2016). Raufaste et al. (2007) which proposed that the contribution of the resultant up lift force (network force and pressure force) exerted on a round

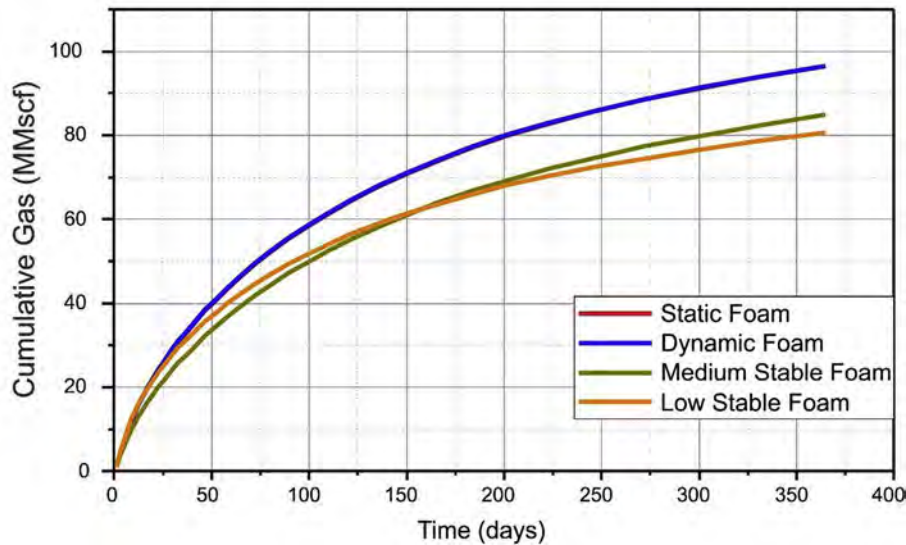


Fig. 10. Cumulative gas production for four different cases.

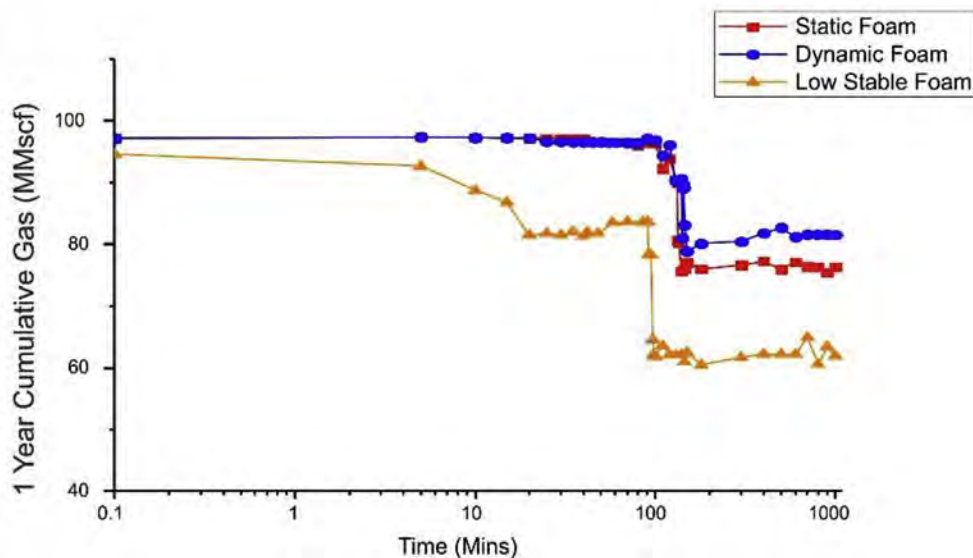


Fig. 11. Cumulative gas production vs. shut-in time.

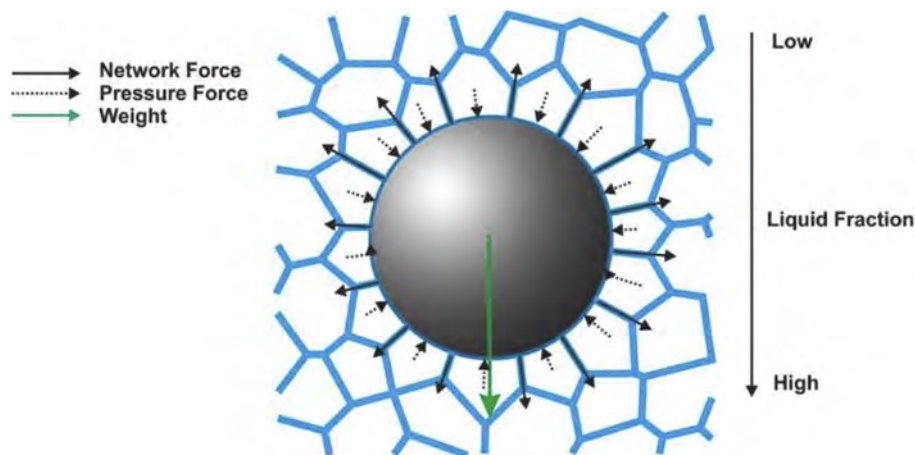


Fig. 12. Forces exert on films and bubbles in a proppant. Gravity (green arrow), network force (black solid arrow), pressure force (black dash arrow). (For interpretation of the references to colour in this figure legend, the reader is referred to the web version of this article.)

particle could be expressed by

$$F_{ny} = \frac{0.516}{(1 - Q_g)^{0.25}} \frac{\gamma d_o}{\sqrt{A_b}} \quad (10)$$

Where γ is surface tension, d_o is particle diameter and A_b is bubble area. This formula is consistent with Fig. 3 statement which implies that a high foam quality improves the apparent viscosity due to an increased in the resultant uplift force by drainage. However, after the critical foam quality has been reached, the uplift force exhibits a sharp decline because the bubble diffusion significantly increases the bubble area (A_b). Therefore, the focus of future work should be on dynamic analysis of foam structure changes (bubble size distribution) to predict more realistic proppant transport from rheological data.

7. Conclusions

This experimental and simulated study discovered the relationship between foam stability and fracturing efficiency. The following major conclusions could be drawn:

1. Foam stability is directly proportional to frac productivity, as it influences foam rheology which coupled fracture geometry and proppant transportation.
2. Foam stability is mainly controlled by foam drainage and disproportionation. The crossover point of those two mechanisms called foam critical time is an essential parameter for pumping time design.
3. Long closure time leads to proppant settle and cumulated at the bottom formation, which causes reduction of propped area and fracture productivity. The foam critical and rupture time need to be carefully designed regarding to formation closure time.
4. Foam stability is relative to the treatment time, it influences proppant transportation during placement and redistribution of proppant during closure. Therefore, it also provides useful in formation for production history matching.
5. There are other variables, such as surfactant types, concentrations, shear history and system pressure, which are also important in foam rheology characterization. The best approach is to develop an understanding of foam properties and performance and on site quality control tests. This process requires good on site quality control to avoid any unnecessary treatment condition change to result in foam be less stable.

Acknowledgements

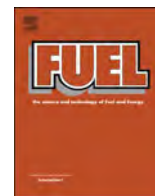
This work was supported by the National Science and Technology Major Project (2016zx04404002). We acknowledge the support of the Fracturing & Acidizing research team lead by Prof. Yang Zhaozhong in providing the experimental research facilities used in this work.

References

- Angarska, J., Stubenrauch, C., Manev, E., 2007. Drainage of foam films stabilized with mixtures of non-ionic surfactants. *Colloids Surfaces A Physicochem. Eng. Aspects* 309 (1–3), 189–197.
- Asadi, M., Conway, M.W., Barree, R.D., 2002. Zero shear viscosity determination of fracturing fluids: an essential parameter. In: *Proppant Transport Characterizations, SPE International Symposium and Exhibition on Formation Damage Control*. Society of Petroleum Engineers, Lafayette, Louisiana.
- Barree, R.D., 1983. *A Practical Numerical Simulator for Three-Dimensional Fracture Propagation in Heterogeneous Media*, Reservoir Simulation Symposium. Society of Petroleum Engineers, San Francisco, CA.
- Bhakta, A., Ruckenstein, E., 1995. Drainage of a standing foam. *Langmuir* 11 (5), 1486–1492.
- Blauer, R.E. and Kohlhaas, C.A., 1974. Formation Fracturing with Foam, 49th Annual Fall Meeting of the Society of Petroleum Engineers of AIME. Society of Petroleum Engineers, Houston, Texas.
- Brakke, K.A., 1992. The surface evolver. 141–165.
- Burke, L.H., Nevison, G.W., Peters, W.E., 2011. Improved Unconventional Gas Recovery with Energized Fracturing Fluids: Montney Example. Society of Petroleum Engineers.
- Craft, J.R., Waddell, S.P., McFtridge, D.G., 1992. CO₂-Foam Fracturing with Methanol Successfully Stimulates Canyon Gas Sand.
- Davies, I.T., Cox, S.J., 2009. Sedimenting discs in a two-dimensional foam. *Colloids Surfaces A Physicochem. Eng. Aspects* 344 (1–3), 8–14.
- Farajzadeh, R., Krastev, R., Zitha, P.L.J., 2008. Foam film permeability: theory and experiment. *Adv. Colloid Interface Sci.* 137 (1), 27–44.
- Fei, Y., et al., 2016. Simulation of hydraulic fracturing with propane-based fluid using a fracture propagation model coupled with multiphase flow simulation in the Cooper Basin, South Australia. *APPEA J.* 56, 415–426.
- Fei, Y., et al., 2017. Experimental investigation of nanotechnology on worm-like micelles for high-temperature foam stimulation. *J. Industrial Eng. Chem.*
- Freeman, E.R., Bilden, D.M. and Hossaini, M., 1986. Delayed Crosslinked Gels: Their Role in Aqueous Foam Fracturing, 56th California Regional Meeting. Society of Petroleum Engineers, Oakland, CA.
- Garbis, S.J., Taylor III, J.L., 1986. The Utility of CO₂ as an Energizing Component for Fracturing Fluids.
- Gaydos, J.S., Harris, P.C., 1980. *Foam Fracturing: Theories, Procedures and Results*. Society of Petroleum Engineers.
- Goelitz, R., Evertz, G.E., 1982. Foam fracturing. In: *The Uinta Basin – a Field Study of the Dakota and Wasatch Formations*. Society of Petroleum Engineers.
- Gu, M., Mohanty, K.K., 2015. Rheology of polymer-free foam fracturing fluids. *J. Petroleum Sci. Eng.* 134, 87–96.
- Harris, P.C., 1985. Dynamic fluid loss characteristics of foam fracturing fluids. *SPE J.*
- Harris, P.C., Walters, H.G., Bryant, J., 2009. Prediction of proppant transport from rheological data. *SPE J.*

- Hohler, R., Cohen-Addad, S., 2005. Rheology of liquid foam. *J. Phys. Condens. Matter* 17 (41), R1041.
- Hutzler, S., Cox, S.J., Wang, G., 2005. Foam drainage in two dimensions. *Colloids Surfaces A Physicochem. Eng. Aspects* 263 (1–3), 178–183.
- Jing, Z., Wang, S., Wang, Z., 2016. Detailed structural and mechanical response of wet foam to the settling particle. *Langmuir* 32 (10), 2419–2427.
- Johnson Jr., R.L., 1995. Fracture treatment modifications and bottomhole treating pressure analysis. In: *The Pictured Cliffs Formation, Rio Arriba County, New Mexico, Production Operations Symposium*. Society of Petroleum Engineers, Oklahoma City, Oklahoma, USA.
- Khade, S.D., Shah, S.N., 2004. New rheological correlations for guar foam fluids. *SPE J.*
- Koehler, S.A., Hilgenfeldt, S., Stone, H.A., 2000. A generalized view of foam Drainage: experiment and theory. *Langmuir* 16 (15), 6327–6341.
- Koehler, S.A., Hilgenfeldt, S., Stone, H.A., 2004. Foam drainage on the microscale: I. Modeling flow through single Plateau borders. *J. Colloid Interface Sci.* 276 (2), 420–438.
- Leonard, R.A., Lemlich, R., 1965. A study of interstitial liquid flow in foam. Part I. Theoretical model and application to foam fractionation. *AIChE J.* 11 (1), 18–25.
- Maestro, A., Rio, E., Drenckhan, W., Langevin, D., Salonen, A., 2014. Foams stabilised by mixtures of nanoparticles and oppositely charged surfactants: relationship between bubble shrinkage and foam coarsening. *Soft Matter* 10 (36), 6975–6983.
- Magrabi, S.A., Dlugogorski, B.Z., Jameson, G.J., 2001. Free drainage in aqueous foams: model and experimental study. *AIChE J.* 47 (2), 314–327.
- Neethling, S.J., Lee, H.T., Cilliers, J.J., 2002. A foam drainage equation generalized for all liquid contents. *J. Phys. Condens. Matter* 14 (3), 331.
- Pokalai, K., Fei, Y., Ahmad, M., Haghighi, M., Gonzalez, M., 2015. Design and optimisation of multi-stage hydraulic fracturing in a horizontal well in a shale gas reservoir in the Cooper Basin, South Australia. *APPEA J.* 55.
- Raufaste, C., Dollet, B., Cox, S., Jiang, Y., Graner, F., 2007. Yield drag in a two-dimensional foam flow around a circular obstacle: effect of liquid fraction. *Eur. Phys. J. E* 23 (2), 217–228.
- Safouane, M., Saint-Jalmes, A., Bergeron, V., Langevin, D., 2006. Viscosity effects in foam drainage: Newtonian and non-newtonian foaming fluids. *Eur. Phys. J. E* 19 (2), 195–202.
- Saint-Jalmes, A., 2006. Physical chemistry in foam drainage and coarsening. *Soft Matter* 2 (10), 836–849.
- Saye, R.I., Sethian, J.A., 2013. Multiscale modeling of membrane rearrangement, drainage, and rupture in evolving foams. *Science* 340 (6133), 720–724.
- Stevenson, P., 2010. Inter-bubble gas diffusion in liquid foam. *Curr. Opin. Colloid & Interface Sci.* 15 (5), 374–381.
- Toney, F.L., Mack, D.J., 1991. The Next Generation of Foam: a Field Study of North-western Oklahoma Foam Fracturing, *Production Operations Symposium*. Society of Petroleum Engineers, Oklahoma City, Oklahoma.
- Wamock Jr., W.E., Harris, P.C., King, D.S., 1985. Successful Field Applications of CO₂-Foam Fracturing Fluids in the Arkansas-Louisiana-Texas Region.
- Wang, J., Nguyen, A.V., Farrokhpay, S., 2016. A critical review of the growth, drainage and collapse of foams. *Adv. Colloid Interface Sci.* 228, 55–70.
- Wanniarachchi, W.A.M., et al., 2015. Current opinions on foam-based hydro-fracturing in deep geological reservoirs. *Geomechanics Geophys. Geo-Energy Geo-Resources* 1 (3), 121–134.
- Weaire, D., 2008. The rheology of foam. *Curr. Opin. Colloid & Interface Sci.* 13 (3), 171–176.

J4: Experimental and Numerical Investigation into Nano-Stabilized Foams in Low Permeability Reservoir Hydraulic Fracturing Applications



Full Length Article

Experimental and numerical investigation into nano-stabilized foams in low permeability reservoir hydraulic fracturing applications



Yang Fei*, Raymond L. Johnson Jr., Mary Gonzalez, Manouchehr Haghighi, Kunakorn Pokalai

Australian School of Petroleum, University of Adelaide, South Australia, Australia

ARTICLE INFO

Keywords:

Foam stability
Hydraulic fracturing
Nanoparticle
Proppant placement

ABSTRACT

Hydraulic fracturing is one of the most effective and efficient methods to enhance oil and gas recovery from reservoirs. Well productivity is mainly determined by the propped dimensions of the fracture. However, the propped dimensions are controlled by proppant transport and proppant placement, of which settling and convection are the controlling mechanisms. In this paper, a new concept is described to overcome the problem of proppant settling during a foam fracturing treatment and prior to fracture closure. This new concept consists of introducing nanoparticles into the base fracturing fluid system to stabilize the foam structure and reduce proppant settling. The results show that foam stability directly influences proppant placement and final fracture conductivity. When foam fracturing fluids experience long closure times, most often as a result of low leakoff, foam breakage occurs. This breakage results in proppant settling and accumulation at the bottom of the fracture, reducing propped dimensions. Whilst, high pumping rates and foam quality provide greater initial propped area, foam stability is major factor controlling the final propped area and productivity. Experimental results show that foam stability increases 2–3-fold in presence of 0.8-wt% silica nanoparticles under 90 °C. The enhancement of foam stability using nanoparticles, particularly foam life-time, allows better proppant suspension, maintains post-fracture conductivity, and minimizes productivity losses. This work is intended to guide the practitioner in the use of nano-stabilized foam to improve unconventional reservoir stimulation.

1. Introduction

The purpose of hydraulic fracturing is to generate a large conductive proppant pack area to improve the flow of reservoir fluids to the wellbore relative to natural flow [1]. Proppants, such as sand, resin coated sand and ceramics, are mixed with fracturing fluids to maintain a higher conductivity channel to increase reservoir fluid flow. However, proppant settling occurs during pumping, particularly with low viscosity fluids, and prior to fracture closure. This settling can result in lower propped height of the vertical fracture. Whilst an adequate vertical fracture may have been created, the total height may be inadequately propped and lead to reduced productivity without some modification made to improve foam stability [2].

Several experimental studies [3–9] and numerical studies [10–15] have been performed to understand the relationship between proppant transportation, distribution and proppant pack conductivity. Fig. 1 shows an illustration of the typical proppant distribution in a vertical fracture at the end of the treatment. With adequate fluid viscosity, proppant settling can be minimized resulting in a more uniform distribution as shown in Fig. 1a. With low viscosity fracturing fluids

(Fig. 1b), a less uniform propped fracture geometry results and can be characterized by a packed bed of proppants at the bottom of the fracture [16–18]. The proppant at the top of the pack, or dune like structure, will experience higher stresses [19] because it is supporting the open arch; this may lead to proppant crushing and additional formation damage (i.e., proppant embedment, fines migration). Therefore, it is generally recognized that failure to achieve sufficient vertical pay coverage with a propped fracture can seriously reduce overall stimulation performance [19–23].

Previously, foams, of varying gas blends and phase percentages, have been used as an alternative to 100% fluid based fracturing fluids in low permeability gas reservoirs for several reasons. These reasons include: minimizing formation damage [24–29]; faster and more complete fracturing fluid clean up [30]; and mitigating environmental impact by reduced water usage [31]. In addition, foams can have better proppant suspension properties relative to water, or low concentration gelled fluids. This suspension is largely the result of foam's micro structure and increased viscosity [32,33]. In addition to gravity forces, proppant settling in foam is dominated by drag forces whilst foam structure is based on elasticity and plasticity [33–35]. However, since

* Corresponding author.

E-mail address: yang.fe@adelaide.edu.au (Y. Fei).

Nomenclature			
ν	Poisson's ratio (dimensionless)	K_s	Packed permeability (md)
E	Young's modulus (Mpsi)	P_{net}	Net pressure (Psi)
w	Fracture width (inch)	P_f	Fluid pressure (Psi)
μ_a	Apparent slurry viscosity (lbm/ft*s)	g	Gravitational Constant ($m^3.kg^{-1}.s^{-2}$)
ρ_s	Slurry bulk density (lbm/ft ³)	g_c	Gravitational units conversion constant (dimensionless)
ρ_l	Liquid phase density (lbm/ft ³)	Z	Vertical distance (ft)
ρ_g	Gas phase density (lbm/ft ³)	S	Distance along fracture surface (ft)
C_v	Volume fraction particles (dimensionless)	v_s	Vertical slurry velocity (ft/s)
Q_g	Foam quality (%)	v_d	Drainage rate (ml/s)
T_F	Formation temperature ($^{\circ}F$)	n_{Liquid}	Base fluid flow behaviour index (dimensionless)
P	Pressure (Psi)	k_{Liquid}	Base fluid flow consistency index (Pa.s ⁿ)
w_s	Packed width (inch)	n_{Foam}	Foam flow behaviour index (dimensionless)
C_f	Baseline conductivity (md.ft)	k_{Foam}	Foam flow consistency index (Pa.s ⁿ)
		$V(t)$	Drained liquid volume at time t (ml)
		$V(t_0)$	Total liquid volume (ml)

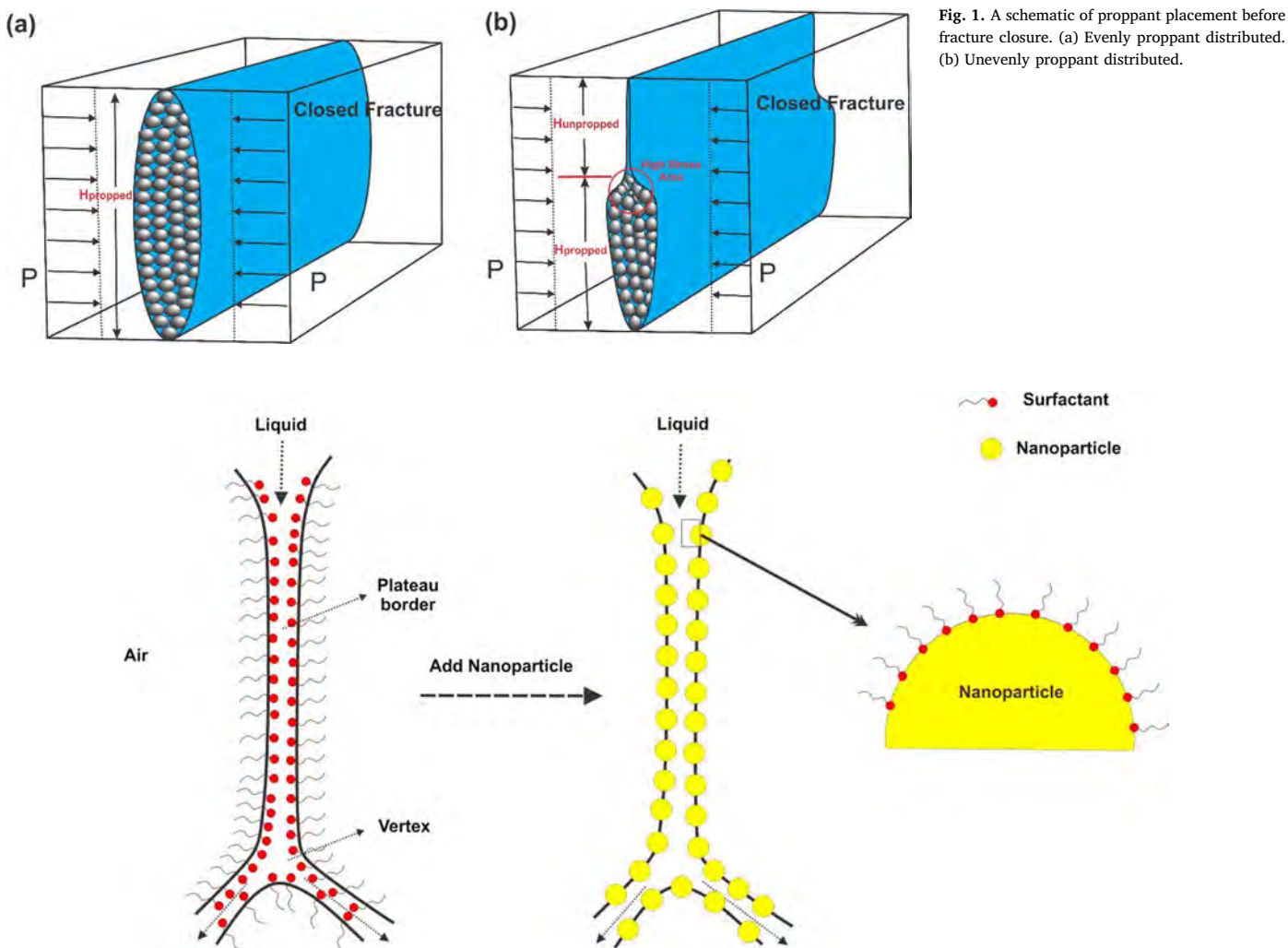


Fig. 2. A schematic diagram of a foam structure filled by surfactant molecules (left) and nanoparticles (right).

foam is naturally an unstable medium, with structure constantly changing, the rheological properties of a foam based fracturing fluid are controlled by foam stability [36,37].

Liquid foam [38] can be unstable due to three mechanisms [39]: drainage caused by gravity segregation [40,41]; coarsening caused by the gas diffusion (or called “disproportionation”) [42]; and bubble coalescence cause by thinning and rupture of the films between bubbles [43]. To counter these effects, increasing the base fluid viscosity by adding polymer and polymer gels have been used to maintain foam

stability [44–47]. However, the limitation of polymer or polymer gels into the foaming system could be confined by the limited increased viscosity. As the viscosity would gradually reduce due to temperature, shear degradation and dilution caused by contacting with reservoir mineral and fluids [48–50]. The viscosity reduction of foaming solution which decrease foam stability. Alternatively, recent research show that nanoparticles can improve the stability of foam [51–54] over prior methods, with some studies [55–59] demonstrating that nanoparticle stabilized foams can survive for weeks or more and even under

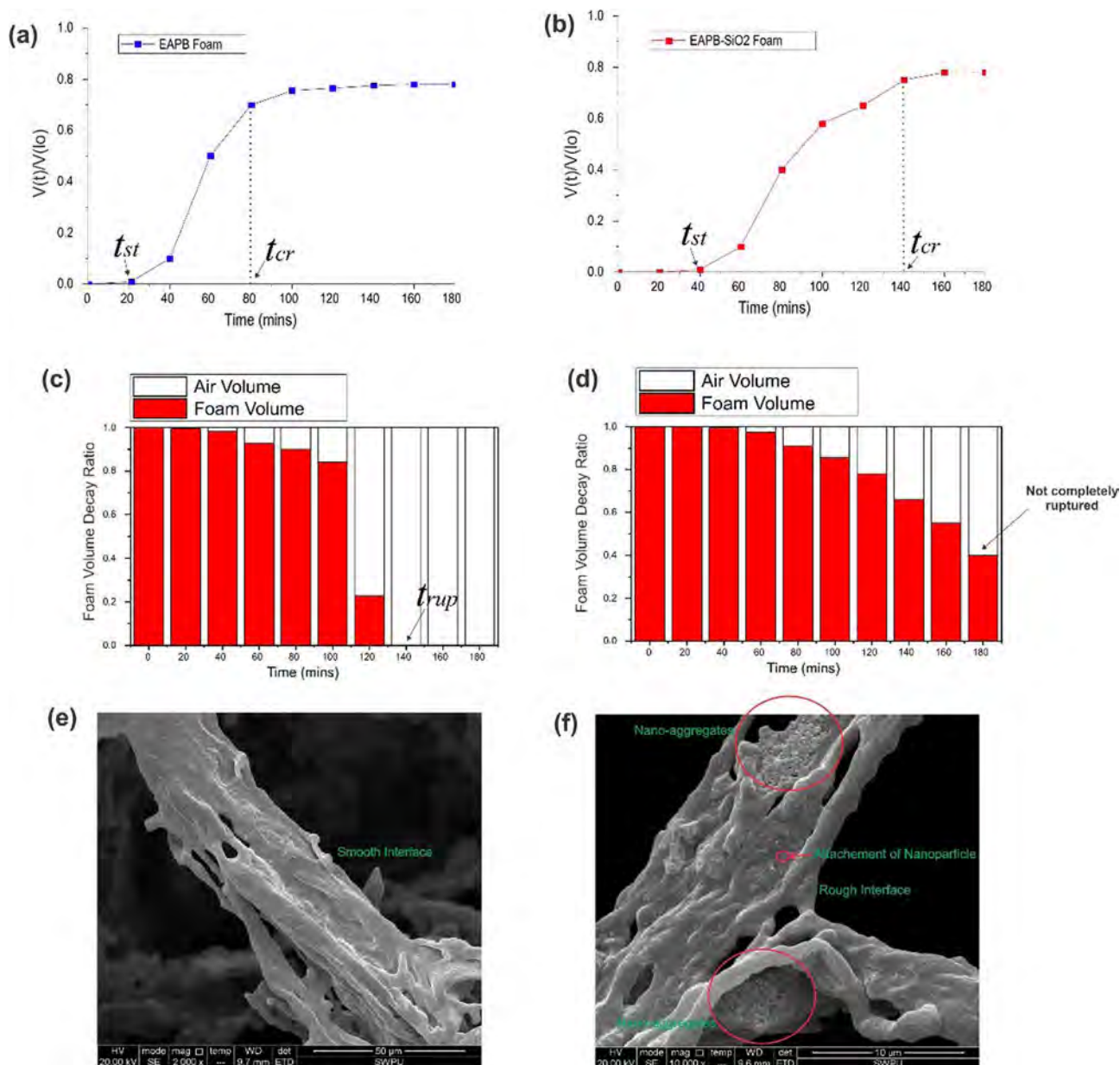


Fig. 3. Results of foam stability experiments with 3% EAPB and EAPB-SiO₂ foam at 90 °C. (a) and (b) illustrate foam drainage rate of EAPB foam & EAPB-SiO₂ foams. (c) and (d) illustrate decay rates of EAPB & EAPB-SiO₂ stabilized foams; (e) and (f) are SEM images of EAPB foam & EAPB-SiO₂ foam gas-water interfaces.

extremely harsh conditions.

Nanoparticles improve foam stability because nanoparticles are adsorbed at the interface and inhibit bubble coalescence by creating a steric barrier; this prevents the advancement of the interfaces [60,61]. Fig. 2 shows a schematic of the foam's interface between bubbles with and without the inclusion of nanoparticles. The attachment energy of nanoparticles in the gas water interface is usually irreversible and its adsorption energy determines the foam stability [62]. In addition, experimental results [62,64,42,65] have reported that the SiO₂ nanoparticles have a synergistic effect on foam stability in addition to surfactant concentration. This is the result of the nanoparticle's influence on the contact angle between the fluid and gas phase. Nanoparticle stabilized foams have been used in enhanced oil recovery [66–69]; however, their reported use in stabilizing foams for hydraulic fracturing treatments are limited.

This study follows previous experimental work [70], highlighting the inclusion of a viscoelastic surfactant with silica nanoparticles. In the previous study, the rheological properties of the foam were

characterized based on experimental results of drainage rate and foam volume decay rate. A foam rheology model was developed from the lab data and integrated into a hydraulic fracturing model to analyse the effect of proppant redistribution after pumping ceases and prior to fracture closing on proppant (e.g. fracture closure). This study attempts to answer the following questions:

1. What is the relationship between foam stability and proppant settling with or without nanoparticles?
2. What is the effect of foam stability on post fracture conductivity and productivity, including varying injection rate, foam quality and shut in time?
3. What special considerations need to be made when designing a foam fracturing treatment, considering these effects?

2. Foam stability experiment

2.1. Materials

As foaming agents, Sodium Dodecyl Sulfate (SDS) and Sodium Dodecyl Benzene Sulfonate (SDBS) were used with 95 wt% active content powders, provided by Chengdu Kelong Co., Ltd, China. The nanoparticle used was a nano fumed silica (with an average size of 40 nm) powder purchased from China Aladdin Chemical Co., Ltd. While erucyl amidopropyl betaine (EAPB) is a zwitterionic surfactant of the betaine type, it was manufactured by “Winsono New Material Technology” (China, Shanghai). All of these chemicals were used without further purification. Deionized water was the base fluid in all of the experimentation. All base fluids were prepared immediately before each experiment at $25 \pm 1^\circ\text{C}$ temperature.

2.2. Sample preparation procedure

The foam sample was prepared using an anionic surfactant mixture consisting of 0.05 wt% SDS and 0.05 wt% SDBS. These foaming agents were added to 100 ml of deionized water using a glass rod to dissolve the powder gently and avoid bubble formation. Then, 3 wt% EAPB was added as a viscosifier using continuous rod rotation. To investigate the effects of the addition of nanoparticles, a second set of experiments were performed including 0.8 wt% silica nanoparticles, which were introduced into the solution after the EAPB addition. Once all additives were completely mixed, the foam is generated by high speed homogenization at 8000 rpm for 1 min using entrained air as the gas phase.

3. Results and discussions

Fig. 3a b shows foam drainage rate of EAPB and EAPB SiO₂ stabilized foams based on normalized drained liquid ($V_{(t)}/V_{(0)}$) versus time. $V_{(t)}$ is the liquid volume that has been drained out of the foam, and $V_{(0)}$ is the total liquid volume in the foam at $t = 0$. Based on this comparison, silica nanoparticles appear to slow gravitational drainage times. In addition, Fig. 3c illustrates that the EAPB foam volume decreases gradually during first 80 min, then sharply declines until no foam remains at 140 min. However, for EAPB SiO₂ foam (Fig. 3d), there is still 40% of foam volume remaining after 180 min. The foam morphologies (Fig. 3e f), based on SEM images of the gas water interface of EAPB foam & EAPB SiO₂ foams, also confirm the nanoparticle adsorption phenomena that results in nanoparticle foam stabilisation.

The purpose of the particle adsorption at the gas water interface is to maintain film thickness, which counters bubble diffusion. When the two bubble surfaces become sufficiently close, attractive forces (i.e.,

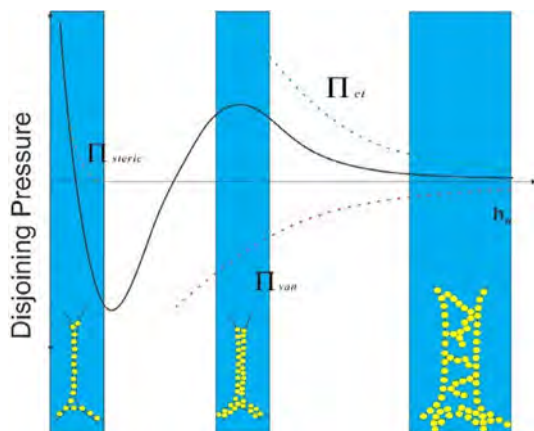


Fig. 4. An example of the disjoining pressure vs. film thickness. Increased layers of nanoparticles in the lamella decrease film thinning. The scale of the nanoparticle layer is for illustration purposes only.

Table 1
Experimental results of foam stability time enhanced by silica nanoparticle.

Name	Value (mins)		Incremental Ratio
	Without SiO ₂	With SiO ₂	
Stable Time	20	40	+100%
Critical Time	80	140	+75%
Rupture Time	140	200	+43%

Table 2
Input data for hydraulic fracturing simulation condition.

Well Parameters	Value
Reservoir Thickness, ft	200
Reservoir pressure, psi	1857
Permeability, mD	0.01
Porosity, %	10
Water saturation, %	50
Gas saturation, %	50
Fracturing Treatment Parameters	
Type Fracturing Fluid	EAPB Foam, EAPB-SiO ₂ Foam & Slickwater
Clean volume, gallon	57,000
Proppant Type, mesh	Ceramic 20/40
Proppant amount, lbs	175,500
Initial foam quality, %	52, 60 & 70
Shut in time, min	0, 60, 120, 180 & Closure
Pumping rate, bpm	10, 20, 30, 40 & 50

van der Waals forces), become significant. As the amplitude of the disturbance increases the likelihood of film rupture becomes more prevalent. Therefore, having a higher number of particles in the adsorbed layers results in a greater film thickness and leads to a lower probability of film rupture. A schematic representation of the geometrical configurations for particles at the bubble interface associated with Derjaguin and Landau, Verwey and Overbeek (DLVO) theory forces are shown in Fig. 4. In summary, foam stabilization occurs by nanoparticle attachment in the film, thickening it, and preventing film rupture.

Finally, foam stability times, or life times, are defined and compared in Table 1. The stable time indicates the time period prior to the start of liquid drainage; the critical time indicates the period when the foam transits from a drainage dominated regime to a disproportionation dominated regime; and the rupture time indicates the point at which the foam structure completely collapses. The inclusion of 0.8 wt% silica nanoparticles increases foam life time (time of stable, critical and rupture) between 43% and 100%, enhancing overall foam stability.

4. Hydraulic fracturing modeling

To evaluate foam stability effects on hydraulic fracturing results, several foam simulations were performed in a planar 3D, hydraulic fracturing model, GOHFER [71]. Three different fluid scenarios were evaluated in the simulator: an EAPB foam; an EAPB SiO₂ stabilized foam; and a low viscosity, or slickwater, non foamed fluid. The reservoir properties and treatment parameters were based on a typical low permeability (i.e., tight) sandstone reservoir and are listed in Table 2. To investigate the relationship between foam stability and post fracture conductivity, the main outputs of proppant concentration were evaluated at: the end of the treatment injection period (i.e., initial shut in time), then during various shut in periods. Finally, the resulting proppant conductivity of each treatment were evaluated at each treatments' point of fracture closure. Fracture proppant concentration is a proxy for tracking potential fracture conductivity prior to fracture closure, since fracture conductivity is based on final proppant concentration and closure stress on the proppant.

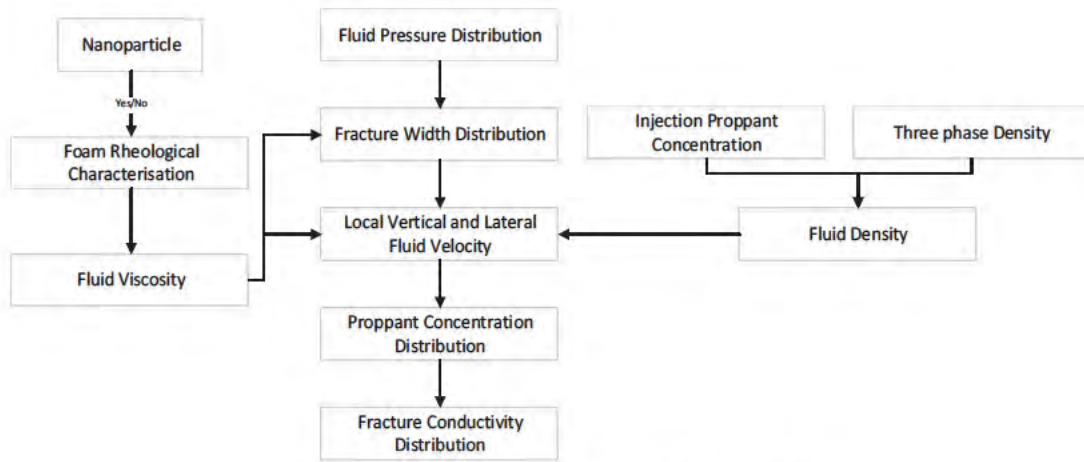


Fig. 5. Workflow of the mathematical formulation for fracturing model.

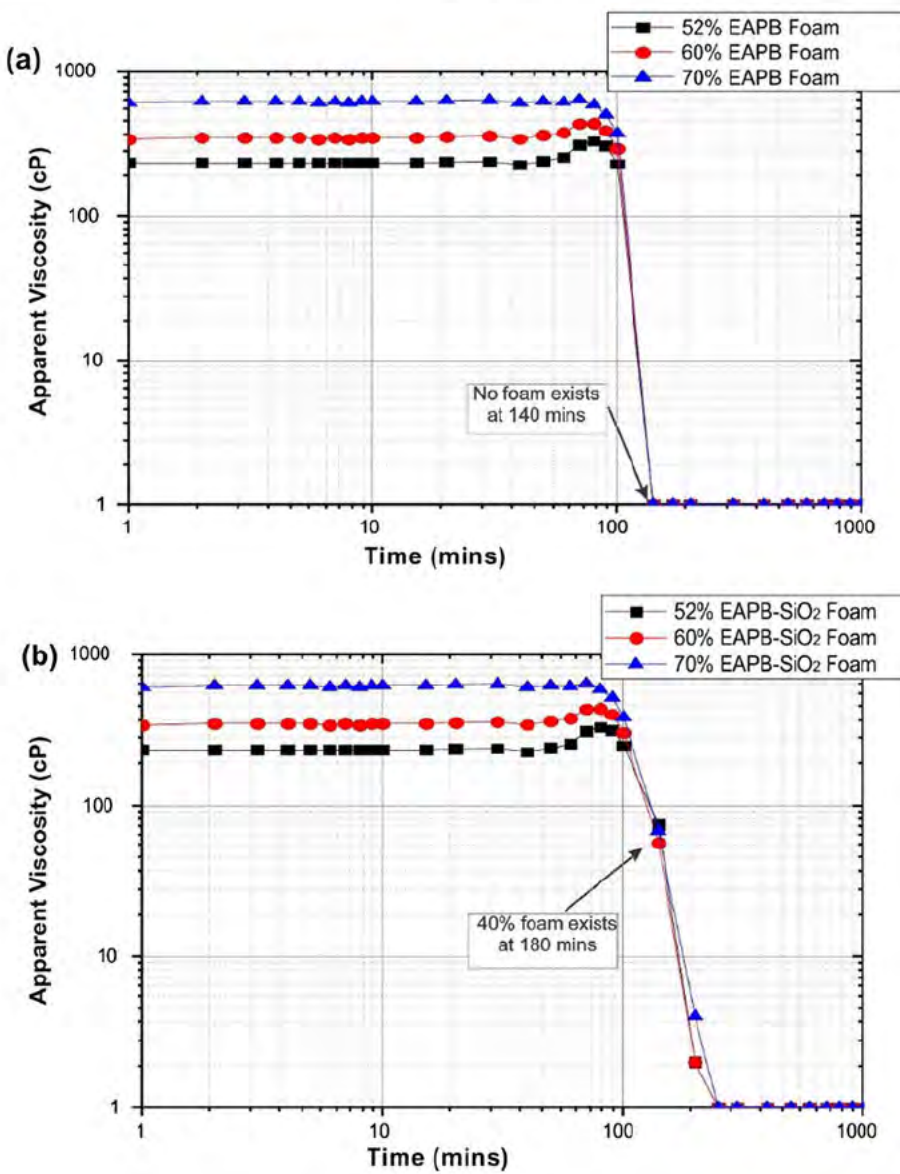


Fig. 6. The rheological properties of EAPB foam and EAPB-SiO₂ foam, based on varying foam quality from 52 to 70%.

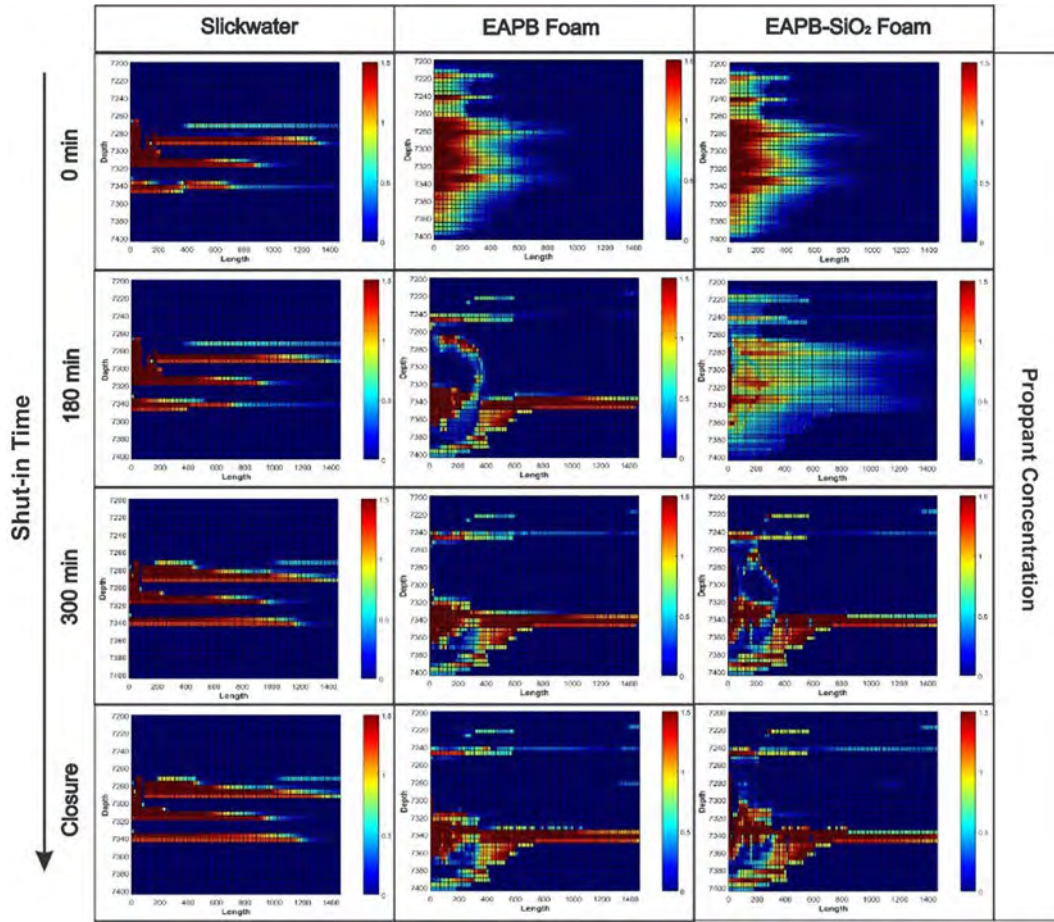


Fig. 7. Proppant concentration distribution (lb/ft²) vs. shut-in time for slickwater, EAPB foam and EAPB-SiO₂ foam with 70% foam quality at 50 bpm of pumping rate.

4.1. Mathematical formulation

The planar 3D hydraulic fracture simulator incorporates a series of sequential finite difference solutions based on a fixed spatial grid [71]. First, fracture fluid pressures (P_f) are calculated based on Poiseuille’s law for flow between parallel plates from the Navier Stoke equations. The distribution of net pressures (P_{net}) results from fluid pressure gradients used in the calculation of the fracture width distribution [72], by:

$$w = \int \frac{(1-\nu^2)}{\pi E r} P_{net} ds \tag{1}$$

where ν is Poisson’s ratio, E is Young’s modulus. The fracture width (w) is obtained by integrating the displacement for a single point load over the surface of the fracture. In addition, the vertical and horizontal components of fluid velocity are provided by the implicit solution of the system of equations generated by the finite difference, fluid flow formulation. These velocity components are used to compute proppant movement within the fracture. The vertical slurry velocity (ft/s) can be estimated [73] by:

$$v_s = \frac{w^2}{12\mu_a} \frac{\partial(\Delta\rho_s gh + 144P_f g_c)}{\partial z} \tag{2}$$

where μ_a is apparent slurry viscosity and ρ_s is the slurry bulk density. The slurry viscosity (μ_a) is dependent on proppant volume fraction and liquid viscosity. The slurry bulk density (ρ_s) can be estimated by the combination of proppant density (ρ_p) and foam density (ρ_f) [73] as:

$$\rho_s = C_v \rho_p + (1-C_v)\rho_f \tag{5}$$

where C_v is volume fraction particles. The foam density relates to foam

quality (Q_g), liquid phase density (ρ_l), and gas phase density (ρ_g), and can be estimated by:

$$\rho_f = Q_g \rho_g + (1-Q_g)\rho_l \tag{6}$$

The gas phase density (ρ_g) can be either the density of CO₂ or N₂ and are a function of pressure (P) and temperature (T_F) [74]:

$$\rho_{CO_2} = [0.6242e^{-0.0079T_F}] \times \frac{P^{(0.0007T_F+0.074)}}{(1 + (P/(800T_F/70))^{-2.8})^{0.357}} \tag{7}$$

$$\rho_{N_2} = \frac{(0.98-0.00045T_F)}{(1 + (P/(8800 + 13T_F))^{-1.1})^{0.95}} \tag{8}$$

The movements of the bulk slurry (v_s) within the fracture can be accelerated by convection as a result of density differences [75]. Slurry mixture density (ρ_s) is significantly increased by the presence of proppant (Eq. (5)). When proppant laden slurry enters a fracture that is initially filled only with pad fluid, the denser slurry tends to gravitationally convect downward, increasing the overall downward particle velocity. Clark and Zhu [76] demonstrated that the role of convection can be assessed with dimensionless number. For power law fluid, the dimensionless number is:

$$N_C = 2 \left(4 + \frac{2}{n} \right)^n \frac{Kq^n}{\Delta\rho g w^{(1+2n)}} \tag{9}$$

where n is flow behavior index and K is consistency index. If N_C is less than one (low viscous medium); gravitational slurry convection is significant. Next, the calculated fluid velocity distribution from Eq. (2) is used to estimate the proppant concentrations at each point in the fracture from a solution of the diffusivity equation in two dimensions [73]:

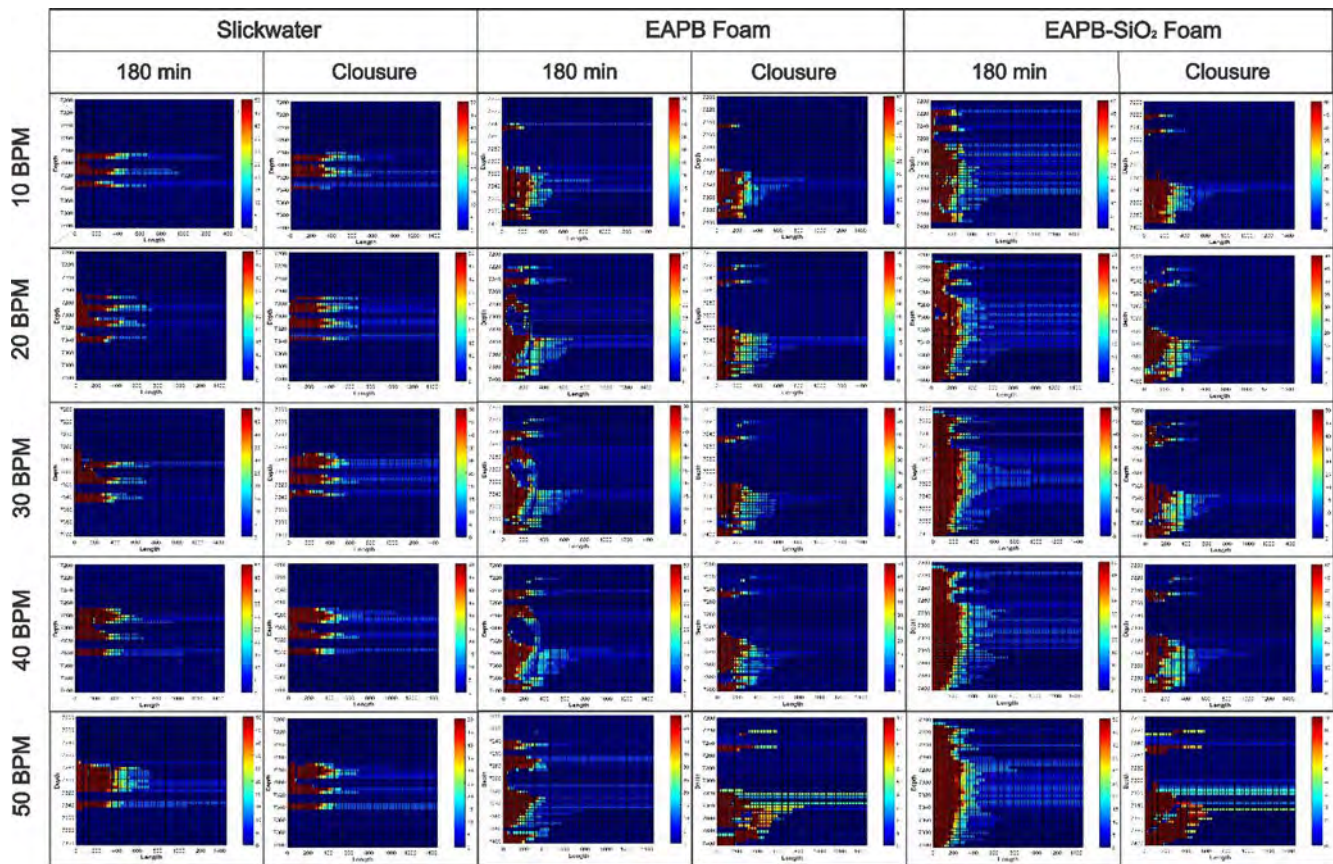


Fig. 8. Fracture conductivity vs. pumping rate for slickwater, EAPB foam and EAPB-SiO₂ foam with 70% foam quality at 180 min & fracture closures.

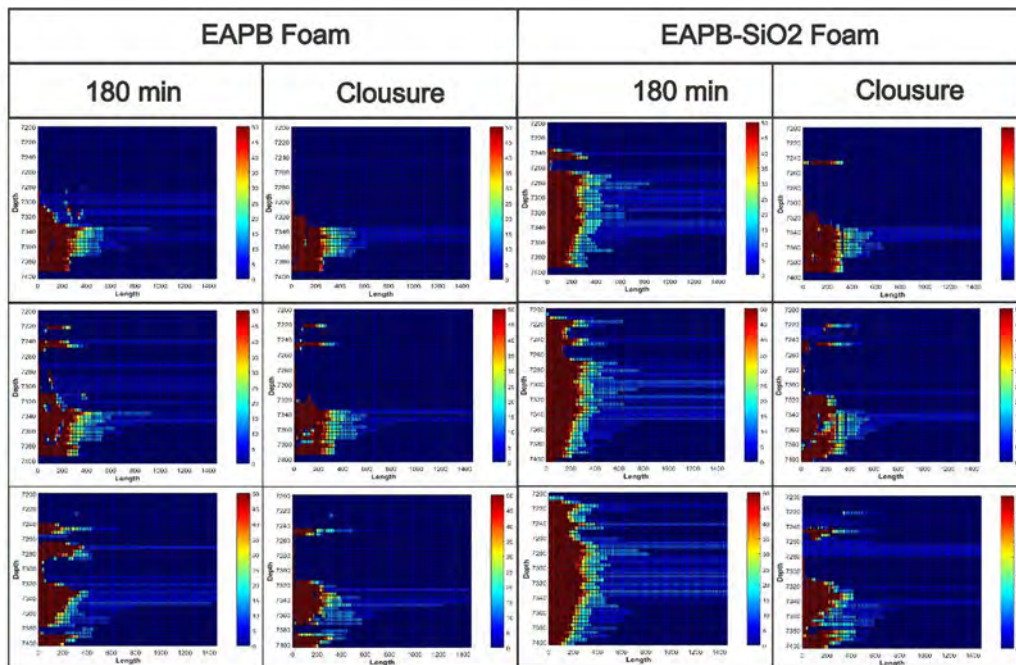


Fig. 9. Fracture conductivity vs. foam quality for both foam cases with 50 bpm of pumping rate at closure time.

$$-v = \frac{\delta C_v}{\delta x} = \frac{\delta C_v}{\delta t} \quad (10)$$

The proppant concentration is dependent on the volume of fluid in the fracture less the fluid leaking off (i.e. leakoff) to the rock matrix. The leakoff in a VES fluid system is non walling building and is

controlled by fluid viscosity leakoff over time. However, the nano particle pseudo crosslinked VES fluid system exhibits wall building leakoff control characteristics [77].

Finally, the final proppant conductivity at fracture closure can be based on the final packed width (w_p) and closure stress; this value is used to calculate baseline conductivity distribution (C_f) [78] by:

$$C_f = k_f w_f = K_s * 1000 * \frac{w_s}{12} \tag{11}$$

where K_s is the proppant packed permeability at a given closure stress. In our case, the same proppant will be used in all models and the closure stress varies only by interval, so the conductivity becomes dependent on the propped fracture width and proportional to the final proppant concentration.

The details of the mathematical formulation workflow are summarized in Fig. 5. To model proppant transport and placement within the fracture, the foam fracturing fluid viscosities were based on rheological properties of a non Newtonian fluid. The foam rheological properties for EAPB foams with and without silica nanoparticles will be described in the next section.

4.2. Foam rheological characterization

In each case, an initial foam quality is assumed then varied upwardly (i.e., 52%, 60% and 70%), with two types of foams EAPB and EAPB SiO₂ stabilized. The drainage rate (v_d) from experimental results (Fig. 3a b) are input into Eq. (12) to generate time dependent foam quality values by:

$$Q_g^t = Q_g^0 + v_d t \tag{12}$$

The time dependence of a complex foam’s rheological properties are predicted by the variance in the two primary base fluid (power law) parameters: n_{Liquid} and k_{Liquid} , then coupled with the foam quality (Q_g^t) to approximate the parameters for the foamed system: n_{Foam} and k_{Foam} . Published experimental correlations [79] have been found to analogously predict the consistency and flow behavior index of these foam fluids by these equations:

$$\frac{n_{Foam}}{n_{Liquid}} = 1 - 0.6633 Q_g^{5.168} \tag{13}$$

$$\frac{k_{Foam}}{k_{Liquid}} = e^{(0.4891 Q_g + 5.6203 Q_g^2)} \tag{14}$$

From the experimental results, the volume of EAPB stabilized foam completely collapses at 140 min; whereas, the foam volume of EAPB SiO₂ stabilized foam remains constant at 40% foam volume after 180 min (Fig. 3c d). Following disassociation, the fluid becomes characterized by the base fluid rheology, which is assumed to be completely degraded by breakers; thus, the fluid eventually reverts to the viscosity of water (1 cp). Using the above results, the apparent viscosity can be plotted in Fig. 6.

5. Results and discussions

Fig. 7 shows the results of proppant concentration distribution

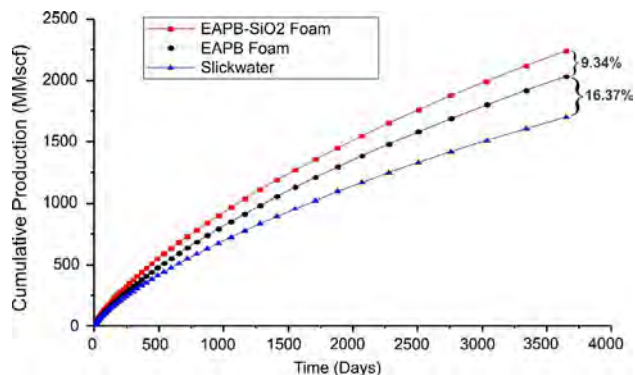


Fig. 10. Productivity forecasting of gas cumulative production for 10-years in the cases of 70% EAPB-SiO₂ foam, 70% EAPB foam and Slickwater with 50 bpm of pumping rate at shut-in 180 min.

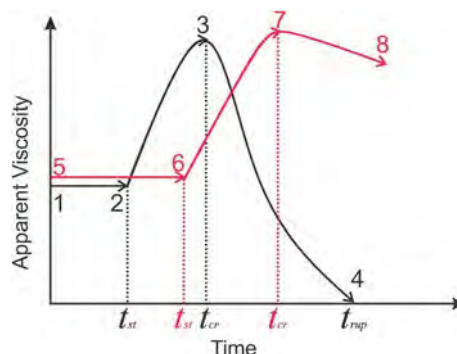
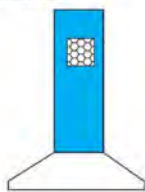
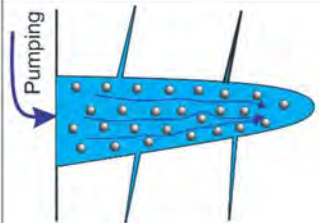
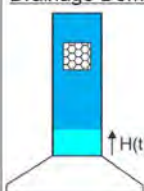

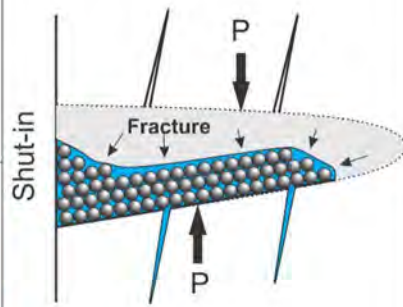
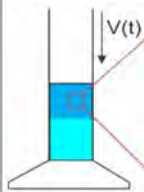
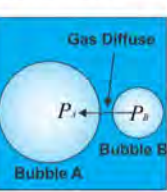
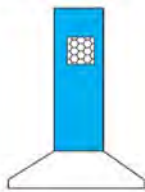
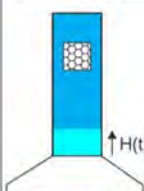
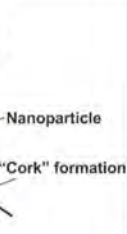
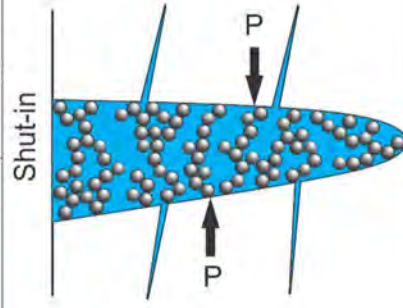
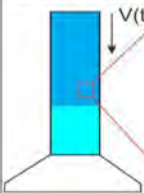
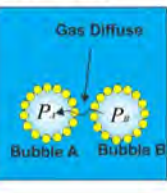


Fig. 11. Example profiles of foam rheology coupled with foam stability factor. The black curve represents a standard unstabilized foam, while the red curve represents a nano-stabilized foam. The time scale is for illustration purposes only.

predicted by the hydraulic fracture modeling using all three fluids: EAPB foams, EAPB SiO₂ foams, and slickwater (based on 100% water based fluid) injected at a pumping rate of 50 bbl/min. Fig. 7 notes the potential progression of proppant redistribution within the fracture from 0 min shut in time (i.e., at the end of injection) to 180 min after shut in, then at fracture closure. The proppant concentration is observed at each of these times and is plotted from 0 (blue) to 1.5 (red) lb/ft². Certainly, the final dimensions at closure are the key dimensions, and the selection of shut in point of 180 min is for evaluation with foam stability experimental results. The use of slickwater fracturing, results in poorer proppant transport and less propped area in compared with either of the two foam cases. The poor proppant transport is caused by the lower viscosity and rapid leakoff rate of the slickwater that results in rapid settling of the proppant particles. For both foam cases, the predicted initial propped geometries are nearly identical. This indicates both foams are stable and maintain adequate viscosity while pumping and provide better proppant transport properties than a slickwater treatment. However, the proppant distribution can be varied along shut in time. For EAPB foam, propped area becomes non uniform, leaving more upper area unpropped within the propped length at early stages. Whereas, for EAPB SiO₂ foam, the propped area remains almost the same at initial as at 180 min shut in; the slow proppant redistribution indicates stabilized foam structure reduces proppant settling rates. However, as a result of low permeability values used in this case, when the fracture closes, the final proppant distribution of two foam cases become nearly identical. This is because during the extended shut in period, the foam tends to become unstable and breakage occurs before fracture closure. Therefore, these results suggest that nano stabilized foams need to be formulated to maintain stability longer than the time of formation closure in order to achieve a more effective proppant distribution.

Next, we can use modeling to evaluate the effects of pumping rate on the propped area based on foam formulations (Fig. 8). For comparison purposes, the fracture conductivity is plotted from 0 (blue) to 50 (red) md*ft. At shut in time = 180 min, total proppant laden area of slickwater is less than that created by EAPB foam and EAPB SiO₂ foam. This confirms the effect of the lower viscosity of slickwater on proppant transport, and ultimately fracture conductivity. For an EAPB foam, sand accumulates at the bottom of the fracture, forming a thinner high conductivity sand bed, a large amount of sand settling, and fluid convection from the upper regions of the fracture independent of pumping rate. For EAPB SiO₂ foam, the fracture conductivity distribution is improved over either the slickwater or EAPB treatments largely as a result of negligible foam stability decline. However, at some point prior to fracture closure, the EAPB SiO₂ foam breakage occurs, there is a loss of viscosity and proppant settling accelerates; under these conditions, the fracture conductivity distribution is reduced based on stability with only minor influences as a result of the pumping rate. These results also compare consistently with previous results of predicted final proppant

Table 3
Stages within foam fracturing treatment based on varying foam stability behaviour.

Type	Process	Foam Behaviour	Fracturing Treatment
Without Nano-particle	1→2	<p>Stable Periods</p> 	
	2→3	<p>Drainage Dominated</p>  	
	3→4	<p>Disproportionation Dominated</p>  	
With Nano-particle	5→6	<p>Stable Periods</p> 	
	6→7	<p>Drainage Dominated</p>  	
	7→8	<p>Disproportionation Dominated</p>  	

distribution (Fig. 7). This confirms that when foam structure is unstable before fracture closure, the final fracture conductivity can be significantly reduced due to proppant settling.

Parametric study of foam quality impact on propped area is also shown in Fig. 9. It shows the size of propped area is direct proportional to the foam quality when foam maintains stable. It appears that higher

foam qualities provide higher viscosities and reduced leakoff. These parameters increase net pressure, and results in fracture height growth and improved proppant transport. However, when fracturing a thin reservoir where there are negative consequences to height growth, using a less stable, low quality foam may be to minimize net pressures and out of interval height growth. As expected a less stable (EAPB

foam) does not create sufficient vertical coverage regardless of foam quality. On contrast, EAPB SiO₂ foams maintaining larger propped areas at initial 180 min shut in by minimizing proppant settling and associated accumulation at the bottom of the fracture. Similar to prior modeling studies [2], proppant laden fluid convects downwardly towards the bottom of the fracture and more settling and poor proppant placement is the result. This is largely because of foam becoming more unstable during the shut in period prior to fracture closure. Therefore, testing and assuring foam quality to maintain proppant support during the shut in period is important to maintain fracture conductivity over the entire targeted interval of the hydraulic fracture.

To demonstrate the impact of resulting conductivity on productivity, simulations of 10 years cumulative production were made for treatments using 70% EAPB foam, 70% EAPB SiO₂ foam and slickwater with 50 bpm of pumping rate. Proppant concentrations at shut in 180 min are used as a proxy for final conductivity to understand the effects of placement on productivity (Fig. 10). Using these values, EAPB SiO₂ foams achieve the highest total gas production with slick water is the smallest. The gap of the cumulative gas production between EAPB SiO₂ stabilized foam and EAPB foam is 9.34%. This difference is the result of EAPB foams beginning to accumulate proppant at the bottom of the fracture, resulting in a smaller propped area. In contrast, for EAPB SiO₂ foams, the fracture geometry is uniformly propped and negligible proppant settling is occurring. The gap of the cumulative gas production between EAPB foam and slickwater is 16.37%, largely the result of the lower viscosity of slickwater. Those observations are consistent with previous proppant concentration studies (Fig. 7). These comparisons highlight the critical role of foam stability and the final position of the proppants, a major contributor to the effectiveness of the post fracture productivity.

6. General guideline of foam treatment design

Therefore, it is important to develop guidelines for foam fracturing designs, based on an understanding of foam rheology and associated foam stability behaviour. Fig. 11 illustrates two different foam rheology profiles representing standard foam (black curve) and nano stabilized foam (red curve); key points in the process a 1–4 for standard and 5–8 for nano stabilized foams. For a standard foam, the rheology experiences a stable period (Fig. 11, points 1–2), and an unstable period (Fig. 11, points 2–4). In a stable period, the foam quality remains relatively unchanged and exhibits a constant foam viscosity. In an unstable period, foam viscosity initially increases due to foam drainage, then decreases sharply by disproportionation (gas diffusion). The stable time (t_{st}), critical time (t_{cr}) and rupture time (t_{rup}) can be experimentally determined to indicate the change of foam behavior (See example of Table 1). For nano stabilized foam, longer stable periods and unstable periods are achieved; this is mainly the result of adsorption of nano particles to prevent bubble coalescence caused by thinning and rupture of the film between bubbles. The foam rheology associated with foam stability behavior can therefore provide useful, and information in foam fracturing treatment, summarized into Table 3. Therefore, it is recommended that pumping and shut in times should be less or equal to foam stable times. This is because foam viscosity is constant during this period, maintaining stable proppant carrying capabilities. In addition, there is a need for better accuracy in hydraulic fracturing models to simulate proppant transport by foam with constant apparent viscosity. For nano stabilized foam, longer stable times area achievable and allow more slurry volume to be pumped with constant apparent viscosity, and create higher productivity. In addition, there is no benefit to use an ultra stable foam in a high permeability reservoir as proppant settling is prevented by rapid fracture closure and before foam breakage occurs. However, for low permeability formations, like unconventional reservoirs, long closure time is expected and can lead to a decrease in final propped area by migration of large amounts of proppant to the bottom of the fracture. Therefore, in low permeability reservoirs there

is an advantage to using ultra stable foams to prevent proppant settling, maintain a larger propped area, and improve productivity. Based on laboratory results, ultra stable foams are achievable by formulations including nanoparticles in the foamed fluid.

7. Conclusions

The purpose of this work is to characterize foam stability and the effect of nanoparticle inclusion on proppant settling during fracture closure. Through this improved understanding, better optimization of hydraulic fracture treatments can be made with foamed fluids in low permeability reservoirs. The major conclusions can be summarized as follows:

1. The apparent viscosity of foam fluids are controlled by foam stability. Instability can promote proppant settling and leads to an unfavorable proppant distribution in the propped fracture. This results in limiting the effective propped area or propping outside the targeted reservoir section. Either effect can reduce overall fracture conductivity and reservoir productivity.
2. Experimental observations indicate foam stability increases 2–3 fold in presence of 0.8 wt% silica nanoparticles. The enhancement of foam life time by nanoparticles can improve fracturing conductivity by preventing proppant settling during fracture closure, reducing overall fracture conductivity and reservoir productivity.
3. Hydraulic fracture modeling suggests that the effective propped area can be controlled by varying the injection rate and foam quality. However, the final distribution of proppant is more affected by closure times. During this period foam stability is primarily affected by foam formulation.
4. Low stability, or slickwater foams cannot achieve sufficient proppant coverage over a thick pay interval when closure time is relatively longer than foam stability.
5. This study suggests further research focused on differing nanoparticles to improve foam stability under harsh environmental conditions to overcome proppant settling issue in high temperature, low permeability, unconventional reservoirs.

Acknowledgements

The authors acknowledge the financial support provided by the National Science and Technology Major Project (2016zx04404002).

References

- [1] Economides MJ, Nolte KG. Reservoir stimulation. New York: Wiley; 2000.
- [2] Johnson Jr. RL. Fracture treatment modifications and bottomhole treating pressure analysis in the pictured cliffs formation, Rio Arriba County, New Mexico. Production operations symposium. Oklahoma City, Oklahoma, USA: Society of Petroleum Engineers; 1995.
- [3] Wu W, Kakkar P, Zhou J, Russell R, Sharma MM. An experimental investigation of the conductivity of unpropped fractures in shales. Hydraulic fracturing technology conference and exhibition. Woodlands, Texas, USA: Society of Petroleum Engineers; 2017.
- [4] Alotaibi MA, Miskimins JL. Slickwater proppant transport in complex fractures: new experimental findings & scalable correlation. SPE annual technical conference and exhibition. Texas, USA: Society of Petroleum Engineers; 2015.
- [5] Li N, Li J, Zhao L, Luo Z, Liu P, Guo Y. Laboratory testing on proppant transport in complex-fracture systems. SPE J 2016.
- [6] Pyrak-Nolte LJ, Morris JP. Single fractures under normal stress: the relation between fracture specific stiffness and fluid flow. Int J Rock Mech Min Sci 2000;37:245–62.
- [7] Beg MS, Kunak AO, Gong M, Zhu D, Hill AD. A systematic experimental study of acid fracture conductivity. SPE Production & Facilities; 1998.
- [8] Fredd CN, McConnell SB, Boney CL, England KW. Experimental study of fracture conductivity for water-fracturing and conventional fracturing applications. SPE J 2001.
- [9] Jansen TA, Zhu D, Hill AD. The effect of rock mechanical properties on fracture conductivity for shale formations. SPE hydraulic fracturing technology conference. Woodlands, Texas, USA: Society of Petroleum Engineers; 2015.
- [10] Shiozawa S, McClure M. Simulation of proppant transport with gravitational settling and fracture closure in a three-dimensional hydraulic fracturing simulator. J Petrol Sci Eng 2016;138:298–314.

- [11] Clark PE, Guler N. Prop transport in vertical fractures: settling velocity correlations. SPE symposium on low permeability. Denver, Colorado: Society of Petroleum Engineers; 1983.
- [12] Liu Y, Leung JY, Chalaturnyk R, Virues CJJ. Fracturing fluid distribution in shale gas reservoirs due to fracture closure, proppant distribution and gravity segregation. Unconventional resources conference. Calgary, Alberta, Canada: Society of Petroleum Engineers; 2017.
- [13] Chang O, Dilmore R, Wang JY. Model development of proppant transport through hydraulic fracture network and parametric study. *J Petrol Sci Eng* 2017;150:224–37.
- [14] Yu W, Zhang T, Du S, Sepelmoori K. Numerical study of the effect of uneven proppant distribution between multiple fractures on shale gas well performance. *Fuel* 2015;142:189–98.
- [15] Zhang G, Li M, Gutierrez M. Numerical simulation of proppant distribution in hydraulic fractures in horizontal wells. *J Nat Gas Sci Eng* 2016.
- [16] Cleary MP. Analysis of mechanisms and procedures for producing favourable shapes of hydraulic fractures. 55th annual fall technical conference and exhibition. Dallas, Texas: Society of Petroleum Engineers; 1980.
- [17] Milton-Taylor D, Stephenson C, Aghian MI. Factors affecting the stability of proppant in propped fractures: results of a laboratory study. 67th annual technical conference and exhibition. Washington, DC: Society of Petroleum Engineers; 1992.
- [18] McLennan JD, Green SJ, Bai M. Proppant placement during tight gas shale stimulation: literature review and speculation. 42th US rock mechanics symposium. San Francisco: American Rock Mechanics Association; 2008.
- [19] Warpinski NR. Stress amplification and arch dimensions in proppant beds deposited by waterfracs. *SPE Production & Operations*; 2010.
- [20] Cipolla CL, Lolon E, Mayerhofer MJ, Warpinski NR. The effect of proppant distribution and un-propped fracture conductivity on well performance in unconventional gas reservoirs. 2009 SPE hydraulic fracturing technology conference. Woodlands, Texas, USA: Society of Petroleum Engineers; 2009.
- [21] Warpinski NR, Mayerhofer MJ, Vincent MC, Cipolla CL, Lolon E. Stimulating unconventional reservoirs: maximizing network growth while optimizing fracture conductivity. SPE unconventional reservoirs conference. Keystone, Colorado, USA: Society of Petroleum Engineers; 2008.
- [22] Babcock RE, Prokop CL, Kehle RO. Distribution of propping agent in vertical fractures. *Drilling and production practice*. New York: American Petroleum Institute; 1967.
- [23] Hou T, Zhang S, Ma X, Shao J, He Y, Lv X, et al. Experimental and theoretical study of fracture conductivity with heterogeneous proppant placement. *J Nat Gas Sci Eng* 2017;37:449–61.
- [24] Shaouf JR, van Zelm LF, de Pater CJ. Damage mechanisms in unconventional-gas-well stimulation—a new look at an old problem. *SPE Production & Operations*; 2011.
- [25] Hurst RE. Use of liquified gases as fracture fluids for dry gas reservoirs. 47th annual fall meeting of AIME. San Antonio, Texas: Society of Petroleum Engineers; 1972.
- [26] Grundmann SR, Lord DL. Foam stimulation. *SPE J* 1983.
- [27] King GE. Foam and nitrified fluid treatments—stimulation techniques and more. 1985–86 distinguished lecturer program. Society of Petroleum Engineers; 1985.
- [28] Ward VL. N₂ and CO₂ in the oil field: stimulation and completion applications. *SPE J* 1986.
- [29] Harris PC. Application of foam fluids to minimize damage during fracturing. SPE international meeting on petroleum engineering. Beijing, China: Society of Petroleum Engineers; 1992.
- [30] Ribeiro L, Sharma M. Fluid selection for energized fracture treatments. SPE hydraulic fracturing technology conference. Woodlands, Texas, USA: Society of Petroleum Engineers; 2013.
- [31] Mack DJ, Harrington LJ. New foams introduce new variables to fracturing. *Oil Gas J* 1990.
- [32] Jing Z, Wang S, Wang Z. Detailed structural and mechanical response of wet foam to the settling particle. *Langmuir* 2016;32:2419–27.
- [33] Wyn A, Davies IT, Cox SJ. Simulations of two-dimensional foam rheology: localization in linear Couette flow and the interaction of settling discs. *Eur Phys J E* 2008;26:81–9.
- [34] Cox SJ, Dollet B, Graner F. Foam flow around an obstacle: simulations of obstacle–wall interaction. *Rheol Acta* 2006;45:403–10.
- [35] Davies IT, Cox SJ. Sedimenting discs in a two-dimensional foam. *Colloids Surf A* 2009;344:8–14.
- [36] Höhler R, Cohen-Addad S. Rheology of liquid foam. *J Phys: Condens Matter* 2005;17:R1041.
- [37] Weaire D. The rheology of foam. *Curr Opin Colloid Interface Sci* 2008;13:171–6.
- [38] Cantat I, Cohen-Addad S, Elias F, Graner F, Höhler R, Pitois O, et al. *Foams: structure and dynamics*. United States of America: Oxford University Press; 2013.
- [39] Wang J, Nguyen AV, Farrokhpay S. A critical review of the growth, drainage and collapse of foams. *Adv Colloid Interface Sci* 2016;228:55–70.
- [40] Angarska J, Stubenrauch C, Manev E. Drainage of foam films stabilized with mixtures of non-ionic surfactants. *Colloids Surf A* 2007;309:189–97.
- [41] Koehler SA, Hilgenfeldt S, Stone HA. A generalized view of foam drainage: experiment and theory. *Langmuir* 2000;16:6327–41.
- [42] Maestro A, Rio E, Drenckhan W, Langevin D, Salonen A. Foams stabilised by mixtures of nanoparticles and oppositely charged surfactants: relationship between bubble shrinkage and foam coarsening. *Soft Matter* 2014;10:6975–83.
- [43] Saye RI, Sethian JA. Multiscale modeling of membrane rearrangement, drainage, and rupture in evolving foams. *Science* 2013;340:720–4.
- [44] Freeman ER, Bilden DM, Hossaini M. Delayed crosslinked gels: their role in aqueous foam fracturing. *SPE-15070-MS*. SPE; 1986.
- [45] Zhao G, Dai C, Zhang Y, Chen A, Yan Z, Zhao M. Enhanced foam stability by adding comb polymer gel for in-depth profile control in high temperature reservoirs. *Colloids Surf A* 2015;482:115–24.
- [46] Huh C, Rossen WR. Approximate pore-level modeling for apparent viscosity of polymer-enhanced foam in porous media. *SPE J* 2008.
- [47] Kantzas A, Allsopp K, Marentette D. Utilization of polymer gels polymer enhanced foams and foamed gels for improving reservoir conformance. 48th annual technical meeting. Calgary, Alberta, Canada: Petroleum Society of Canada; 1997.
- [48] Zhao G, Dai C, Wen D, Fang J. Stability mechanism of a novel three-phase foam by adding dispersed particle gel. *Colloids Surf A* 2016;497:214–24.
- [49] Dupas A, Henaut I, Rousseau D, Poulain P, Tabary R, Argillier J-F, et al. Impact of polymer mechanical degradation on shear and extensional viscosities: toward better injectivity forecasts in polymer flooding operations. SPE international symposium on oilfield chemistry. Society of Petroleum Engineers; 2013.
- [50] Samuelson ML, Constien VG. Effects of high temperature on polymer degradation and cleanup. Annual technical conference and exhibition. Society of Petroleum Engineers; 1996.
- [51] Carn F, Colin A, Pitois O, Vignes-Adler M, Backov R. Foam drainage in the presence of nanoparticle surfactant mixtures. *Langmuir* 2009;25:7847–56.
- [52] Zhu Y, Pei X, Jiang J, Cui Z, Binks BP. Responsive aqueous foams stabilized by silica nanoparticles hydrophobized in situ with a conventional surfactant. *Langmuir* 2015;31:12937–43.
- [53] Carl A, Bannuscher A, von Klitzing R. Particle stabilized aqueous foams at different length scales: synergy between silica particles and alkylamines. *Langmuir* 2015;31:1615–22.
- [54] Lv Q, Li Z, Li B, Shi D, Zhang C, Li B. Silica nanoparticles as a high-performance filtrate reducer for foam fluid in porous media. *J Ind Eng Chem* 2017;45:171–81.
- [55] Binks BP, Horozov TS. Aqueous foams stabilized solely by silica nanoparticles. *Angew Chem* 2005;44:3722–5.
- [56] Alargova RG, Warhadpande DS, Paunov VN, Velev OD. Foam super stabilization by polymer microrods. *Langmuir* 2004;20:10371–4.
- [57] Fujii S, Ryan AJ, Armes SP. Long-range structural order, Moiré patterns, and iridescence in latex-stabilized foams. *J Am Chem Soc* 2006;128:7882–6.
- [58] Dickinson E, Ettelaie R, Kostakis T, Murray BS. Factors controlling the formation and stability of air bubbles stabilized by partially hydrophobic silica nanoparticles. *Langmuir* 2004;20:8517–25.
- [59] Gonzenbach Urs T, Studart André R, Tervoort Elena, Gauckler LJ. Ultrastable particle-stabilized foams. *Angew Chem Int Ed* 2006;3526–30.
- [60] Stocco A, Garcia-Moreno F, Manke I, Banhart J, Langevin D. Particle-stabilised foams: structure and aging. *Soft Matter* 2011;7:631–7.
- [61] Bournival G, Ata S, Wanless EJ. The roles of particles in multiphase processes: particles on bubble surfaces. *Adv Colloid Interface Sci* 2015;225:114–33.
- [62] Binks BP, Kirkland M, Rodrigues JA. Origin of stabilisation of aqueous foams in nanoparticle–surfactant mixtures. *Soft Matter* 2008;4:2373–82.
- [63] Sun Q, Li Z, Wang J, Li S, Li B, Jiang L, et al. Aqueous foam stabilized by partially hydrophobic nanoparticles in the presence of surfactant. *Colloids Surf A* 2015;471:54–64.
- [64] Zargartalebi M, Barati N, Kharrat R. Influences of hydrophilic and hydrophobic silica nanoparticles on anionic surfactant properties: interfacial and adsorption behaviors. *J Petrol Sci Eng* 2014;119:36–43.
- [65] Hunter TN, Pugh RJ, Franks GV, Jameson GJ. The role of particles in stabilising foams and emulsions. *Adv Colloid Interface Sci* 2008;137:57–81.
- [66] Espinoza DA, Caldelas FM, Johnston KP, Bryant SL, Huh C. Nanoparticle-stabilized supercritical CO₂ foams for potential mobility control applications. SPE improved oil recovery symposium. Tulsa, Oklahoma, USA: Society of Petroleum Engineers; 2010.
- [67] Yu J, An C, Mo D, Liu N, Lee RL. Study of adsorption and transportation behavior of nanoparticles in three different porous media. 18th SPE improved oil recovery symposium. Tulsa, Oklahoma, USA: Society of Petroleum Engineers; 2012.
- [68] Sun Q, Li Z, Li S, Jiang L, Wang J, Wang P. Utilization of surfactant-stabilized foam for enhanced oil recovery by adding nanoparticles. *Energy Fuels* 2014;28:2384–94.
- [69] Sun Q, Li Z, Wang J, Li S, Jiang L, Zhang C. Properties of multi-phase foam and its flow behavior in porous media. *RSC Adv* 2015;5:67676–89.
- [70] Fei Y, Zhu J, Xu B, Li X, Gonzalez M, Haghighi M. Experimental investigation of nanotechnology on worm-like micelles for high-temperature foam stimulation. *J Ind Eng Chem* 2017.
- [71] Barree RD. A practical numerical simulator for three-dimensional fracture propagation in heterogeneous media. Reservoir simulation symposium. San Francisco, CA: Society of Petroleum Engineers; 1983.
- [72] Barree RD, Conway MW. Experimental and numerical modeling of convective proppant transport. 69th SPE annual technical conference. New Orleans, LA, USA: Society of Petroleum Engineers; 1994.
- [73] Barree RD, Conway MW. Experimental and numerical modeling of convective proppant transport. *SPE J* 1995.
- [74] Barree RD, Conway M, Gilbert JV. An effective model for pipe friction estimation in hydraulic fracturing treatments. SPE rocky mountain petroleum technology conference. Denver, Colorado, USA: Society of Petroleum Engineers; 2009.
- [75] Cleary MP, Fonseca A. Proppant convection and encapsulation in hydraulic fracturing: practical implications of computer and laboratory simulations. 67th annual technical conference and exhibition. Washington, DC: Society of Petroleum Engineers; 1992.
- [76] Clark PE, Zhu Q. Convective transport of propping agents during hydraulic fracturing. SPE eastern regional meeting. Columbus, Ohio: Society of Petroleum Engineers; 1996.
- [77] Huang T, Crews JB. Nanotechnology applications in viscoelastic surfactant stimulation fluids. *SPE Production & Operations*; 2008.
- [78] Barree RD, Miskimins JL, Conway MW, Duenkel R. Generic correlations for proppant pack conductivity. SPE hydraulic fracturing technology. The Woodlands, Texas, USA: Society of Petroleum Engineers; 2016.
- [79] Khade SD, Shah SN. New rheological correlations for guar foam fluids. *SPE J* 2004.